

**Sensing via Analyte-Triggered Gelation: Molecular Design and
Implementation**

by

Jing Chen

**A dissertation submitted in partial fulfillment
of the requirements for the degree of
Doctor of Philosophy
(Chemistry)
in the University of Michigan
2012**

Doctoral Committee:

**Assistant Professor Anne J. McNeil, Chair
Professor Adam J. Matzger
Professor Mark M. Banaszak-Holl
Associate Professor Jinsang Kim**

谨以此文，献给我的父亲母亲。

To Mom and Dad, for your unconditional love and support.

ACKNOWLEDGEMENTS

First, I want to thank my advisor, Prof. Anne J. McNeil, for her patience, guidance, and encouragement during the past four and half years. As an excellent scientist, she re-defined passion, intelligence, hard work and persistence for me. I would like to thank her for allowing me to participate in paper writing, grant and paper review and generating my own research ideas. All these experiences have rendered me to grow from an amateur to a mature chemist.

I am deeply indebted to Prof. Adam Matzger for his helpful suggestions throughout my PhD education as well as for allowing me to explore various instruments in his lab for my research. Those were not only fun experiences, but also transformed me into a well-rounded materials chemist.

I also want to thank Prof. Mark Banazsak Holl and Prof. Jinsang Kim for serving on the committee of my PhD dissertation and candidacy exam. Their challenging questions and insightful advice have pushed my research to a higher level.

I want to thank Dr. Jeff Kampf for all the single crystal structure determinations. I would also like to thank Dr. Kai Sun from the EMAL facility for his help on SEM, TEM and AFM experiments.

I want to thank my collaborators on the quantitative gel-based sensor project: Dr. Abdul Rehman and Prof. Xiangqun Zeng at Oakland University, Ariel Hecht and Prof. Raoul Kopelman from Chemistry Department at UM, Jeffrey Gregory and Prof. Khalil Najafi, Dr. Scott Green and Prof. Yegosh Gianchandina from EECS Department at UM.

I am also deeply indebted to my colleagues Dr. Maria Muro-Small and Weiwei Wu, who have closely collaborated with me on the gelation structure-property relationships project and the TATP sensing project, respectively.

I would like to thank the Matzger lab members for training me on their instruments, especially Dr. Vilimali Lopez-Mejias for her help on Raman spectroscopy and Hirshfeld surface analysis.

I want to thank all the past and present members from the McNeil lab: Yash Adhia, Zack Bryan, Dan Dawson, Dr. Raja Kaliappan, Kelsey King, Dr. Erica Lanni, Se Ryeon Lee, Jonas Locke, Cheryl Moy, Dr. Ed Palermo, Tracy Schloemer, Karen Sanders, Danielle Zurcher and many more, for asking challenging research questions, providing insightful suggestions and making our lab a happy place to work.

I would also like to thank all my friends in Ann Arbor (and all over the US), for making my life more than just chemistry. In particular, I want to thank Xiao Liu, Yipei Wang, Xin Liu, Wenjing Chen, Lyra Chang, Chenxi Shen, Liuling Gong, Di Gao, Yan Yin, Zihui Li, Xiaoming Zhu and Jie Luo. Thank you for being amazing companions, for sharing together all the joys and sadness, and inspiring me with other possibilities about career and life.

I also want to thank my dear friends from China, Xiaoyu Bian and Yanmin Zhong, for always being there to listen and for creating many warm memories throughout our fifteen years of friendship. I would also like to thank my cousin, Yanjun Chen, for loving me a like a real sister. Without their non-stop support and encouragement from thousand miles away, I wouldn't have conquered all the difficulties and challenges during my PhD education.

Last but not least, I want to thank my parents. I owe every single success, if any, to my dad and mom. They are the most selfless parents in the world for letting me go wherever I want and for encouraging me to follow my dreams. They have given me complete freedom, continuous support and unconditional love in my whole life and never ask for anything in return. I sincerely dedicate this dissertation to them with the hope that this can be something they are proud of.

Table of Contents

Dedication.....	ii
Acknowledgements.....	iii
List of Figures.....	vi
List of Tables.....	viii
List of Charts.....	ix
List of Schemes.....	x
List of Appendices.....	xi
Chapter	
I. Introduction: Molecular Gels and Their Applications.....	1
II. Analyte-Triggered Gelation: Initiating Self-Assembly via Oxidation-Induced Planarization.....	9
III. Comparing Molecular Gelators and Nongelators Based on Solubilities and Solid-State Interactions.....	17
IV. Dissolution Parameter Reveal Role of Structure and Solvent in Molecular Gelation.....	33
V. Detection of a Peroxide-based Explosive via Molecular Gelation.....	48
VI. Development towards Quantitative Gel-Based Sensors.....	56
VII. Conclusion and Future Directions.....	65
Appendices.....	69

List of Figures

- Figure 2.1** Scanning electron micrograph of the gel formed by **2** (26 mM) in 1/1.25/3.75 of CH₃CN/DMSO/H₂O.....12
- Figure 2.2** Adding an aqueous solution of CAN to **1** (26 mM, 4/1 DMSO/H₂O, left) produces **2** and gelation (2/1 DMSO/H₂O, right).....12
- Figure 2.3** Adding NO to a mixture of **1** in CH₃CN (43 mM, upper left) results in oxidation to **2** (upper right). Adding an aliquot of DMSO/H₂O results in a solution for **1** (lower left) and a gel for **2** (lower right).....13
- Figure 3.1** Plot of rt solubility versus molecular structure in 1/1 DMSO/H₂O (○, ●) and 1/2 EtOH/H₂O (□, ■). The gelators are denoted by the filled-in symbols (●, ■). (Note that there are two x-axes. For an alternative representation, see Appendix 2).....21
- Figure 3.2** Plots of ΔH_{diss} (A) and ΔS_{diss} (B) versus molecular structure in 1/1 DMSO/H₂O (○, ●) and 1/2 EtOH/H₂O (□, ■). The gelators are denoted by filled-in symbols (■, ●). (Note that there are two x-axes. For an alternative representation, see Appendix 2).....22
- Figure 3.3** Single-crystal X-ray structures for (A) **6d**, (B) **2a**, and (C) **1a**. H-atoms were omitted for clarity.....24
- Figure 3.4** Percent relative contribution of the intermolecular interactions in each crystal structure based on Hirshfeld surface analysis.....24
- Figure 4.1** PXRD patterns for dipeptide gelator **1a**: (A) Form I (top) and the air-dried gel (bottom), and (B) Form II (top) with the freeze-dried gel (bottom).....38
- Figure 4.2** Plot of the (A) ΔH_{diss} and (B) ΔS_{diss} versus molecular structure (Gelators are dark gray, and nongelators are light gray).....40
- Figure 5.1** A gel forms within 30 min of adding solid TATP (2.5 mg) to a vial containing thiol **1** (36 mM) and TsOH (1.3 M) in MeOH.....50
- Figure 5.2** Adding solid TATP (1.5 mg) to a MeOH solution containing TsOH (1.3 M) and **1** (36 mM) led to gel formation within 8 min.....52

Figure 6.1 Plot of (A) elastic modulus (G') versus gelator concentration; (B) elastic modulus (G') versus time during gelation.....	57
Figure 6.2 Vibration frequency and amplitude of quartz crystal tuning fork in air (solid line) and in DI H ₂ O (dash line).....	59
Figure 6.4 Magnetoelastic sensing system.....	61

List of Tables

Table 2.1 Time to 90% Conversion in the NO-induced Oxidation of 1	14
Table 3.1 Critical gel concentrations for gelators 1-4	20
Table 4.1 Critical gel concentrations (cgc) for 1a-c and 2a-c	34
Table 6.1 QCM vibration frequency shift versus gelator concentration.....	60
Table 6.2 Vibration frequency and amplitude of magnetoelastic sensor in different samples.....	62
Table 6.3 Vibration frequency and amplitude in gel samples with different [2] prepared via good/bad solvent or heating/cooling.....	63

List of Charts

Chart 3.1 Molecular structures of pyridines 1-8	18
Chart 4.1 Dipeptide-based gelators (1a-c ; 2a-c) and nongelators (1d,e ; 3a-c)..	36
Chart 4.2 Pyridine-based gelators (4-7) and nongelators (8-11).....	37
Chart 5.1 Molecular structures of cystine derivatives 3-7	51
Chart 6.1 Molecular structure of gelator 1 and 2	56

List of Schemes

Scheme 1.1	Schematic illustration of molecular gel formation.....	1
Scheme 1.2	Illustration of a gel-based sensor.....	4
Scheme 1.3	Design strategy (top) and molecular implementation (bottom) of a gel-based NO sensor.....	5
Scheme 2.1	Molecular structures and X-ray crystal structures of 1 and 2	11

List of Appendices

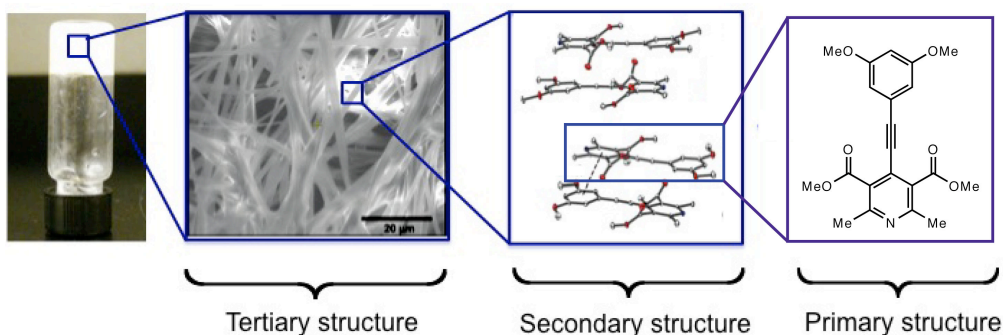
Appendix 1. Appendix to Chapter 2: Analyte-Triggered Gelation: Initiating Self-Assembly via Oxidation-Induced Planarization.....	69
Appendix 2. Appendix to Chapter 3: Comparing Molecular Gelators and Nongelators Based on Solubilities and Solid-State Interactions.....	97
Appendix 3. Appendix to Chapter 4: Dissolution Parameter Reveal Role of Structure and Solvent in Molecular Gelation.....	218
Appendix 4. Appendix to Chapter 5: Detection of a Peroxide-based Explosive via Molecular Gelation.....	280

Chapter 1

Introduction: Molecular Gels and Their Applications

Gels exist in every aspect of our life, from food to cosmetics.¹ Gels are viscoelastic materials that behave as solids rheologically even though more than 99% of their weight is composed of liquid. Based on the type of linkages that constitute the gels, they can be categorized into polymer gels and molecular gels. Polymer gels are formed through crosslinking (either chemical or physical) of the covalently-bonded polymer chains. Common polymer gels include poly(acrylic acid), poly(ethylene glycol), polyamide and poly(vinyl alcohol).² Molecular gels are formed via solely non-covalent interactions between small molecules.³ Although the exact gelation mechanism is still not clear, it is believed that molecular gel formation is initiated by small molecules assembling into low dimensional aggregates, which further entangle or interweave to construct a three dimensional (3D) network that provides high surface tension to immobilize solvent (Scheme 1.1). The driving forces behind molecular gel formation are non-covalent interactions such as hydrogen-bonding, π -stacking, van der Waals interactions, ionic interactions, hydrophobic effects, etc.

Scheme 1.1 Schematic illustration of molecular gel formation.



Designing gelators is challenging, because predicting what molecules will gel is difficult. Although numerous gelators have been reported, the controlling factors in gelation are still unknown. Hanabusa proposed that the presence of intermolecular interactions to build intertwining macro-aggregates is essential to enable gelation.⁴ As a result, research efforts towards designing gelators are mainly focused on promoting one-dimensional (1D) intermolecular interactions to allow formation of high aspect-ratio aggregates that intertwine. A frequently used approach is derivatizing known gelator frameworks to create new ones. However, small modifications on gelators can easily disrupt gelling ability, thus most gelators have been discovered by serendipity or via a trial-and-error approach.

To establish design principles for small molecule gelators, enormous efforts have focused on elucidating the structure-property relationships in gelation. For example, the relationship between peptide structures and its gelation ability has been extensively studied, by systematically modifying the side chain of the amino acids, peptide sequence and length, and the aromatic end groups.⁵ These studies revealed that peptides with non-bulky amino acid residues (e.g., glycine, alanine, serine) tend to be gelators. In contrast, peptides with increased steric hindrance (e.g., leucine, isoleucine, valine) are more likely to be nongelators. Interestingly, peptides with bulky aromatic side chains (e.g., phenylalanine, pentafluoro-phenylalanine) are efficient gelators, which indicated that a delicate balance between hydrophilic and hydrophobic fragments is crucial for designing peptide gelators.^{5b} However, hydrophobicity is difficult to quantify, rendering the discovery of new peptide gelators still a screening process.

Another seminal study of structure-property relationships in gelation was performed on the aromatic-linker-steroid (ALS) type gelator framework.⁶ The steric and electronic effects on the aromatic ring, the length and flexibility of the linker and the steric effect on the steroid were examined. It was concluded that stronger π - π stacking, and rigid and linear molecular structures improve gelation ability and subtle changes on the steroid are detrimental to gelation. Also, odd-even effects on gelation were observed when changing the aliphatic linkers.⁷ A new gelator was successfully designed based on these conclusions.⁸

Nevertheless, the limitation of these structure-property relationship studies is the lack of generality. The relationships concluded from one molecular framework are not applicable to another, making the discovery of gelators by design still an unsolved challenge. Moreover, due to the complex structure-property relationships in molecular gels, engineering of physical properties (e.g., cgc, gel strength, fiber morphology) of gel materials is even harder. As a result, very few of the reported gelators have found practical applications because of their undesired mechanical properties. To develop more general guidelines for designing gelators, correlation between molecular properties (i.e., solubility and solid-state interactions) and gelation ability were examined.⁹ We found that room temperature solubility and the presence of 1D solid-state interactions are not correlated with gelation ability; instead, dissolution enthalpy and entropy are found to be higher for gelators than nongelators, indicating these parameters might be key factors in molecular gelation. If general, this finding will be a useful guideline to predict and design gelators for various exciting applications.

Despite the elusive structure-property relationships in gelation, molecular gels have been applied as matrix materials in tissue engineering,¹⁰ catalysis¹¹ and hybrid materials synthesis.¹² In the meantime, due to their responsive nature to external stimuli (e.g., temperature, solvents,^{13a} pH, ionic strength,^{13b} light,^{13c} ultrasound,^{13d} and chemicals), molecular gels have also been actively investigated in the areas of regenerative medicine,¹⁴ drug delivery,¹⁵ and pollutant remediation.¹⁶

Utilizing gels for bio- and chemical sensing however, is less-explored territory. Existing methods for bio/chemical sensing range from those based on sophisticated instruments to those that are convenient and portable. High-end instruments, although providing high accuracy and sensitivity, are expensive and often require laborious sample preparation. As a result, their applications for on-site detection are limited. On the other hand, portable sensors that utilize changes in absorption or fluorescence provide fast response and high sensitivity; however, signals from colorimetric/fluorescent sensors are sometimes ambiguous. Moreover, those sensors are not applicable when the samples are

colored or fluorescent. In contrast, gel-based sensors utilize a solution-to-gel physical change to provide unambiguous read-out with little interference from sample color or opacity, thus are potential alternatives to colorimetric sensors. Typically, there are three important components in a gel-based sensor: (1) non-gelling precursor, (2) gelator and (3) a chemical reaction that utilizes the analyte to convert the precursor into gelator (Scheme 1.2).

Scheme 1.2 Illustration of a gel-based sensor

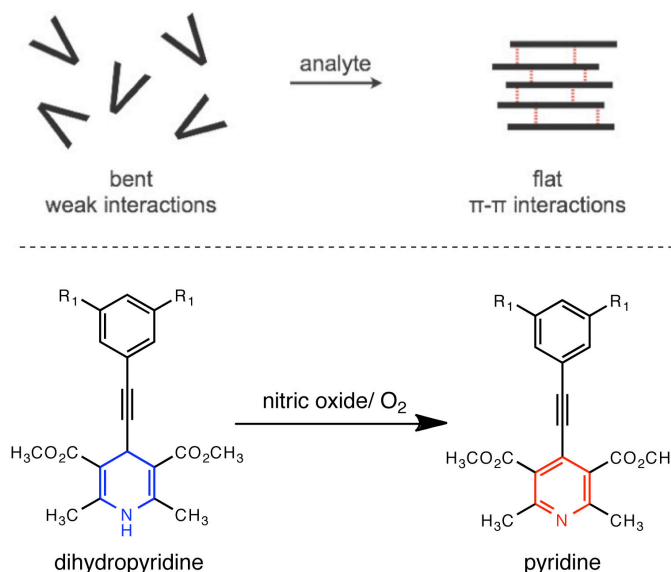


Several gelation-based biosensors have been reported before our entry into the field.¹⁷ For example, Xu and coworkers reported the first gel-based enzyme sensor in 2007,^{17a} where the presence of lactamase cleaved a sterically-hindered solubilizing group off a nongelling precursor to release a peptide gelator, leading to in situ gel formation. A similar design strategy was applied to develop a phosphatase sensor, which undergoes a solution-to-gel transition when the phosphatase hydrolyzes a phosphate group off the nongelling precursor and produces a gelator.¹⁸ Although these are proof-of-principle examples of gel-based sensors, the design strategy is limited to changing the solubility of precursors to induce gelation, which limits the analyte to mainly enzymes or acids/bases.¹⁹ To expand the horizon of gel-based sensors, new design strategies for gelation are necessary.

Instead of altering solubility to induce gelation, we hypothesized that increasing the intermolecular interactions of nongelling precursors can also produce gelators and trigger gel formation. As a proof of concept, we designed and developed a gel-based nitric oxide (NO) sensor.²⁰ In this sensor, a non-planar structure was designed as the precursor, which is not likely to gel due to the lack of obvious 1D interactions. We envisioned an analyte-involved chemical reaction that converts the non-planar precursor into a planar molecule might substantially enhance 1D intermolecular interactions and lead to gelation. To

implement this design strategy, a non-planar dihydropyridine framework was synthesized as precursor and gelation was successfully triggered by an NO-induced oxidation, which converted dihydropyridine into planar pyridine (Scheme 1.3).

Scheme 1.3 Design strategy (top) and molecular implementation (bottom) of a gel-based NO sensor.



With the increasing number of new gelators, another challenge facing the field of molecular gels is the lack of practical utility of existing gelators, presumably because gelation ability of molecules is susceptible to the changes of condition and careful optimizations are required to identify suitable systems for both gelation and application. To explore the practical utility of a known gelator, we coupled an H_2O_2 -induced thiol-to-disulfide oxidation to generate the gelator and develop a TATP sensor for the detection of mg quantities of TATP within minutes. Our work on developing this TATP sensor also demonstrated the essential optimizations from a known gelator to an actual sensor.²¹

All gelation-based sensors that have been developed so far are qualitative sensors, giving only a yes/no signal. In the last chapter, efforts toward the development of quantitative gel-based sensors are discussed. To find a suitable quantification technique in a gel medium, we explored a series of tools such as a

rheometer, a micro-rheometer, piezoelectric sensors, and a magnetoelastic sensor. We believe that the incorporation of quantitative detection will expand the application scope of gel-based sensors.

In summary, our work presented here expands the scope of gelation-based sensors by developing a nitric oxide gel-based sensor through increasing 1D interactions between molecules. Meanwhile, we explored the practical utility of a known gelator by developing and optimizing a TATP gel-based sensor from it. Furthermore, we initiated the development of quantitative gel-based sensor by testing several methods for the measurement of gel viscosity and identified a magnetoelastic sensor as a suitable approach. Last but not least, our work also provides evidence for dissolution parameters being important factors in gelation via in-depth structure-property relationship studies on a pyridine framework. If general to other molecular frameworks, this finding will become a useful guideline for designing new gelators for various applications.

References:

(1) For recent reviews, see: (a) Peppas, N. A.; Hilt, J. Z.; Khademhosseini, A.; Langer, R. *Adv. Mater.* **2006**, *18*, 1345-1360. (b) Hughes, N. E.; Marangoni, A. G.; Wright, A. J.; Rogers, M. A.; Rush, J. W. E. *Trends Food Sci. Technol.* **2009**, *20*, 470-480.

(2) (a) Laftah, W. A.; Hashim, S.; Ibrahim, A. N. *Polym.-Plast. Technol.* **2011**, *50*, 1475-1486. (b) Peppas, N. A.; Bures, P.; Leobandung, W.; Ichikawa, H. *Eur. J. Pharm. Biopharm.* **2000**, *50*, 27-46.

(3) (a) *Molecular Gels: Materials with Self-Assembled Fibrillar Networks*; Weiss, R. G., Terech, P., Eds.; Springer: Dordrecht, The Netherlands, 2006. (b) Low Molecular Mass Gelator; *Topics in Current Chemistry*, Vol. 256; Springer: Berlin, Heidelberg, 2005. For recent reviews, see: (a) Piepenbrock, M.-O. M.; Lloyd, G. O.; Clarke, N.; Steed, J. W. *Chem. Rev.* **2010**, *110*, 1960-2004. (b) Banerjee, S.; Das, R. K.; Maitra, U. *J. Mater. Chem.* **2009**, *19*, 6649-6687. (c) Hirst, A. R.; Escuder, B.; Miravet, J. F.; Smith, D. K. *Angew. Chem., Int. Ed.* **2008**, *47*, 8002-8018. (d) Sangeetha, N. M.; Maitra, U. *Chem. Soc. Rev.* **2005**, *34*, 821-836. de Loos, M.; (e) Feringa, B. L.; van Esch, J. H. *Eur. J. Org. Chem.* **2005**, 3615-3631. (f) Estroff, L. A.; Hamilton, A. D. *Chem. Rev.* **2004**, *104*, 1201-1218.

(4) Hanabusa, K.; Yamada, M.; Kimura, M.; Shirai, H. *Angew. Chem., Int. Ed.* **1996**, *35*, 1949-1951.

(5) (a) Cheng, G.; Castelletto, V.; Moulton, C. M.; Newby, G. E.; Hamley, I. W. *Langmuir* **2010**, *26*, 4990-4998. (b) Ma, M.; Kuang, Y.; Gao, Y.; Zhang, Y.; Gao, P.; Xu, B. *J. Am. Chem. Soc.* **2010**, *132*, 2719-2728. (c) Pashuck, E. T.; Cui, H.; Stupp, S. I. *J. Am. Chem. Soc.* **2010**, *132*, 6041-6046. (d) Ryan, D. M.; Anderson, S. B.; Nilsson, B. L. *Soft Matter* **2010**, *6*, 3220-3231. (e) Ryan, D. M.; Anderson, S. B.; Senguen, F. T.; Youngman, R. E.; Nilsson, B. L. *Soft Matter* **2010**, *6*, 475-479. (f) Niece, K. L.; Czeisler, C.; Sahni, V.; Tysseling-Mattiace, V.; Pashuck, E. T.; Kessler, J. A.; Stupp, S. I. *Biomaterials* **2008**, *29*, 4501-4509. (g) Mitra, R. N.; Das, D.; Roy, S.; Das, P. K. *J. Phys. Chem. B* **2007**, *111*, 14107-14113.

(6) (a) Lin, Y.-C.; Weiss, R. G. *Liq. Cryst.* **1989**, *4*, 367-384. (b) Lin, Y.-C.; Weiss, R. G. *Macromolecules*, **1987**, *20*, 414-417. (c) Weiss, R. G.; Lin, Y.-C. US Pat., 4 790 961, 1988.

(7) (a) Cirkel, P.A.; van der Ploeg, J. P. M.; Koper, G. J. M. *Prog. Colloid Polym. Sci.* **1997**, *105*, 204-208. (b) Aliotta, F. *Trends Phys. Chem.* **1997**, *6*, 31-53. (c) Murata, K.; Aoki, M.; Suzuki, T.; Harada, T.; Kawabata, H.; Komri, T.; Olrseto, F.; Ueda, K.; Shinkai, S. *J. Am. Chem. Soc.* **1994**, *116*, 6664-6676. (d) Mukkamala, R.; Weiss, R. G. *Langmuir* **1996**, *12*, 1474-1482. (e) Lin, Y.-C.; Kachar, B.; Weiss, R. G. *J. Am. Chem. Soc.* **1989**, *111*, 5542-5551. (f) Ishi-i, T.; Iguchi, R.; Snip, E.; Ikeda, M.; Shinkai, S. *Langmuir* **2001**, *17*, 5825-5833. (g) Mukkamala, R.; Weiss, R. G. *J. Chem. Soc., Chem. Commun.* **1995**, 375-376. (h) Lu, L.; Cocker, T. M.; Bachman, R. E.; Weiss, R. G. *Langmuir* **2000**, *16*, 20-34.

(8) Klawonn, T.; Gansauer, A.; Winkler, I.; Lauterbach, T.; Franke, D.; Nolte, R. J. M.; Feiters, M. C.; Borner, H.; Hentschel, J.; Dotz, K. H. *Chem. Commun.* **2007**, 1894-1895.

(9) (a) Chen, J.; Kampf, J. W.; McNeil, A. J. *Langmuir* **2010**, *26*, 13076-13080. (b) Muro-Small, M. L.; Chen, J.; McNeil, A. J. *Langmuir* **2011**, *27*, 13248-13253.

(10) For recent examples on tissue engineering applications, see: (a) Ryan, D. M.; Nilsson, B. L. *Polym. Chem.* **2012**, *3*, 18-33; (b) Collier, J. H.; Rudra, J. S.; Gasiorowski, J. Z.; Jung, J. P. *Chem. Soc. Rev.* **2010**, *39*, 3413-3424.

(11) For a recent review, see: Escuder, B.; Rodriguez-Llansola, F.; Miravet, J. F. *New J. Chem.* **2010**, *34*, 1044-1054.

(12) For recent reviews on templated-synthesis, see: (a) Bideau, J. L.; Viau, L.; Vioux, A. *Chem. Soc. Rev.* **2011**, *40*, 907-925. (b) Brizard, A.; Oda, R.; Huc, I. *Topics Curr. Chem.* **2005**, *256*, 167-218. (c) Jung, J. H.; Shinkai, S. *Topics Curr. Chem.* **2004**, *248*, 223-260.

(13) (a) Jonkheijm, P.; van der Schoot, P.; Schenning, A. P. H. J.; Meijer, E. W.

Science **2006**, *313*, 80-83. (b) Meada, H. *Chem. Eur. J.* **2008**, *14*, 11274-11282. (c) Wang, C.; Chen, Q.; Sun, F.; Zhang, D.; Zhang, G.; Huang, Y.; Zhao, R.; Zhu, D. *J. Am. Chem. Soc.* **2010**, *132*, 3092-3096. (d) Berdelang, D.; Cameral, F.; Margeson, J. C.; Leek, D. M.; Schmutz, M.; Zaman, Md. B.; Yu, K.; Soldatov, D. V.; Ziessel, R.; Ratcliffe, C. I.; Ripmeester, J. A. *J. Am. Chem. Soc.* **2008**, *130*, 3313-3315.

(14) For recent reviews on regenerative medicine, see: (a) Matson, J. B.; Stupp, S. I. *Chem. Commun.* **2012**, *48*, 26-33. (b) Matson, J. B.; Zha, R. H.; Stupp, S. I. *Curr. Opin. Solid State Mater. Sci.* **2011**, *15*, 225-235.

(15) For recent examples of drug-delivery, see: (a) Mao, L.; Wang, H.; Tan, M.; Ou, L.; Kong, D.; Yang, Y. *Chem. Commun.* **2012**, *48*, 395-397. (b) Wang, H.; Yang, C.; Wang, L.; Kong, D.; Zhang, Y.; Yang, Z. *Chem. Commun.* **2011**, *47*, 4439-4441. (c) Li, X.; Li, J.; Gao, Y.; Kuang, Y.; Shi, J.; Xu, B. *J. Am. Chem. Soc.* **2010**, *132*, 17707-17709. (d) Zhao, Y.; Tanaka, M.; Kinoshita, T.; Higuchi, M.; Tan, T. *J. Controlled Release* **2010**, *147*, 392-399. (e) Zhao, F.; Ma, M. L.; Xu, B. *Chem. Soc. Rev.* **2009**, *38*, 883-891.

(16) (a) Rodriguez-Llansola, F.; Escuder, B.; Miravet, J. F.; Hermida-Merino, D.; Hamley, I. W.; Cardin, C. J.; Hayes, W. *Chem. Commun.* **2010**, *46*, 7960-7962. (b) Adhikari, B.; Palui, G.; Banerjee, A. *Soft Matter*, **2009**, *5*, 3452-3460.

(17) For recent reviews, see: (a) Yang, Z.; Xu, Bing *Acc. Chem. Res.* **2008**, *41*, 315-325. (b) Gao, Y.; Yang, Z.; Kuang, Y.; Ma, M.; Li, J.; Zhao, F.; Xu, B. *Biopolymers*, **94**, 19-31. (c) Yang, Z.; Ho, P.-L.; Liang, G.; Chow, K. H.; Wang, Q.; Cao, Y.; Guo, Z.; Xu, B. *J. Am. Chem. Soc.* **2007**, *129*, 266-267.

(18) Yang, Z.; Xu, B. *Chem. Commun.* **2004**, 2424-2425.

(19) (a) Hirst, A. R.; Coates, I. A.; Boucheteau, T. R.; Miravet, J. F.; Escuder, B.; Castelletto, V.; Hamley, I. W.; Smith, D. K. *J. Am. Chem. Soc.* **2008**, *130*, 9113-9121. (b) Yang, Z.; Liang, G.; Xu, B. *Acc. Chem. Res.* **2008**, *41*, 315-326. (c) Das, A. K.; Collins, R.; Ulijn, R. V. *Small* **2008**, *4*, 279-287. (d) Shome, A.; Debnath, S.; Das, P. K. *Langmuir* **2008**, *24*, 4280-4288.

(20) Chen, J.; McNeil, A. J. *J. Am. Chem. Soc.* **2008**, *130*, 16496-16497.

(21) Chen, J.; Wu, W.; McNeil, A. J. *submitted*, 2012.

Chapter 2¹

Analyte-Triggered Gelation: Initiating Self-Assembly via Oxidation-Induced Planarization

Molecular gels have been studied for over 160 years¹ and are now used in exciting applications such as regenerative medicine,² drug-delivery,³ biosensing,⁴ and environmental remediation.⁵ Despite their great utility, many applications have relied on a narrow set of gelator structures because there is simply no predictive model to guide their invention. The challenge in designing new gelators is that many factors can influence their self-assembly, including molecular structure and medium effects (e.g., pH, ionic strength, temperature, solvent identity⁶). Creating a stimuli-induced gelation is even more challenging because of the additional need to design a precursor molecule that does not form a gel.

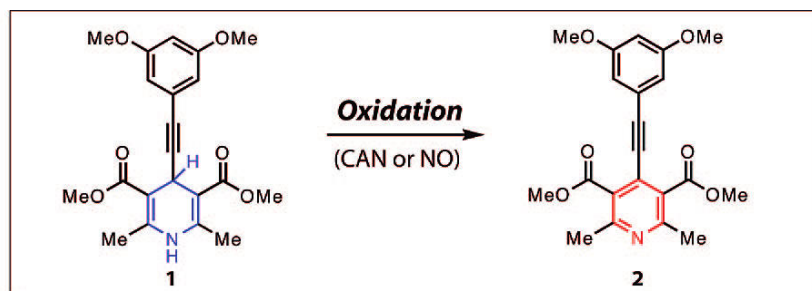
Since gelation occurs when molecules self-assemble, design strategies have traditionally focused on promoting this process by changing the solubility or solvent-molecule interactions;⁷ for example, Xu⁸ and Ulijn⁹ have used enzymes to cleave a solubilizing group or add an insoluble moiety, and others have used pH to protonate or deprotonate a precursor.¹⁰ Although successful, this approach has been limited. An alternative and underutilized approach is to promote self-assembly by triggering changes in the intermolecular or molecule-molecule interactions; for example, light-induced isomerizations¹¹ and employing additives¹² have been used to influence molecular packing. Although it may be difficult to *predict* whether the molecular change will more strongly effect the solubility or intermolecular interactions, we believe the second approach will

¹ Reproduced with permission from Chen, J.; McNeil, A. J. "Analyte-Triggered Gelation: Initiating Self-Assembly via Oxidation-Induced Planarization." *J. Am. Chem. Soc.* **2008**, *130*, 16496-16497. Copyright 2008 American Chemical Society.

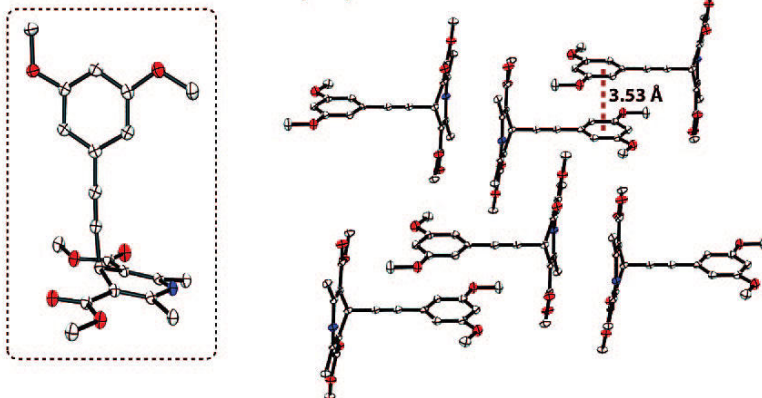
prove more useful for *designing* new triggered gels. As evidence, we describe the successful design of a new analyte-induced gelation using this strategy. Specifically, an oxidation-induced planarization is used to trigger self-assembly and gelation through donor-acceptor π -stacking interactions.

Dihydropyridine **1** was designed as the precursor for the following reasons: (1) Nonplanar **1** should not form a gel due to an absence of obvious 1-D intermolecular interactions. (2) The molecular framework becomes planar upon oxidation to **2** (due to a change in hybridization) which should promote π -stacking.¹³ (3) The electron-rich aryl ethynylene should interact with the electron poor pyridine in **2** through intermolecular donor-acceptor interactions. As a result, it was predicted that **2** would form a gel under conditions where **1** either precipitated or remained in solution.

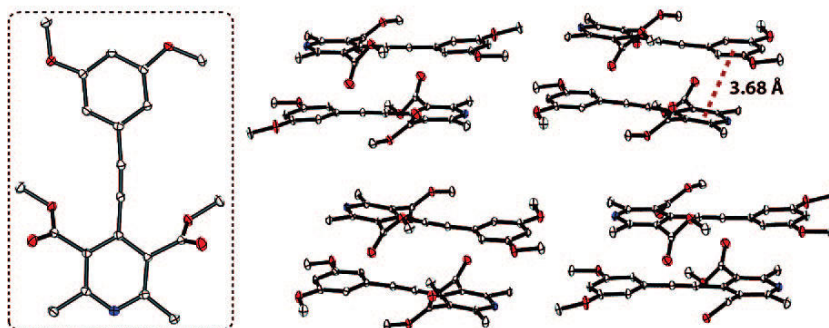
Scheme 2.1 Molecular structures and X-ray crystal structures of **1** and **2**.



X-ray crystal structure, **1**



X-ray crystal structure, **2**



Indeed, pyridine **2** forms a gel in mixtures of water with DMSO, alcohols, acetone, and DMF, whereas **1** either precipitates or remains in solution at the same concentrations.^{14,15} The critical gel concentration of **2** is 16 mM (0.6 wt %) at 2/1 DMSO/H₂O and 25 °C. Scanning electron microscopy revealed that the gel consists of high-aspect-ratio fibers under all conditions examined (Figure 2.1 and Appendix 1). Single crystal X-ray diffraction confirmed that the solid-state packing for **1** and **2** are remarkably different, with oxidized **2** showing predominantly 1-D

π -stacking with donor-acceptor interactions (Scheme 2.1¹⁶); powder X-ray diffraction on the cryo-dried gel confirms that the packing motif in the gel fibers is similar. Raman spectroscopy on single fibers to determine the molecular orientation within the fibers revealed that the π -stacking direction is coincident with the fiber axis (see Appendix 1).

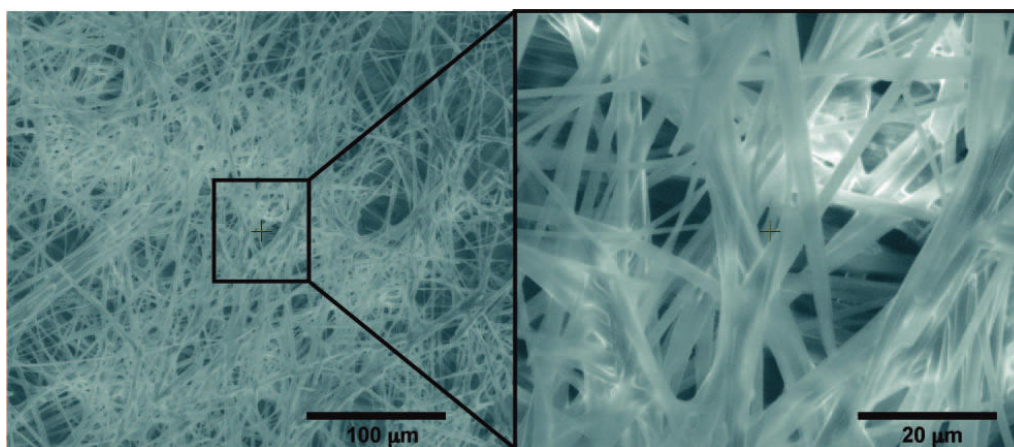


Figure 2.1 Scanning electron micrograph of the gel formed by **2** (26 mM) in 1/1.25/3.75 of CH₃CN/DMSO/H₂O.

To test the proposed oxidation-induced gelation a strong oxidant was first used: cerium(IV) ammonium nitrate (CAN).¹⁷ In situ IR spectroscopy indicated that the oxidation is quantitative within 15 s in DMSO/H₂O. As anticipated, a gel formed after slow¹⁸ addition of an aqueous solution of CAN to **1** in DMSO/H₂O at room temperature (Figure 2.2). Note that this gelation is not due to a change in solvent-molecule interactions because **1** and **2** exhibit similar solubilities under the final reaction conditions.¹⁹

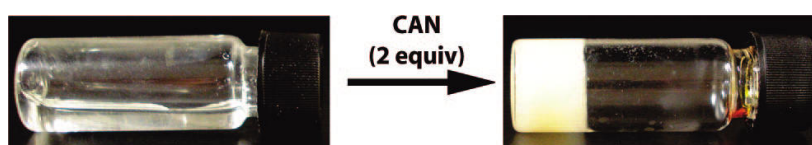


Figure 2.2 Adding an aqueous solution of CAN to **1** (26 mM, 4/1 DMSO/H₂O, left) produces **2** and gelation (2/1 DMSO/H₂O, right).

Given this successful result an oxidation-induced gelation was attempted with a weaker oxidant, nitric oxide (NO). NO is an appealing analyte because elevated concentrations in exhaled breath is a biomarker for many diseases.²⁰ NO has been shown to catalytically oxidize related dihydropyridines under an aerobic atmosphere.²¹ Using NO as an oxidant presented a challenge because it is insoluble in DMSO²² and reacts with alcohols and water in the presence of oxygen. Therefore the NO-induced oxidation was performed in CH₃CN. Syringe injection of NO (1 equiv) oxidizes **1** in 75 min. Table 2.1 depicts the reaction times to 90% conversion for various equivalents of NO. Comparing entries 1 and 4 reveal that although the reaction is catalytic in NO, the reaction time is substantially slower at lower NO concentrations.

After oxidation a gel formed at room temperature when DMSO/H₂O was added. Control studies showed that the NO-induced oxidation is essential to gel formation since an unexposed solution of **1** does not form a gel upon identical treatment of DMSO/H₂O (Figure 2.3).

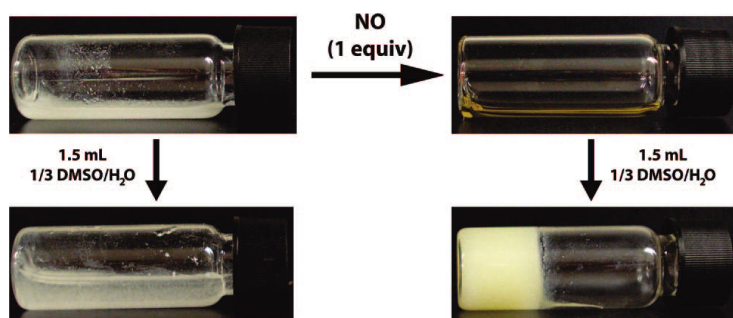


Figure 2.3 Adding NO to a mixture of **1** in CH₃CN (43 mM, upper left) results in oxidation to **2** (upper right). Adding an aliquot of DMSO/H₂O results in a solution for **1** (lower left) and a gel for **2** (lower right).

In summary, we invented a new analyte-triggered gelation by employing a molecular design strategy based on a change in intermolecular interactions. Specifically, an oxidation-induced planarization with concomitant donor-acceptor interactions was shown to trigger gel formation. Though the present case exploits π -stacking, the general strategy of using an analyte to introduce gel-promoting intermolecular interactions can be applied using other noncovalent interactions

such as H-bonding, solvophobic, and electrostatic attraction. We believe that by employing signal amplification these analyte-triggered gelations can be used in chemical sensing. Our current efforts are focused on developing methods for amplification using functionalized polymers.

Table 2.1 Time to 90% Conversion in the NO-induced Oxidation of **1**^a

Entry	Equiv. NO	Time^b (min)
1	0.25	2900
2	0.50	140
3	1	75
4	10	< 1

a. Reaction conditions: 13 mmol **1** in 0.3 mL CH₃CN, 1 atm O₂, rt. *b.* Conversions were determined by HPLC analysis using 1,3-dinitrobenzene as an internal standard.

References:

(1) (a) *Molecular Gels: Materials with Self-Assembled Fibrillar Networks*; Weiss, R. G., Terech, P., Eds.; Springer: Dordrecht, The Netherlands, 2006. (b) Low Molecular Mass Gelator; *Topics in Current Chemistry*, Vol. 256; Springer: Berlin, Heidelberg, 2005. For recent reviews, see: (c) Sangeetha, N. M.; Maitra, U. *Chem. Soc. Rev.* **2005**, *34*, 821-836. de Loos, M.; Feringa, B. L.; van Esch, J. H. *Eur. J. Org. Chem.* **2005**, 3615-3631. Estroff, L. A.; Hamilton, A. D. *Chem. Rev.* **2004**, *104*, 1201-1218.

(2) For a recent example, see: Tysseling-Mattiace, V. M.; Sahni, V.; Niece, K. L.; Birch, D.; Czeisler, C.; Fehlings, M. G.; Stupp, S. I.; Kessler, J. A. *J. Neurosci.* **2008**, *28*, 3814-3823. Silva, G. A.; Czeisler, C.; Niece, K. L.; Beniash, E.; Harrington, D. A.; Kessler, J. A.; Stupp, S. I. *Science* **2004**, *303*, 1352-1355.

(3) For a recent review: Vintiloiu, A.; Leroux, J.-C. *J. Controlled Release* **2008**, *125*, 179-192.

(4) For recent examples, see: Yang, Z.; Ho, P.-L.; Liang, G.; Chow, K. H.; Wang, Q.; Cao, Y.; Guo, Z.; Xu, B. *J. Am. Chem. Soc.* **2007**, *129*, 266-267. Yang, Z.; Xu, B. *Chem. Commun.* **2004**, 2424-2425.

(5) For a recent example, see: Bardelang, D.; Camerel, F.; Margeson, J. C.; Leek, D. M.; Schmutz, M.; Zaman, M. B.; Yu, K.; Soldatov, D. V.; Ziessel, R.; Ratcliffe, C. I.; Ripmeester, J. A. *J. Am. Chem. Soc.* **2008**, *130*, 3313-3315.

(6) For example, an effect of the solvent chain length was reported to play an unknown but measurable role in molecular self-assembly; Jonkheijm, P.; van der Schoot, P.; Schenning, A. P. H. J.; Meijer, E. W. *Science* **2006**, *313*, 80-83.

(7) Hirst, A. R.; Coates, I. A.; Boucheteau, T. R.; Miravet, J. F.; Escuder, B.; Castelletto, V.; Hamley, I. W.; Smith, D. K. *J. Am. Chem. Soc.* **2008**, *130*, 9113-9121.

(8) For a recent review, see: Yang, Z.; Liang, G.; Xu, B. *Acc. Chem. Res.* **2008**, *41*, 315-326.

(9) For a recent example, see: Das, A. K.; Collins, R.; Ulijn, R. V. *Small* **2008**, *4*, 279-287.

(10) For a recent example, see: Shome, A.; Debnath, S.; Das, P. K. *Langmuir* **2008**, *24*, 4280-4288.

(11) For a recent example, see: Matsumoto, S.; Yamaguchi, S.; Ueno, S.; Komatsu, H.; Ikeda, M.; Ishizuka, K.; Iko, Y.; Tabata, K. V.; Aoki, H.; Ito, S.; Noji, H.; Hamachi, I. *Chem. Eur. J.* **2008**, *14*, 3977-3986.

(12) For a review of two-component gels, see: Hirst, A. R.; Smith, D. K. *Chem. Eur. J.* **2005**, *11*, 5496-5508.

(13) For related examples, see: (a) Zang, L.; Che, Y.; Moore, J. S. *Acc. Chem. Res.* **2008**, *41*, 1596-1608. (b) Ajayaghosh, A.; Praveen, V. K. *Acc. Chem. Res.* **2007**, *40*, 644-656. (c) Hoeben, F. J. M.; Jonkheijm, P.; Meijer, E. W.; Schenning, A. P. H. J. *Chem. Rev.* **2005**, *105*, 1491-1546.

(14) For rheological measurements on these gels, see Appendix 1.

(15) For the role of the 2,6-dimethyl substituents in a related gelator, see: Baddeley, C.; Yan, Z.; King, G.; Woodward, P. M.; Badjic, J. D. *J. Org. Chem.* **2007**, *72*, 7270-7278.

(16) X-ray crystal structure images were generated using ORTEP-3. H-atoms were omitted for clarity.

(17) Pfister, J. R. *Synthesis* **1990**, 689-690. See also: Nair, V.; Deepthi, A. *Chem. Rev.* **2007**, *107*, 1862-1891.

(18) Note that rapidly adding CAN in one aliquot lead to a precipitate.

(19) The equilibrium solubilities were measured by UV-vis spectroscopy in 2/1 DMSO/H₂O at room temperature: **1** (0.29 ± 0.04 mg/mL) and **2** (0.61 ± 0.07 mg/mL).

(20) Lim, K. G.; Mottram, C. *Chest* **2008**, *133*, 1232-1242.

(21) (a) Zhu, X.-Q.; Zhao, B.-J.; Cheng, J.-P. *J. Org. Chem.* **2000**, *65*, 8158-8163. (b) Itoh, T.; Nagata, K.; Matsuya, Y.; Miyazaki, M.; Ohsawa, A. *J. Org. Chem.* **1997**, *62*, 3582-3585.

(22) (a) Shaw, A. W.; Vosper, A. J. *J. Chem. Soc., Faraday Trans. 1* **1977**, *73*, 1239-1244. (b) *Dimethyl sulfoxide (DMSO) Solubility Data; Bulletin #102B*; Gaylord Chemical Company, L.L.C.: Slidell, LA, 2007.

Chapter 3²

Comparing Molecular Gelators and Nongelators Based on Solubilities and Solid-State Interactions

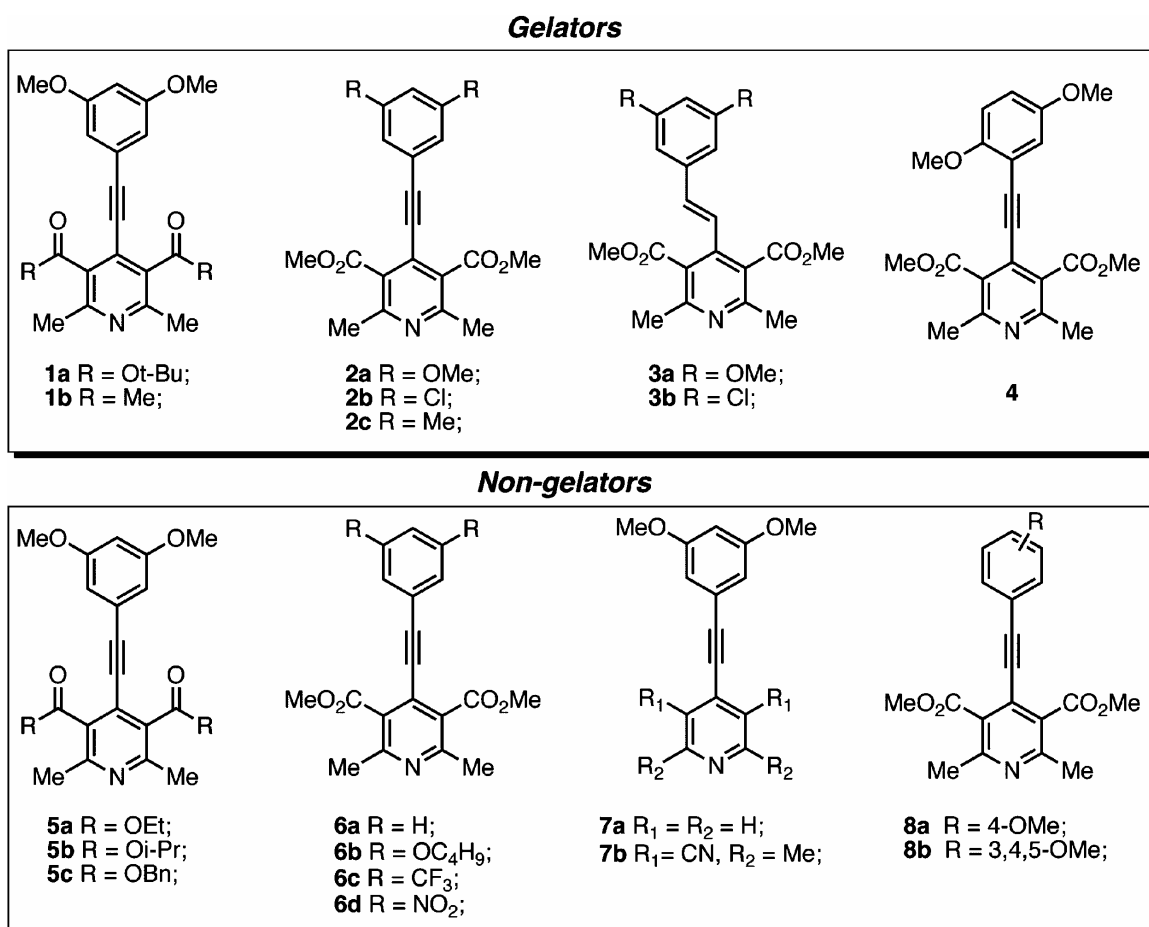
Molecular gels^{1,2} are increasingly being investigated for diverse applications, including chemical sensing,³ bioresponsive materials,⁴ regenerative medicine,⁵ and environmental remediation.⁶ It was recently estimated that over 1000 small-molecule based gelators have been reported in the literature.⁷ Although many of these gelators were discovered serendipitously, we^{3b,6a} and others⁸ have proposed strategies for designing new gelators. These strategies are based on an early hypothesis by Hanabusa et al.,⁹ who suggested that an important criterion for gelators is that they exhibit unidirectional or 1D intermolecular interactions. In addition, an optimal solubility (not too soluble or insoluble) is considered essential for molecular gelators.¹⁰ Despite these criteria, discovering new molecular gelators remains a largely empirical endeavor and subtle changes to their structures have had unpredictable effects on their gelation ability.¹¹ As a result, efforts to improve gel properties or applications by modifying the gelator structure have not been straightforward. A fundamental understanding of the relationship between molecular structure and gelation ability is needed to advance this field.

We recently reported on the design and discovery of a pyridine-based gelator (**2a**) for sensing nitric oxide.^{3b} The planar, conjugated molecule exhibited 1D donor-acceptor π - π interactions in the solid-state, consistent with Hanabusa et al.'s criterion for gelators. To improve the sensors detection limit, subsequent studies focused on modifications to the gelator scaffold; substituents that were

² Reproduced with permission from Chen, J.; Kampf, J. W.; McNeil, A. J. "Comparing Molecular Gelators and Nongelators based on Solubilities and Solid-State Interactions." *Langmuir* **2010**, *26*, 13076-13080. Copyright 2010 American Chemical Society.

anticipated to lower the solubility or enhance π - π interactions were added. Surprisingly, these efforts did not lead to an improved gelator; instead, a confusing relationship between molecular structure and gelation ability emerged. Consequently, we initiated comprehensive studies on all these compounds and present herein compelling evidence that gelators and nongelators cannot be distinguished based simply on their room temperature solubility or presence of 1D intermolecular interactions. Instead, the majority of gelators exhibited different thermodynamic parameters for dissolution than the nongelators. Finally, a comparison of structure-property relationships among the eight gelators revealed that, in some cases, the gel properties correlate with solubility or 1D interactions.

Chart 3.1 Molecular structure of pyridines 1-8.



Pyridines **1-8** (Chart 3.1) were synthesized via two different pathways depending on the nature of R1. In one route, initial Hantzsch condensation of 3-(trimethylsilyl)propionaldehyde and a β -ketoester,¹² followed by deprotection¹³ and Sonogashira cross-coupling with aryl halides¹⁴ provided the penultimate dihydropyridines. Alternatively, the dihydropyridines were prepared through initial Sonogashira cross-coupling of propargyl alcohol and aryl halides,¹⁵ followed by oxidation¹⁶ and Hantzsch condensation with either a β -diketone¹² or 3-aminocrotononitrile.¹⁷ All dihydropyridines were then oxidized using cerium(IV) ammonium nitrate to produce pyridines **1-8** in high yields.¹⁸ (Note that **3a**, **3b**, and **7a** were synthesized via alternative routes.) The experimental procedures and characterization data for all compounds can be found in Appendix 2.

All pyridines were screened for gelation in a range of organic solvent/water mixtures (e.g., DMSO, DMF, THF, acetone, and alcohols) via heating and cooling the solutions. Samples that were stable to inversion of the vial were identified as gelators. In total, eight gelators were discovered (**1a**, **1b**, **2a**, **2b**, **2c**, **3a**, **3b**, and **4**). Rheological measurements were used to confirm that each gel exhibited viscoelastic properties. The critical gel concentrations (cgc) are summarized in Table 3.1. The cgc's range from 4 to 30 mg/mL in 1/1 DMSO/H₂O and 1/2 EtOH/H₂O and are similar to other small molecule-based gelators. The gel microstructures were characterized by scanning electron microscopy, and all gels showed fiber-like morphologies. The experimental protocols and data for all these studies can be found in Appendix 2.

A qualitative survey of Chart 3.1 suggests an unpredictable relationship between molecular structure and gelation ability. For example, simply varying the alkyl ester from Me (**2a**) to Et (**5a**) converts a gelator into a nongelator. Given this result, it was not surprising that the i-Pr ester (**5b**) is also a nongelator; the trend does not continue, however, as the t-Bu ester (**1a**) is a gelator. In another striking example, both the 3,5- and 2,5-dimethoxy substituted pyridines (**2a** and **4**, respectively) are gelators while the less substituted 4-methoxy (**8a**) and more substituted 3,4,5- trimethoxy (**8b**) pyridines are nongelators. On the other hand, changing the triple bond of gelator **2a** (and **2b**) into a double bond in **3a** (and **3b**)

led to the discovery of two additional gelators. Finally, electron-poor arenes such as the Cl-substituted arenes (**2b** and **3b**) are gelators while others such as CF₃- and NO₂-substituted arenes (**6c** and **6d**, respectively) are nongelators. These results highlight how subtle changes in structure can have unpredictable effects on gelation ability and are consistent with other qualitative structure-gelation ability comparisons in the literature.¹¹ Together, these studies motivate the need for a quantitative depiction of the relationship between molecular structure and gelation ability.

Table 3.1. Critical gel concentrations for gelators **1-4**.

Pyridine	cgc (mg/mL)	cgc (mg/mL)
	(1/1 DMSO/H ₂ O)	(1/2 EtOH/H ₂ O)
1a	30 ± 1	--
1b	6 ± 1	9 ± 1
2a	4.5 ± 0.5	9 ± 1
2b	13 ± 1	13 ± 1
2c	21 ± 1	28 ± 1
3a	18 ± 1	18 ± 1
3b	13 ± 1	13 ± 1
4	7.0 ± 0.5	13 ± 1

The mechanism of gel formation is believed to be similar to crystallization; that is, nuclei or small clusters of self-assembled molecules initially form in a supersaturated solution and then growth occurs once a critical size is reached.¹⁹ It is unsurprising, therefore, that solubility is often discussed in the context of gelation. Until now, no studies have compared solubilities between structurally related gelators and nongelators to determine whether it is a distinguishing characteristic. Herein, we report the solubility, dissolution enthalpies (ΔH_{diss}), and dissolution entropies (ΔS_{diss}) for all 19 pyridines in two different solvents. The solubilities were measured on powder samples obtained directly from column

chromatography using UV-vis spectroscopy. A van't Hoff plot of $\ln(\chi)$ (where χ is the mole fraction of pyridine in solution) versus $1/T$ provided ΔH_{diss} and ΔS_{diss} (Appendix 2).²⁰ The results are highlighted in Figures 3.1 and 3.2. Overall, the results show that there is no obvious correlation between room temperature solubility and gelation ability; however, there is a trend in the thermodynamic parameters for dissolution.

The room temperature solubilities of the bulk powders were compared in two different organic solvent/water combinations (1/1 DMSO/H₂O and 1/2 EtOH/H₂O), and several unexpected outcomes were readily apparent (Figure 3.1; gelators are denoted by the filled-in symbols): Some of the most and least soluble pyridines are gelators. Moreover, the nongelators exhibited similar solubilities to each of the gelators. Overall, the range of solubilities was surprisingly broad and spanned nearly 3 orders of magnitude (0.002-1.0 mg/mL).

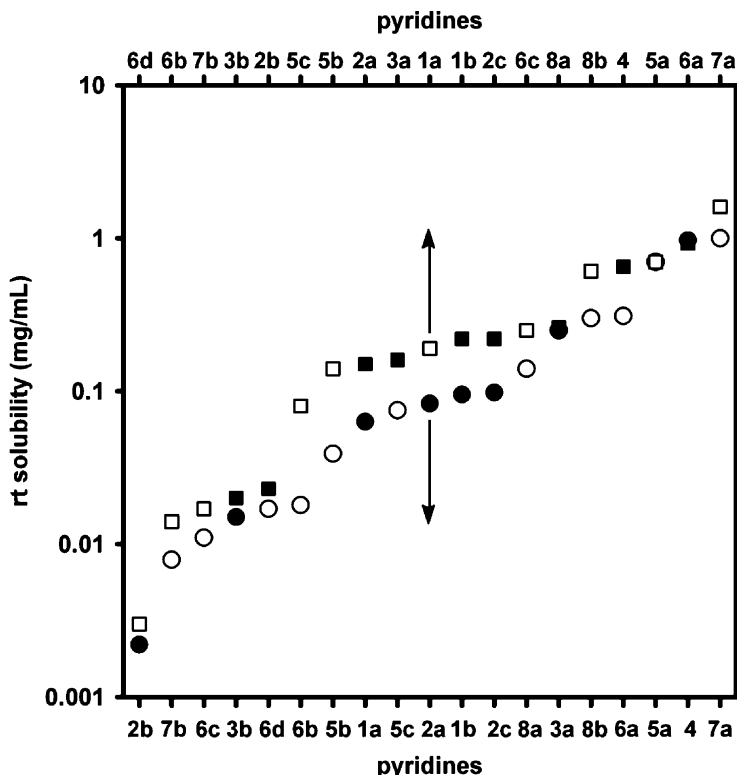


Figure 3.1 Plot of rt solubility versus molecular structure in 1/1 DMSO/H₂O (o, ●) and 1/2 EtOH/H₂O (□, ■). The gelators are denoted by the filled-in symbols (●, ■). (Note that there are two x-axes. For an alternative representation, see Appendix 2).

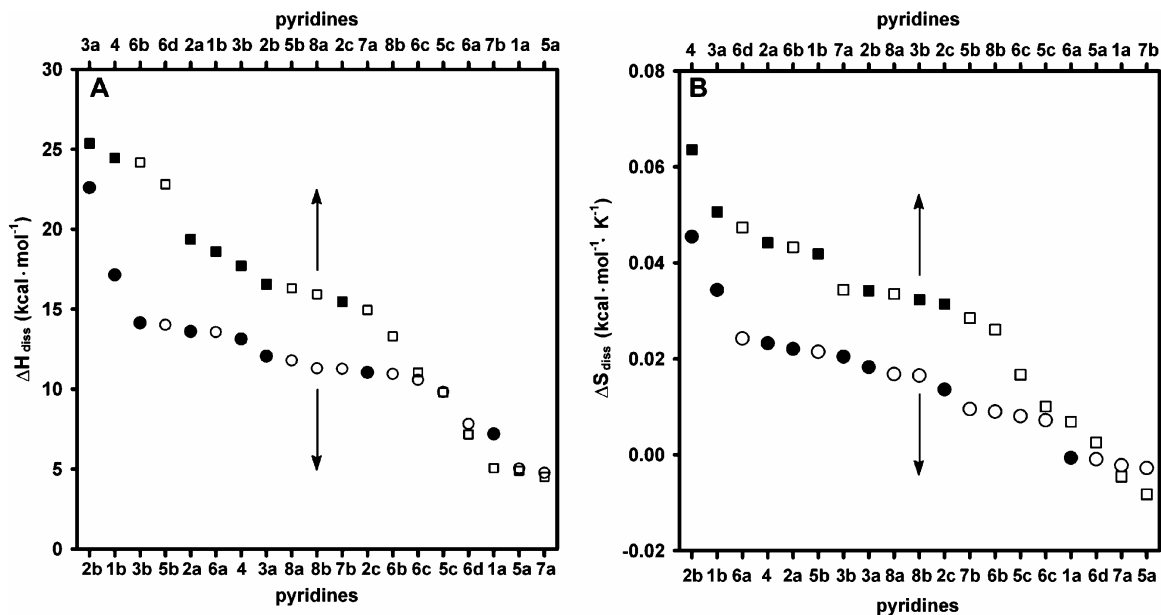


Figure 3.2 Plots of ΔH_{diss} (A) and ΔS_{diss} (B) versus molecular structure in 1/1 DMSO/H₂O (○,●) and 1/2 EtOH/H₂O (□,■). The gelators are denoted by filled-in symbols (■,●). (Note that there are two x-axes. For an alternative representation, see Appendix 2)

The solubilities of the bulk powders were then measured at higher temperatures, and van't Hoff analysis provided the dissolution enthalpies (ΔH_{diss}) and entropies (ΔS_{diss}).²⁰ These values correspond to the thermodynamic parameters for dissolution of the bulk solid. As seen in Figure 3.2, the majority of gelators exhibit the highest values of dissolution enthalpies and entropies whereas the majority of nongelators have the lowest values. These results are consistent with the idea that gelators have stronger intermolecular interactions (ΔH_{diss}) and more order (ΔS_{diss}) in the solid state. This interpretation is most valid when the packing in the solid state is similar to that of the gel fibers, but it is also a reasonable approximation when the packing is dissimilar because polymorphs of organic compounds typically exhibit similar solubilities.²¹ Though the overall trend in the different solvent mixtures is similar, the rankings (highest to lowest) are quite different, suggesting that the influence of solvent on ΔH_{diss} and ΔS_{diss} is structure-dependent.²² For example, gelator **3a** exhibited a much larger difference in dissolution enthalpy between the two solvents than gelator **2a** (13.3 versus 5.4 kcal/mol, respectively). Given their structural similarities, these

dramatic solvent effects are not easily understood. It is notable that similar absolute values of ΔH_{diss} (11-25 kcal/mol) and ΔS_{diss} (0.03-0.07 kcal/mol·K) were found in the only other study that has reported dissolution enthalpies and entropies of gelators, despite the differences in gelator structure (lysine-based versus pyridine-based gelators) and solvent (toluene versus organic solvent/water).¹⁰ Combined, these results suggest that the trend in dissolution parameters between gelators and nongelators may be more general.

Because the majority of molecular gels exhibit microstructures with highly anisotropic fibers, it has been predicted that 1D intermolecular interactions are the driving force for this 1D growth.^{9,23} This hypothesis remains speculative because the molecular packing in gel fibers is often unknown. Definitive structural information can be obtained using single-crystal X-ray crystallography; however, such studies have been limited by the difficulty in obtaining X-ray quality single crystals of gelator molecules. Moreover, this information is only useful if the molecular packing in the single crystal is similar to that in the gel fibers.²⁴⁻²⁶ Few studies have compared molecular packing of both gelators and nongelators via single-crystal and powder X-ray diffraction.²⁷ Herein, we report 11 single-crystal X-ray structures of six gelators and five nongelators, and an analysis of their intermolecular interactions in the solid state.²⁸ Powder patterns were simulated for each single-crystal X-ray structure and compared to the observed diffraction patterns of the bulk powders and gels in 1/1 DMSO/H₂O (Appendix 2). Only three gelators had similar molecular packing in the single crystal and gel fibers (**1a**, **2a**, and **2c**), and as a result the following discussion will focus on comparisons between these gelators and the five nongelators. The results are highlighted in Figures 3.3 and 3.4.

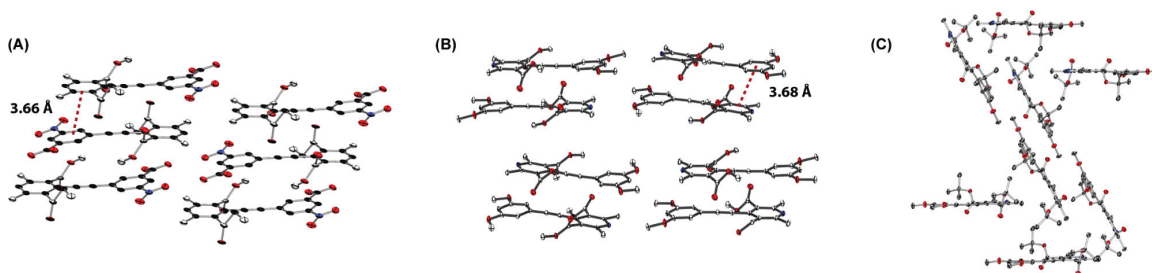


Figure 3.3 Single-crystal X-ray structures for (A) **6d**, (B) **2a**, and (C) **1a**. H-atoms were omitted for clarity.

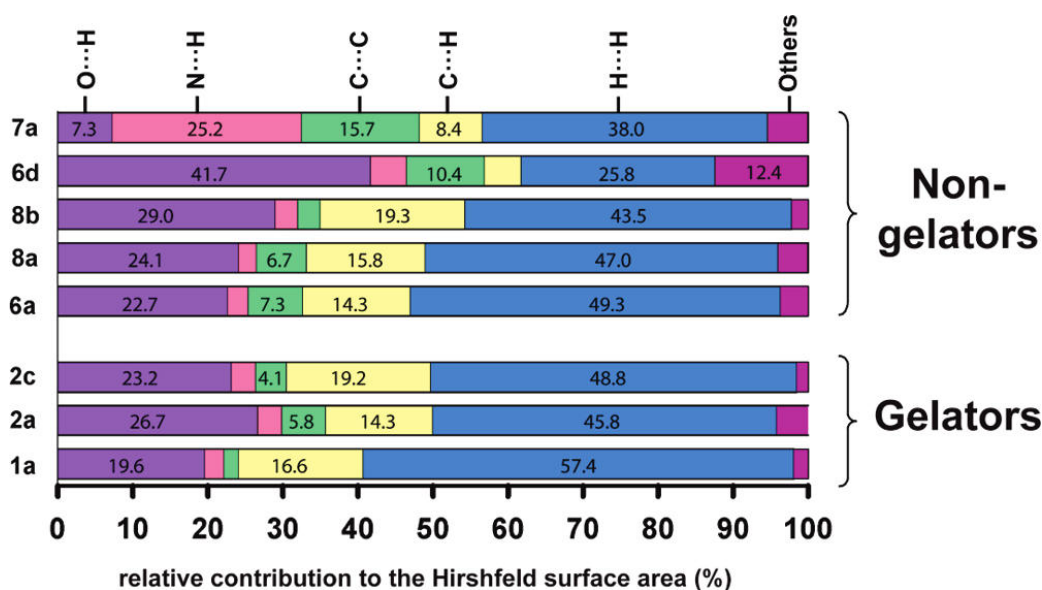


Figure 3.4 Percent relative contribution of the intermolecular interactions in each crystal structure based on Hirshfeld surface analysis.

Overall, there is no clear distinction between gelators and nongelators based on molecular packing. Qualitative analyses of the molecular packing led to two interesting observations: (1) The presence of 1D noncovalent interactions is not unique to gelators; for example, nongelator **6d** and gelator **2a** both exhibit π - π interactions between neighboring molecules where the overall orientation of these interactions is along one dimension (3.66 and 3.68 Å, respectively, Figure 3.3A and B). (2) 1D noncovalent interactions may be unnecessary for gelation; for example, gelator **1a** exhibited a herringbone pattern, with no persistent 1D interactions (Figure 3.3C). These results are consistent with Dastidar and co-workers, who examined gelators with a more directional intermolecular

interaction (H-bonding) and found that 1D interactions were not exclusive to gelators and, in some cases, were not necessary for gelation.²⁷

A more quantitative analysis of molecular packing was obtained using Hirshfeld surface analysis. The Hirshfeld surfaces were calculated for each single-crystal X-ray structure to identify the nature and extent of the intermolecular interactions in the solid state.²⁹ These surfaces represent the space occupied by a molecule in the unit cell and provide information about the intermolecular interactions. For the two X-ray crystal structures (**2a** and **3a**) that contained more than one molecule in the asymmetric unit cell, an average of surface areas was used. Figure 3.4 depicts the relative contribution of van der Waals (C···C, C···H, and H···H) and hydrogen-bonding (O···H and N···H) intermolecular interactions to the Hirshfeld surface area. Surprisingly, three of the five nongelators (i.e., **6a**, **8a**, and **8b**) exhibited Hirshfeld surfaces that are similar to those of the gelators. These results suggest that the nature and extent of intermolecular interactions are not unique to gelators.

The gelator solubilities, dissolution parameters, and intermolecular interactions were compared to elucidate the relationship between molecular structure, solvent identity, and gel properties. A correlation between rt solubility and cgc was observed for gelator **2a** in varying ratios of DMSO/H₂O (Figure S101A in the Appendix 2); for example, an increase in the proportion of bad solvent (H₂O) led to both a lower solubility and cgc for gelator **2a**. However, when different good solvents were used, there was no trend between cgc and solubility (Figure S101B in Appendix 2); for example, the solubility of **2a** is 17 times higher in 1/1 DMF/H₂O than in 1/1 DMSO/H₂O, yet the cgc's are nearly equivalent (3.6 versus 4.5 mg/mL). Similarly, there was no correlation between solubility and cgc when all eight gelators were compared in a single solvent system (Figure S102 in Appendix 2); for example, gelators **1a** and **2a** exhibit similar solubilities (0.06 versus 0.083 mg/mL), yet gelator **1a** has the highest cgc (30 mg/mL) while gelator **2a** has the lowest cgc (4.5 mg/mL) in 1/1 DMSO/H₂O. Together, these results suggest that the rt solubility and cgc are not strongly correlated, in contrast to the results of Smith and co-workers.¹⁰ Moreover, no correlation

between gel properties (e.g., cgc or T_{gel}) and solvent polarity was observed, in contrast to results by Hanabusa et al.³⁰ and others.³¹ These differences are likely due to the fact that cgc is not simply dependent on gelator solubility but also depends on gel microstructure, which often varies with changes in solvent³² and gelator structure.

On the other hand, a modest correlation between cgc and thermodynamic parameters for dissolution exists; for example, in 1/1 DMSO/H₂O, gelators **1a**, **2c**, and **3a** have the highest cgc's and the lowest dissolution enthalpies and entropies. Similarly, in 1/2 EtOH/H₂O, gelator **2c** has the lowest dissolution enthalpy and entropy and the highest cgc. Smith and co-workers observed a similar correlation among lysine-based gelators.¹⁰ The correlations are not perfect, however, as the gelators with the highest ΔH_{diss} and ΔS_{diss} in 1/1 DMSO/H₂O (**2b**) and 1/2 EtOH/H₂O (**3a**) do not have the lowest cgc's. Combined, these results imply that, among gelators, a complex relationship exists between molecular structure, solvent identity, and gel properties.

A correlation between gel properties and the extent of 1D interactions was observed among the three gelators with matching single-crystal and X-ray powder diffraction patterns. Hirshfeld surface analysis provided a relative ranking of the gelators based on the extent of C \cdots C interactions (**1a** < **2c** < **2a**), which correspond almost exclusively to π - π interactions. The reverse ranking is obtained for cgc's in 1/1 DMSO/H₂O (**2a** < **2c** < **1a**), consistent with the notion that π - π interactions enhance gelation. Likewise, gelator **1a**, which did not exhibit any 1D intermolecular interactions, is the weakest gel in 1/1 DMSO/H₂O and does not form gels in 1/2 EtOH/H₂O. Combined, these results imply that, among gelators, the nature and extent of noncovalent interactions does correlate with gel properties (e.g., cgc and gel strength).

In the present study, the solubilities and solid-state interactions were compared for a series of 19 structurally related pyridines (8 gelators and 11 nongelators) with the aim of understanding the relationship between molecular structure and gelation ability. These results provided compelling evidence that gelators and nongelators cannot be distinguished based simply on their room

temperature solubilities or the presence (and absence) of 1D intermolecular interactions. Excitingly, we found that the majority of gelators have higher dissolution enthalpies and entropies, consistent with stronger intermolecular interactions and more order in the solid-state. Current efforts in our group aim to determine the generality of these results by examining other classes of gelators.

References:

(1) (a) Smith, D. K. *Molecular Gels - Nanostructured Soft Materials*. In *Organic Nanostructures*; Steed, J. W., Atwood, J. L., Eds.; Wiley-VCH: Weinheim, 2008; pp 111-154. (b) *Molecular Gels: Materials with Self-Assembled Fibrillar Networks*; Weiss, R. G., Terech, P., Eds.; Springer: Dordrecht, The Netherlands, 2006. (c) *Low Molecular Mass Gelators*; Fages, F., Ed.; Topics in Current Chemistry Vol. 256; Springer: Berlin, Heidelberg, 2005.

(2) For recent reviews, see: (a) Piepenbrock, M. -O. M.; Lloyd, G. O.; Clarke, N.; Steed, J. W. *Chem. Rev.* **2010**, *110*, 1960-2004. (b) Banerjee, S.; Das, R. K.; Maitra, U. *J. Mater. Chem.* **2009**, *19*, 6649-6687. (c) Hirst, A. R.; Escuder, B.; Miravet, J. F.; Smith, D. K. *Angew. Chem., Int. Ed.* **2008**, *47*, 8002-8018. (d) Sangeetha, N. M.; Maitra, U. *Chem. Soc. Rev.* **2005**, *34*, 821-836. (e) de Loos, M.; Feringa, B. L.; van Esch, J. H. *Eur. J. Org. Chem.* **2005**, 3615-3631. (f) Estroff, L. A.; Hamilton, A. D. *Chem. Rev.* **2004**, *104*, 1201-1217. (g) Abdallah, D. J.; Weiss, R. G. *Adv. Mater.* **2000**, *12*, 1237-1247. (h) Terech, P.; Weiss, R. G. *Chem. Rev.* **1997**, *97*, 3133-3159.

(3) For recent examples, see: (a) Kim, T. H.; Kim, D. G.; Lee, M.; Lee, T. S. *Tetrahedron* **2010**, *66*, 1667-1672. (b) Chen, J.; McNeil, A. J. *J. Am. Soc. Chem.* **2008**, *130*, 16496-16497. (c) Mukhopadhyay, P.; Iwashita, Y.; Shirakawa, M.; Kawano, S.-I.; Fujita, N.; Shinkai, S. *Angew. Chem., Int. Ed.* **2006**, *45*, 1592-1595.

(4) For recent reviews, see: (a) Gao, Y.; Yang, Z.; Kuang, Y.; Ma, M.-L.; Li, J.; Zhao, F.; Xu, B. *Pept. Sci.* **2010**, *94*, 19-31. (b) Williams, R. J.; Mart, R. J.; Ulijn, R. V. *Pept. Sci.* **2010**, *94*, 107-117. (c) Yang, Z.; Liang, G.; Xu, B. *Acc. Chem. Res.* **2008**, *41*, 315-326. (d) Ulijn, R. V.; Bibi, N.; Jayawarna, V.; Thornton, P. D.; Todd, S. J.; Mart, R. J.; Smith, A. M.; Gough, J. E. *Mater. Today* **2007**, *10*, 40-48.

(5) For recent reviews, see: (a) Webber, M. J.; Kessler, J. A.; Stupp, S. I. *J. Intern. Med.* **2010**, *267*, 71-88. (b) Jung, J. P.; Gasiorowski, J. Z.; Collier, J. H. *Pept. Sci.* **2010**, *94*, 49-59. (c) Yang, Y.; Khoe, U.; Wang, X.; Horii, A.; Yokoi, H.; Zhang, S. *Nano Today* **2009**, *4*, 193-210. (d) Xu, B. *Langmuir* **2009**, *25*, 8375-8377. (e) Gelain, F.; Horii, A.; Zhang, S. *Macromol. Biosci.* **2007**, *7*, 544-551.

(6) (a) King, K. N.; McNeil, A. J. *Chem. Commun.* **2010**, *46*, 3511-3513. (b) Adhikari, B.; Palui, G.; Banerjee, A. *Soft Matter* **2009**, *5*, 3452-3460. (c) Bardelang, D.; Camerel, F.; Margeson, J. C.; Leek, D. M.; Schmutz, M.; Zaman, Md. B.; Yu, K.; Soldatov, D. V.; Ziessel, R.; Ratcliffe, C. I.; Ripmeester, J. A. *J. Am. Soc. Chem.* **2008**, *130*, 3313-3315. (d) Debnath, S.; Shome, A.; Dutta, S.; Das, P. K. *Chem. Eur. J.* **2008**, *14*, 6870-6881. (e) Trivedi, D. R.; Dastidar, P. *Chem. Mater.* **2006**, *18*, 1470-1478. (f) Trivedi, D. R.; Ballabh, A.; Dastidar, P.; Ganguly, B. *Chem. Eur. J.* **2004**, *10*, 5311-5322. (g) Trivedi, D. R.; Ballabh, A.; Dastidar, P. *Chem. Mater.* **2003**, *15*, 3971-3973. (h) Bhattacharya, S.; Krishnan-Ghosh, Y. *Chem. Commun.* **2001**, 185-186.

- (7) van Esch, J. H. *Langmuir* **2009**, *25*, 8392-8394.
- (8) The crystal engineering approach has been used by Dastidar et al. to identify new organic salt-based gelators. This approach appends supramolecular synthons (e.g., ammonium dicarboxylates) to organic molecules to enhance 1D interactions. For a recent review, see: Dastidar, P. *Chem. Soc. Rev.* **2008**, *37*, 2699-2715. For a more general review on crystal engineering, see: Desiraju, G. R. *Angew. Chem., Int. Ed.* **2007**, *46*, 8342-8356.
- (9) Hanabusa, K.; Yamada, M.; Kimura, M.; Shirai, H. *Angew. Chem., Int. Ed.* **1996**, *35*, 1949-1951.
- (10) Hirst, A. R.; Coates, I. A.; Boucheteau, T. R.; Miravet, J. F.; Escuder, B.; Castelletto, V.; Hamley, I. W.; Smith, D. K. *J. Am. Chem. Soc.* **2008**, *130*, 9113-9121.
- (11) For examples of remarkable changes in gelation ability with minimal changes in structure, see: (a) Ma, M.; Kuang, Y.; Gao, Y.; Zhang, Y.; Gao, P.; Xu, B. *J. Am. Chem. Soc.* **2010**, *132*, 2719-2728. (b) Karthik Kumar, K.; Elango, M.; Subramanian, V.; Mohan Das, T. *New J. Chem.* **2009**, *33*, 1570-1577. (c) Yang, Z.; Liang, G.; Ma, M.; Gao, Y.; Xu, B. *J. Mater. Chem.* **2007**, *17*, 850-854. (d) de Loos, M.; van Esch, J. H.; Kellogg, R. M.; Feringa, B. L. *Tetrahedron* **2007**, *63*, 7285-7301. (e) Menger, F. M.; Caran, K. L. *J. Am. Chem. Soc.* **2000**, *122*, 11679-11691. (f) Garner, C. M.; Terech, P.; Allegraud, J.-J.; Mistrot, B.; Nguyen, P.; de Geyer, A.; Rivera, D. *J. Chem. Soc., Faraday Trans.* **1998**, *94*, 2173-2179. (g) See also ref 25g.
- (12) Li, A.-H.; Chang, L.; Ji, X.-D.; Melman, N.; Jacobson, K. A. *Bioconjugate Chem.* **1999**, *10*, 667-677.
- (13) Chanteau, S. H.; Tour, J. M. *Tetrahedron Lett.* **2001**, *42*, 3057-3060.
- (14) Mio, M. J.; Kopel, L. C.; Braun, J. B.; Gadzikwa, T. L.; Hull, K. L.; Brisbois, R. G.; Markworth, C. J.; Grieco, P. A. *Org. Lett.* **2002**, *4*, 3199-3202.
- (15) Ozeki, M.; Muroyama, A.; Kajimoto, T.; Watanabe, T.; Wakabayashi, K.; Node, M. *Synlett* **2009**, 1781-1784.
- (16) Washio, T.; Yamaguchi, R.; Abe, T.; Nambu, H.; Anada, M.; Hashimoto, S. *Tetrahedron* **2007**, *63*, 12037-12046.
- (17) Hafiz, I. S. A.; Ramiz, M. M. M.; Mahmoud, F. F.; Darwish, E. S. *J. Chem. Sci.* **2008**, *120*, 339-345.
- (18) Pfister, J. R. *Synthesis* **1990**, 689-690. See also: Nair, V.; Deepthi, A. *Chem.*

Rev. **2007**, 107, 1862-1891.

(19) For recent examples of gelation studies which support the nucleation growth mechanism, see: (a) Li, J.-L.; Liu, X.-Y. *J. Phys. Chem. B* **2009**, 113, 15467-15472. (b) Rogers, M. A.; Marangoni, A. G. *Langmuir* **2009**, 25, 8556-8566. (c) Huang, X.; Raghavan, S. R.; Terech, P.; Weiss, R. G. *J. Am. Chem. Soc.* **2006**, 128, 15341-15352. (d) Tan, G.; John, V. T.; McPherson, G. L. *Langmuir* **2006**, 22, 7416-7420. (e) Lescanne, M.; Grondin, P.; d'Aleo, A.; Fages, F.; Pozzo, J. -L.; Mondain Monval, O.; Reinheimer, P.; Colin, A. *Langmuir* **2004**, 20, 3032-3041.

(20) (a) Mullin, J. W. *Solutions and Solubility. Crystallization*, 3rd ed.; Butterworth-Heinemann: Oxford, 1992; pp 81-127. (b) Belny, D. H. M.; Mullin, J. W. *J. Chem. Eng. Data* **1987**, 32, 9-10.

(21) Solubility differences were shown to be less than a factor of 2 among polymorphs, see: Pudipeddi, M.; Serajuddin, A. T. M. *J. Pharm. Sci.* **2005**, 94, 929-939.

(22) (a) Solvent-dependent melting enthalpies were observed for bisamide- and bisurea-based gelators by DSC, see: Zweep, N.; Hopkinson, A.; Meetsma, A.; Browne, W. R.; Feringa, B. L.; van Esch, J. H. *Langmuir* **2009**, 25, 8802-8809. (b) Solvent-independent melting enthalpies were observed for cholesterol-based gelators, see: Murata, K.; Aoki, M.; Suzuki, T.; Harada, T.; Kawabata, H.; Komori, T.; Ohseto, F.; Ueda, K.; Shinkai, S. *J. Am. Chem. Soc.* **1994**, 116, 6664-6676.

(23) This concept has precedent in the crystallization literature. For example, see: (a) Davey, R.; Garside, J. *Crystal Morphology. From Molecules to Crystallizers: An Introduction to Crystallization*; Oxford University Press: Oxford, 2000; pp 36-43. (b) Weissbuch, I.; Popovitz-Biro, R.; Lahav, M.; Leiserowitz, L. *Acta Crystallogr.* **1995**, B51, 115-148. (c) Hartman, P.; Bennema, P. *J. Cryst. Growth* **1980**, 49, 145-156.

(24) There are many reports of gelator single-crystal X-ray structures that were not compared to the gel powder diffraction patterns. For examples, see: (a) Olive, A. G. L.; Raffy, G.; Allouchi, H.; Leger, J. -M.; Del Guerso, A.; Desvergne, J. -P. *Langmuir* **2009**, 25, 8606-8614. (b) Adarsh, N. N.; Kumar, D. K.; Dastidar, P. *Tetrahedron* **2007**, 63, 7386-7396. (c) Trivedi, D. R.; Ballabh, A.; Dastidar, P. *Cryst. Growth Des.* **2006**, 6, 763-768. (d) Gronwald, O.; Shinkai, S. *Chem. Eur. J.* **2001**, 7, 4329-4334. (e) Lu, L.; Cocker, M.; Bachman, R. E.; Weiss, R. G. *Langmuir* **2000**, 16, 20-34. (f) Tamaru, S.-I.; Luboradzki, R.; Shinkai, S. *Chem. Lett.* **2001**, 336-337. (g) Luboradzki, R.; Gronwald, O.; Ikeda, M.; Shinkai, S.; Reinhoudt, D. N. *Tetrahedron* **2000**, 56, 9595-9599. (h) Menger, F. M.; Yamasaki, Y.; Catlin, K. K.; Nishimi, T. *Angew. Chem., Int. Ed.* **1995**, 34, 585-586. (i) See also ref 31b.

(25) For examples of gelator single-crystal X-ray structures that do not match the gel diffraction patterns, see: (a) Das, U. K.; Trivedi, D. R.; Adarsh, N. N.; Dastidar, P. *J. Org. Chem.* **2009**, *74*, 7111-7121. (b) Wang, Y.; Tang, L.; Yu, J. *Cryst. Growth Des.* **2008**, *8*, 884-889. (c) Kumar, D. K.; Jose, D. A.; Das, A.; Dastidar, P. *Chem. Commun.* **2005**, 4059-4061. (d) Sangeetha, N. M.; Bhat, S.; Choudhury, A. R.; Maitra, U.; Terech, P. *J. Phys. Chem. B* **2004**, *108*, 16056-16063. (e) Kumar, D. K.; Jose, D. A.; Dastidar, P.; Das, A. *Langmuir* **2004**, *20*, 10413-10418. (f) Ballabh, A.; Trivedi, D. R.; Dastidar, P. *Chem. Mater.* **2003**, *15*, 2136-2140. (g) van Esch, J.; Schoonbeek, F.; de Loos, M.; Kooijman, H.; Spek, A. L.; Kellogg, R. M.; Feringa, B. L. *Chem. Eur. J.* **1999**, *5*, 937-950. (h) Ostuni, E.; Kamaras, P.; Weiss, R. G. *Angew. Chem., Int. Ed.* **1996**, *35*, 1324-1326.

(26) For examples of gelator single-crystal X-ray structures that match the gel diffraction patterns, see: (a) Piepenbrock, M.-O. M.; Lloyd, G. O.; Clarke, N.; Steed, J. W. *Chem. Commun.* **2008**, 2644-2646. (b) Terech, P.; Sangeetha, N. M.; Maitra, U. *J. Phys. Chem. B* **2006**, *110*, 15224-15233. (c) Makarevic, J.; Jokic, M.; Raza, Z.; Stefanic, Z.; Kojic-Prodic, B.; Zinic, M. *Chem. Eur. J.* **2003**, *9*, 5567-5580. (d) Abdallah, D. J.; Sirchio, S. A.; Weiss, R. G. *Langmuir* **2000**, *16*, 7558-7561. (e) See also ref 3b.

(27) For studies comparing gelators and nongelators with matching powder and single-crystal X-ray diffraction data, see: (a) Sahoo, P.; Adarsh, N. N.; Chacko, G. E.; Raghavan, S. R.; Puranik, V. G.; Dastidar, P. *Langmuir* **2009**, *25*, 8742-8750. (b) Ballabh, A.; Adalder, T. K.; Dastidar, P. *Cryst. Growth Des.* **2008**, *8*, 4144-4149. (c) Trivedi, D. R.; Dastidar, P. *Cryst. Growth Des.* **2006**, *6*, 2114-2121. (d) Ballabh, A.; Trivedi, D. R.; Dastidar, P. *Chem. Mater.* **2006**, *18*, 3795-3800. (e) Trivedi, D. R.; Ballabh, A.; Dastidar, P. *J. Mater. Chem.* **2005**, *15*, 2606-2614. (f) See also ref 6e and 6f.

(28) Note that the single-crystal X-ray structure of **2a** was previously reported; see ref 3b.

(29) (a) Spackman, M. A.; Jayatilaka, D. *Cryst. Eng. Comm.* **2009**, *11*, 19-32. (b) McKinnon, J. J.; Jayatilaka, D.; Spackman, M. A. *Chem. Commun.* **2007**, 3814-3816. (c) McKinnon, J. J.; Spackman, M. A.; Mitchell, A. S. *Acta Crystallogr.* **2004**, *B60*, 627-668. (d) Lopez-Mejías, V.; Kampf, J. W.; Matzger, A. J. *J. Am. Chem. Soc.* **2009**, *131*, 4554-4555.

(30) Hanabusa, K.; Matsumoto, M.; Kimura, M.; Kakehi, A.; Shirai, H. *J. Colloid Interface Sci.* **2000**, *224*, 231-244.

(31) (a) Hirst, A. R.; Smith, D. K. *Langmuir* **2004**, *20*, 10851-10857. (b) Makarevic, J.; Jokic, M.; Peric, B.; Tomisic, V.; Kojic-Prodic, B.; Zinic, M. *Chem. Eur. J.* **2001**, *7*, 3328-3341. (c) Brinksma, J.; Feringa, B. L.; Kellogg, R. M.; Vreeker, R.; van Esch, J. *Langmuir* **2000**, *16*, 9249-9255.

(32) For recent examples and discussions of the complex role of solvent in gelation, see: (a) Caplar, V.; Frkanec, L.; Vujicic, N. S.; Zinic, M. *Chem. Eur. J.* **2010**, *16*, 3066-3082. (b) Zhu, G.; Dordick, J. S. *Chem. Mater.* **2006**, *18*, 5988-5995. (c) Bhattacharya, S.; Pal, A. *J. Phys. Chem. B* **2008**, *112*, 4918-4927. See also: Jonkheijm, P.; van der Schoot, P.; Schenning, A. P. H. J.; Meijer, E. W. *Science* **2006**, *313*, 80-83.

Chapter 4³

Dissolution Parameters Reveal Role of Structure and Solvent in Molecular Gelation

Many low molecular weight molecules have been discovered (often serendipitously) to form gels in organic and aqueous solvents.^{1,2} Because gelation is reversible and can be responsive to stimuli, these materials are being widely investigated for applications in medicine,^{3,4} materials science,⁵ and environmental science.^{6,7} Yet the design and discovery of new gelators remains a significant challenge.⁸ More than a decade ago, Hanabusa et al. suggested that the presence of one-dimensional (1D) intermolecular interactions is important for gelation.⁹ The premise is that these interactions promote preferential, 1D growth, leading to the anisotropic fibers often observed in molecular gelation. We and others have successfully utilized this concept to design new gelators based on 1D interactions observed in the solid state.^{7a,10}

Despite these successes, gelation has remained a largely empirical phenomenon because many molecules exhibit 1D interactions in the solid state and do not form gels. To advance this field, an improved understanding of the relationship between structure and gelation ability is needed.¹¹

Although theoretical and experimental approaches to understanding gelation have been reported, few studies have compared gelators to nongelators. For example, Adams, Day and co-workers applied crystal structure prediction methods to elucidate why switching the dipeptide sequence converts a gelator into a nongelator.¹² The results suggested that the propensity to form 1D hydrogen-bonded networks correlated with gelation ability, although solvent was

³ Reproduced in part with permission from Muro-Small, M. L.; Chen, J.; McNeil, A. J. "Dissolution Parameters Reveal Role of Structure and Solvent in Molecular Gelation." *Langmuir* **2011**, *27*, 13248-13253. Copyright 2011 American Chemical Society.

excluded from these analyses and none of the predicted crystal structures matched the gel structure. In a different example, Shinkai and co-workers observed that nongelators exhibited higher melting enthalpies than gelators, and attributed this effect to stronger “cohesive” forces present in nongelators.¹³

In 2010, we reported a series of 19 pyridine-based compounds, of which 8 were identified as gelators.¹⁴ An analysis of single crystal X-ray structures revealed that the gelators and nongelators were indistinguishable based on the presence or absence of 1D intermolecular interactions. In addition, the gelators and nongelators were indistinguishable based on the nature and extent of their intermolecular interactions in the solid state. Nevertheless, these studies revealed that there is a correlation between thermodynamic dissolution parameters and gelation ability. Specifically, the gelators exhibited higher dissolution enthalpies and entropies than nongelators. To determine the generality of this relationship, we have now expanded these initial studies to include peptide-based gelators and nongelators. Peptides were selected because they represent the largest class of molecular gelators^{15,16} and their gelation ability is highly sensitive to sequence and structure.¹⁷⁻¹⁹ In addition, peptide-based gelators are utilized in many biomedical applications, including cell culture,²⁰ drug-delivery,²¹ and regenerative medicine.²² Furthermore, the self-assembly of peptides, unlike that of the pyridines, is driven by intermolecular H-bonding interactions. We report herein that, among the two different classes of compounds (dipeptides and pyridines) and three different solvent mixtures (HCl/H₂O, DMSO/H₂O and EtOH/H₂O), a consistent trend is observed between the dissolution parameters and gelation ability. The key conclusion is that the strength of the intermolecular interactions (inasmuch as they are reflected in the dissolution enthalpy) is more relevant than their directionality. Combined, these studies suggest that converting a nongelator into a gelator can occur when structural modifications or a change in solvent lead to increases in these dissolution parameters.

Dipeptides **1-3** were synthesized by Dr. Maria Muro-Small, using standard peptide coupling methods (see Appendix 3). Xu and co-workers previously

identified dipeptides **2a-c** as nongelators.²³ However, she found that these compounds formed gels under our screening conditions (Table 4.1).

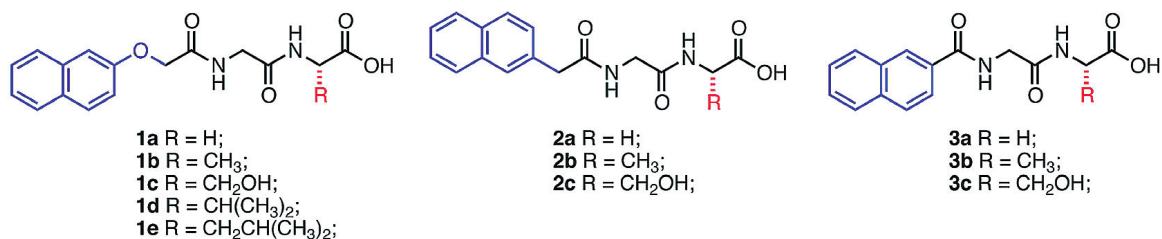
Table 4.1. Critical gel concentrations (cgc) for **1a-c** and **2a-c**.^a

Gelator	cgc (wt %)	cgc (mM)
1a	0.09 ± 0.01	3.1 ± 0.1
1b	0.06 ± 0.02	2.0 ± 0.4
1c	0.10 ± 0.02	2.9 ± 0.5
2a	0.15 ± 0.01	5.0 ± 0.2
2b	0.40 ± 0.02	13 ± 1
2c	0.42 ± 0.04	11 ± 1

^aCritical gel concentrations were determined by heating/cooling in aqueous solutions (pH = 2).

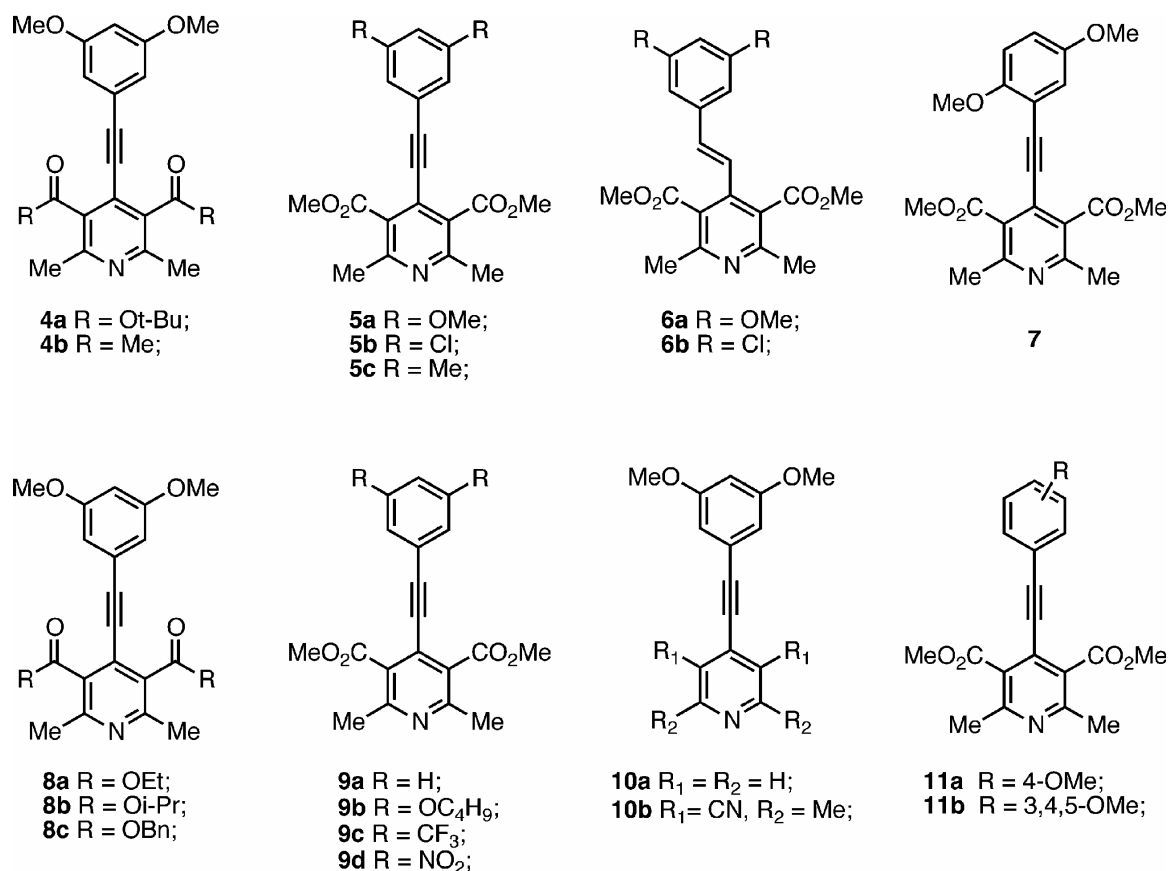
These differences in gelation may be due to the different methods used for gel screening (i.e., heating/cooling versus lowering the pH²⁴), which could influence the kinetics of the self-assembly process, or to the concentrations examined, as **2a-c** are relatively weak gelators with high critical gel concentrations (cgc > 0.1 wt %). Using the heat/cool gel screening protocol, dipeptides **1a-c** were also identified by Maria as gelators while **1d,e** and **3a-c** were identified as nongelators,²⁵ consistent with the results of Xu and co-workers.²³ Examining the structures in Chart 4.1 reveals that deletion of a methylene unit in the naphthylbased amide can convert a gelator (e.g., **2a**) into a nongelator (e.g., **3a**). The impact of this seemingly minor structural change on gelation ability highlights the need for an improved understanding of the relationship between structure and gelation ability.

Chart 4.1 Dipeptide-based gelators (**1a-c**; **2a-c**) and nongelators (**1d,e**; **3a-c**)



Pyridines **4-11** were synthesized by me as described previously (Chart 4.2).¹⁴ The pyridines were screened for gelation using the heat/cool procedure in a range of organic solvent/water mixtures. Under these conditions, pyridines **4-7** were identified as gelators and pyridines **8-11** as nongelators.²⁵ In two complementary solvent systems, 1/1 DMSO/H₂O and 1/2 EtOH/H₂O, the cgc's range from 4 to 30 mg/mL (0.4-3.0 wt %).¹⁴ Gelation is highly sensitive to structure, as the 3,5- and 2,5-dimethoxy substituted pyridines (**5a** and **7**, respectively) are gelators whereas the less substituted 4-methoxy (**11a**) and more substituted 3,4,5-trimethoxy (**11b**) pyridines are nongelators.

Chart 4.2 Pyridine-based gelators (**4-7**) and nongelators (**8-11**)



The equilibrium solubilities were measured at various temperatures ranging from 25 to 80 °C using UV-vis absorption spectroscopy. The dissolution enthalpies (ΔH_{diss}) and entropies (ΔS_{diss}) were determined from the van't Hoff plots (see Figures S15-S17 and S30-S35 in Appendix 3).²⁶ In our initial report, the solubilities of pyridines **4-11** were measured after 2 h.¹⁴ We report herein the equilibrium solubilities, which were measured after 24 h. Although the absolute values of ΔH_{diss} and ΔS_{diss} have changed for most compounds, the overall trends remain the same. Powder X-ray diffraction (PXRD) was performed on the solid before and after the solubility measurements to determine whether any solid-solid transitions occurred during heating (see Figures S20-S29 and S36-S69 in Appendix 3).

As described below, several of the dipeptides and pyridines underwent solid-solid transitions during the solubility measurements. Most of these compounds

were excluded from the subsequent discussions, except when the solid form matched the gel form as determined by PXRD.

In a series of PXRD experiments on the dipeptides performed by Maria, dipeptide gelator **1a** exhibited several different forms, depending on its thermal history. For example, the solid isolated from synthesis (Form I) underwent a solid-solid transition during the solubility measurements (with heating) to generate Form II.²⁷ Because PXRD of the wet gel was unsuccessful, the gel was dried under ambient conditions with slow solvent evaporation. The resulting PXRD pattern matched that of Form I (Figure 4.1A). Alternatively, when the gel was dried via lyophilization, the gel PXRD pattern matched that of Form II (Figure 4.1B). These results highlight the challenges associated with using a “dried” gel sample for comparison. As a result of these complexities, gelator **1a** was not included in the data analysis. Dipeptide nongelator **1e** was also excluded from these studies because it exhibited a solid-solid transition with heating (see Figure S23 in Appendix 3). The remainder of the dipeptides did not undergo any solid-solid transitions with heating and were therefore included in the subsequent dissolution parameter comparisons.

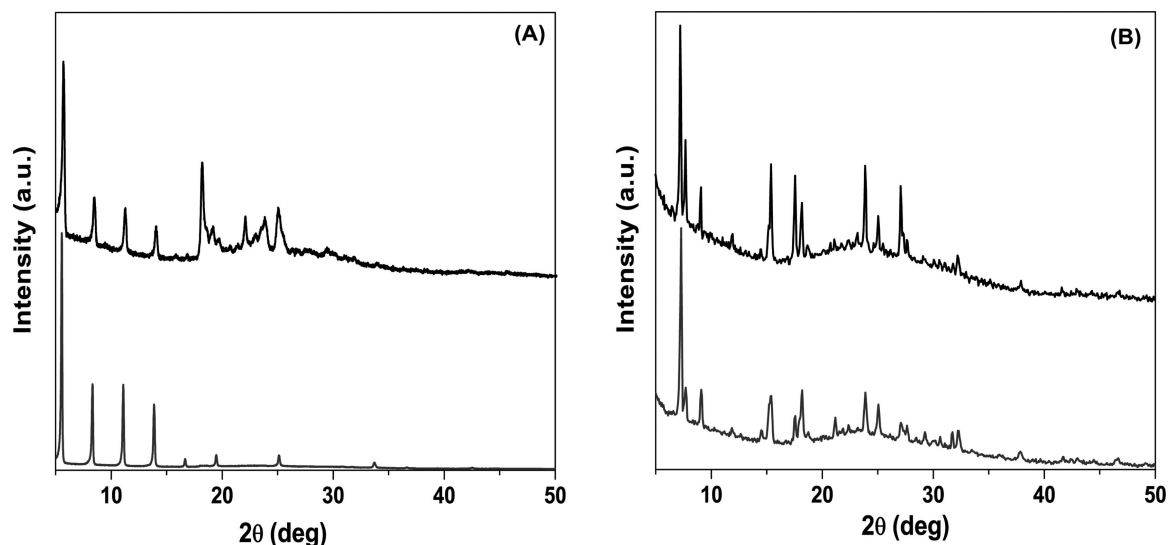


Figure 4.1. PXRD patterns for dipeptide gelator **1a**: (A) Form I (top) and the air-dried gel (bottom), and (B) Form II (top) with the freeze-dried gel (bottom).

In PXRD experiments on pyridines **4-11** performed by me, nongelator **9a** underwent a solid-solid transition in both 1/1 DMSO/H₂O and 1/2 EtOH/H₂O

(Figures S45 and S62 in Appendix 3). Note that the form present after heating is different for the two different solvent conditions, illustrating the critical role of solvent in these transformations. Pyridine nongelator **8b** also exhibited a solid-solid transition in 1/2 EtOH/H₂O, but no transition was observed in 1/1 DMSO/H₂O (Figures S61 and S44 in Appendix 3), again highlighting the solvent contribution to these processes. Because these are nongelators, there is no gel form to compare any of these PXRD patterns. As a result, the data from these two compounds were not included in the dissolution parameter comparisons.

In contrast, pyridine gelator **7** exhibited a solid-solid transition with heating in 1/2 EtOH/H₂O and the gel PXRD matched the heated form (Form II, Figure S60 in Appendix 3). Therefore, the solubility measurements were performed on Form II and these results are included in the comparisons.

As seen in Figure 4.2, the majority of gelators exhibited higher dissolution enthalpies (ΔH_{diss}) and entropies (ΔS_{diss}) than the nongelators, regardless of the structure or solvent system. These results suggest that gelators have stronger intermolecular interactions and more order in the solid state than nongelators. However, this simple interpretation ignores the solvent contribution and the observed solvent-dependent data suggest that this contribution is important.²⁸

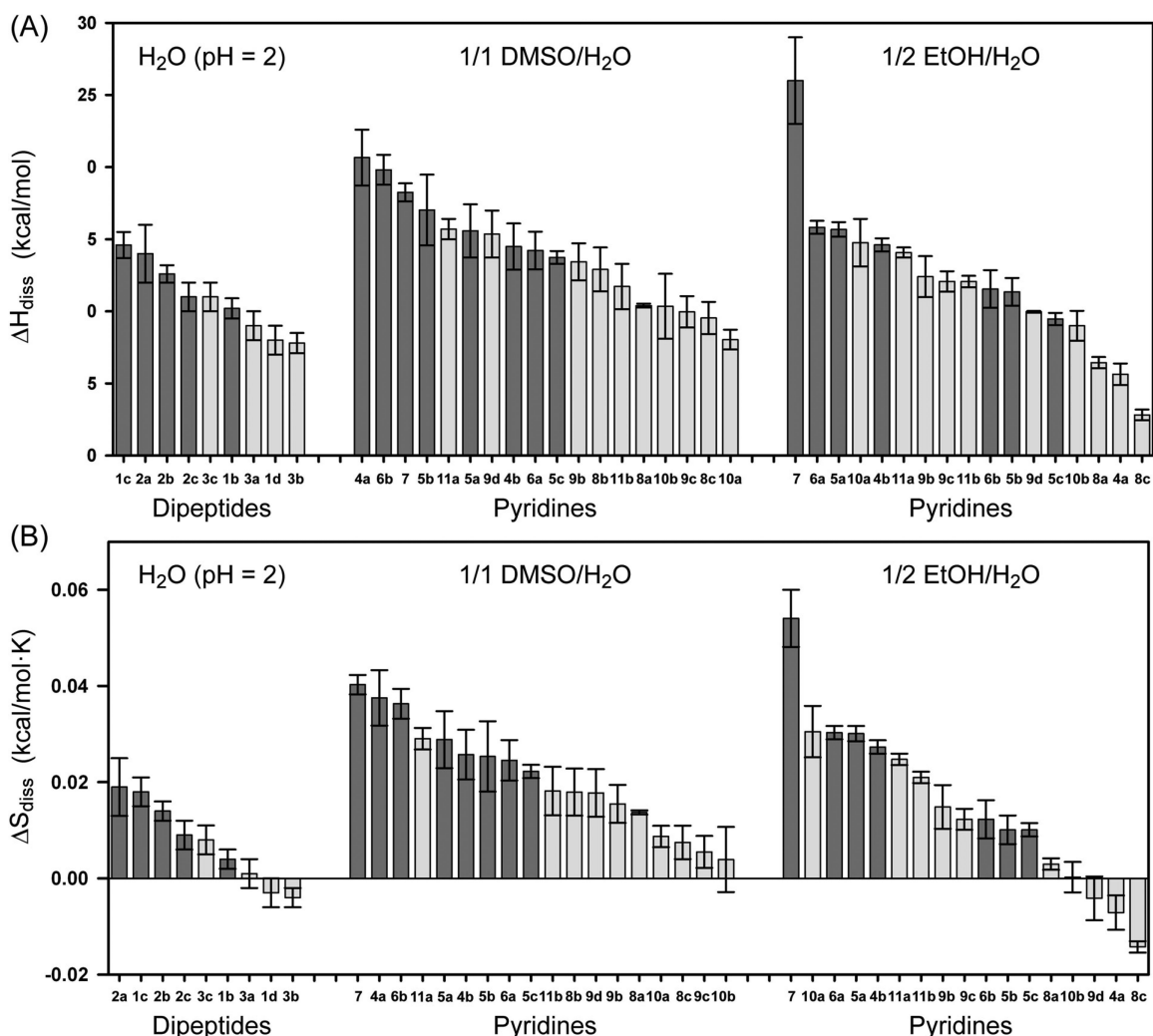


Figure 4.2 Plot of the (A) ΔH_{diss} and (B) ΔS_{diss} versus molecular structure. (Gelators are dark gray, and nongelators are light gray)

Instead, the trends in dissolution enthalpy can be rationalized based on changes in the solid-state interactions ($\sim\Delta H_{\text{sublimation}}$) and the solvent-solute interactions ($\sim\Delta H_{\text{solvation}}$) as a function of the compound structure and solvent composition. For a class of structurally related compounds within the same solvent system, the higher dissolution enthalpies exhibited by the gelators suggests that gelators have stronger solid-state interactions or weaker solvent-solute interactions (or both) than the nongelators. For the same compound in different solvent systems, a large change in dissolution enthalpy when changing solvents suggests that the solvent-solute interactions are significantly different under these conditions.

For example, pyridine gelator **4a** exhibited a large dissolution enthalpy in 1/1 DMSO/H₂O (21 kcal/mol) and a small dissolution enthalpy in 1/2 EtOH/H₂O (5.6 kcal/mol), suggesting a significant change in the solvent-solute interactions from weak interactions in the former to strong interactions in the latter. This interpretation is consistent with the significantly different room temperature solubilities for **4a** in the two solvent systems (0.0034 and 0.20 mM, respectively). Overall, these data are remarkably consistent with the fact that **4a** is a gelator in the former and a nongelator in the latter. It is instructive to compare these data with another compound: Pyridine gelator **5a** exhibited similar dissolution enthalpies in both 1/1 DMSO/H₂O (16 kcal/mol) and 1/2 EtOH/H₂O (15.7 kcal/mol), and it formed a gel in both solvent conditions. The room temperature solubilities of **5a** were also similar (0.28 and 0.39 mM), suggesting that the solvent-solute interactions are similar in both solvent systems.

In a different example, Cl-substituted gelators **5b** and **6b** exhibited large changes in dissolution enthalpy when the solvent system was changed ($\Delta\Delta H_{\text{diss}} = 6$ and 8 kcal/mol), whereas methoxy-substituted gelators **5a** and **6a** exhibited small changes ($\Delta\Delta H_{\text{diss}} = 0.3$ and 1.8 kcal/mol). These results can also be rationalized in terms of a change (or lack thereof) in the solvent-solute interactions, and are consistent with the differences in room temperature solubilities (see Table S5 in Appendix 3).

Although dissolution enthalpies can provide insight into the role of structure and solvent in molecular gelation, it remains challenging to explain at the molecular level the impact of a single functional group transformation on dissolution and gelation (e.g., t-butyl (**4a**) versus methyl (**5a**) ester). The Hansen²⁹ and Hildebrand³⁰ solubility parameters, which have been used to probe solvent-dependent gelations based on the contributions of dispersive, polar, and hydrogen-bonding interactions between solvent and solute, could provide this level of insight. The limitation is that obtaining these parameters requires extensive testing of each compound in many different solvents. The combined approach, using dissolution enthalpy to identify interesting pairs of compounds and then determining their solubility parameters, should provide a more

comprehensive view of solvent/structure effects in gelation.

Though the overall trends (gelator versus nongelator) are similar for the dipeptides and pyridines, the absolute values are quite different. For example, the range of ΔH_{diss} for the dipeptide gelators is 10-15 kcal/mol, whereas the range for pyridine gelators is 14-21 kcal/mol in 1/1 DMSO/H₂O. These results indicate that gelators and nongelators are not distinguishable based on an absolute value of ΔH_{diss} or ΔS_{diss} . Rather, within each class of compounds and solvent system, the gelators exhibit the highest dissolution enthalpies and entropies. Overall, these results provide compelling evidence that there is a relationship between dissolution parameters and gelation ability.

Smith and co-workers previously reported a correlation between cgc and ΔH_{diss} among lysine-based gelators;³¹ that is, gelators with the highest ΔH_{diss} exhibited the lowest cgc's. In contrast, no apparent relationship was observed between cgc and ΔH_{diss} with the pyridine- and dipeptide-based gelators. For example, dipeptide gelators **1b** and **2c** exhibited similar dissolution enthalpies, yet **1b** has the lowest cgc (2.0 mM) while **2c** has one of the highest cgc's (11 mM). Similarly, pyridine gelator **4a** has the highest ΔH_{diss} in 1/1 DMSO/H₂O and yet it also has the highest cgc. One explanation is that gels made from pyridine gelator **4a** consisted of short, needlelike structures, rather than the long, flexible fibers observed using gelators with lower cgc's.¹⁴ These results reflect the fact that cgc is not simply dependent on gelator properties (e.g., ΔH_{diss}) but also depends on other factors, including the gel microstructure.

A correlation between thermodynamic dissolution parameters and gelation ability was observed despite the significant differences in molecular structure, self-assembly motif, and solvent identity. These results suggest that structural- or solvent-based changes that influence these dissolution parameters can be used to convert a nongelator into a gelator. As a result, our current efforts are focused on developing methods to predict dissolution enthalpies to inform the design of new and improved gelators. These studies have also provided preliminary insight into the critical role of solvent in gelation by examining the changes in dissolution parameters as a function of solvent identity. Because solvent-dependent

gelations are commonly observed yet poorly understood, these solvent-solute relationships will be the subject of further study using the approach described herein.

References:

(1) (a) Smith, D. K. Molecular Gels-Nanostructured Soft Materials. In *Organic Nanostructures*; Steed, J. W., Atwood, J. L., Eds.; Wiley-VCH: Weinheim, 2008; pp 111-154. (b) *Molecular Gels: Materials with Self-Assembled Fibrillar Networks*; Weiss, R. G., Terech, P., Eds.; Springer: Dordrecht, The Netherlands, 2006. (c) *Low Molecular Mass Gelators*; Fages, F., Ed.; Topics in Current Chemistry Vol. 256; Springer: Berlin, Heidelberg, 2005.

(2) For recent reviews, see: (a) Piepenbrock, M.-O. M.; Lloyd, G. O.; Clarke, N.; Steed, J. W. *Chem. Rev.* **2010**, *110*, 1960-2004. (b) Banerjee, S.; Das, R. K.; Maitra, U. *J. Mater. Chem.* **2009**, *19*, 6649-6687. (c) Hirst, A. R.; Escuder, B.; Miravet, J. F.; Smith, D. K. *Angew. Chem., Int. Ed.* **2008**, *47*, 8002-8018. (d) Sangeetha, N. M.; Maitra, U. *Chem. Soc. Rev.* **2005**, *34*, 821-836. (e) de Loos, M.; Feringa, B. L.; van Esch, J. H. *Eur. J. Org. Chem.* **2005**, 3615-3631. (f) Estroff, L. A.; Hamilton, A. D. *Chem. Rev.* **2004**, *104*, 1201-1217.

(3) For a recent perspective, see: Stupp, S. I. *Nano Lett.* **2010**, *10*, 4783-4786.

(4) For a recent review, see: Cui, H.; Webber, M. J.; Stupp, S. I. *Biopolymers* **2010**, *94*, 1-18. See also refs 20, 21, and 22.

(5) For recent examples, see: (a) Das, R. K.; Bhat, S.; Banerjee, S.; Aymonier, C.; Loppinet-Serani, A.; Terech, P.; Maitra, U.; Raffy, G.; Desvergne, J.-P.; Del Guerso, A. *J. Mater. Chem.* **2011**, *21*, 2740-2750. (b) Tsai, W.-W.; Tevis, I. D.; Tayi, A. S.; Cui, H.; Stupp, S. I. *J. Phys. Chem. B* **2010**, *114*, 14778-14786. (c) Coates, I. A.; Smith, D. K. *J. Mater. Chem.* **2010**, *20*, 6696-6702. (d) Vadehra, G. S.; Wall, B. D.; Diegelmann, S. R.; Tovar, J. D. *Chem. Commun.* **2010**, *46*, 3947-3949. (e) Dutta, S.; Das, D.; Dasgupta, A.; Das, P. K. *Chem.-Eur. J.* **2010**, *16*, 1493-1505. (f) Jiang, J.; Wang, T.; Liu, M. *Chem. Commun.* **2010**, *46*, 7178-7180. (g) Adhikari, B.; Banerjee, A. *Chem.-Eur. J.* **2010**, *16*, 13698-13705.

(6) For recent examples of molecular gel-based sensors, see: (a) Kim, T. H.; Kim, D. G.; Lee, M.; Lee, T. S. *Tetrahedron* **2010**, *66*, 1667-1672. (b) Chen, J.; McNeil, A. J. *J. Am. Soc. Chem.* **2008**, *130*, 16496-16497.

(7) For recent examples of molecular gel-based remediation methods, see: (a) King, K. N.; McNeil, A. J. *Chem. Commun.* **2010**, *46*, 3511-3513. (b) Adhikari, B.; Palui, G.; Banerjee, A. *Soft Matter* **2009**, *5*, 3452-3460. (c) Bardelang, D.; Camerel, F.; Margeson, J. C.; Leek, D. M.; Schmutz, M.; Zaman, Md. B.; Yu, K.; Soldatov, D. V.; Ziessel, R.; Ratcliffe, C. I.; Ripmeester, J. A. *J. Am. Soc. Chem.* **2008**, *130*, 3313-3315.

(8) For example, seemingly minor structural changes can convert gelators into nongelators. For reference, see: (a) Ma, M.; Kuang, Y.; Gao, Y.; Zhang, Y.; Gao, P.; Xu, B. *J. Am. Chem. Soc.* **2010**, *132*, 2719-2728. (b) Karthik Kumar, K.; Elango, M.; Subramanian, V.; Mohan Das, T. *New J. Chem.* **2009**, *33*, 1570-

1577. (c) de Loos, M.; van Esch, J. H.; Kellogg, R. M.; Feringa, B. L. *Tetrahedron* **2007**, *63*, 7285-7301. (d) Menger, F. M.; Caran, K. L. *J. Am. Chem. Soc.* **2000**, *122*, 11679-11691. (e) Garner, C. M.; Terech, P.; Allegraud, J.-J.; Mistrot, B.; Nguyen, P.; deGeyer, A.; Rivera, D. *J. Chem. Soc., Faraday Trans.* **1998**, *94*, 2173-2179.

(9) Hanabusa, K.; Yamada, M.; Kimura, M.; Shirai, H. *Angew. Chem., Int. Ed.* **1996**, *35*, 1949-1951.

(10) The crystal engineering approach has been used by Dastidar et al. to identify new organic salt-based gelators. For a recent review, see: Dastidar, P. *Chem. Soc. Rev.* **2008**, *37*, 2699-2715. For a more general review on crystal engineering, see: Desiraju, G. R. *Angew. Chem., Int. Ed.* **2007**, *46*, 8342-8356.

(11) For a recent perspective, see: van Esch, J. H. *Langmuir* **2009**, *25*, 8392-8394.

(12) Adams, D. J.; Morris, K.; Chen, L.; Serpell, L. C.; Bacsá, J.; Day, G. M. *Soft Matter* **2010**, *6*, 4144-4156.

(13) Gronwald, O.; Sakurai, K.; Luboradzki, R.; Kimura, T.; Shinkai, S. *Carbohydr. Res.* **2001**, *331*, 307-318.

(14) Chen, J.; Kampf, J. W.; McNeil, A. J. *Langmuir* **2010**, *26*, 13076-13080.

(15) For recent reviews, see: (a) Truong, W. T.; Su, Y.; Meijer, J. T.; Thordarson, P.; Braet, F. *Chem.-Asian J.* **2011**, *6*, 30-42. (b) Adams, D. J. *Macromol. Biosci.* **2011**, *11*, 160-173. (c) Zhang, Y.; Kuang, Y.; Gao, Y.; Xu, B. *Langmuir* **2011**, *27*, 529-537. (d) Adams, D. J.; Topham, P. D. *Soft Matter* **2010**, *6*, 3707-3721. (e) Jung, J. P.; Gasiórowski, J. Z.; Collier, J. H. *Biopolymers* **2010**, *94*, 49-59. (f) Yang, Y.; Khoe, U.; Wang, X.; Horii, A.; Yokoi, H.; Zhang, S. *Nano Today* **2009**, *4*, 193-210. (g) Xu, B. *Langmuir* **2009**, *25*, 8375-8377. (h) Suzuki, M.; Hanabusa, K. *Chem. Soc. Rev.* **2009**, *38*, 967-975. (i) Higashi, N.; Koga, T. *Adv. Polym. Sci.* **2008**, *219*, 27-68. (j) Ulijn, R. V.; Smith, A. M. *Chem. Soc. Rev.* **2008**, *37*, 664-675.

(16) For examples of naphthalene-derivatized dipeptide gelators, see: (a) Chen, L.; Revel, S.; Morris, K.; Serpell, L. C.; Adams, D. J. *Langmuir* **2010**, *26*, 13466-13471. (b) Chen, L.; Morris, K.; Laybourn, A.; Elias, D.; Hicks, M. R.; Rodger, A.; Serpell, L.; Adams, D. J. *Langmuir* **2010**, *26*, 5232-5242. (c) Chen, L.; Revel, S.; Morris, K.; Adams, D. J. *Chem. Commun.* **2010**, *46*, 4267-4269. (d) Liang, G.; Yang, Z.; Zhang, R.; Li, L.; Fan, Y.; Kuang, Y.; Gao, Y.; Wang, T.; Lu, W. W.; Xu, B. *Langmuir* **2009**, *25*, 8419-8422. (e) Yang, Z.; Ho, P.-L.; Liang, G.; Chow, K.H.; Wang, Q.; Cao, Y.; Guo, Z.; Xu, B. *J. Am. Chem. Soc.* **2007**, *129*, 266-267. (f) Yang, Z.; Liang, G.; Xu, B. *Chem. Commun.* **2006**, 738-740. (g) See also ref 23.

(17) For recent examples of structure-property relationships amongst peptide gelators, see: (a) Cheng, G.; Castelletto, V.; Moulton, C. M.; Newby, G. E.; Hamley, I. W. *Langmuir* **2010**, *26*, 4990–4998. (b) Ma, M.; Kuang, Y.; Gao, Y.; Zhang, Y.; Gao, P.; Xu, B. *J. Am. Chem. Soc.* **2010**, *132*, 2719–2728. (c) Pashuck, E. T.; Cui, H.; Stupp, S. I. *J. Am. Chem. Soc.* **2010**, *132*, 6041–6046. (d) Ryan, D. M.; Anderson, S. B.; Nilsson, B. L. *Soft Matter* **2010**, *6*, 3220–3231. (e) Ryan, D. M.; Anderson, S. B.; Senguen, F. T.; Youngman, R. E.; Nilsson, B. L. *Soft Matter* **2010**, *6*, 475–479. (f) Niece, K. L.; Czeisler, C.; Sahni, V.; Tysseling-Mattiace, V.; Pashuck, E. T.; Kessler, J. A.; Stupp, S. I. *Biomaterials* **2008**, *29*, 4501–4509. (g) Mitra, R. N.; Das, D.; Roy, S.; Das, P. K. *J. Phys. Chem. B* **2007**, *111*, 14107–14113.

(18) For recent examples of structure-property relationships amongst nonpeptidic gelators, see: (a) Liu, J.-W.; Ma, J.-T.; Chen, C.-F. *Tetrahedron* **2011**, *67*, 85–91. (b) Baddeley, C.; Yan, Z.; King, G.; Woodward, P. M.; Badjic, J. D. *J. Org. Chem.* **2007**, *72*, 7370–7278. (c) See also refs 8 and 14.

(19) Adams and co-workers have suggested that gelation properties of fluorenyl- and naphthyl-peptides correlate with hydrophobicity. For reference, see: (a) Adams, D. J.; Mullen, L. M.; Berta, M.; Chen, L.; Frith, W. J. *Soft Matter* **2010**, *6*, 1971–1980. (b) See also ref 16a.

(20) For recent examples, see: (a) Panda, J. J.; Dua, R.; Mishra, A.; Mitra, B.; Chauhan, V. S. *ACS Appl. Mater. Interfaces* **2010**, *2*, 2839–2848. (b) Galler, K. M.; Aulisa, L.; Regan, K. R.; D'Souza, R. N.; Hartgerink, J. D. *J. Am. Chem. Soc.* **2010**, *132*, 3217–3223. (c) Zhou, M.; Smith, A. M.; Das, A. K.; Hodson, N. W.; Collins, R. F.; Ulijn, R. V.; Gough, J. E. *Biomaterials* **2009**, *30*, 2523–2530. (d) Jayawarna, V.; Richardson, S. M.; Hirst, A. R.; Hodson, N. W.; Saiani, A.; Gough, J. E.; Ulijn, R. V. *Acta Biomater.* **2009**, *5*, 934–943. (e) Banwell, E. F.; Abelardo, E. S.; Adams, D. J.; Birchall, M. A.; Corrigan, A.; Donald, A. M.; Kirkland, M.; Serpell, L. C.; Butler, M. F.; Woolfson, D. N. *Nat. Mater.* **2009**, *8*, 596–600.

(21) For recent examples, see: (a) Wang, H.; Yang, C.; Wang, L.; Kong, D.; Zhang, Y.; Yang, Z. *Chem. Commun.* **2011**, *47*, 4439–4441. (b) Li, X.; Li, J.; Gao, Y.; Kuang, Y.; Shi, J.; Xu, B. *J. Am. Chem. Soc.* **2010**, *132*, 17707–17709. (c) Zhao, Y.; Tanaka, M.; Kinoshita, T.; Higuchi, M.; Tan, T. *J. Controlled Release* **2010**, *147*, 392–399. (d) Naskar, J.; Palui, G.; Banerjee, A. *J. Phys. Chem. B* **2009**, *113*, 11787–11792. (e) Gao, Y.; Kuang, Y.; Guo, Z.-F.; Guo, Z.; Krauss, I. J.; Xu, B. *J. Am. Chem. Soc.* **2009**, *131*, 13576–13577. (f) Kim, J.-K.; Anderson, J.; Jun, H.-W.; Repka, M. A.; Jo, S. *Mol. Pharmaceutics* **2009**, *6*, 978–985. (g) Zhao, F.; Ma, M. L.; Xu, B. *Chem. Soc. Rev.* **2009**, *38*, 883–891.

(22) For recent examples, see: (a) Chow, L. W.; Bitton, R.; Webber, M. J.; Carvajal, D.; Shull, K. R.; Sharma, A. K.; Stupp, S. I. *Biomaterials* **2011**, *32*, 1574–1582. (b) Huang, Z.; Newcomb, C. J.; Bringas, P., Jr.; Stupp, S. I.; Snead, M. L. *Biomaterials* **2010**, *31*, 9202–9211. (c) Webber, M. J.; Kessler, J. A.; Stupp,

S. I. *J. Intern. Med.* **2010**, *267*, 71–88. (d) Chow, L. W.; Wang, L.-J.; Kaufman, D. B.; Stupp, S. I. *Biomaterials* **2010**, *31*, 6154–6161. (e) Shah, R. N.; Shah, N. A.; Lim, M. M. D.; Hsieh, C.; Nuber, G.; Stupp, S. I. *Proc. Natl. Acad. Sci. U.S.A.* **2010**, *107*, 3293–3298. (f) Mata, A.; Geng, Y.; Henrikson, K. J.; Aparicio, C.; Stock, S. R.; Satcher, R. L.; Stupp, S. I. *Biomaterials* **2010**, *31*, 6004–6012.

(23) Yang, Z.; Liang, G.; Ma, M.; Gao, Y.; Xu, B. *J. Mater. Chem.* **2007**, *17*, 850–854.

(24) Both the absolute pH and the rate of change in pH have been demonstrated to influence the resulting gel properties. For examples, see: (a) Tang, C.; Smith, A. M.; Collins, R. F.; Ulijn, R. V.; Saiani, A. *Langmuir* **2009**, *25*, 9447–9453. (b) Adams, D. J.; Butler, M. F.; Frith, W. J.; Kirkland, M.; Mullen, L.; Sanderson, P. *Soft Matter* **2009**, *5*, 1856–1862. (c) See also ref 16b.

(25) Note that these compounds were screened for gelation at concentrations that are significantly higher than their room temperature solubilities. As a result, all of the nongelators resulted in some form of precipitation.

(26) (a) Mullin, J. W. Solutions and Solubility. *Crystallization*, 3rd ed.; Butterworth-Heinemann: Oxford, 1992; pp 81-127. (b) Beiny, D. H. M.; Mullin, J. W. *J. Chem. Eng. Data* **1987**, *32*, 9-10.

(27) Note that the mixture remained heterogeneous during this transformation (Form I → Form II).

(28) (a) Solvent-dependent melting enthalpies were observed for bisamide- and bisurea-based gels; see: Zweep, N.; Hopkinson, A.; Meetsma, A.; Browne, W. R.; Feringa, B. L.; van Esch, J. H. *Langmuir* **2009**, *25*, 8802–8809. (b) Solvent-independent melting enthalpies were observed for cholesterol-based gels; see: Murata, K.; Aoki, M.; Suzuki, T.; Harada, T.; Kawabata, H.; Komori, T.; Ohseto, F.; Ueda, K.; Shinkai, S. *J. Am. Chem. Soc.* **1994**, *116*, 6664–6676.

(29) Raynal, M.; Bouteiller, L. *Chem. Commun.* **2011**, *47*, 8271–8273.

(30) Hirst, A. R.; Smith, D. K. *Langmuir* **2004**, *20*, 10851–10857.

(31) Hirst, A. R.; Coates, I. A.; Boucheteau, T. R.; Miravet, J. F.; Escuder, B.; Castelletto, V.; Hamley, I. W.; Smith, D. K. *J. Am. Chem. Soc.* **2008**, *130*, 9113–9121.

Chapter 5⁴

Detecting a Peroxide-based Explosive via Molecular Gelation

The continued safety of civilian and military personnel requires methods for on-site explosives detection. Existing methods range from those based on high-end instrumentation, which provide both accuracy and sensitivity, to those without instrumentation, which are portable but less accurate and less sensitive.¹ The ideal method depends on both the location, method of sampling, and sense of urgency.

Triacetone triperoxide (TATP) is a peroxide-based explosive that is easily accessible due to its facile synthesis from commercially available reagents (i.e., acetone, hydrogen peroxide, and acid). As a consequence, several recent terrorist plots have relied on TATP.² Portable TATP sensors have been developed and a few are commercialized.³ Several of these methods rely on spectrometers to detect changes in absorption or emission spectra of dyes, and most methods involve time-intensive sample pre-treatment to convert TATP into more reactive components. Suslick and co-workers recently reported a colorimetric array-based sensor for detecting TATP vapours that utilizes an in-line acid catalyst for decomposition and a flatbed scanner for analysis.⁴ The system has both a fast response time and the ability to discriminate TATP from other common oxidants. Several methods based on visual detection have also been reported. For example, Finney and Malashikhin detected TATP based on an increase in fluorescence of a dye (with UV illumination) that is observable with the naked eye.⁵ We describe herein an alternative instrument-free approach, wherein the presence of TATP triggers a solution-to-gel phase transition.

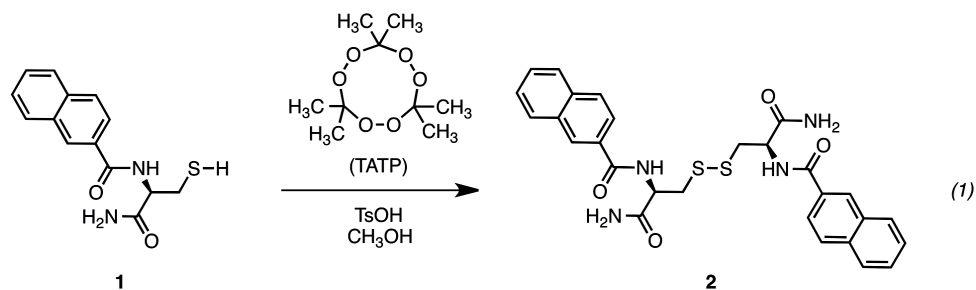
Gel-based sensors provide an unambiguous visual change in the material's

⁴ Reproduced in part from Chen, J.; Wu, W.; McNeil, A. J. submitted, 2012

physical properties and, in contrast to colorimetric and fluorescent sensors, there is no interference from opaque or colored samples. The detection process typically involves an analyte-triggered chemical reaction, which converts a nongelator into a gelator, followed by gel formation. Response times can vary from seconds to minutes depending on the analyte concentration as well as the rate of the chemical reaction. To date, we have developed gelation-based sensors for nitric oxide,^{6a} Hg²⁺ ions,^{6b} and several proteases.^{6c}

A gelation-based sensor requires three components: (1) a nongelling reactant, (2) a gelling product, and (3) an analyte-mediated chemical reaction to convert the reactant into product.

We initially selected L-cysteine derivative **1** (a nongelator) as reactant based on the known peroxide-induced thiol-to-disulfide reaction as well as the reported gelation ability of disulfide **2** (eq 1).⁷ Disulfide-based gelators were first reported in 1892⁸ and were more recently studied by Menger⁷ and Bradley.^{9,10} Disulfide **2** has one of the lowest critical gel concentrations (cgc) known for small molecules (0.25 mM in 25/75 DMSO/H₂O), and it forms gels in a variety of organic solvents. A low cgc is important for sensing because in many cases the analyte is a stoichiometric reagent in the chemical transformation. As a result, sensors based on gelators with lower cgc will detect lower analyte concentrations.



Thiol **1** and disulfide **2** were synthesized from commercially available L-cysteine methyl ester (Appendix 4). No reaction was observed when thiol **1** was treated directly with TATP. To generate a stronger oxidant, the TATP was first treated with *p*-toluenesulfonic acid (TsOH) in methanol (MeOH) to presumably generate H₂O₂ and acetone in situ from the degradation of TATP.¹¹ This mixture was then added to thiol **1** and a gel was observed within 30 min (Figure 5.1). It is important to note that no gel was observed without TATP, indicating a negligible

background rate of oxidation (Appendix 4).¹² Based on these promising initial results, the system was further optimized to develop a gelation-based sensor with an even lower detection limit and faster response time.

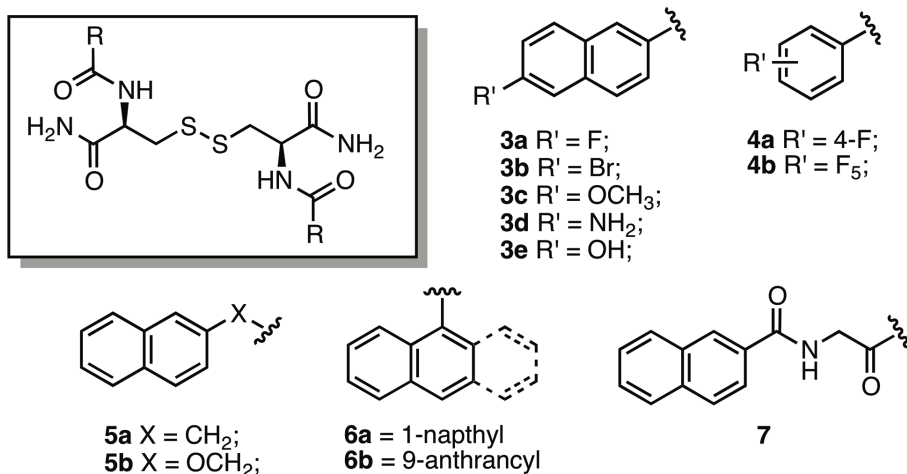


Figure 5.1. A gel forms within 30 min of adding TATP (2.5 mg) to a vial containing thiol **1** (36 mM) and TsOH (1.3 M) in MeOH.

One approach to lowering the detection limit is to modify the structure of disulfide **2** to identify an alternative gelator with a lower cgc (Appendix 4). (Note that the cgc of **2** is 4.5 mM in MeOH.) Because of the largely unpredictable relationship between structure and gelation ability,¹³ several different approaches were investigated. For example, previous studies of peptide- and disulfide-based gelators have shown improvements in cgc with halogen substitution and attributed these results to increased hydrophobicity.^{9,14} In this case, however, halogenated disulfides **3a** and **4a** exhibited higher cgcs (6.5 mM and 25 mM, respectively) than disulfide **2** while both **3b** and **4b** were nongelators. Electron-donating substituents were also added at the 6-position to enhance the intermolecular interactions but none of these compounds (**3c-3e**) formed gels under these conditions. Because π -stacking was suggested to be important in the self-assembly of these disulfide-based gelators,⁷ compounds **5a-5b** and **6a-6b** were synthesized and screened for gelation. Extending the linker length in **5a** led to a nongelator, as did changing the point of attachment (**6a**) and extending the aromatic unit (**6b**). In contrast, using the larger linker (**5b**) led to a gelator, albeit with a higher cgc (8.5 mM). Because intermolecular H-bonding is also suggested to drive the self-assembly of these disulfides,⁷ a glycine residue was inserted between the naphthyl and amide residues (**7**). This amino acid-based compound did not form gels under these conditions. Overall, these results highlight the challenges involved in the design and discovery of new gelators.¹³ In total, three new gelators were discovered through these efforts.¹⁵ Among all the

compounds synthesized, the original disulfide (**2**) remained the best gelator for the TATP sensor because it had the lowest cgc in MeOH. Thus, further optimizations were performed using disulfide **2**.

Chart 5.1 Molecular structure of cystine derivatives **3-7**.



To decrease the response time, the TATP degradation and thiol oxidation reaction rates were independently optimized. Rate studies were first performed on the TsOH-mediated decomposition of TATP. As noted above, the main decomposition products have been suggested to be H₂O₂ and acetone.¹¹ To provide support for this proposal, the degradation reaction was performed in the presence of 2,4-dinitrophenyl hydrazine, which reacts with any acetone present to form a hydrazone.¹⁶ Approximately 30% of the expected acetone was trapped as hydrazone (Appendix 4). Based on the mechanism of acetone formation, this result suggests that H₂O₂ is also generated during this reaction. Rate studies revealed a fractional order (0.7) dependence on [TsOH] for the TATP degradation (Appendix 4). Rate studies were then performed on the H₂O₂-mediated oxidation of thiol **1**, which revealed an approximate first-order dependence on [H₂O₂] (Appendix 4). Combined, these results suggest that increasing the rate of TATP degradation (by increasing the [TsOH]) will increase both the oxidation and gelation rates. However, a background reaction involving esterification of the amide in **2** became significant at higher TsOH concentrations

(Appendix 4). The optimized TsOH concentration was empirically determined to be 36 equivalents relative to thiol **1** (Appendix 4).¹⁷

To lower the detection limit, we investigated the impact of decreasing the reaction volume. A decrease in reaction volume will decrease the quantity of TATP required to form a gel based on the reaction stoichiometry. For example, while 20 mg of TATP is required to gel a 4 mL solution of **1** (36 mM in MeOH), only 2 mg of TATP is required to gel a 0.4 mL of the same solution. A further decrease in detection limit can be obtained by decreasing the diameter of the container while keeping the overall volume constant. This effect is attributed to an increase in the surface area, which increases the interactions of the solvent and gel fibers with the container walls.¹⁹ As evidence, the cgc of **2** decreases from 4.6 mM in a 13 mm inner diameter vial to 2.0 mM in 4.6 mm inner diameter vial using 0.5 mL of MeOH.

Using all of these optimized conditions, a simple one-pot method was developed. Specifically, **1** (36 mM), TsOH (1.3 M) and TATP (1.5 mg) were pre-mixed and then transferred to a small tube, where gelation was observed within 8 min (Figure 5.2).¹² Note that faster response times can be obtained with higher concentrations of TATP. For example, gelation occurs within 2 min when 12 mg of TATP is added (Appendix 4). Overall, this method is convenient and simple to use and interpret.

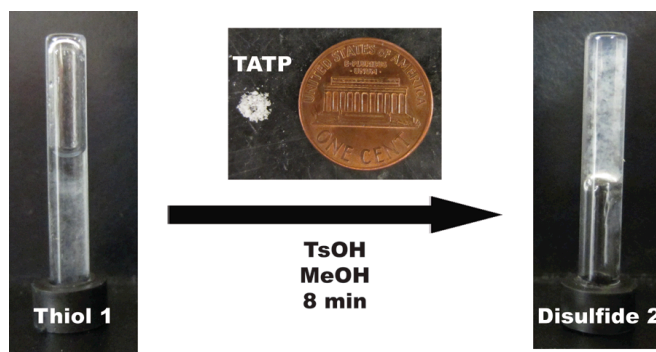


Figure 5.2. Gel formation is observed within 8 min of mixing **1** (36 mM), TsOH (1.3 M) and TATP (1.5 mg) in MeOH.

Similar to most portable TATP sensors, this gel-based sensor is also sensitive to other hydrogen-based peroxides and strong oxidants such as bleach, Cr³⁺,

Cr^{6+} and peracetic acid (Appendix 4). Fortunately, none of these oxidants have a similar white powder appearance to TATP and can therefore be distinguished. In addition, oxidants with similar white powder formulations, such as potassium iodide, potassium chlorate and benzyl peroxide do not trigger gelation even under acidic conditions (Appendix 4).

In summary, a convenient and portable gel-based sensor for detecting mg quantities of solid TATP is reported. Given that hundreds of grams of TATP are used in improvised explosive devices, milligram-sized samples should be readily accessible. The sensor is based on a TATP-triggered gelation via a thiol-to-disulfide oxidation reaction. Although modifying the original structure did not produce a better gelator, optimizing the oxidation and gelation rates, as well as the reaction volume and container size improved both the detection limit and response times. Overall, we believe that this sensor is complimentary to the traditional colorimetric and fluorescent approaches used in TATP detection, with the added advantages of unambiguous signal read-out and no instrumentation needed.

References:

(1) For recent reviews, see: (a) Salinas, Y.; Martínez-Máñez, R.; Marcos, M. D.; Sancenón, F.; Costero, A. M.; Parra, M.; Gil, S. *Chem. Soc. Rev.* **2012**, *41*, 1261-1296. (b) Mäkinen, M.; Nousiainen, M.; Sillanpää, M. *Mass Spec. Rev.* **2011**, *30*, 940-973. (c) Germain, M. E.; Knapp, M. J. *Chem. Soc. Rev.* **2009**, *38*, 2543-2555. (d) Singh, S. *J. Hazard. Mater.* **2007**, *144*, 15-28. (e) Moore, D. S. *Rev. Sci. Instrum.* **2004**, *75*, 2499-2512.

(2) M. Jacoby, *Chem. Eng. News* **2009**, *87* (22), 10-13.

(3) For reviews on sensing peroxide-based explosives, see: (a) Burks, R. M.; Hage, D. S. *Anal. Bioanal. Chem.* **2009**, *395*, 301-313. (b) Schulte-Ladbeck, R.; Vogel, M.; Karst, U. *Anal. Bioanal. Chem.* **2006**, *386*, 559-565.

(4) Lin, H.; Suslick, K. S. *J. Am. Chem. Soc.* **2010**, *132*, 15519-15521. See also: Lin, H.; Jang, M.; Suslick, K. S. *J. Am. Chem. Soc.* **2011**, *133*, 16786-16789.

(5) Malashikhin, S.; Finney, N. S. *J. Am. Chem. Soc.* **2008**, *130*, 12846-12847.

(6) (a) Chen, J.; McNeil, A. J. *J. Am. Chem. Soc.* **2008**, *130*, 16496-16497. (b) King, K. N.; McNeil, A. J. *Chem. Commun.* **2010**, *46*, 3511-3513. (c) Bremmer, S. C.; Chen, J.; McNeil, A. J.; Soellner, M. B. *Chem. Commun.* **2012**, *48*, 5482-5484.

(7) (a) Menger, F. M.; Caran, K. L. *J. Am. Chem. Soc.* **2000**, *122*, 11679-11691. (b) Menger, F. M.; Yamasaki, Y.; Catlin, K. K.; Nishimi, T. *Angew. Chem. Int. Ed.* **1995**, *34*, 585-586. (c) Menger, F. M.; Venkatasubban, K. S. *J. Org. Chem.* **1978**, *43*, 3413-3414.

(8) Brenzinger, K. *Zeitsch. Physiol. Chem.* **1892**, *16*, 552-588. See also: (a) Gortner, R. A.; Hoffman, W. F. *J. Am. Chem. Soc.* **1921**, *43*, 2199-2202. (b) Wolf, C. G. L.; Rideal, E. K. *Biochem. J.* **1922**, *16*, 548-555.

(9) Matteucci, M.; Bhalay, G.; Bradley, M. *J. Peptide Sci.* **2004**, *10*, 318-325.

(10) For examples of other disulfide-based gelators, see (a) Milanese, L.; Hunter, C. A.; Tzokova, N.; Waltho, J. P.; Tomas, S. *Chem. Eur. J.* **2011**, *17*, 9753-9761. (b) Lyon, R. P.; Atkins, W. M. *J. Am. Chem. Soc.* **2001**, *123*, 4408-4413.

(11) Armitt, D.; Zimmermann, P.; Ellis-Steinborner, S. *Rapid Commun. Mass Spectrom.* **2008**, *22*, 950-958.

(12) Although thiol **1** is stable for months in the solid-state under ambient conditions, it slowly undergoes oxidation to disulfide **2** in MeOH over time (e.g., 35% conversion after 21 days). When TsOH is present, a competing esterification reaction occurs (see Appendix 4).

(13) Although the rational design of gelators remains a challenge, some of the key factors relevant to gelation are being uncovered. For recent examples, see: (a) Xu, H.; Song, J.; Tian, T.; Feng, R. *Soft Matter* **2012**, *8*, 3478-3486. (b) Raynal, M.; Bouteiller, L. *Chem. Commun.* **2011**, *47*, 8271-8273. (c) Muro-Small, M. L.; Chen, J.; McNeil, A. J. *Langmuir* **2011**, *27*, 13248-13253. (d) Chen, J.; Kampf, J. W.; McNeil, A. J. *Langmuir* **2010**, *26*, 13076-13080. (e) Hirst, A. R.; Smith, D. K. *Langmuir* **2004**, *20*, 10851-10857.

(14) For recent examples of halogenated peptide-based gelators, see: (a) Ryan, D. M.; Anderson, S. B.; Nilsson, B. L. *Soft Matter* **2010**, *6*, 3220-3231. (b) Ryan, D. M.; Anderson, S. B.; Senguen, F. T.; Youngman, R. E.; Nilsson, B. L. *Soft Matter* **2010**, *6*, 475-479.

(15) Elucidation the origin of these structure-property relationships was difficult because X-ray quality single-crystals could not be obtained for any of these compounds.

(16) For a recent review, see: Uchiyama, S.; Inada, Y.; Kunugita, N. *J. Chromatogr., B.* **2011**, *879*, 1282-1289. See also: (a) Allen, C. F. H. *J. Am. Chem. Soc.* **1930**, *52*, 2955-2959. (b) Brady, O. L. *J. Chem. Soc.* **1931**, 756-759.

(17) Under these conditions, disulfide **2** undergoes esterification over the course of 3 d (see Appendix 4).

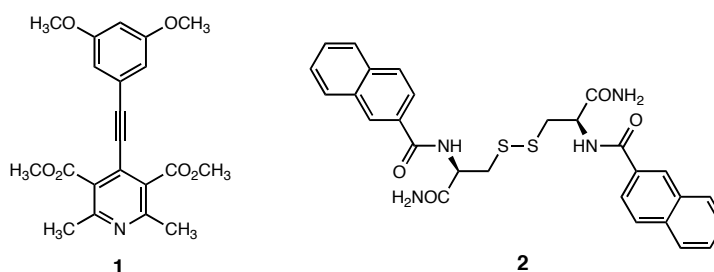
(18) S. R. Raghavan and B. H. Cipriano, Gel Formation: Phase Diagram Using Tabletop Rheology and Calorimetry. In *Molecular Gels: Materials with Self-Assembled Fibrillar Network*, R. G. Weiss and P. Terech, Eds., Springer: The Netherlands, 2006; 241-252.

Chapter 6

Development of Quantitative Gel-Based Sensors

The nitric oxide and TATP gel-based sensors described in Chapter 2 and Chapter 5 are qualitative sensors that can only indicate if an analyte is present or absent. Although convenient to use, these qualitative sensors lack the ability to distinguish different analyte concentrations. Moreover, the detection limit of a qualitative gel-based sensor is determined by gelator's critical gelation concentration (cgc). A threshold of analyte concentration can be determined only when a stable gel is formed. In contrast, quantitative gel-based sensor can potentially detect lower analyte concentrations when an unstable gel or viscous solution is formed. The main challenge in the development of quantitative gel-based sensor is to find a suitable method to correlate gel properties with analyte concentrations. In this chapter, measurements of gel viscosity on a rheometer, a micro-rheometer, piezoelectric sensors and a magnetoelastic sensor will be discussed.

Chart 6.1 Molecular structure of gelator **1** and **2**.



Elastic modulus (G') is often used to describe a gel's mechanical toughness. A stiffer gel (i.e., at higher gelator concentration) will have a higher elastic modulus. Besides elastic modulus, gel viscosity could also be an indicator for the mechanical property of a gel. Based on the observation that gels with higher

elastic modulus are more viscous and less likely to flow, we hypothesized that gel viscosity is proportional to the gel modulus.

Analogous to a quantitative colorimetric sensor, where the absorbance correlates to analyte concentration and can be quantified via a spectrophotometer, we hypothesized that in a gel-based sensor, gelation time and the elastic modulus (G') of the gel may correlate to the gelator (analyte) concentration. Preliminary data of gel modulus/gelation time versus gelator concentrations were obtained on a rheometer¹ using pyridine gelator **1** (Figure 6.1). Gels formed at higher gelator concentrations did show higher modulus (G') and required less gelation times (Figure 6.1B). Although these preliminary results are promising, a rheometer is a large and expensive instrument and requires time-intensive sample preparation, and is therefore not suitable as a portable gel-based sensor.

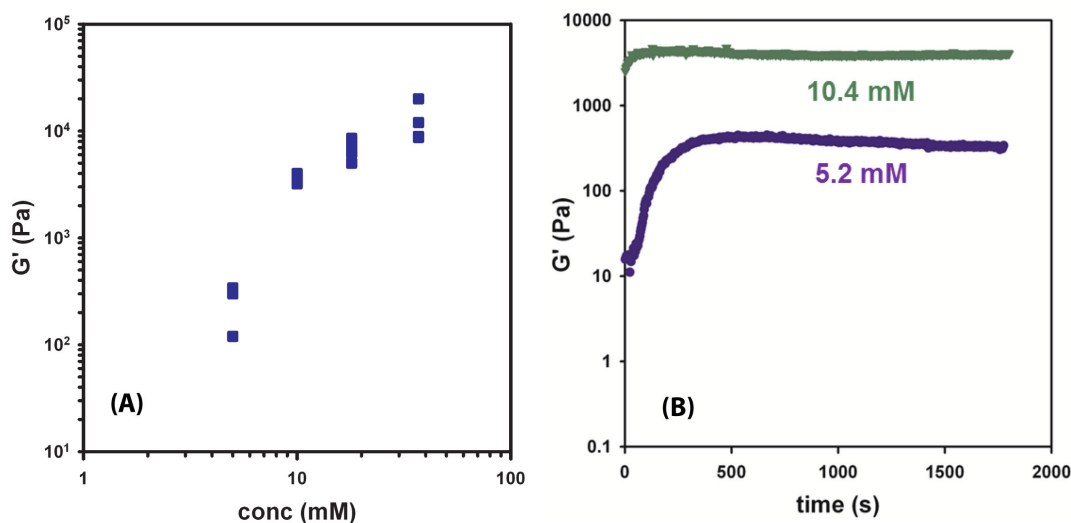


Figure 6.1. Plot of (A) elastic modulus (G') versus gelator concentration; (B) Plot of elastic modulus (G') versus time during gelation.

One alternative to a conventional rheometer is to utilize micro-rheology. Several micro-rheological techniques (e.g., sonorheometry,² magnetic micro-rheology³) have been previously reported as viscosity and chemical sensors.⁴ In

collaboration with Prof. Raoul Kopelman and Ariel Hecht (UM, Chemistry), magnetic micro-rheology was used to measure viscosity in gels. The specific micro-rheology set-up involved three components: (1) magnetic micro-beads that have an average size of $\sim 10 \mu\text{m}$; (2) a magnetic field to induce rotation of beads; and (3) an optical microscope coupled to a charge-coupled device (CCD) to monitor the bead motions. The rotation of the magnetic particle is highly sensitive to the medium viscosity: the more viscous the system is, the more slowly the particles rotate.⁴ Therefore, we expected a drastic decrease in rotation speed when the sample transforms from solution-to-gel.

To perform micro-rheology on a gel sample, a small portion of micro-bead-doped gel of **1** in 1/1 DMSO/H₂O was transferred to a glass slide and the rotation of magnetic beads was monitored under the microscope. A control was performed in neat solvent (1/1 DMSO/H₂O). Surprisingly, we did not observe any differences in the rotation speed between the gel sample and the control, indicating no viscosity differences. There were two possible reasons to account for this result: (1) The destruction of the fiber network by sample handling generated large pores (significantly larger than the beads) between gel fibers, therefore the bead motions were only affected by the viscosity of solvent trapped within the loose fibers. Unfortunately, monitoring the micro-beads rotation directly from an intact gel was unsuccessful due to the opacity of sample. (2) The size of mesh in the fibrous network might be too large compared to the size of the magnetic beads. To further test the feasibility of micro-rheology in gel medium, larger bead sizes should be considered.

To avoid direct visualization, a piezoelectric resonator⁵ was utilized to detect viscosity changes in the gel medium. Piezoelectric materials vibrate at their resonant frequency under an external AC circuit and the vibration is sensitive to environmental changes (e.g., temperature, humidity, viscosity and chemical additives). By correlating the vibration frequency/amplitude with medium changes, piezoelectric materials have found use in temperature, humidity, viscosity and chemical sensing.⁶ However, these materials have not been applied in a high-viscosity medium like molecular gels.

To test the feasibility of a piezoelectric resonator in gel medium, we collaborated with Prof. Khali Najafi and Jeffrey Gregory (UM, EECS) and utilized a quartz crystal tuning fork sensor to monitor gel formation. The instrumental set-up included a quartz crystal tuning fork (resonant frequency 32.7 kHz), an external driving circuit and an oscilloscope for signal read-out. The tuning fork was submerged in different samples and the damping (decrease) of frequency and amplitude was recorded. In air, the tuning fork vibrated at its resonant frequency of 32.7 kHz; when submerged in deionized (DI) H₂O, expected frequency damping (from 32.7 kHz to 29.2 kHz) and amplitude damping (from 8000 to 60) were observed together with obvious peak broadening (Figure 6.2). However, when the tuning fork was submerged in a gel of **1** in 1/1 DMSO/H₂O, a vibration signal was not observed, indicating complete damping of the resonator.

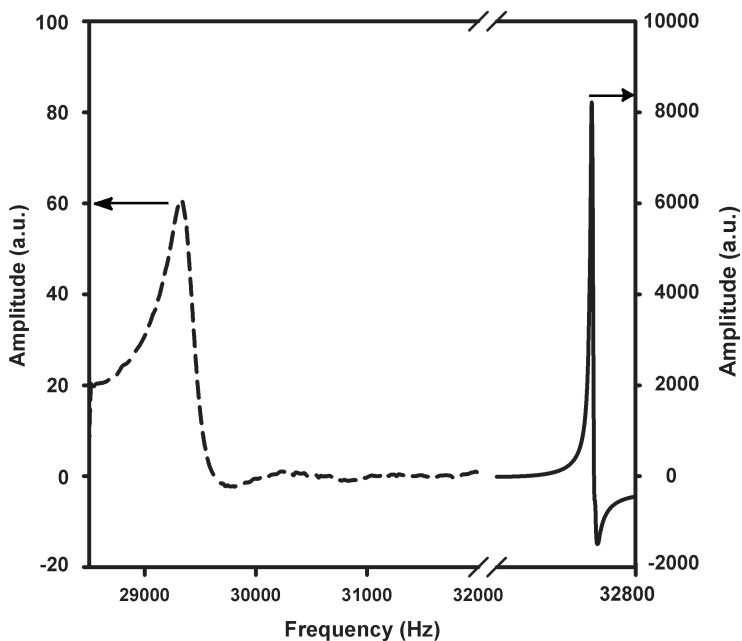


Figure 6.2. Vibration frequency and amplitude of quartz crystal tuning fork in air (solid line) and in DI H₂O (dash line).

To look for a more robust piezoelectric sensor, a disk-geometry of quartz crystal resonator (quartz crystal microbalance, QCM)⁷ was examined in gel environment. The working mechanism of a QCM is similar to that of a tuning fork. With the disk-shape resonator placed at the bottom of the sample, QCM is able

to detect changes in both viscosity and mass-loading.⁸ Using the QCM set-up in Prof. Xiangqun Zeng's laboratory (Oakland University, Chemistry), we were able to test the robustness of QCM in gel materials. We hypothesized that when gel concentration increases, a denser fiber network will deposit onto the QCM, thus more significant damping will be observed. During the measurement, an unstable gel was formed in situ by the addition of H₂O to a DMSO solution of gelator **1**. Although significant (but not complete) damping of vibration frequency upon gel formation was observed, the degree of damping was not proportional to the gel concentration (Table 6.1). We suspected that precipitate or loose gel fibers that formed at low gelation concentrations might have higher mobility and deposit faster on the sensor disk than the interweaving network formed at high concentrations. As a result, more significant damping was observed at low concentrations. Meanwhile, we also observed that at high gelator concentrations where stable gels were formed, the vibration frequency of QCM remained unchanged regardless of gel concentrations. This phenomenon might be explained by the generation of a solvent layer between the fiber network and the sensor, resulting in detection of only the liquid layer. Combined, these preliminary results suggested that the quartz crystal was not suitable for quantifying the viscosity changes in molecular gels.

Table 6.1 QCM vibration frequency shift versus gelator concentration.

<i>[1]</i> (mg/mL)	1.0	2.5	5.0	7.5
Frequency Shift (Hz)	-785	-1275	-970	-680

Our most recent quantification method has been focused on a magnetoelastic sensor. Magnetoelastic sensors vibrate at their resonant frequency under an AC magnetic field and the shift of vibration frequency can reveal environmental changes (e.g., pressure, liquid viscosity and mass-loading).⁹ The advantages of magnetoelastic sensor, compared to the piezoelectric counterpart, include facile tuning of resonant frequency, easy handling of the resonator, the flexibility of

remote sensing and most importantly, the successful demonstration as a viscosity sensor in a polymer hydrogel medium.¹⁰ In recent collaboration with Prof. Yogesh Gianchandani and Dr. Scott Green (UM, EECS), the correlation between vibration damping and gel concentrations was examined using a home-built magnetoelastic sensor. The instrumental set-up involved a magnetoelastic resonator, an external AC magnetic field generated by an AC circuit, and a signal receiver and analyzer (Figure 6.4).

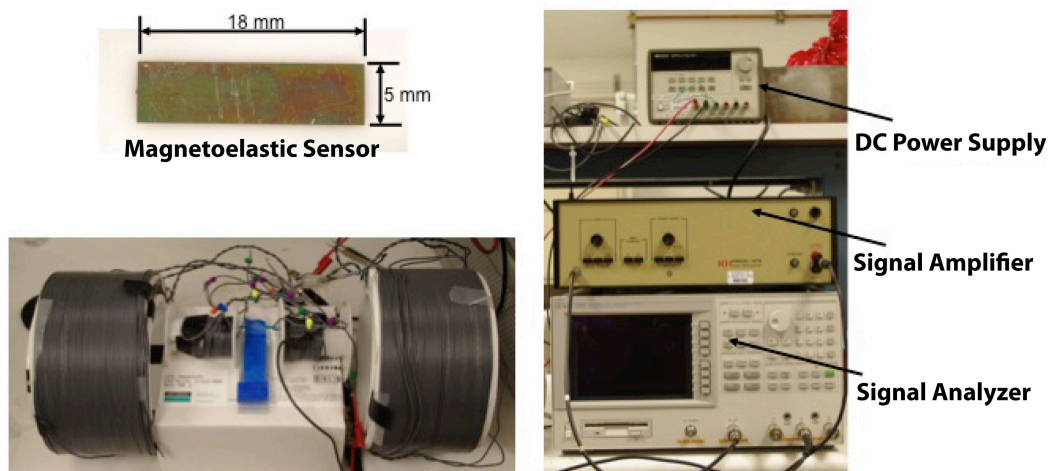


Figure 6.4 Magnetoelastic sensing system.

To test its sensitivity and robustness, a wireless magnetoelastic resonator (18 mm x 5 mm) was subjected to air, solvent and gel samples and the damping of resonant frequency was monitored. Although the vibration amplitude decreased when the resonator was moved from air to solution, the vibration frequency, a more reliable indicator for damping, remained unchanged. However, both the vibration frequency and amplitude were significantly dampened when it was submerged in a gel of **2**, demonstrating robustness for operation in gel medium. Note that the observation of damping was only observed when the resonator was incorporated in the sample prior to gel formation. When the resonator was inserted into a pre-formed gel sample, vibration damping was negligible (Table 6.1). We hypothesized that the insertion of resonator created a solvent layer between the sensor and the gel fibers, therefore it was only detecting the

viscosity of solvent. Alternatively, the insertion of the sensor could also cause mechanical breakdown the fibers, leading to the decrease of viscosity.

Table 6.2. Vibration frequency and amplitude of magnetoelastic sensor in different samples.

<i>Sample</i>	<i>Vibration Frequency, F_0 (kHz)</i>	<i>Vibration Amplitude (a.u.)</i>
Air	120.3 ± 0.3	18.5 ± 0.5
1/1 DMSO/H ₂ O	120.6 ± 0.3	11 ± 1
Suspension of 2	120.2 ± 0.1	12.3 ± 0.8
Unstable gel #1 ^a	120.3 ± 0.5	11.3 ± 0.8
Stable gel #2 ^a	118.9 ± 0.1	12.2 ± 0.6
Unstable gel #3 ^b	116.8 ± 0.6	2.3 ± 0.4

a. the sensor was inserted after gel formation; b. sensor was incorporated in the solution prior to gelation.

The correlation between vibration frequency/amplitude and gel concentrations was further investigated. To ensure damping was observed, all samples were prepared by submerging the magnetoelastic sensor in a series of DMSO solution with different concentrations of **2** and then adding H₂O to trigger gel formation. Vibration frequency and amplitude were then measured for each sample. However, a clear correlation between frequency/amplitude and gelator concentrations was not observed. Although vibration frequency initially decreased when the gelator concentration increased, the frequency gradually increased at higher gelator concentrations. We speculated that this result was due to the inconsistency in sample preparation caused by the complex gelation kinetics via the good/bad solvent approach. By switching to a more reproducible sample preparation method (i.e., heating/cooling), we observed larger damping (ΔF_0 7.9 kHz via heating/cooling versus 2.3 kHz via good/bad solvent) when gelator concentration went from 0.75 to 3.0 mg/mL. To determine if a correlation between vibration frequency/amplitude and gelator concentration exists, more data points via the heating/cooling method are needed.

Table 6.3 Vibration frequency and amplitude in gel samples with different [2] prepared via good/bad solvent or heating/cooling.

[2] (mg/mL)	<i>Good/bad solvent</i>		<i>Heating/cooling</i>	
	F ₀ (kHz)	Amplitude (a.u.)	F ₀ (kHz)	Amplitude (a.u.)
0.75	115.1 ± 0.4	9 ± 1	109.9 ± 0.1	6.9 ± 0.1
1.6	115.4 ± 0.3	16 ± 1	--	--
2.3	111.1 ± 0.1	6.2 ± 0.3	--	--
3.0	111.4 ± 0.3	6.7 ± 0.3	102.0 ± 0.2	3.1 ± 0.3
4.3	114.6 ± 0.1	8.6 ± 0.3	--	--
5.6	116.6 ± 0.5	9.1 ± 0.7	--	--

(--) indicates untested conditions.

In the future, several issues need to be addressed before a quantitative gel-based sensor is fully developed. First of all, heating/cooling is not an ideal sample preparation method because it requires an extra step for detection, rendering real-time quantification of analyte difficult. Moreover, for heat-sensitive analytes, sample preparation via heating/cooling is not feasible. Therefore, it is essential to develop reliable and in-situ sample preparation protocol by screening different good/bad solvent pairs, controlling the addition rate of bad solvent and optimizing the wait time for gelation. Secondly, examining the generality of the correlation between resonator vibration and gelator concentrations across different classes of gelators is necessary. Last but not least, the detection limit and sensitivity should be evaluated by applying quantitative gel-based sensor to the detection of analytes of interest (e.g., NO, TATP).

In conclusion, we explored a series quantification tools from conventional rheometer, micro-rheometer, piezoelectric sensors, to magnetoelastic sensor to measure changes in gel modulus/viscosity. We identified a magnetoelastic sensor as a promising lead because it demonstrated sufficient robustness and sensitivity in the gel medium. Experiments towards elucidating the correlation

between resonator vibration and gel concentrations via heating/cooling sample preparation method are ongoing in our laboratory.

References:

- (1) Adhia, Y. J.; McNeil, A. J. unpublished data.
- (2) Mauldin Jr., F. W.; Viola, F.; Hamer, T. C.; Ahmed, E. M.; Crawford, S. B.; Haverstick, D. M.; Lawrence, M. B.; Walker, W. F. *Clinica Chimica Acta* **2010**, *411*, 638-644.
- (3) Behrend, C. J.; Anker, J. N.; McNaughton, B. H.; Brasuel, M.; Philbert, M. A.; Kopelman, R. *J. Phys. Chem. B.* **2004**, *108*, 10408-10414.
- (4) Anker, J. N.; Behrend, C. J.; Huang, H.; Kopelman, R. *J. Magn. Magn. Mater.* **2005**, *293*, 655-662.
- (5) Kudo, S. *Jpn. J. Appl. Phys.* **2007**, *46*, 4704-4708.
- (6) Zhang, J.; O'Shea, S. *Sensors and Actuators B* **2003**, *94*, 65-72.
- (7) Buttry, D. A.; Ward, M. D. *Chem. Rev.* **1992**, *92*, 1355-1379.
- (8) (a) Rehman, A.; Hamilton, A.; Chung, A.; Baker, G.; Wang, Z.; Zeng, X. *Anal. Chem.* **2011**, *83*, 7823-7833. (b) Shang, Y.; Singh, P.; Chisti, M.; Mernaugh, R.; Zeng, X. *Anal. Chem.* **2011**, *83*, 8928-8936.
- (9) Grimes, C. A.; Mungle, C. S.; Zeng, K.; Jain, M. K.; Dreschel, W. R.; Paulose, M.; Ong, K. G. *Sensors* **2002**, *2*, 294-313.
- (10) Green, S. R.; Gianchandani, Y. B. *J. Micromech. Microeng.* **2010**, *20*, 075040-075052.

Chapter 7

Conclusion and Future Directions

Molecular gels have attracted broad interests in the past two decades, finding potential applications in drug delivery,¹ regenerative medicine,² tissue engineering,³ environmental remediation,⁴ catalysis,⁵ and synthesis of hybrid materials.⁶ Bio-/chemical sensing via molecular gelation is a less-explored area.⁷ Although several gel-based enzyme sensors had been developed,⁸ the sensor design strategy was limited to decreasing solubility to trigger gelation. Instead, we hypothesized that increasing intermolecular interactions can also induce gel formation. As a proof of concept, a nitric oxide (NO) gel-based sensor was successfully designed, utilizing an NO-induced nonplanar-to-planar structural change to enhance intermolecular π - π interactions and lead to gelation.⁹ Despite this new design strategy, designing gelators for specific applications still remains a challenge because gelation is difficult to predict. To elucidate the controlling factors in molecular gelation, we performed structure-property relationship studies in a class of pyridine derivatives and found that dissolution parameters (i.e., dissolution enthalpy and entropy) correlate with gelation ability.¹⁰ In general, this finding could provide helpful insights for designing new gelators by identifying molecules that have high dissolution enthalpies and entropies (via simulations) as potential gelators.

Compared to designing new gelators, increasing the practical utility of known gelators is much less explored. During the development of our triacetone triperoxide (TATP) gel-based sensor, an H_2O_2 -induced thiol-to-disulfide oxidation was utilized to convert a soluble precursor to a known gelator. Further optimizations of gelator structure, reaction rate, sample volume and container size were performed for the TATP sensor, highlighting the important factors one should investigate to develop sensitive and efficient gel-based sensors.¹¹

Finally, some preliminary results towards the development of quantitative gel-based sensor were discussed in this work. To measure the viscosity of gel, a series of methods were explored and a magnetoelastic sensor was identified as a promising quantification method because it is robust and sensitive enough in gel medium.

Although several gel-based sensors have been reported by us^{7a,9,12} and other,¹³ low sensitivity and selectivity still remain the major limitations to overcome. Low sensitivity of a gel-based sensor is originated from the stoichiometric chemical reaction between analyte and sensing precursor. To address this sensitivity issue, our group has designed systems in which the analyte serves as a catalyst,^{7b} introduced additives to reduce cgc,¹⁴ and incorporated a signal amplification method to release multiple copies of gelator in response to one analyte.¹⁵ On the other hand, low selectivity is caused by the non-specific chemical reaction between the precursor and analyte. To improve sensor selectivity, highly specific chemical reactions need to be employed in sensor design or an array of parallel gel-based sensors might be useful to exclude possible interferences.

To expand both the structural scope and the applications of molecular gelators, future directions will focus on further understanding the complex structure-property relationships in molecular gelation to obtain universal design strategy for gelation. Besides identifying new molecular properties that distinguish gelators from nongelators, efforts should also focus on elucidating how molecular structures can affect the morphologies of secondary structures (e.g., fibers, ribbons) and the physical interactions between them, which will shed light on designing efficient gelators. Meanwhile, developing strategies to tailor or engineer gel properties (i.e., mechanical strength, opacity) continues to attract significant attention.¹⁶ For example, a variety of additives have been utilized to increase branching or bundling of gel fibers^{16a,16b} to enhance the degree of crosslinking and produce molecular gels with high moduli. Future directions might also include the engineering of fiber surfaces to introduce strong specific non-

covalent interactions (e.g., H-bonding^{16b}, electrostatics, metal-ligand complexation) for crosslinking. Last but not least, integrating molecular gels with practical applications is one of the ultimate goals of the field. In the past decade, several pH-sensitive amphiphilic peptide gelators have made significant progress in tissue engineering and regeneration.² Recent applications of molecular gel fibers in nanoelectronics¹⁷ and explosive detection^{7a} also indicate a promising outlook of the materials.¹⁸

References:

(1) For recent examples of drug-delivery, see: (a) Mao, L.; Wang, H.; Tan, M.; Ou, L.; Kong, D.; Yang, Y. *Chem. Commun.* **2012**, *48*, 395-397. (b) Wang, H.; Yang, C.; Wang, L.; Kong, D.; Zhang, Y.; Yang, Z. *Chem. Commun.* **2011**, *47*, 4439-4441. (c) Li, X.; Li, J.; Gao, Y.; Kuang, Y.; Shi, J.; Xu, B. *J. Am. Chem. Soc.* **2010**, *132*, 17707-17709. (d) Zhao, Y.; Tanaka, M.; Kinoshita, T.; Higuchi, M.; Tan, T. *J. Controlled Release* **2010**, *147*, 392-399. (e) Zhao, F.; Ma, M. L.; Xu, B. *Chem. Soc. Rev.* **2009**, *38*, 883-891.

(2) For recent reviews on regenerative medicine, see: (a) Matson, J. B.; Stupp, S. I. *Chem. Commun.* **2012**, *48*, 26-33. (b) Matson, J. B.; Zha, R. H.; Stupp, S. I. *Curr. Opin. Solid State Mater. Sci.* **2011**, *15*, 225-235.

(3) For recent examples on tissue engineering applications, see: (a) Ryan, D. M.; Nilsson, B. L. *Polym. Chem.* **2012**, *3*, 18-33; (b) Collier, J. H.; Rudra, J. S.; Gasiorowski, J. Z.; Jung, J. P. *Chem. Soc. Rev.* **2010**, *39*, 3413-3424.

(4) (a) Rodriguez-Llansola, F.; Escuder, B.; Miravet, J. F.; Hermida-Merino, D.; Hamley, I. W.; Cardin, C. J.; Hayes, W. *Chem. Commun.* **2010**, *46*, 7960-7962. (b) Adhikari, B.; Palui, G.; Banerjee, A. *Soft Matter* **2009**, *5*, 3452-3460.

(5) For a recent review, see: Escuder, B.; Rodriguez-Llansola, F.; Miravet, J. F. *New J. Chem.* **2010**, *34*, 1044-1054.

(6) For recent reviews on synthesis hybrid materials, see: (a) Bideau, J. L.; Viau, L.; Vioux, A. *Chem. Soc. Rev.* **2011**, *40*, 907-925. (b) Brizard, A.; Oda, R.; Huc, I. *Topics Curr. Chem.* **2005**, *256*, 167-218. (c) Jung, J. H.; Shinkai, S. *Topics Curr. Chem.* **2004**, *248*, 223-260.

(7) For recent examples of bio-/chemical sensing, see: (a) Kartha, K. K.; Babu, S. S.; Srinivasan, S.; Ajayaghosh, A. *J. Am. Chem. Soc.* **2012**, *134*, 4834-4841. (b) Bremmer, S. C.; Chen, J.; McNeil, A. J.; Soellner, M. B. *Chem. Commun.* **2012**, *48*, 5482-5484.

- (8) For recent reviews, see: (a) Yang, Z.; Xu, B. *Acc. Chem. Res.* **2008**, *41*, 315-325. (b) Gao, Y.; Yang, Z.; Kuang, Y.; Ma, M.; Li, J.; Zhao, F.; Xu, B. *Biopolymers*, **94**, 19-31. (c) Yang, Z.; Ho, P.-L.; Liang, G.; Chow, K. H.; Wang, Q.; Cao, Y.; Guo, Z.; Xu, B. *J. Am. Chem. Soc.* **2007**, *129*, 266-267.
- (9) Chen, J.; McNeil, A. J. *J. Am. Chem. Soc.* **2008**, *130*, 16496-16497.
- (10) (a) Muro-Small, M. L.; Chen, J.; McNeil, A. J. *Langmuir* **2011**, *27*, 13248-13253. (b) Chen, J.; Kampf, J. W.; McNeil, A. J. *Langmuir* **2010**, *26*, 13076-13080.
- (11) Chen, J.; Wu, W.; McNeil, A. J. manuscript in preparation, 2012.
- (12) King, K. N.; McNeil, A. J. *Chem. Commun.* **2010**, *46*, 3511-3513.
- (13) (a) Kawano, S.-I.; Fujita, N.; Shinkai, S. *Chem. Eur. J.* **2005**, *11*, 4735-4742. (b) Mukhopadhyay, P.; Iwashita, Y.; Shirakawa, M.; Kawano, S.-I.; Fujita, N.; Shinkai, S. *Angew. Chem. Int. Ed.* **2006**, *45*, 1592-1595. (c) Zhang, Y.-M.; Lin, Q.; Wei, T.-B.; Qin, X.-P.; Li, Y. *Chem. Commun.* **2009**, 6074-6076.
- (14) Adhia, Y. J.; Schloemer, T. H.; Perez, M. T.; McNeil, A. J. *Soft Matter* **2012**, *8*, 430-434.
- (15) Zurcher, D.; Moy, C. L.; McNeil, A. J. unpublished data.
- (16) (a) Li, J.-L.; Yuan, B.; Liu, X.-Y.; Wang, X.-G.; Wang, R.-Y. *Cryst. Growth Des.* **2011**, *11*, 3227-3234. (b) Numata, M.; Sugiyasu, K.; Kishida, T.; Haraguchi, S.; Fujita, N.; Park, S. M.; Yun, Y. J.; Kim, B. H.; Shinkai, S. *Org. Biomol. Chem.* **2008**, *6*, 712-718. See also: Karinaga, R.; Jeong, Y.; Shinkai, S.; Kaneko, K.; Sakurai, K. *Langmuir* **2005**, *21*, 9398-9401. (c) Diaz, D. D.; Rajagoal, K.; Strable, E.; Schneider, J.; Finn, M. G. *J. Am. Chem. Soc.* **2006**, *128*, 6065-6067.
- (17) Hong, J.-P.; Um, M.-C.; Nam, S.-R.; Hong, S.-I.; Lee, S. *Chem. Commun.* **2009**, 310-312.
- (18) (a) Dawn, A.; Shiraki, T.; Haraguchi, S.; Tamaru, S.; Shinkai, S. *Chem. Asian. J.* **2011**, *6*, 266-282. (b) Aida, T.; Meijer, E. W.; Stupp, S. I. *Science* **2012**, *335*, 813-817.

Appendix 1

Appendix to Chapter 2: Analyte-Triggered Gelation: Initiating Self-Assembly via Oxidation-Induced Planarization

Materials:

Silica gel (40-63 μm) was purchased from SiliCycle. All other reagent grade materials were purchased from Aldrich, Alfa Aesar, Acros or Fisher and used without further purification unless otherwise noted.

General Experimental:

General Procedure for Heat/Cool-induced Gelation: A 4 mL vial was charged with **2** and an organic solvent/H₂O mixture. The mixture was heated to 80 °C to form a homogeneous solution and allowed to cool to 25 °C to form a gel.

General Procedure for CAN-Triggered Gelation: A 4 mL glass vial was charged with a stir bar, **1** (10 mg, 26 μmol), DMSO (0.7 mL) and H₂O (0.15 mL). The mixture was stirred to give a homogeneous solution. An aqueous solution of ceric ammonium nitrate (CAN) (28 mg, 46 μmol , 0.15 mL H₂O) was added dropwise over 5 min. A gel was formed at the end of CAN addition.

General Procedure for Nitric Oxide-Triggered Gelation: A 4 mL glass vial equipped with a stir bar was charged with **1** (5 mg, 13 μmol) and CH₃CN (0.3 mL) and was sealed with a PTFE/red rubber septum cap. O₂ was purged through the mixture. NO (0.30 mL, 1 equiv) was injected via syringe into the reaction mixture, which was kept stirring until it was homogeneous. For gelation, 1.5 mL of 1/3 DMSO/H₂O mixture was added to the above solution to form a gel.

To measure the reaction rate, 1 mL CH₂Cl₂ was added to dilute the reaction mixture. Aliquots of 10 μL were taken and diluted with 1.5 mL CH₂Cl₂ and analyzed by HPLC using 1,3-dinitrobenzene as an internal standard.

General Procedure for Equilibrium Solubility Measurement: A 4 mL glass vial equipped with a stir bar was charged with **1** (5 mg), DMSO (0.8 mL) and H₂O (0.4 mL). The mixture was stirred vigorously overnight to reach equilibrium. Undissolved **1** was removed by filtration, and the filtrate was diluted with DMSO/H₂O (2/1). The concentration of the diluted solution was measured via UV-Vis spectroscopy using a calibration curve. Equilibrium solubility of **2** was measured according to the same procedure.

NMR Spectroscopy: ¹H and ¹³C NMR spectra for all compounds were acquired in CDCl₃ on a Varian MR400 Spectrometer operating at 400 MHz and 100MHz, respectively. The chemical shift data are reported in units of δ (ppm) relative to tetramethylsilane (TMS) and referenced with residual CHCl₃.

X-ray Crystallography: Colorless plates of **1** were grown by slow evaporation of a DMF/water solution at 25 °C. A crystal of dimensions 0.39 x 0.24 x 0.10 mm was mounted on a Bruker SMART APEX CCD-based X-ray diffractometer equipped with a low temperature device and fine focus Mo-target X-ray tube (λ = 0.71073Å) operated at 1500 W power (50 kV, 30 mA). The X-ray intensities were measured at 85(2) K; the detector was placed at a distance 5.055 cm from the crystal. A total of 4590 frames were collected with a scan width of 0.5° in ω and 0.45° in Φ with an exposure time of 25 s/frame. The integration of the data yielded a total of 25689 reflections to a maximum 2θ value of 57.00° of which 4660 were independent and 3782 were greater than 2σ(I). The final cell constants were based on the xyz centroids of 9264 reflections above 10σ(I). Analysis of the data showed negligible decay during data collection; the data were processed with SADABS and corrected for absorption. The structure was solved and refined with the Bruker SHELXTL software package^[1], using the space group P1bar with Z = 2 for the formula C₂₁H₂₃NO₆. All non-hydrogen atoms were refined anisotropically with the hydrogen atoms placed in idealized positions with the exception of the hydrogen participating in hydrogen bonding. Full matrix least-squares refinement based on F² converged at R1 = 0.0429 and wR2 = 0.1121 [based on I > 2σ(I)], R1 = 0.0540 and wR2 = 0.1183 for all data. Additional details are presented in Figure S9~S11.

Colorless plates of **2** were crystallized from a methanol/water solution at 25 °C. A crystal of dimensions 0.35 x 0.34 x 0.06 mm was mounted on a standard Bruker SMART-APEX CCD-based X-ray diffractometer equipped with a low temperature device and fine focus Mo-target X-ray tube ($\lambda = 0.71073 \text{ \AA}$) operated at 1500 W power (50 kV, 30 mA). The X-ray intensities were measured at 85(2) K; the detector was placed at a distance 5.055 cm from the crystal. A total of 3101 frames were collected with a scan width of 0.5° in ω and 0.45° in Φ with an exposure time of 20 s/frame. The frames were integrated with the Bruker SAINT software package^[1] with a narrow frame algorithm. The integration of the data yielded a total of 99584 reflections to a maximum 2θ value of 56.76° of which 18840 were independent and 15068 were greater than $2\sigma(I)$. The final cell constants were based on the xyz centroids of 9824 reflections above $10\sigma(I)$. Analysis of the data showed negligible decay during data collection; the data were processed with SADABS and corrected for absorption. The structure was solved and refined with the Bruker SHELXTL (version 2008/3) software package^[1], using the space group $P1\bar{6}$ with $Z = 8$ for the formula $C_{21}H_{21}NO_6$. There are four crystallographically independent molecules in the asymmetric unit. All non-hydrogen atoms were refined anisotropically with the hydrogen atoms placed in idealized positions. Full-matrix least-squares refinement based on F^2 converged at $R1 = 0.0399$ and $wR2 = 0.1038$ [based on $I > 2\sigma(I)$], $R1 = 0.0538$ and $wR2 = 0.1126$ for all data. Additional details are presented in Figure S9~S11.

Powder X-ray Diffraction: Powder X-ray diffraction (PXRD) patterns were collected at ambient temperature using a Rigaku R-Axis SPIDER diffractometer with an imaging plate detector using graphite monochromated Cu-K α radiation (1.5406 \AA). For collections at room temperature, samples were mounted on a cryoloop. To obtain powder patterns with minimized preferred orientation, images were collected for 5 minutes while rotating the sample about the ϕ -axis at $10^\circ \cdot s^{-1}$ while oscillating ω between 120° and 180° at $1^\circ \cdot s^{-1}$ with χ set at 45° . Images were integrated from 2.5° to 50° 2θ with a 0.02° step size with the AreaMax^[2] software package. Powder patterns were processed in Jade Plus^[3] to calculate peak positions and intensities. Temperature was controlled with an Oxford Cryostream Plus.

Scanning Electron Microscopy: Gels were prepared as explained on p 67. Wet gels were placed in a SEM holder mounted onto SEM stubs with copper tape, and observed using

the low-vacuum mode of a Philips XL30FEG scanning electron microscope (SEM) using a 15-kV accelerating voltage. Images were digitally recorded and processed using Adobe Illustrator.

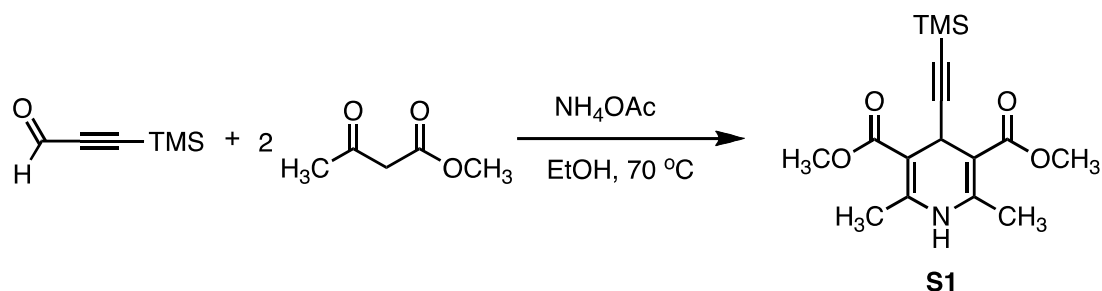
Raman Spectroscopy: Raman spectra were obtained using a Renishaw inVia Raman Microscope equipped with a Leica microscope, RenCam CCD detector, 633 nm He-Ne laser, 1200 lines/mm grating, and 50 μm slit. Spectra were collected in extended scan mode in the range of 3600-100 cm^{-1} and analyzed using the WiRE 2.0 software package. Calibration was performed using a silicon standard.

Rheology: The viscoelastic properties of a gel of **2** were characterized using an advanced rheometric expansion system (ARES) rheometer (Rheometrics Scientific) equipped with 25 mm parallel plates under small-amplitude oscillatory shear strain. The average gap between the plates was 1 mm, and applied strains 0.1%. The frequency-dependent elastic ($G'(\omega)$) and loss ($G''(\omega)$) shear moduli were measured at 298 K by performing frequency, ω , sweeps from 0.1 to 100 rad/s. Strain sweeps verified that all reported measurements were within the linear viscoelastic regime.

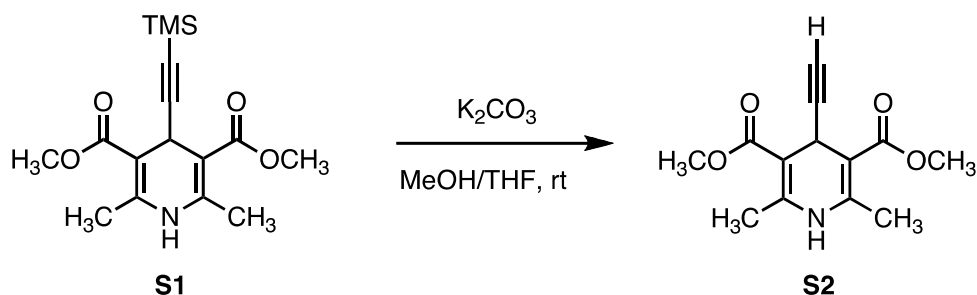
High Performance Liquid Chromatography: HPLC was performed on a Varian ProStar 210 HPLC using Waters μ -Porasil 10 μm silica (3.9 x 300 mm) column. Samples were run using 70/30 hexane/EtOAc as the eluent at 1 mL/min. An internal standard (1,3-dinitrobenzene) was used for quantitative measurement. Retention times for the dinitrobenzene standard, **2** and **1** were 5.29, 10.67 and 15.87 min, respectively.

UV-visible Spectroscopy: UV-Vis spectra were taken on a Perkin-Elmer Lambda 850 UV-visible Spectrophotometer. Calibration curves were measured at $\lambda = 350$ nm for **1** and $\lambda = 304$ nm for **2**.

Synthetic Procedures

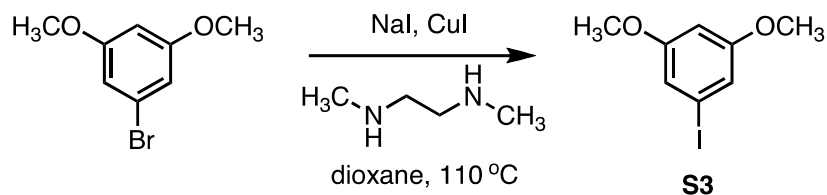


S1^[4]: A 25 mL Schlenk tube was equipped with a stir bar. Sequentially, ammonium acetate (0.53 g, 6.8 mmol), methyl acetoacetate (0.75 mL, 6.8 mmol), EtOH (5 mL) and 3-trimethylsilylpropynal (0.60 mL, 3.4 mmol) were added to the flask. The tube was sealed and the reaction mixture was heated to 70 °C overnight. After cooling to room temperature, the reaction mixture was concentrated in vacuo and then purified by column chromatography using 20/80 hexanes/EtOAc as the eluent to give 0.993 g of **S1** as a light yellow crystalline solid (90% yield). HRMS (ESI): Calcd. for C₁₆H₂₃NO₄Si, 344.1294 [M+Na]⁺; found, 344.1297. Elemental Analysis: Calcd. for C₁₆H₂₃NO₄Si: C, 62.64; H, 6.07; N, 5.62; found: C, 62.60; H, 5.97; N, 5.45.

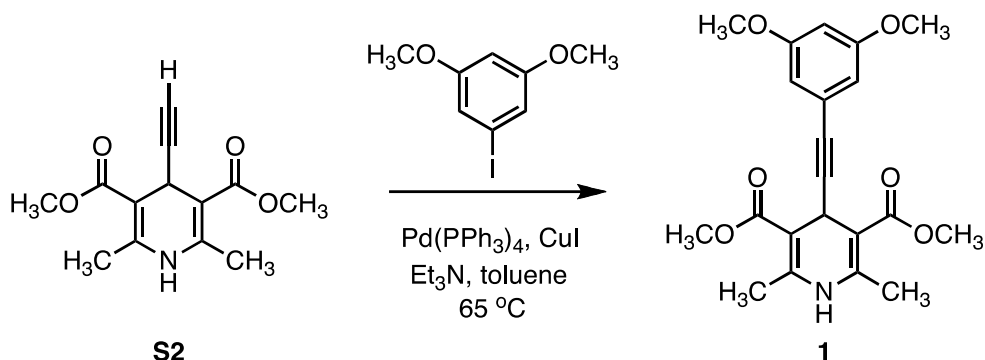


S2^[5]: A 100 mL round-bottom flask was equipped with a stir bar. Sequentially, **S1** (0.30 g, 1.0 mmol), potassium carbonate (1 g, 7.2 mmol), MeOH (10 mL) and THF (10 mL) were added to the flask. The reaction mixture was stirred vigorously at room temperature overnight. Excess potassium carbonate was removed by filtration. The filtrate was concentrated in vacuo and washed with ethanol to give 0.215 g of **S2** as a white solid (83% yield). HRMS (ESI): Calcd. for C₁₃H₁₅NO₄, 272.0899 [M+Na]⁺; found, 272.0903.

Elemental Analysis: Calcd. for C₁₃H₁₅NO₄: C, 59.78; H, 7.21; N, 4.36; found: C, 59.58; H, 7.11; N, 4.22.

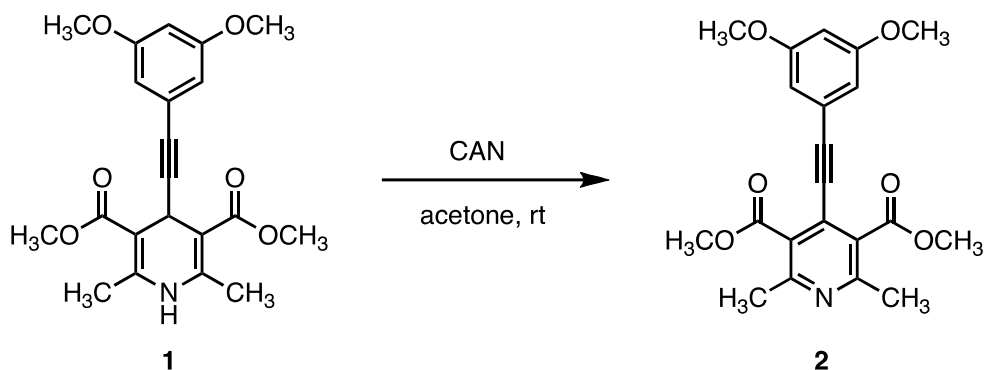


S3^[6]: A 25 mL Schlenk tube equipped with a stir bar was oven-dried, cooled under vacuum and charged with N₂. Sequentially, 1-bromo-3,5-dimethoxybenzene (4.0 g, 18 mmol), sodium iodide (5.4 g, 36 mmol), copper iodide (0.172 g, 0.90 mmol), *N,N'*-dimethylethylenediamine (0.20 mL, 1.8 mmol) and dioxane (15 mL) were added to the flask. The reaction mixture was degassed with N₂ for 10 min and then heated to 110 °C overnight. After cooling to room temperature, the reaction mixture was quenched with NH₄OH (30%, 5 mL) and poured into water (50 mL). The aqueous mixture was extracted with CH₂Cl₂ (3 x 30 mL). The organic layer was dried over anhydrous Na₂SO₄ and concentrated in vacuo to give 4.14 g of **S3** as a light yellow crystalline solid (85% yield). HRMS (ESI): Calcd. for C₈H₉IO₂, 286.9502 [M+Na]⁺; found, 286.9511.



1^[7]: A 50 mL Schlenk tube equipped with a stir bar was oven-dried, cooled under vacuum and charged with N₂. Sequentially, **S2** (0.735 g, 2.95 mmol), **S3** (1.10 g, 4.20 mmol), copper iodide (82 mg, 0.43 mmol), triethylamine (5 mL) and toluene (25 mL) were added to the flask. The reaction mixture was purged with N₂ for 10 min before Pd(PPh₃)₄ (100 mg, 0.087 mmol) was added. The reaction mixture was heated to 65 °C overnight. After cooling to room temperature, the reaction mixture was diluted with

CH₂Cl₂ (25 mL) and washed with saturated aq. NH₄Cl (3 x 20 mL). The organic layer was dried over anhydrous Na₂SO₄, concentrated in vacuo and purified by column chromatography using 50/50 hexane/EtOAc as the eluent to give a light yellow solid. The solid was recrystallized from methylene chloride/hexane to give 0.982 g of **1** as a white fluffy solid (92% yield). HRMS (ESI): Calcd. for C₂₁H₂₃NO₆, 408.1423 [M+Na]⁺; found, 408.1423. Elemental Analysis: Calcd. for C₂₁H₂₃NO₆: C, 65.44; H, 6.02; N, 3.63; found: C, 65.50; H, 5.97; N, 3.64.



2: A 50 mL round-bottom flask was equipped with a stir bar. Sequentially, **1** (0.588 g, 1.53 mmol), ceric ammonium nitrate (1.67 g, 3.05 mmol) and acetone (15 mL) were added to the flask. The reaction mixture was stirred at room temperature vigorously overnight. The reaction mixture was concentrated in vacuo and washed with H₂O (10 mL). A second aliquot of H₂O (20 mL) was added to the reaction mixture and extracted with CH₂Cl₂ (3 x 10 mL). The organic layer was concentrated in vacuo and purified by column chromatography using 50/50 hexane/EtOAc as the eluent to give 0.565 g of **2** as a white solid (96% yield). HRMS (ESI): Calcd. for C₂₁H₂₁NO₆, 384.1447 [M+H]⁺; found, 384.1452. Elemental Analysis: Calcd. for C₂₁H₂₁NO₆: C, 65.79; H, 5.52; N, 3.65; found: C, 65.88; H, 5.58; N, 3.61.

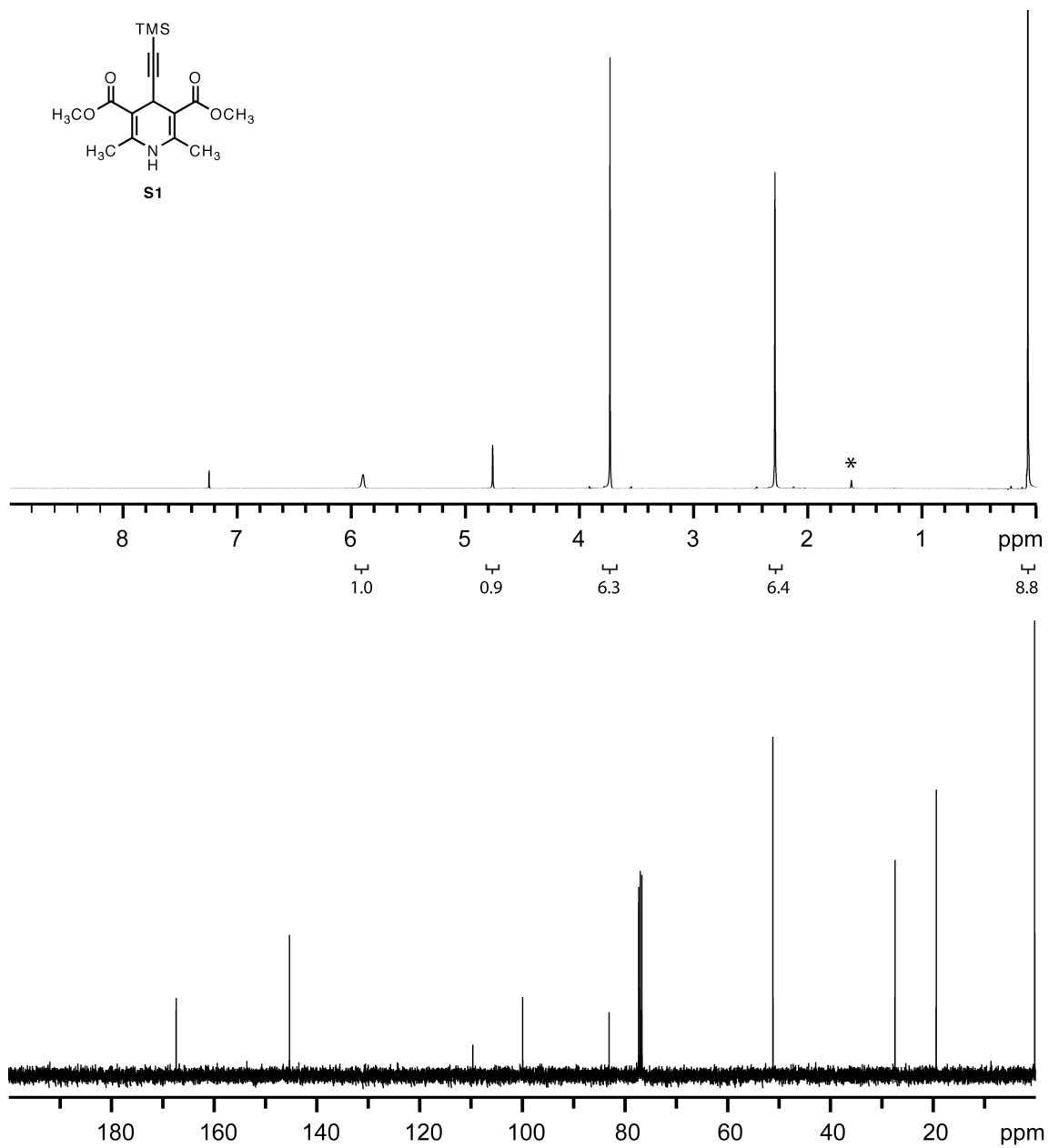


Figure S1. ^1H and ^{13}C NMR spectra of **S1**. ^1H NMR (400 MHz, CDCl₃) δ 5.70 (s, 1H), 4.77 (s, 1H), 3.75 (s, 6H), 2.31 (s, 6H), 0.09 (s, 9H). ^{13}C NMR (100 MHz, CDCl₃) δ 167.39, 145.32, 109.61, 99.90, 80.10, 51.16, 27.40, 19.36, 0.195. * denotes H₂O peak

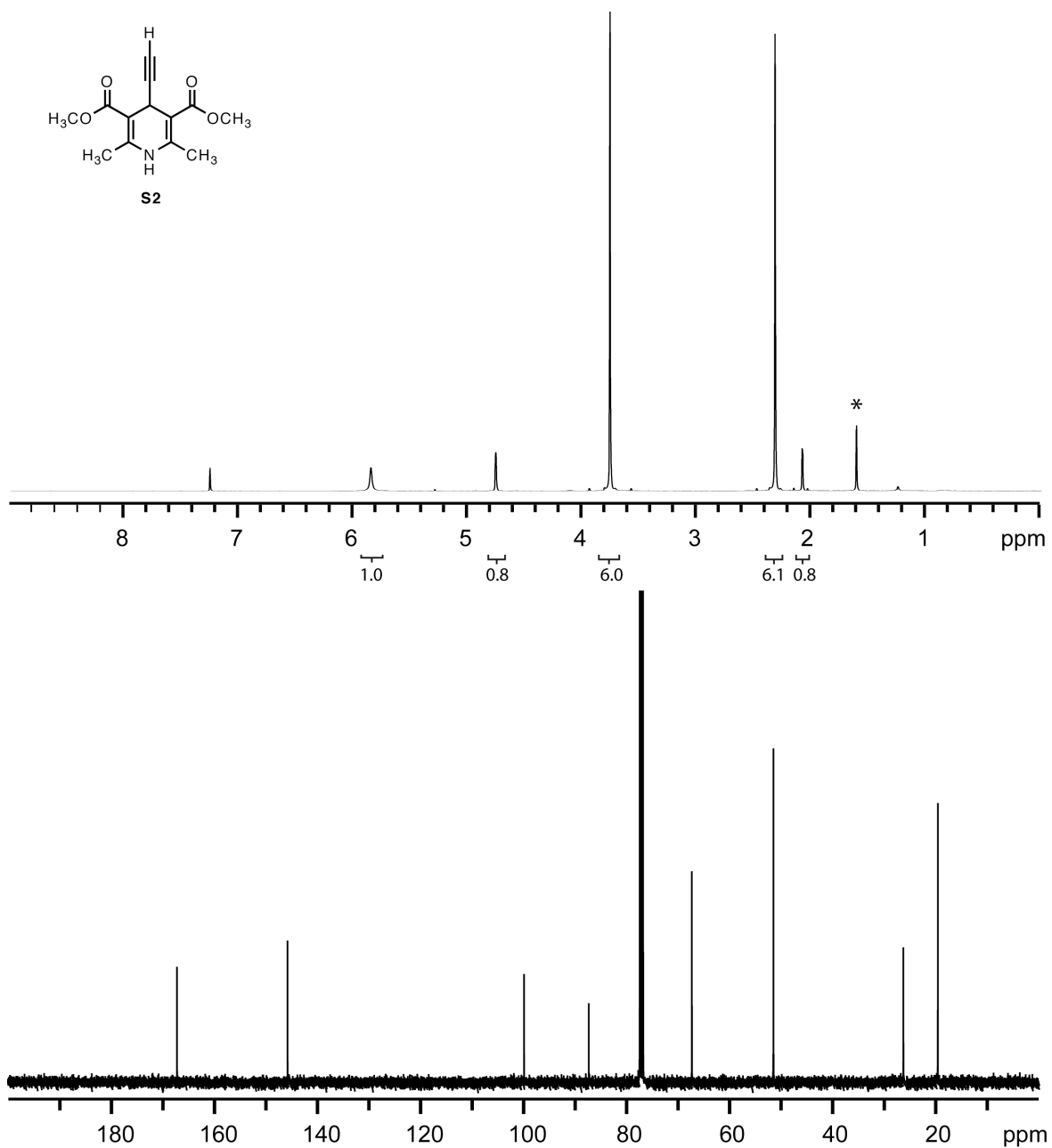


Figure S2. ¹H and ¹³C NMR spectra of **S2**. ¹H NMR (400 MHz, CDCl₃) δ 5.85 (s, 1H), 4.76 (s, 1H), 3.76 (s, 6H), 2.32 (s, 6H), 2.08 (s, 1H). ¹³C NMR (100 MHz, CDCl₃) δ 167.17, 145.72, 99.80, 87.23, 67.22, 51.38, 26.15, 19.47. * denotes H₂O peak.

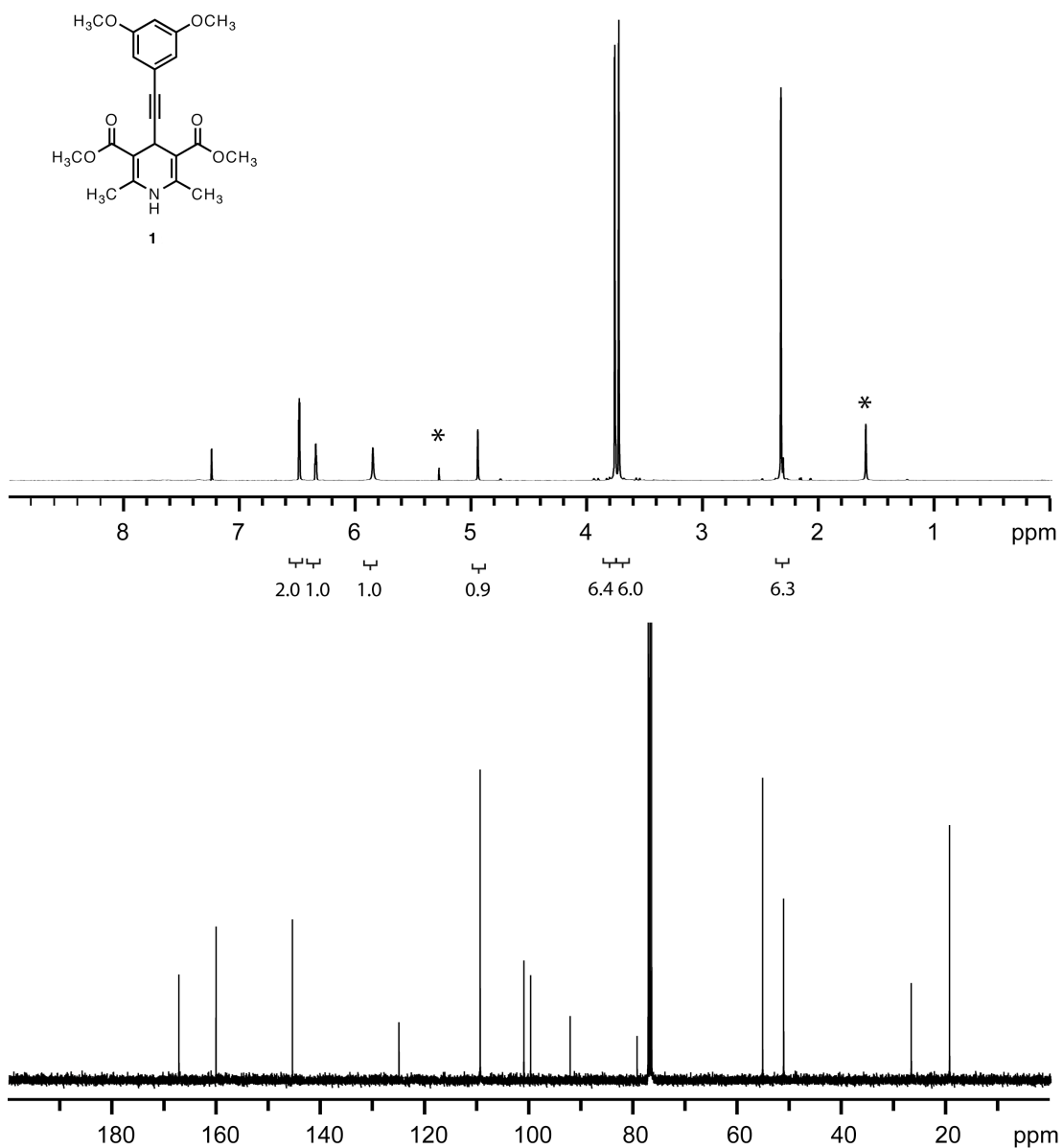


Figure S3. ¹H and ¹³C NMR spectra of **1**. ¹H NMR (400 MHz, CDCl₃) δ 6.50 (s, 2H), 6.36 (s, 1H), 5.87 (s, 1H), 4.96 (s, 1H), 3.77 (s, 6H), 3.74 (s, 6H), 2.34 (s, 6H). ¹³C NMR (100 MHz, CDCl₃) δ 167.40, 160.28, 145.62, 125.17, 109.58, 101.20, 99.91, 92.32, 79.46, 55.37, 51.34, 26.85, 19.50. * denote H₂O and CH₂Cl₂ peaks.

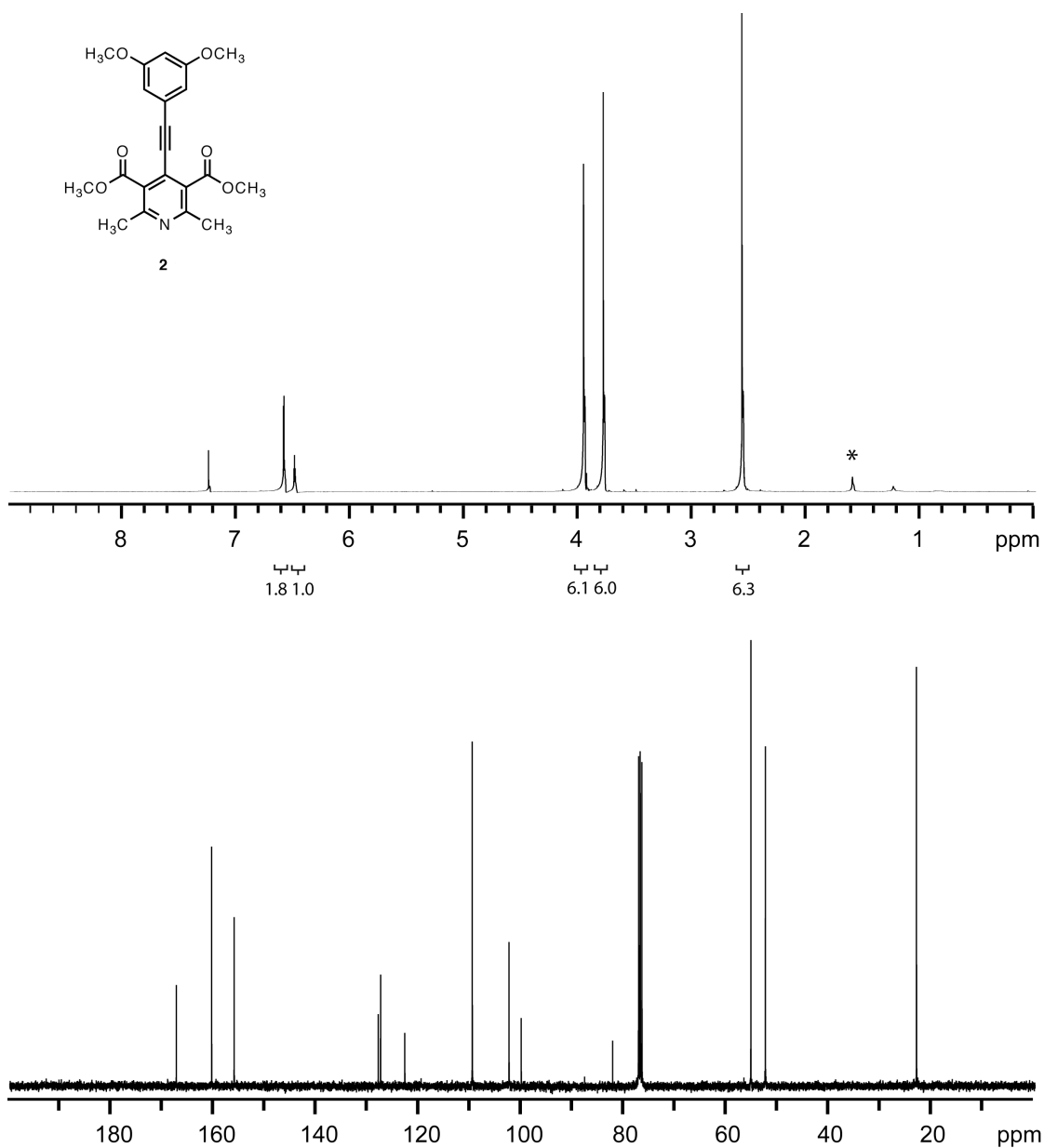


Figure S4. ^1H and ^{13}C NMR spectra of **2**. ^1H NMR (400 MHz, CDCl_3) δ 6.60 (s, 2H), 6.50 (s, 1H), 3.97 (s, 6H), 3.80 (s, 6H), 2.58 (s, 6H). ^{13}C NMR (100 MHz, CDCl_3) δ 167.51, 160.62, 156.23, 128.14, 127.67, 122.94, 109.79, 102.62, 100.23, 82.43, 55.45, 52.61, 23.14. * denotes H_2O peak.

Gelation Tests



Figure S5. Gel of **2** (26 mM, formed by heat/cool-induced gelation) in a series of organic solvent/water mixtures.

Table S1. Critical gel concentration (cgc) of **2** in a series of organic solvent/water mixtures at 25 °C.

Solvent (v/v)	cgc (mg/mL)
MeOH/H ₂ O (2/1)	6.2
EtOH/H ₂ O (1/1.4)	10
iPrOH/H ₂ O (1/3)	5.6
DMSO/H ₂ O (2/1)	6
DMF/H ₂ O (1.1/1)	3.7
Acetone/H ₂ O (1/1.2)	20

Solubility Tests

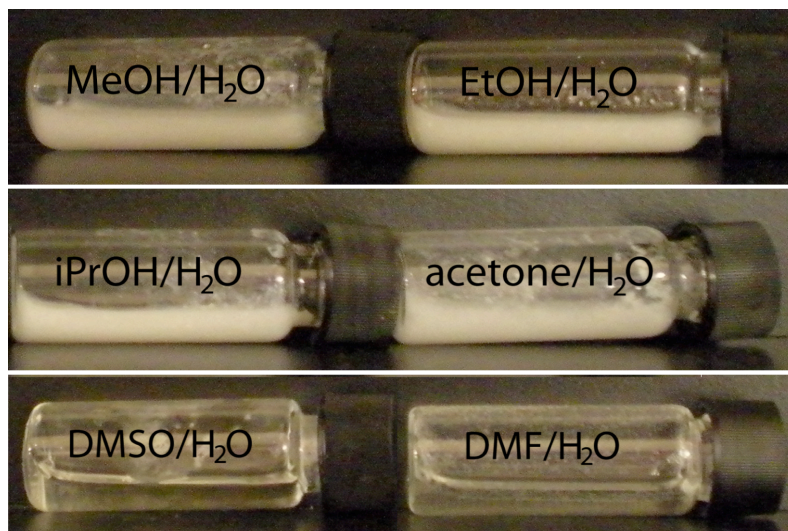


Figure S6. Solution/precipitates of **1** (26 mM, prepared by heat/cool method) in a series of organic solvent/water mixtures.

Table S2. **1** (26 mM) in a series of organic solvent/water mixtures after one heat/cool cycle.

Solvent (v/v)	State
MeOH/H ₂ O (2/1)	P
EtOH/H ₂ O (1/1.4)	P
iPrOH/H ₂ O (1/3)	P
DMSO/H ₂ O (2/1)	S
DMF/ H ₂ O (1.1/1)	S
acetone/H ₂ O (1/1.2)	P

P: Precipitate **S:** Solution

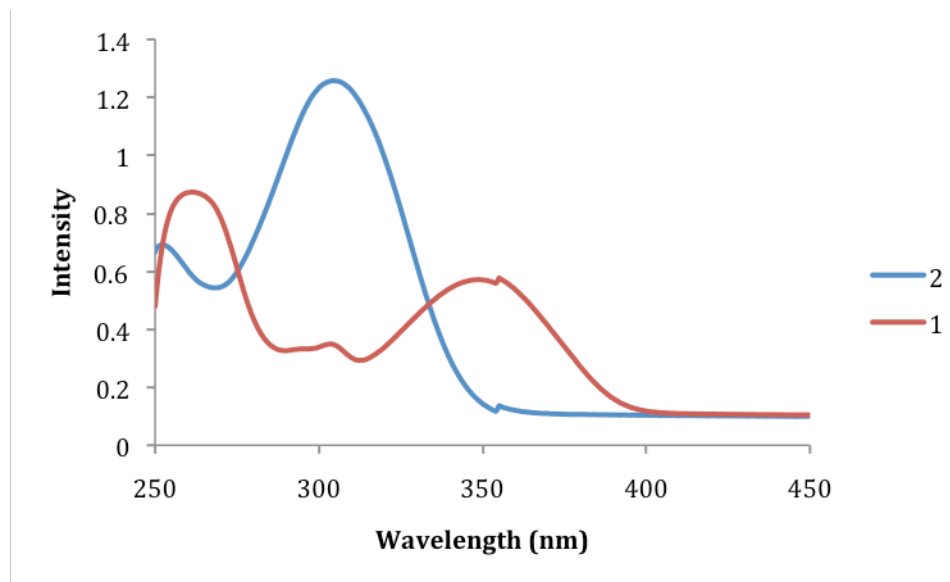


Figure S7. UV-Vis spectra of **1** (red) and **2** (blue) in DMSO/H₂O (2/1).

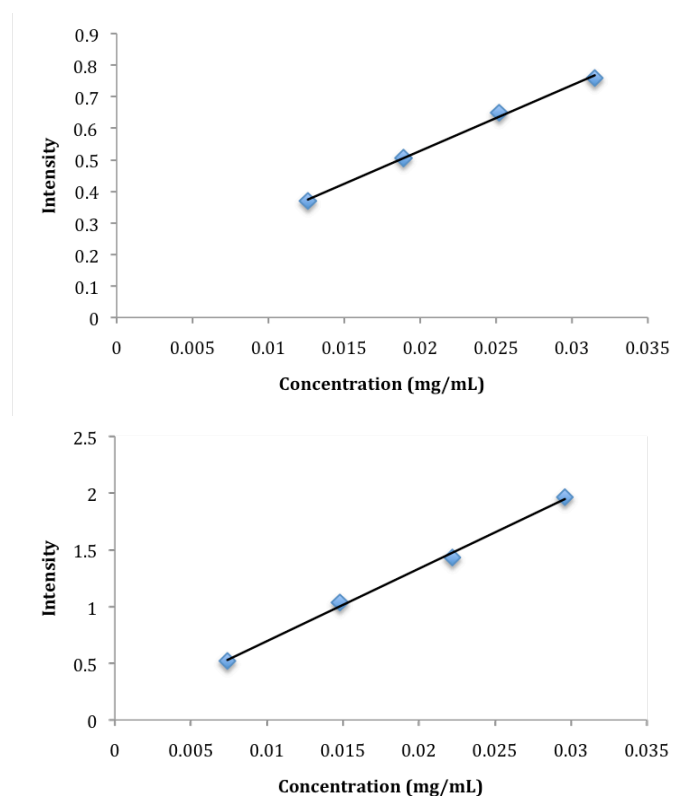


Figure S8. Calibration curve of **1** (top) and **2** (bottom) in DMSO/H₂O (2/1).

Table S3. Equilibrium solubility of **1** and **2** at 25 °C.

Solvent (v/v)	Solubility of 1 (mg/mL)	Solubility of 2 (mg/mL)
DMSO/H ₂ O (2/1)	0.29 ± 0.04	0.61 ± 0.07

X-ray Crystal Structures

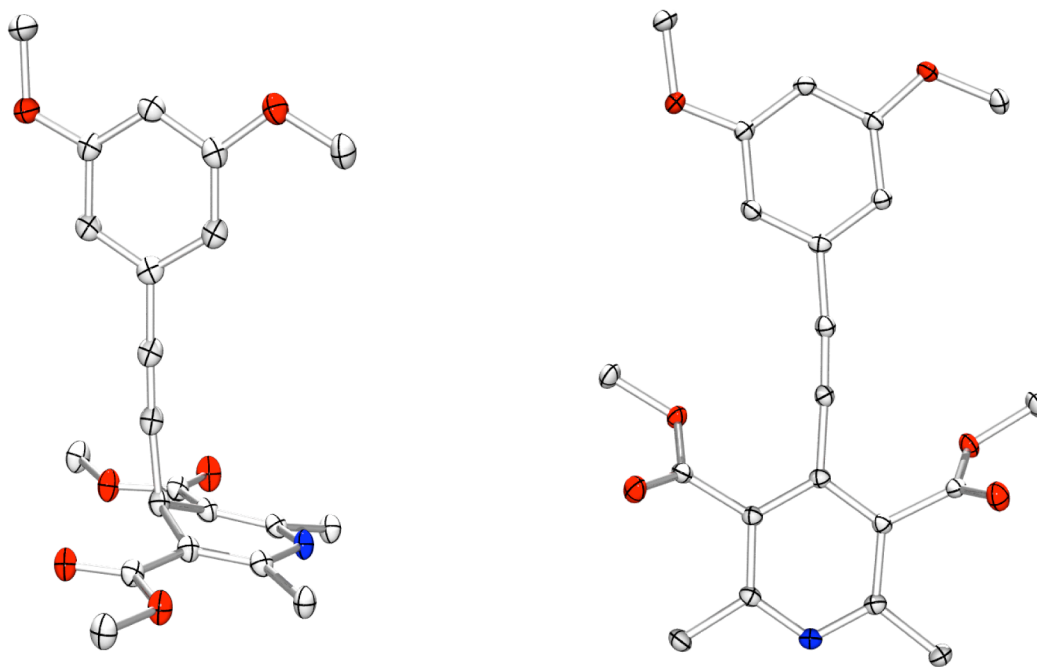


Figure S9. Crystal structures of **1** (left) and **2** (right). Torsion angle between the two arenes in **1** is 109.6°. Torsion angle between the two arenes in **2** is -7.6°.

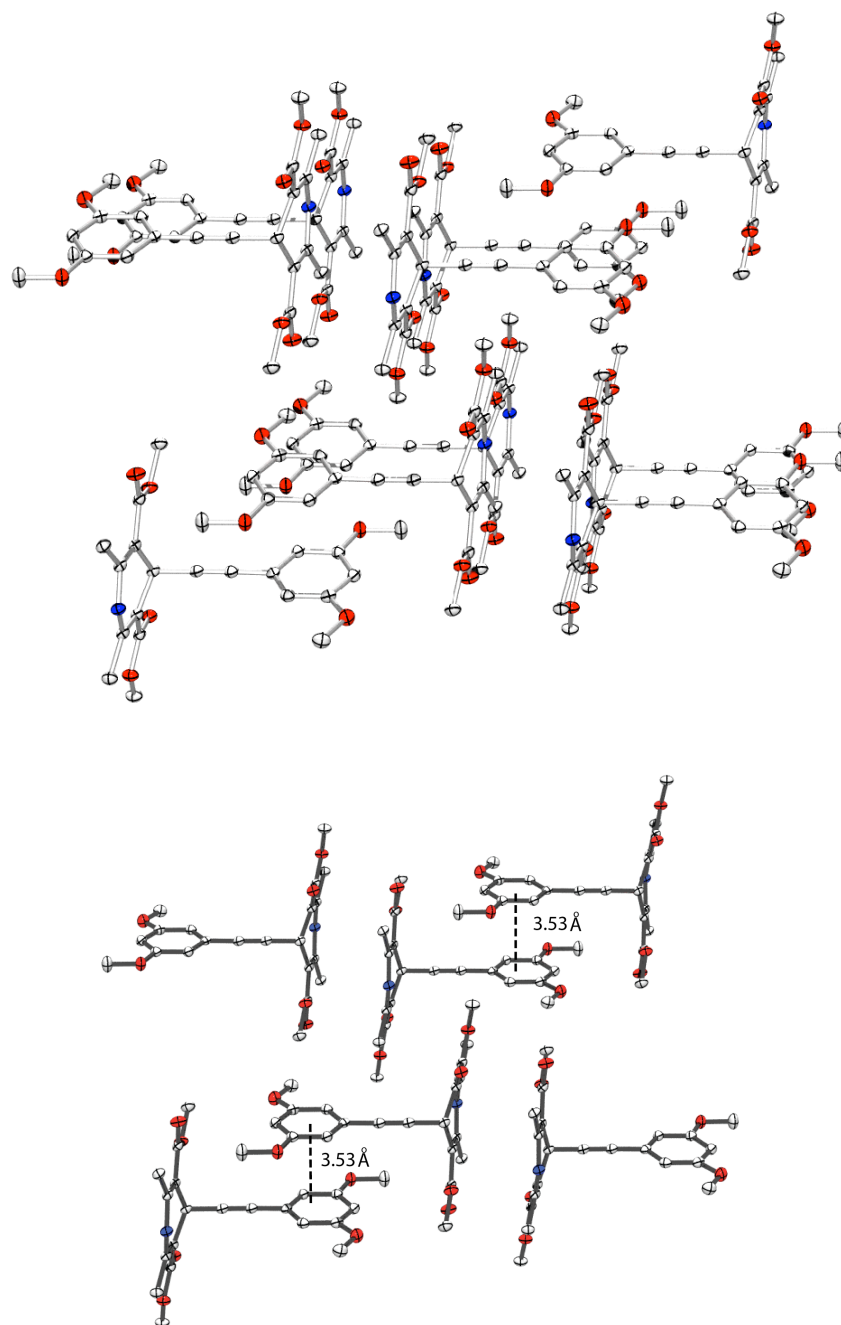


Figure S10. The solid state packing of **1** (top). A simplified version of packing (bottom). The average distance between two bis-methoxybenzene rings is 3.53 Å.

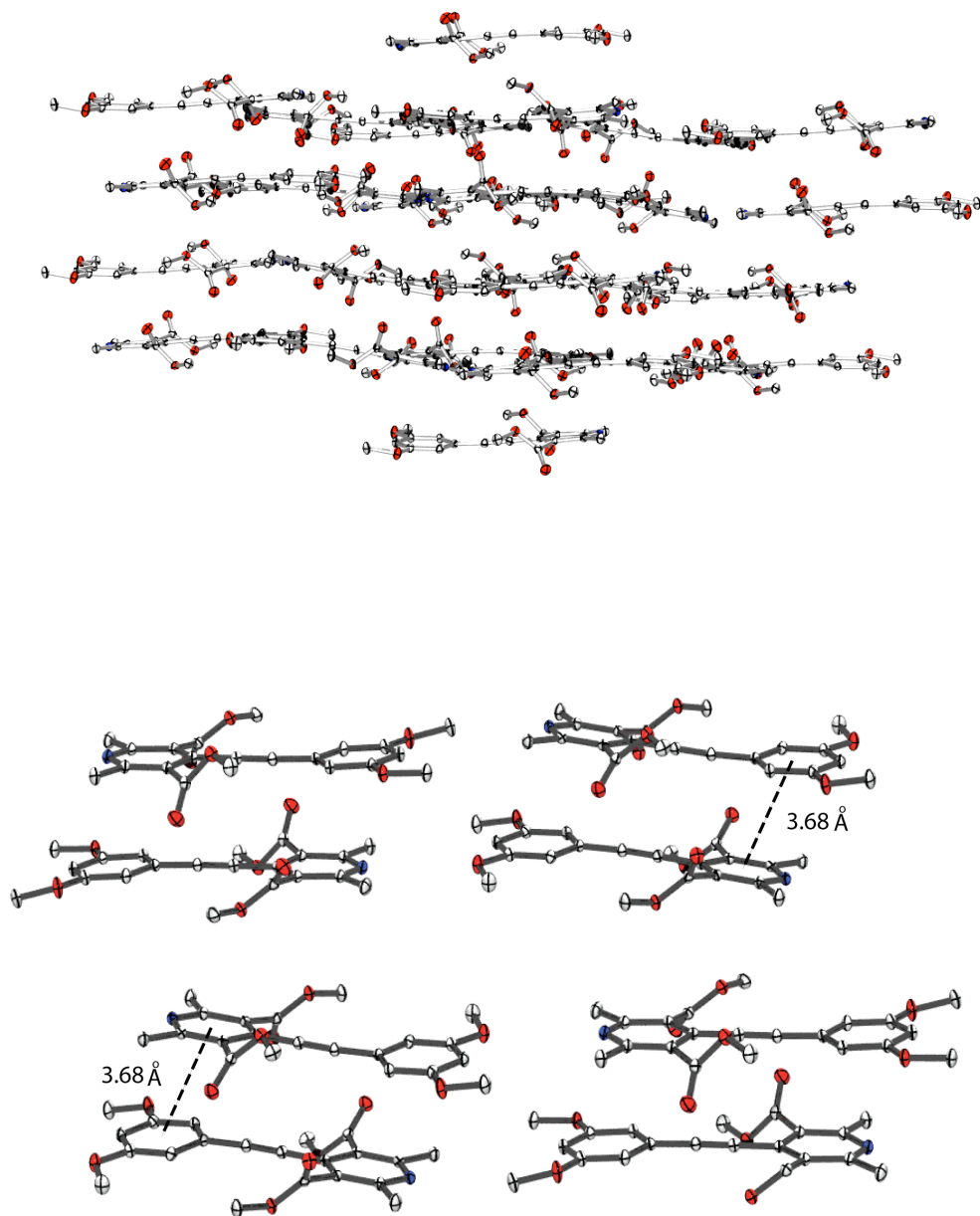


Figure S11. The solid state packing of **2** (top). A simplified version of packing (bottom). The average distance between two C≡C is 3.50 Å, and the average distance between electron-rich bis-methoxybenzene ring and electron-deficient pyridine ring is 3.68 Å.

SEM Images

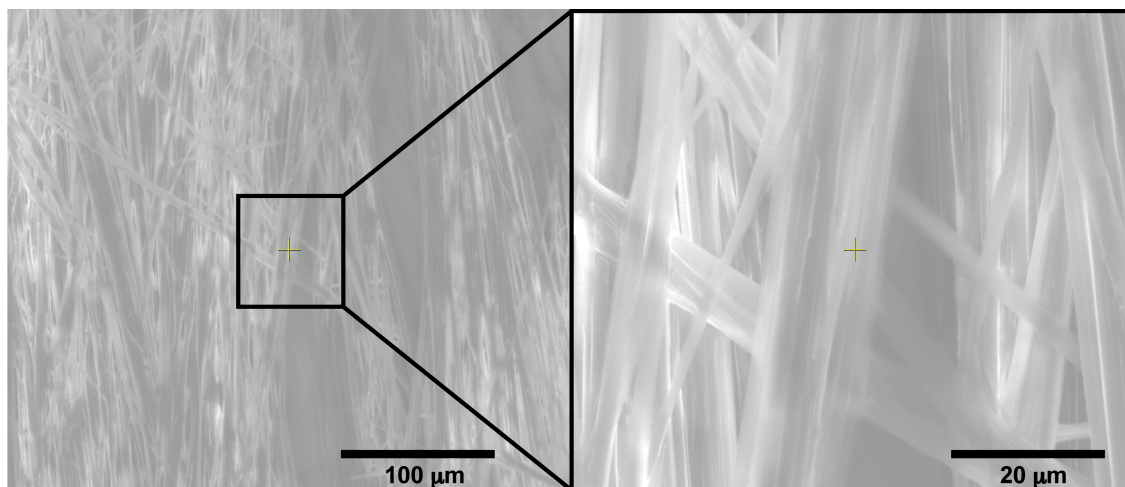


Figure S12. SEM images of fibers obtained from heat/cool-induced gelation of **2** (26 mM) in 2/1 DMSO/H₂O. The image to the right is at higher magnification.

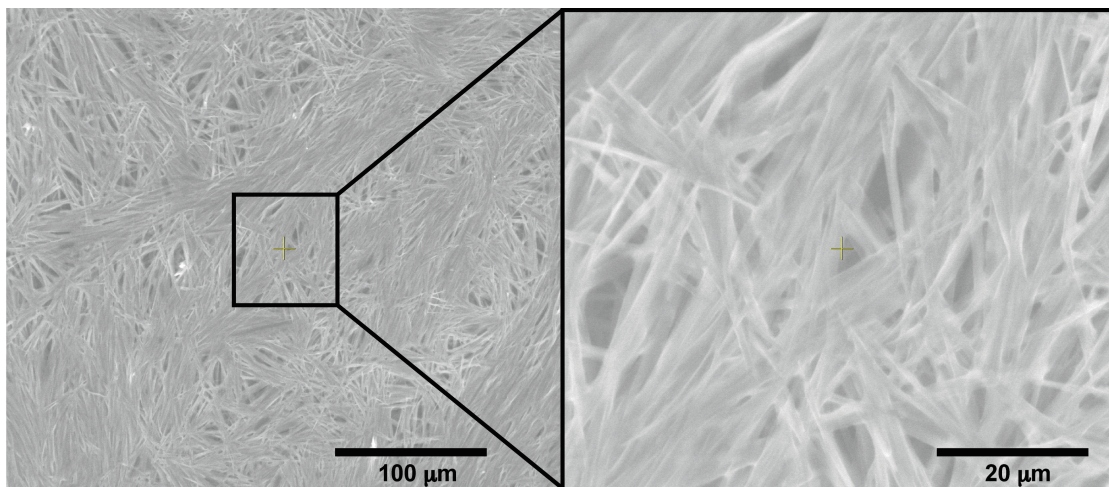


Figure S13. SEM images of fibers obtained from CAN-triggered gelation of **2** (26 mM). The image to the right is at higher magnification.

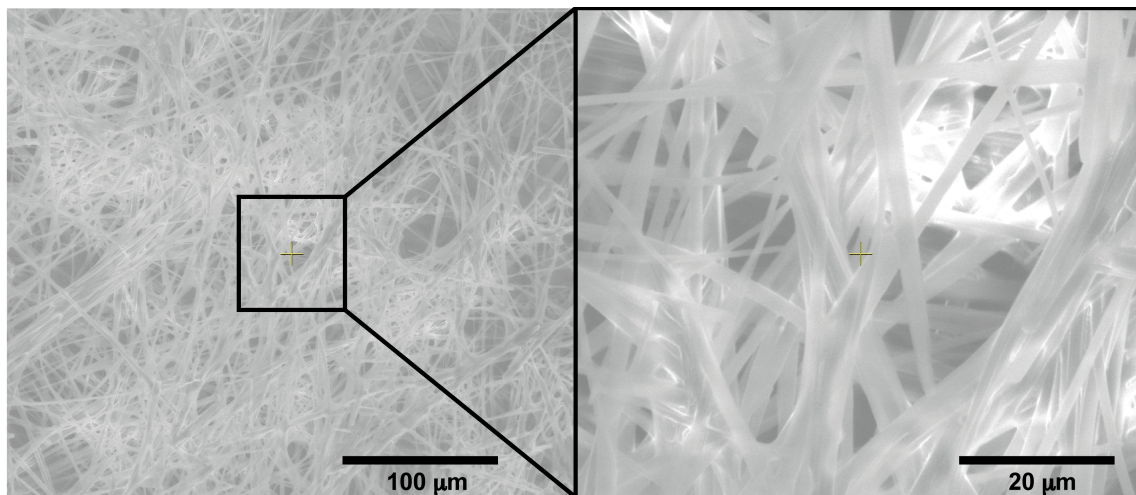


Figure S14. SEM images of fibers obtained from gelation of **2** (7.2 mM) after reaction with NO. The image to the right is at higher magnification.

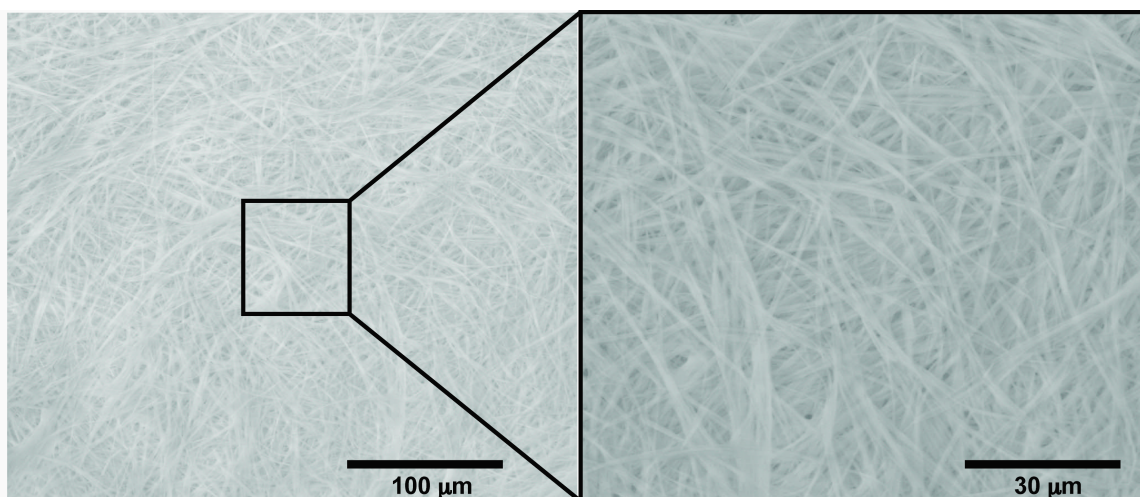


Figure S15. SEM images of fibers obtained from heat/cool-induced gelation of **2** (26 mM) in 1/1 MeOH/H₂O. The image to the right is at higher magnification.

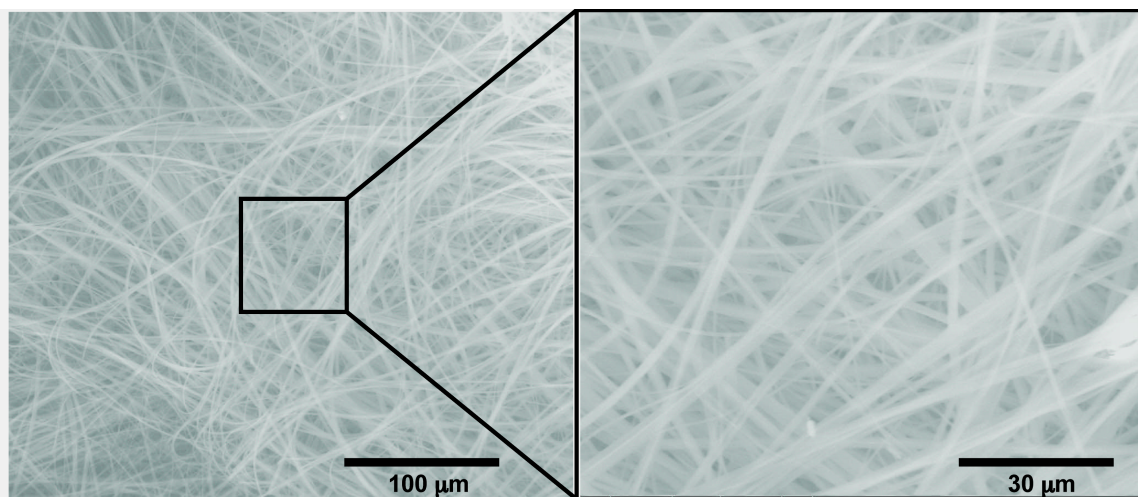


Figure S16. SEM images of fibers obtained from heat/cool-induced gelation of **2** (26 mM) in 1/2 EtOH/H₂O. The image to the right is at higher magnification.

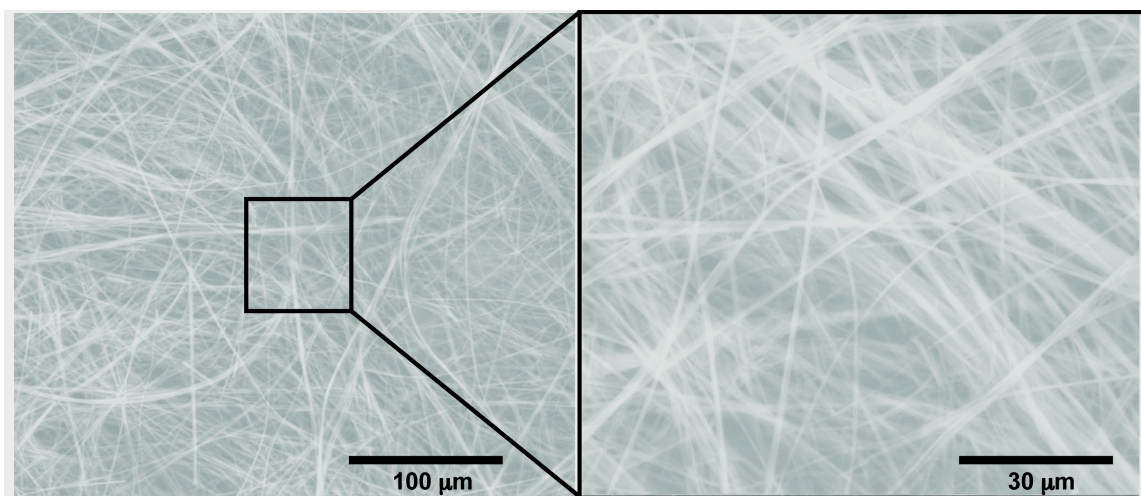


Figure S17. SEM images of fibers obtained from heat/cool-induced gelation of **2** (26 mM) in 1/3 iPrOH/H₂O. The image to the right is at higher magnification.

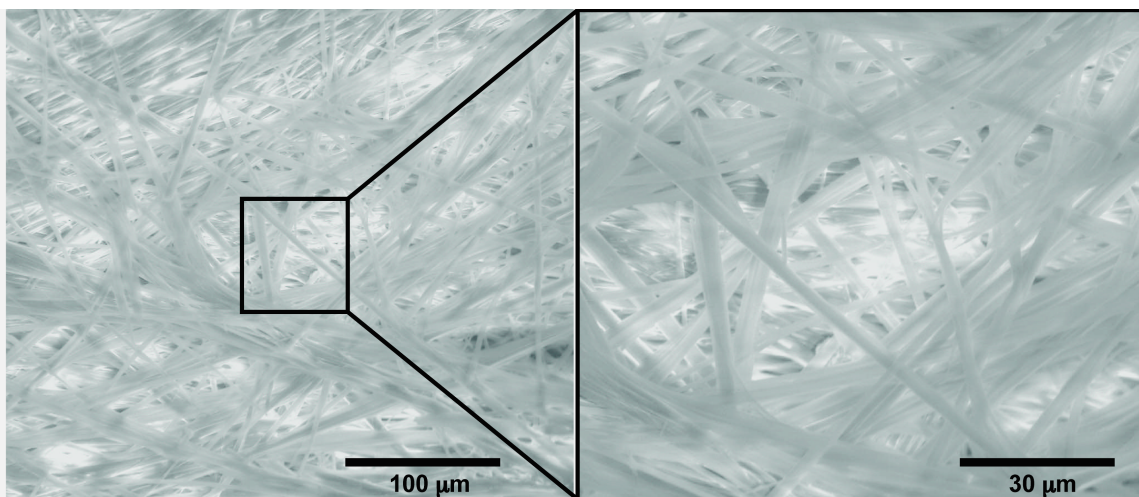


Figure S18. SEM images of fibers obtained from heat/cool-induced gelation of **2** (26 mM) in 1/1 DMF/H₂O. The image to the right is at higher magnification.

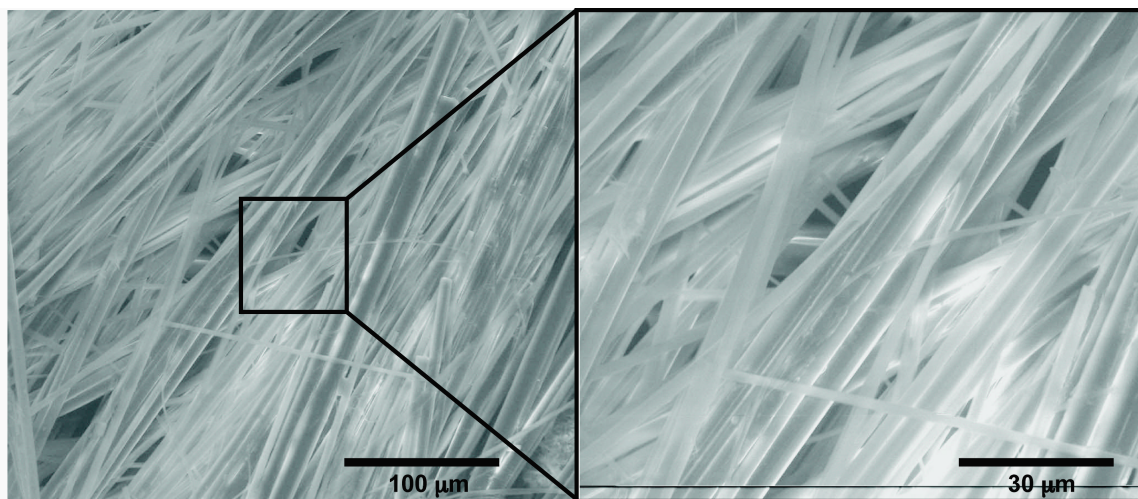


Figure S19. SEM images of fibers obtained from heat/cool-induced gelation of **2** (26 mM) in 1/1 acetone/H₂O. The image to the right is at higher magnification.

Powder X-ray Diffraction

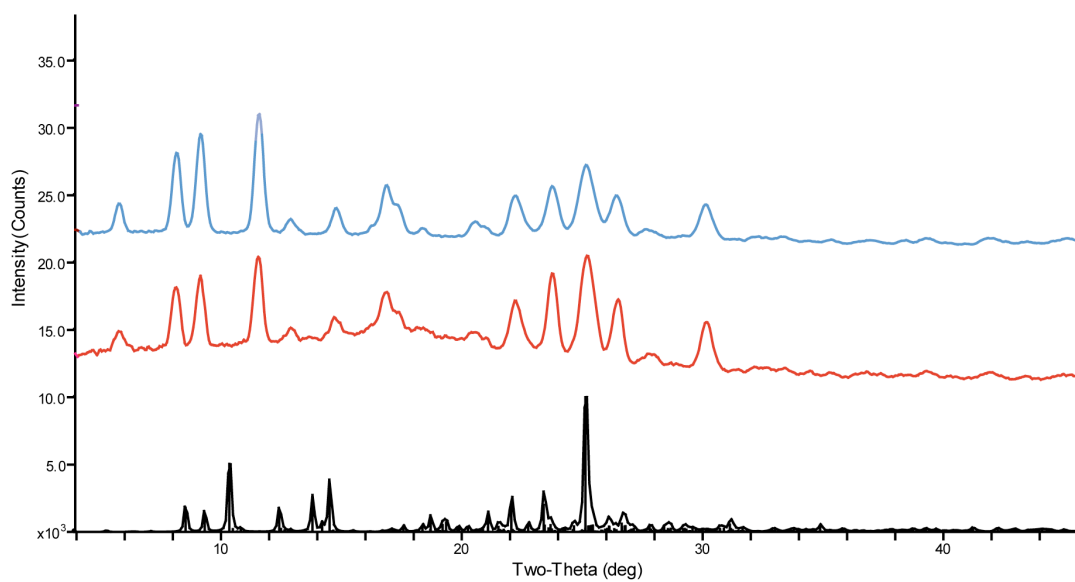


Figure S20. Powder X-ray diffraction of solid powder of **2** (blue), cryo-gel of **2** in acetone/H₂O (red) and powder X-ray simulation of **2** from single crystal structure (black). Note that the simulation from single crystal of **2** shared similar pattern with powder X-ray diffraction. The peak shift is due to the different temperatures used in the two experiments; Single crystal X-ray diffraction was performed at 85K while powder X-ray diffraction at 298K.

Raman Spectroscopic Data

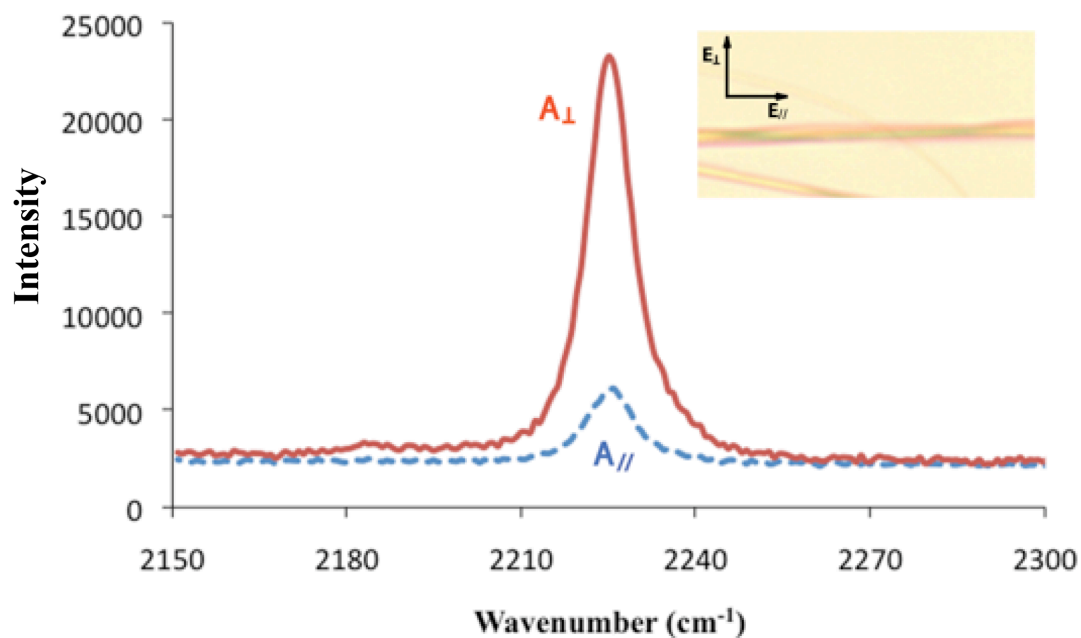


Figure S21. Raman spectra of **2** in gel (26 mM in 2/1 DMSO/H₂O) at C≡C stretching region (2225 cm⁻¹~2227 cm⁻¹). Spectra were taken on single fibers at two conditions: Fiber axis was parallel to laser (A_∥). Fiber long axis was perpendicular to laser (A_⊥). This sample was representative of the gel.

Rheological Tests

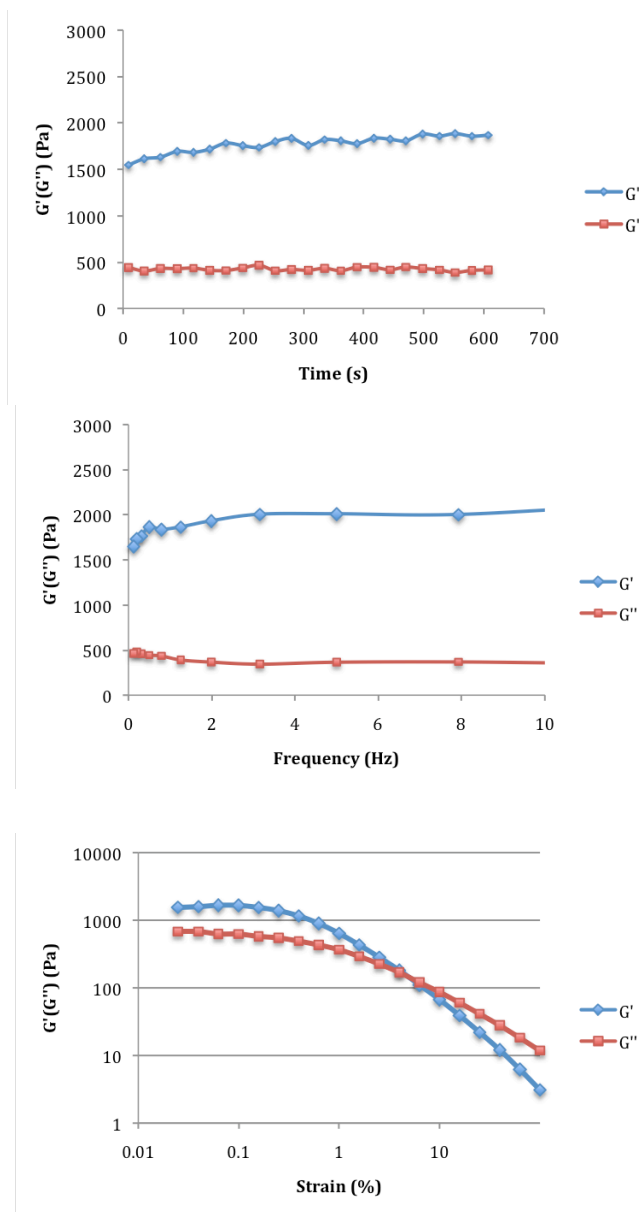


Figure S22. Viscoelastic properties of a 26 mM gel of **2** in DMSO/H₂O (2/1). **(top)** Time sweep under a constant strain (0.1%) and constant frequency (1Hz). Note that $G'(\omega)$ is three times greater than $G''(\omega)$. Both values remain constant during test time (10 min), indicating temporal stability of the gel. **(middle)** Frequency sweep using a constant strain (0.1%). Both $G'(\omega)$ and $G''(\omega)$ are independent of frequency from 0.1 Hz to 10 Hz. **(bottom)** Strain sweep under constant frequency (1 Hz). Before 0.1% deformation, $G'(\omega)$ is independence of the applied strain. Above 0.1% strain, the gel breaks down.

CAN-Triggered Gelations

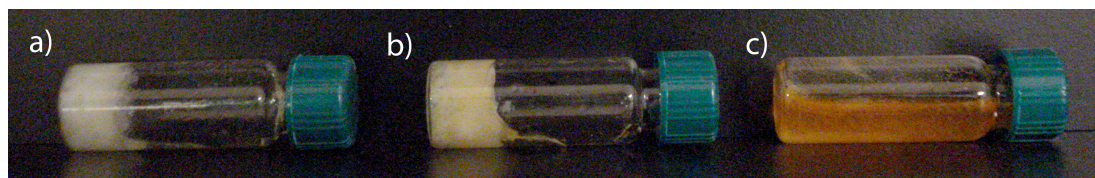
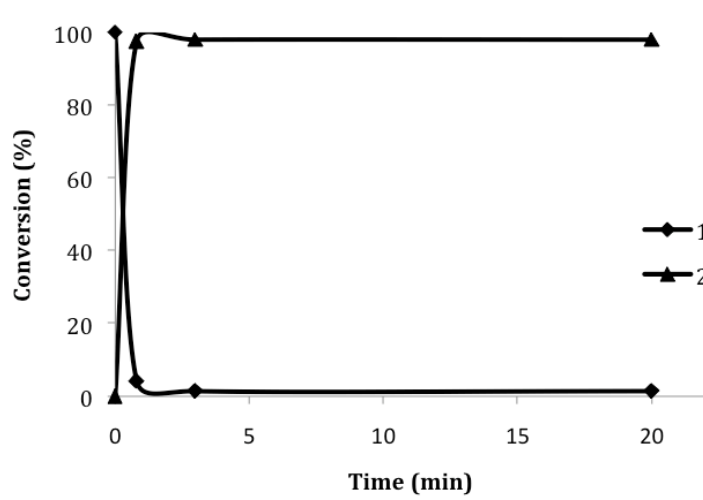


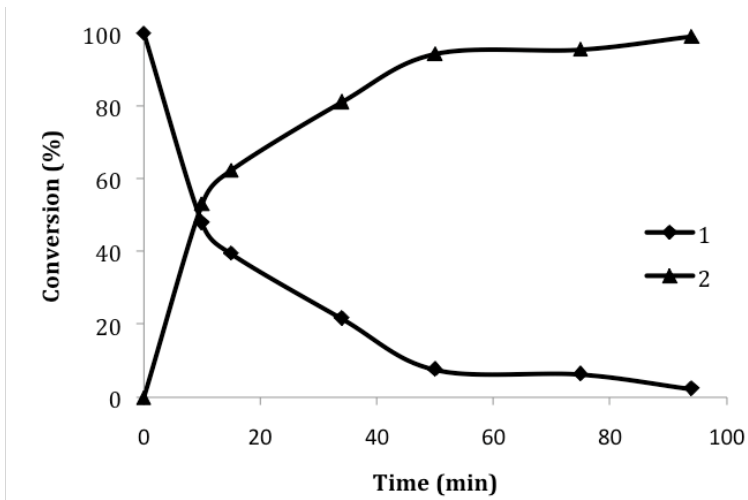
Figure S23. CAN-induced oxidation of **1** in 2/1 DMSO/H₂O at (a) 8 mg/mL (above cgc); (b) 6 mg/mL, (at cgc); (c) 4 mg/mL, (below cgc).

Data for Nitric Oxide Reaction

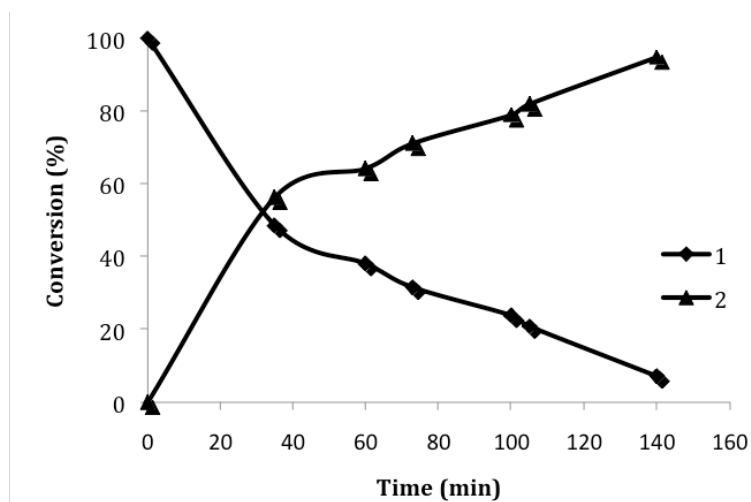
(a)



(b)



(c)



(d)

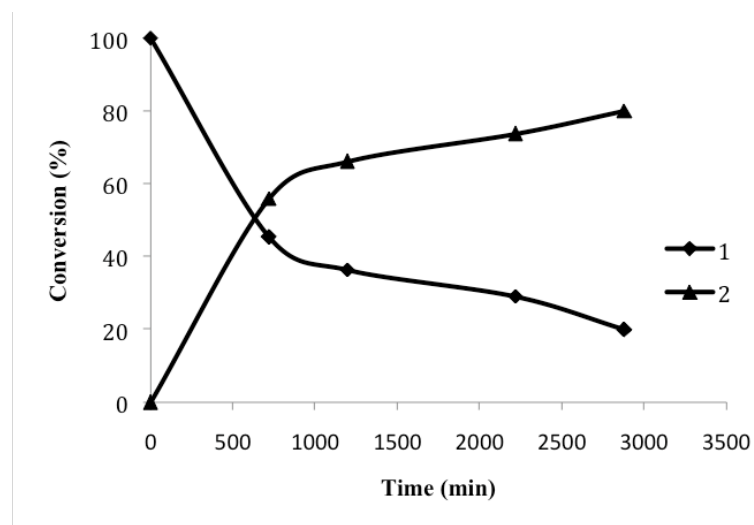


Figure S24. Reaction rates for oxidation of **1** by (a) 10 equiv (b) 1 equiv (c) 0.5 equiv (d) 0.25 equiv of NO.

References

1. Software for X-ray Crystallography: (a) Sheldrick, G.M. SHELXTL, v. 2008/3; Bruker Analytical X-ray, Madison, WI, 2008. (b) Sheldrick, G.M. SADABS, v. 2008/1. Program for Empirical Absorption Correction of Area Detector Data, University of Gottingen: Gottingen, Germany, 2008. (c) Saint Plus, v. 7.34, Bruker Analytical X-ray, Madison, WI, 2006.
2. AreaMax 2.0.0.4 ed.; Rigaku, 2005.
3. Jade Plus 8.2 ed.; Materials Data, Inc, 1995-2007
4. Li, A.-H.; Chang, L.; Ji, X.-D.; Melman, N.; Jacobson, K. A. *Bioconjugate Chem.* **1999**, *10*, 667-677.
5. Chanteau, S. H.; Tour, J. M. *Tetrahedron Lett.* **2001**, *42*, 3057-3060.
6. Klapars, A.; Buchwald, S.L. *J. Am. Chem. Soc.* **2002**, *124*, 14844-14845.
7. Mio, M. J.; Kopel, L. C.; Braun, J.B.; Gadzikwa, T. L.; Hull, K. L.; Brisbois, R. G.; Markworth, C. J.; Grieco, P.A. *Org. Lett.* **2002**, *4*, 3199-3202.

Appendix 2

Appendix to Chapter 3: Comparing Molecular Gelators and Non-gelators based on Solubilities and Solid-state Interactions

I. Materials

Column chromatography was performed on SiliCycle silica gel (40-63 μm) or using a Biotage Isolera One flash purification system. Thin layer chromatography was performed on Merck TLC plates pre-coated with silica gel 60 F254. All reagent grade materials and solvents were purchased from Aldrich, Acros, EMD, or Fisher and used without further purification unless otherwise noted. **S1**, **S6**, and **2a** were prepared according to literature procedures.¹

II. General Experimental

NMR Spectroscopy

Unless otherwise noted, ^1H and ^{13}C NMR spectra for all compounds were acquired in CDCl_3 on a Varian MR400 or a Varian Inova 400 Spectrometer operating at 400 and 100 MHz, respectively. The chemical shift data are reported in units of δ (ppm) relative to tetramethylsilane (TMS) and referenced with residual solvent. Multiplicities are reported as follows: singlet (s), broad singlet (br s), doublet (d), doublet of doublet (dd), triplet (t), multiplet (m).

Mass Spectrometry

HRMS data were obtained on a Micromass AutoSpec Ultima Magnetic Sector mass spectrometer.

Rheology

Rheological measurements were taken on an AR2000ex rheometer (TA Instruments) with a 25 mm serrated parallel plate. A hot solution (gelator and solvent) was loaded onto a pre-heated Peltier plate at 90 $^\circ\text{C}$. The gap was then fixed at 650 μm . The sample

was then cooled to 20 °C to allow gel formation. A solvent trap was used to limit solvent evaporation. After 30 min, the sample was pre-sheared under a stress of 0.1 Pa for 30 s before conducting the frequency sweep and oscillating stress sweep experiments. All measurements were repeated an average of 2-3 times to ensure reproducibility. The frequency sweep experiment was performed under 0.1 Pa stress with a frequency range from 0.628 rad/s to 628 rad/s (i.e., 0.1 Hz-100 Hz). The oscillating stress sweep experiment was performed at 1 Hz, with a stress range from 0.03 Pa to 150 Pa.

Scanning Electron Microscopy

Wet gel samples were loaded onto a stainless steel SEM holder and mounted with copper tape. The gels were observed using the low-vacuum mode of a Philips XL30FEG scanning electron microscope (SEM) using a 15-kV accelerating voltage. The images were digitally recorded and processed using Adobe Illustrator.

UV-Vis Spectrometry

UV-Vis spectra were taken on a Perkin-Elmer Lambda 850 UV-visible Spectrometer. Calibration curves were measured at λ_{max} for all compounds.

Melting Point

Melting points were measured on a MeltTemp 3.0, with a ramping rate of 2 °C/min.

X-ray crystallography

Colorless plates of **1a** were crystallized from a MeOH/H₂O solution at 23 °C. A crystal of dimensions 0.24 x 0.18 x 0.04 mm was mounted on a standard Bruker SMART-APEX CCD-based X-ray diffractometer equipped with a low temperature device and fine focus Mo-target X-ray tube ($\lambda = 0.71073 \text{ \AA}$) operated at 1500 W power (50 kV, 30 mA). The X-ray intensities were measured at 85(2) K; the detector was placed at a distance 5.055 cm from the crystal. A total of 2490 frames were collected with a scan width of 0.5° in ω and 0.45° in Φ with an exposure time of 30 s/frame. The frames were integrated with the Bruker SAINT software package with a narrow frame algorithm. The integration of the data yielded a total of 55660 reflections to a maximum 2θ value of 56.56° of which 6222 were independent and 5020 were greater than $2s(I)$. The final cell constants were based on the xyz centroids of 9985 reflections above $10s(I)$. Analysis of the data showed negligible decay during data collection; the data were processed with SADABS and

corrected for absorption. The structure was solved and refined with the Bruker SHELXTL (version 2008/4) software package,² using the space group P2(1)/c with Z = 4 for the formula C₂₇H₃₃NO₆. All non-hydrogen atoms were refined anisotropically with the hydrogen atoms placed in idealized positions. Full-matrix least-squares refinement based on F² converged at R1 = 0.0426 and wR2 = 0.1038 [based on I > 2σ(I)], R1 = 0.0557 and wR2 = 0.1126 for all data.

Colorless plates of **1b form-1** were grown by slow evaporation of a DMF/H₂O solution at 25 °C. A crystal of dimensions 0.40 x 0.33 x 0.10 mm mounted on a Bruker SMART APEX CCD-based X-ray diffractometer equipped with a low temperature device and fine focus Mo-target X-ray tube (λ = 0.71073 Å) operated at 1500 W power (50 kV, 30 mA). The X-ray intensities were measured at 200(2) K; the detector was placed at a distance 5.055 cm from the crystal. A total of 2750 frames were collected with a scan width of 0.5° in ω and 0.45° in Φ with an exposure time of 25 s/frame. The integration of the data yielded a total of 43911 reflections to a maximum 2θ value of 56.60° of which 9177 were independent and 7082 were greater than 2s(I). The final cell constants were based on the xyz centroids of 9849 reflections above 10s(I). Analysis of the data showed negligible decay during data collection; the data were processed with SADABS and corrected for absorption. The structure was solved and refined with the Bruker SHELXTL (version 2008/4) software package,² using the space group P1̄ with Z = 4 for the formula C₂₁H₂₁NO₄. There are two crystallographically independent molecules in the asymmetric unit. All non-hydrogen atoms were refined anisotropically with the hydrogen atoms placed in idealized positions. Full matrix least-squares refinement based on F² converged at R1 = 0.0474 and wR2 = 0.1274 [based on I > 2σ(I)], R1 = 0.0634 and wR2 = 0.1402 for all data.

Colorless needles of **1b form-2** were grown by slow evaporation of a MeOH/H₂O solution at 25 °C. A crystal of dimensions 0.46 x 0.04 x 0.03 mm mounted on a Bruker SMART APEX CCD-based X-ray diffractometer equipped with a low temperature device and fine focus Mo-target X-ray tube (λ = 0.71073 Å) operated at 1500 W power (50 kV, 30 mA). The X-ray intensities were measured at 85(2) K; the detector was placed at a distance 6.055 cm from the crystal. A total of 2640 frames were collected with a scan width of 0.5° in ω and 0.45° in Φ with an exposure time of 60 s/frame. The integration of the data yielded a total of 34333 reflections to a maximum 2θ value of 52.98° of which 4213 were independent and 3031 were greater than 2s(I). The final cell constants were

based on the xyz centroids of 7824 reflections above $10\sigma(I)$. Analysis of the data showed negligible decay during data collection; the data were processed with SADABS and corrected for absorption. The structure was solved and refined with the Bruker SHELXTL (version 2008/4) software package,² using the space group $P2(1)/c$ with $Z = 4$ for the formula $C_{21}H_{27}NO_6$. All non-hydrogen atoms were refined anisotropically with the hydrogen atoms placed in idealized positions with the exception of the hydrogen participating in hydrogen bonding. Full matrix least-squares refinement based on F^2 converged at $R1 = 0.0478$ and $wR2 = 0.1200$ [based on $I > 2\sigma(I)$], $R1 = 0.0737$ and $wR2 = 0.1363$ for all data.

Colorless plates of **2c** were crystallized from a DMF/H₂O solution at 23 °C. A crystal of dimensions 0.21 x 0.14 x 0.09 mm was mounted on a standard Bruker SMART-APEX CCD-based X-ray diffractometer equipped with a low temperature device and fine focus Mo-target X-ray tube ($\lambda = 0.71073 \text{ \AA}$) operated at 1500 W power (50 kV, 30 mA). The X-ray intensities were measured at 85(2) K; the detector was placed at a distance 5.055 cm from the crystal. A total of 2590 frames were collected with a scan width of 0.5° in w and 0.45° in Φ with an exposure time of 30 s/frame. The frames were integrated with the Bruker SAINT software package with a narrow frame algorithm. The integration of the data yielded a total of 42132 reflections to a maximum 2θ value of 56.66° of which 4615 were independent and 3798 were greater than $2\sigma(I)$. The final cell constants were based on the xyz centroids of 9941 reflections above $10\sigma(I)$. Analysis of the data showed negligible decay during data collection; the data were processed with SADABS and corrected for absorption. The structure was solved and refined with the Bruker SHELXTL (version 2008/4) software package,² using the space group $P2(1)/n$ with $Z = 4$ for the formula $C_{21}H_{21}NO_4$. All non-hydrogen atoms were refined anisotropically with the hydrogen atoms placed in idealized positions. Full-matrix least-squares refinement based on F^2 converged at $R1 = 0.0427$ and $wR2 = 0.1112$ [based on $I > 2\sigma(I)$], $R1 = 0.0534$ and $wR2 = 0.1199$ for all data.

Colorless needles of **3a** were crystallized from a DMF/H₂O solution at 23 °C. A crystal of dimensions 0.46 x 0.14 x 0.08 mm was mounted on a standard Bruker SMART-APEX CCD-based X-ray diffractometer equipped with a low temperature device and fine focus Mo-target X-ray tube ($\lambda = 0.71073 \text{ \AA}$) operated at 1500 W power (50 kV, 30 mA). The X-ray intensities were measured at 85(2) K; the detector was placed at a distance 5.055 cm from the crystal. A total of 1460 frames were collected with a scan width of 0.5° in w

and 0.45° in Φ with an exposure time of 30 s/frame. The frames were integrated with the Bruker SAINT software package with a narrow frame algorithm. The integration of the data yielded a total of 79584 reflections to a maximum 2θ value of 56.60° of which 14510 were independent and 10988 were greater than $2s(I)$. The final cell constants were based on the xyz centroids of 9990 reflections above $10s(I)$. Analysis of the data showed negligible decay during data collection; the data were processed with SADABS and corrected for absorption. The structure was solved and refined with the Bruker SHELXTL (version 2008/4) software package,² using the space group $P2(1)/n$ with $Z = 12$ for the formula $C_{21}H_{23}NO_6$. There are three crystallographically independent molecules in the asymmetric unit. All non-hydrogen atoms were refined anisotropically with the hydrogen atoms placed in idealized positions. Full-matrix least-squares refinement based on F^2 converged at $R1 = 0.0506$ and $wR2 = 0.1196$ [based on $I > 2\sigma(I)$], $R1 = 0.0726$ and $wR2 = 0.1314$ for all data.

Colorless needles of **5b** were crystallized from a MeOH/H₂O solution at 25 °C. A crystal of dimensions 0.46 x 0.12 x 0.10 mm was mounted on a standard Bruker SMART-APEX CCD-based X-ray diffractometer equipped with a low temperature device and fine focus Mo-target X-ray tube ($\lambda = 0.71073 \text{ \AA}$) operated at 1500 W power (50 kV, 30 mA). The X-ray intensities were measured at 85(2) K; the detector was placed at a distance 5.060 cm from the crystal. A total of 5190 frames were collected with a scan width of 0.5° in ω and 0.45° in Φ with an exposure time of 20 s/frame. The frames were integrated with the Bruker SAINT software package with a narrow frame algorithm. The integration of the data yielded a total of 50928 reflections to a maximum 2θ value of 56.66° of which 2833 were independent and 2533 were greater than $2s(I)$. The final cell constants were based on the xyz centroids of 9972 reflections above $10s(I)$. Analysis of the data showed negligible decay during data collection; the data were processed with SADABS and corrected for absorption. The structure was solved and refined with the Bruker SHELXTL (version 2008/4) software package,² using the space group $C2/c$ with $Z = 4$ for the formula $C_{25}H_{29}NO_6$. All non-hydrogen atoms were refined anisotropically with the hydrogen atoms placed in idealized positions. The molecule lies on a two-fold axis in the crystal lattice. Full-matrix least-squares refinement based on F^2 converged at $R1 = 0.0375$ and $wR2 = 0.0993$ [based on $I > 2\sigma(I)$], $R1 = 0.0415$ and $wR2 = 0.1036$ for all data.

Colorless blocks of **6a** were crystallized from a MeOH/H₂O solution at 23 °C. A crystal of dimensions 0.33 x 0.21 x 0.14 mm was mounted on a standard Bruker SMART APEX CCD-based X-ray diffractometer equipped with a low-temperature device and fine-focus Mo-target X-ray tube ($\lambda = 0.71073 \text{ \AA}$) operated at 2000 W power (50 kV, 30 mA). The X-ray intensities were measured at 200(2) K; the detector was placed at a distance 5.055 cm from the crystal. A total of 4095 frames were collected with a scan width of 0.5° in ω and 0.45° in Φ with an exposure time of 30 s/frame. Indexing was performed by use of the CELL_NOW program which indicated that the crystal was a two-component, non-merohedral twin. The frames were integrated with the Bruker SAINT software package with a narrow frame algorithm. The integration of the data yielded a total of 56656 reflections to a maximum 2θ value of 52.72° of which 7196 were independent and 6473 were greater than $2\sigma(I)$. The final cell constants were based on the xyz centroids of 5040 reflections above $10\sigma(I)$. Analysis of the data showed negligible decay during data collection; the data were processed with TWINABS and corrected for absorption. For this refinement, single reflections from component one as well as composite reflections containing a contribution from this component were used. Merging of the data was performed in TWINABS and an HKLF 5 format file was used for refinement. The structure was solved and refined with the Bruker SHELXTL (version 2008/4) software package, using the space group P1bar with $Z = 4$ for the formula C₁₉H₁₇NO₄•H₂O. All non-hydrogen atoms were refined anisotropically with the hydrogen atoms placed in idealized positions with the exception of the hydrogens involved in H-bonding which were allowed to refine isotropically. The twin domains are related by a 179.5 degree rotation about the direct and reciprocal (0 1 0) axis and a refined twin volume fraction of 0.428(2). Full-matrix least-squares refinement based on F^2 converged at $R1 = 0.0434$ and $wR2 = 0.1221$ [based on $I > 2\sigma(I)$], $R1 = 0.0493$ and $wR2 = 0.1265$ for all data.

Colorless needles of **6d** were crystallized from a DMF/H₂O solution at 23 °C. A crystal of dimensions 0.48 x 0.03 x 0.03 mm was mounted on a standard Bruker SMART-APEX CCD-based X-ray diffractometer equipped with a low temperature device and fine focus Mo-target X-ray tube ($\lambda = 0.71073 \text{ \AA}$) operated at 1500 W power (50 kV, 30 mA). The X-ray intensities were measured at 85(2) K; the detector was placed at a distance 5.055 cm from the crystal. A total of 2446 frames were collected with a scan width of 0.5° in ω and 0.45° in Φ with an exposure time of 60 s/frame. The frames were integrated with the Bruker SAINT software package with a narrow frame algorithm. The integration of the

data yielded a total of 16859 reflections to a maximum 2θ value of 52.84° of which 3766 were independent and 2403 were greater than $2s(I)$. The final cell constants were based on the xyz centroids of 3707 reflections above $10s(I)$. Analysis of the data showed negligible decay during data collection; the data were processed with SADABS and corrected for absorption. The structure was solved and refined with the Bruker SHELXTL (version 2008/4) software package,² using the space group P1bar with $Z = 2$ for the formula $C_{27}H_{33}NO_6$. All non-hydrogen atoms were refined anisotropically with the hydrogen atoms placed in idealized positions. Full-matrix least-squares refinement based on F^2 converged at $R1 = 0.0776$ and $wR2 = 0.1779$ [based on $I > 2\sigma(I)$], $R1 = 0.1183$ and $wR2 = 0.1986$ for all data.

Yellow blocks of **7b** were crystallized from a DMF/MeOH solution at 23°C . A crystal of dimensions $0.44 \times 0.23 \times 0.12$ mm was mounted on a standard Bruker SMART-APEX CCD-based X-ray diffractometer equipped with a low temperature device and fine focus Mo-target X-ray tube ($\lambda = 0.71073 \text{ \AA}$) operated at 1500 W power (50 kV, 30 mA). The X-ray intensities were measured at $85(2) \text{ K}$; the detector was placed at a distance 5.055 cm from the crystal. A total of 3415 frames were collected with a scan width of 0.5° in w and 0.45° in Φ with an exposure time of 20 s/frame. The frames were integrated with the Bruker SAINT software package with a narrow frame algorithm. The integration of the data yielded a total of 23787 reflections to a maximum 2θ value of 56.64° of which 4036 were independent and 3554 were greater than $2s(I)$. The final cell constants were based on the xyz centroids of 9962 reflections above $10s(I)$. Analysis of the data showed negligible decay during data collection; the data were processed with SADABS and corrected for absorption. The structure was solved and refined with the Bruker SHELXTL (version 2008/4) software package, using the space group P1bar with $Z = 2$ for the formula $C_{19}H_{15}N_3O_2$. All non-hydrogen atoms were refined anisotropically with the hydrogen atoms placed in idealized positions. Full-matrix least-squares refinement based on F^2 converged at $R1 = 0.0477$ and $wR2 = 0.1384$ [based on $I > 2\sigma(I)$], $R1 = 0.0525$ and $wR2 = 0.1430$ for all data.

Colorless prisms of **8a** were crystallized from a DMF/H₂O solution at 25°C . A crystal of dimensions $0.21 \times 0.17 \times 0.16$ mm was mounted on a standard Bruker SMART-APEX CCD-based X-ray diffractometer equipped with a low temperature device and fine focus Mo-target X-ray tube ($\lambda = 0.71073 \text{ \AA}$) operated at 1500 W power (50 kV, 30 mA). The X-

ray intensities were measured at 85(2) K; the detector was placed at a distance 5.060 cm from the crystal. A total of 4095 frames were collected with a scan width of 0.5° in w and 0.45° in Φ with an exposure time of 20 s/frame. The frames were integrated with the Bruker SAINT software package with a narrow frame algorithm. The integration of the data yielded a total of 30832 reflections to a maximum 2θ value of 56.60° of which 4308 were independent and 3750 were greater than $2s(I)$. The final cell constants were based on the xyz centroids of 9987 reflections above $10s(I)$. Analysis of the data showed negligible decay during data collection; the data were processed with SADABS and corrected for absorption. The structure was solved and refined with the Bruker SHELXTL (version 2008/4) software package,² using the space group $P1\bar{1}$ with $Z = 2$ for the formula $C_{20}H_{19}NO_5$. All non-hydrogen atoms were refined anisotropically with the hydrogen atoms placed in idealized positions. Full-matrix least-squares refinement based on F^2 converged at $R1 = 0.0397$ and $wR2 = 0.1076$ [based on $I > 2\sigma(I)$], $R1 = 0.0456$ and $wR2 = 0.1144$ for all data.

Colorless needles of **8b** were crystallized from a DMSO/H₂O solution at 25 °C. A crystal of dimensions 0.44 x 0.08 x 0.08 mm was mounted on a standard Bruker SMART-APEX CCD-based X-ray diffractometer equipped with a low temperature device and fine focus Mo-target X-ray tube ($\lambda = 0.71073 \text{ \AA}$) operated at 1500 W power (50 kV, 30 mA). The X-ray intensities were measured at 85(2) K; the detector was placed at a distance 5.060 cm from the crystal. A total of 2540 frames were collected with a scan width of 0.6° in w and 0.45° in Φ with an exposure time of 30 s/frame. The frames were integrated with the Bruker SAINT software package with a narrow frame algorithm. The integration of the data yielded a total of 39475 reflections to a maximum 2θ value of 52.82° of which 4254 were independent and 2983 were greater than $2s(I)$. The final cell constants were based on the xyz centroids of 7836 reflections above $10s(I)$. Analysis of the data showed negligible decay during data collection; the data were processed with SADABS and corrected for absorption. The structure was solved and refined with the Bruker SHELXTL (version 2008/4) software package,² using the space group $P2(1)/c$ with $Z = 4$ for the formula $C_{22}H_{23}NO_7$. All non-hydrogen atoms were refined anisotropically with the hydrogen atoms placed in idealized positions. Full-matrix least-squares refinement based on F^2 converged at $R1 = 0.0512$ and $wR2 = 0.1173$ [based on $I > 2\sigma(I)$], $R1 = 0.0804$ and $wR2 = 0.1331$ for all data.

Powder X-ray Diffraction

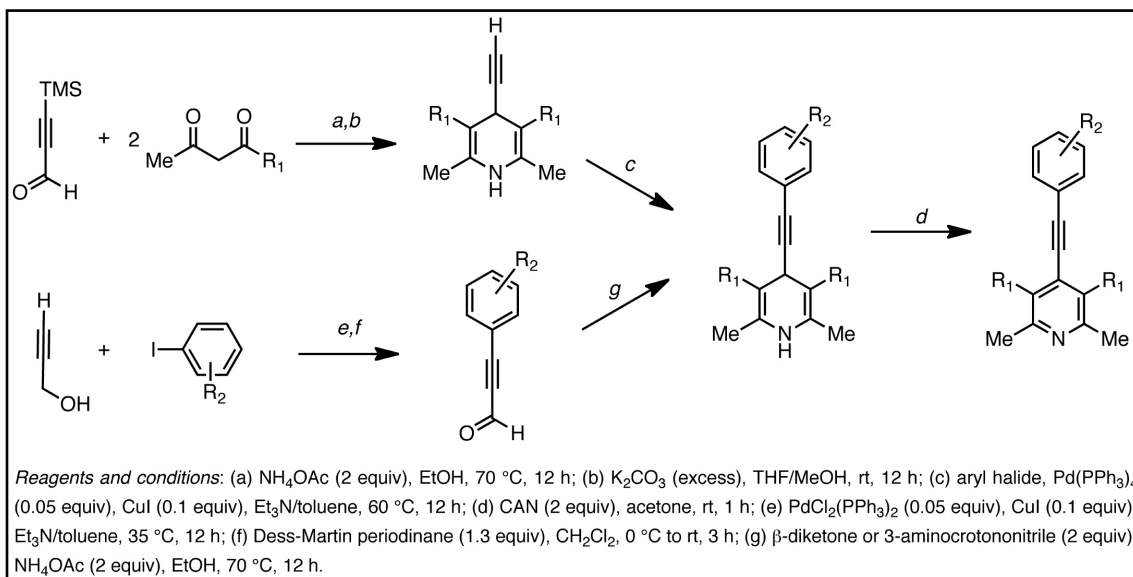
Powder X-ray diffraction (PXRD) patterns were collected at ambient temperature using a Rigaku R-Axis SPIDER diffractometer with an imaging plate detector and graphite monochromated Cu-K α radiation (1.5406 Å). The samples were mounted on a cryoloop. The temperature was controlled with an Oxford Cryostream Plus. To obtain powder patterns with minimized preferred orientation, images were collected for 5 min while rotating the sample about the φ -axis at 10° s⁻¹ while oscillating ω between 120° and 180° at 1° s⁻¹ with χ set at 45°. The images were integrated from 2 θ ranging between 2.5° to 50° with a 0.02° step size with the AreaMax software package.³ The powder diffraction patterns were processed in Jade Plus⁴ to calculate peak positions and intensities. Background subtraction was performed for the in situ gel diffraction patterns to remove the scattering contribution from solvent.

Hirshfeld Surface Analysis

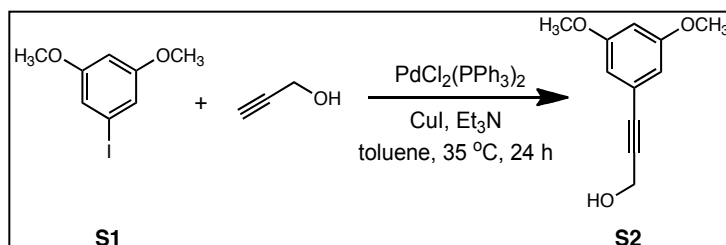
Hirshfeld surfaces for each molecule in the asymmetric unit of the single crystal of **1a**, **1b** (both forms), **2a**, **2c**, **3a**, **5b**, **6a**, **6d**, **7b**, **8a** and **8b** were constructed using the program Crystal Explorer v2.0.⁵ The Hirshfeld surface is defined as the partitioning of space in the crystal where the electron distribution of the sum of spherical atoms for the molecule (promolecule), contributes more than twice the electron distribution of the corresponding sum of the whole crystal (procrystal). These surfaces are derived from Hirshfeld's stockholders partitioning which are described in detail elsewhere.^{6,7} Each point on the surface is color-coded according to the fraction of the total surface area contained in the bin.

The crystallographic information files were uploaded to the program after normalization of the C-H bond length to average neutron values (1.083 Å). The 3D Hirshfeld surfaces were then calculated. The 2D fingerprint plots and their decompositions into different intermolecular contacts are extracted from the 3D Hirshfeld surfaces. For example, areas where hydrogen is the closest atom inside the surface and oxygen is the closest atom outside the surface (and *vice versa*) are colored for O \cdots H interactions. Consequently, the area of the colored surface is summed and then divided by the total Hirshfeld surface area to determine the relative contribution of the O \cdots H interactions.⁷

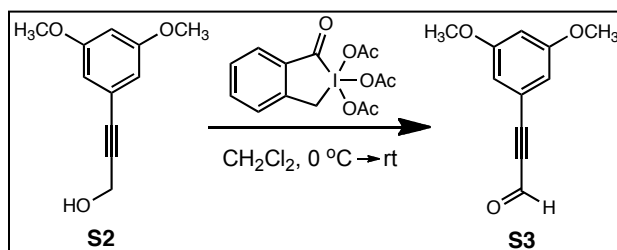
III. Synthetic Procedures



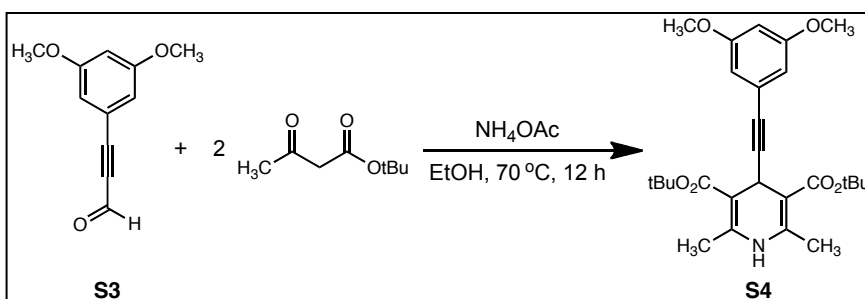
Scheme S1. Syntheses scheme for pyridines 1-8.



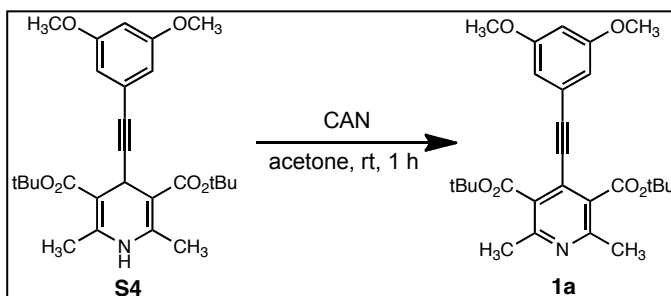
S2.⁹ A 50 mL Schlenk flask was equipped with a stir bar, oven-dried, cooled under vacuum and charged with N_2 . Sequentially, **S1** (7.6 g, 29 mmol), CuI (0.55 g, 2.9 mmol), Et_3N (6 mL), propargyl alcohol (1.6 g, 29 mmol), $\text{PdCl}_2(\text{PPh}_3)_2$ (0.98 g, 1.4 mmol) and toluene (30 mL) were added. The flask was sealed and heated to 35 °C. After 24 h, the mixture was diluted with CH_2Cl_2 , washed with saturated aq NH_4Cl (2 x 50 mL) and brine (1 x 50 mL). The organic layer was separated, dried over MgSO_4 , filtered and concentrated in vacuo. The crude product was purified by column chromatography using 50/50 EtOAc/hexanes as eluent to give 5.1 g of a yellow oil (93% yield). HRMS (ESI): Calcd for $\text{C}_{11}\text{H}_{12}\text{O}_3$, 193.0865 $[\text{M} + \text{H}]^+$; Found, 193.0859.



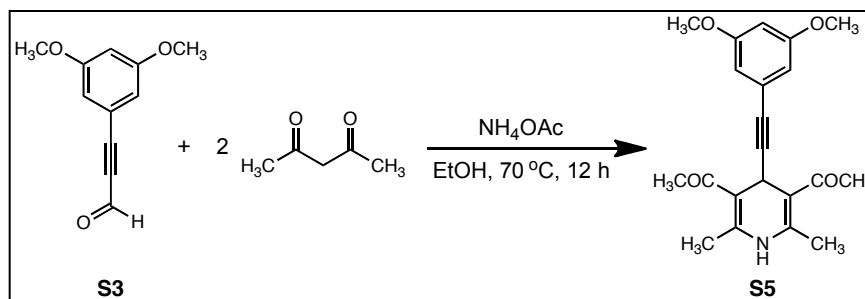
S3.¹⁰ A 250 mL round bottom flask was equipped with a stir bar. **S2** (6.4 g, 33 mmol) and CH_2Cl_2 (50 mL) were added. The solution was cooled to 0 °C and then Dess-Martin periodinane (17 g, 40 mmol) was added in one portion. The ice-bath was removed and the reaction was allowed to warm to rt. After 3 h, the mixture was filtered. The filtrate was washed with saturated aq Na_2CO_3 (2 x 50 mL) and 10% aq $\text{Na}_2\text{S}_2\text{O}_3$ (2 x 50 mL). The organic layer was separated, dried over anhydrous MgSO_4 , filtered and concentrated in vacuo. The crude product was purified by column chromatography using 15/85 EtOAc/hexanes as the eluent to give 4.9 g of a colorless crystalline solid (78% yield). HRMS (ESI): Calcd for $\text{C}_{11}\text{H}_{10}\text{O}_3$, 190.0630 M^+ ; Found, 190.0626.



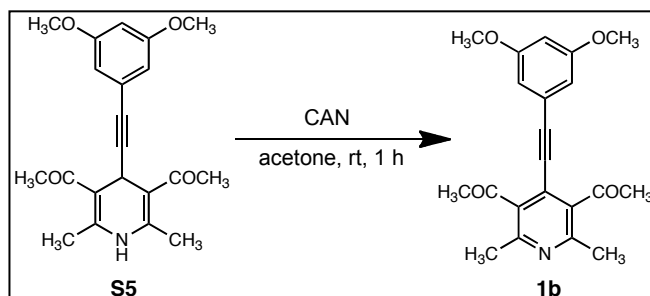
S4.¹¹ A 50 mL round bottom flask was equipped with a stir bar. Sequentially, **S3** (0.35 g, 1.8 mmol), *t*-butyl acetoacetate (0.58 g, 3.7 mmol), NH_4OAc (0.28 g, 3.7 mmol) and EtOH (20 mL) were added. The solution was stirred at 70 °C for 12 h. After cooling to rt, a white precipitate formed. The precipitate was isolated by filtration, washed with hexanes (~20 mL) and EtOH (~20 mL) and dried under vacuum to give 0.48 g yellow solid (56% yield). HRMS (ESI): Calcd for $\text{C}_{27}\text{H}_{35}\text{NO}_6$, 492.2362 $[\text{M} + \text{Na}]^+$; Found, 492.2369.



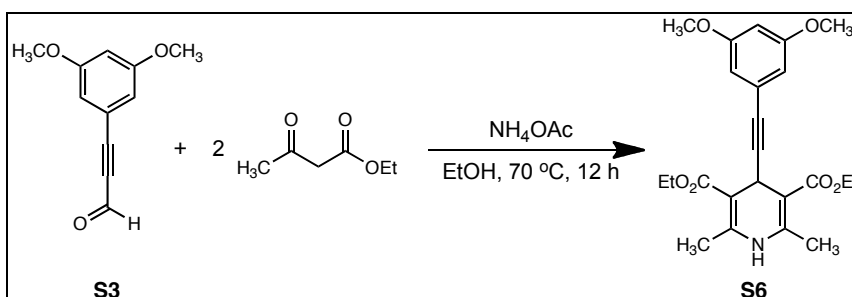
1a.¹² A 50 mL round bottom flask was equipped with a stir bar. **S4** (0.48 g, 1.0 mmol) and acetone (20 mL) were added and stirred to give a homogeneous solution. To this solution, cerium ammonium nitrate (1.1 g, 2.0 mmol) was added portion wise. The mixture was stirred at rt for 1 h. Then the mixture was concentrated in vacuo. The resulting solid was dissolved in CH_2Cl_2 and extracted with H_2O (3 x 20 mL). The organic layer was separated, dried over anhydrous MgSO_4 , filtered and concentrated in vacuo. The crude product was purified by column chromatography using 50/50 EtOAc/hexanes as the eluent to give 0.41 g of a white solid (85% yield). HRMS (ESI): Calcd for $\text{C}_{27}\text{H}_{33}\text{NO}_6$, 468.2386 $[\text{M} + \text{H}]^+$; Found, 468.2377. Elemental Analysis: Calcd. for $\text{C}_{27}\text{H}_{33}\text{NO}_6$: C, 69.36; H, 7.11; N, 3.00; O, 20.53; Found: C, 68.65; H, 7.14; N, 2.93; O, 21.28.



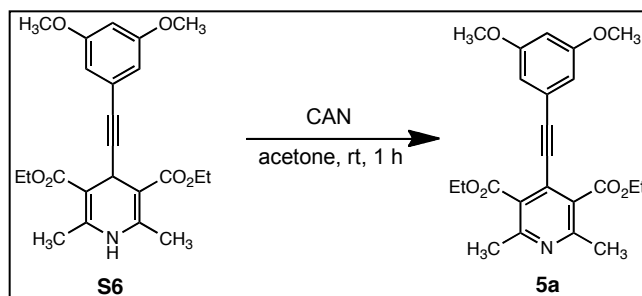
S5 was synthesized using the same procedure as **S4** (Page 107). Filtration and washing with hexanes (~20 mL) and EtOH (~20 mL) gave 0.25 g of a bright yellow solid (52% yield). HRMS (ESI): Calcd for $\text{C}_{21}\text{H}_{23}\text{NO}_4$, 376.1525 $[\text{M} + \text{Na}]^+$; Found, 376.1519.



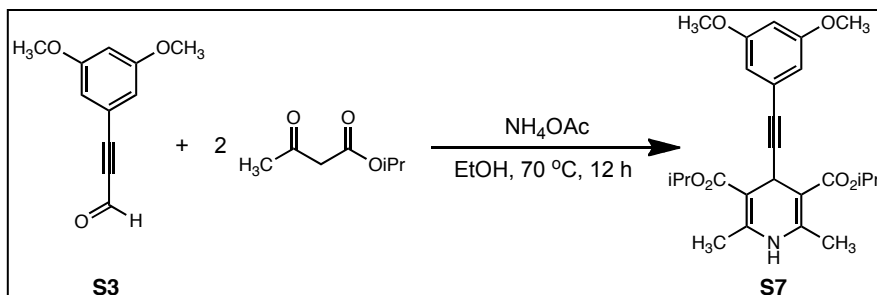
1b was synthesized using the same procedure as **1a** (Page 108). Column chromatography using 50/50 hexanes/EtOAc as the eluent gave 0.54 g of a white solid (91% yield). HRMS (ESI): Calcd for $C_{21}H_{21}NO_4$, 352.1549 $[M + H]^+$; Found, 352.1546. Elemental Analysis: Calcd for $C_{21}H_{21}NO_4$: C, 71.78; H, 6.02; N, 3.99; O, 18.21; Found: C, 71.64; H, 6.03; N, 4.01; O, 18.32.



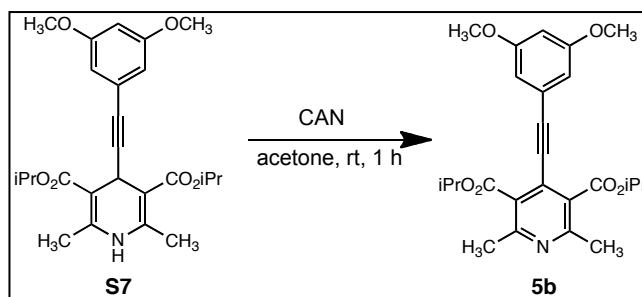
S6 was synthesized using the same procedure as **S4** (Page 107). Filtration and washing with hexanes (~20 mL) and EtOH (~20 mL) gave 0.19 g of a light brown solid (58% yield). HRMS (ESI): Calcd for $C_{23}H_{27}NO_6$, 436.1736 $[M + Na]^+$; Found, 436.1730.



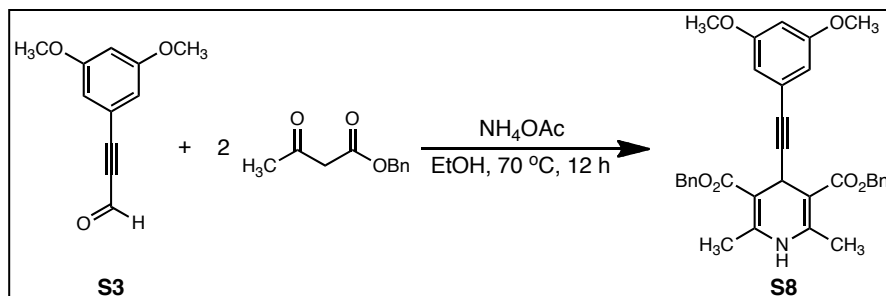
5a was synthesized using the same procedure as **1a** (Page 108). Column chromatography using 50/50 hexanes/EtOAc as the eluent gave 0.16 g of a light yellow oil (100% yield). HRMS (ESI): Calcd for $C_{23}H_{25}NO_6$, 412.1760 $[M + H]^+$; Found, 412.1745.



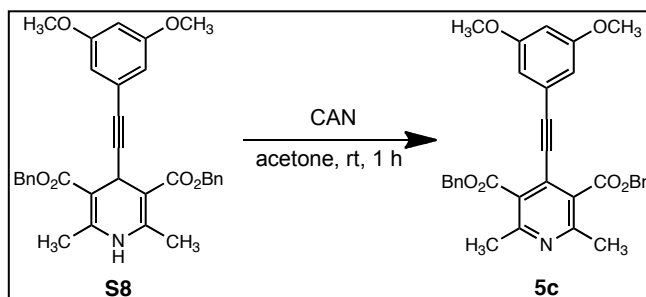
S7 was synthesized using the same procedure as **S4** (Page 107). Filtration and washing with hexanes (~20 mL) and EtOH (~20 mL) gave 0.13 g of a pale yellow solid (58% yield). HRMS (ESI): Calcd for $C_{25}H_{31}NO_6$, 464.2049 $[M + Na]^+$; Found, 464.2045.



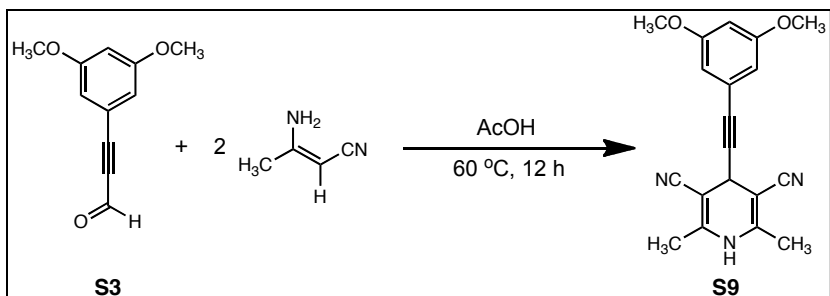
5b was synthesized using the same procedure as **1a** (Page 108). Column chromatography using 50/50 hexane/EtOAc as the eluent gave 0.11 g of a dark yellow solid (85% yield). HRMS (ESI): Calcd for $C_{25}H_{29}NO_6$, 440.2073 $[M + H]^+$; Found, 440.2074.



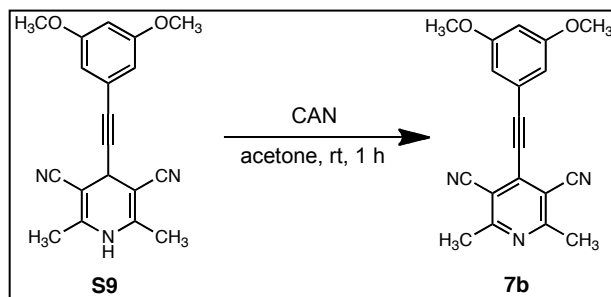
S8 was synthesized using the same procedure as **S4** (Page 107). Column chromatography using 50/50 hexanes/ EtOAc as the eluent gave 0.12 g of a yellow solid (54% yield). HRMS (ESI): Calcd for $\text{C}_{33}\text{H}_{31}\text{NO}_6$, 560.2044 $[\text{M} + \text{Na}]^+$; Found, 560.2033.



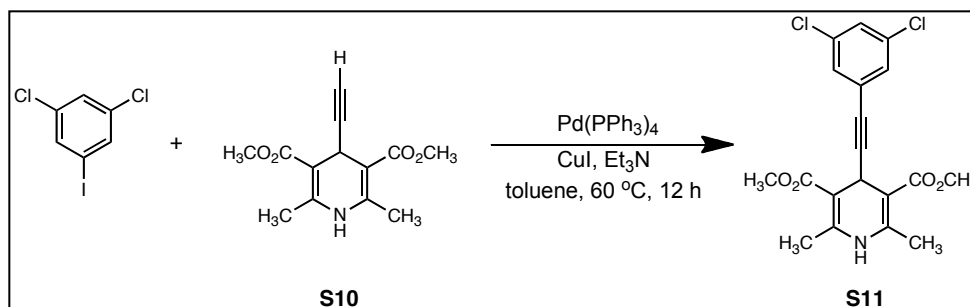
5c was synthesized using the same procedure as **1a** (Page 108). Column chromatography using 50/50 hexane/ EtOAc as the eluent gave 0.15 g of a yellow oil (49% yield). HRMS (ESI): Calcd for $\text{C}_{33}\text{H}_{29}\text{NO}_6$, 536.2073 $[\text{M} + \text{H}]^+$; Found, 536.2072.



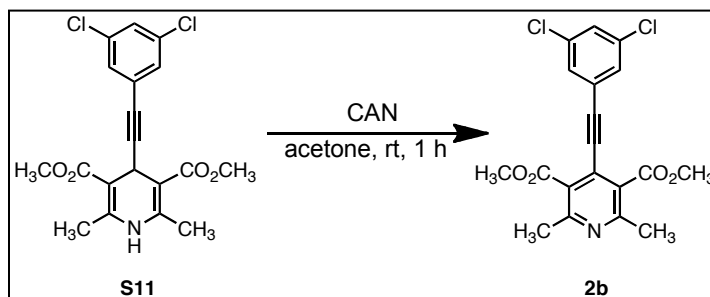
S9.¹³ A 50 mL round bottom flask was equipped with a stir bar. Sequentially, **S3** (0.20 g, 1.1 mmol), 3-aminocrotononitrile (0.17 g, 2.2 mmol), and AcOH (20 mL) were added. The mixture was stirred at 60 °C for 12 h. After cooling to rt, a yellow precipitate formed. The precipitate was filtered, washed with H₂O and dried under vacuum to give 0.17 g of a pale yellow solid (52% yield). Additionally, H₂O was added to the filtrate and a dark yellow solid precipitated. The second precipitate was filtered and purified by column chromatography using 50/50 EtOAc/hexanes as the eluent to give 0.077 g of a bright yellow solid (24% yield). HRMS (ESI): Calcd for C₁₉H₁₇N₃O₂, 342.1218 [M + Na]⁺; Found, 342.1206.



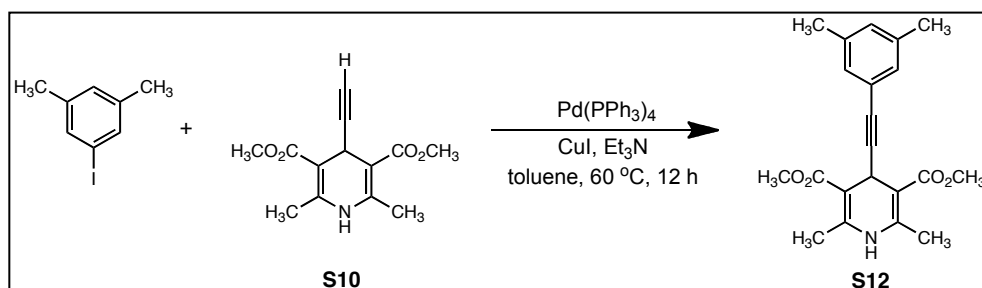
7b was synthesized using the same procedure as **1a** (Page 108). Column chromatography using 50/50 hexanes/EtOAc as the eluent gave 0.050 g of a bright yellow solid (100% yield). HRMS (ESI): Calcd. for $C_{19}H_{15}N_3O_2$, 318.1243 $[M + H]^+$; Found, 318.1229.



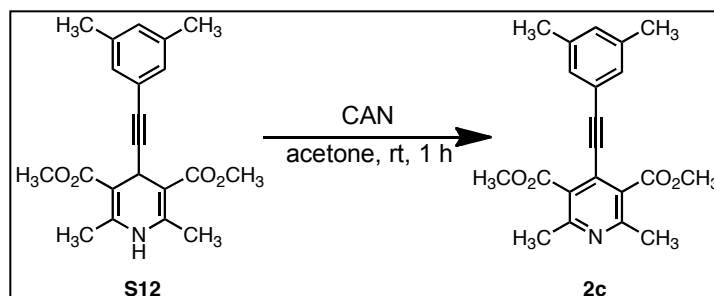
S11.¹⁴ A 25 mL Schlenk flask was equipped with a stir bar, oven-dried, cooled under vacuum and refilled with N_2 . Sequentially, **S10** (0.50 g, 2.0 mmol), CuI (0.038 g, 0.20 mmol), Et_3N (3 mL), 1-iodo-3,5-dichlorobenzene (0.46 g, 2.0 mmol), $Pd(PPh_3)_4$ (0.060 g, 0.050 mmol) and toluene (10 mL) were added. The flask was sealed and heated to 60 $^\circ\text{C}$ for 12 h. The mixture was cooled to rt and a precipitate formed. The precipitate was filtered, dissolved in CH_2Cl_2 , washed with saturated aq NH_4Cl (2 x 20 mL) and brine (1 x 20 mL). The organic layer was separated, dried over anhydrous $MgSO_4$, filtered and concentrated in vacuo to give 0.76 g of a white solid (96% yield). HRMS (ESI): Calcd for $C_{19}H_{17}Cl_2NO_4$, 394.0613 $[M + Na]^+$; Found, 394.0604.



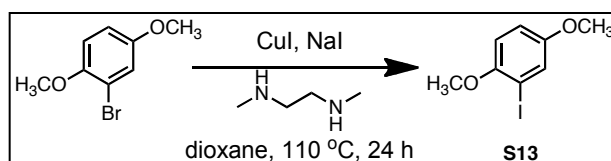
2b was synthesized using the same procedure as **1a** (Page 108). Column chromatography using 50/50 hexanes/EtOAc as the eluent gave 0.31 g of a white fluffy solid. (81% yield). HRMS (ESI): Calcd for $C_{19}H_{15}Cl_2NO_4$, 392.0456 $[M + H]^+$; Found, 392.0453. Elemental Analysis: Calcd for $C_{19}H_{15}Cl_2NO_4$: C, 58.18; H, 3.85; N, 3.57; O, 16.32; Cl, 18.08; Found: C, 58.28; H, 3.72; N, 3.58; O, 16.43; Cl, 17.99.



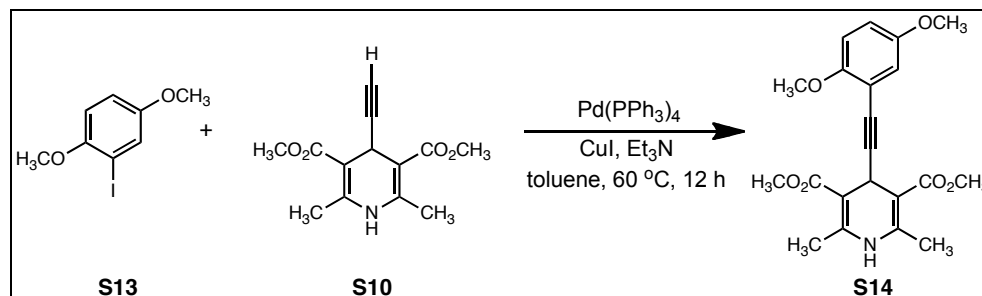
S12 was synthesized using the same procedure as **S11** (Page 113). After workup, 0.28 g of a white solid was obtained (98% yield). HRMS (ESI): Calcd for $C_{21}H_{23}NO_4$, 376.1525 $[M + Na]^+$; Found, 376.1508.



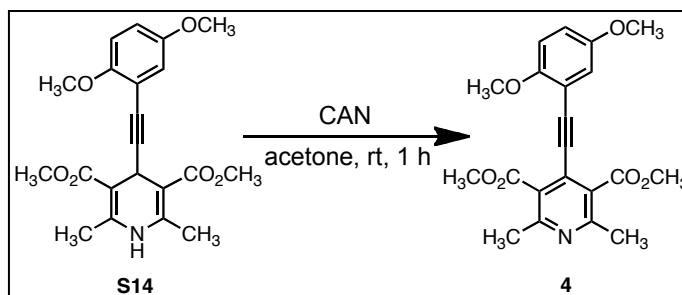
2c was synthesized using the same procedure as **1a** (Page 108). Column chromatography using 50/50 hexanes/EtOAc as the eluent gave 0.20 g of a white crystalline solid (91% yield). HRMS (ESI): Calcd for $C_{21}H_{21}NO_4$, 352.1549 $[M + H]^+$; Found, 352.1538. Elemental Analysis: Calcd for $C_{21}H_{21}NO_4$: C, 71.78; H, 6.02; N, 3.99; O, 18.21; Found: C, 71.49; H, 5.98; N, 3.92; O, 18.61.



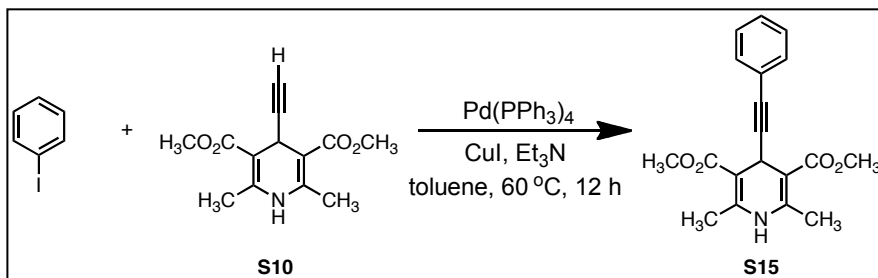
S13.¹⁵ A 25 mL Schlenk flask equipped with a stir bar was oven-dried, cooled under vacuum and charged with N_2 . Sequentially, 1-bromo-3,6-dimethoxybenzene (1.0 g, 18 mmol), sodium iodide (5.4 g, 36 mmol), copper iodide (0.17 g, 0.90 mmol), *N,N'*-dimethylethylenediamine (0.20 mL, 1.8 mmol), and toluene (15 mL) were added to the flask. The reaction mixture was degassed with N_2 for 10 min and heated to 110 °C. After 24 h, the reaction mixture was cooled to rt, quenched with 30% aq NH_4OH (5 mL) and poured into water (50 mL). The aqueous solution was extracted with CH_2Cl_2 (3 x 30 mL). The organic layer was separated, dried over anhydrous Na_2SO_4 , filtered and concentrated in vacuo to give 1.0 g of a yellow oil (85% yield). HRMS (ESI): Calcd for $C_8H_9IO_2$, 263.9647 M^+ ; Found, 263.9656.



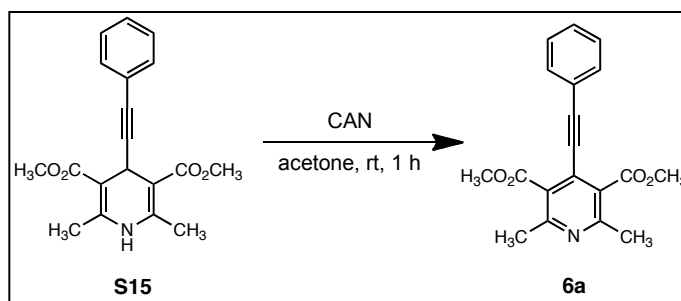
S14 was synthesized using the same procedure as **S11** (Page 113). Column chromatography using 50/50 hexanes/EtOAc as the eluent gave 0.26 g of a white solid (60% yield). HRMS (ESI): Calcd for $\text{C}_{21}\text{H}_{23}\text{NO}_6$, 408.1423 $[\text{M} + \text{Na}]^+$; Found, 408.1412.



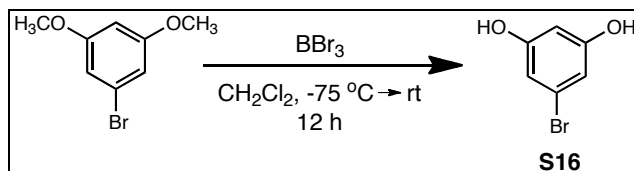
4 was synthesized using the same procedure as **1a** (Page 108). Column chromatography using 50/50 hexanes/EtOAc as the eluent gave 0.24 g of a bright yellow crystalline solid (81% yield). HRMS (ESI): Calcd for $\text{C}_{21}\text{H}_{21}\text{NO}_6$, 384.1447 $[\text{M} + \text{H}]^+$; Found, 384.1448. Elemental Analysis: Calcd for $\text{C}_{21}\text{H}_{21}\text{NO}_6$: C, 65.79; H, 5.52; N, 3.65; O, 25.04; Found: C, 65.67; H, 5.52; N, 3.66; O, 25.15.



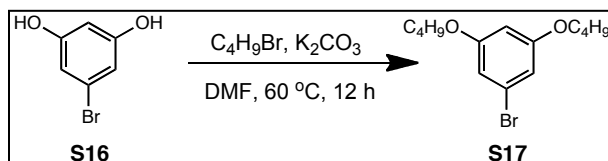
S15 was synthesized using the same procedure as **S11** (Page 113). After workup, 0.65 g of a white solid was obtained (92% yield). HRMS (ESI): Calcd for $\text{C}_{19}\text{H}_{19}\text{NO}_4$, 348.1212 $[\text{M} + \text{Na}]^+$; Found, 348.1208.



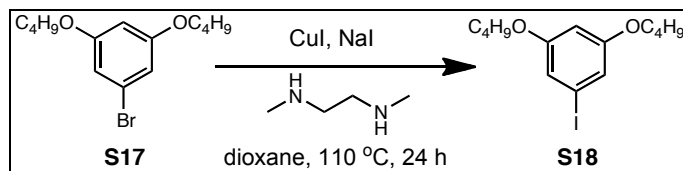
6a was synthesized using the same procedure as **1a** (Page 108). Column chromatography using 50/50 hexanes/ EtOAc as the eluent gave 0.33 g of a white solid (83% yield). HRMS (ESI): Calcd for $\text{C}_{19}\text{H}_{17}\text{NO}_4$, 324.1236 $[\text{M} + \text{H}]^+$; Found, 324.1229.



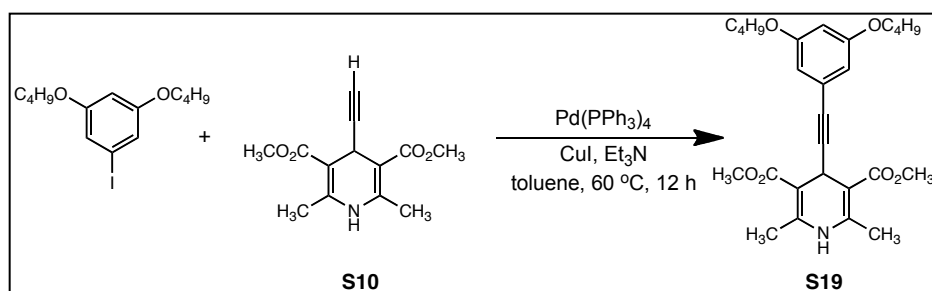
S16.¹⁶ A 50 mL two-neck round bottom flask was charged with a stir bar, oven-dried and cooled to rt under N₂. The flask was charged with 1-bromo-3,5-dimethoxybenzene (1.0 g, 4.6 mmol), CH₂Cl₂ (20 mL) and cooled to -75 °C. To this solution, boron tribromide (1M, 13.8 mL, 13.8 mmol) was added slowly over 30 min. After 30 min, the cold bath was removed and the reaction was warmed to rt and stirred for 12 h. The solution was poured into ice/water (20 mL) and extracted with EtOAc (3 x 20 mL). The organic layer was washed with H₂O (2 x 20 mL), dried over anhydrous MgSO₄, filtered and concentrated in vacuo. The crude product was purified by column chromatography using 50/50 EtOAc/hexanes as the eluent to give 0.86 g of a light brown oil (100% yield). HRMS (ESI): Calcd for C₆H₅BrO₂, 187.9473 M⁺; Found, 187.9470.



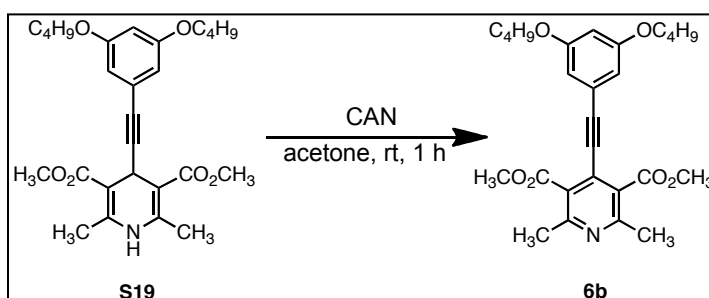
S17.¹⁷ A 50 mL round bottom flask was charged with a stir bar, **S16** (0.87 g, 4.6 mmol), n-butylbromide (1.9 g, 14 mmol), K₂CO₃ (excess) and DMF (20 mL). The mixture was stirred at rt for 24 h. The reaction mixture was then poured into H₂O (20 mL) and extracted with ether (3 x 20 mL). The organic layer was washed with H₂O (3 x 20 mL), dried over anhydrous MgSO₄, filtered and concentrated in vacuo. The crude product was purified by column chromatography using 30/70 EtOAc/hexanes as the eluent to give 1.2 g of a light brown oil (87% yield). HRMS (ESI): Calcd for C₁₄H₂₁BrO₂, 301.0803 [M + H]⁺; Found, 301.0807.



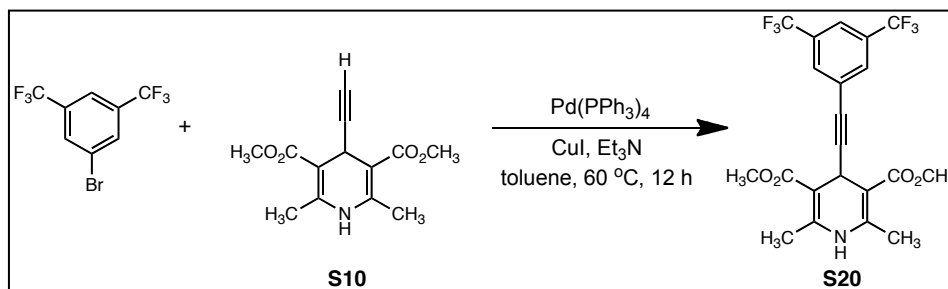
S18 was synthesized using the same procedure as **S13** (Page 115). Extraction with CH_2Cl_2 gave 0.29 g of a light brown oil (83% yield). HRMS (ESI): Calcd for $\text{C}_{14}\text{H}_{21}\text{IO}_2$, 349.0659 $[\text{M} + \text{H}]^+$; Found, 349.0651.



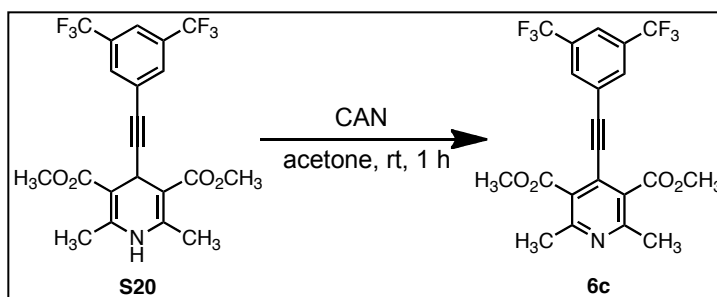
S19 was synthesized using the same procedure as **S11** (Page 113). After workup, 0.36 g of a white solid was obtained (76% yield). HRMS (ESI): Calcd for $\text{C}_{27}\text{H}_{35}\text{NO}_6$, 492.2362 $[\text{M} + \text{Na}]^+$; Found, 492.2363.



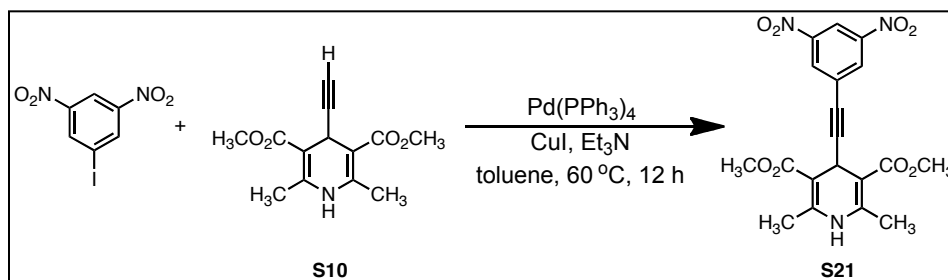
6b was synthesized using the same procedure as **1a** (Page 108). Column chromatography using 50/50 hexanes/EtOAc as the eluent gave 0.24 g of a pale yellow crystalline solid (70% yield). HRMS (ESI): Calcd for $\text{C}_{27}\text{H}_{33}\text{NO}_6$, 468.2386 $[\text{M} + \text{H}]^+$; Found, 468.2375.



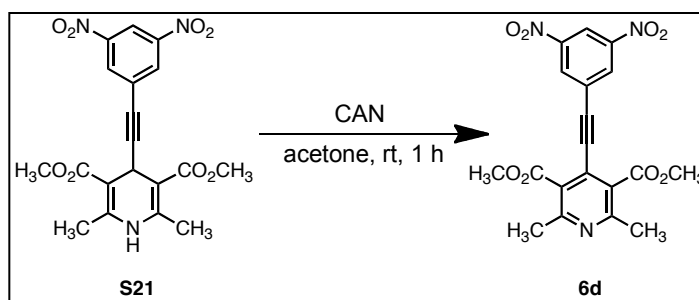
S20 was synthesized using the same procedure as **S11** (Page 113). After workup, 0.71 g of a white solid was obtained (96% yield). HRMS (ESI): Calcd for $\text{C}_{21}\text{H}_{17}\text{F}_6\text{NO}_4$, 484.0959 $[\text{M} + \text{Na}]^+$; Found, 484.0937.



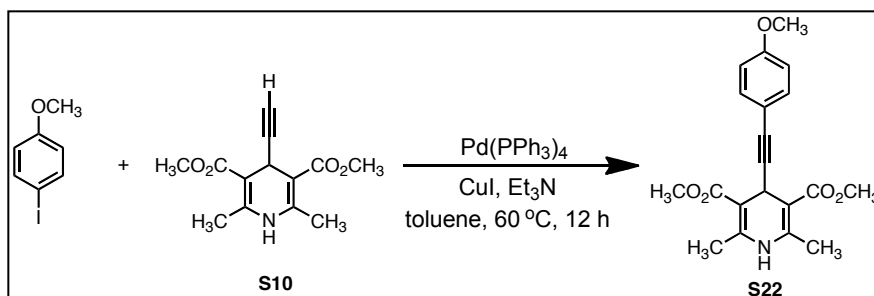
6c was synthesized using the same procedure as **1a** (Page 108). Column chromatography using 50/50 hexanes/EtOAc as the eluent gave 0.60 g of a white solid (93% yield). HRMS (ESI): Calcd for $\text{C}_{21}\text{H}_{15}\text{F}_6\text{NO}_4$, 460.0984 $[\text{M} + \text{H}]^+$; Found, 460.0975.



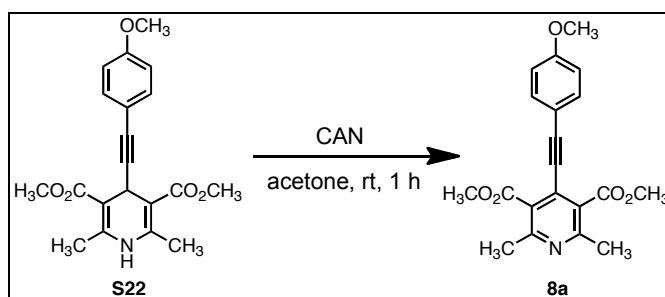
S21 was synthesized using the same procedure as **S11** (Page 113). After workup, 0.17 g of a white solid was obtained (89% yield). HRMS (ESI): Calcd for $\text{C}_{19}\text{H}_{17}\text{N}_3\text{O}_8$, 438.0913 $[\text{M} + \text{Na}]^+$; Found, 438.0907.



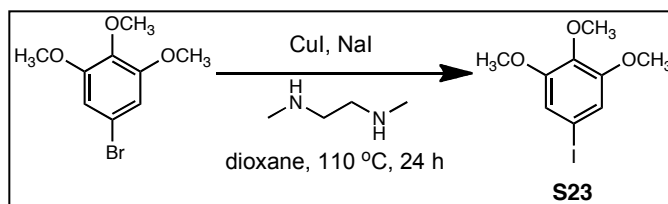
6d was synthesized using the same procedure as **1a** (Page 108). Column chromatography using 50/50 hexanes/EtOAc as the eluent gave 0.095 g of a white solid (77% yield). HRMS (ESI): Calcd for $\text{C}_{19}\text{H}_{15}\text{N}_3\text{O}_8$, 414.0922 $[\text{M} + \text{H}]^+$; Found, 414.0922.



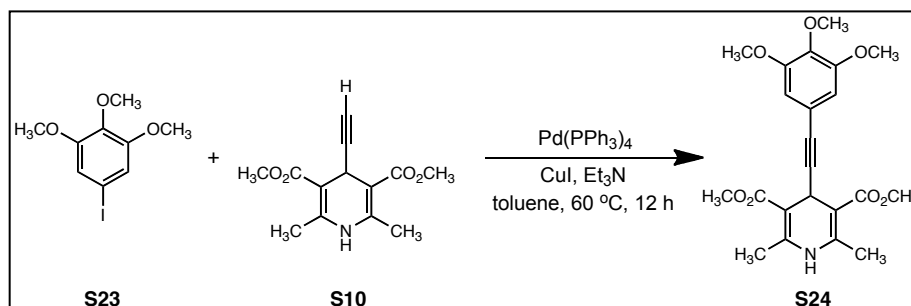
S22 was synthesized using the same procedure as **S11** (Page 113). After workup, 0.27 g of a white solid was obtained (91% yield). HRMS (ESI): Calcd for $\text{C}_{20}\text{H}_{21}\text{NO}_5$, 378.1317 $[\text{M} + \text{Na}]^+$; Found, 378.1300.



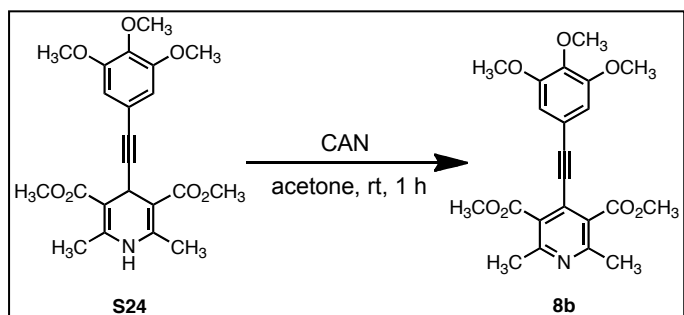
8a was synthesized using the same procedure as **1a** (Page 108). Column chromatography using 50/50 hexanes/EtOAc as the eluent gave 0.19 g of a pale yellow solid (83% yield). HRMS (ESI): Calcd for $\text{C}_{20}\text{H}_{19}\text{NO}_5$, 354.1341 $[\text{M} + \text{H}]^+$; Found, 354.1344.



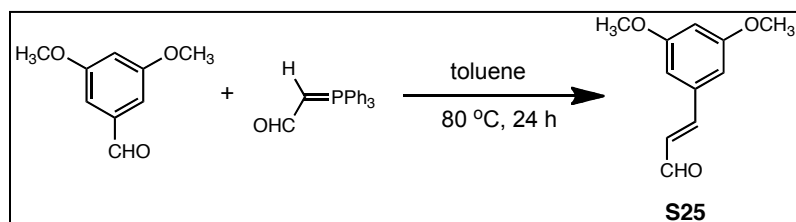
S23 was synthesized using the same procedure as **S13** (Page 117). Extraction with CH_2Cl_2 gave 0.21 g of a white solid (90% yield). HRMS (ESI): Calcd for $\text{C}_{15}\text{H}_{23}\text{IO}_3$, 316.9651 $[\text{M} + \text{Na}]^+$; Found, 316.9641.



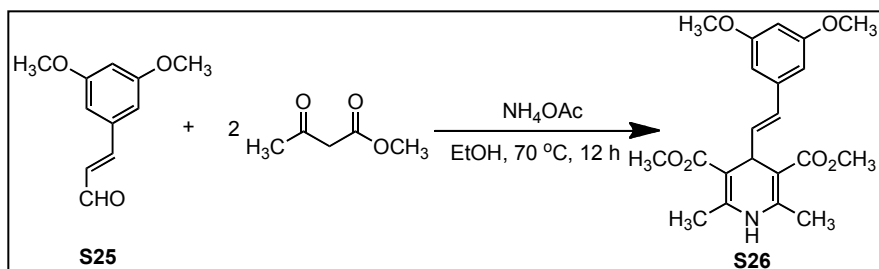
S24 was synthesized using the same procedure as **S11** (Page 113). After workup, 0.26 g of a white solid was obtained (61% yield). HRMS (ESI): Calcd for $\text{C}_{22}\text{H}_{25}\text{NO}_7$, 438.1529 $[\text{M} + \text{Na}]^+$; Found, 438.1508.



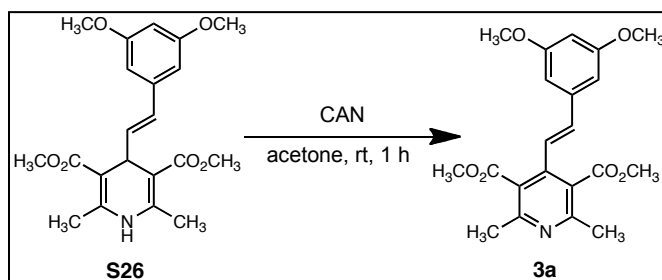
8b was synthesized using the same procedure as **1a** (Page 108). Column chromatography using 50/50 hexanes/EtOAc as the eluent gave 0.16 g of an orange crystalline solid (71% yield). HRMS (ESI): Calcd for $C_{22}H_{23}NO_7$, 414.1553 $[M + H]^+$; Found, 414.1549.



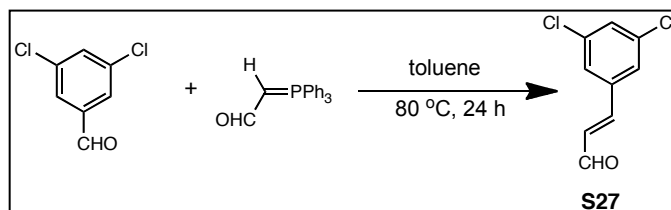
S25.¹⁸ A 50 mL round bottom flask was equipped with a stir bar. Sequentially, 3,5-dimethoxybenzaldehyde (0.75 g, 0.45 mmol), toluene (30 mL) and (triphenylphosphoranylidene)acetaldehyde (1.4 g, 0.45 mmol) were added. The mixture was stirred at 80 °C for 24 h. After cooling to rt, the mixture was concentrated in vacuo and purified by column chromatography using 10/90 EtOAc/hexanes as the eluent to give 0.50 g of a colorless crystalline solid (58% yield). HRMS (ESI): Calcd for $C_{11}H_{12}O_3$, 193.0865 $[M + H]^+$; Found, 193.0865.



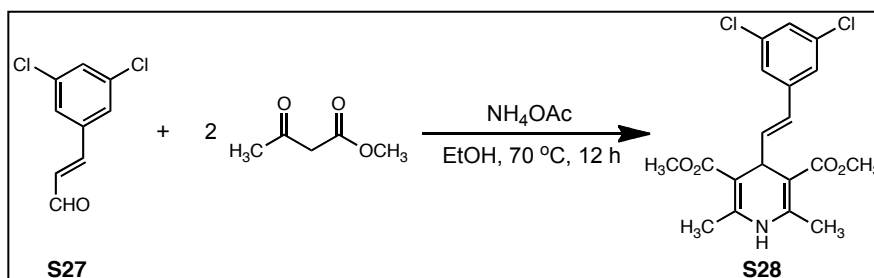
S26. A 50 mL round bottom flask was equipped with a stir bar. Sequentially, **S25** (0.50 g, 2.6 mmol), methyl acetoacetate (0.60 g, 5.2 mmol), NH_4OAc (0.40 g, 5.2 mmol) and EtOH (20 mL) were added. The mixture was stirred at 70 °C for 12 h. After cooling to rt, a precipitate formed. The precipitate was filtered, washed with hexanes and EtOH and dried under vacuum to give 0.75 g of a pale yellow solid (81% yield). HRMS (ESI): Calcd for $\text{C}_{21}\text{H}_{25}\text{NO}_6$, 410.1580 $[\text{M} + \text{Na}]^+$; Found, 410.1563.



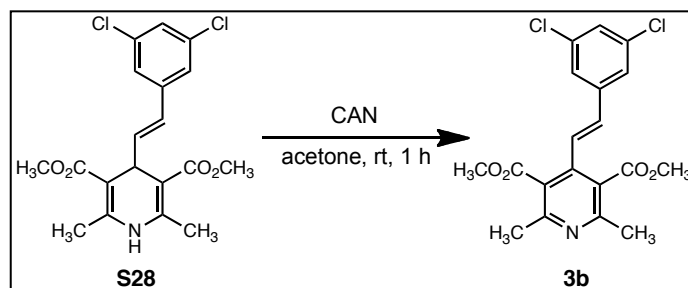
3a was synthesized using the same procedure as **1a** (Page 108). Column chromatography using 50/50 hexanes/EtOAc as the eluent gave 0.20 g of a white solid (82% yield). HRMS (ESI): Calcd for $\text{C}_{21}\text{H}_{25}\text{NO}_6$, 386.1604 $[\text{M} + \text{H}]^+$; Found, 386.1593. Elemental Analysis: Calcd for $\text{C}_{21}\text{H}_{25}\text{NO}_6$: C, 65.44; H, 6.02; N, 3.63; O, 24.91; Found: C, 64.83; H, 5.97; N, 3.63; O, 25.57.



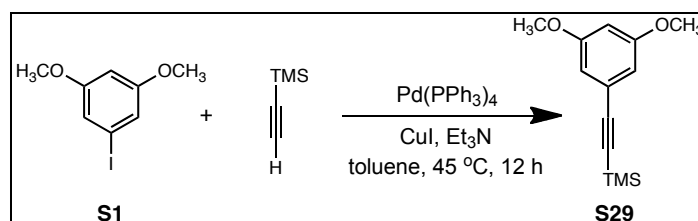
S27 was synthesized using the same procedure as **S25** (Page 124). Column chromatography using 10/90 EtOAc/hexanes as the eluent gave 0.37 g of a white solid (64% yield). HRMS (ESI): Calcd for $C_9H_6Cl_2O$, 199.9796 M^+ ; Found, 199.9800.



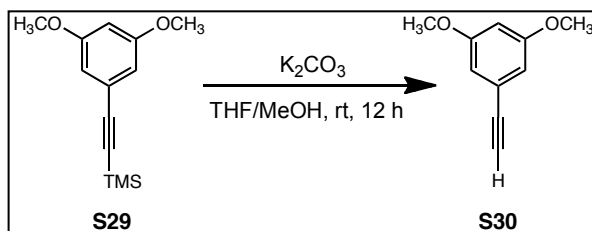
S28 was synthesized using the same procedure as **S26** (Page 125). After workup, 0.32 g of a white fluffy solid was obtained (81% yield). HRMS (ESI): Calcd for $C_{19}H_{19}Cl_2NO_4$, 418.0589 $[M + Na]^+$; Found, 418.0585.



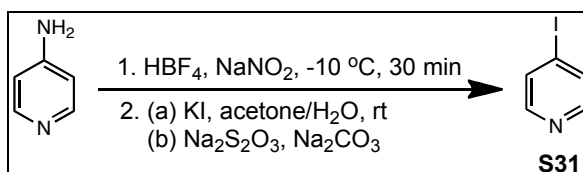
3b was synthesized using the same procedure as **1a** (Page 108). Column chromatography using 50/50 hexanes/EtOAc as the eluent gave 0.14 g of a white fluffy solid (68% yield). HRMS (ESI): Calcd for $C_{19}H_{17}Cl_2NO_4$, 394.0613 $[M + H]^+$; Found, 394.0603. Elemental Analysis: Calcd for $C_{19}H_{17}Cl_2NO_4$: C, 57.88; H, 4.35; N, 3.55; O, 16.23; Cl, 17.99; Found: C, 58.05; H, 4.24; N, 3.58; O, 16.36; Cl, 17.77.



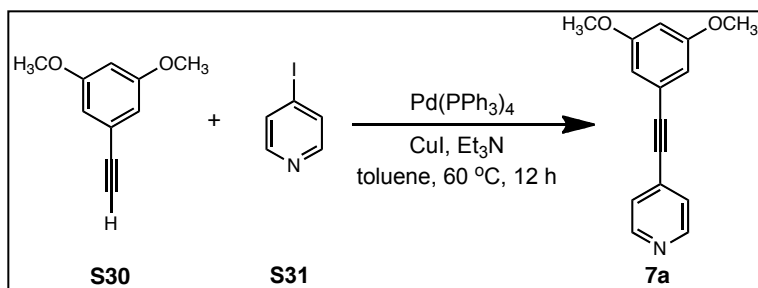
S29. A 50 mL Schlenk flask was equipped with a stir bar, oven-dried, cooled under vacuum and refilled with N_2 . Sequentially, **S1** (2.6 g, 10 mmol), CuI (0.19 g, 1.0 mmol), Et_3N (10 mL), ethynyl(trimethyl)silane (0.98 g, 10 mmol), $Pd(PPh_3)_4$ (0.57 g, 0.5 mmol) and toluene (25 mL) were added. The flask was sealed and heated to $60^\circ C$ for 12 h. The mixture was then cooled to rt and diluted with CH_2Cl_2 (~25 mL), washed with saturated aq NH_4Cl (2 x 20 mL) and brine (1 x 20 mL). The organic layer was separated, dried over anhydrous $MgSO_4$, filtered and concentrated in vacuo. The crude product was purified by column chromatography using 95/5 hexanes/EtOAc as the eluent to give 2.3 g of a white solid (98% yield). HRMS (ESI): Calcd for $C_{16}H_{24}O_2Si$, 234.1076 M^+ ; Found, 234.1069.



S30.¹⁹ A 50 mL round bottom flask was charged with a stir bar, **S29** (2.2 g, 9.4 mmol), K_2CO_3 (excess), MeOH (15 mL) and THF (15 mL). The mixture was stirred at rt for 12 h. The mixture was then filtered. The filtrate was concentrated in vacuo to give a yellow solid which was purified via column chromatography using 10/90 EtOAc/hexanes to give 1.3 g of a white solid (88% yield). HRMS (ESI): Calcd for $C_{10}H_{10}O_2$, 162.0681 M^+ ; Found, 162.0674.



S31.²⁰ A 50 mL round bottom flask was charged with a stir bar. Sequentially, 4-aminopyridine (0.50 g, 5.3 mmol) and HBF_4 (48% in H_2O , 4.5 mL, 25 mmol) were added. The solution was stirred at $-10\text{ }^\circ\text{C}$ for 10 min and $NaNO_2$ (0.395 g, 4.6 mmol) was added portion wise over 10 min. The reaction was stirred for an additional 30 min to give a white precipitate. The precipitate was isolated by filtration and added in portions to a solution of KI (1.4 g, 8.4 mmol), acetone (3.4 mL) and H_2O (5.1 mL). The heterogeneous mixture turned brown and was further stirred for 10 min. To the mixture, saturated aq $Na_2S_2O_3$ (~ 20 mL) was added to decolorize and saturated aq Na_2CO_3 was added until the pH was neutral. The mixture was extracted with ether (3 x 20 mL). The organic layer was separated, washed with H_2O (2 x 50 mL) and brine (1 x 50 mL), dried over anhydrous $MgSO_4$, filtered and concentrated in vacuo. The crude product was purified by column chromatography using 25/75 ether/chloroform as the eluent to give 0.70 g of a white solid (64% yield). HRMS (ESI): Calcd for C_5H_4IN , 205.9467 $[M + H]^+$; Found, 205.9476.



7a. A 25 mL Schlenk flask was equipped with a stir bar, oven-dried, cooled under vacuum and refilled with N₂. Sequentially, **S30** (0.21 g, 1.3 mmol), **S31** (0.26 g, 1.3 mmol), CuI (0.025 g, 0.13 mmol), Et₃N (3 mL), Pd(PPh₃)₄ (0.050 g, 0.043 mmol) and toluene (10 mL) were added. The flask was sealed and heated to 60 °C for 12 h. The mixture was then cooled to rt and a precipitate formed. The precipitate was filtered, dissolved in CH₂Cl₂, washed with saturated aq NH₄Cl (2 x 20 mL) and brine (1 x 20 mL). The organic layer then dried over anhydrous MgSO₄, filtered and concentrated in vacuo. The crude product was purified by column chromatography using 50/50 hexanes/EtOAc as the eluent to give 0.23 g of a yellow solid (75% yield). HRMS (ESI): Calcd for C₁₅H₁₃NO₂, 240.1025 [M + H]⁺; found, 240.1026.

IV. ^1H and ^{13}C NMR Spectra

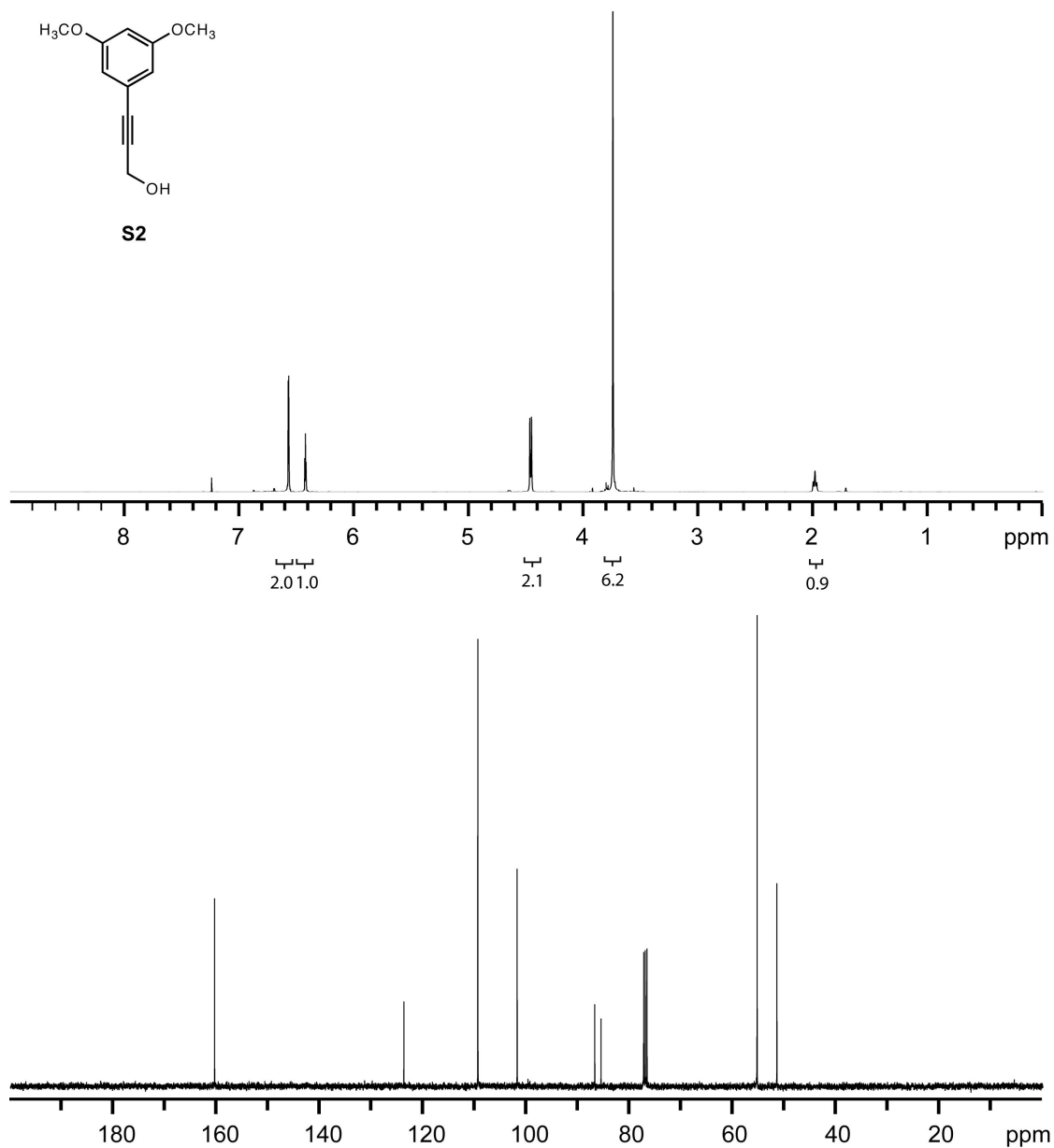


Figure S1. ^1H and ^{13}C NMR spectra of **S2**. ^1H NMR (400 MHz, CDCl_3) δ 6.59 (d, $J = 2.4$ Hz, 2H), 6.44 (t, $J = 2.4$ Hz, 1H), 4.48 (d, $J = 6.0$ Hz, 2H), 3.76 (s, 6H), 2.00 (t, $J = 6.0$ Hz, 1H). ^{13}C NMR (100 MHz, CDCl_3) δ 160.47, 123.81, 109.48, 101.86, 86.82, 85.61, 55.38, 51.55.

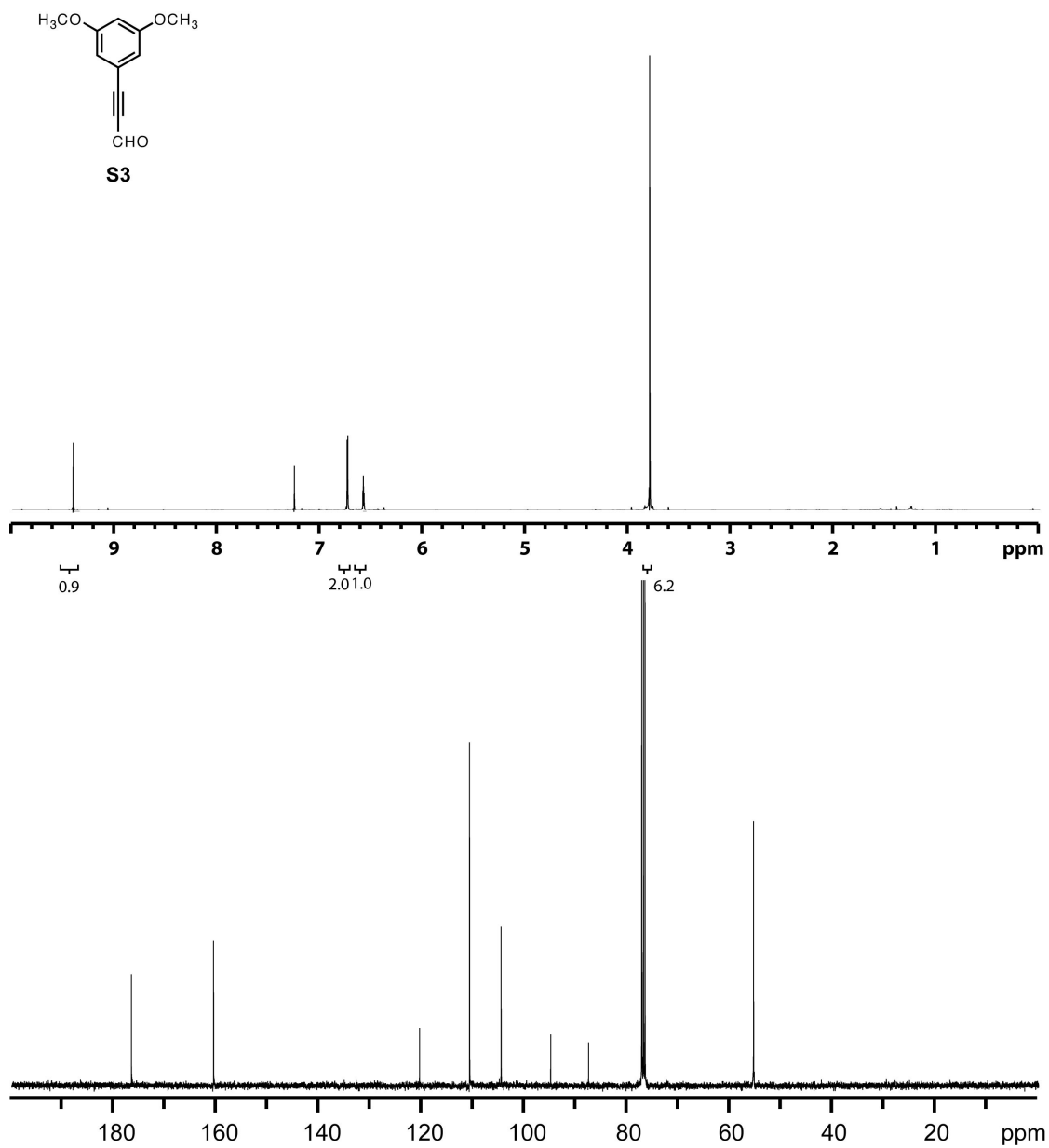


Figure S2. ¹H and ¹³C NMR spectra of **S3**. ¹H NMR (400 MHz, CDCl₃) δ 9.41 (s, 1H), 6.72 (d, *J* = 2.4 Hz, 2H), 6.58 (t, *J* = 2.4 Hz, 1H), 3.80 (s, 6H). ¹³C NMR (100 MHz, CDCl₃) δ 176.70, 160.69, 120.58, 110.84, 104.71, 95.04, 87.68, 55.54.

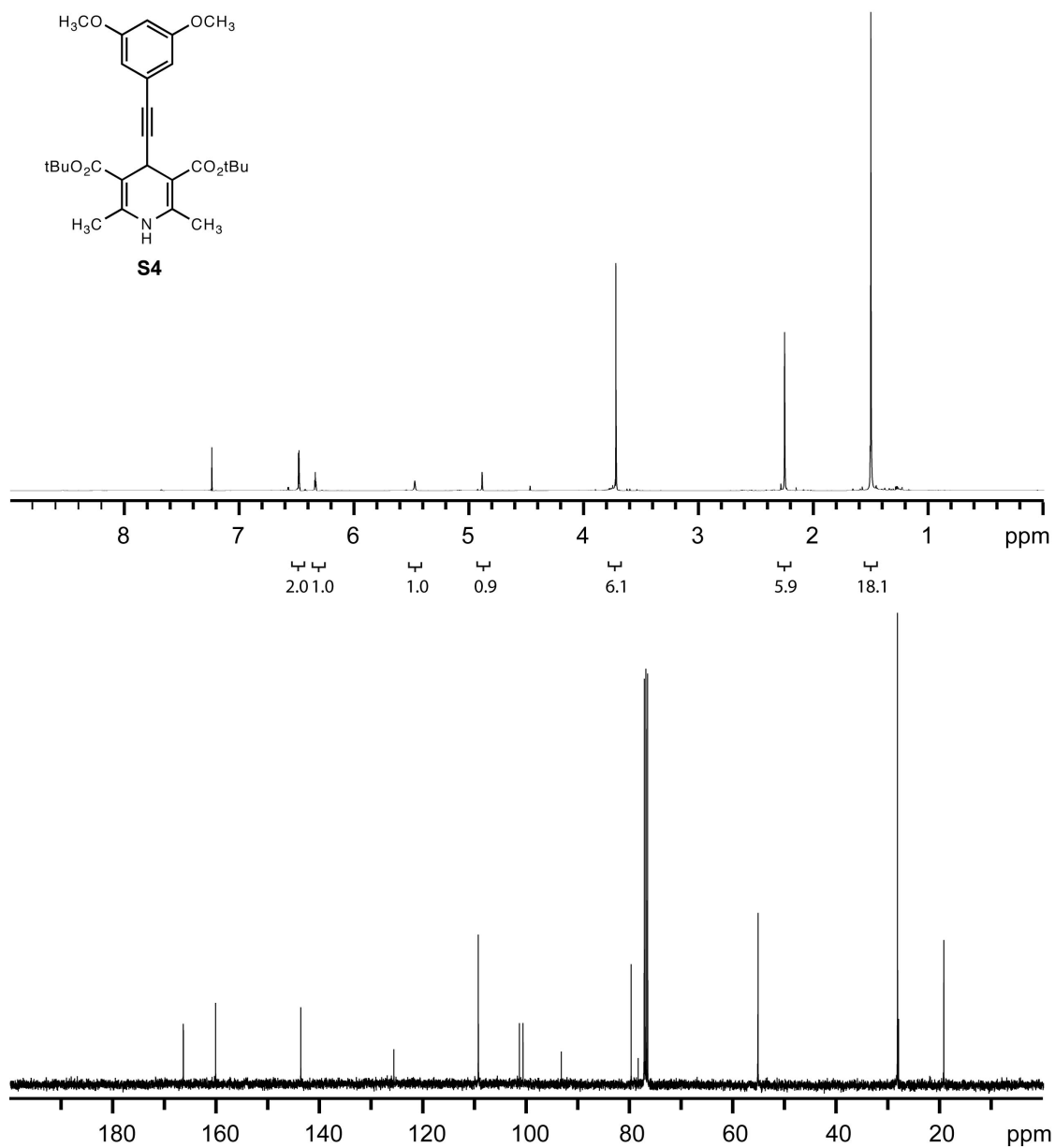


Figure S3. ^1H and ^{13}C NMR spectra of **S4**. ^1H NMR (400 MHz, CDCl_3) δ 6.49 (d, $J = 2.4$ Hz, 2H), 6.35 (t, $J = 2.4$ Hz, 1H), 5.48 (s, 1H), 4.89 (s, 1H), 3.73 (s, 6H), 2.26 (s, 6H), 1.51 (s, 18H). ^{13}C NMR (100 MHz, CDCl_3) δ 166.52, 160.26, 143.79, 125.77, 109.42, 101.47, 100.78, 93.37, 79.85, 78.50, 55.29, 28.30, 28.11, 19.34.

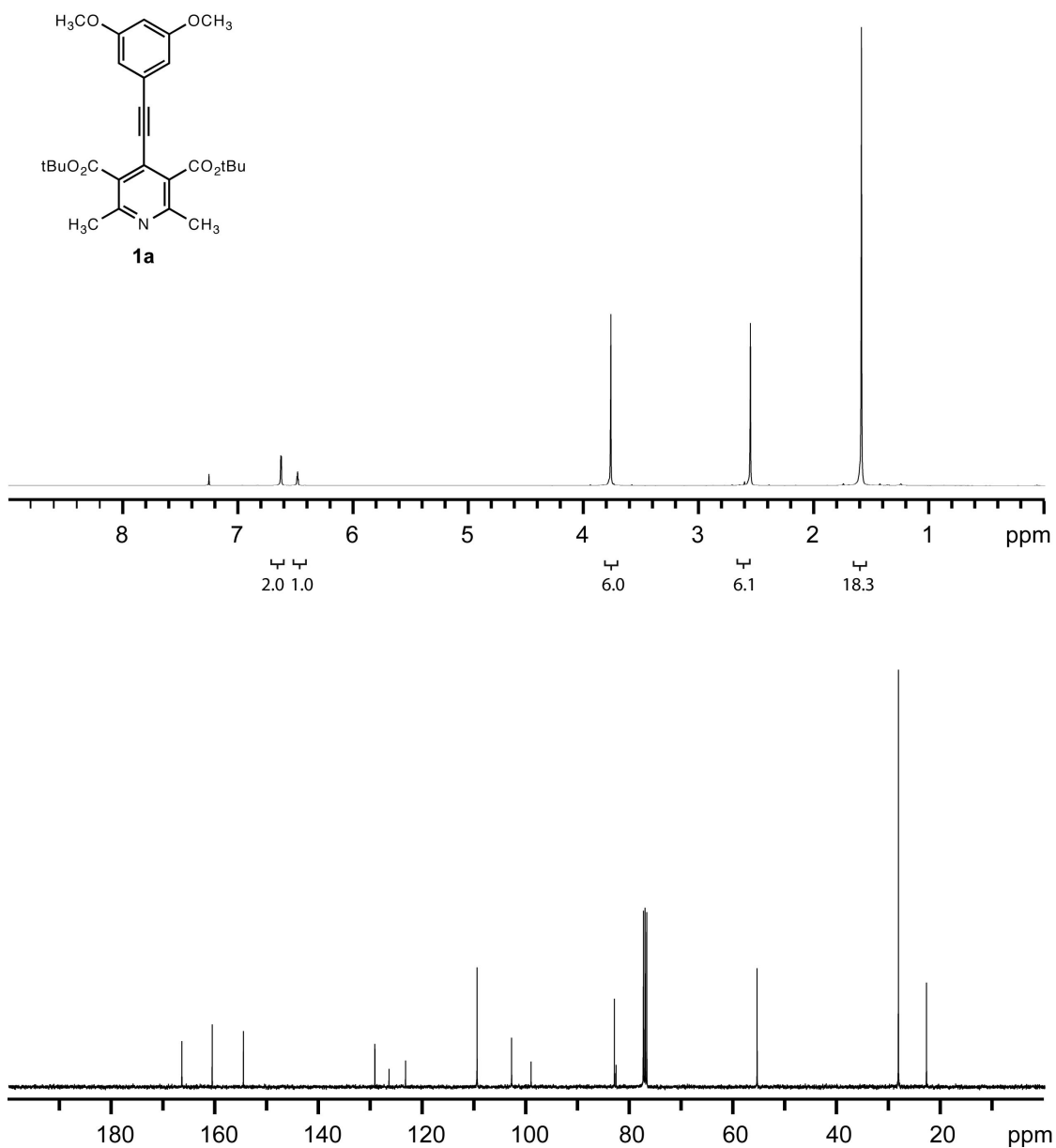


Figure S4. ^1H and ^{13}C NMR spectra of **1a**. ^1H NMR (400 MHz, CDCl_3) δ 6.63 (d, J = 2.4 Hz, 2H), 6.49 (t, J = 2.4 Hz, 1H), 3.77 (s, 6H), 2.56 (s, 6H), 1.59 (s, 18H). ^{13}C NMR (100 MHz, CDCl_3) δ 166.36, 160.51, 154.49, 129.11, 126.39, 123.20, 109.40, 102.73, 98.96, 82.86, 82.57, 55.35, 28.07, 22.65.

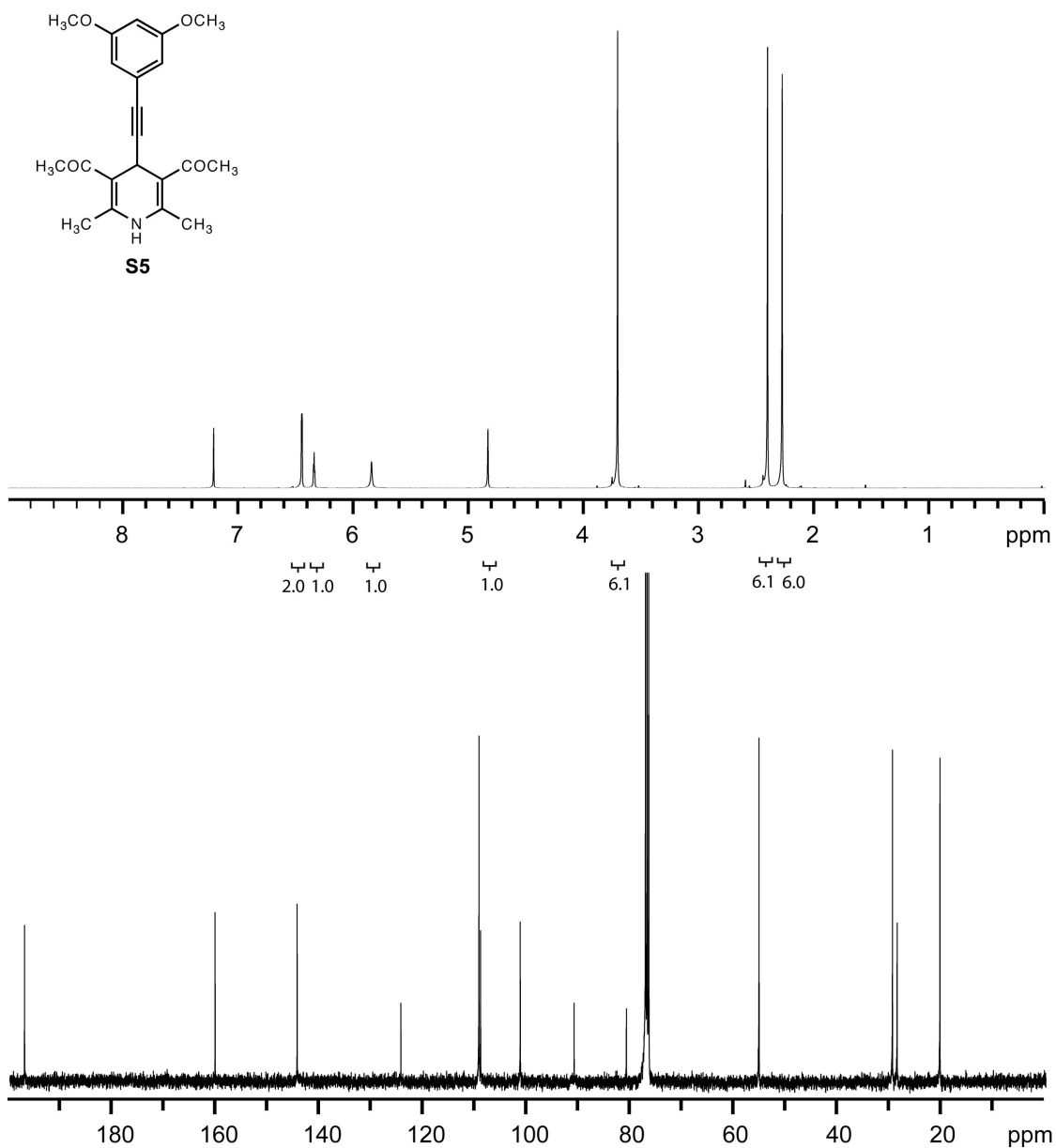


Figure S5. ^1H and ^{13}C NMR spectra of **S5**. ^1H NMR (400 MHz, CDCl_3) δ 6.49 (d, J = 2.4 Hz, 2H), 6.38 (t, J = 2.4 Hz, 1H), 5.89 (s, 1H), 4.88 (s, 1H), 3.75 (s, 6H), 2.45 (s, 6H), 2.32 (s, 6H). ^{13}C NMR (100 MHz, CDCl_3) δ 197.17, 160.39, 144.56, 124.53, 109.47, 109.15, 101.49, 91.10, 81.02, 55.41, 29.66, 28.76, 20.49.

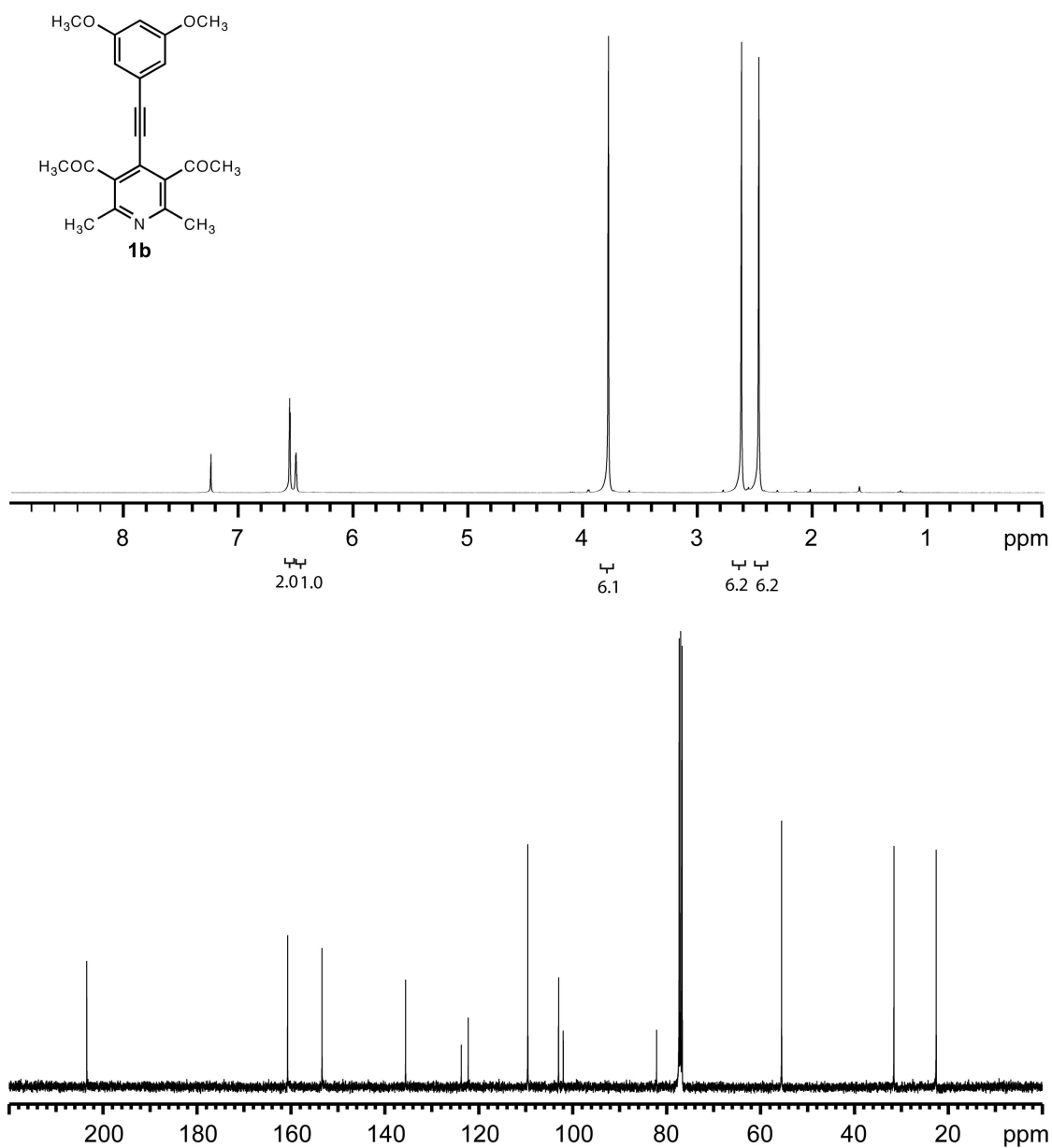


Figure S6. ^1H and ^{13}C NMR spectra of **1b**. ^1H NMR (400 MHz, CDCl_3) δ 6.57 (d, $J = 2.4$ Hz, 2H), 6.52 (t, $J = 2.0$ Hz, 1H), 3.80 (s, 6H), 2.64 (s, 6H), 2.49 (s, 6H). ^{13}C NMR (100 MHz, CDCl_3) δ 203.46, 160.69, 153.38, 135.55, 123.69, 122.23, 109.54, 102.99, 101.97, 82.11, 55.48, 31.56, 22.58.

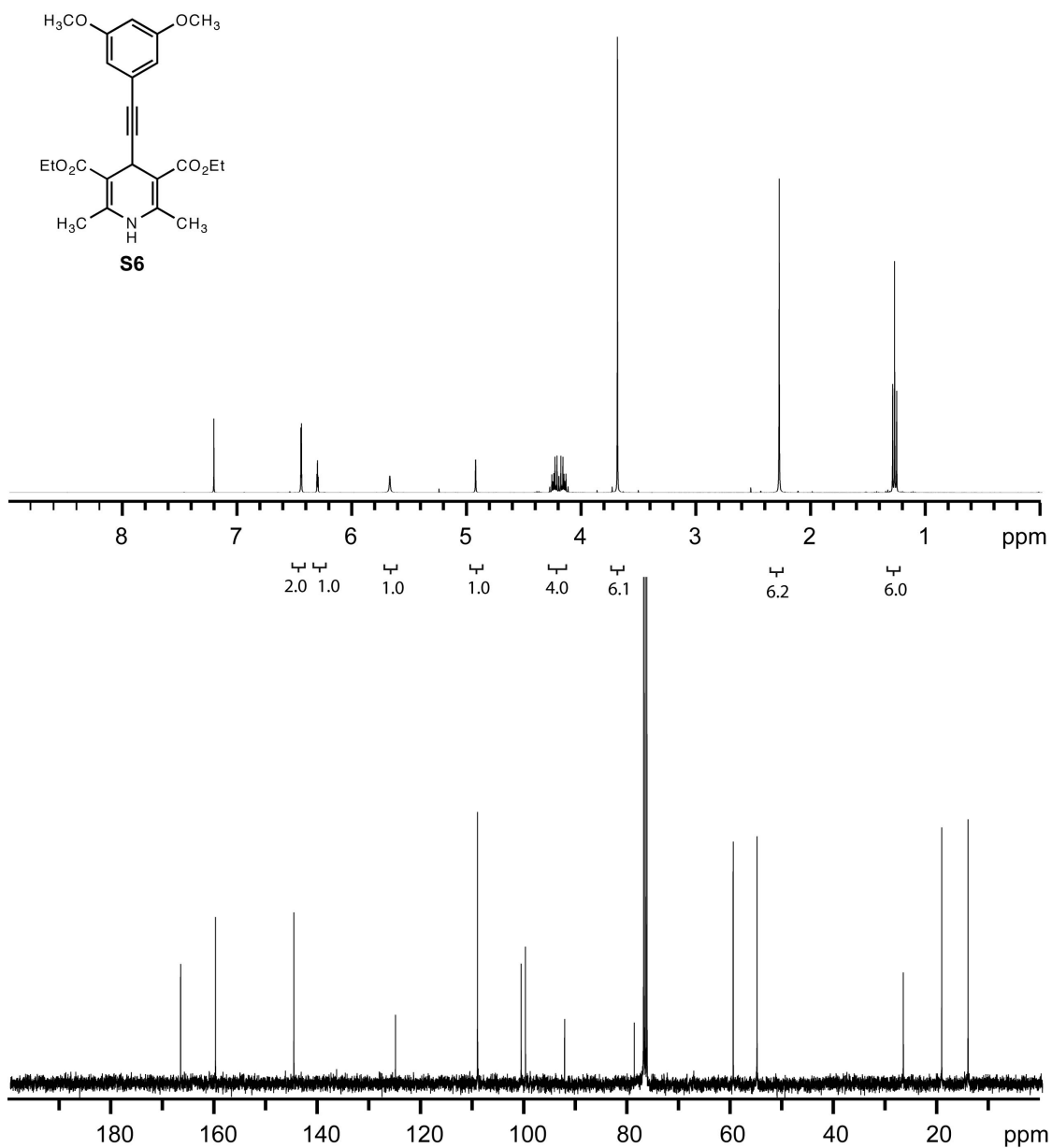


Figure S7. ^1H and ^{13}C NMR spectra of **S6**. ^1H NMR (400 MHz, CDCl_3) δ 6.50 (d, $J = 2.4$ Hz, 2H), 6.35 (t, $J = 2.4$ Hz, 1H), 5.73 (s, 1H), 4.98 (s, 1H), 4.25 (doublet of sextet, $J = 6.8$ Hz, $J = 3.6$ Hz, 4H), 3.74 (s, 6H), 2.33 (s, 6H), 1.33 (t, $J = 7.2$ Hz, 6H). ^{13}C NMR (100 MHz, CDCl_3) δ 167.02, 160.26, 145.09, 125.40, 109.50, 101.06, 100.21, 92.64, 79.13, 59.97, 55.34, 27.01, 19.57, 14.48.

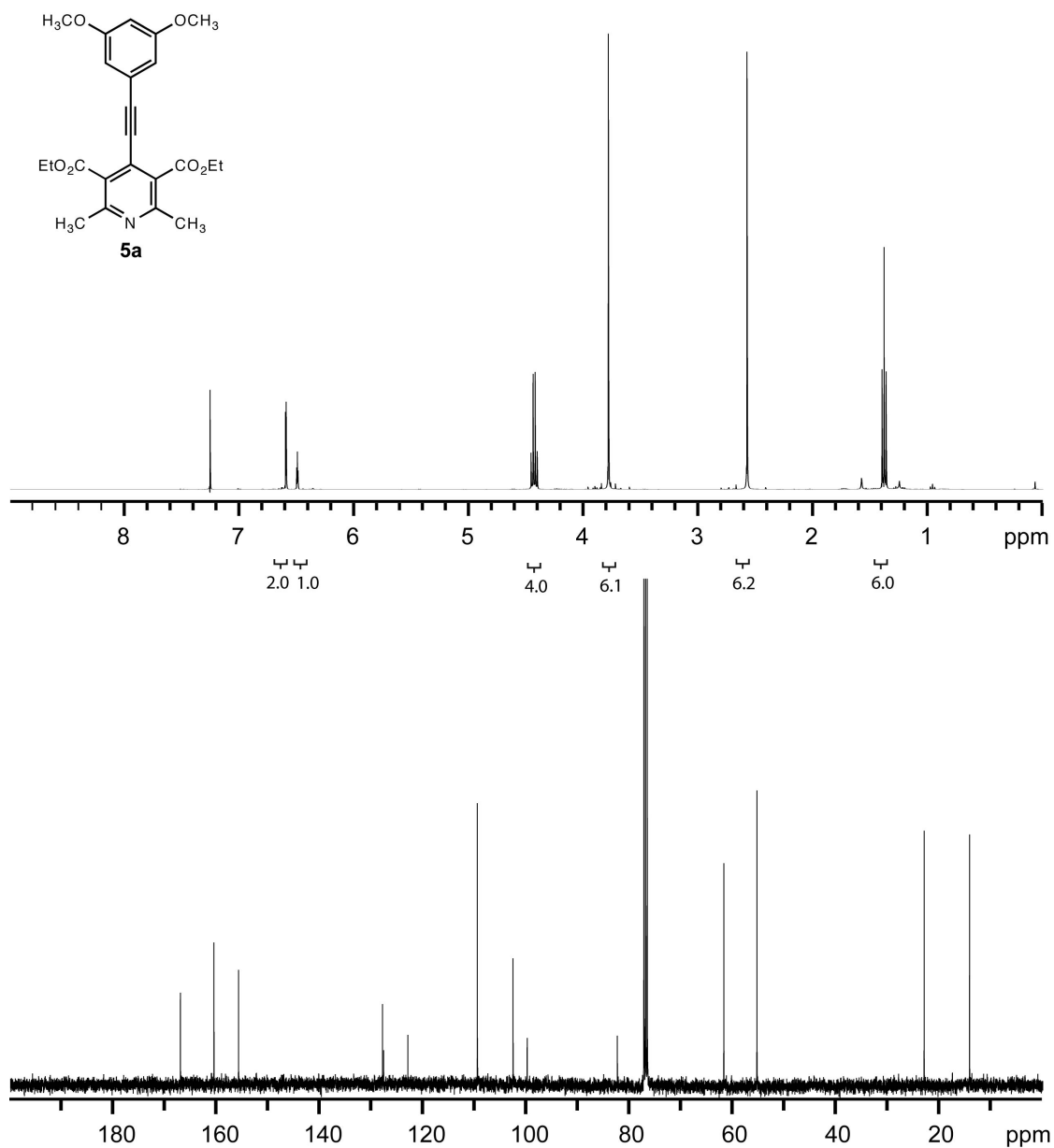


Figure S8. ^1H and ^{13}C NMR spectra of **5a**. ^1H NMR (400 MHz, CDCl_3) δ 6.58 (d, $J = 2.4$ Hz, 2H), 6.48 (t, $J = 2.4$ Hz, 1H), 4.42 (q, $J = 7.2$ Hz, 4H), 3.77 (s, 6H), 2.56 (s, 6H), 1.37 (t, $J = 7.2$ Hz, 6H). ^{13}C NMR (100 MHz, CDCl_3) δ 167.09, 160.59, 155.83, 127.94, 127.72, 123.02, 109.57, 102.65, 99.93, 82.45, 61.82, 55.42, 23.02, 14.22.

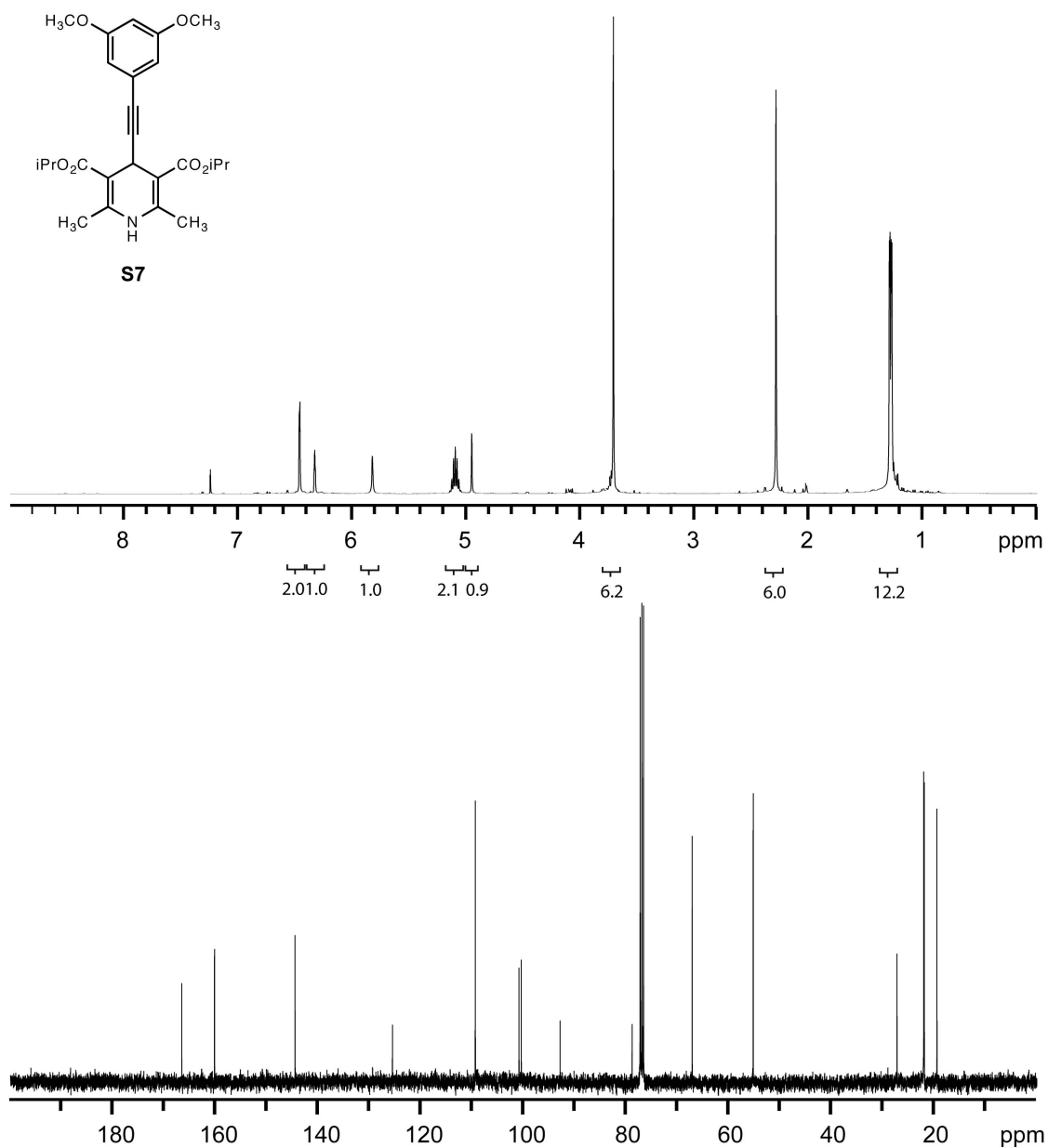


Figure S9. ^1H and ^{13}C NMR spectra of **S7**. ^1H NMR (400 MHz, CDCl_3) δ 6.48 (d, $J = 2.4$ Hz, 2H), 6.35 (t, $J = 2.4$ Hz, 1H), 5.84 (s, 1H), 5.11 (septet, $J = 6.4$ Hz, 2H), 4.97 (s, 1H), 3.73 (s, 6H), 2.30 (s, 6H), 1.30 (d, $J = 6.4$ Hz, 12H). ^{13}C NMR (100 MHz, CDCl_3) δ 166.63, 160.24, 144.56, 125.57, 109.44, 100.93, 100.48, 92.93, 78.88, 67.19, 55.30, 27.28, 22.06, 19.49.

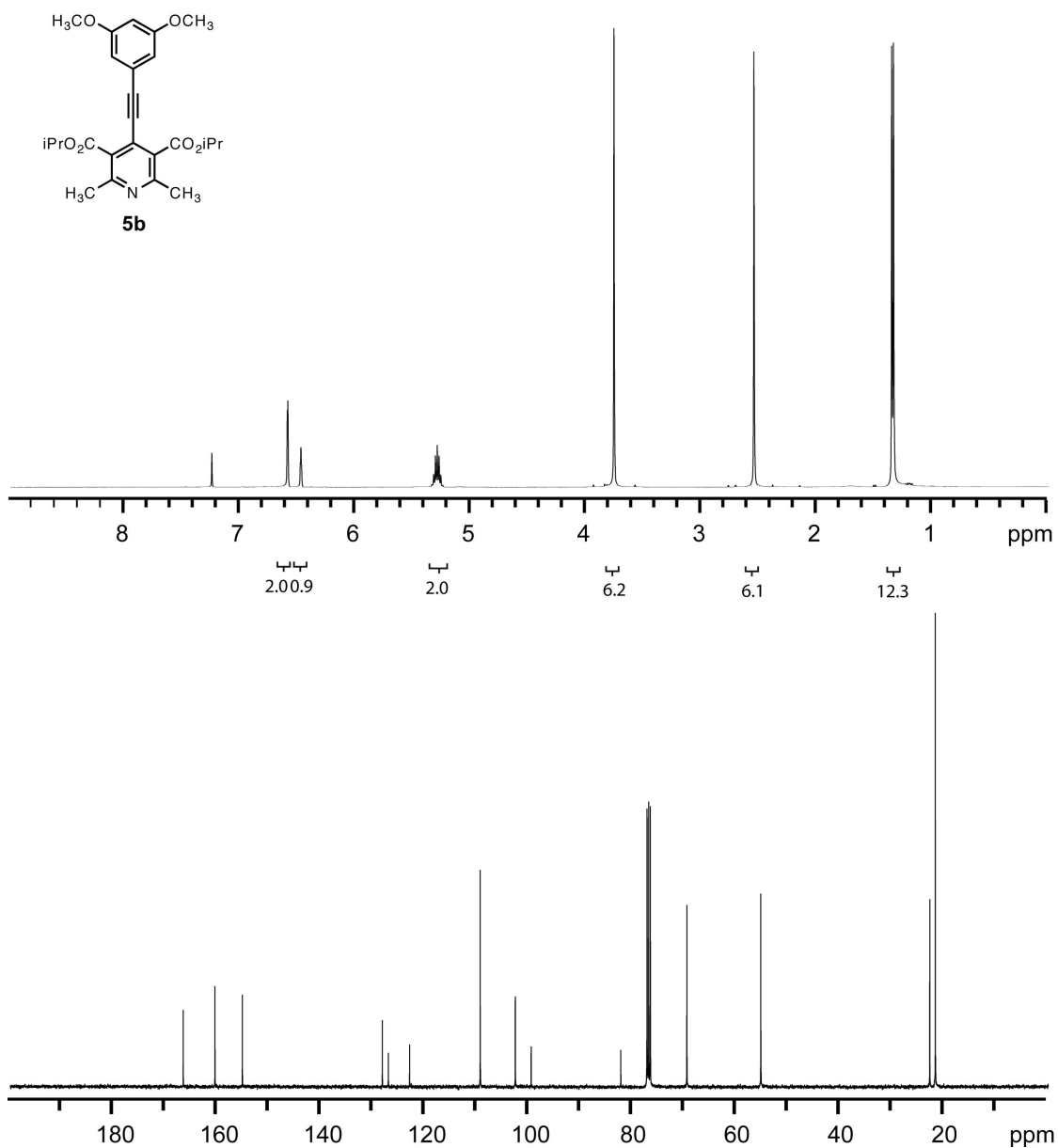


Figure S10. ^1H and ^{13}C NMR spectra of **5b**. ^1H NMR (400 MHz, CDCl_3) δ 6.60 (d, $J = 2.0$ Hz, 2H), 6.49 (t, $J = 2.0$ Hz, 1H), 5.31 (septet, $J = 6.4$ Hz, 2H), 3.77 (s, 6H), 2.56 (s, 6H), 1.36 (d, $J = 6.4$ Hz, 12H). ^{13}C NMR (100 MHz, CDCl_3) δ 166.67, 160.56, 155.28, 128.31, 127.16, 123.06, 109.46, 102.70, 99.65, 82.38, 69.66, 55.41, 22.86, 21.79.

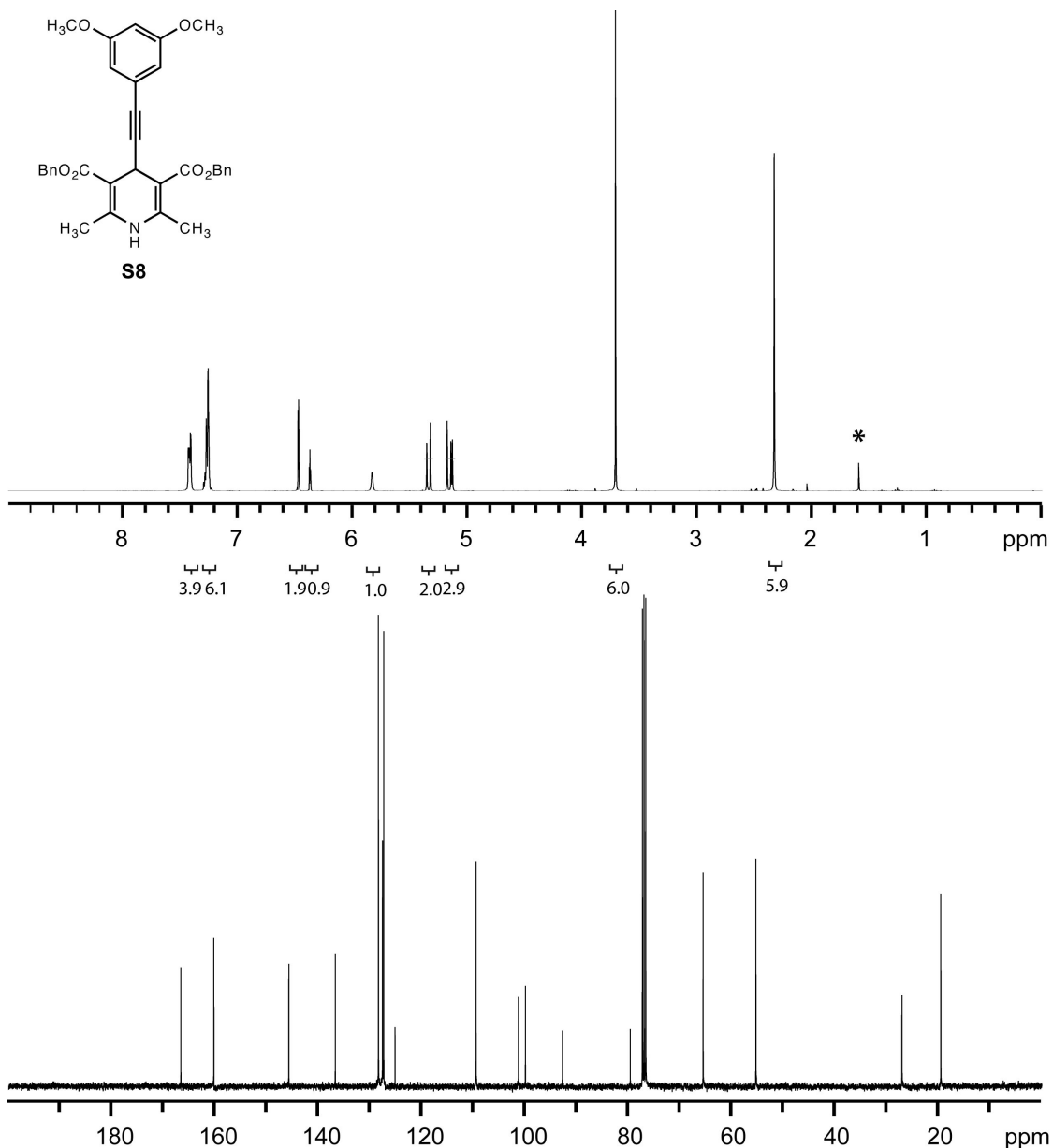


Figure S11. ^1H and ^{13}C NMR spectra of **S8**. ^1H NMR (400 MHz, CDCl_3) δ 7.42 (m, 4H), 7.28 (m, 6H), 6.48 (d, $J = 2.4$ Hz, 2H), 6.38 (t, $J = 2.2$ Hz, 1H), 5.84 (s, 1H), 5.25 (dd, $J = 18.4$ Hz, $J = 12.8$ Hz, 2H), 5.14 (s, 1H), 3.72 (s, 6H), 2.33 (s, 6H). ^{13}C NMR (100 MHz, CDCl_3) δ 166.66, 160.28, 145.77, 136.78, 128.43, 127.64, 127.40, 125.21, 109.53, 101.32, 99.98, 92.82, 79.68, 65.59, 55.37, 27.10, 19.59. (*denotes H_2O peak)

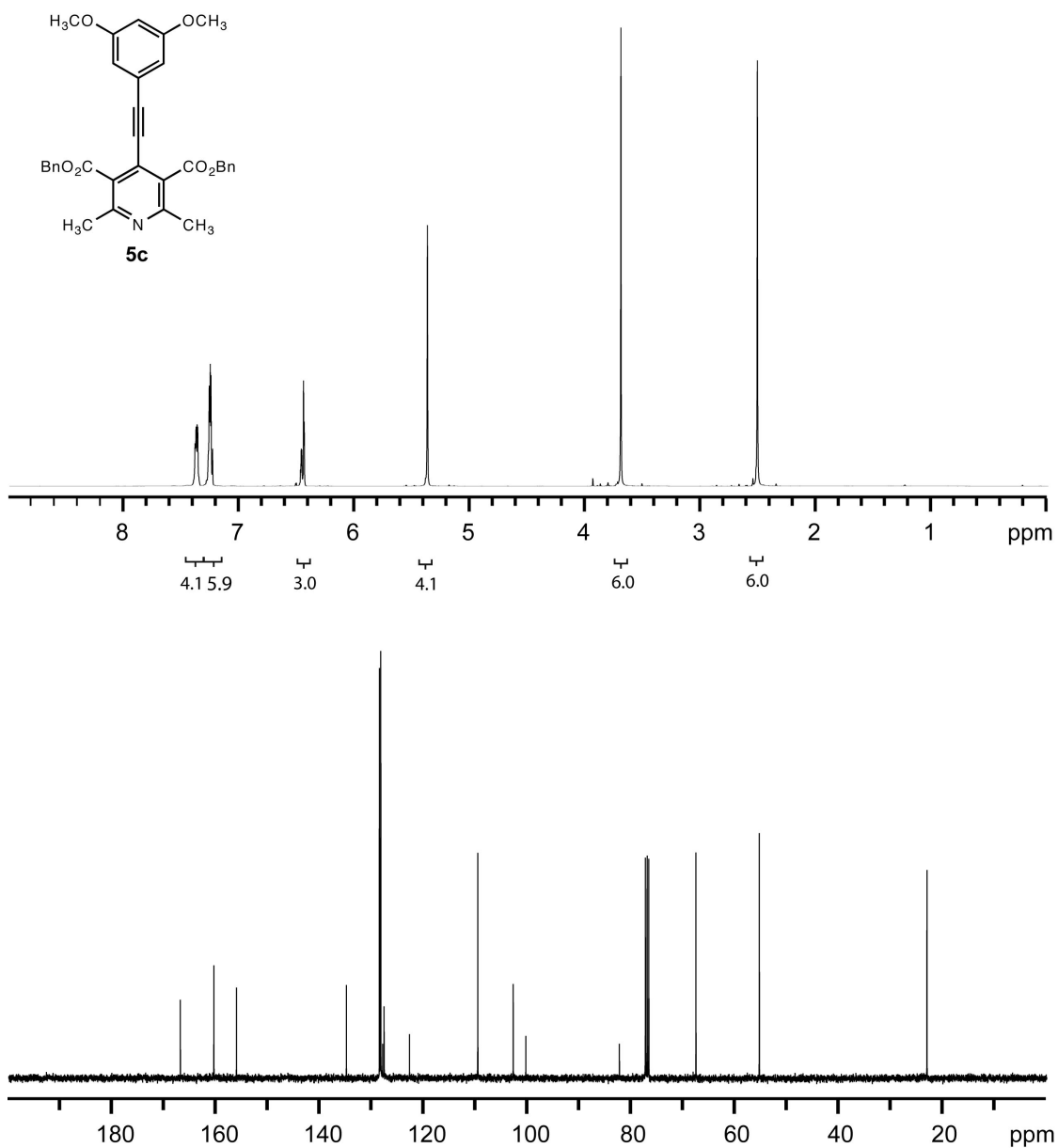


Figure S12. ^1H and ^{13}C NMR spectra of **5c**. ^1H NMR (400 MHz, CDCl_3) δ 7.38 (m, 4H), 7.26 (m, 6H), 6.46 (m, 3H), 5.38 (s, 4H), 3.70 (s, 6H), 2.52 (s, 6H). ^{13}C NMR (100 MHz, CDCl_3) δ 166.93, 160.48, 156.13, 134.95, 128.59, 128.44, 128.33, 127.97, 127.68, 122.79, 109.64, 102.81, 100.39, 82.34, 67.61, 55.40, 23.10.

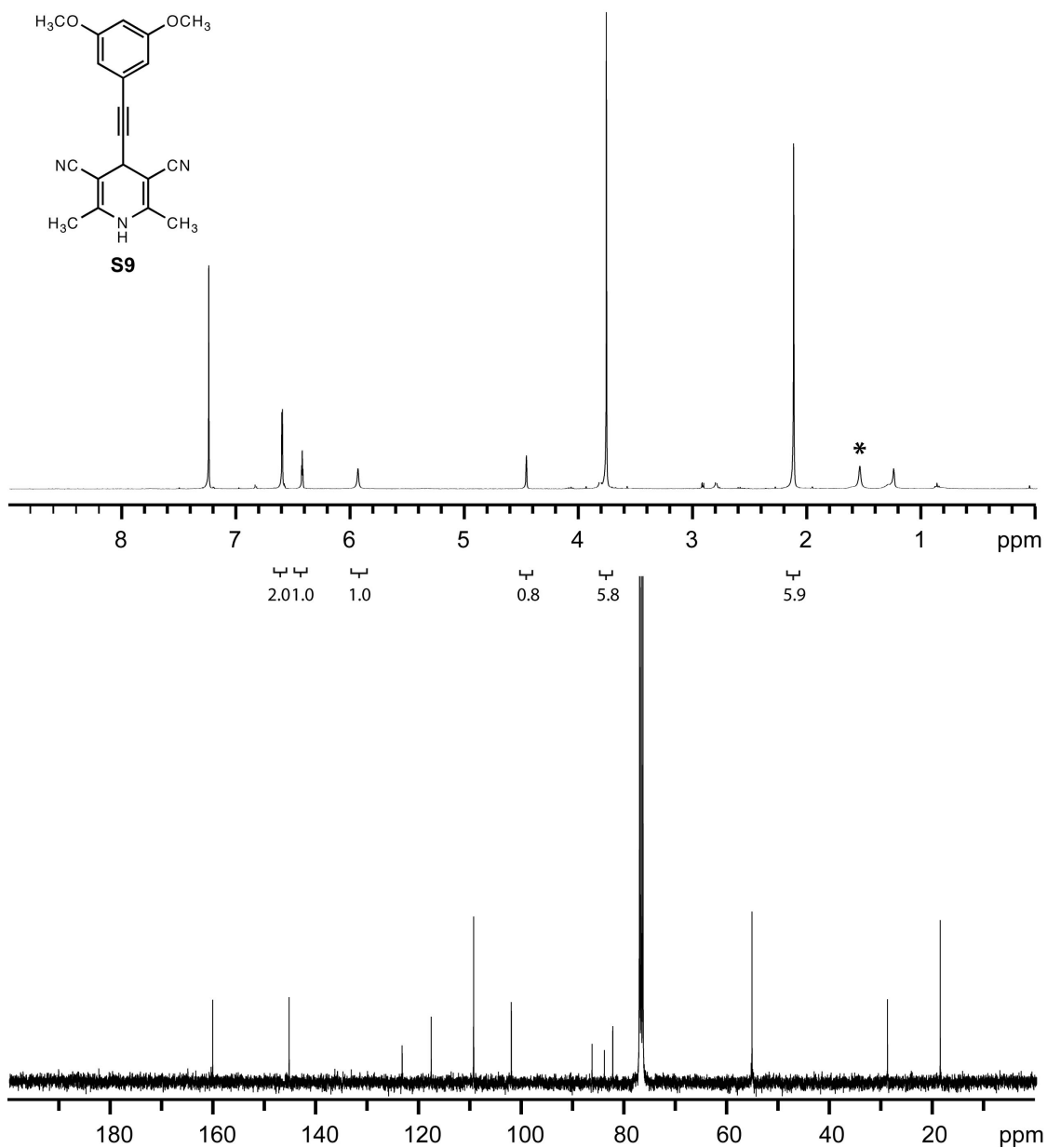


Figure S13. ¹H and ¹³C NMR spectra of **S9**. ¹H NMR (400 MHz, CDCl₃) δ 6.61 (d, *J* = 2.4 Hz, 2H), 6.44 (t, *J* = 2.2 Hz, 1H), 5.95 (s, 1H), 4.47 (s, 1H), 3.77 (s, 6H), 2.13 (s, 6H). ¹³C NMR (100 MHz, CDCl₃) δ 160.43, 145.55, 123.55, 117.90, 109.64, 102.30, 86.59, 84.19, 82.54, 55.45, 29.08, 18.81. (*denotes H₂O peak)

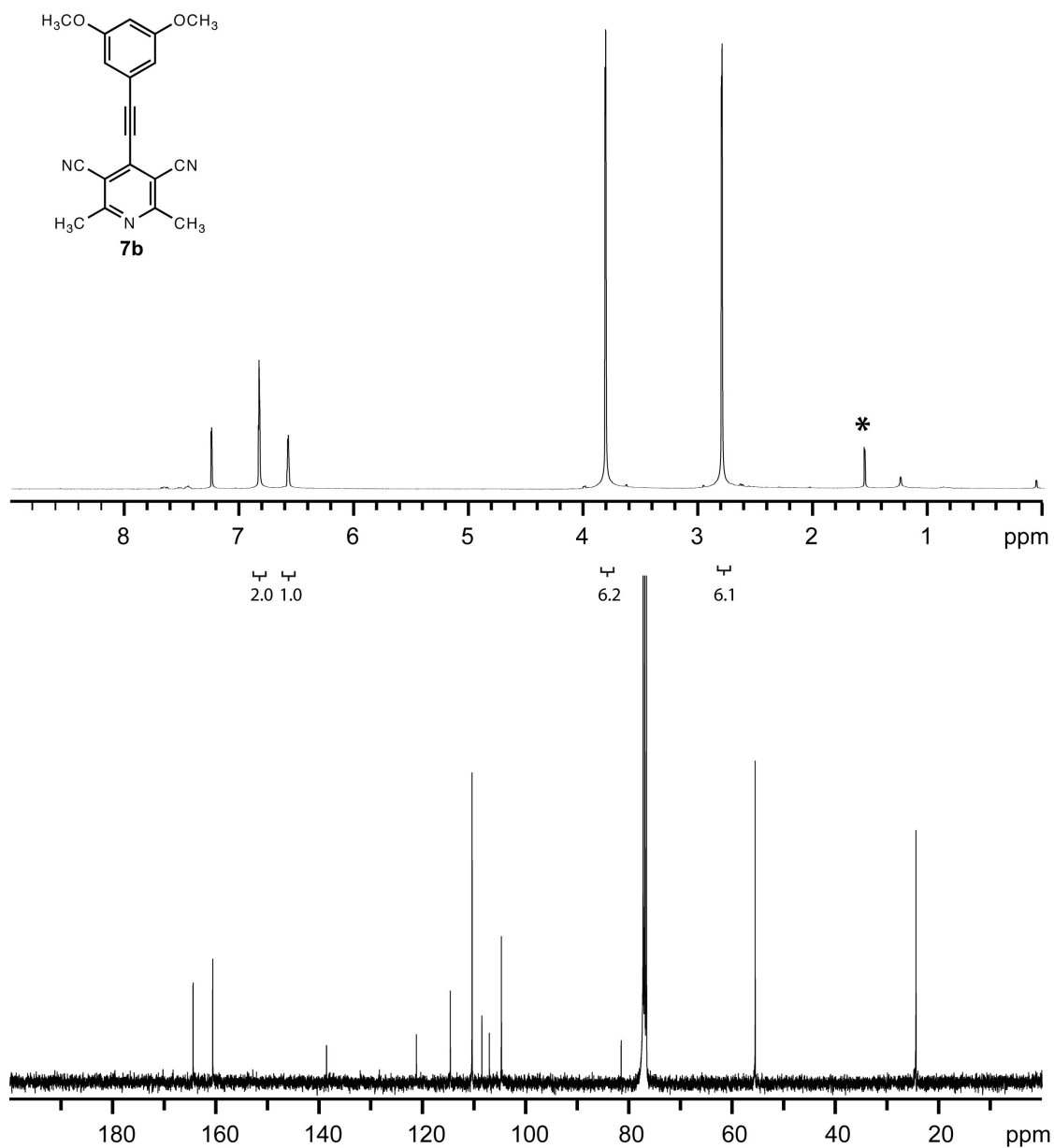


Figure S14. ^1H and ^{13}C NMR spectra of **7b**. ^1H NMR (400 MHz, CDCl_3) δ 6.85 (d, $J = 2.4$ Hz, 2H), 6.59 (t, $J = 2.2$ Hz, 1H), 3.83 (s, 6H), 2.82 (s, 6H). ^{13}C NMR (100 MHz, CDCl_3) δ 164.51, 160.71, 138.66, 121.26, 114.68, 110.47, 108.57, 107.13, 104.78, 81.59, 55.61, 24.47. (*denotes H_2O peak)

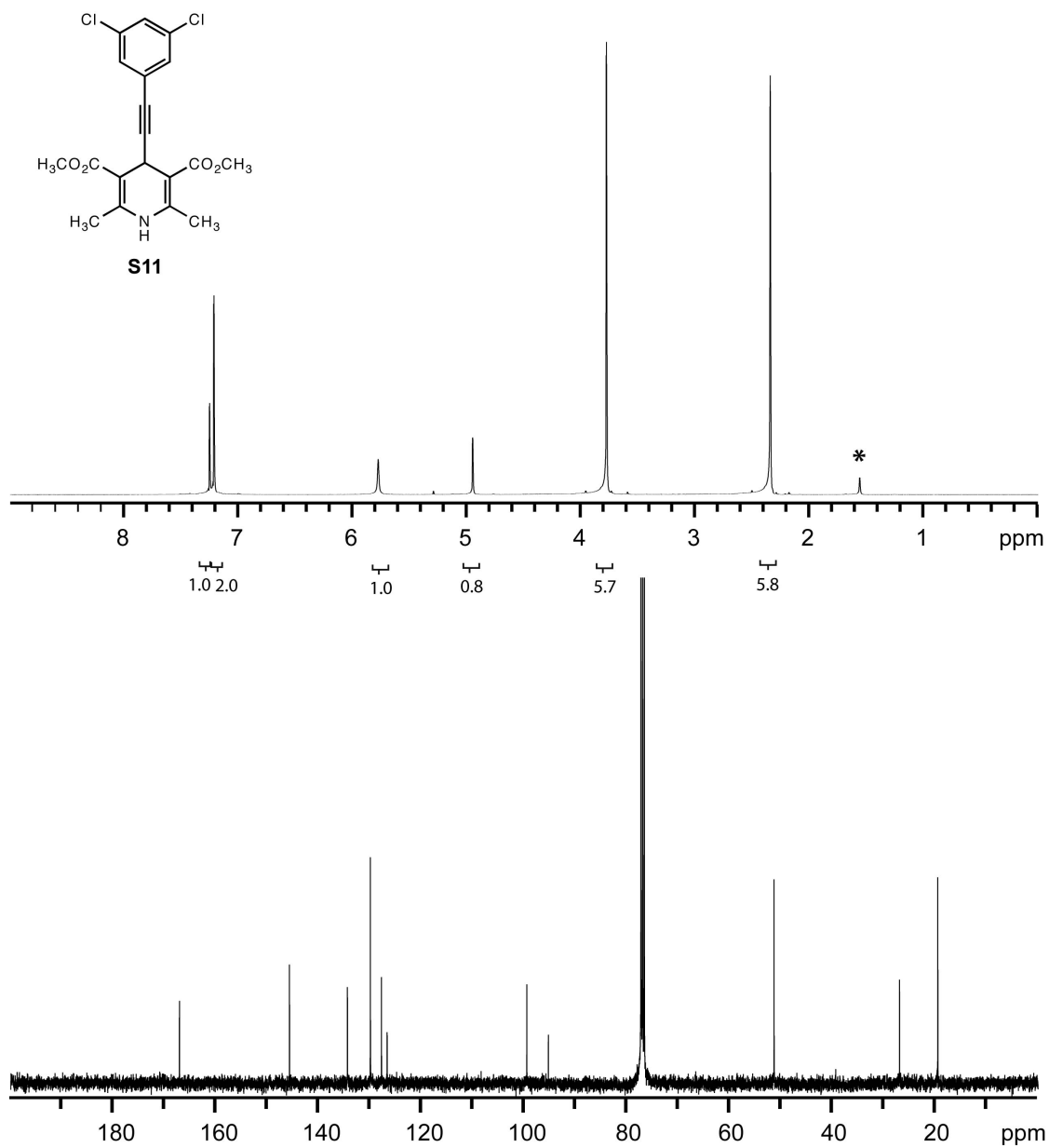


Figure S15. ^1H and ^{13}C NMR spectra of **S11**. ^1H NMR (400 MHz, CDCl_3) δ 7.25 (d, $J = 1.6$ Hz, 1H), 7.22 (d, $J = 1.2$ Hz, 2H), 5.78 (s, 1H), 4.95 (s, 1H), 3.78 (s, 6H), 2.35 (s, 6H). ^{13}C NMR (100 MHz, CDCl_3) δ 167.38, 145.97, 134.68, 130.22, 128.06, 126.96, 99.77, 95.57, 51.64, 27.23, 19.78. (*denotes H_2O peak)

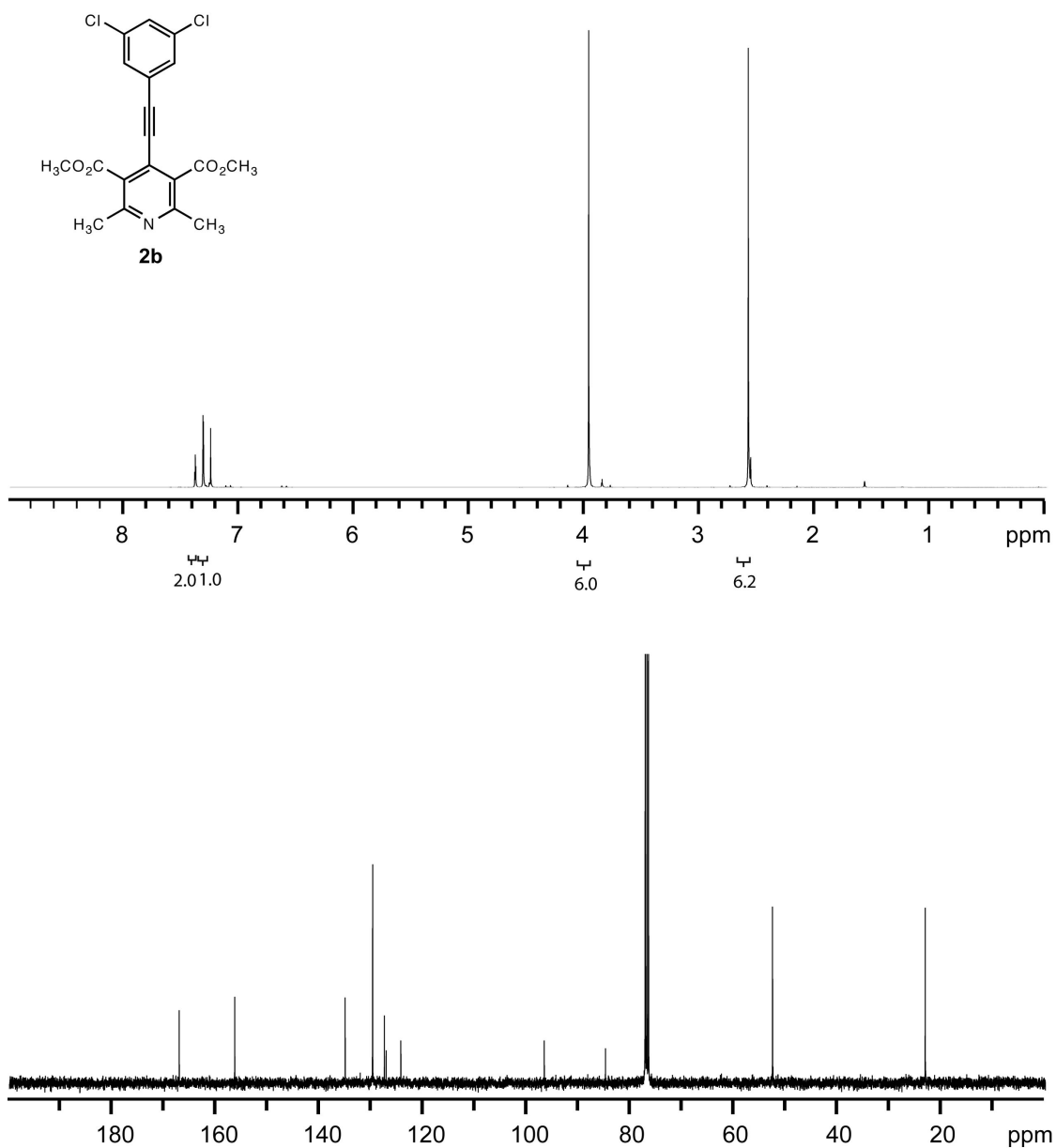


Figure S16. ^1H and ^{13}C NMR spectra of **2b**. ^1H NMR (400 MHz, CDCl_3) δ 7.39 (t, J = 1.8 Hz, 1H), 7.32 (d, J = 1.6 Hz, 2H), 3.98 (s, 6H), 2.59 (s, 6H). ^{13}C NMR (100 MHz, CDCl_3) δ 167.21, 156.50, 135.18, 129.90, 129.88, 127.60, 127.27, 124.43, 96.75, 84.94, 52.70, 23.23.

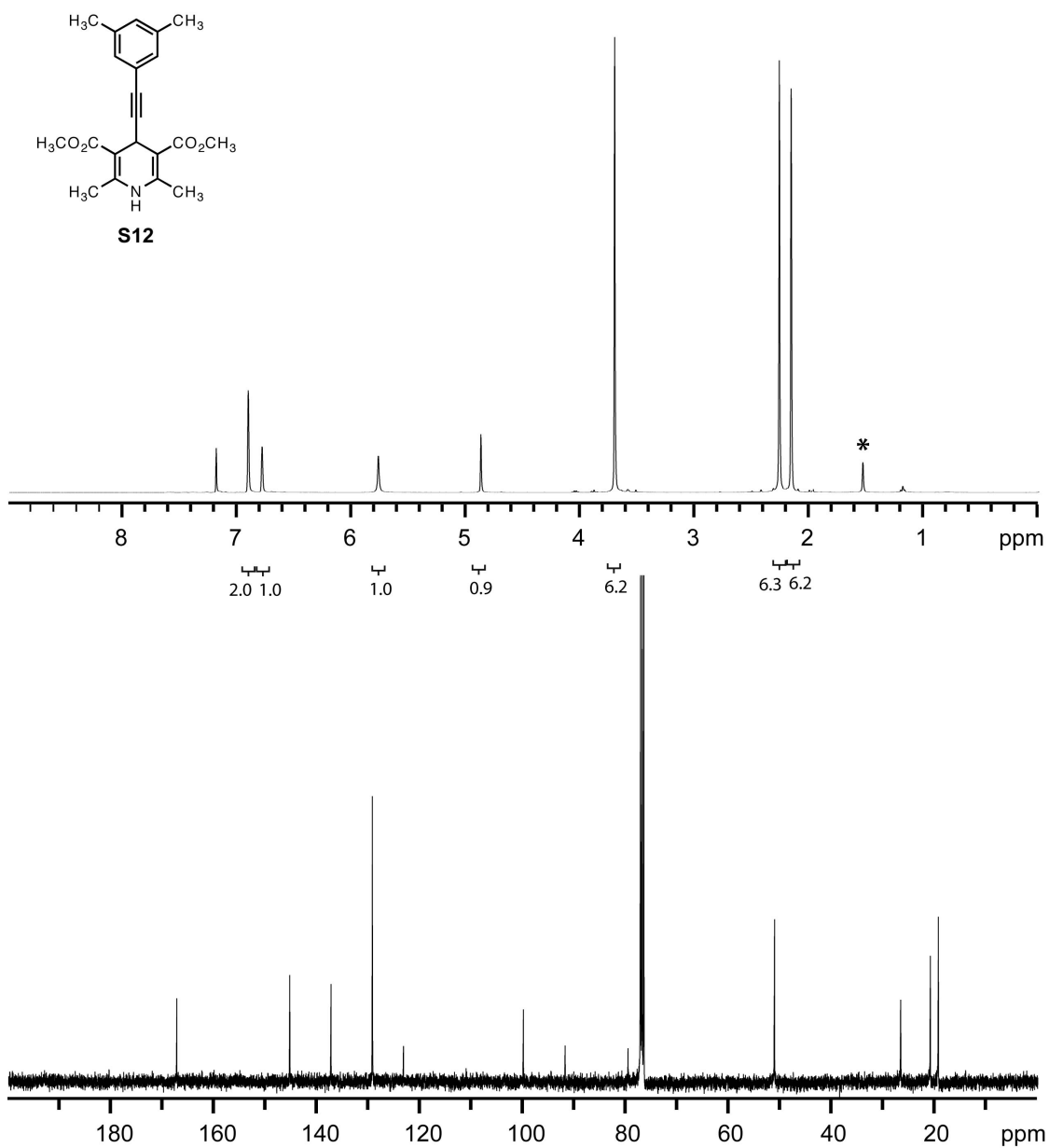


Figure S17. ^1H and ^{13}C NMR spectra of **S12**. ^1H NMR (400 MHz, CDCl_3) δ 6.91 (brs, 2H), 6.79 (brs, 1H), 5.78 (s, 1H), 4.88 (s, 1H), 3.71 (s, 6H), 2.27 (s, 6H), 2.17 (s, 6H). ^{13}C NMR (100 MHz, CDCl_3) δ 167.32, 145.38, 137.36, 129.32, 123.28, 99.98, 91.87, 79.64, 51.19, 26.68, 20.91, 19.36. (*denotes H_2O peak)

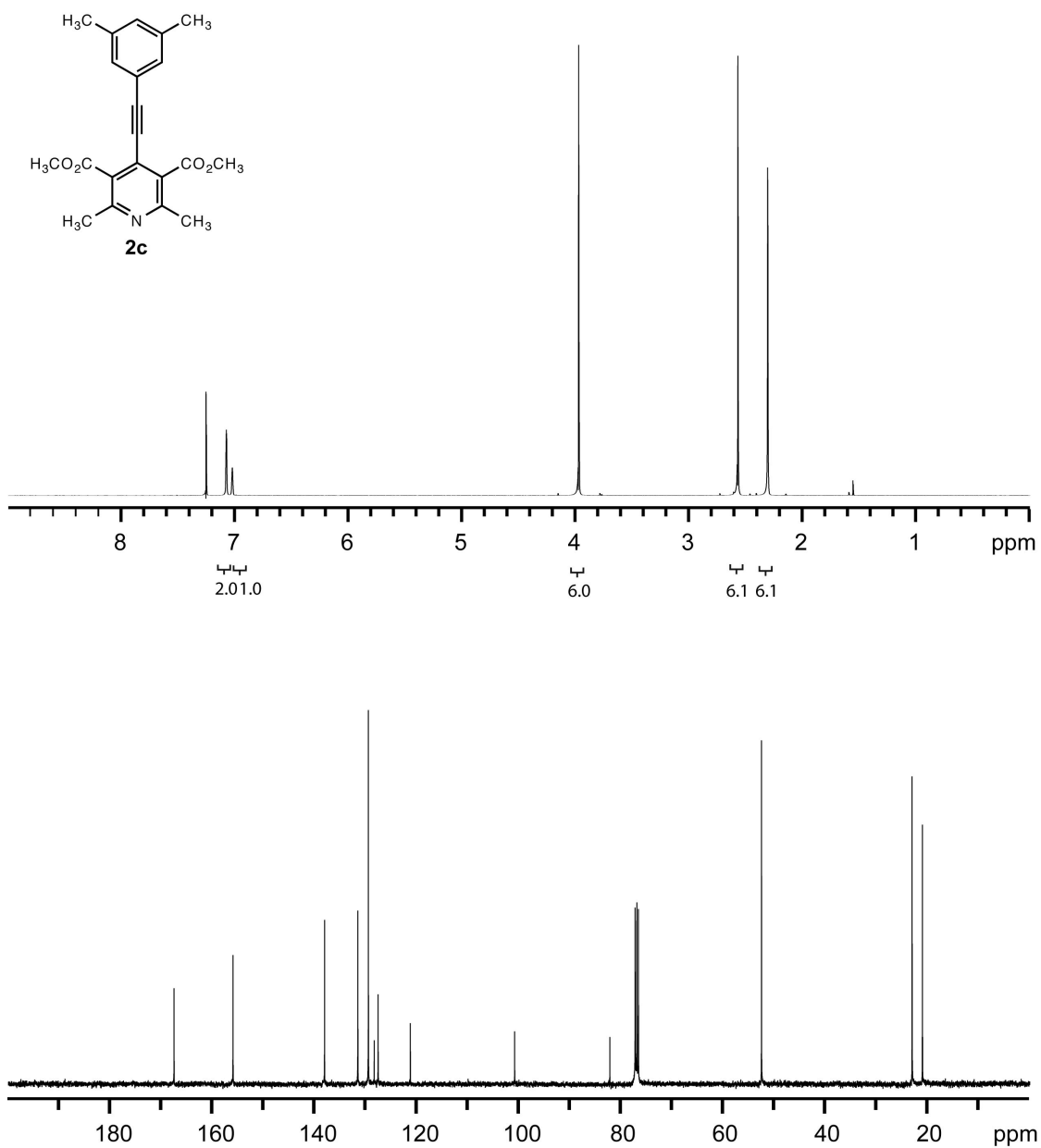


Figure S18. ¹H and ¹³C NMR spectra of **2c**. ¹H NMR (400 MHz, CDCl₃) δ 7.08 (brs, 2H), 7.03 (brs, 1H), 3.98 (s, 6H), 2.58 (s, 6H), 2.31 (s, 6H). ¹³C NMR (100 MHz, CDCl₃) δ 167.64, 156.08, 138.15, 131.64, 129.57, 128.43, 127.66, 121.34, 100.93, 82.28, 52.63, 23.14, 21.12.

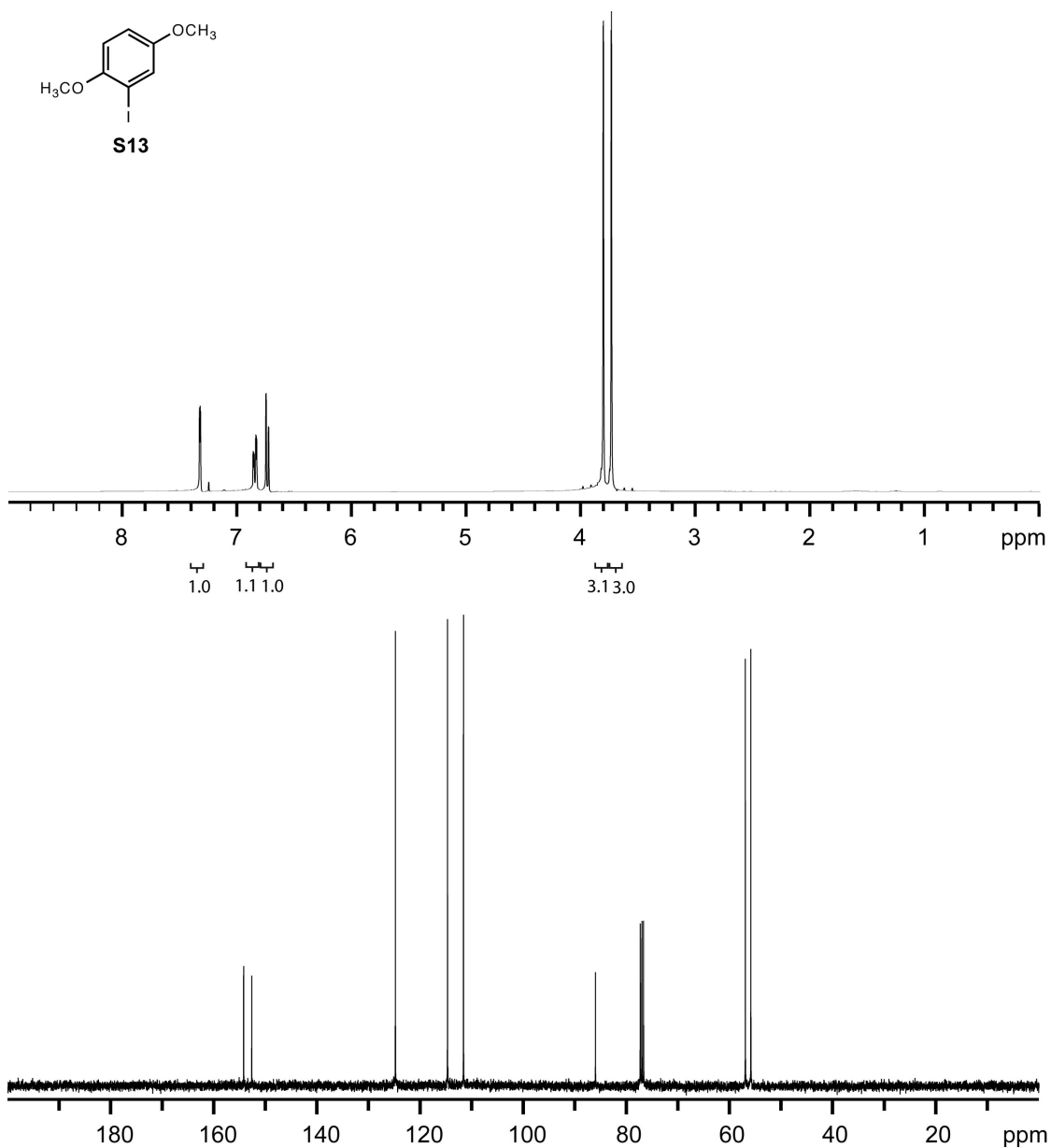


Figure S19. ^1H and ^{13}C NMR spectra of **S13**. ^1H NMR (400 MHz, CDCl_3) δ 7.33 (d, $J = 2.8$ Hz, 1H), 6.85 (dd, $J = 8.8$ Hz, $J = 2.8$ Hz, 1H), 6.74 (d, $J = 8.8$ Hz, 1H), 3.81 (s, 3H), 3.74 (s, 3H). ^{13}C NMR (100 MHz, CDCl_3) δ 154.28, 152.72, 124.85, 114.74, 111.65, 86.06, 56.99, 55.93.

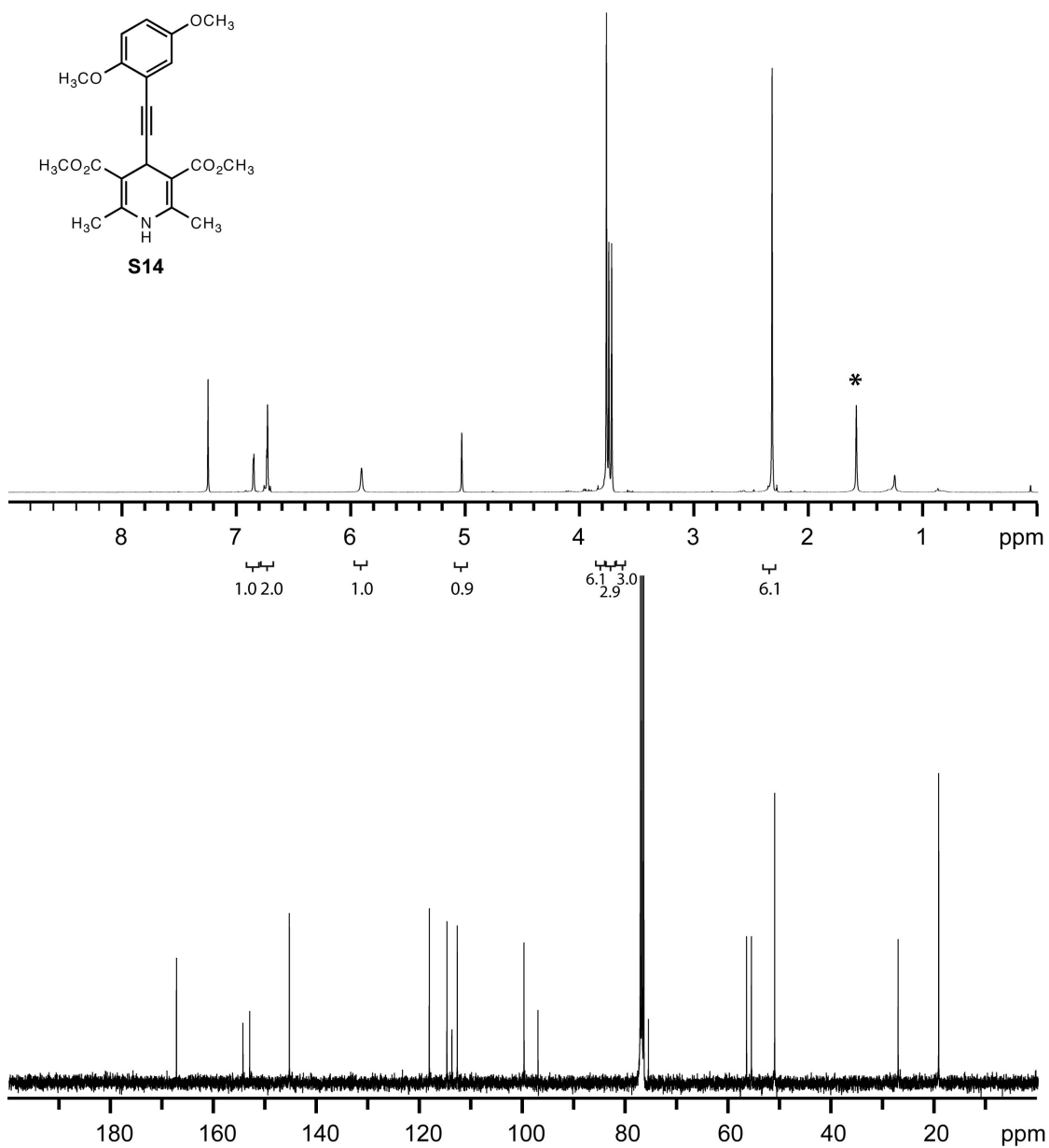


Figure S20. ¹H and ¹³C NMR spectra of **S14**. ¹H NMR (400 MHz, CDCl₃) δ 6.86 (m, 1H), 6.74 (m, 2H), 5.92 (s, 1H), 5.04 (s, 1H), 3.78 (s, 6H), 3.76 (s, 3H), 3.73 (s, 3H), 2.33 (s, 6H). ¹³C NMR (100 MHz, CDCl₃) δ 167.46, 157.56, 153.25, 145.54, 118.36, 114.92, 113.95, 112.91, 99.94, 97.23, 75.78, 56.71, 55.77, 51.25, 27.26, 19.38. (*denotes H₂O peak)

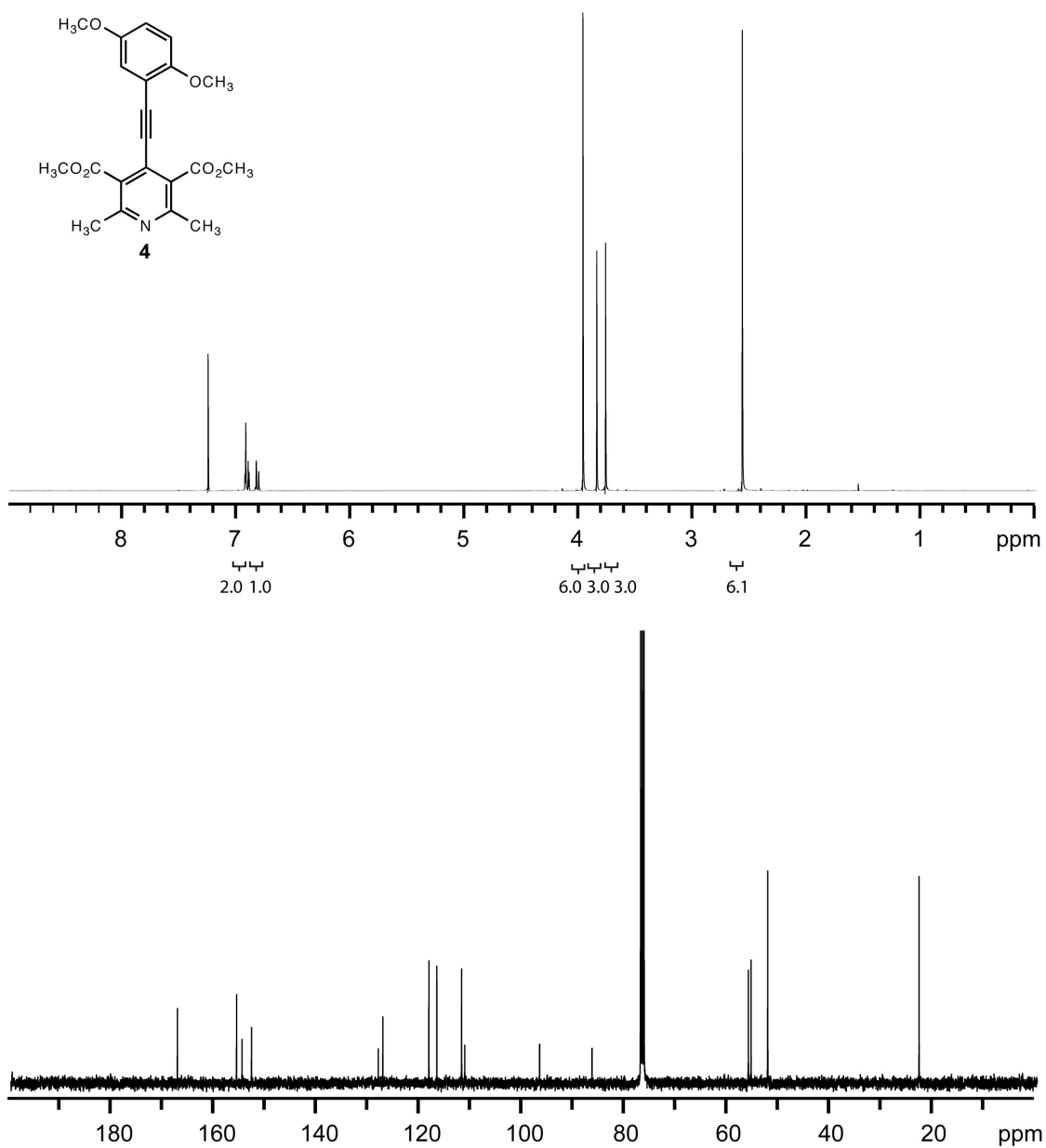


Figure S21. ¹H and ¹³C NMR spectra of **4**. ¹H NMR (400 MHz, CDCl₃) δ 6.92 (m, 2H), 6.82 (d, *J* = 8.4 Hz, 1H), 3.97 (s, 6H), 3.85 (s, 3H), 3.77 (s, 3H), 2.57 (s, 6H). ¹³C NMR (100 MHz, CDCl₃) δ 167.56, 156.03, 154.97, 153.12, 128.41, 127.54, 118.56, 117.01, 112.19, 111.57, 96.98, 86.78, 56.30, 55.79, 52.54, 23.05.

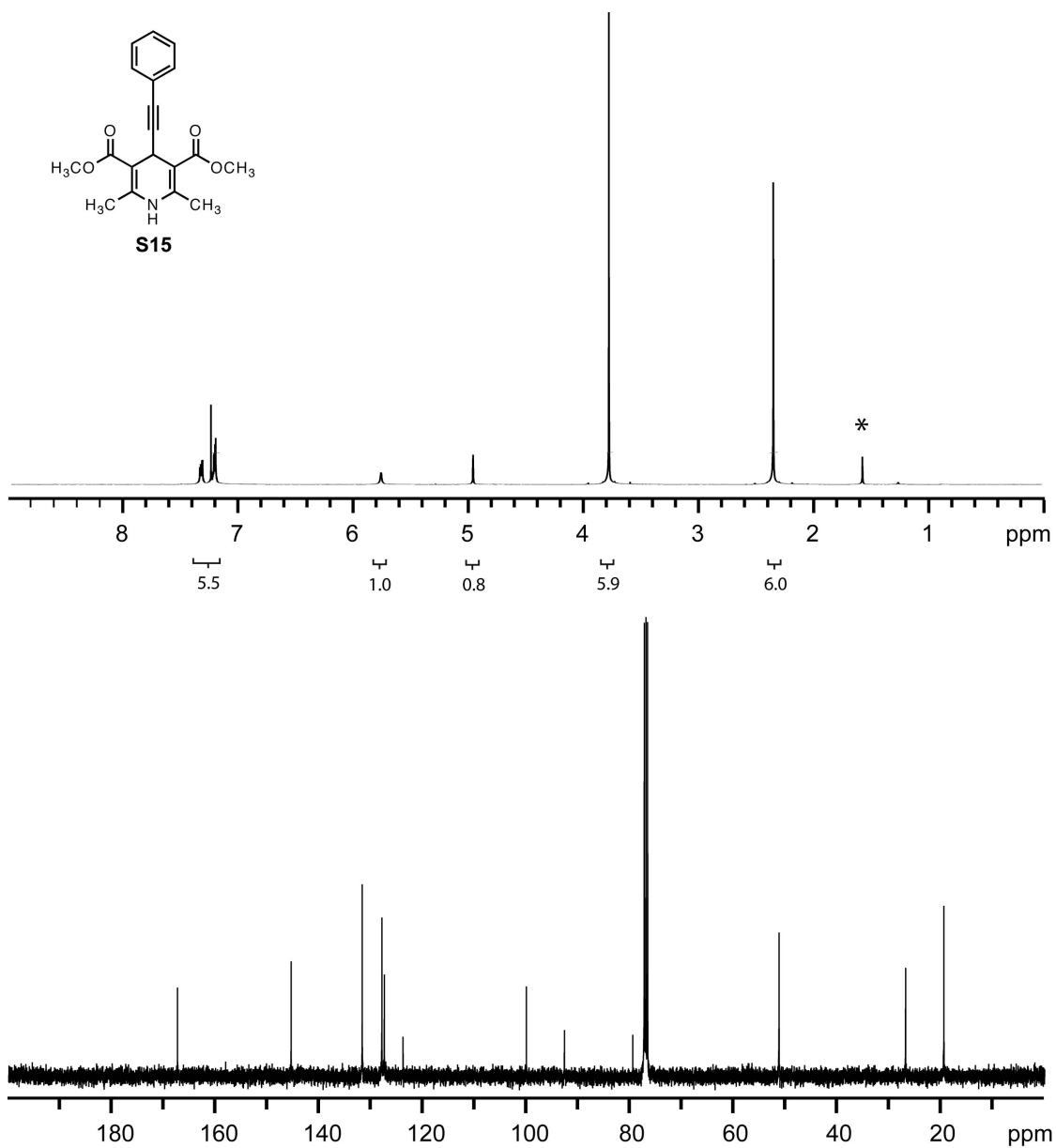


Figure S22. ^1H and ^{13}C NMR spectra of **S15**. ^1H NMR (400 MHz, CDCl_3) δ 7.30 (m, 5H), 5.77 (s, 1H), 4.97 (s, 1H), 3.78 (s, 6H), 2.34 (s, 6H). ^{13}C NMR (100 MHz, CDCl_3) δ 167.40, 145.49, 131.77, 127.96, 127.50, 123.88, 100.07, 92.73, 79.53, 51.30, 26.89, 19.48. (*denotes H_2O peak)

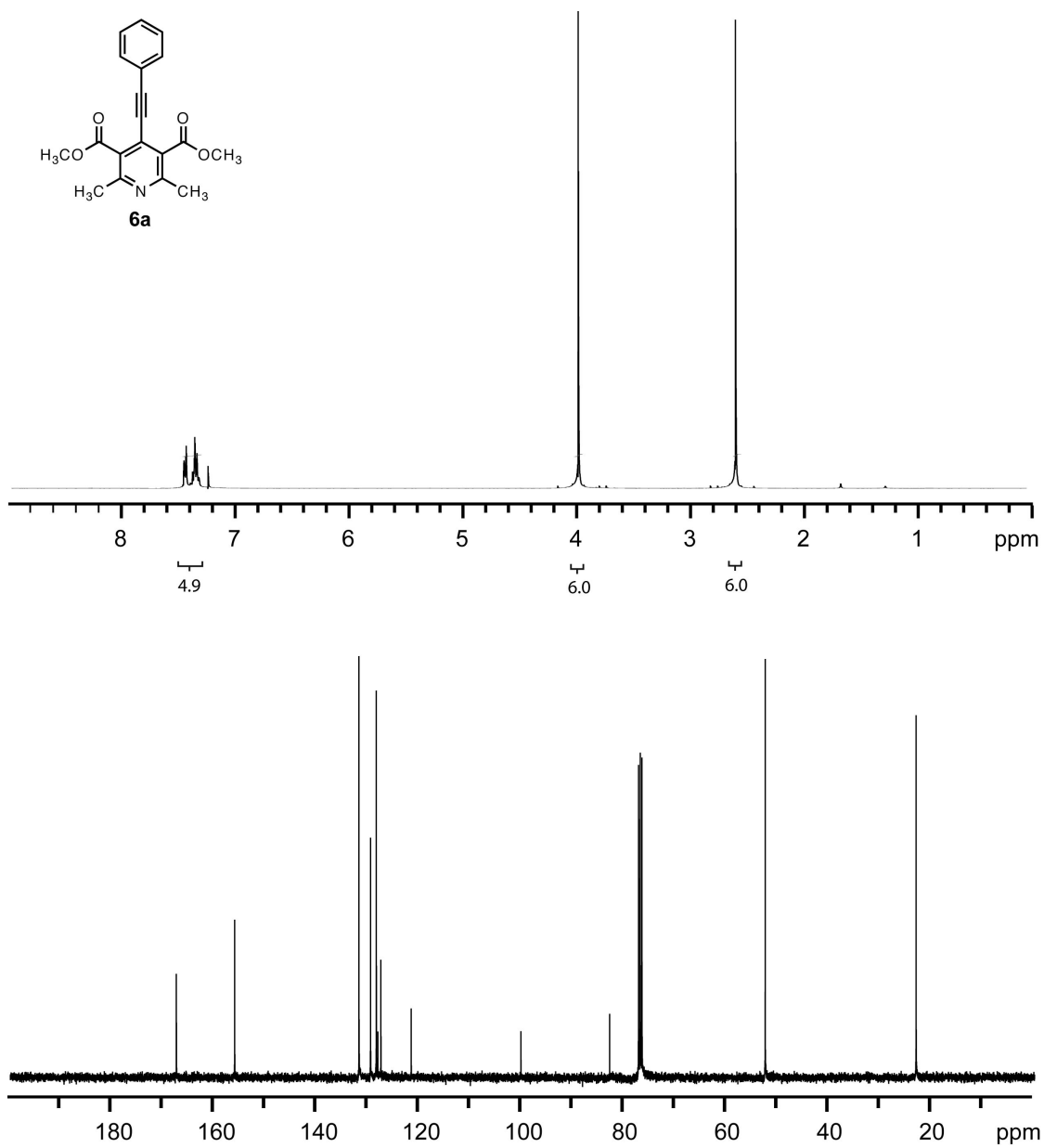


Figure S23. ¹H and ¹³C NMR spectra of **6a**. ¹H NMR (400 MHz, CDCl₃) δ 7.41 (m, 5H), 3.97 (s, 6H), 2.58 (s, 6H). ¹³C NMR (100 MHz, CDCl₃) δ 167.57, 156.19, 131.92, 129.67, 128.53, 128.24, 127.65, 121.73, 100.31, 83.00, 52.61, 23.15.

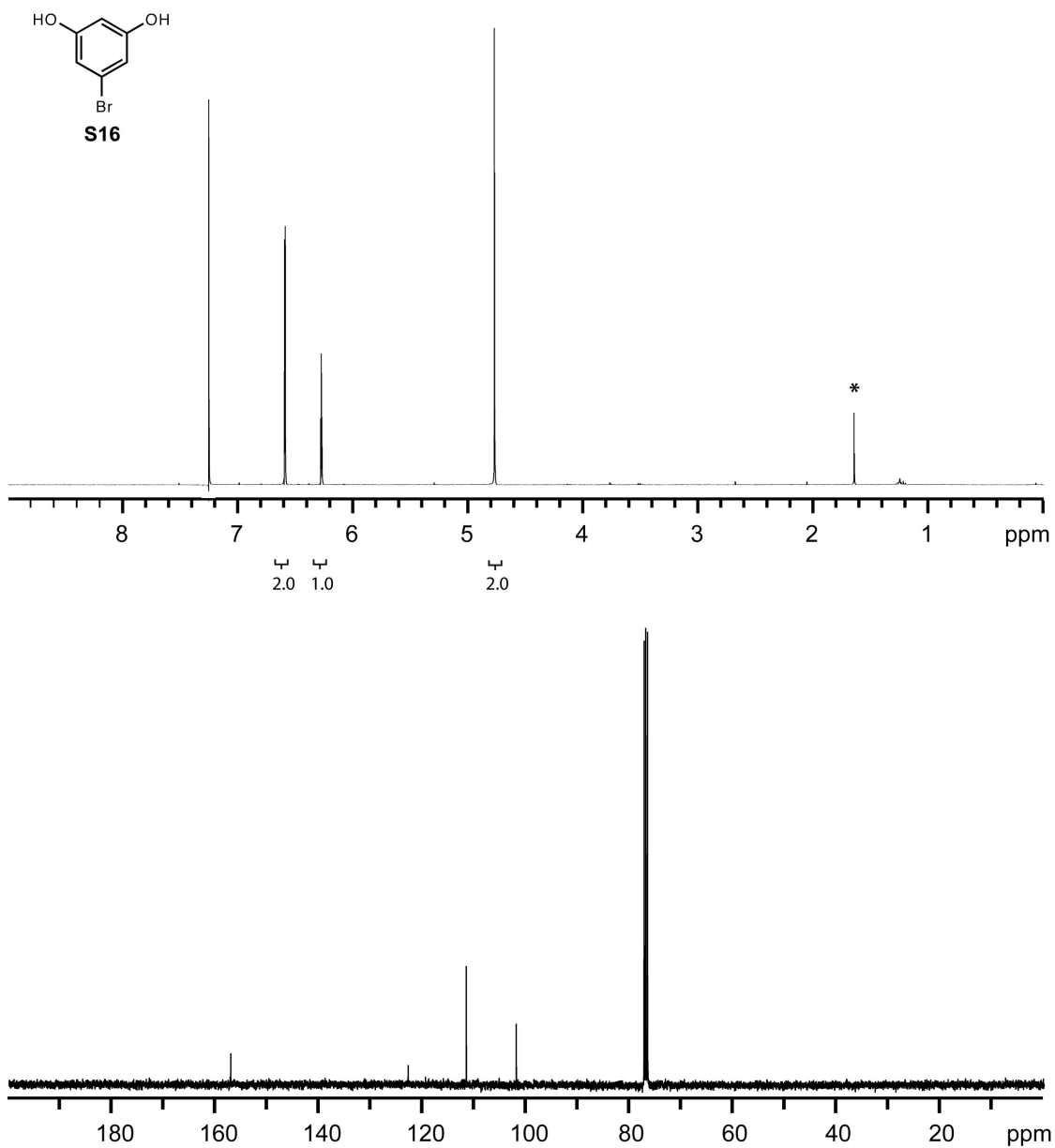


Figure S24. ^1H and ^{13}C NMR spectra of **S16**. ^1H NMR (400 MHz, CDCl_3) δ 6.60 (d, J = 2.4 Hz, 2H), 6.28 (t, J = 2.0 Hz, 1H), 4.78 (s, 2H). ^{13}C NMR (100 MHz, CDCl_3) δ 157.18, 122.90, 111.66, 102.00. (*denotes H_2O peak)

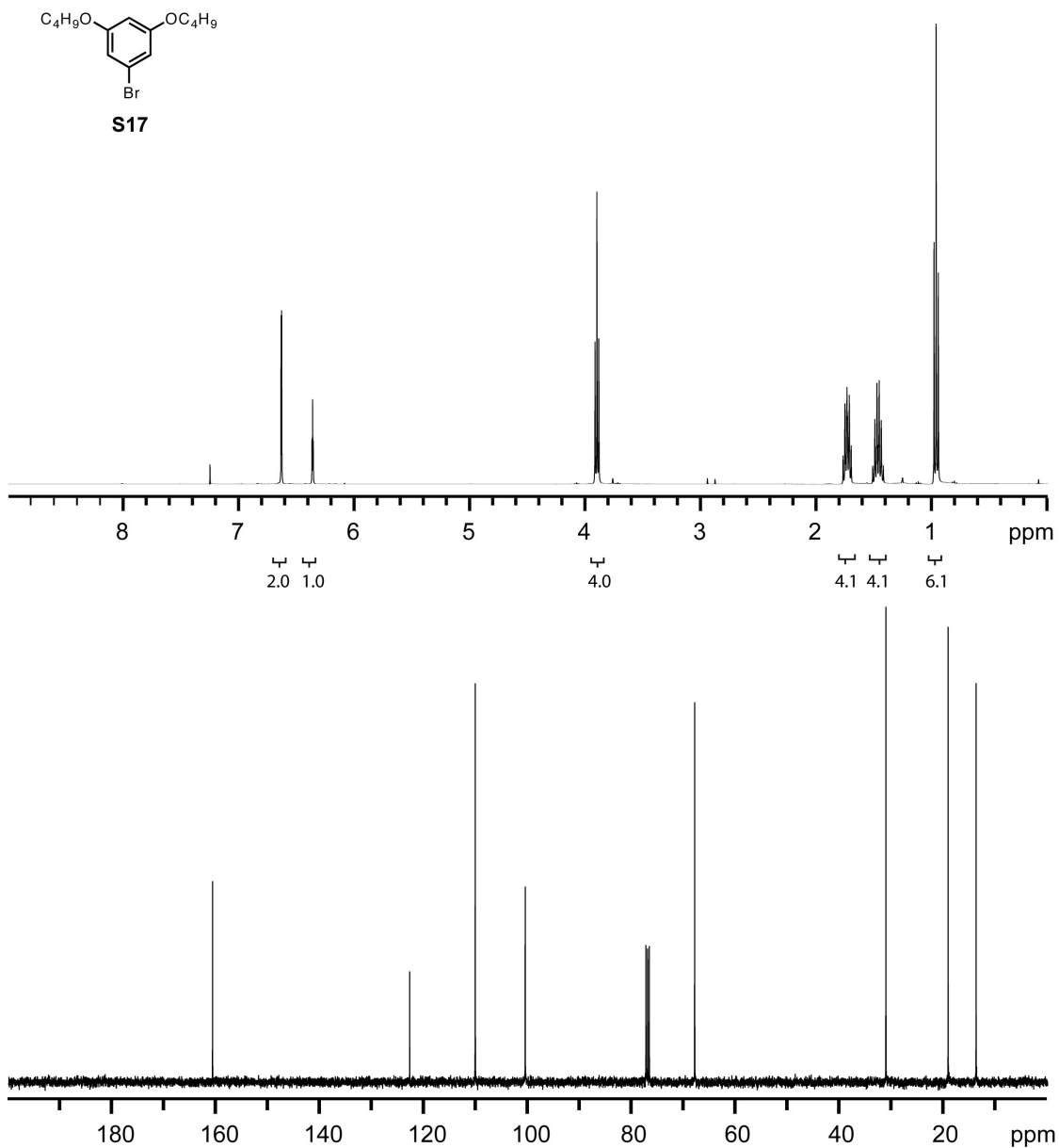


Figure S25. ^1H and ^{13}C NMR spectra of **S17**. ^1H NMR (400 MHz, CDCl_3) δ 6.65 (d, J = 2.4 Hz, 2H), 6.37 (t, J = 2.0 Hz, 1H), 3.91 (t, J = 6.4 Hz, 4H), 1.74 (m, 4H), 1.48 (m, 4H), 0.97 (t, J = 7.2 Hz, 6H). ^{13}C NMR (100 MHz, CDCl_3) δ 160.75, 122.81, 110.19, 100.57, 67.96, 31.16, 19.19, 13.80.

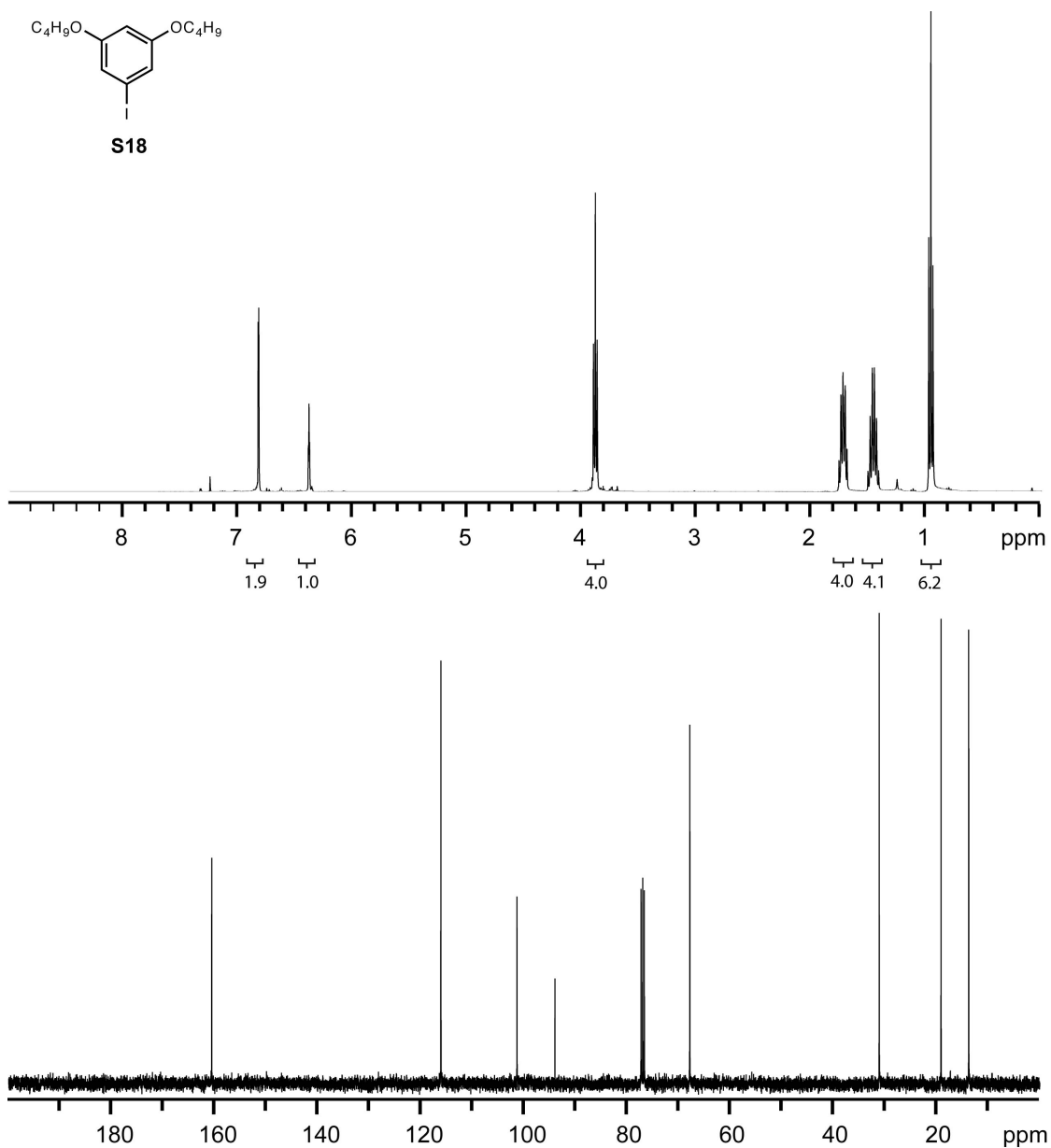


Figure S26. ^1H and ^{13}C NMR spectra of **S18**. ^1H NMR (400 MHz, CDCl_3) δ 6.84 (d, J = 2.4 Hz, 2H), 6.40 (t, J = 2.0 Hz, 1H), 3.90 (t, J = 6.8 Hz, 4H), 1.74 (m, 4H), 1.47 (m, 4H), 0.97 (t, J = 7.2 Hz, 6H). ^{13}C NMR (100 MHz, CDCl_3) δ 160.62, 116.18, 101.42, 94.06, 67.91, 31.18, 19.19, 13.82.

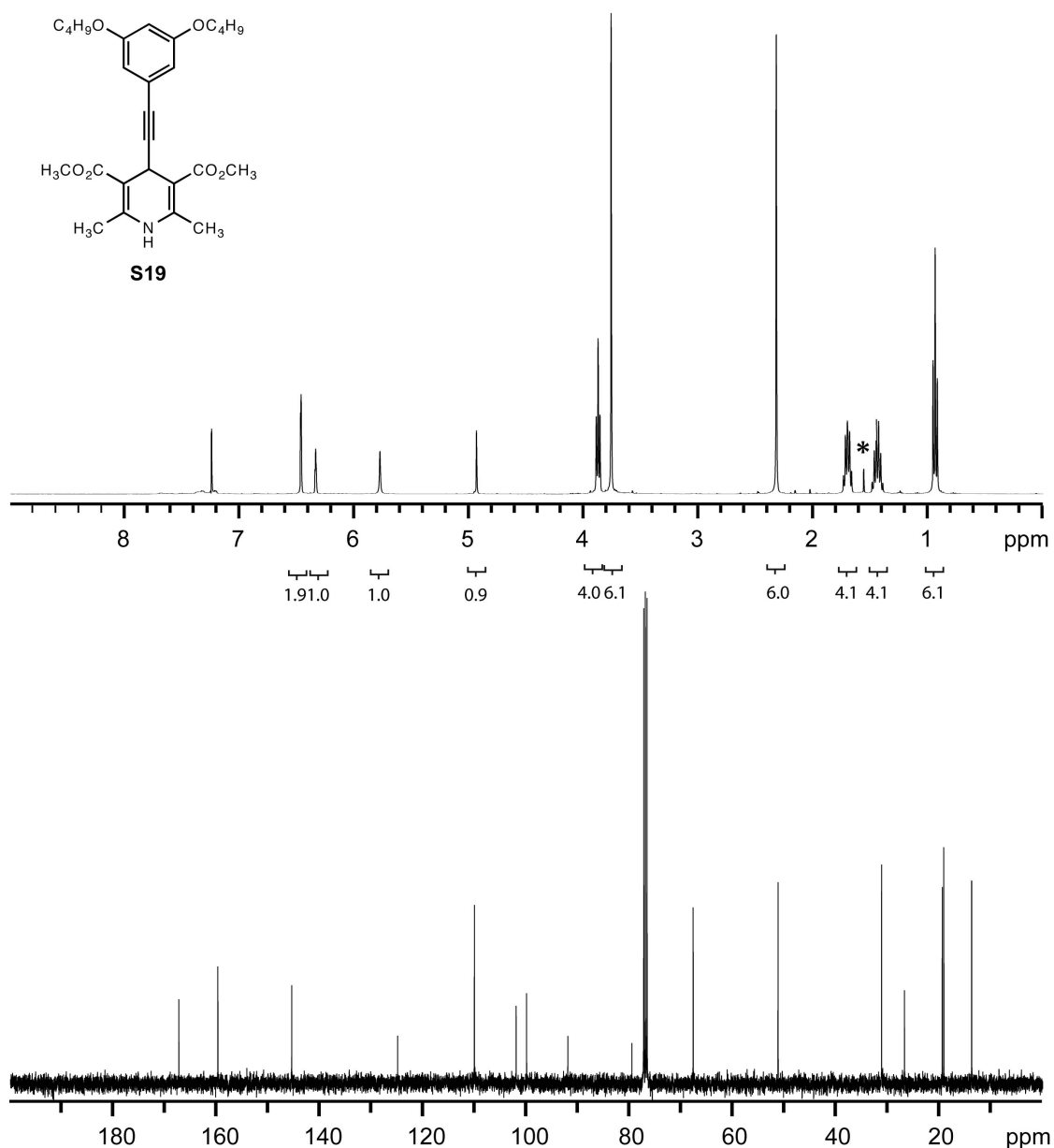


Figure S27. ^1H and ^{13}C NMR spectra of **S19**. ^1H NMR (400 MHz, CDCl_3) δ 6.48 (d, $J = 1.6$ Hz, 2H), 6.35 (t, $J = 2.0$ Hz, 1H), 5.79 (s, 1H), 4.95 (s, 1H), 3.89 (t, $J = 6.8$ Hz, 4H), 3.78 (s, 6H), 2.34 (s, 6H), 1.72 (m, 4H), 1.47 (m, 4H), 0.95 (t, $J = 7.2$ Hz, 6H). ^{13}C NMR (100 MHz, CDCl_3) δ 167.38, 159.81, 145.50, 124.99, 110.12, 102.30, 100.01, 92.02, 79.62, 67.74, 51.29, 31.23, 26.81, 19.48, 19.18, 13.79. (*denotes H_2O peak)

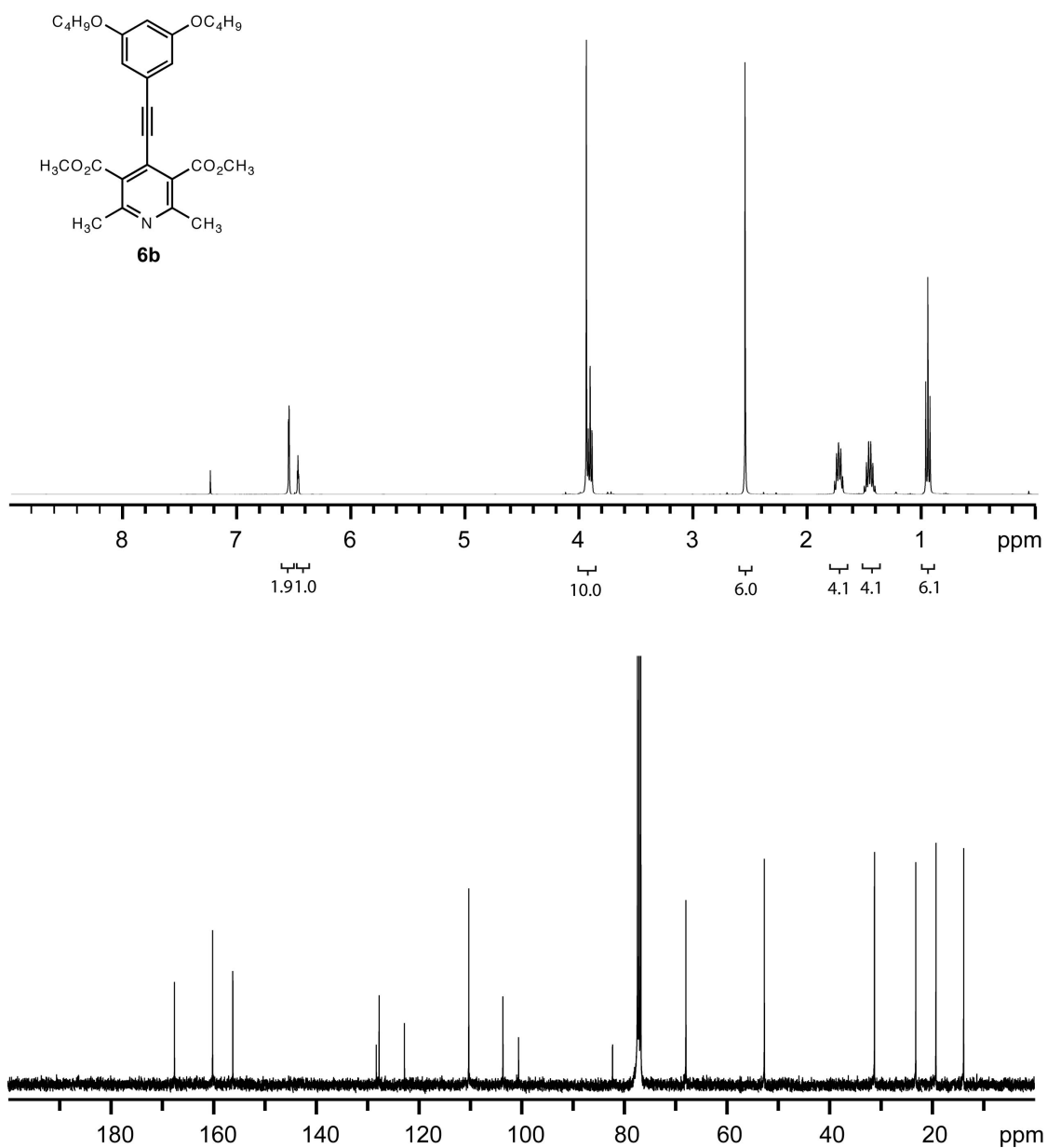


Figure S28. ^1H and ^{13}C NMR spectra of **6b**. ^1H NMR (400 MHz, CDCl_3) δ 6.56 (d, $J = 2.0$ Hz, 2H), 6.49 (t, $J = 2.4$ Hz, 1H), 3.96 (s, 6H), 3.93 (t, $J = 6.4$ Hz, 4H), 2.57 (s, 6H), 1.76 (m, 4H), 1.47 (m, 4H), 0.97 (t, $J = 7.2$ Hz, 6H). ^{13}C NMR (100 MHz, CDCl_3) δ 167.54, 160.13, 156.18, 128.23, 127.68, 122.74, 110.21, 103.56, 100.51, 82.20, 67.92, 52.62, 31.17, 23.13, 19.19, 13.80.

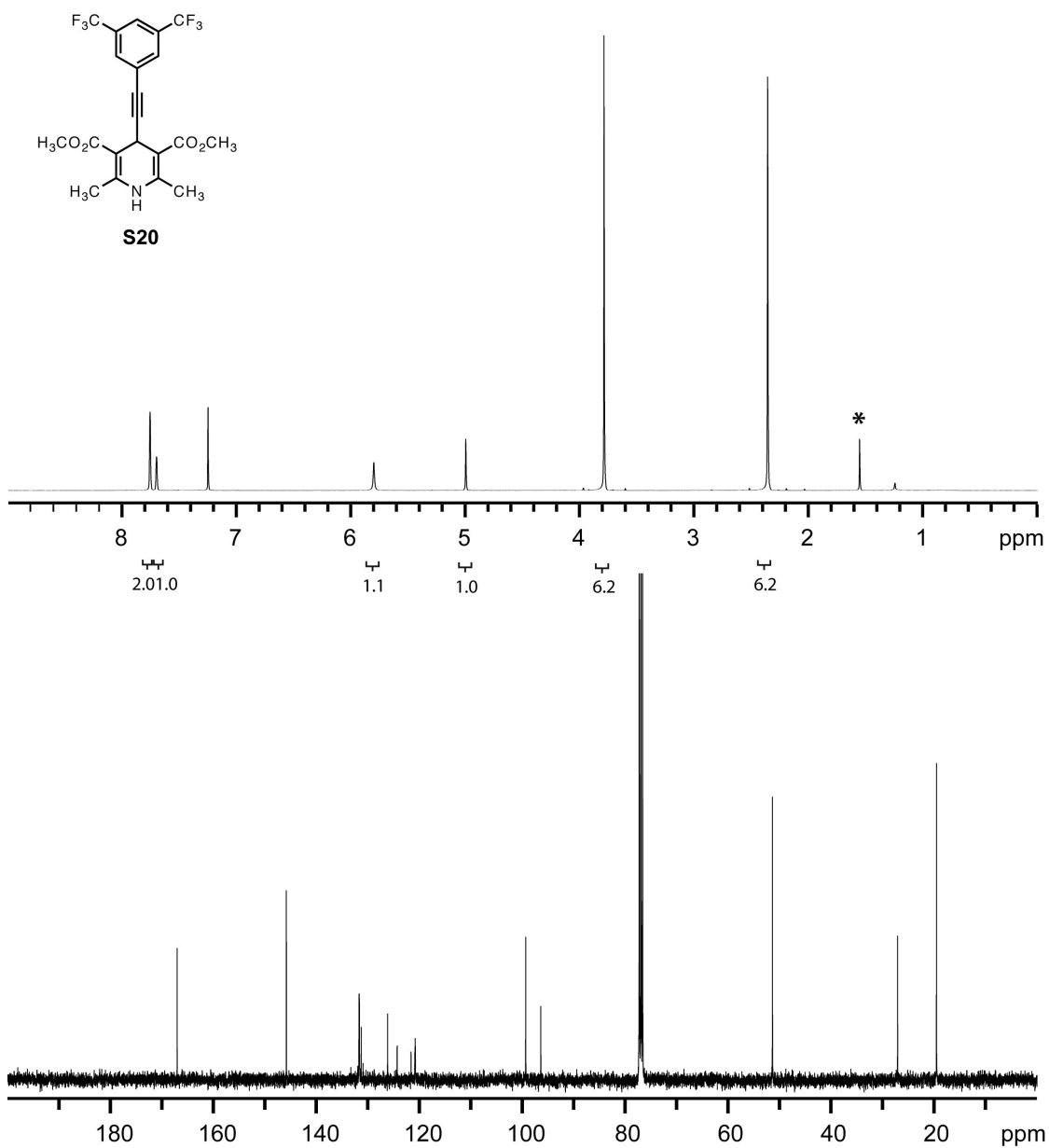


Figure S29. ^1H and ^{13}C NMR spectra of **S20**. ^1H NMR (400 MHz, CDCl_3) δ 7.76 (brs, 2H), 7.71 (brs, 1H), 5.81 (s, 1H), 5.00 (s, 1H), 3.79 (s, 6H), 2.63 (s, 6H). ^{13}C NMR (100 MHz, CDCl_3) δ 167.10, 145.88, 131.70 (q, $J_{\text{CF}} = 16.2$ Hz), 131.33, 126.21, 124.36, 121.65, 120.88 (m), 99.38, 96.45, 51.45, 27.11, 19.57. (*denotes H_2O peak)

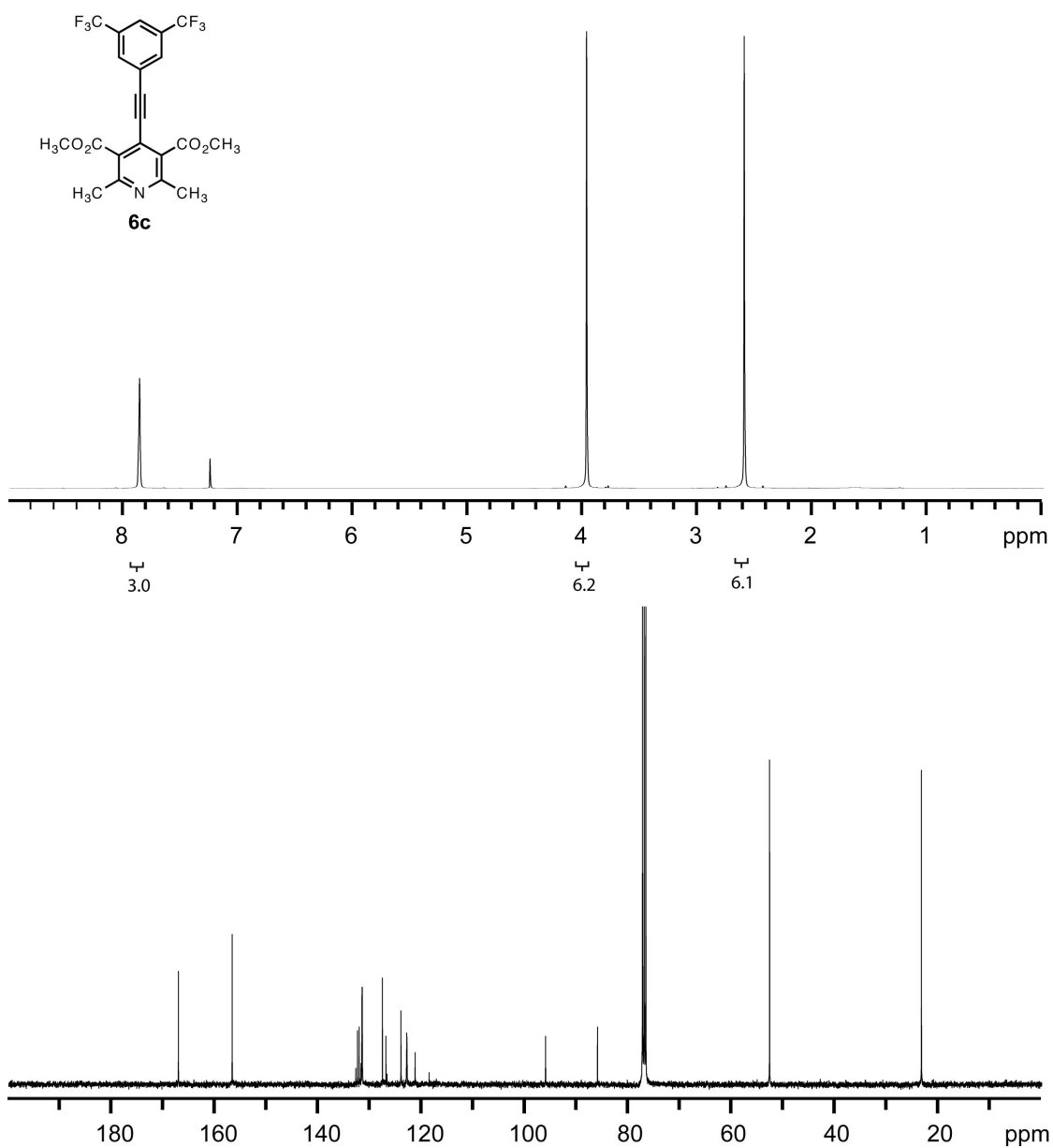


Figure S30. ^1H and ^{13}C NMR spectra of **6c**. ^1H NMR (400 MHz, CDCl_3) δ 7.87 (brs, 3H), 3.98 (s, 6H), 2.61 (s, 6H). ^{13}C NMR (100 MHz, CDCl_3) δ 167.15, 156.74, 132.31 (q, $J_{\text{CF}} = 33.4$ Hz), 131.58, 127.65, 126.98, 124.07, 122.94, 121.33, 96.08, 86.03, 52.72, 23.33.

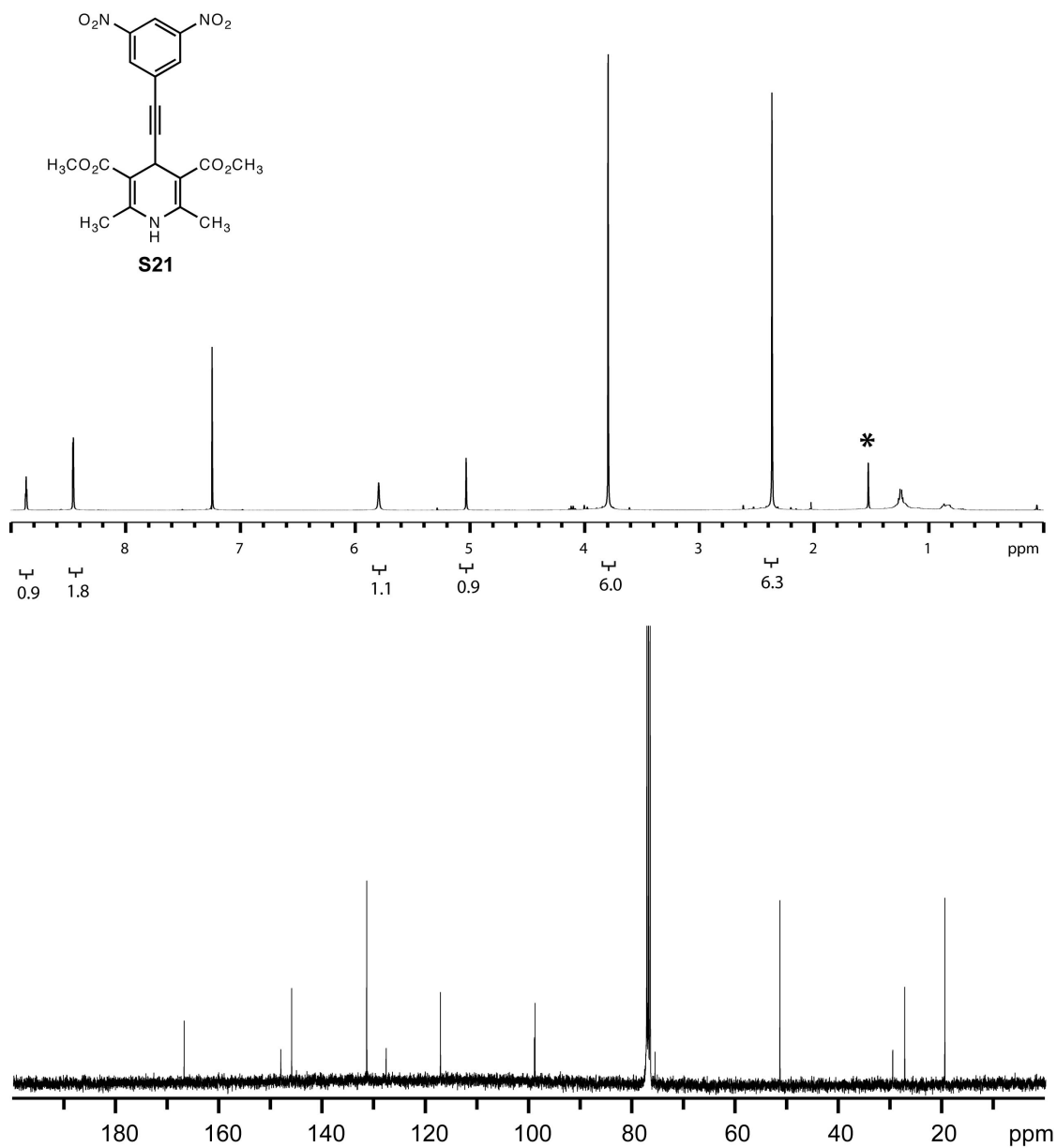


Figure S31. ^1H and ^{13}C NMR spectra of **S21**. ^1H NMR (400 MHz, CDCl_3) δ 8.87 (t, $J = 1.6$ Hz, 1H), 8.46 (d, $J = 2.0$ Hz, 2H), 5.80 (s, 1H), 5.03 (s, 1H), 3.80 (s, 6H), 2.37 (s, 6H). ^{13}C NMR (100 MHz, CDCl_3) δ 166.94, 148.20, 146.10, 131.57, 127.81, 117.28, 99.02, 75.71, 51.53, 29.68, 27.36, 19.60. (*denotes H_2O peak)

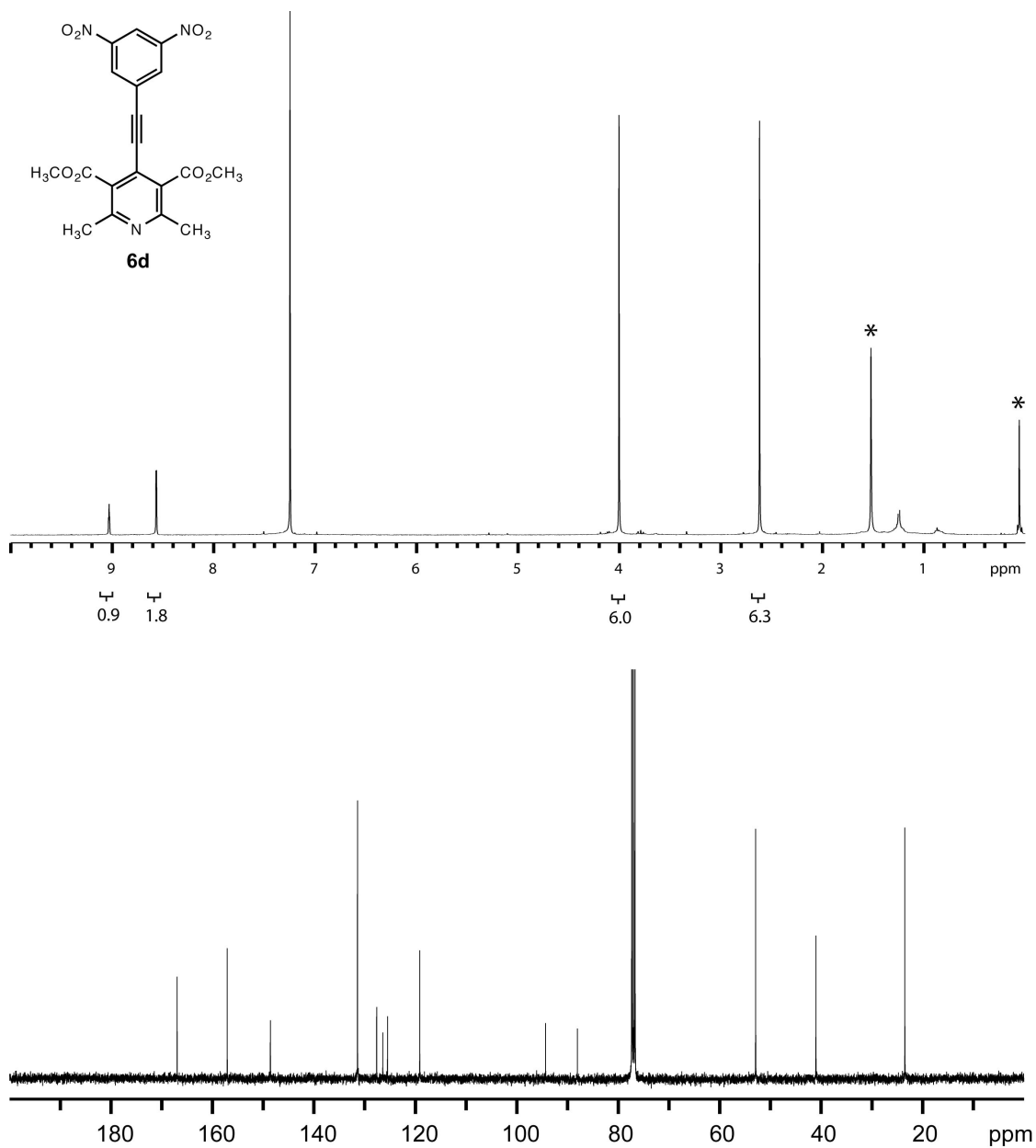


Figure S32. ^1H and ^{13}C NMR spectra of **6d**. ^1H NMR (400 MHz, CDCl_3) δ 9.03 (t, $J = 2.0$ Hz, 1H), 8.57 (d, $J = 1.6$ Hz, 2H), 4.01 (s, 6H), 2.62 (s, 6H). ^{13}C NMR (100 MHz, CDCl_3) δ 166.96, 157.08, 148.58, 131.41, 127.61, 126.42, 125.47, 119.12, 94.32, 88.05, 52.91, 41.02, 23.49. (*denotes H_2O and TMS peak)

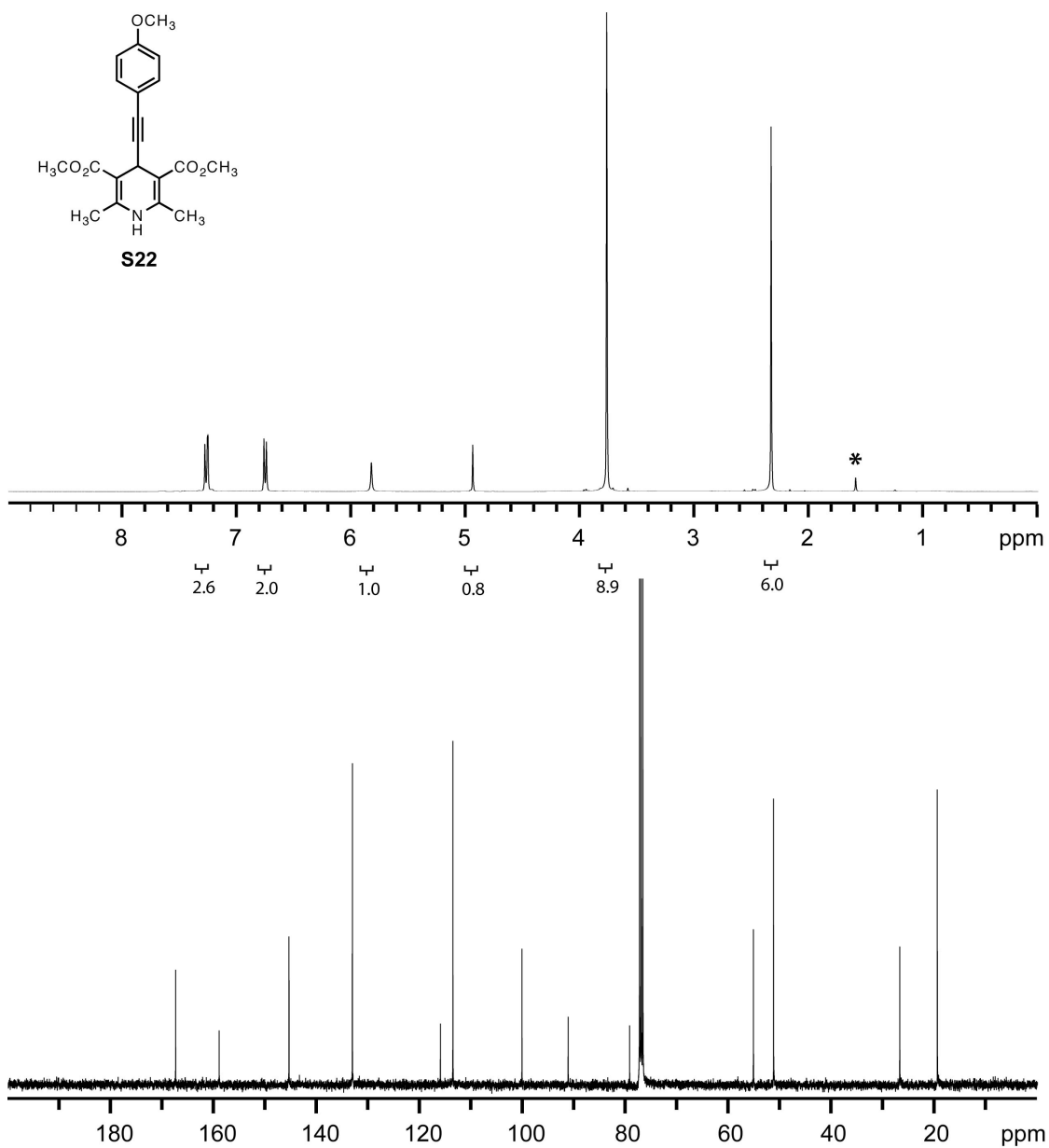


Figure S33. ^1H and ^{13}C NMR spectra of **S22**. ^1H NMR (400 MHz, CDCl_3) δ 7.27 (d, $J = 8.8$ Hz, 2H), 6.76 (d, $J = 8.8$ Hz, 2H), 5.83 (s, 1H), 4.94 (s, 1H), 3.77 (s, 9H), 2.33 (s, 6H). ^{13}C NMR (100 MHz, CDCl_3) δ 167.47, 159.01, 145.44, 133.13, 116.02, 113.59, 100.17, 91.21, 79.27, 55.22, 51.31, 26.79, 19.49. (*denotes H_2O peak)

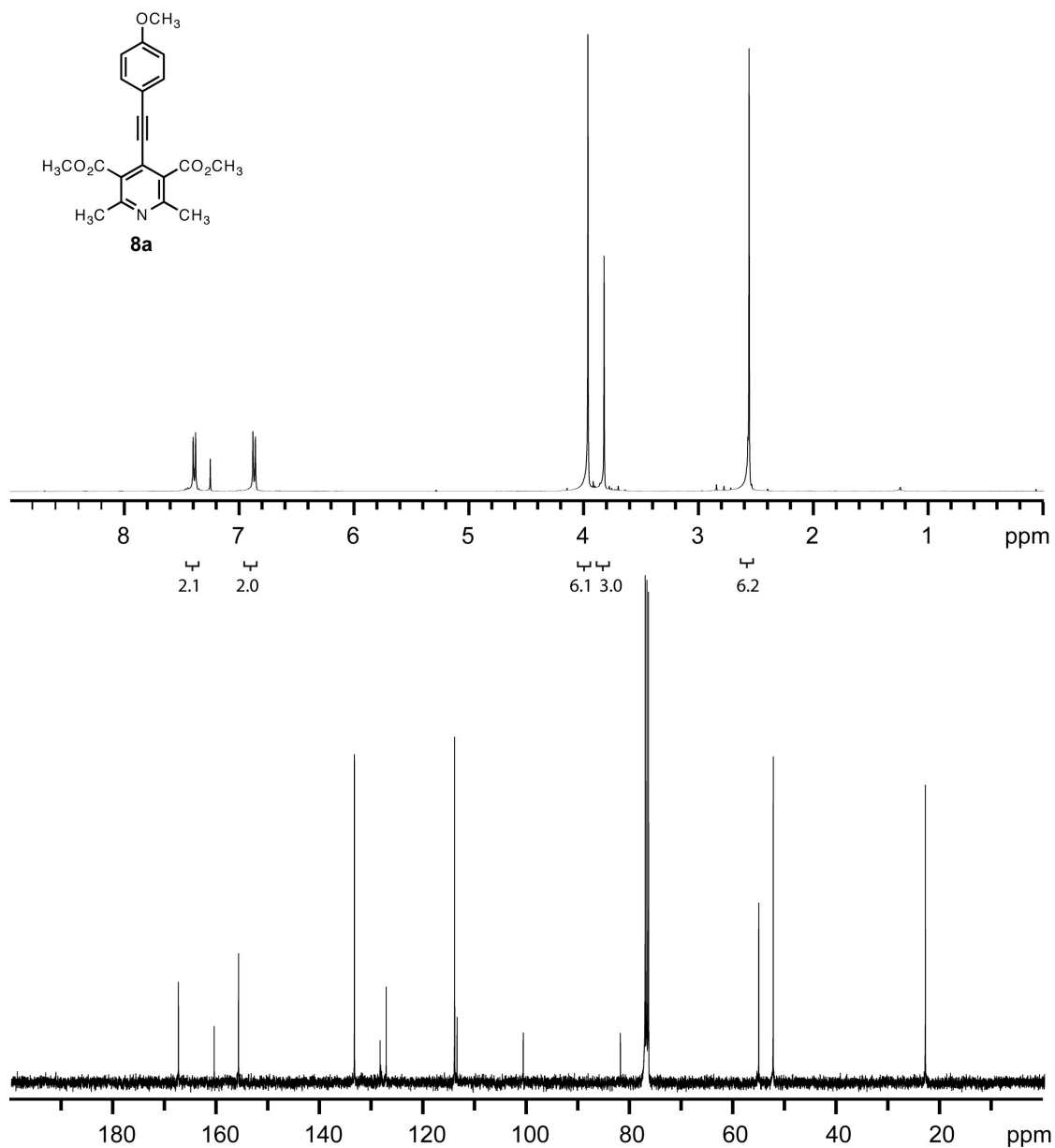


Figure S34. ¹H and ¹³C NMR spectra of **8a**. ¹H NMR (400 MHz, CDCl₃) δ 7.41 (d, *J* = 8.8 Hz, 2H), 6.88 (d, *J* = 8.8 Hz, 2H), 3.97 (s, 6H), 3.83 (s, 3H), 2.57 (s, 6H). ¹³C NMR (100 MHz, CDCl₃) δ 167.67, 160.73, 156.04, 133.61, 128.64, 127.46, 114.21, 113.75, 100.94, 82.14, 55.36, 52.55, 23.11. (*denotes H₂O peak)

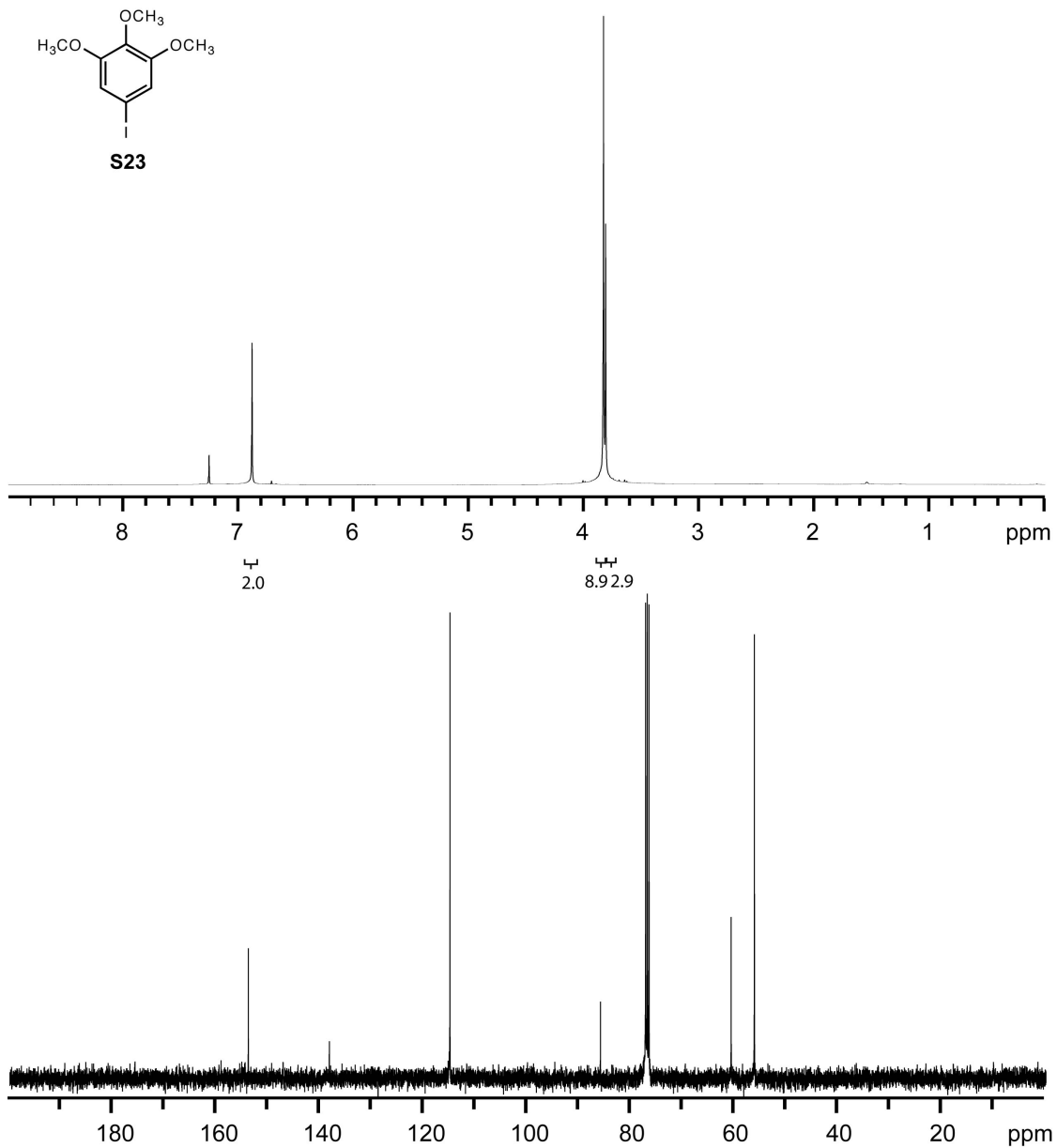


Figure S35. ¹H and ¹³C NMR spectra of **S23**. ¹H NMR (400 MHz, CDCl₃) δ 6.89 (s, 2H), 3.83 (s, 9H), 3.82 (s, 3H). ¹³C NMR (100 MHz, CDCl₃) δ 153.98, 138.35, 115.06, 86.02, 60.80, 56.32.

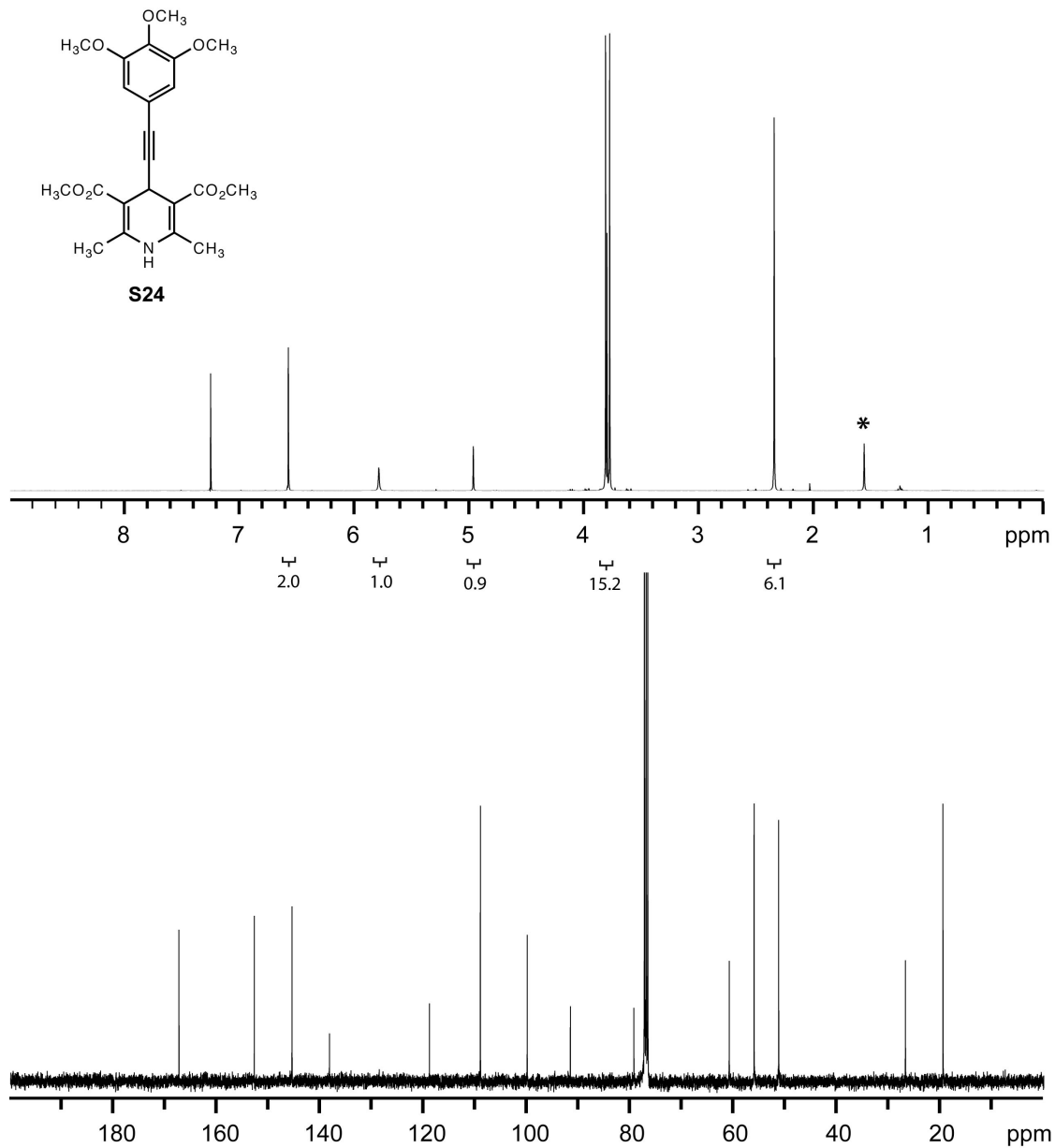


Figure S36. ^1H and ^{13}C NMR spectra of **S24**. ^1H NMR (400 MHz, CDCl_3) δ 6.58 (s, 2H), 5.80 (s, 1H), 4.97 (s, 1H), 3.82 (s, 6H), 3.81 (s, 3H), 3.79 (s, 6H), 2.35 (s, 6H). ^{13}C NMR (100 MHz, CDCl_3) δ 167.40, 152.81, 145.52, 138.28, 118.92, 109.07, 100.01, 91.66, 79.37, 60.91, 56.11, 51.34, 26.81, 19.55. (*denotes H_2O peak)

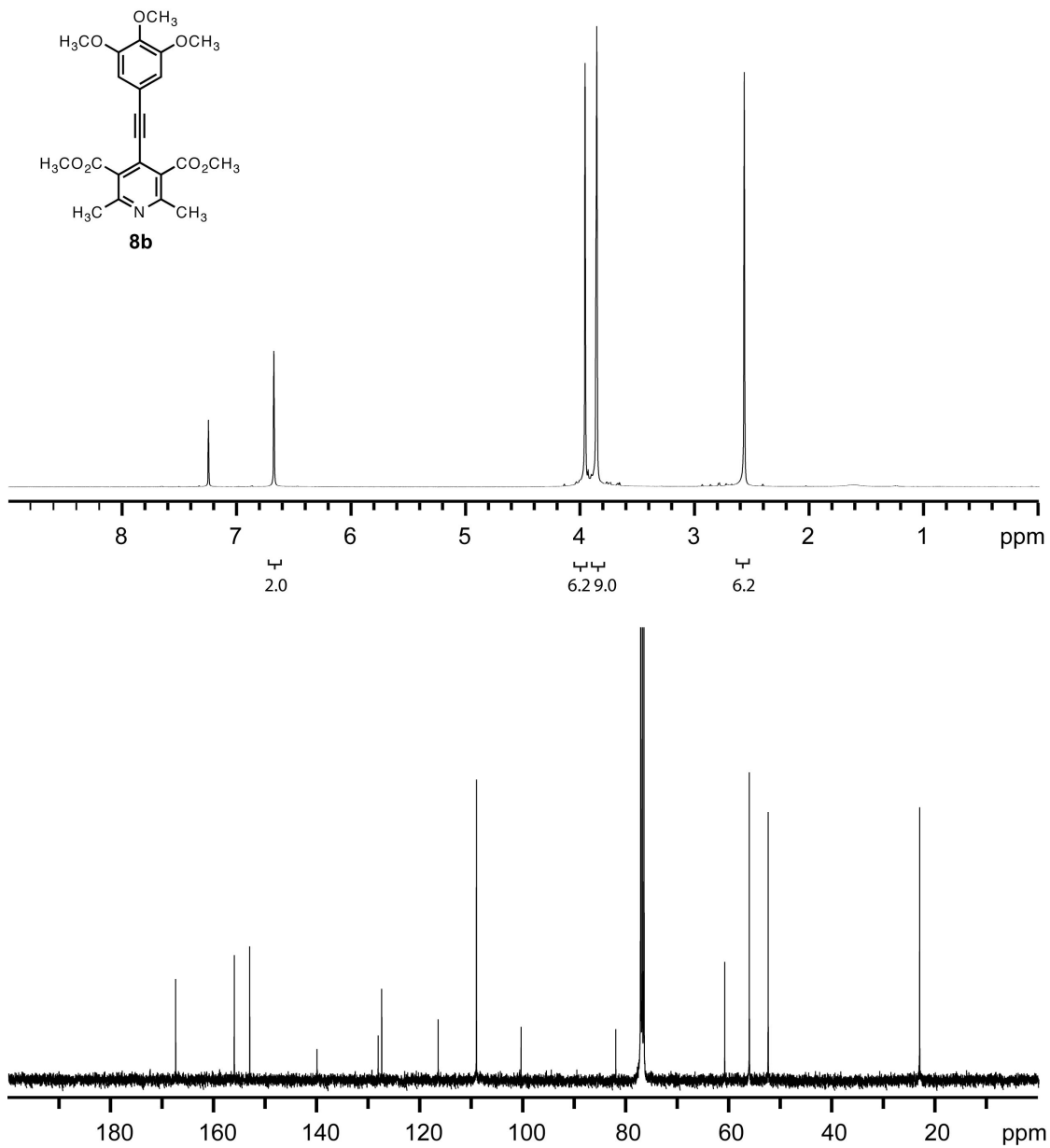


Figure S37. ¹H and ¹³C NMR spectra of **8b**. ¹H NMR (400 MHz, CDCl₃) δ 6.69 (s, 2H), 3.97 (s, 6H), 3.87 (s, 9H), 2.58 (s, 6H). ¹³C NMR (100 MHz, CDCl₃) δ 167.57, 156.20, 153.20, 140.12, 128.27, 127.58, 116.61, 109.20, 100.53, 82.15, 61.01, 56.23, 52.57, 23.16.

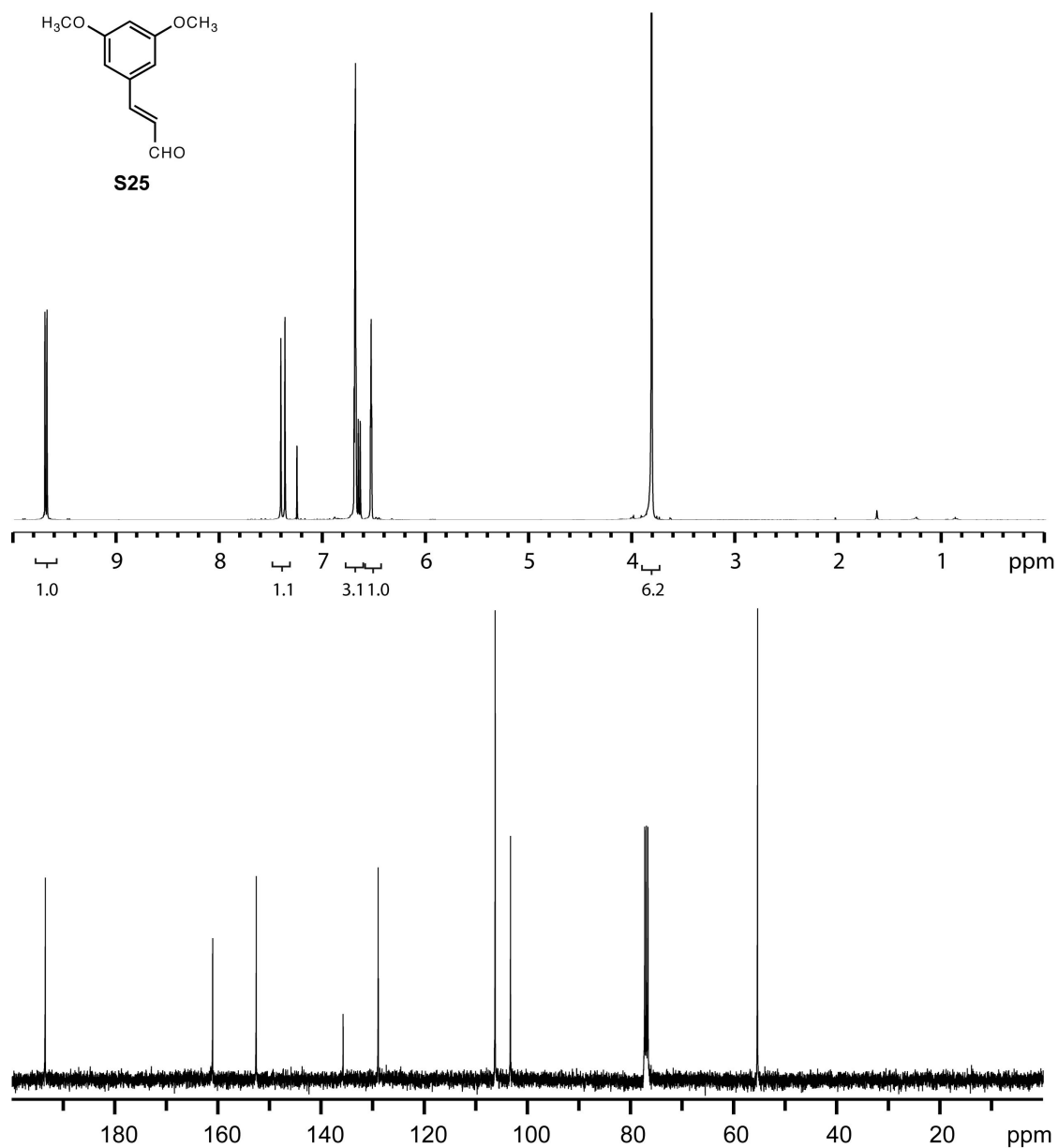


Figure S38. ¹H and ¹³C NMR spectra of **S25**. ¹H NMR (400 MHz, CDCl₃) δ 9.69 (d, *J* = 7.6 Hz, 1H), 7.39 (d, *J* = 15.6 Hz, 1H), 6.70 (d, *J* = 2.4 Hz, 2H), 6.65 (d, *J* = 8.0 Hz, 1H), 6.54 (t, *J* = 2.0 Hz, 1H), 3.82 (s, 6H). ¹³C NMR (100 MHz, CDCl₃) δ 193.58, 161.13, 152.67, 135.82, 129.01, 106.34, 103.36, 55.46.

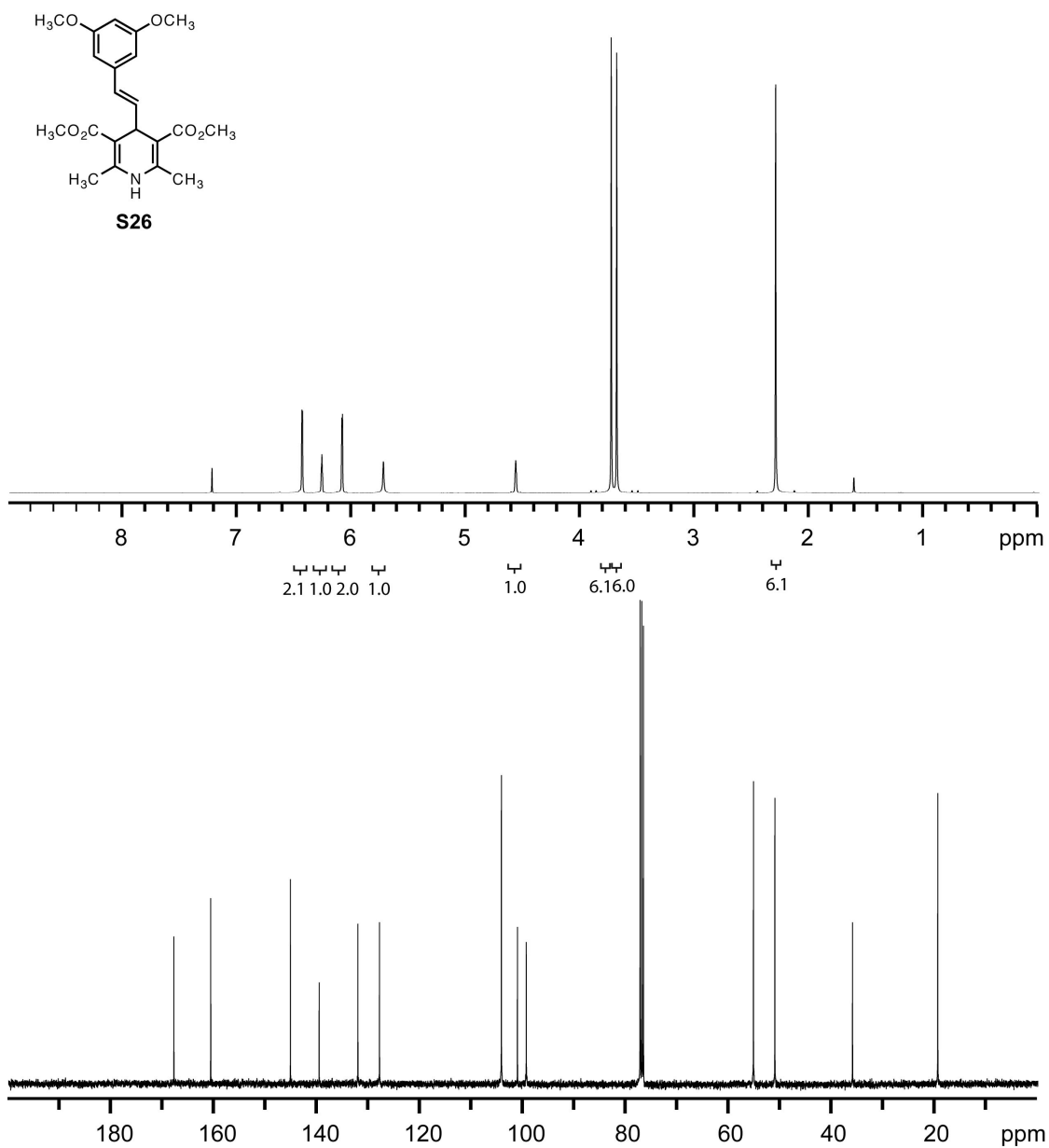


Figure S39. ^1H and ^{13}C NMR spectra of **S26**. ^1H NMR (400 MHz, CDCl_3) δ 6.47 (d, J = 2.4 Hz, 2H), 6.30 (s, 1H), 6.12 (d, J = 2.0 Hz, 2H), 5.76 (s, 1H), 4.61 (s, 1H), 3.77 (s, 6H), 3.72 (s, 6H), 2.33 (s, 6H). ^{13}C NMR (100 MHz, CDCl_3) δ 167.89, 160.73, 145.24, 139.67, 132.13, 127.94, 104.26, 101.14, 99.42, 55.29, 51.13, 36.03, 19.47.

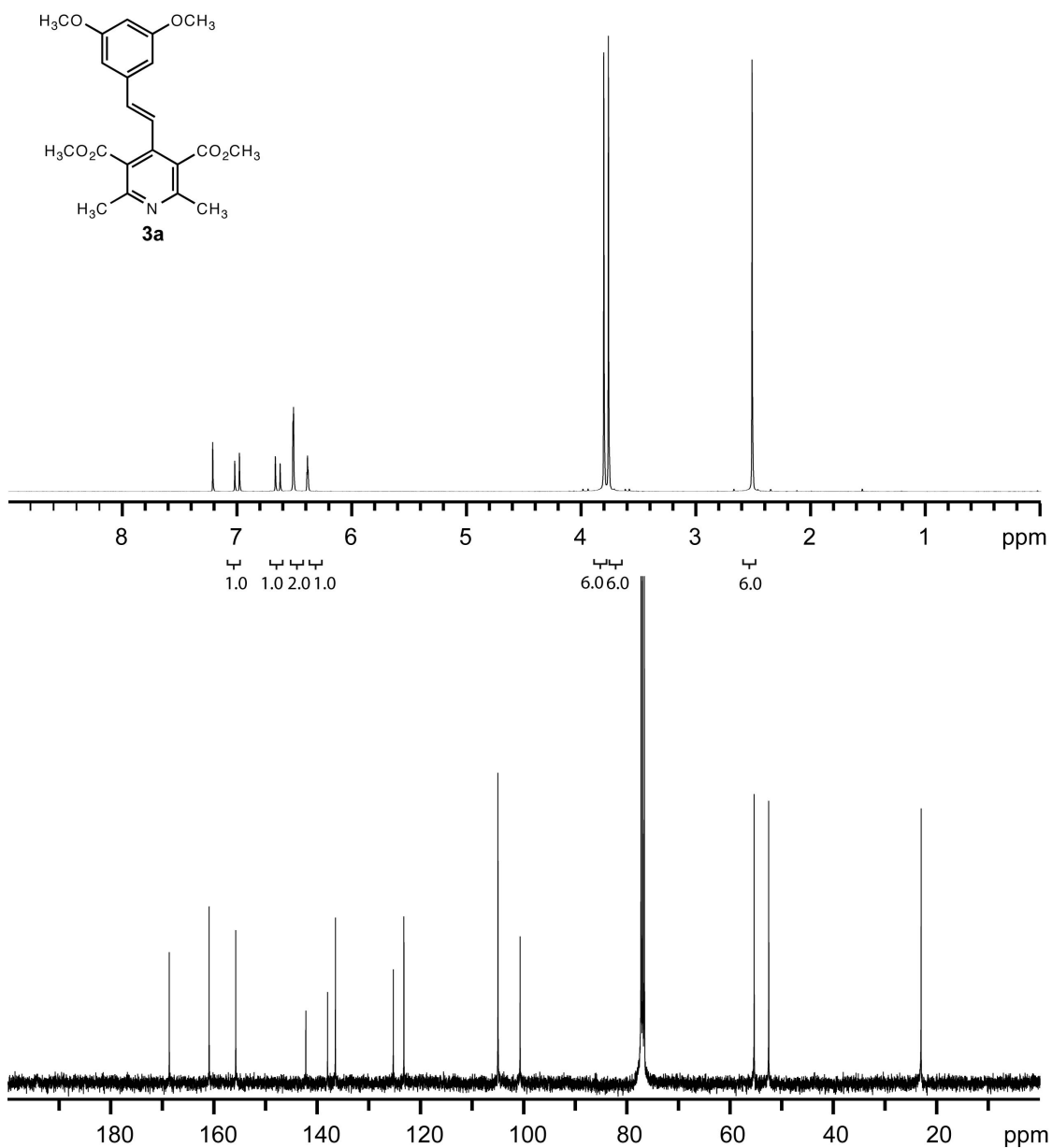


Figure S40. ^1H and ^{13}C NMR spectra of **3a**. ^1H NMR (400 MHz, CDCl_3) δ 7.05 (d, $J = 16.4$ Hz, 1H), 6.69 (d, $J = 16.4$ Hz, 1H), 6.56 (d, $J = 2.0$ Hz, 2H), 6.43 (t, $J = 2.0$ Hz, 1H), 3.85 (s, 6H), 3.81 (s, 6H), 2.56 (s, 6H). ^{13}C NMR (100 MHz, CDCl_3) δ 168.73, 161.01, 155.86, 142.28, 138.07, 136.55, 125.33, 123.28, 105.05, 100.76, 55.41, 52.59, 23.06.

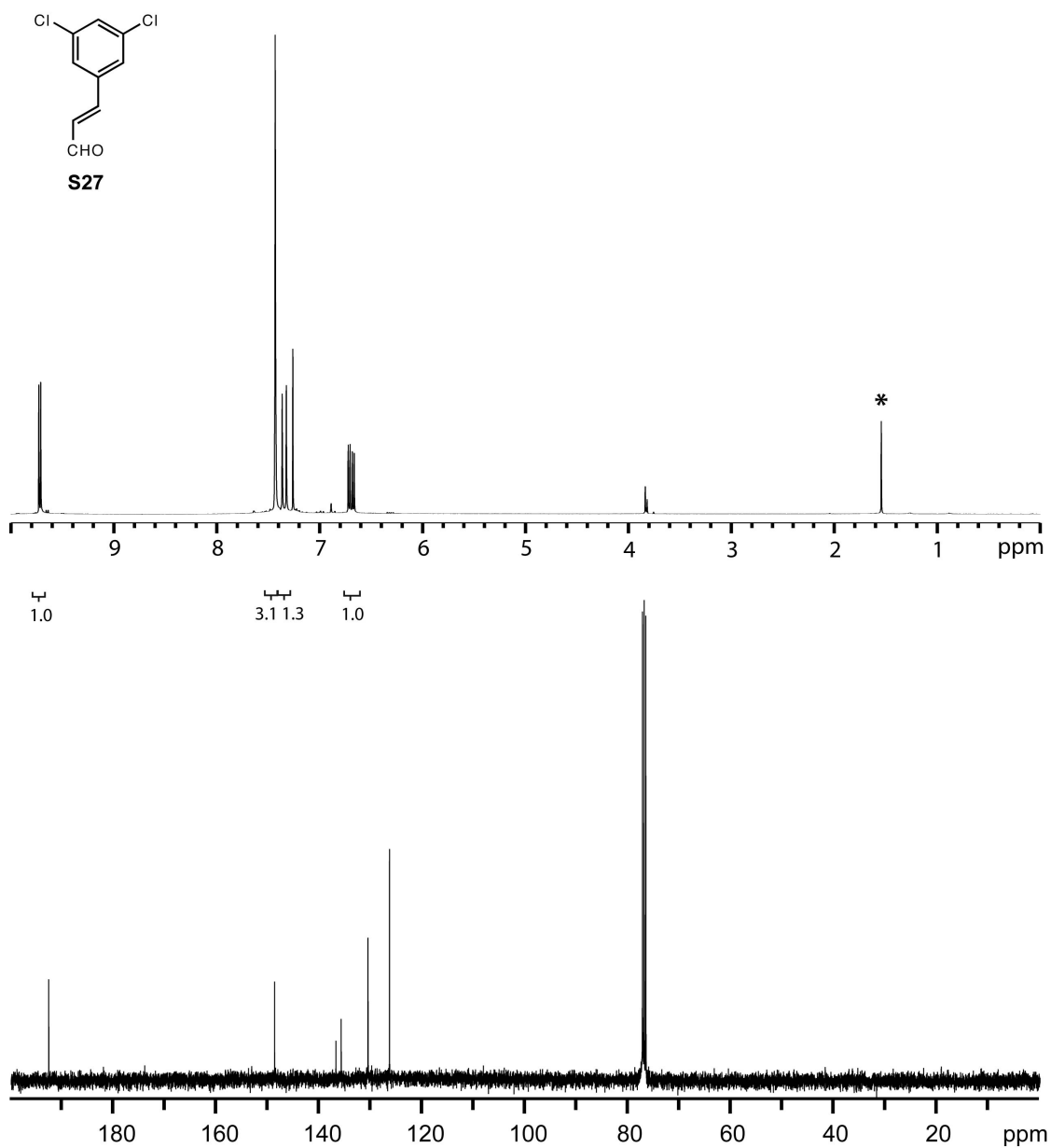


Figure S41. ^1H and ^{13}C NMR spectra of **S27**. ^1H NMR (400 MHz, CDCl_3) δ 9.72 (d, $J = 7.6$ Hz, 1H), 7.43 (s, 3H), 7.34 (d, $J = 16.0$ Hz, 1H), 6.69 (dd, $J = 16.0$ Hz, $J = 7.2$ Hz, 1H). ^{13}C NMR (100 MHz, CDCl_3) δ 192.68, 148.80, 136.88, 135.85, 130.66, 130.63, 126.46. (*denotes H_2O peak)

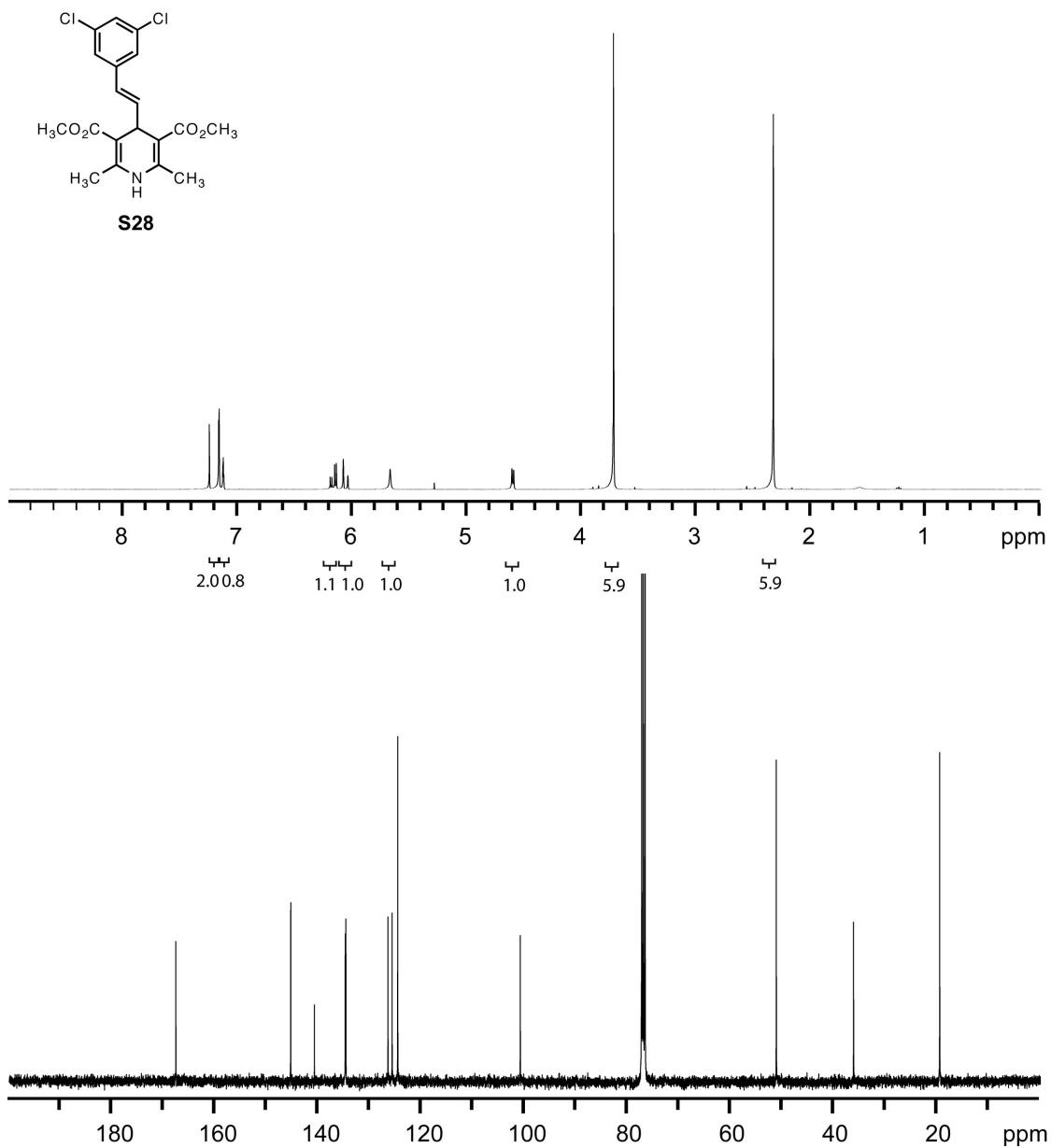


Figure S42. ^1H and ^{13}C NMR spectra of **S28**. ^1H NMR (400 MHz, CDCl_3) δ 7.17 (m, 2H), 7.14 (m, 1H), 6.19 (dd, $J = 16.0$ Hz, $J = 6.4$ Hz, 1H), 6.05 (d, $J = 16.0$ Hz, 1H), 5.68 (s, 1H), 4.61 (d, $J = 6.0$ Hz, 1H), 3.73 (s, 6H), 2.34 (s, 6H). ^{13}C NMR (100 MHz, CDCl_3) δ 167.91, 145.63, 141.04, 135.06, 134.92, 126.77, 125.96, 124.88, 101.11, 51.47, 36.49, 19.78.

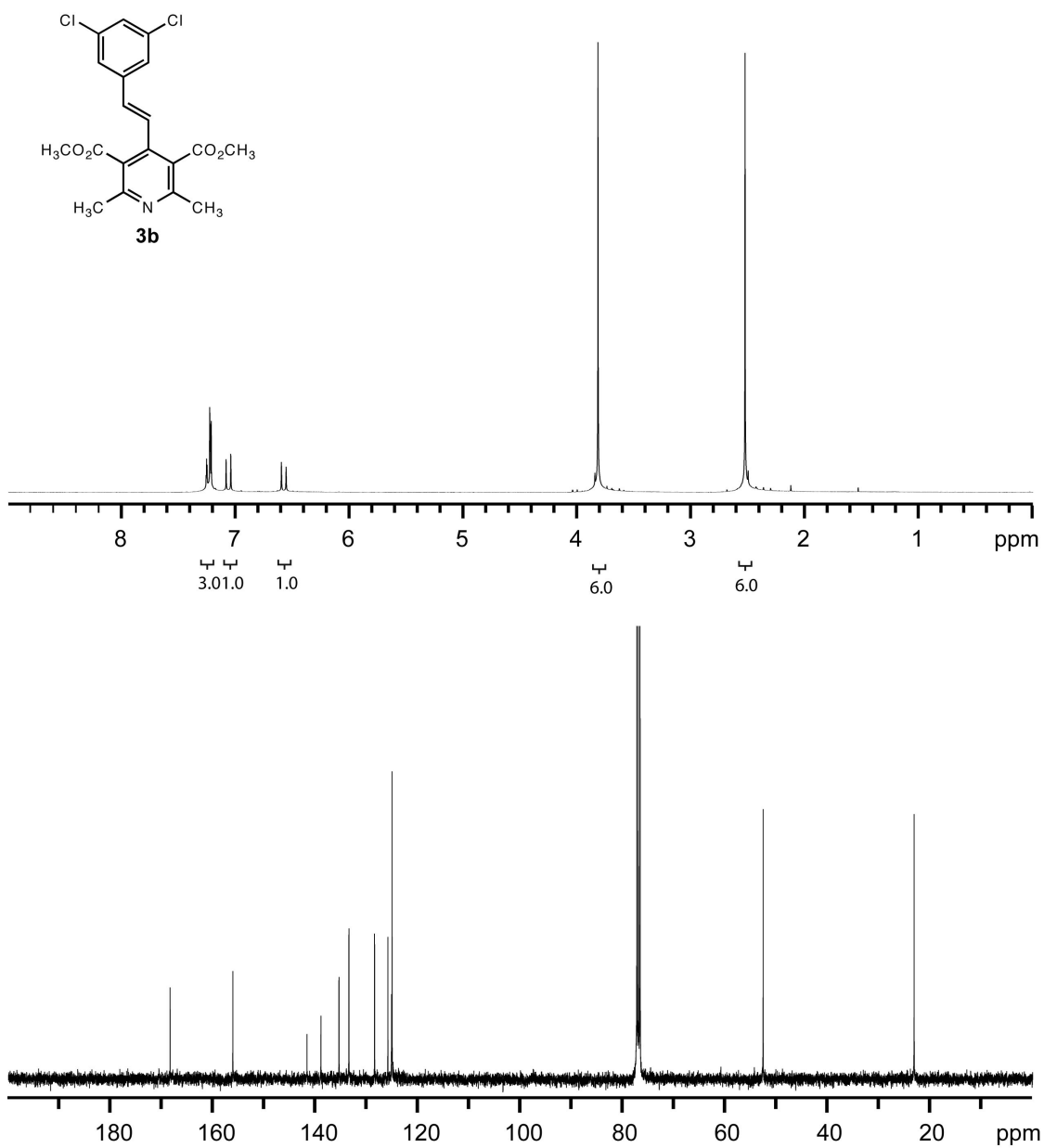


Figure S43. ^1H and ^{13}C NMR spectra of **3b**. ^1H NMR (400 MHz, CDCl_3) δ 7.25 (m, 3H), 7.07 (d, $J = 16.4$ Hz, 1H), 6.58 (d, $J = 16.8$ Hz, 1H), 3.82 (s, 6H), 2.53 (s, 6H). ^{13}C NMR (100 MHz, CDCl_3) δ 168.45, 156.20, 141.73, 139.00, 135.47, 133.54, 128.53, 125.93, 125.23, 125.11, 52.68, 23.19.

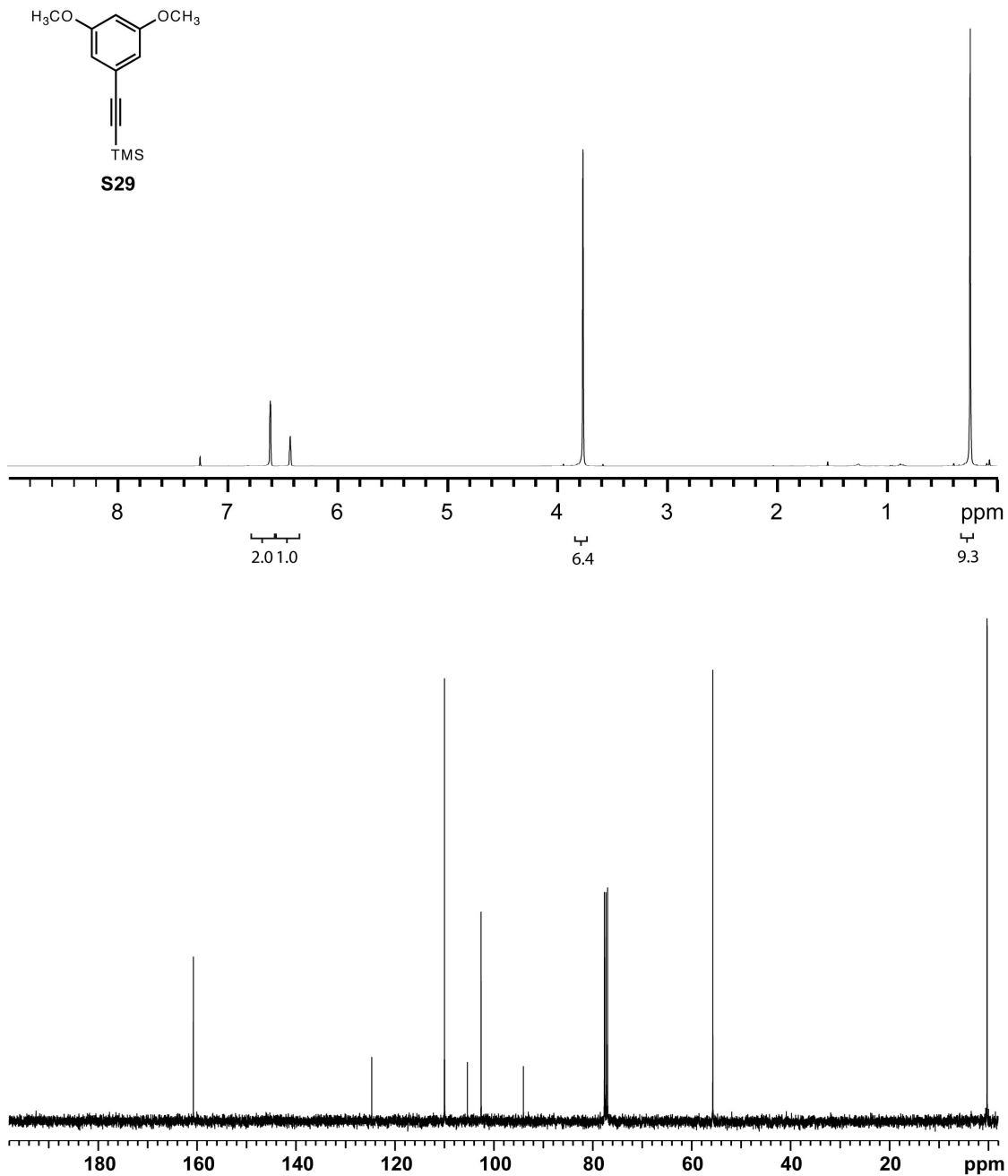


Figure S44. ¹H and ¹³C NMR spectra of **S29**. ¹H NMR (400 MHz, CDCl₃) δ 6.62 (m, 2H), 6.44 (m, 1H), 3.78 (s, 6H), 0.26 (s, 9H). ¹³C NMR (100 MHz, CDCl₃) δ 160.42, 124.34, 109.64, 105.00, 102.24, 93.67, 55.38, 0.20.

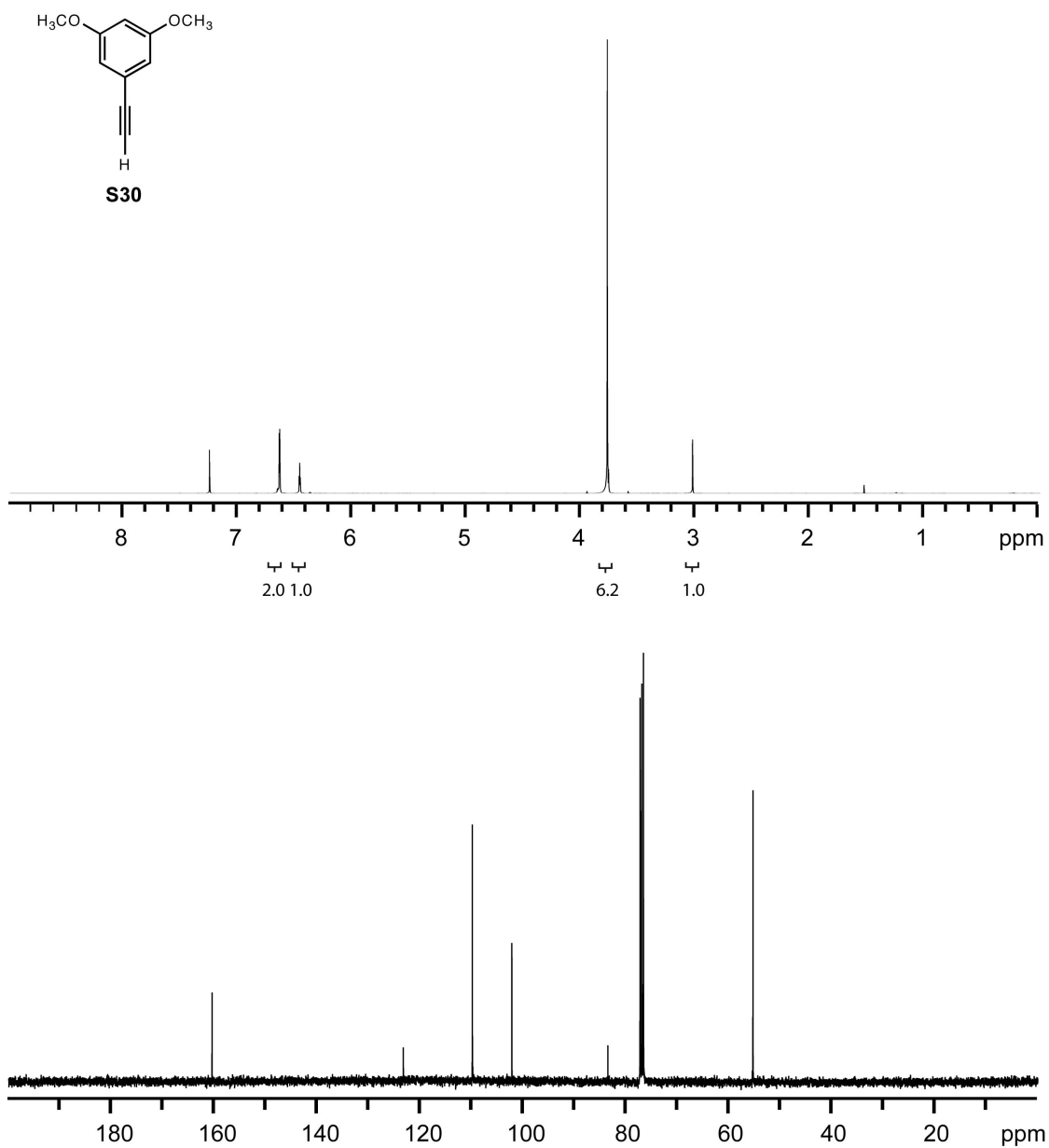


Figure S45. ^1H and ^{13}C NMR spectra of **S30**. ^1H NMR (400 MHz, CDCl_3) δ 6.58 (d, J = 2.4 Hz, 2H), 6.40 (t, J = 2.4 Hz, 1H), 3.71 (s, 6H), 2.97 (s, 1H). ^{13}C NMR (100 MHz, CDCl_3) δ 160.48, 123.31, 109.91, 102.23, 83.58, 55.39.

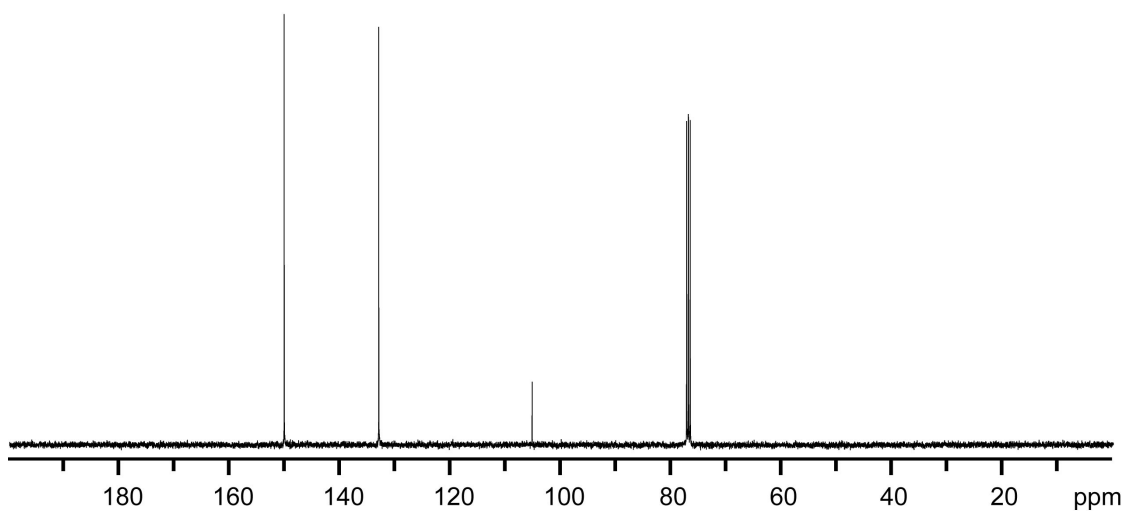
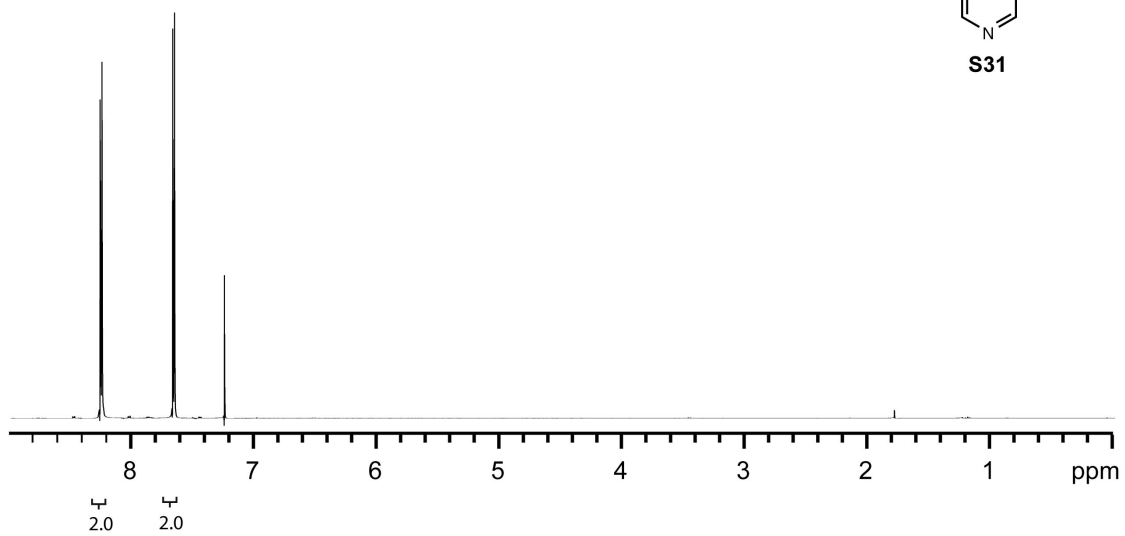
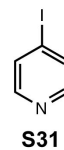


Figure S46. ¹H and ¹³C NMR spectra of **S31**. ¹H NMR (400 MHz, CDCl₃) δ 8.27 (m, 2H), 7.67 (m, 2H). ¹³C NMR (100 MHz, CDCl₃) δ 150.26, 133.11, 105.34.

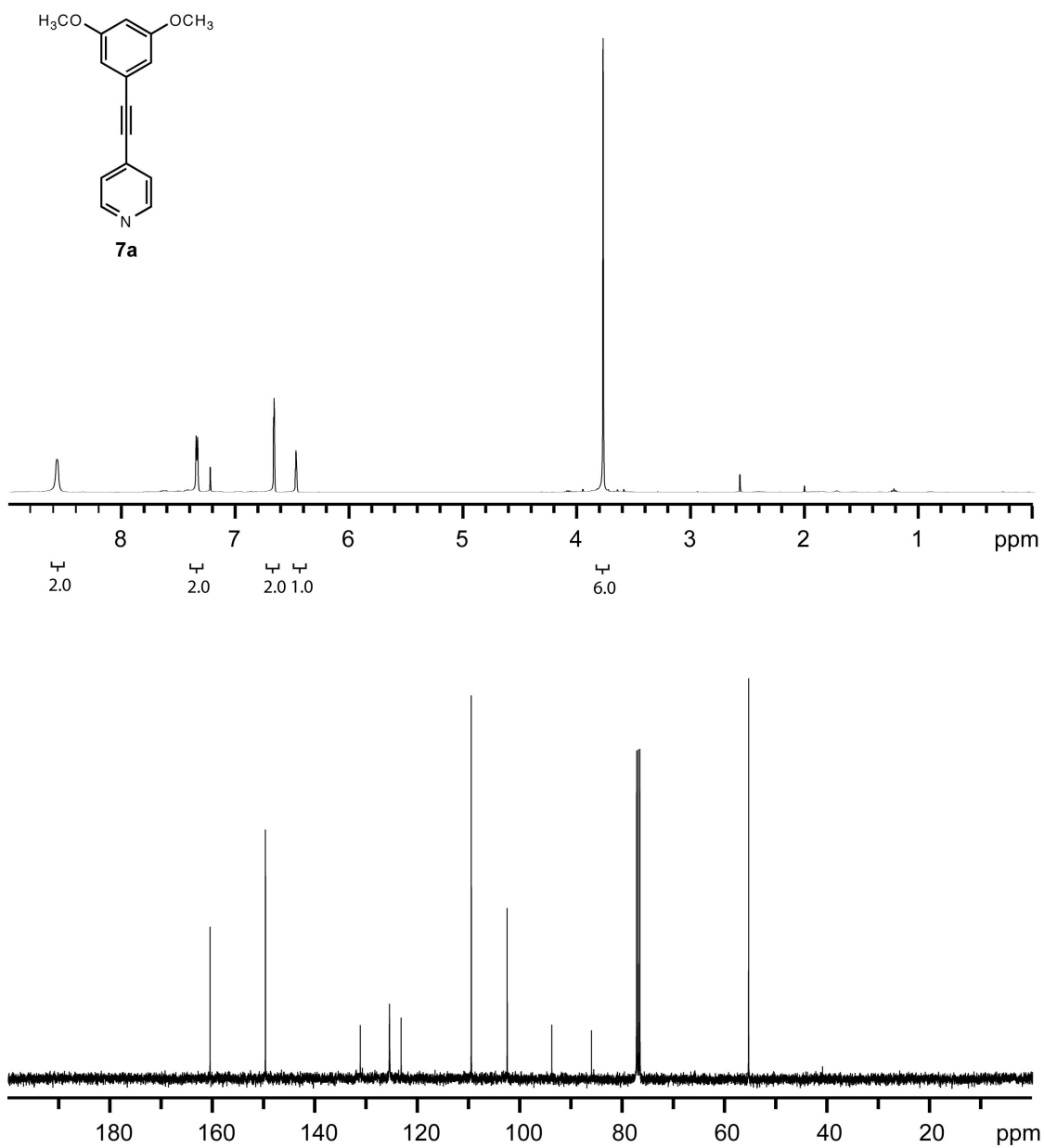


Figure S47. ^1H and ^{13}C NMR spectra of **7a**. ^1H NMR (400 MHz, CDCl_3) δ 8.61 (d, $J = 2.8$ Hz, 2H), 7.38 (d, $J = 4.8$ Hz, 2H), 6.70 (s, 2H), 6.51 (s, 1H), 3.81 (s, 6H). ^{13}C NMR (100 MHz, CDCl_3) δ 160.60, 149.78, 131.26, 125.56, 123.29, 109.59, 102.58, 93.88, 86.11, 55.46.

V. Procedures for Determining c_{gc} and T_g

c_{gc} : A 4 mL vial was charged with 10 mg of gelator and 0.10 mL 1/1 DMSO/H₂O. The mixture was heated to dissolve, then cooled to rt to allow gel formation. Additional aliquots of 1/1 DMSO/H₂O were added and the heat/cool cycle was continued until the gels were unstable to vial inversion. The last concentration of a stable gel was recorded as its c_{gc} . The c_{gc} in 1/2 EtOH/H₂O was measured following the same procedure.

Table S1. Summary of critical gel concentrations (c_{gc})

Pyridine	c_{gc} (mg/mL) in 1/1 DMSO/H ₂ O	c_{gc} (mg/mL) in 1/2 EtOH/H ₂ O
1a	30 ± 1	--
1b	6 ± 1	9 ± 1
2a	4.5 ± 0.5	9 ± 1
2b	13 ± 1	13 ± 1
2c	21 ± 1	28 ± 1
3a	18 ± 1	18 ± 1
3b	13 ± 1	13 ± 1
4	7.0 ± 0.5	13 ± 1

T_g : Gels of **1b**, **2a**, **2b**, **3b**, and **4** (at 13 mg/mL) and gels of **1a**, **2c**, **3a** (at 30 mg/mL) were formed via heating and cooling in 1/1 DMSO/H₂O in a sealed 4 mL vial. The gels were then equilibrated at each temperature for 1 h (using 1 °C increments). After equilibration, the vial was inverted; if an unstable gel was observed, the temperature was recorded as gelation temperature (T_g). Each reported T_g is an average of 3 runs.

Table S2. Summary of T_g

Pyridine	T_g (°C)
1a	42 ± 2
1b	40 ± 1
2a	62 ± 2
2b	50 ± 1
2c	53 ± 2
3a	46 ± 1
3b	70 ± 2
4	42 ± 1

VI. Rheological Properties of Gels in 1/1 DMSO/H₂O

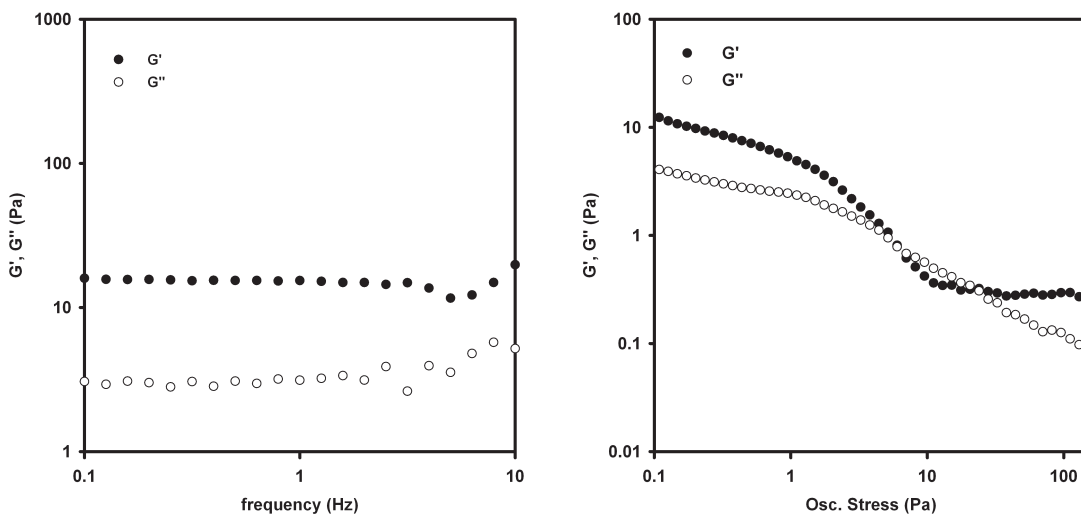


Figure S48. Frequency sweep and oscillating stress sweep of an in situ gel of **1a** (30 mg/mL). The gel network breaks down up to 10Hz.

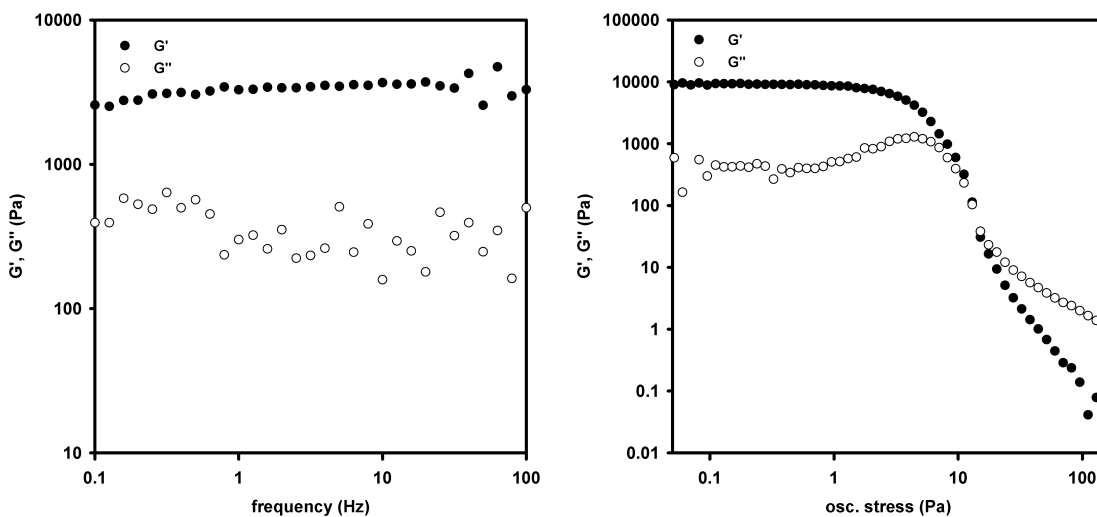


Figure S49. Frequency sweep and oscillating stress sweep of an in situ gel of **1b** (13 mg/mL).

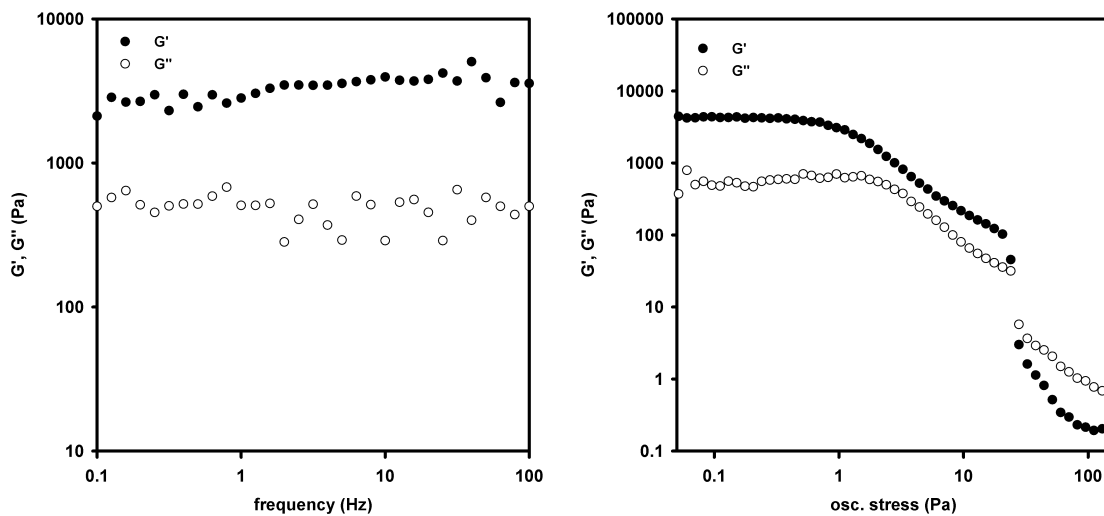


Figure S50. Frequency sweep and oscillating stress sweep of an in situ gel of **2a** (13 mg/mL).

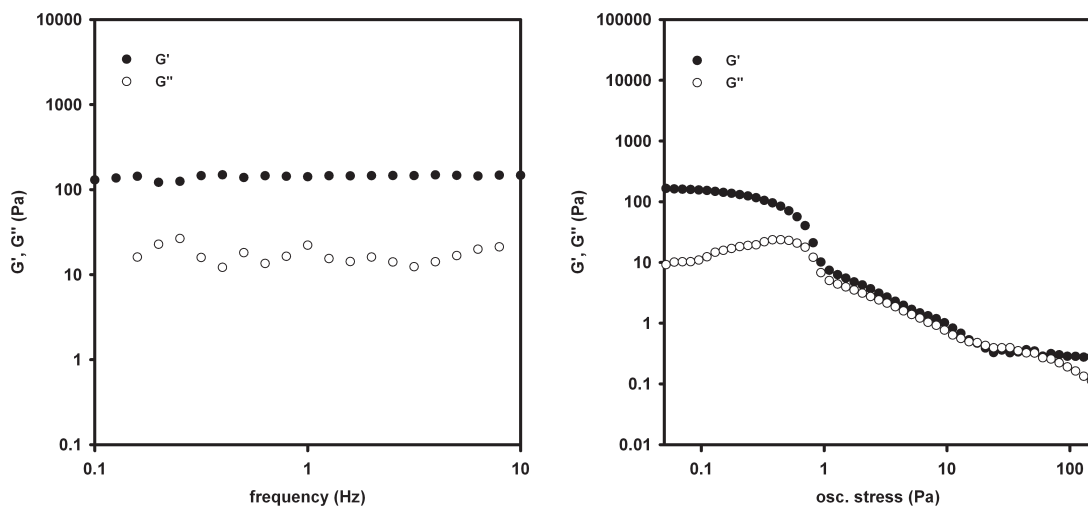


Figure S51. Frequency sweep and oscillating stress sweep of an in situ gel of **2b** (13 mg/mL). The gel network breaks down up to 10 Hz.

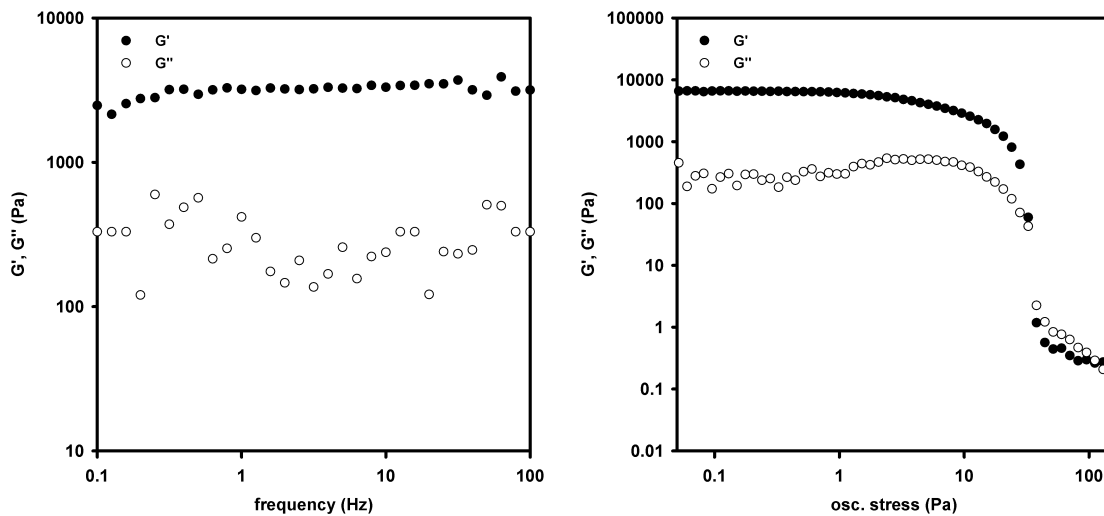


Figure S52. Frequency sweep and oscillating stress sweep of an in situ gel of **2c** (13 mg/mL).

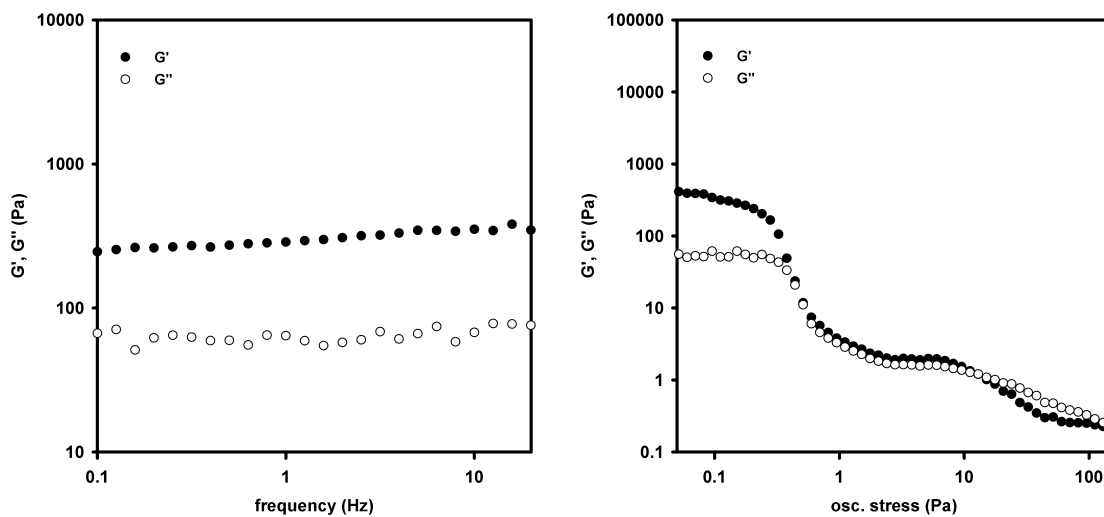


Figure S53. Frequency sweep and oscillating stress sweep of an in situ gel of **3a** (13 mg/mL). The gel network breaks down up to 20 Hz.

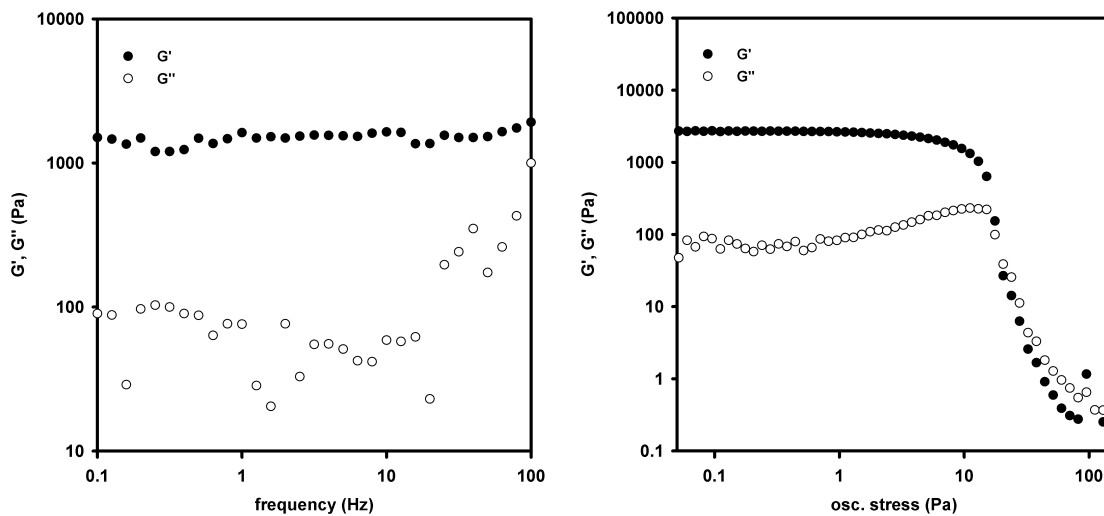


Figure S54. Frequency sweep and oscillating stress sweep of an in situ gel of **3b** (30 mg/mL).

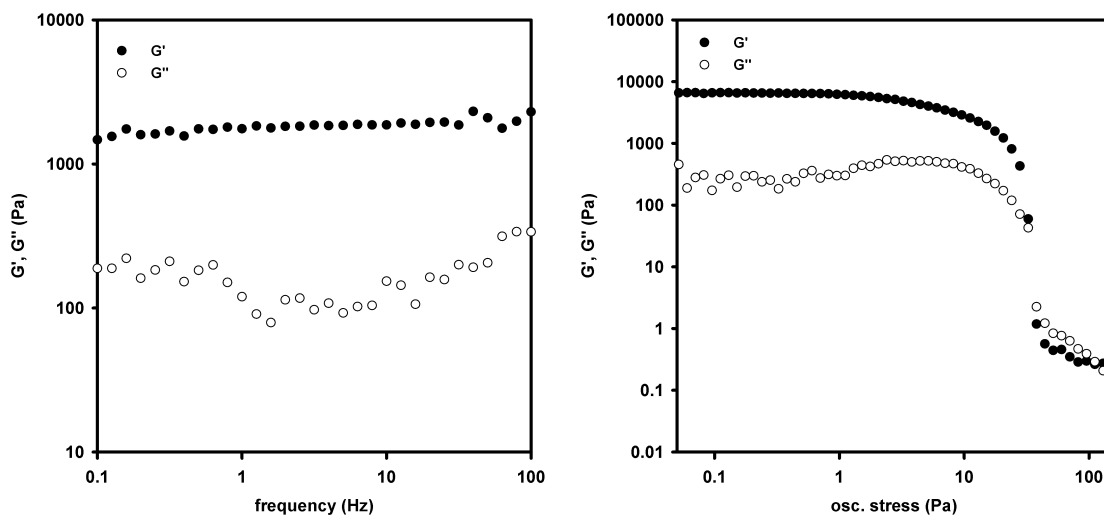


Figure S55. Frequency sweep and oscillating stress sweep of an in situ gel of **4** (13 mg/mL).

VII. Microscope Images of Gels

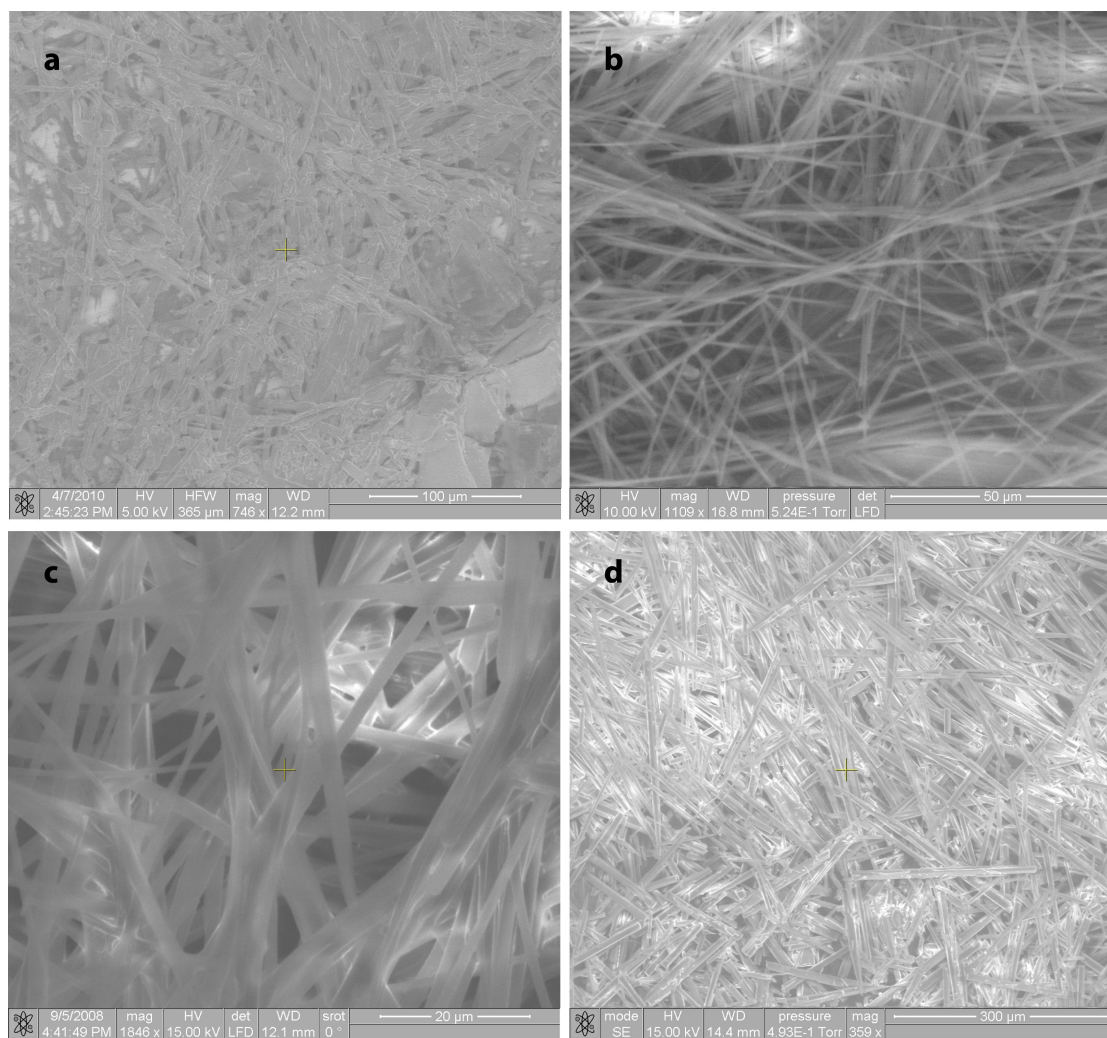


Figure S56. Scanning electron microscope images of pyridine gels in 1/1 DMSO/H₂O: (a) **1a** (30 mg/mL), (b) **1b** (6 mg/mL), (c) **2a** (4.5 mg/mL), and (d) **2b** (13 mg/mL).

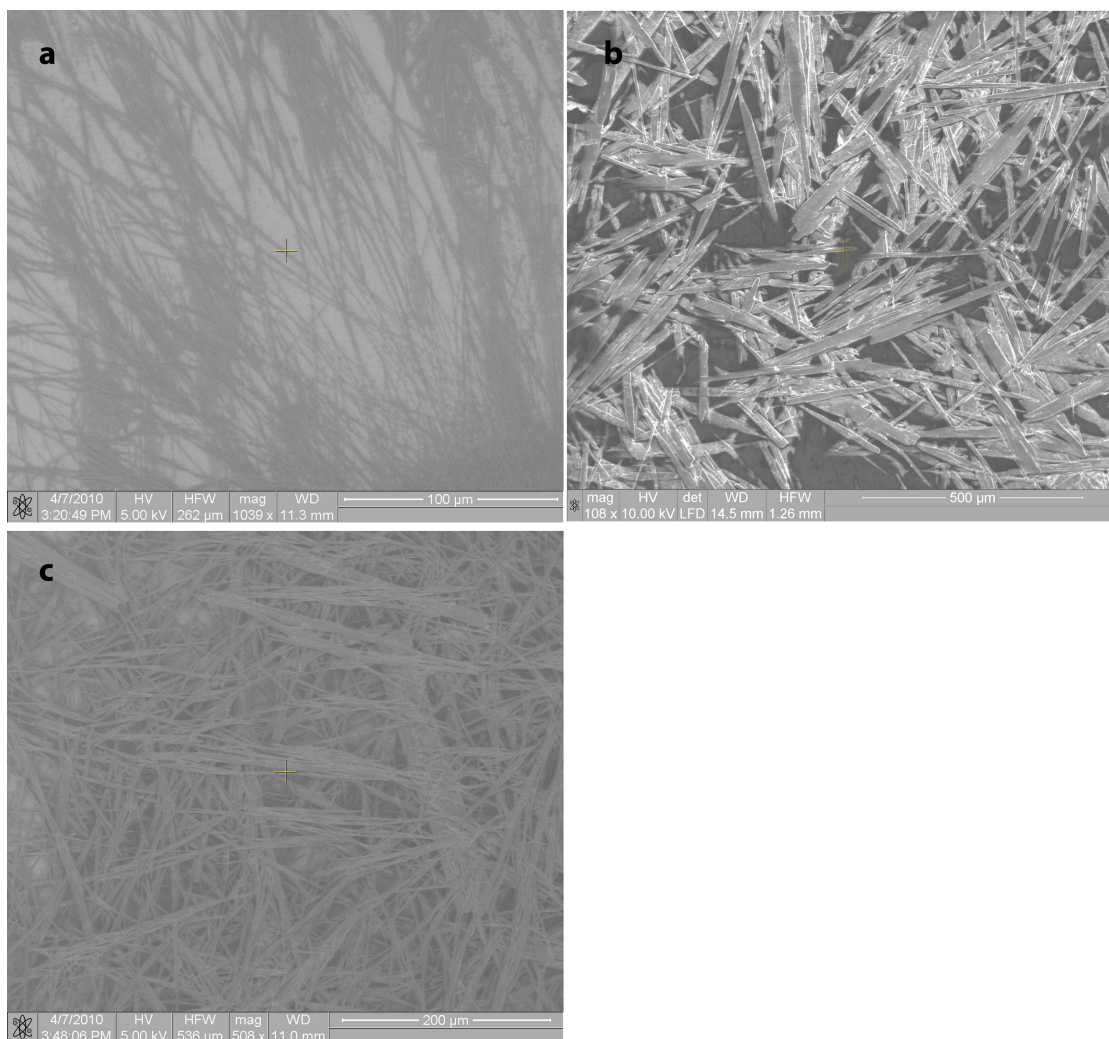


Figure S57. Scanning electron microscopic images of pyridine gels in 1/1 DMSO/H₂O: (a) **2c** (21 mg/mL), (b) **3a** (18 mg/mL), (c) **3b** (13) mg/mL.

The gel of pyridine **4** in 1/1 DMSO/H₂O dissolved upon exposure to the electron beam; therefore, an optical microscope image was recorded instead.

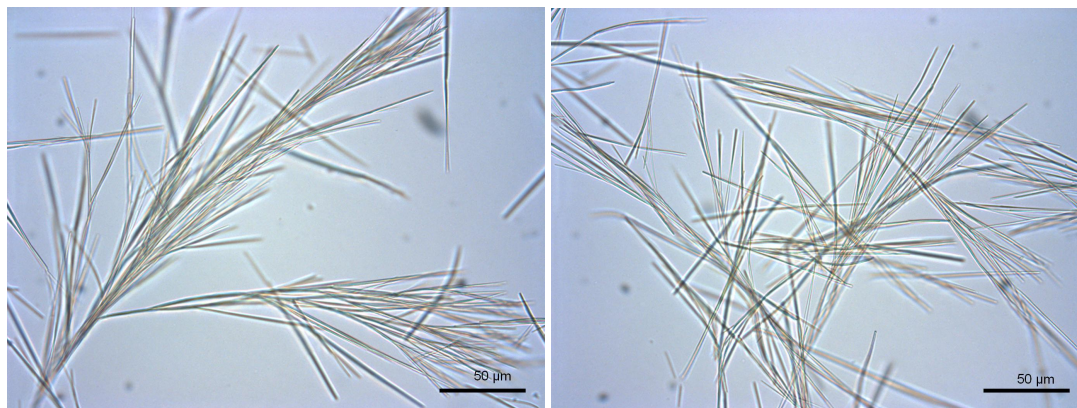


Figure S58. Optical microscope image of pyridine **4** (7 mg/mL) in 1/1 DMSO/H₂O.

VIII. Procedure for Measuring Solubility

A 4 mL vial was charged with a stir bar, pyridine (10 mg) and 1/1 DMSO/H₂O (2 mL). The mixture was stirred at rt for 6 h and then equilibrated without stirring for an additional 12 h. The entire mixture was then passed through a GPC filter (0.2 μm) to remove the undissolved solid. An aliquot (10 μL – 1 mL) of the filtrate was then diluted with 1/1 DMSO/H₂O. The [pyridine] in solution was determined using UV-Vis spectroscopy and a calibration curve. The rt solubilities in 1/2 EtOH/H₂O were measured following the same procedure.

Table S3. Summary of rt solubilities

Pyridine	solubility (mg/mL) in 1/1 DMSO/H₂O	solubility (mg/mL) in 1/2 EtOH/H₂O
1a	0.06 ± 0.01	0.19 ± 0
1b	0.095 ± 0.002	0.22 ± 0.01
2a	0.083 ± 0.005	0.15 ± 0
2b	0.0018 ± 0.0002	0.023 ± 0.002
2c	0.10 ± 0.01	0.22 ± 0.01
3a	0.25 ± 0.01	0.16 ± 0.01
3b	0.015 ± 0.005	0.020 ± 0.002
4	0.97 ± 0.03	0.65 ± 0.05
5a	0.70 ± 0.00	0.7 ± 0.1
5b	0.039 ± 0.005	0.14 ± 0
5c	0.075 ± 0.001	0.080 ± 0.002
6a	0.31 ± 0.02	0.93 ± 0
6b	0.018 ± 0.001	0.014 ± 0.001
6c	0.011 ± 0.002	0.25 ± 0.02
6d	0.017 ± 0.002	0.0030 ± 0.0004
7a	1.0 ± 0.0	1.6 ± 0.1
7b	0.0079 ± 0.0004	0.017 ± 0.001
8a	0.14 ± 0.01	0.26 ± 0.02
8b	0.30 ± 0.01	0.61 ± 0.01

Control Experiment for rt Solubility Measurement

A stable gel (5 mg/mL) and unstable gel (3 mg/mL) of **2a** were formed in 1/1 DMSO/H₂O (2 mL) in a 4 mL vial. In a different 4 mL vial, the bulk solid of **2a** (10 mg) was stirred in 1/1 DMSO/H₂O (2 mL) at rt for 6 h. All samples were then equilibrated for an additional 12 h. Each mixture was passed through a GPC filter (0.2 μm) to remove the gel fibers or undissolved solid. An aliquot (50 μL) of each filtrate was then diluted with 1/1 DMSO/H₂O (3 mL). The [pyridine] in solution was determined using UV-Vis spectroscopy and a calibration curve.

Table S4. Room Temperature Solubility of **2a** Measured from Different Methods

	Stable Gel	Unstable Gel	Bulk Solid
solubility (mg/mL)	0.10 ± 0.01	0.10 ± 0.01	0.089 ± 0.009

General Procedure for Measuring ΔH_{diss} and ΔS_{diss}

A 4 mL vial was charged with pyridine (20 mg) and 1/1 DMSO/H₂O (2 mL). The mixture was then equilibrated at each temperature for 1 h. An aliquot of the solution (100 μ L) was taken with a 250 μ L syringe and placed in a 4 mL vial. The syringe was then rinsed with DMSO (100 μ L). The rinse was combined with the original aliquot and was further diluted with DMSO (~3.5 mL). The [pyridine] in solution was determined using UV-Vis spectroscopy and a calibration curve.

To minimize sampling error, the solubility was determined by taking three aliquots from each sample and averaging them. Then, three different samples were used to calculate the average solubility at that temperature.

Dissolution enthalpies and entropies in 1/2 EtOH/H₂O were measured following the same procedure.

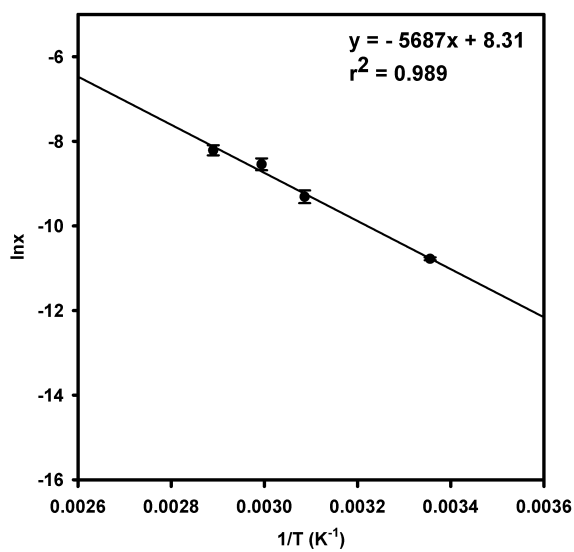


Figure S59. A representative van't Hoff plot for **8b** in 1/1 DMSO/H₂O.²¹

Table S5. Raw data for Figure S59.

Temperature (K)	Solubility (mg/mL)	Mole fraction χ	Relative error
346	3.9 ± 0.5	$27 \pm 3 \times 10^{-5}$	0.12
334	2.8 ± 0.4	$20 \pm 3 \times 10^{-5}$	0.14
324	1.3 ± 0.2	$9 \pm 1 \times 10^{-5}$	0.15
298	0.30 ± 0.01	$2.1 \pm 0.1 \times 10^{-5}$	0.033

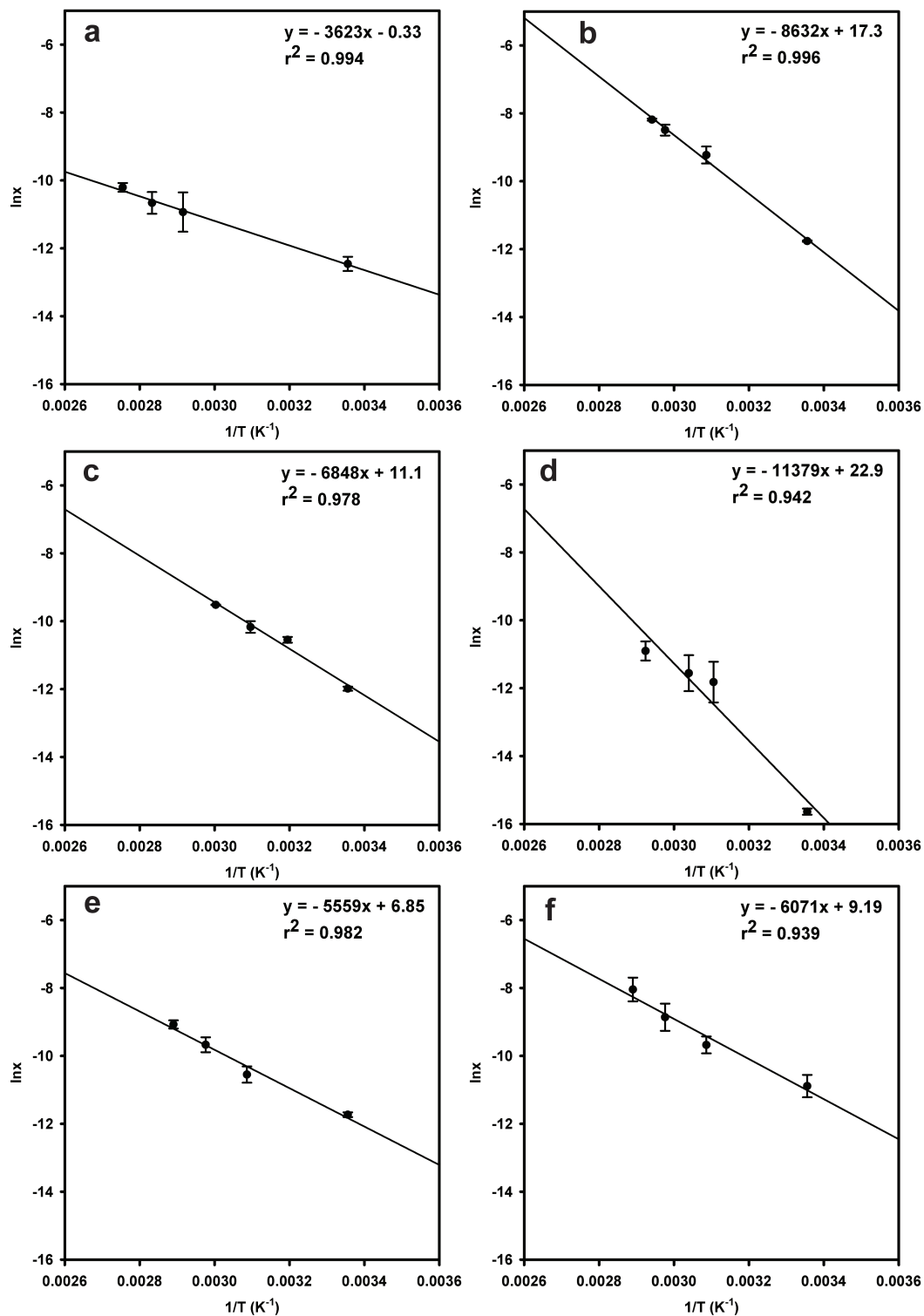


Figure S60. Van't Hoff plot for (a) **1a**, (b) **1b**, (c) **2a**, (d) **2b**, (e) **2c**, (f) **3a** in 1/1 DMSO/H₂O.

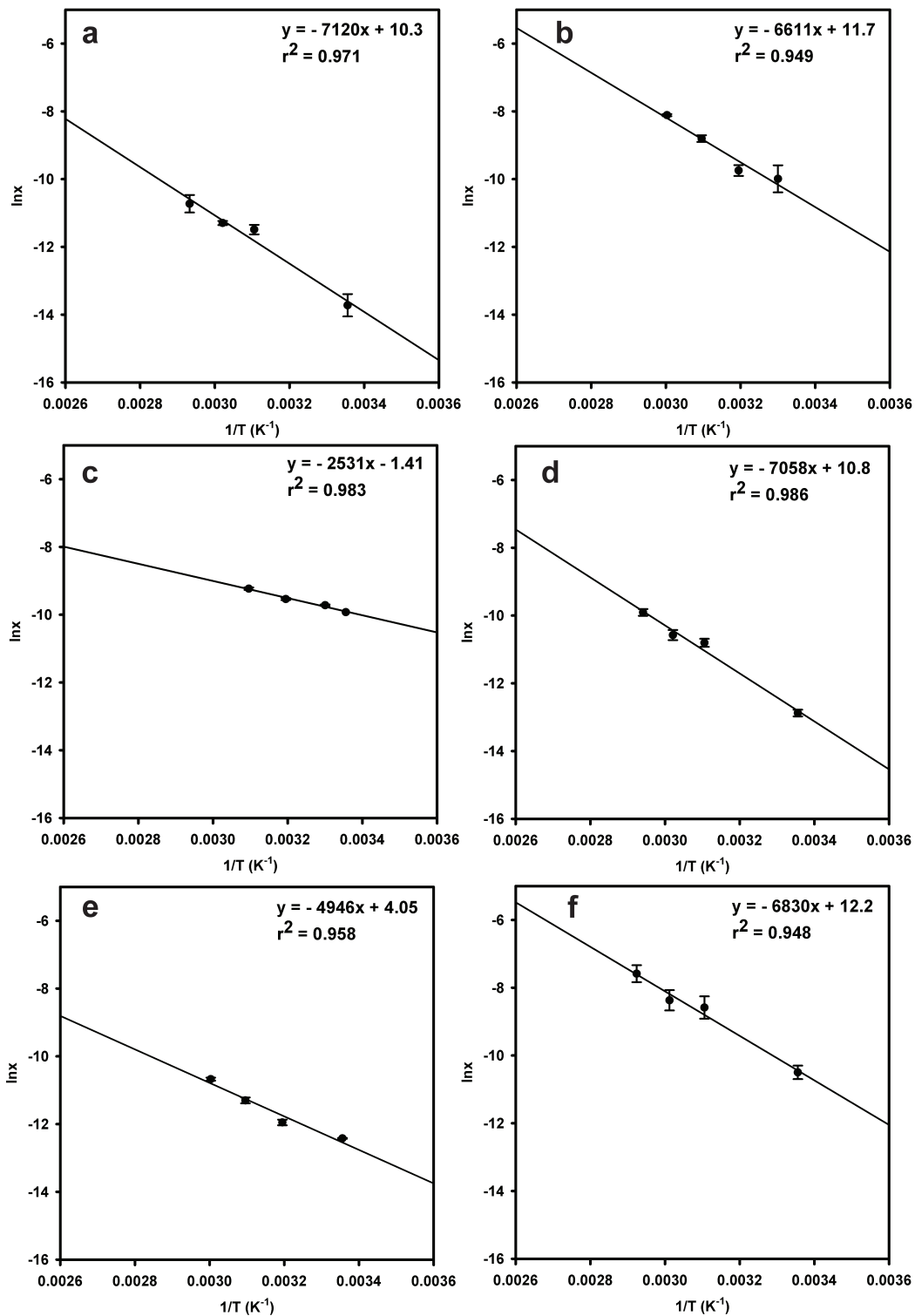


Figure S61. Van't Hoff plot for (a) **3b**, (b) **4**, (c) **5a**, (d) **5b**, (e) **5c**, (f) **6a** in 1/1 DMSO/ H_2O .

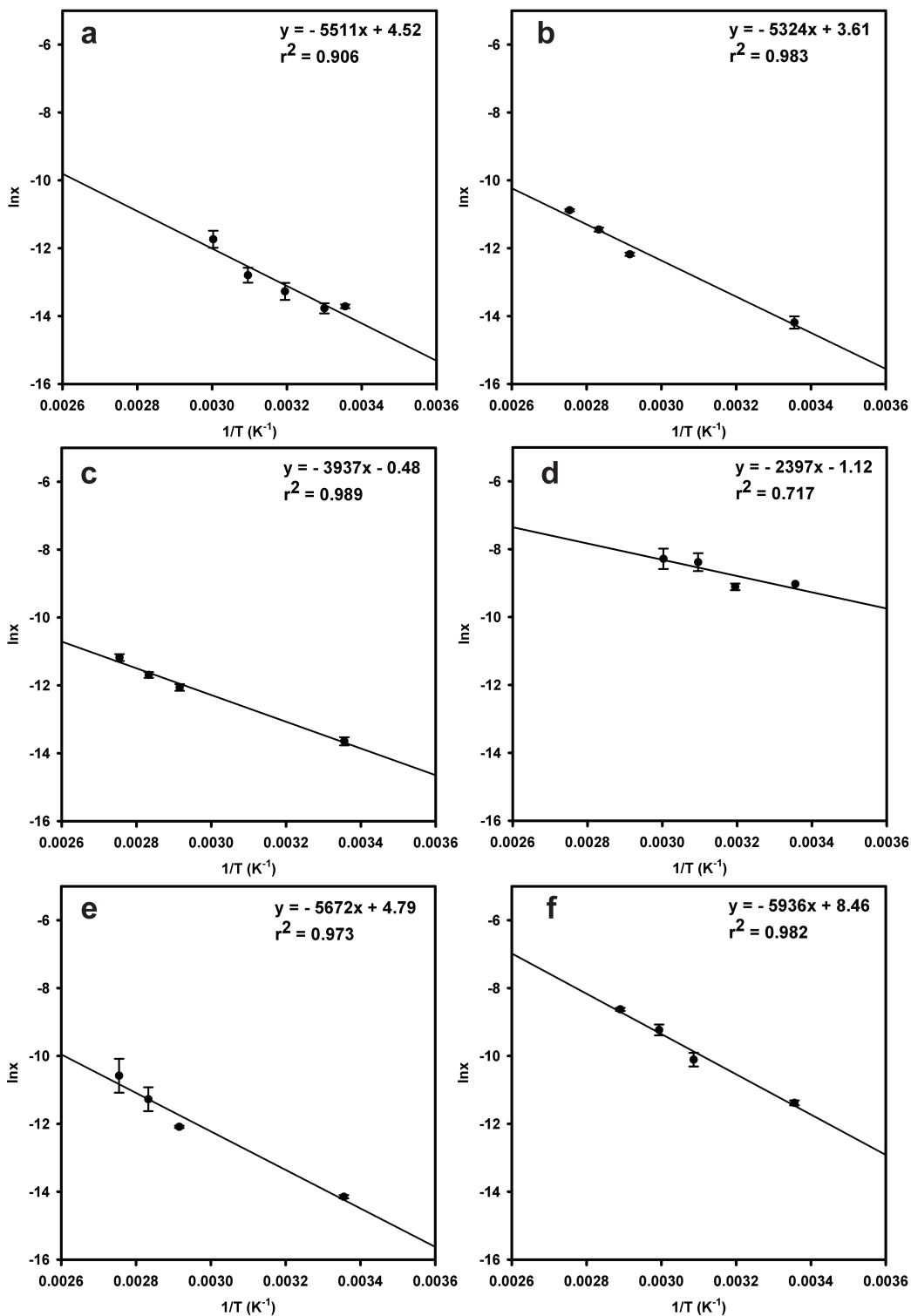


Figure S62. Van't Hoff plot for (a) **6b**, (b) **6c**, (c) **6d**, (d) **7a**, (e) **7b**, (f) **8a** in 1/1 DMSO/H₂O.

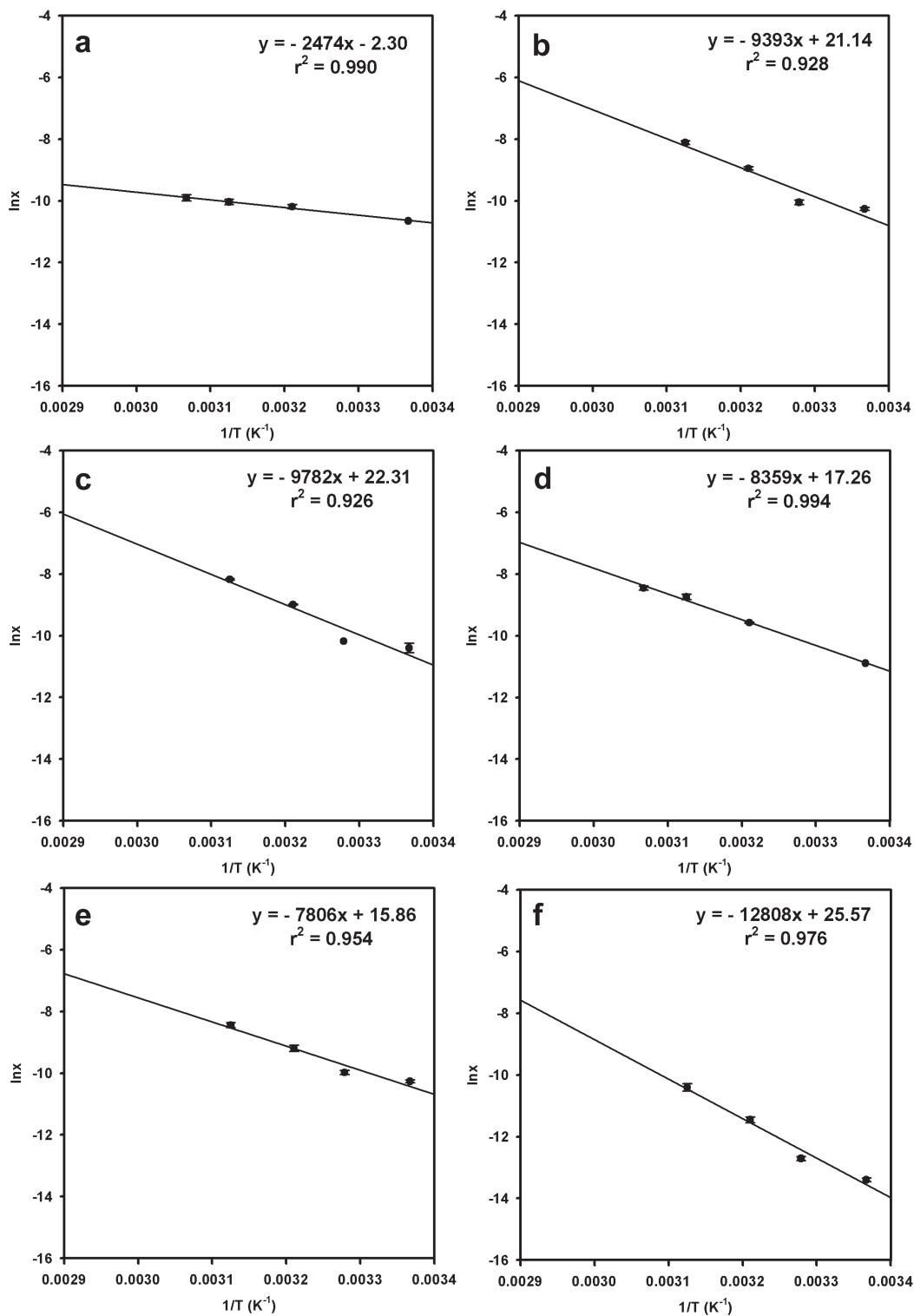


Figure S63. Van't Hoff plot for (a) **1a** (b) **1b**, (c) **2a**, (d) **2b**, (e) **2c**, (f) **3a** in 1/2 EtOH/H₂O.

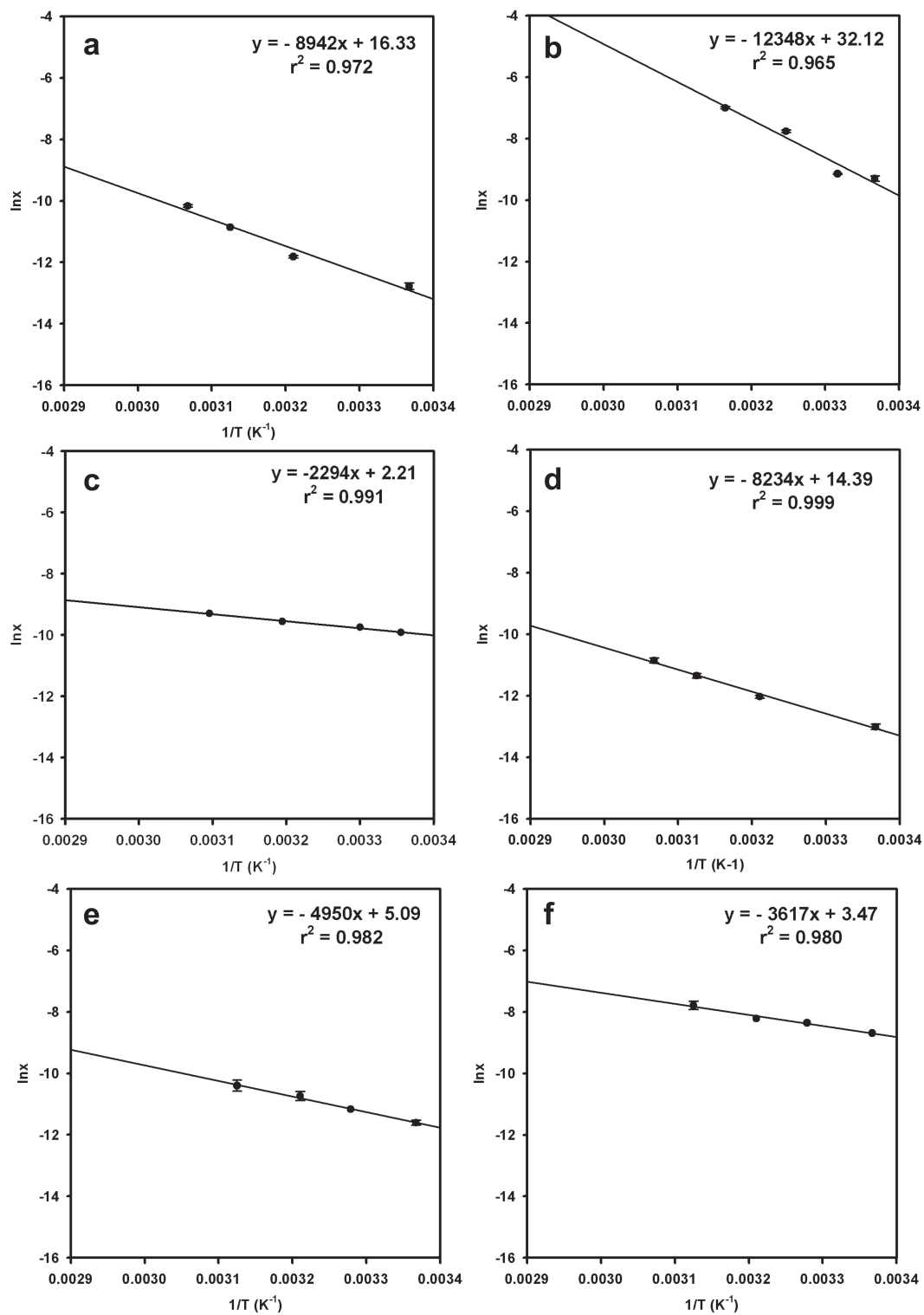


Figure S64. Van't Hoff plot for (a) **3b**, (b) **4**, (c) **5a**, (d) **5b**, (e) **5c**, (f) **6a** in 1/2 EtOH/H₂O

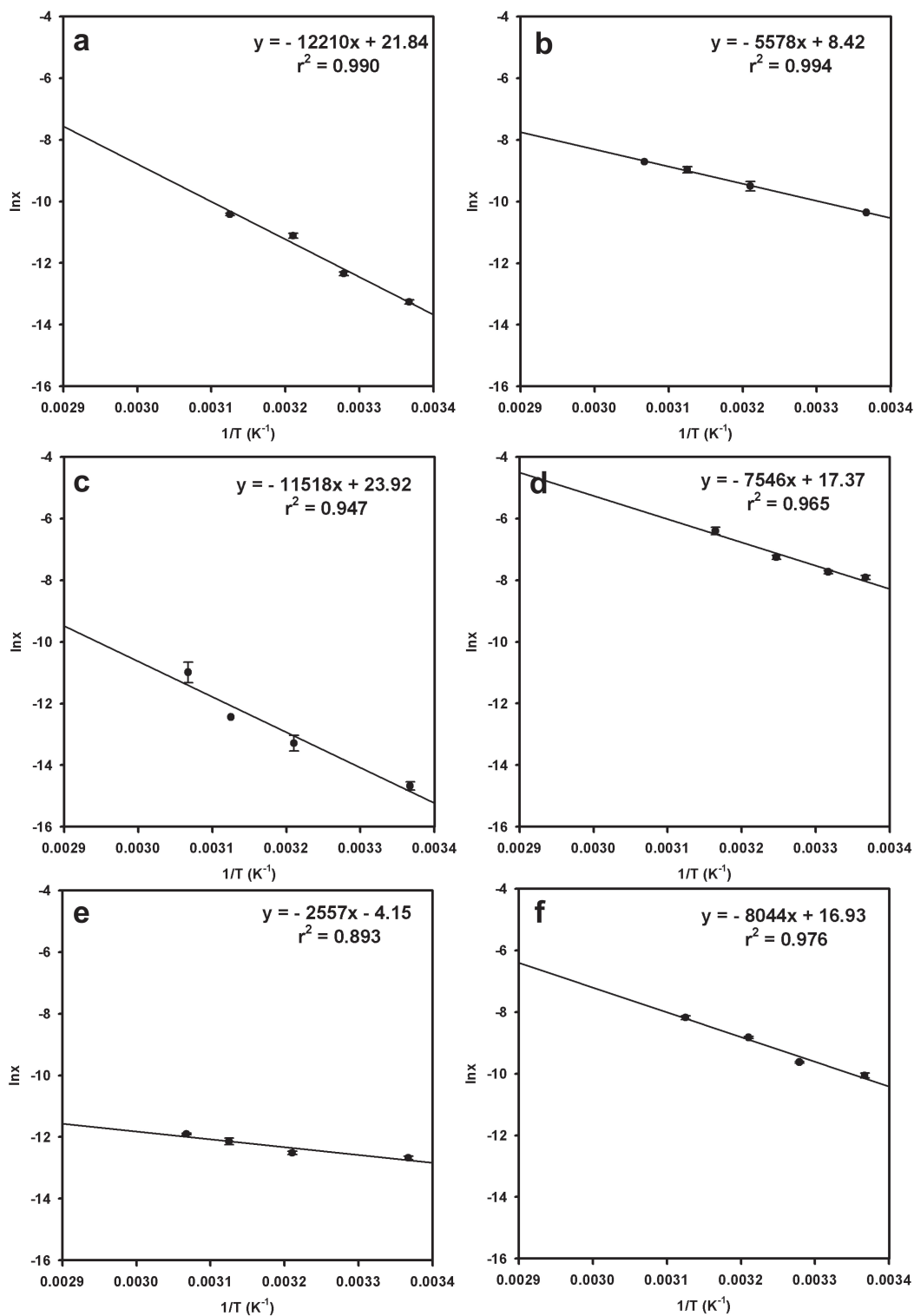


Figure S65. Van't Hoff plot for (a) **6b**, (b) **6c**, (c) **6d**, (d) **7a**, (e) **7b**, (f) **8a** in 1/2 EtOH/H₂O.

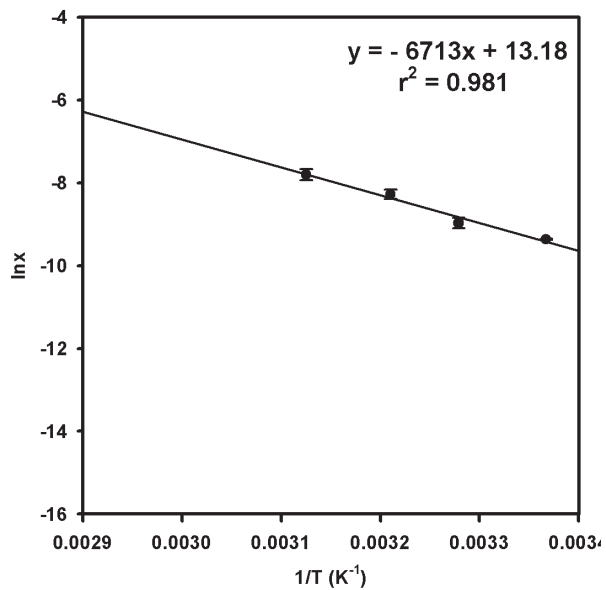


Figure S66. Van't Hoff plot for **8b** in 1/2 EtOH/H₂O.

Table S6. Summary of dissolution enthalpies and entropies of pyridines **1-8**.

Pyridine	ΔH_{diss}	ΔS_{diss}	ΔH_{diss}	ΔS_{diss}
	(kcal/mol)	(kcal/mol/K)	(kcal/mol)	(kcal/mol/K)
	ln 1/1	ln 1/1	ln 1/2	ln 1/2
	DMSO/H ₂ O	DMSO/H ₂ O	EtOH/H ₂ O	EtOH/H ₂ O
1a	7.19	-0.000655	4.90	-0.00455
1b	17.1	0.0343	18.6	0.0419
2a	14.0	0.0220	19.4	0.0442
2b	22.6	0.0455	16.6	0.0342
2c	11.0	0.0136	15.5	0.0314
3a	12.1	0.0182	25.4	0.0506
3b	14.1	0.0204	17.7	0.0323
4	13.1	0.0232	24.4	0.0636
5a	5.03	-0.00280	4.51	0.00255
5b	14.0	0.0214	16.3	0.0285
5c	9.82	0.00804	9.80	0.0101
6a	13.6	0.0242	7.16	0.00687
6b	10.9	0.00897	24.2	0.0432
6c	10.6	0.00717	11.0	0.0167
6d	7.81	-0.000953	22.8	0.0474
7a	4.76	-0.00222	14.9	0.0344
7b	11.3	0.00951	5.06	-0.00822
8a	11.8	0.0168	15.9	0.0335
8b	11.3	0.0165	13.3	0.0261

IX. Melting Points

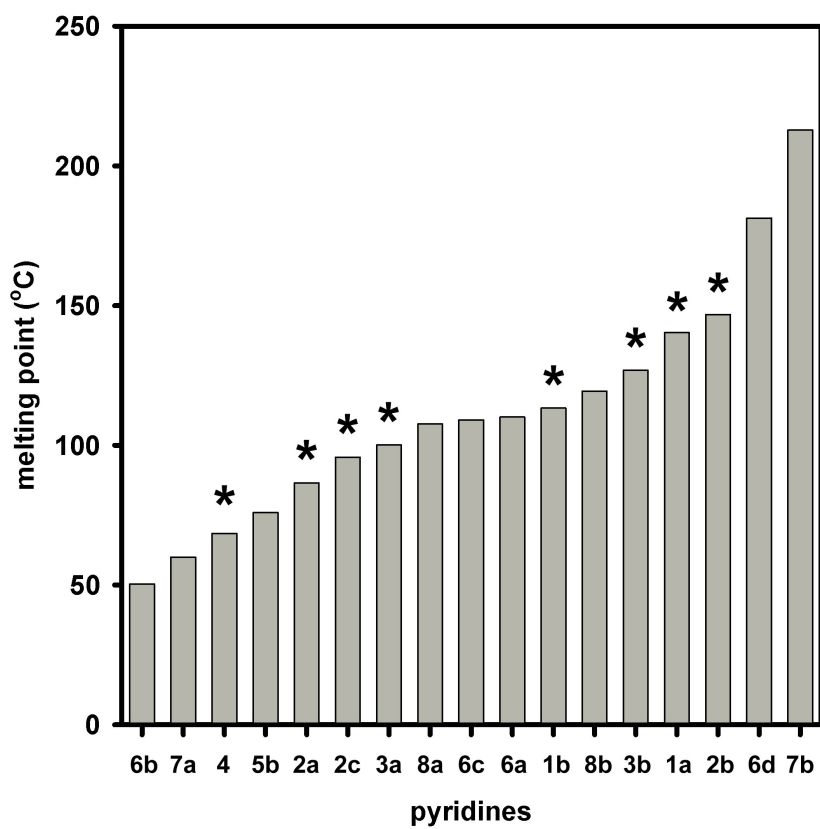


Figure S67. Melting points for pyridines 1-8 (*denotes a gelator).

X. Single-crystal X-ray Structures

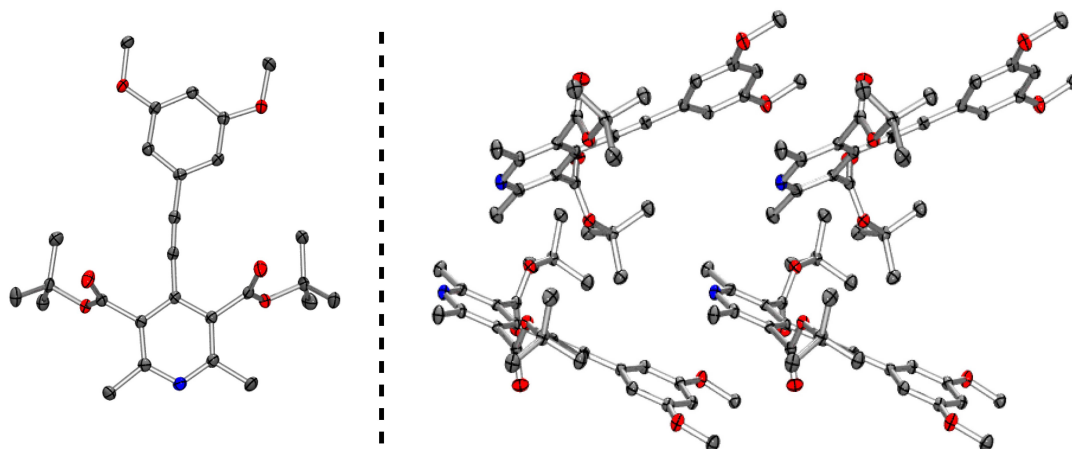


Figure S68. Single-crystal X-ray structure of **1a** (left) and the solid-state packing in the crystal (right).

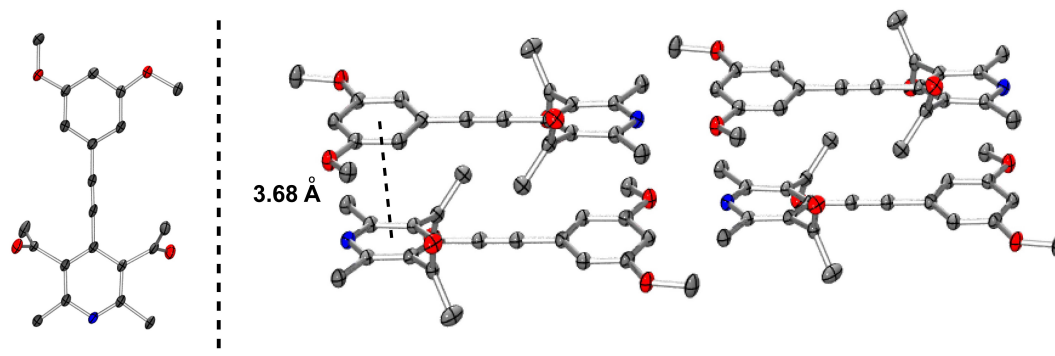


Figure S69. Single-crystal X-ray structure of **1b form-1** (left) and the solid-state packing in the crystal (right).

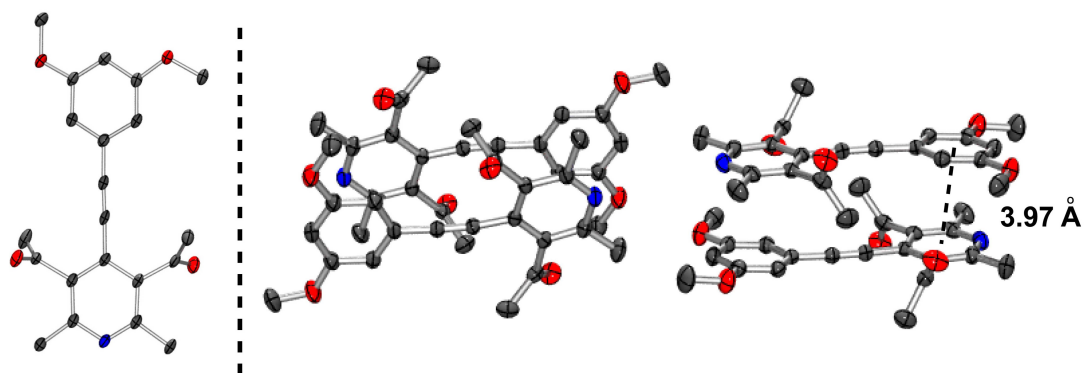


Figure S70. Single-crystal X-ray structure of **1b form-2** (left) and the solid-state packing in the crystal (right).

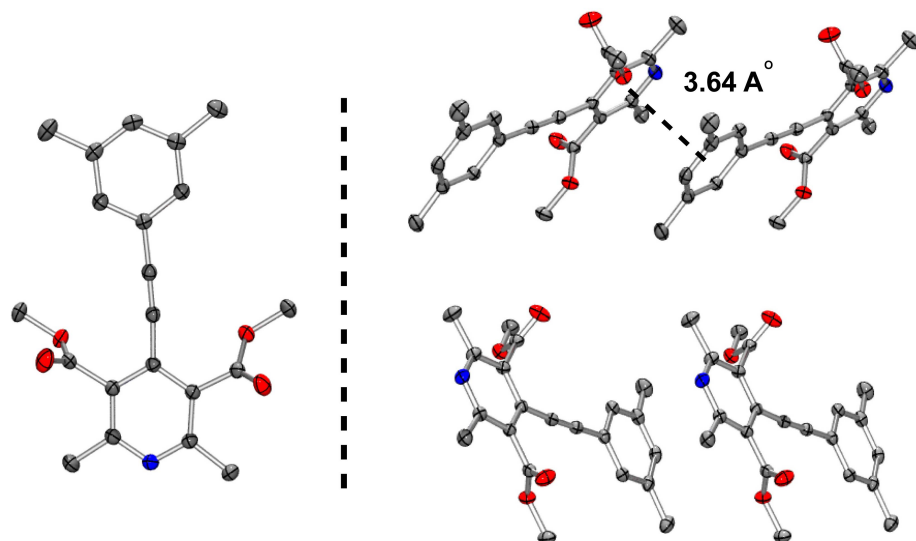


Figure S71. Single-crystal X-ray structure of **2c** (left) and the solid-state packing in the crystal (right).

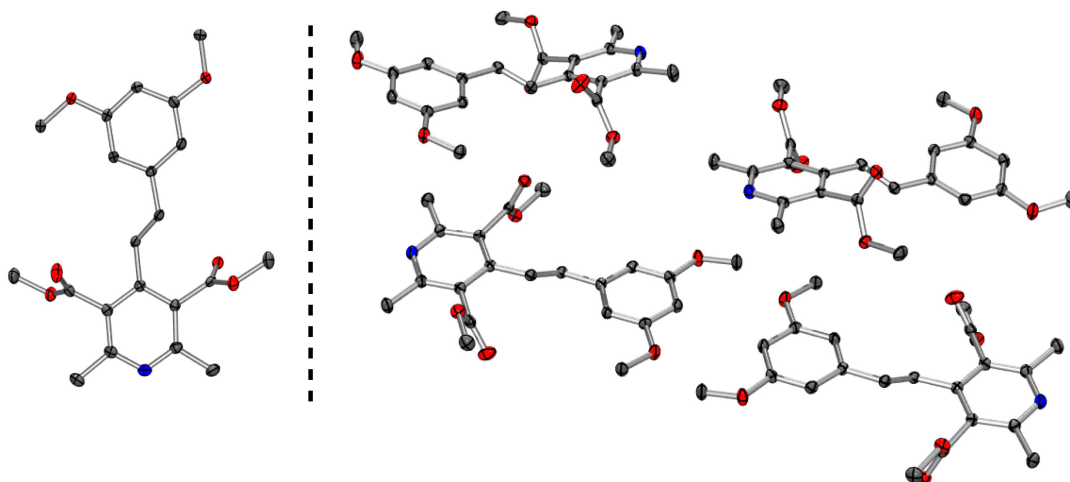


Figure S72. Single-crystal X-ray structure of **3a** (left) and the solid-state packing in the crystal (right).

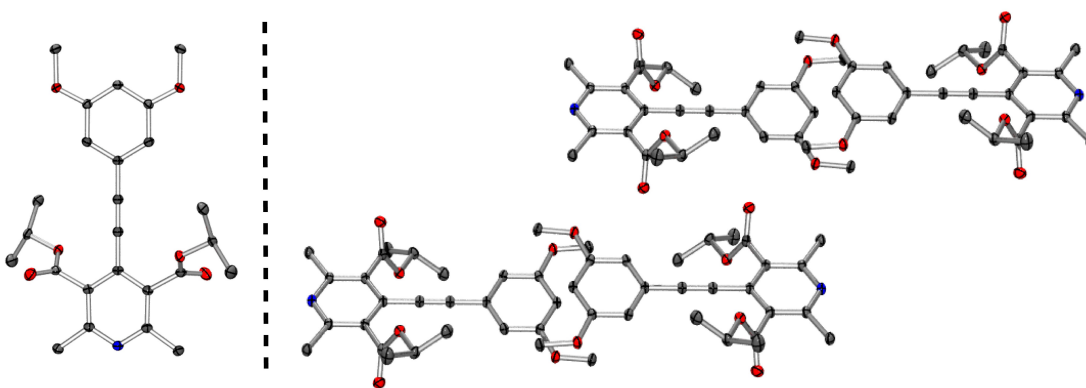


Figure S73. Single-crystal X-ray structure of **5c** (left) and the solid-state packing in the crystal (right).

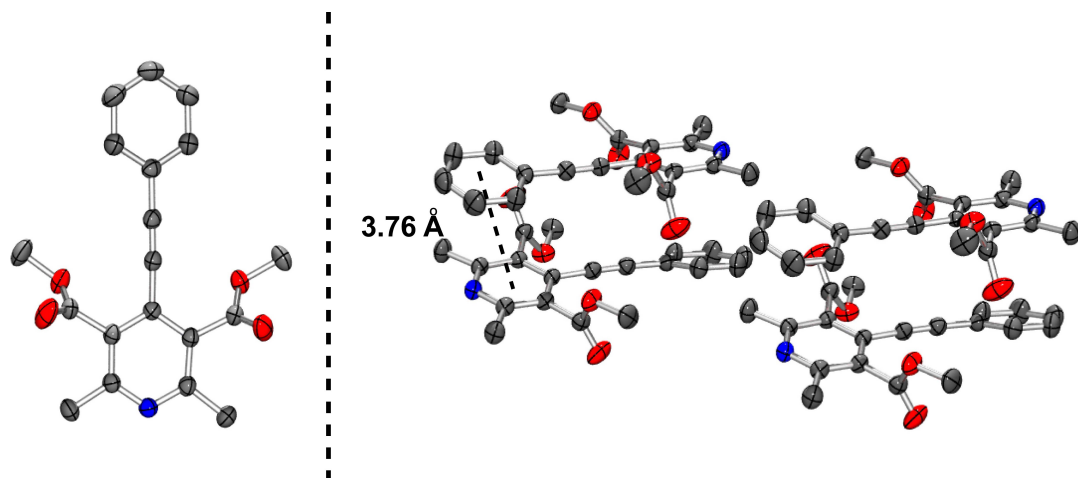


Figure S74. Single-crystal X-ray structure of **6a** (left) and the solid-state packing in the crystal (right).

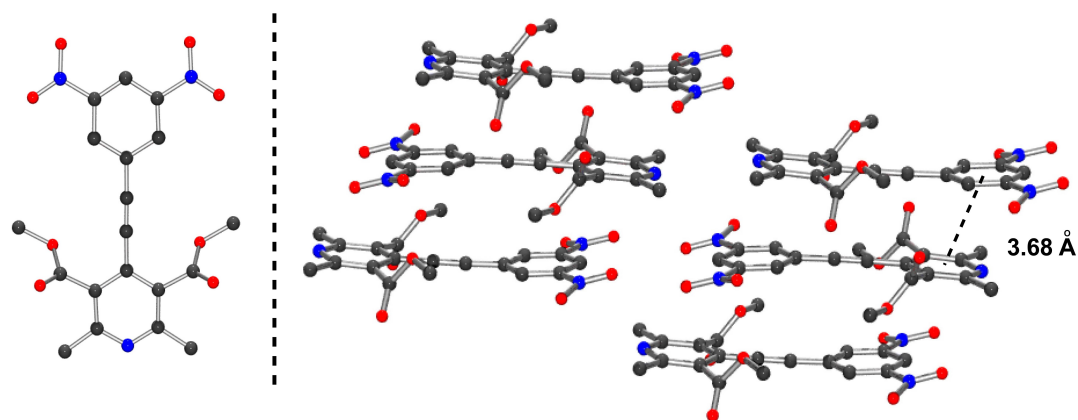


Figure S75. Single-crystal X-ray structure of **6d** (left) and the solid-state packing in the crystal (right).

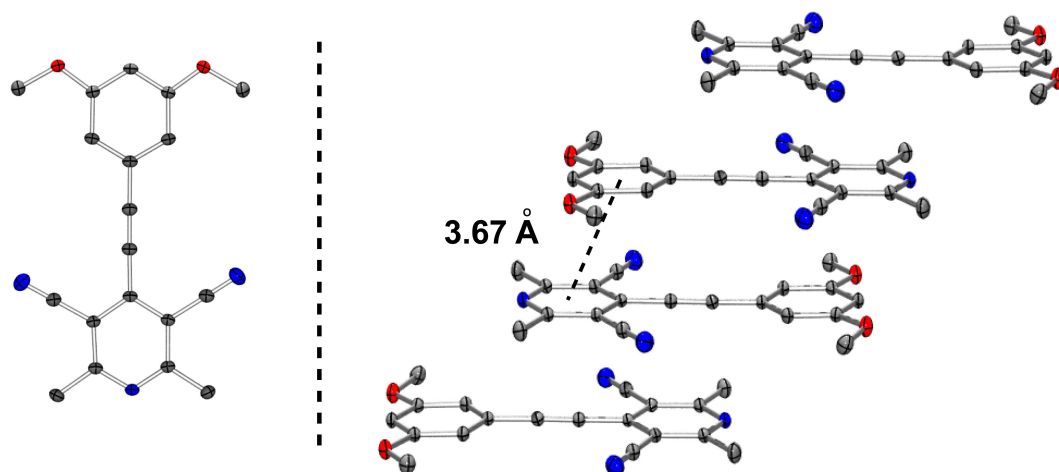


Figure S76. Single-crystal X-ray structure of **7a** (left) and the solid-state packing in the crystal (right).

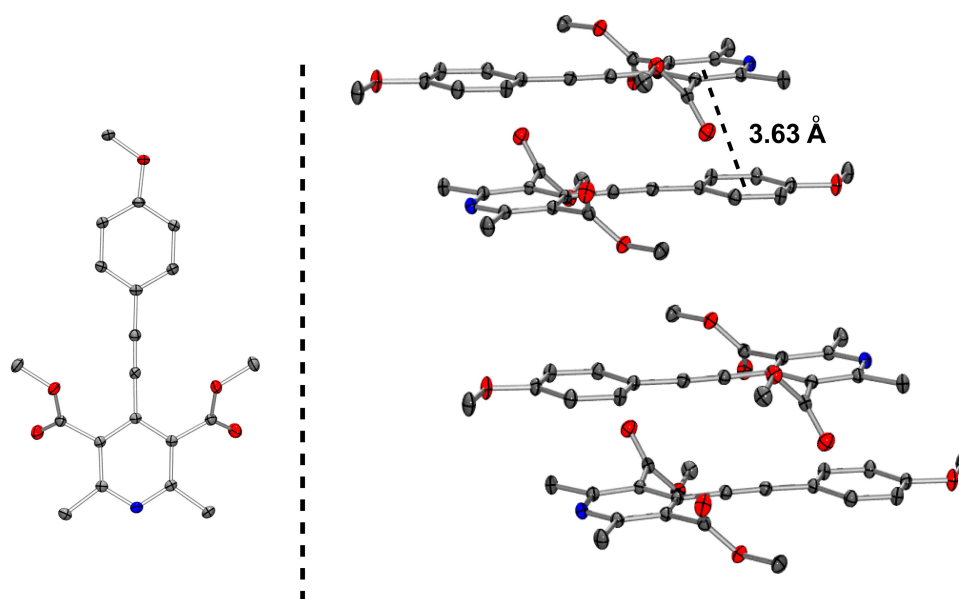


Figure S77. Single crystal X-ray structure of **8a** (left) and the solid-state packing in the crystal (right).

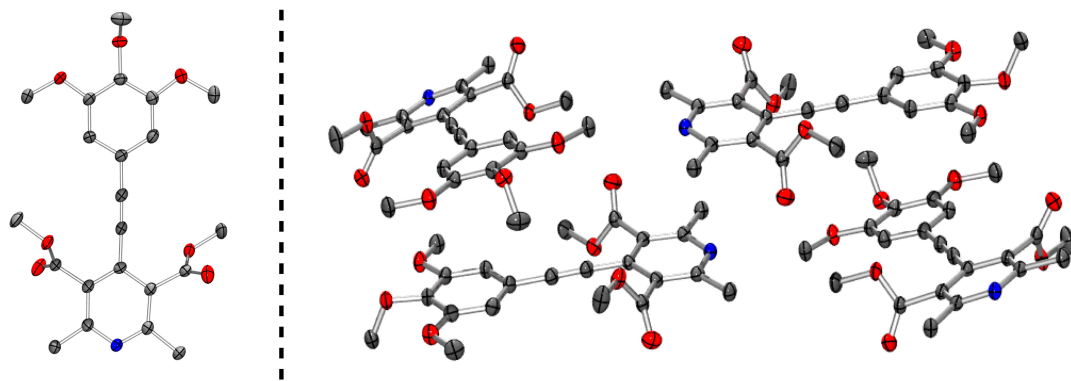


Figure S78. Single-crystal X-ray structure of **8b** (left) and the solid-state packing in the crystal (right).

XI. Powder X-ray Diffraction Patterns

For each experiment, the “bulk solid” refers to the material isolated after column chromatography and concentration in vacuo. In situ gels were formed in 1/1 DMSO/H₂O at their respective cgc.

In each figure, the top line depicts the difference (via subtraction) between the two diffraction patterns.

Comparisons between the bulk solid and the gel.

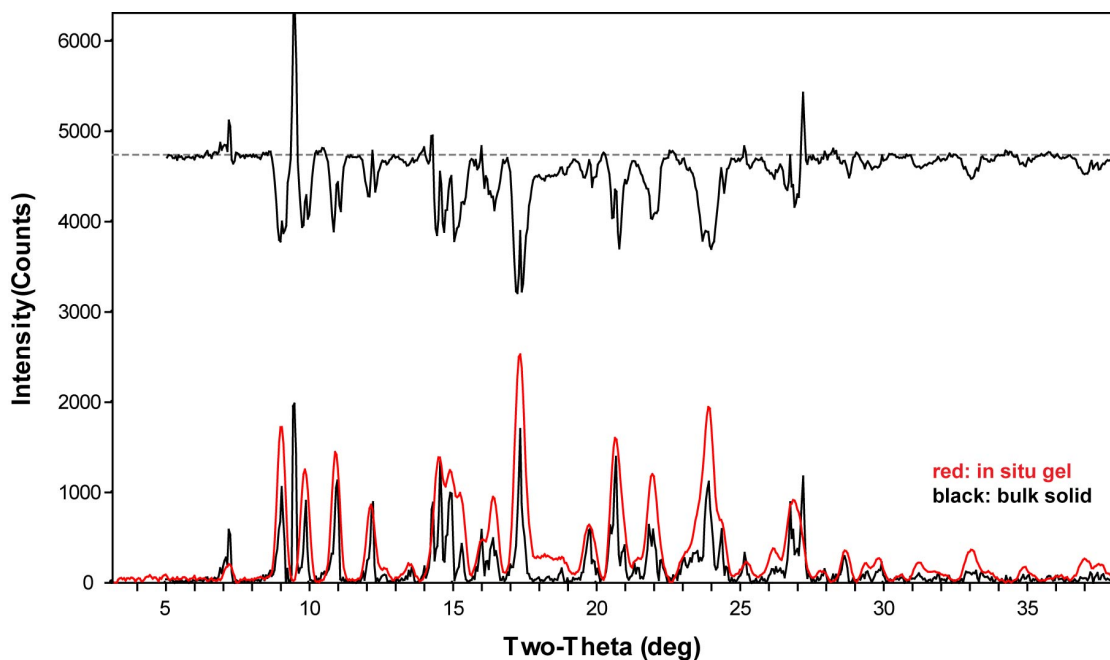


Figure S79. PXRD patterns for **1a** from the in situ gel (red) and bulk solid (black).

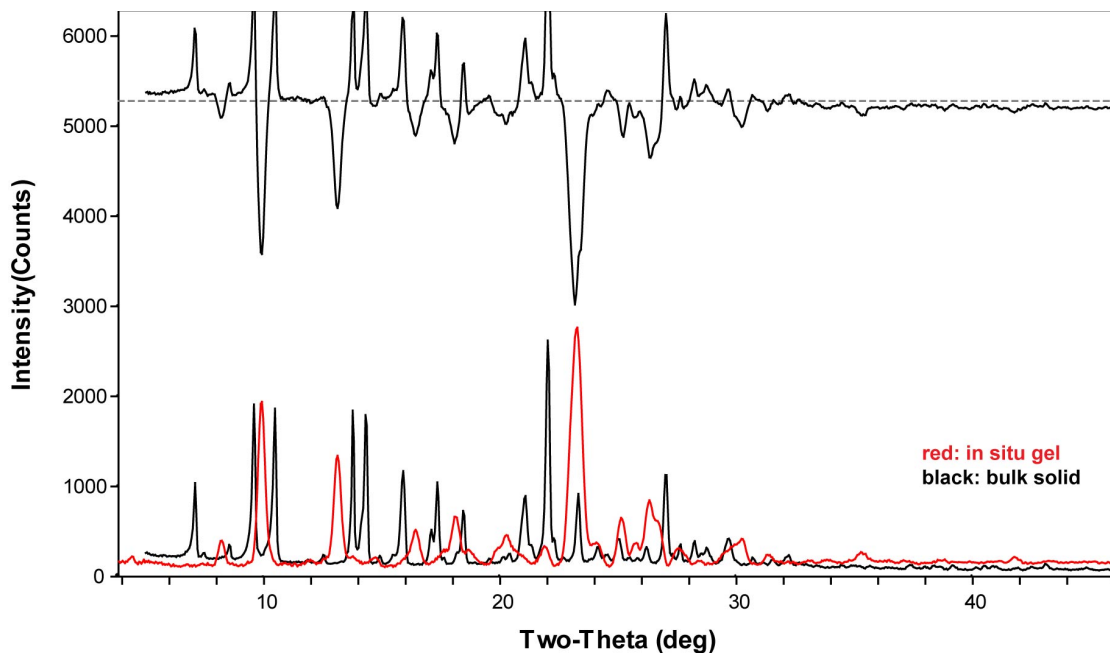


Figure S80. PXRD patterns for **1b** from the in situ gel (red) and bulk solid (black).

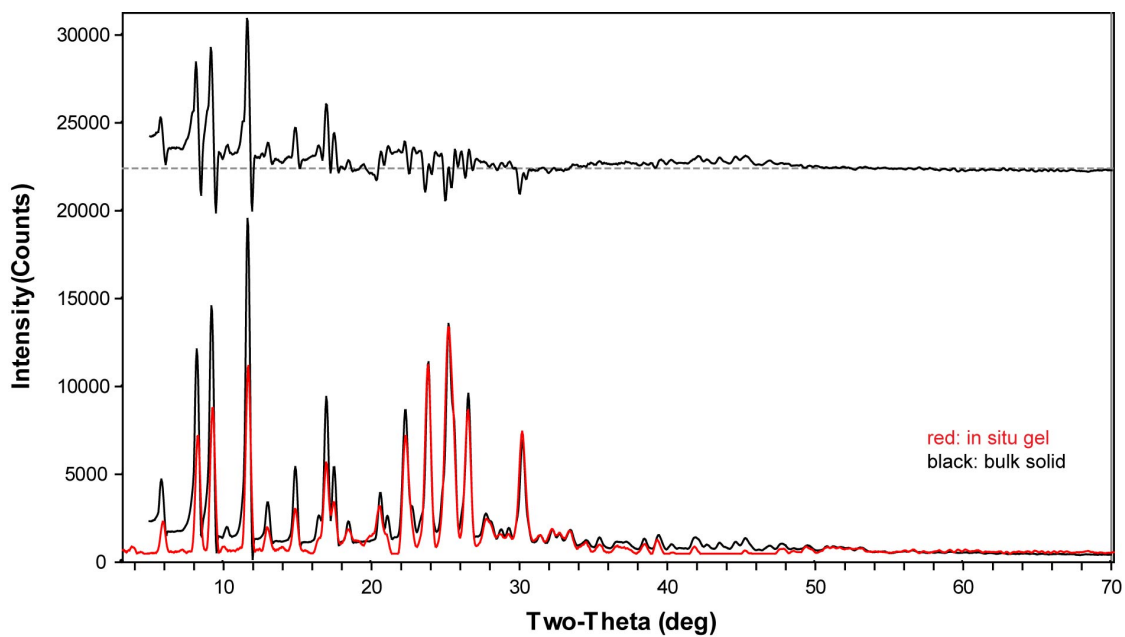


Figure S81. PXRD patterns for **2a** from the in situ gel (red) and bulk solid (black).

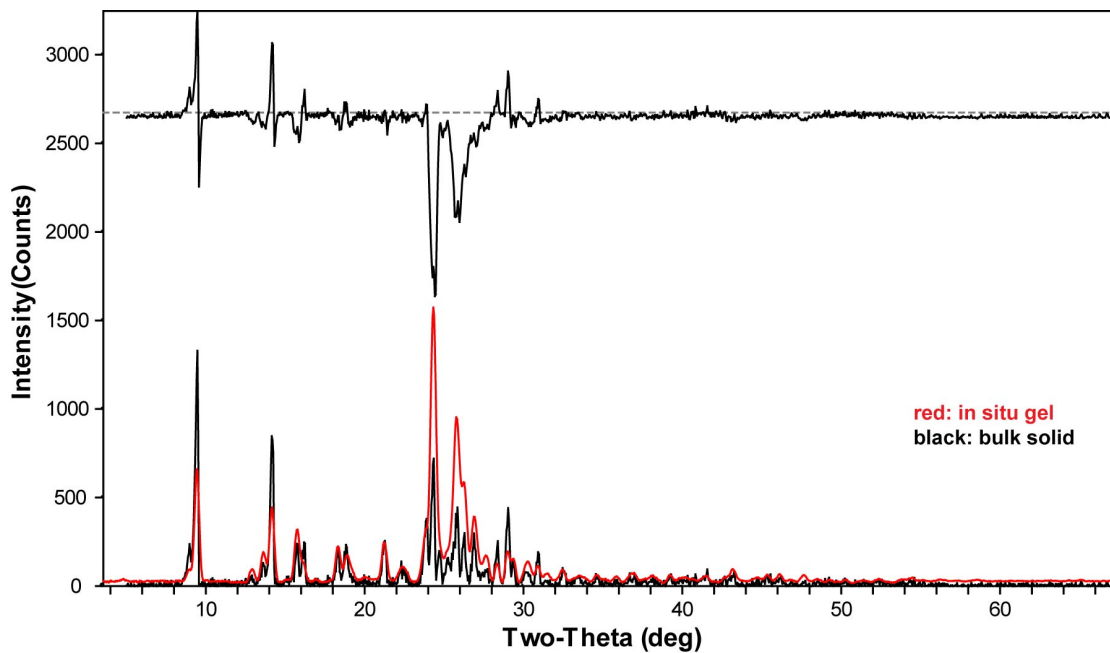


Figure S82. PXRD patterns for **2b** from the in situ gel (red) and bulk solid (black).

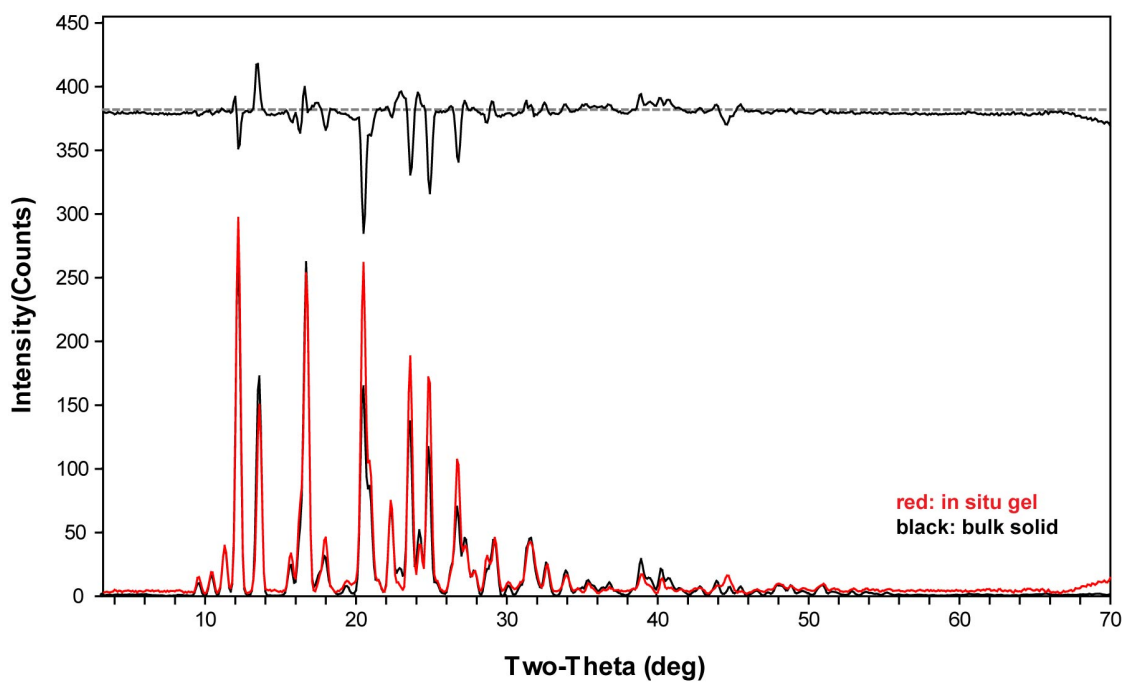


Figure S83. PXRD patterns for **2c** from the in situ gel (red) and bulk solid (black).

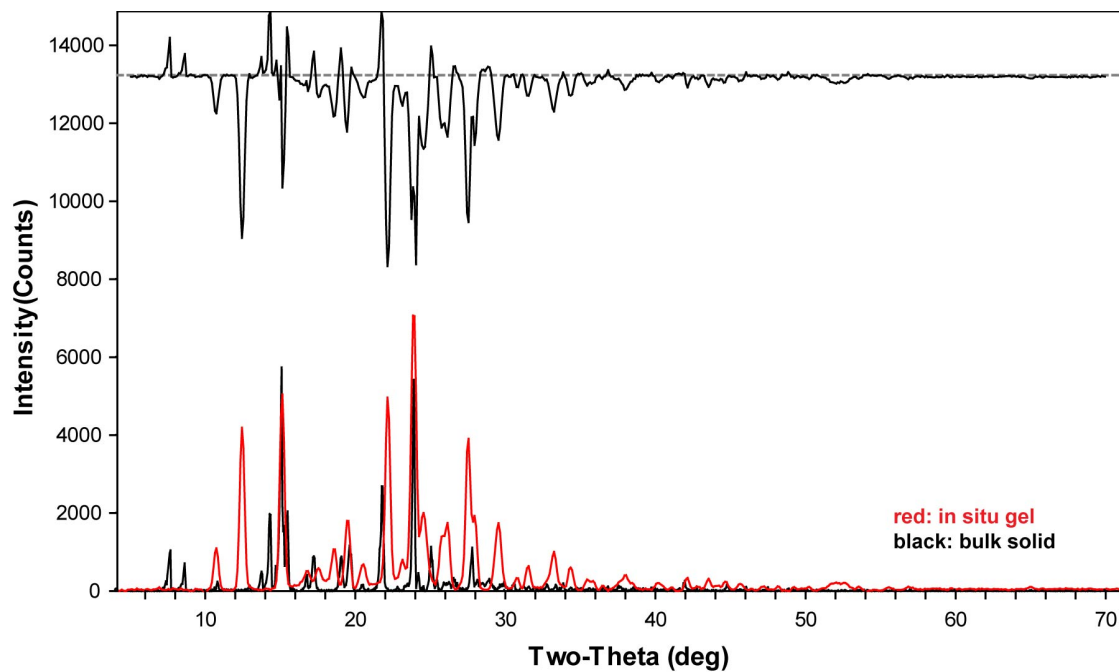


Figure S84. PXRD patterns for **3a** from the in situ gel (red) and bulk solid (black).

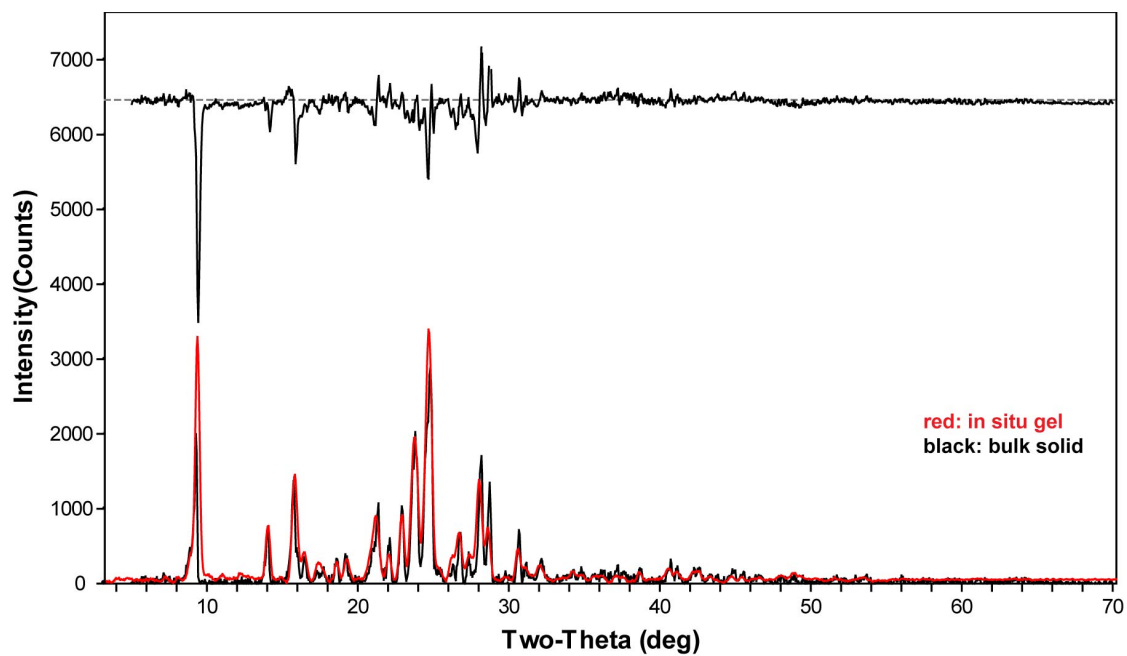


Figure S85. PXRD patterns for **3b** from the in situ gel (red) and bulk solid (black).

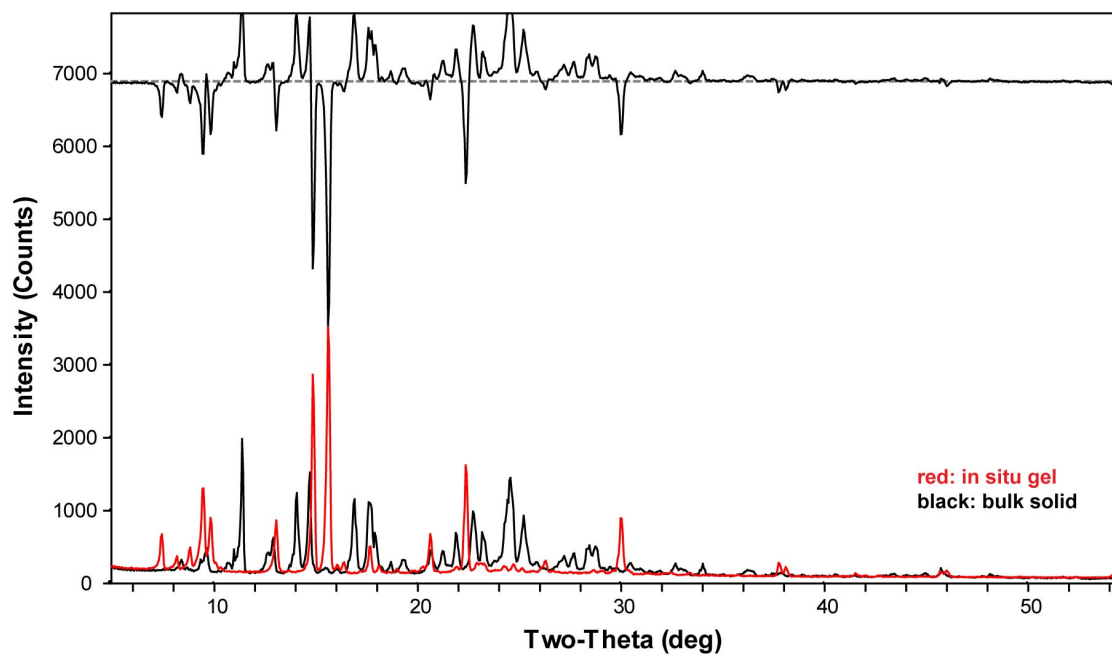


Figure S86. PXRD patterns for **4** from the in situ gel (red) and bulk solid (black).

Comparisons between the gel and a simulation from the single-crystal X-ray structure.

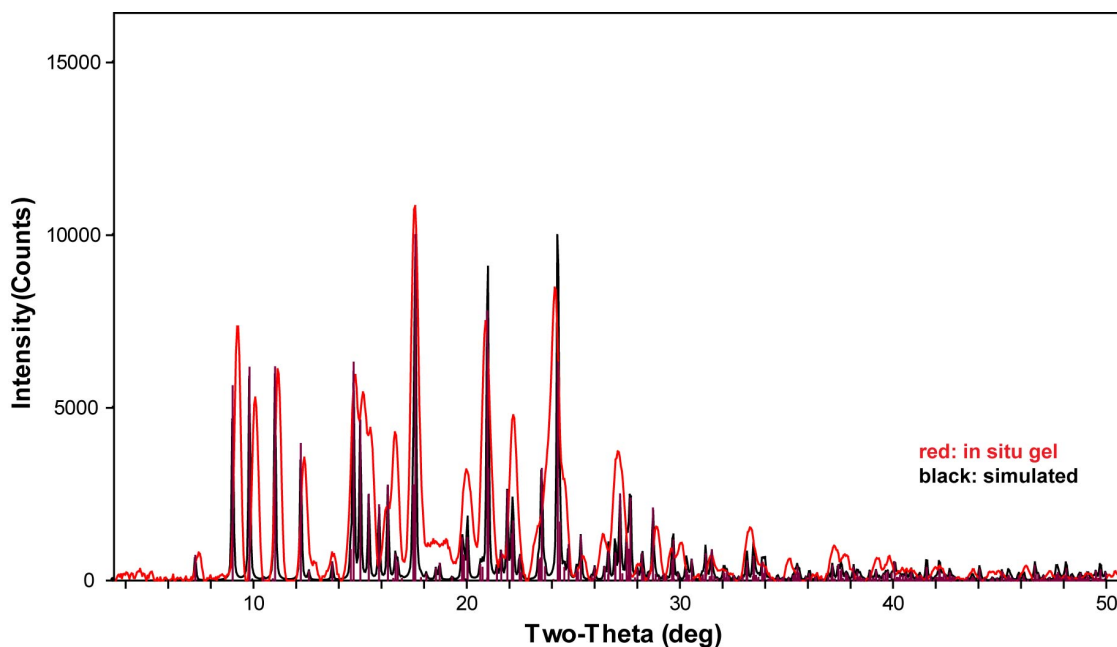


Figure S87. PXRD patterns for **1a** from the in situ gel (red) and a simulation from the single-crystal X-ray structure (black).

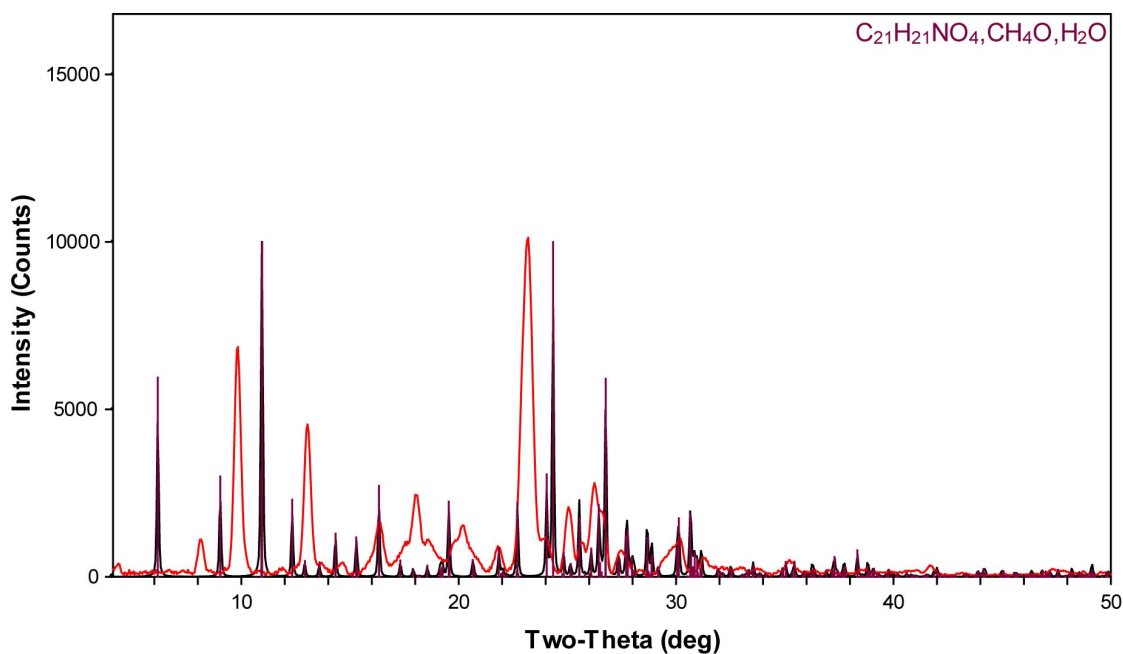


Figure S88. PXRD patterns for **1b** from the in situ gel (red) and a simulation from the single-crystal X-ray structure form-1 (black). Note that H₂O and MeOH molecules are in the single-crystal.

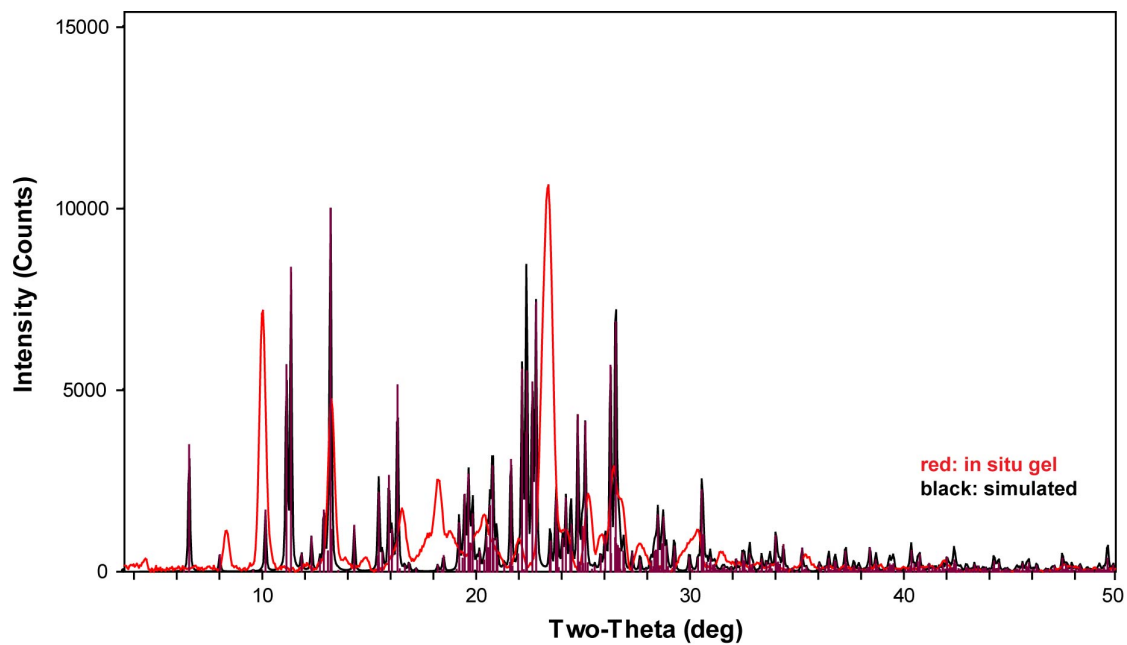


Figure S89. PXRD patterns for **1b** from the in situ gel (red) and a simulation from the single-crystal X-ray structure form-2 (black).

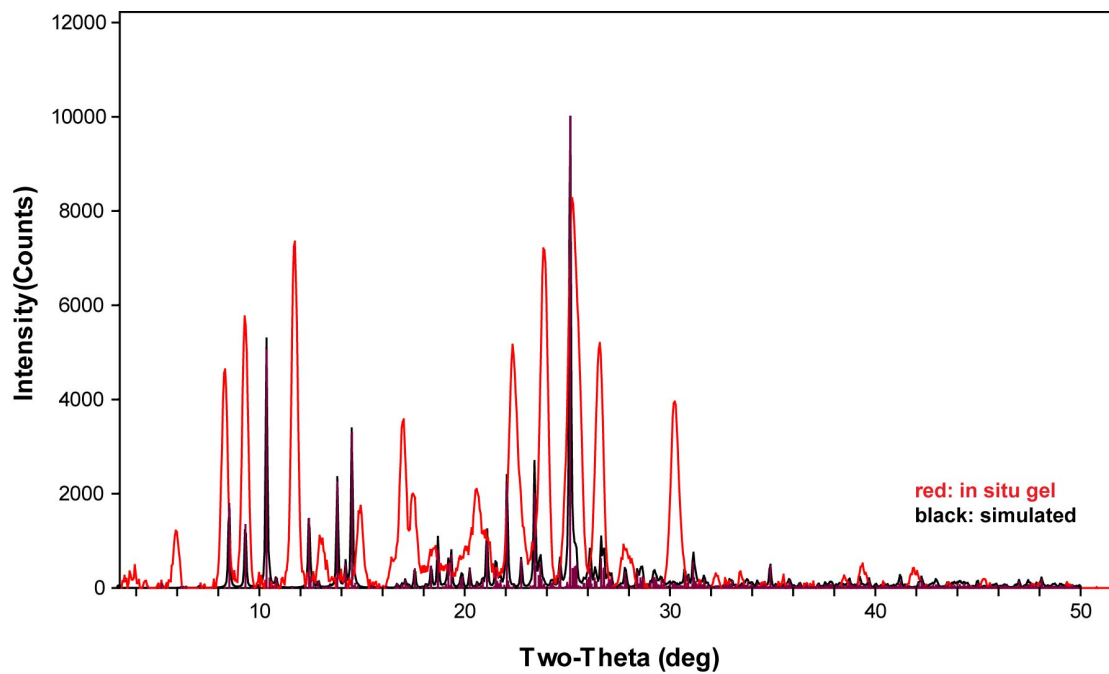


Figure S90. PXRD patterns for **2a** from the in situ gel (red) and a simulation from the single-crystal X-ray structure (black).

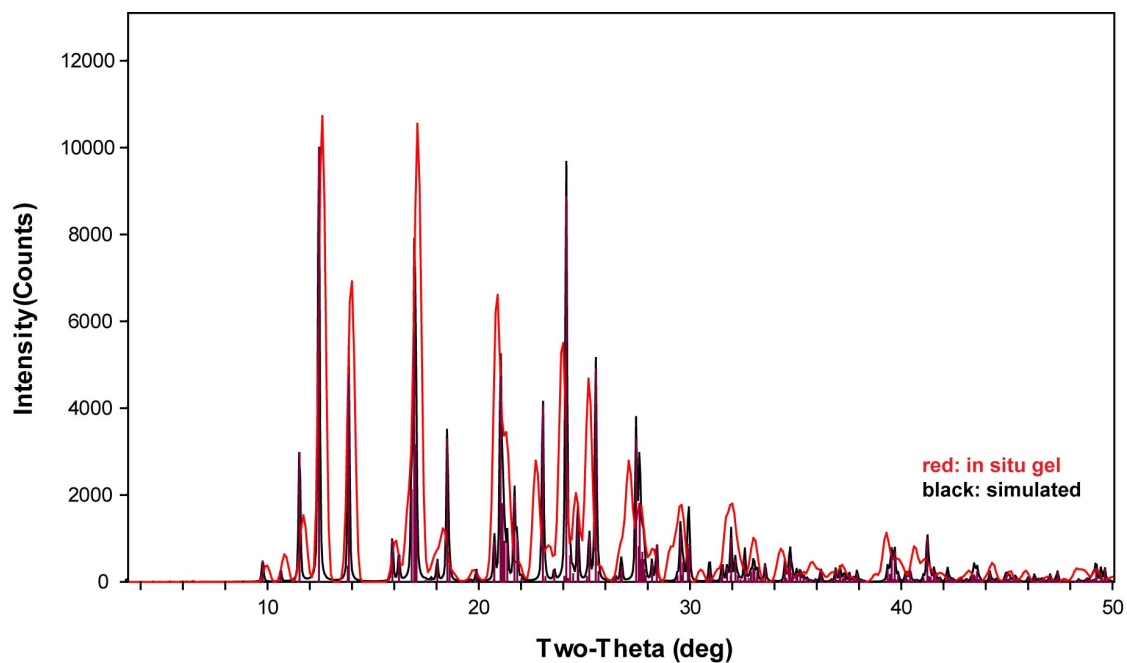


Figure S91. PXRD patterns for **2c** from the in situ gel (red) and a simulation from the single-crystal X-ray structure (black).

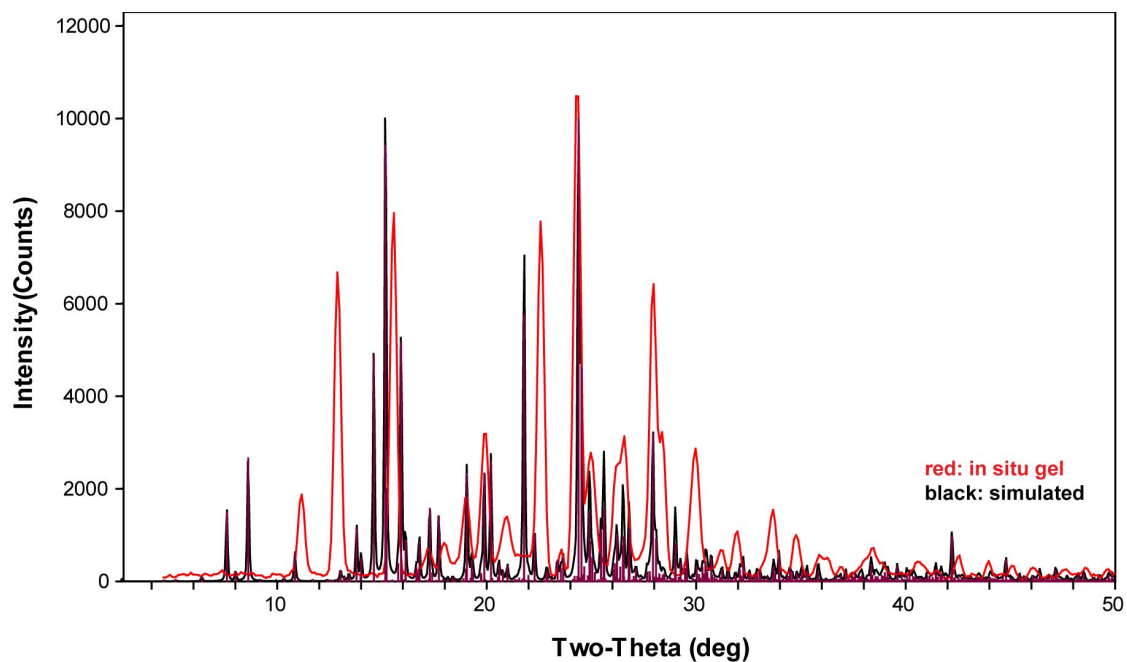


Figure S92. PXRD patterns for **3a** from the in situ gel (red) and a simulation from the single-crystal X-ray structure (black).

Comparisons between the bulk solid and the simulation from the single-crystal X-ray structure.

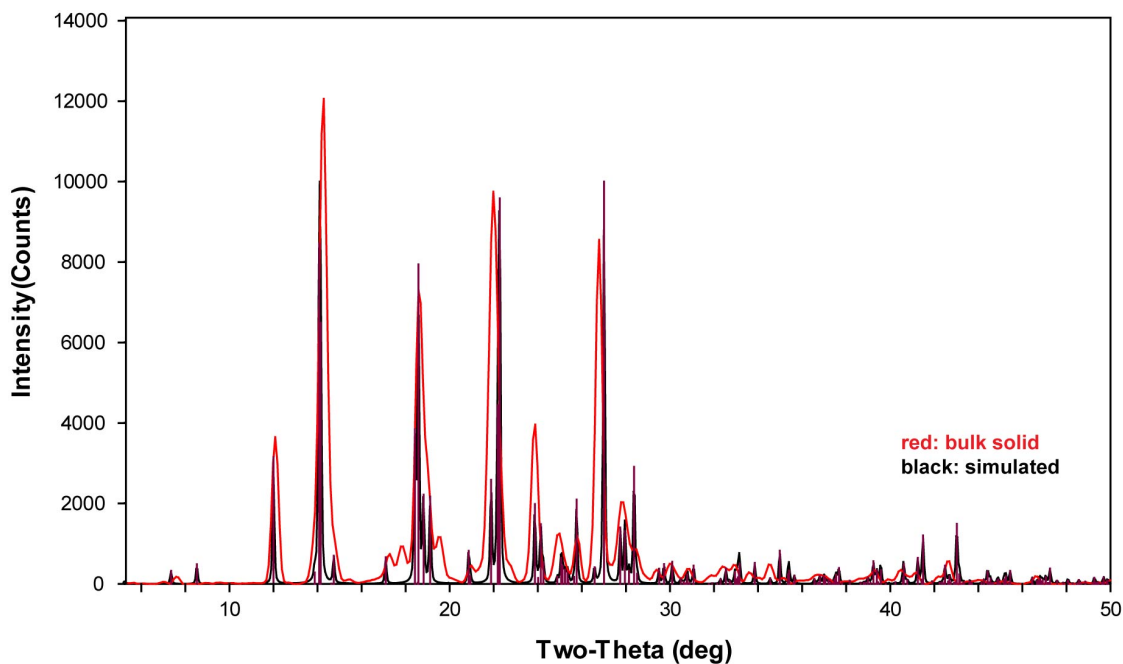


Figure S93. PXRD patterns for **5b** from the bulk solid (red) and a simulation from the single-crystal X-ray structure (black).

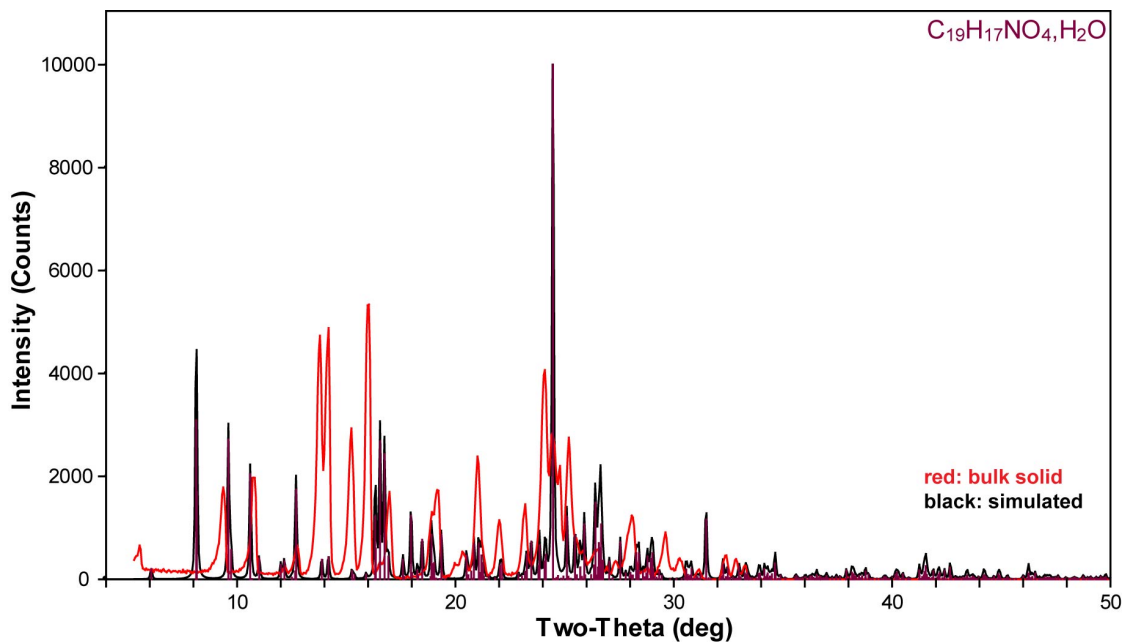


Figure S94. PXRD patterns for **6a** from the bulk solid (red) and a simulation from the single-crystal X-ray structure (black). Note that H₂O molecules are in the single-crystal of **6a**.

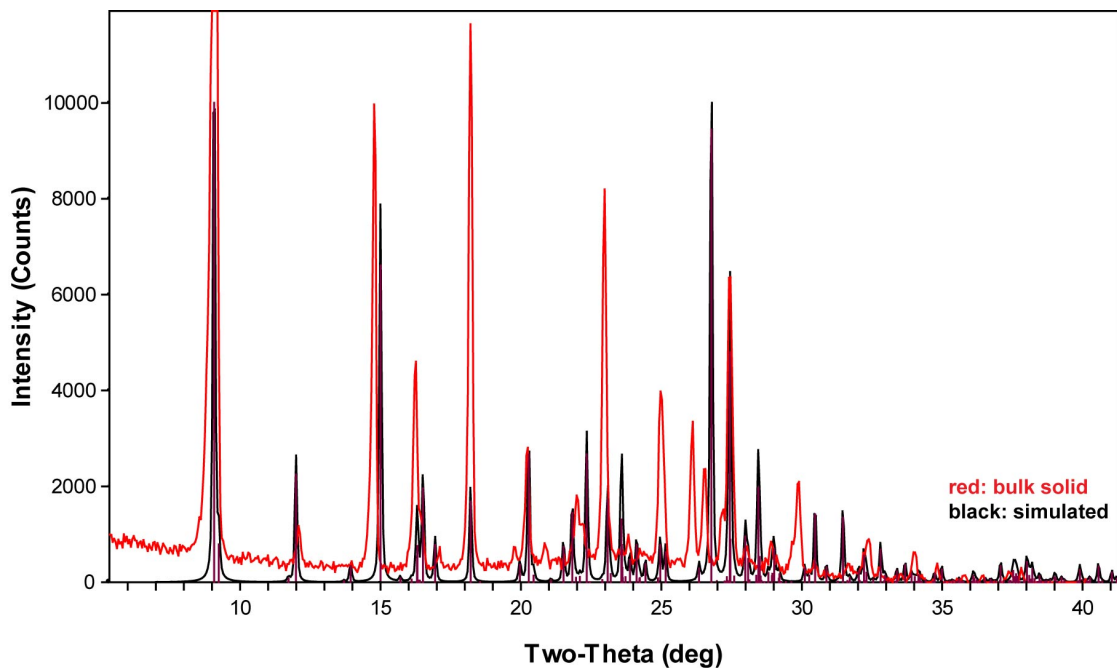


Figure S95. PXRD patterns for **6d** from the bulk solid (red) and a simulation from the single-crystal X-ray structure (black).

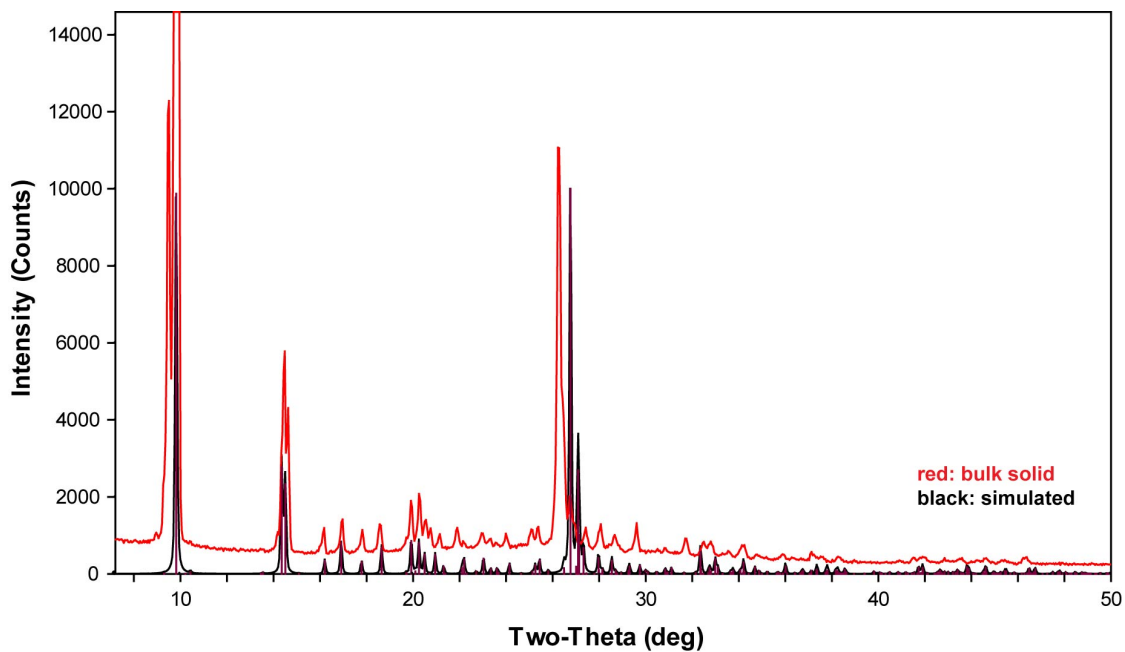


Figure S96. PXRD patterns for **7a** from bulk solid (red) and a simulation from the single-crystal X-ray structure (black).

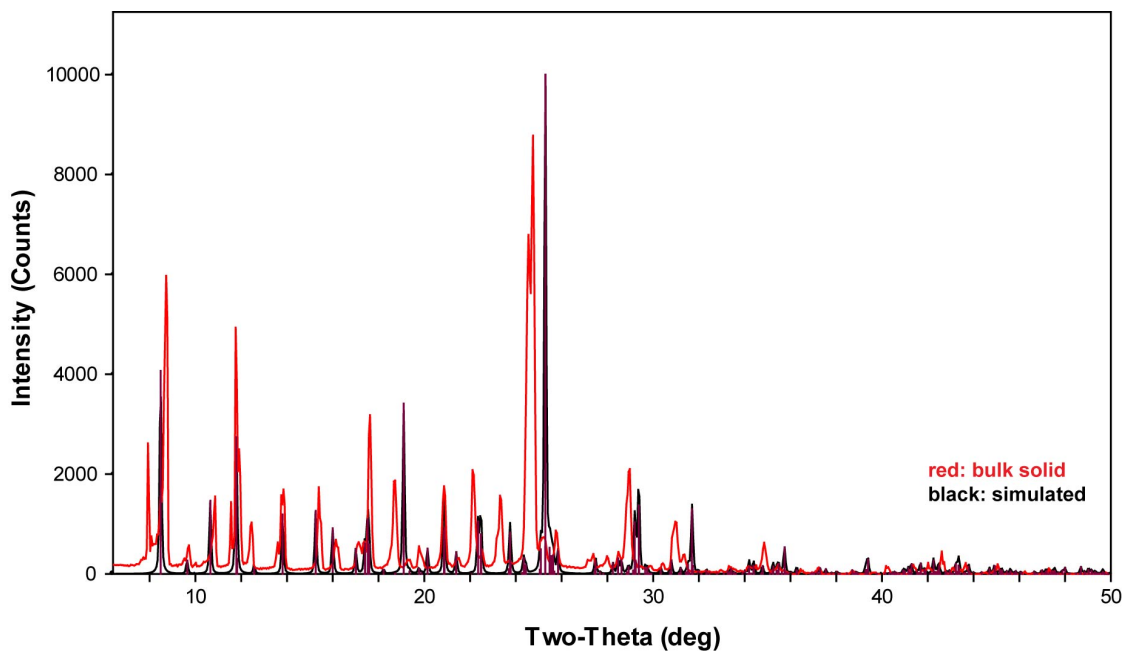


Figure S97. PXRD patterns for **8a** from the bulk solid (red) and a simulation from the single-crystal X-ray structure (black).

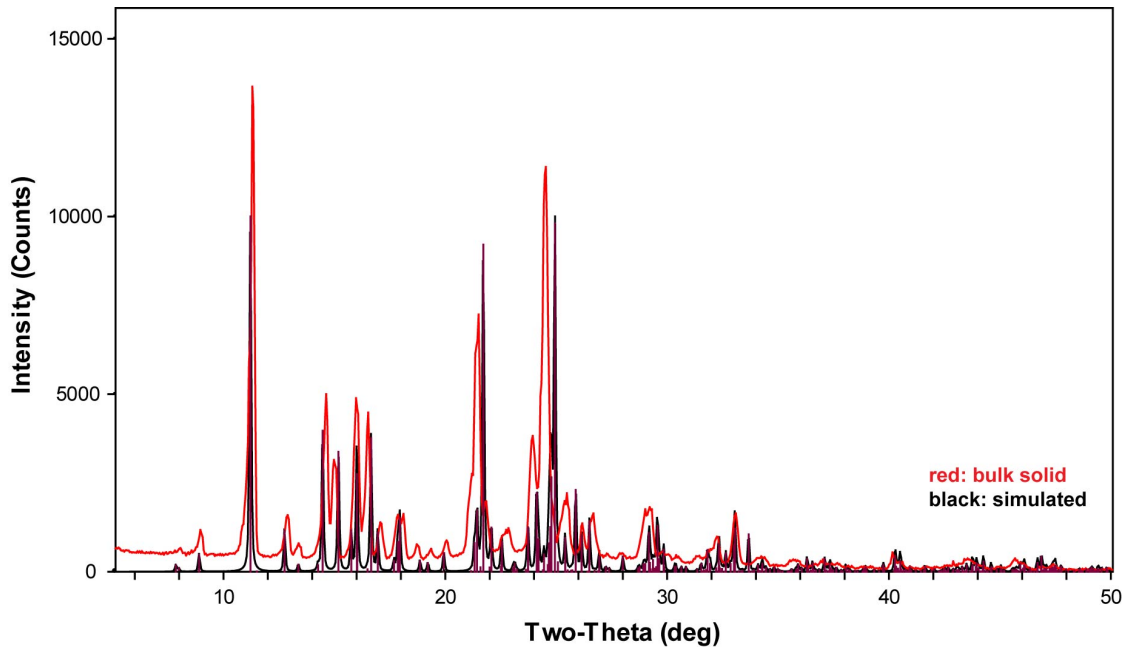


Figure S98. PXRD patterns for **8b** from the bulk solid (red) and a simulation from the single-crystal X-ray structure (black).

XII. Hirshfeld Surface Analysis Results

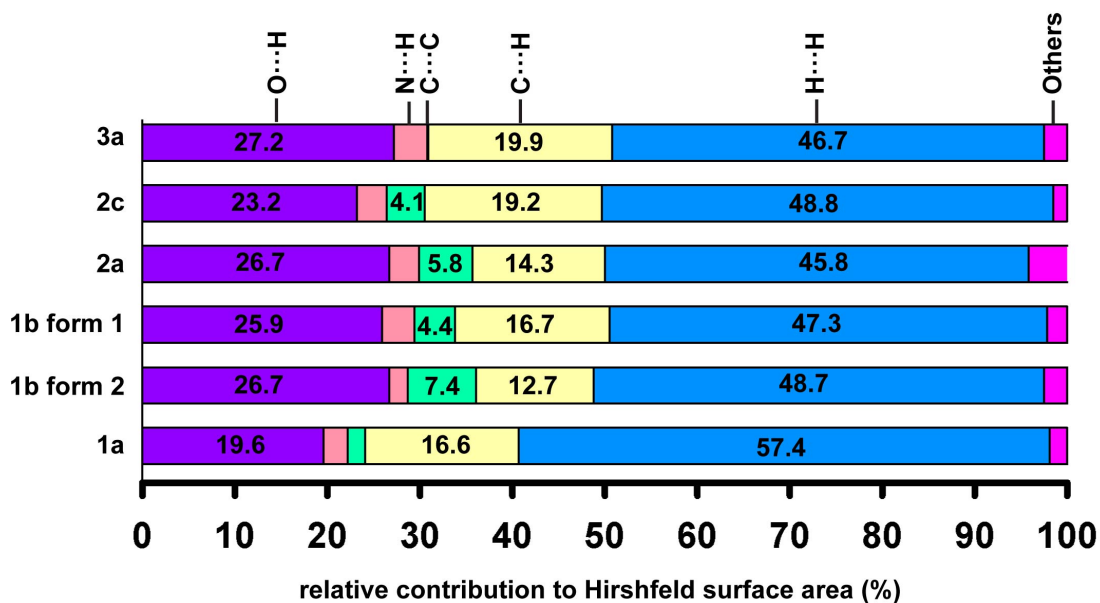


Figure S99. Hirshfeld surface analysis of gelators.

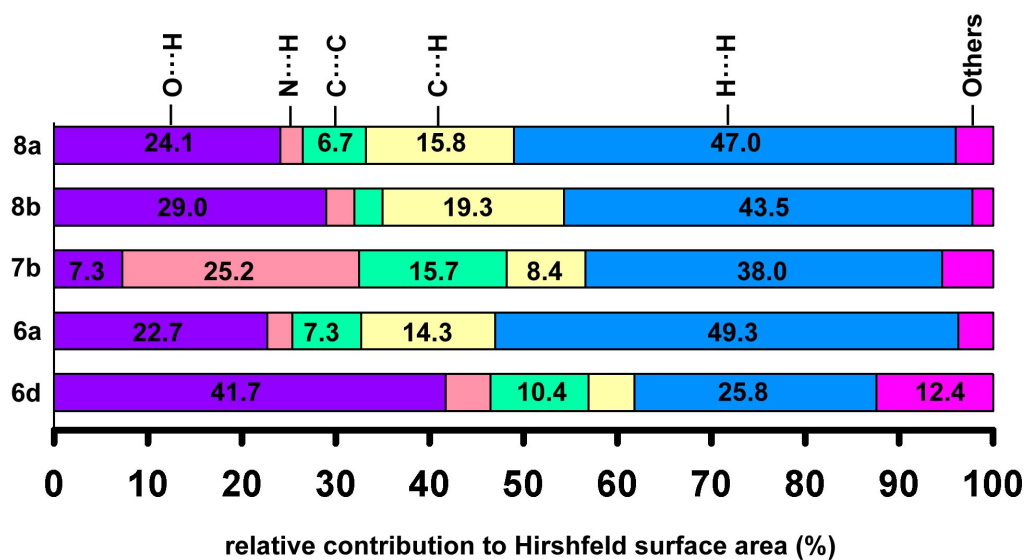


Figure S100. Hirshfeld surface analysis of non-gelators.

XIII. Solubility versus cgc Comparisons for Gelators

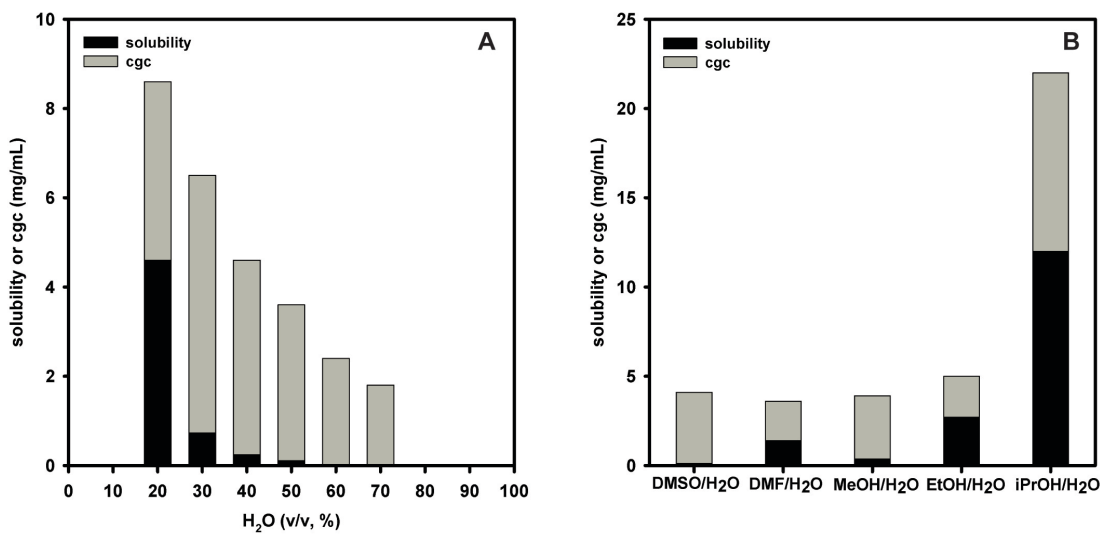


Figure S101. (A) Solubility versus cgc of **2a** in DMSO/H₂O. (B) Solubility versus cgc of **2a** in 1/1 (v/v) organic solvent/H₂O mixtures.

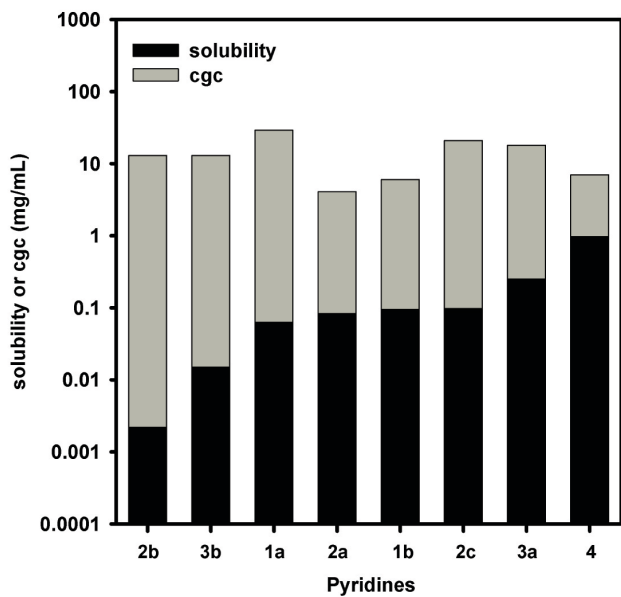


Figure S102. Solubility versus cgc of gelators **1-4** in 1/1 (v/v) DMSO/H₂O.

XIV. References

1. Chen, J.; McNeil, A. J. *J. Am. Chem. Soc.* **2008**, *130*, 16496-16497.
2. (a) Sheldrick, G.M. SHELXTL, v. 2008/4; Bruker Analytical X-ray, Madison, WI, 2008. (b) Saint Plus, v. 7.60A, Bruker Analytical X-ray, Madison, WI, 2009. (c) Sheldrick, G.M. SADABS, v. 2008/1. Program for Empirical Absorption Correction of Area Detector Data, University of Gottingen: Gottingen, Germany, 2008.
3. AreaMax 2.0.0.4 ed.; Rigaku, 2005.
4. Jade Plus 8.2 ed.; Materials Data, Inc, 1995-2007.
5. S. K. Wolff, D. J. Grimwood, J.J. McKinnon, D. Jayatilaka, M. A. Spackmen, *CrystalExplorer* 1.6, 2006, University of Western Australia, Perth, <http://www.theochem.uwa.edu.au/CrystalExplorer>. Version 2.0.
6. McKinnon J. J.; Spackman, M. A.; Mitchell, A. S. *Acta Cryst.* **2004**, *B60*, 627-668.
7. (a) McKinnon J. J.; Jayatilaka, D.; Spackman, M. A. *Chem. Commun.* **2007**, 3814-3816. (b) Spackman, M. A.; Jayatilaka, D. *Cryst. Eng. Comm.* **2009**, *11*, 19-32.
8. Lopes-Mejias, V.; Kampf, J. W.; Matzger, A. J. *J. Am. Chem. Soc.* **2009**, *131*, 4554-4555.
9. Ozeki, M.; Muroyama, A.; Kajimoto, T.; Watanabe, T.; Wakabayashi, K.; Node, M. *Synlett* **2009**, 1781-1784.
10. Washio, T.; Yamaguchi, R.; Abe, T.; Nambu, H.; Anada, M.; Hashimoto, S. *Tetrahedron* **2007**, *63*, 12037-12046.
11. Li, A.-H.; Chang, L.; Ji, X.-D.; Melman, N.; Jacobson, K. A. *Bioconjugate Chem.* **1999**, *10*, 667-677.
12. Pfister, J. R. *Synthesis* **1990**, 689-690.
13. Hafiz, I. S. A.; Ramiz, M. M. M.; Mahmoud, F. F.; Darwish, E. S. *J. Chem. Sci.* **2008**, *120*, 339-345.
14. Mio, M. J.; Kopel, L. C.; Braun, J. B.; Gadzikwa, T. L.; Hull, K. L.; Brisbois, R. G.; Markworth, C. J.; Grieco, P.A. *Org. Lett.* **2002**, *4*, 3199-3202.
15. Klapars, A.; Buchwald, S.L. *J. Am. Chem. Soc.* **2002**, *124*, 14844-14845.
16. Azagarsamy, M. A.; Sokkalingam, P.; Thayumanavan, S. *J. Am. Chem. Soc.* **2009**, *131*, 14184-14185.

17. Li, W.-S.; Yamamoto, Y.; Fukushima, T.; Saeki, A.; Seki, S.; Tagawa, S.; Masunaga, H.; Sasaki, S.; Takata, M.; Aida, T. *J. Am. Chem. Soc.* **2008**, *130*, 8886-8887.
18. Zu, L.; Zhang, S.; Xie, H.; Wang, W. *Org. Lett.* **2009**, *11*, 1627-1630.
19. Chanteau, S. H.; Tour, J. M. *Tetrahedron Lett.* **2001**, *42*, 3057-3060.
20. Spivey, A. C.; Shukla, L.; Hayler, J. F. *Org. Lett.* **2007**, *9*, 891-894.
21. Hirst, A. R.; Coates, I. A.; Boucheteau, T. R.; Miravet, J. F.; Escuder, B.; Castelletto, V.; Hamley, I. W.; Smith, D. K. *J. Am. Chem. Soc.* **2008**, *130*, 9113-9121.

Appendix 3

Appendix to Chapter 4: Dissolution Parameters Reveal Role of Structure and Solvent in Molecular Gelation

I. General Experimental

Commercially available reagents and solvents for the synthetic procedures were obtained from Sigma-Aldrich, Acros Organic, and Fisher Scientific and used as received. The syntheses reported are adapted from published literature procedures. Compounds **4a-11b** were synthesized according to previously reported procedures.¹

¹H NMR and ¹³C{H}-NMR spectra were recorded on a Varian 500 spectrometer. All chemical shifts are referenced to the residual solvent signals and previously referenced to TMS. Splitting patterns are designated as s (singlet), d (doublet), t (triplet), q (quartet), and m (multiplet).

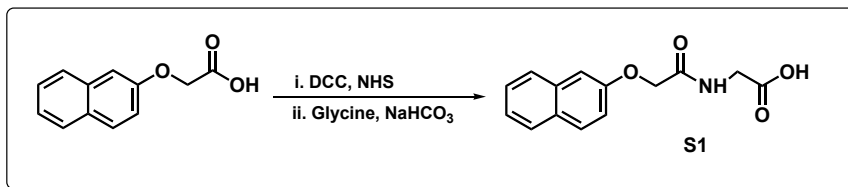
UV-Vis spectra were taken on a Perkin-Elmer Lambda 850 UV-visible Spectrometer. For peptides, all UV-Vis measurements were taken in acetonitrile and the extinction coefficients were determined at the I_{\max} . For pyridines, solvents used in UV-Vis measurements were DMSO and EtOH.

Powder X-ray diffraction (PXRD) patterns were measured in a Bruker D8 Advance diffractometer equipped with a 1.6 kW sealed tube X-ray source (Cu) and a LynxEye linear position sensitive detector. The system features a 60 mm sealed Göbel mirror that creates a highly parallel incident beam and suppresses $K\beta$ radiation. The samples were loaded onto a microscope slide at rt with a 2θ range from 5° to 50° with a step size of 0.07°.

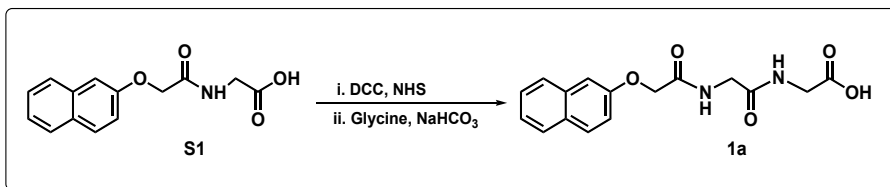
To determine the critical gelation concentration (cgc), weighed amounts of **1a-c** and **2a-c** (2 mg – 10 mg) were placed in a 4 mL vial with a starting volume of 1 mL of water (pH = 2, HCl). The mixtures were heated until clear solutions were obtained and cooled at rt until gel formation was observed. The volume of the solutions was systematically

modified by increments of 0.1 mL followed by the heat/cool procedure until an unstable gel was observed. The last concentration of a stable gel was recorded as its cgc. For each gelator, the cgc reported is the average of three independent measurements. For pyridines **4a-11b**, cgc was measured in 1/1 DMSO/H₂O and 1/2 EtOH/H₂O via heat/cool procedure.

II. Syntheses²

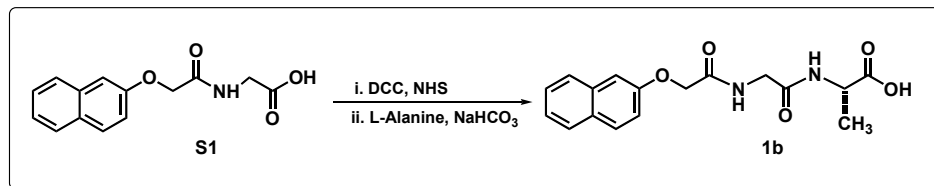


S1. In a round-bottom flask, 2-naphthoxy acetic acid (0.404 g, 1.99 mmol) and *N*-hydroxy-succinimide (NHS) (0.232 g, 2.01 mmol) were dissolved in 20 mL of CHCl₃ at rt. To this mixture, *N,N'*-dicyclohexylcarbodiimide (DCC) (0.432 g, 2.11 mmol) was added and the final mixture stirred at rt for 30 min. The precipitate was filtered off and the filtrate, which contains the intermediate, was evaporated under reduced pressure obtaining a grey solid that was submitted to the next reaction without further purification. Glycine (0.149 g, 1.99 mmol) and NaHCO₃ (0.336 g, 3.99 mmol) were dissolved in 20 mL of water at rt and the solid obtained previously was dissolved in 30 mL of acetone and added to the aqueous solution. After overnight reaction at rt, the solvent was evaporated under reduced pressure, and the residue re-dissolved in water (~10 mL). The insoluble solid was filtered off and the filtrate was acidified to pH = 3 with dilute HCl, yielding the product as a white precipitate. The solid was filtered, washed with water (3 x 10 mL), and dried under vacuum overnight (0.403 g; 78% yield).

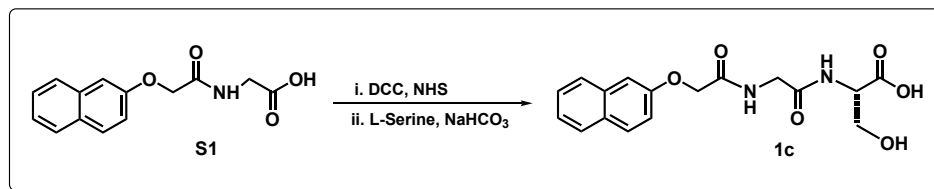


1a. In a round-bottom flask, **S1** (0.350 g, 1.35 mmol) and NHS (0.155 g, 1.35 mmol) were dissolved in 20 mL of CHCl₃ at rt. To this mixture, DCC (0.306 g, 1.49 mmol) was added and the final mixture stirred at rt for 30 min. The precipitate was filtered off and the filtrate, which contains the intermediate, was evaporated under reduced pressure obtaining a white solid that was submitted to the next reaction without further purification.

Glycine (0.101 g, 1.35 mmol) and NaHCO₃ (0.227 g, 2.70 mmol) were dissolved in 20 mL of water at rt and the solid obtained previously was dissolved in 30 mL of acetone and added to the aqueous solution. After overnight reaction at rt, the solvent was evaporated under reduced pressure, and the residue re-dissolved in water (~10 mL). The insoluble solid was filtered off and the filtrate was acidified to pH = 3 with dilute HCl, yielding the product as a white precipitate (gel-like). The solid was filtered, washed with water (3 x 10 mL), and dried under vacuum overnight (0.314 g; 74% yield).

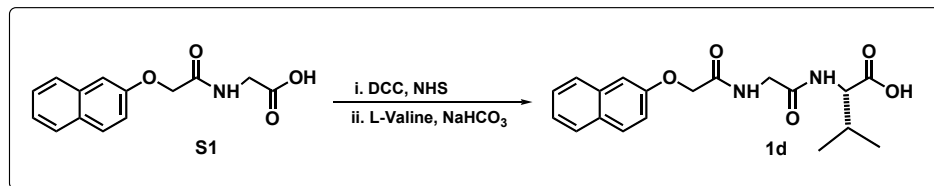


1b. In a round-bottom flask, **S1** (0.298 g, 1.15 mmol) and NHS (0.138 g, 1.20 mmol) were dissolved in 25 mL of CHCl₃ at rt. To this mixture, DCC (0.261 g, 1.27 mmol) was added and the final mixture stirred at rt for 30 min. The precipitate was filtered off and the filtrate, which contains the intermediate, was evaporated under reduced pressure obtaining a white solid that was submitted to the next reaction without further purification. L-Alanine (0.106 g, 1.19 mmol) and NaHCO₃ (0.195 g, 2.32 mmol) were dissolved in 20 mL of water at rt and the solid obtained previously was dissolved in 30 mL of acetone and added to the aqueous solution. After overnight reaction at rt, the solvent was evaporated under reduced pressure, and the residue re-dissolved in water (~10 mL). The insoluble solid was filtered off and the filtrate was acidified to pH = 3 with dilute HCl, yielding the product as a white precipitate (gel-like). The solid was filtered, washed with water (3 x 10 mL), and dried under vacuum overnight (0.295 g; 78% yield).

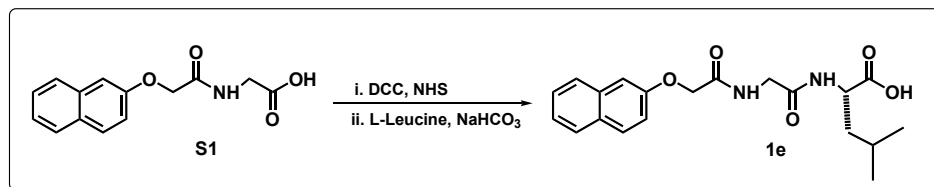


1c. In a round-bottom flask, **S1** (0.149 g, 0.575 mmol) and NHS (0.066 g, 0.573 mmol) were dissolved in 15 mL of CHCl₃ at rt. To this mixture, DCC (0.135 g, 0.654 mmol) was added and the final mixture stirred at rt for 30 min. The precipitate was filtered off and the filtrate, which contains the intermediate, was evaporated under reduced pressure obtaining a white solid that was submitted to the next reaction without further purification.

L-Serine (0.060 g, 0.57 mmol) and NaHCO₃ (0.103 g, 1.23 mmol) were dissolved in 10 mL of water at rt and the solid obtained previously was dissolved in 15 mL of acetone and added to the aqueous solution. After overnight reaction at rt, the solvent was evaporated under reduced pressure, and the residue re-dissolved in water (~10 mL). The insoluble solid was filtered off and the filtrate was acidified to pH = 3 with dilute HCl, yielding the product as a white precipitate (gel-like). The solid was filtered, washed with water (3 x 10 mL), and dried under vacuum overnight (0.153 g; 77% yield).

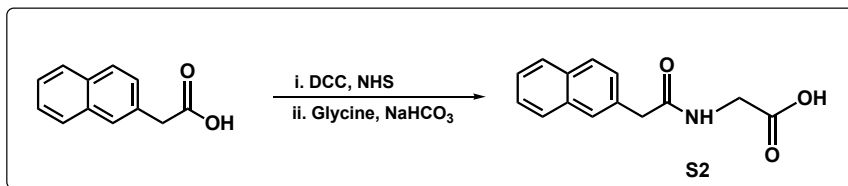


1d. In a round-bottom flask, **S1** (0.250 g, 0.964 mmol) and NHS (0.111 g, 0.964 mmol) were dissolved in 20 mL of CHCl₃ at rt. To this mixture, DCC (0.224 g, 1.06 mmol) was added and the final mixture stirred at rt for 30 min. The precipitate was filtered off and the filtrate, which contains the intermediate, was evaporated under reduced pressure obtaining a white solid that was submitted to the next reaction without further purification. L-Valine (0.117 g, 1.00 mmol) and NaHCO₃ (0.163 g, 1.94 mmol) were dissolved in 20 mL of water at rt and the solid obtained previously was dissolved in 30 mL of acetone and added to the aqueous solution. After overnight reaction at rt, the solvent was evaporated under reduced pressure, and the residue re-dissolved in water (~10 mL). The insoluble solid was filtered off and the filtrate was acidified to pH = 3 with dilute HCl, yielding the product as a white precipitate. The solid was filtered, washed with water (3 x 10 mL), and dried under vacuum overnight (0.115 g; 33% yield).

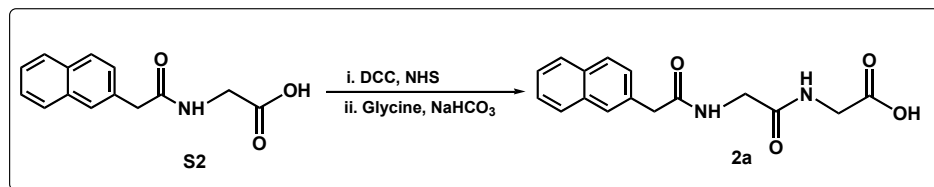


1e. In a round-bottom flask, **S1** (0.300 g, 1.16 mmol) and NHS (0.133 g, 1.16 mmol) were dissolved in 25 mL of CHCl₃ at rt. To this mixture, DCC (0.258 g, 1.28 mmol) was added and the final mixture stirred at rt for 30 min. The precipitate was filtered off and the filtrate, which contains the intermediate, was evaporated under reduced pressure obtaining a white solid that was submitted to the next reaction without further purification.

L-Leucine (0.158 g, 1.16 mmol) and NaHCO₃ (0.195 g, 2.32 mmol) were dissolved in 20 mL of water at rt and the solid obtained previously was dissolved in 30 mL of acetone and added to the aqueous solution. After overnight reaction at rt, the solvent was evaporated under reduced pressure, and the residue re-dissolved in water (~10 mL). The insoluble solid was filtered off and the filtrate was acidified to pH = 3 with dilute HCl, yielding the product as a white precipitate. The solid was filtered, washed with water (3 x 10 mL), and dried under vacuum overnight (0.385 g; 89% yield).

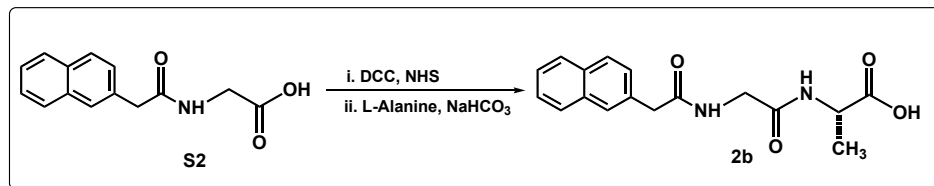


S2. In a round-bottom flask, 2-naphthyl acetic acid (0.999 g, 5.36 mmol) and NHS (0.659 g, 5.73 mmol) were dissolved in 20 mL of CHCl₃ at rt. To this mixture, DCC (1.11 g, 5.39 mmol) was added and the final mixture stirred at rt for 30 min. The precipitate was filtered off and the filtrate, which contains the intermediate, was evaporated under reduced pressure obtaining a white solid that was submitted to the next reaction without further purification. Glycine (0.409 g, 5.45 mmol) and NaHCO₃ (0.902 g, 10.74 mmol) were dissolved in 40 mL of water at rt and the solid obtained previously was dissolved in 60 mL of acetone and added to the aqueous solution. After overnight reaction at rt, the solvent was evaporated under reduced pressure, and the residue re-dissolved in water (~10 mL). The insoluble solid was filtered off and the filtrate was acidified to pH = 3 with dilute HCl, yielding the product as a white precipitate. The solid was filtered, washed with water (3 x 10 mL), and dried under vacuum overnight (0.999 g; 77% yield).

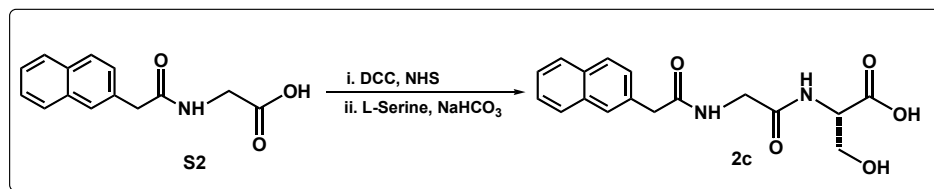


2a. In a round-bottom flask, **S2** (0.296 g, 1.22 mmol) and NHS (0.144 g, 1.25 mmol) were dissolved in 30 mL of CHCl₃ at rt. To this mixture, DCC (0.278 g, 1.35 mmol) was added and the final mixture stirred at rt for 30 min. The precipitate was filtered off and the filtrate, which contains the intermediate, was evaporated under reduced pressure obtaining a white solid that was submitted to the next reaction without further purification.

Glycine (0.093 g, 1.24 mmol) and NaHCO₃ (0.224 g, 2.67 mmol) were dissolved in 20 mL of water at rt and the solid obtained previously was dissolved in 30 mL of acetone and added to the aqueous solution. After overnight reaction at rt, the solvent was evaporated under reduced pressure, and the residue re-dissolved in water (~10 mL). The insoluble solid was filtered off and the filtrate was acidified to pH = 3 with dilute HCl, yielding the product as a white precipitate. The solid was filtered, washed with water (3 x 10 mL), and dried under vacuum overnight (0.219 g; 60% yield).

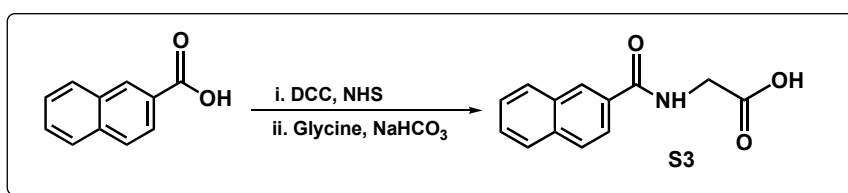


2b. In a round-bottom flask, **S2** (0.202 g, 0.830 mmol) and NHS (0.080 g, 0.699 mmol) were dissolved in 20 mL of CHCl₃ at rt. To this mixture, DCC (0.183 g, 0.888 mmol) was added and the final mixture stirred at rt for 30 min. The precipitate was filtered off and the filtrate, which contains the intermediate, was evaporated under reduced pressure obtaining a white solid that was submitted to the next reaction without further purification. L-Alanine (0.076 g, 0.853 mmol) and NaHCO₃ (0.146 g, 1.74 mmol) were dissolved in 20 mL of water at rt and the solid obtained previously was dissolved in 30 mL of acetone and added to the aqueous solution. After overnight reaction at rt, the solvent was evaporated under reduced pressure, and the residue re-dissolved in water (~10 mL). The insoluble solid was filtered off and the filtrate was acidified to pH = 3 with dilute HCl. The solid did not precipitate after acidification. Instead, the solution was kept overnight at rt to induce precipitation. The solid was filtered, washed with water (3 x 10 mL), and dried under vacuum overnight (0.078 g; 35% yield).

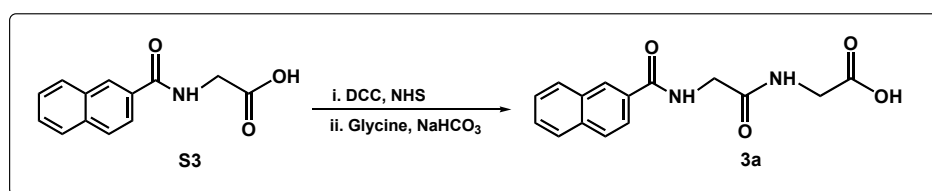


2c. In a round-bottom flask, **S2** (0.299 g, 1.23 mmol) and NHS (0.143g, 1.24 mmol) were dissolved in 25 mL of CHCl₃ at rt. To this mixture, DCC (0.286 g, 1.39 mmol) was added and the final mixture stirred at rt for 30 min. The precipitate was filtered off and the filtrate, which contains the intermediate, was evaporated under reduced pressure

obtaining a white solid that was submitted to the next reaction without further purification. L-Serine (0.128 g, 1.22 mmol) and NaHCO₃ (0.218 g, 2.59 mmol) were dissolved in 20 mL of water at rt and the solid obtained previously was dissolved in 30 mL of acetone and added to the aqueous solution. After overnight reaction at rt, the solvent was evaporated under reduced pressure, and the residue re-dissolved in water (~10 mL). The insoluble solid was filtered off and the filtrate was acidified to pH = 3 with dilute HCl. The solid did not precipitate after acidification. Instead, the solution was kept overnight at rt to induce precipitation. The solid was filtered, washed with water (3 x 10 mL), and dried under vacuum overnight (0.215 g; 53% yield).

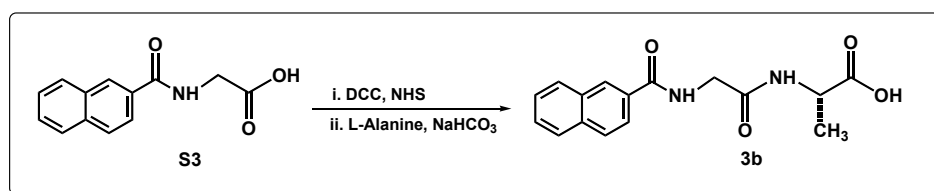


S3. In a round-bottom flask, 2-naphthoic acid (0.999 g, 5.80 mmol) and NHS (0.666 g, 5.79 mmol) were dissolved in 50 mL of CHCl₃ at rt. To this mixture, DCC (1.34 g, 6.50 mmol) was added and the final mixture stirred at rt for 30 min. The precipitate was filtered off and the filtrate, which contains the intermediate, was evaporated under reduced pressure obtaining a white solid that was submitted to the next reaction without further purification. Glycine (0.436 g, 5.81 mmol) and NaHCO₃ (0.985 g, 11.72 mmol) were dissolved in 40 mL of water at rt and the solid obtained previously was dissolved in 60 mL of acetone and added to the aqueous solution. After overnight reaction at rt, the solvent was evaporated under reduced pressure, and the residue re-dissolved in water (~10 mL). The insoluble solid was filtered off and the filtrate was acidified to pH = 3 with dilute HCl, yielding the product as a white precipitate. The solid was filtered, washed with water (3 x 10 mL), and dried under vacuum overnight (1.083 g; 81% yield).

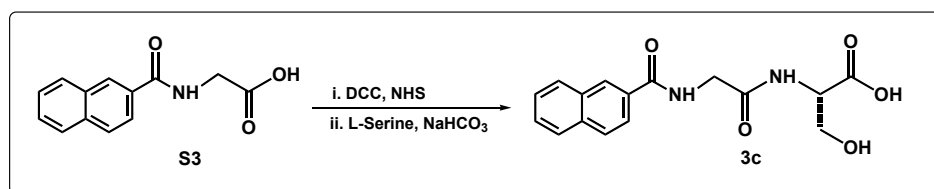


3a. In a round-bottom flask, **S3** (0.150 g, 0.654 mmol) and NHS (0.0860 g, 0.748 mmol) were dissolved in 15 mL of CHCl₃ at rt. To this mixture, DCC (0.158 g, 0.767 mmol) was added and the final mixture stirred at rt for 30 min. The precipitate was filtered off and

the filtrate, which contains the intermediate, was evaporated under reduced pressure obtaining a white solid that was submitted to the next reaction without further purification. Glycine (0.0670 g, 0.893 mmol) and NaHCO₃ (0.145 g, 1.73 mmol) were dissolved in 15 mL of water at rt and the solid obtained previously was dissolved in 20 mL of acetone and added to the aqueous solution. After overnight reaction at rt, the solvent was evaporated under reduced pressure, and the residue re-dissolved in water (~10 mL). The insoluble solid was filtered off and the filtrate was acidified to pH = 3 with dilute HCl, yielding the product as a white precipitate. The solid was filtered, washed with water (3 x 10 mL), and dried under vacuum (0.073 g; 39% yield).



3b. In a round-bottom flask, **S3** (0.300 g, 1.31 mmol) and NHS (0.151 g, 1.31 mmol) were dissolved in 20 mL of CHCl₃ at rt. To this mixture, DCC (0.297 g, 1.44 mmol) was added and the final mixture stirred at rt for 30 min. The precipitate was filtered off and the filtrate, which contains the intermediate, was evaporated under reduced pressure obtaining a white solid that was submitted to the next reaction without further purification. L-Alanine (0.117 g, 1.31 mmol) and NaHCO₃ (0.220 g, 2.62 mmol) were dissolved in 20 mL of water at rt and the solid obtained previously was dissolved in 30 mL of acetone and added to the aqueous solution. After overnight reaction at rt, the solvent was evaporated under reduced pressure, and the residue re-dissolved in water (~10 mL). The insoluble solid was filtered off and the filtrate was acidified to pH = 3 with dilute HCl, yielding the product as a white precipitate. The solid was filtered, washed with water (3 x 10 mL), and dried under vacuum overnight (0.105 g; 27% yield).



3c. In a round-bottom flask, **S3** (0.300 g, 1.31 mmol) and NHS (0.151 g, 1.31 mmol) were dissolved in 20 mL of CHCl₃ at rt. To this mixture, DCC (0.297 g, 1.44 mmol) was added and the final mixture stirred at rt for 30 min. The precipitate was filtered off and

the filtrate, which contains the intermediate, was evaporated under reduced pressure obtaining a white solid that was submitted to the next reaction without further purification. L-Serine (0.138 g, 1.31 mmol) and NaHCO_3 (0.220 g, 2.62 mmol) were dissolved in 20 mL of water at rt and the solid obtained previously was dissolved in 30 mL of acetone and added to the aqueous solution. After overnight reaction at rt, the solvent was evaporated under reduced pressure, and the residue re-dissolved in water (~10 mL). The insoluble solid was filtered off and the filtrate was acidified to pH = 3 with dilute HCl, yielding the product as a white precipitate. The solid was filtered, washed with water (3 x 10 mL), and dried under vacuum overnight (0.289 g; 71% yield).

III. ^1H NMR and ^{13}C NMR Spectra.

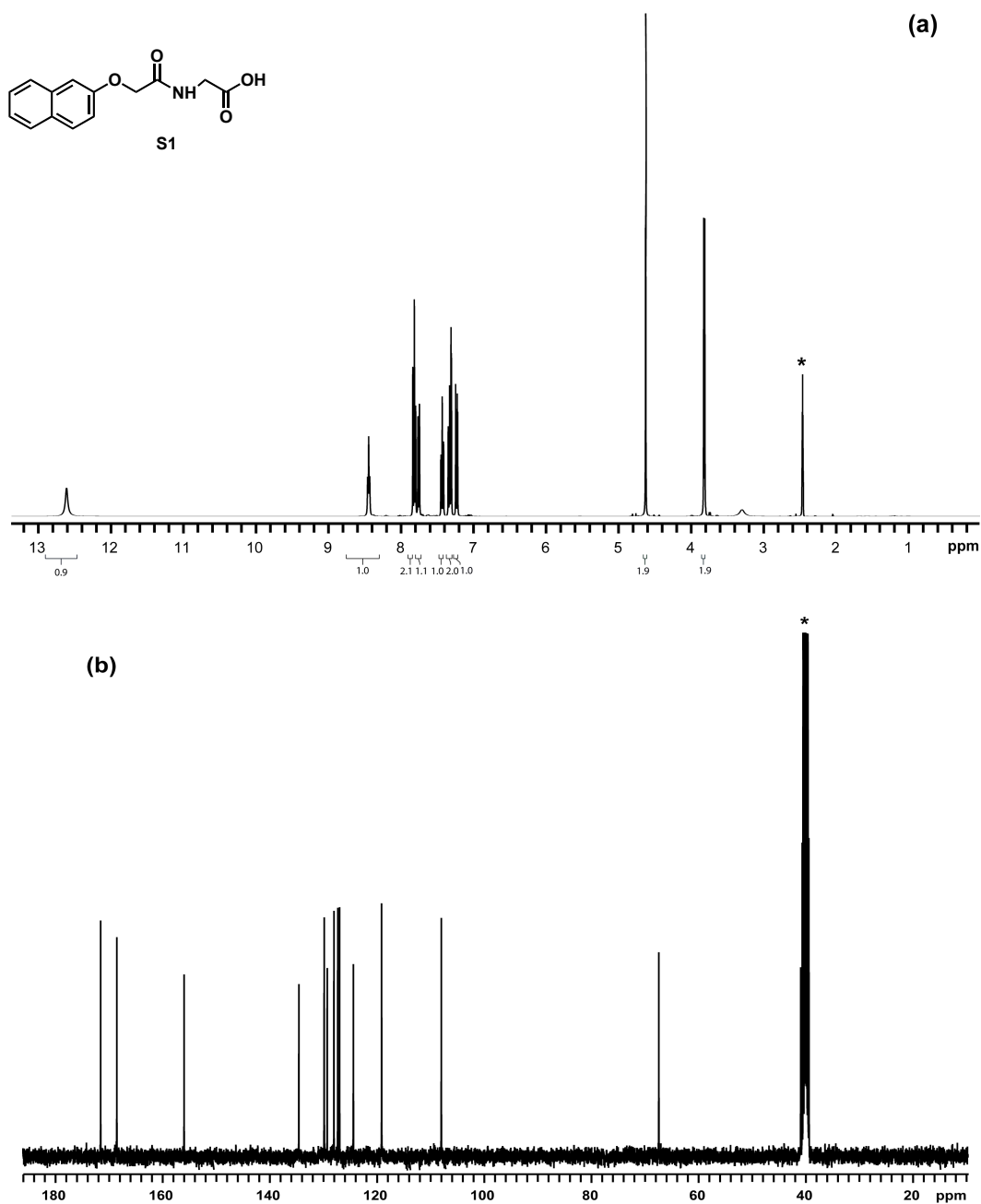


Figure S1. (a) ^1H NMR and (b) ^{13}C NMR spectra of **S1**. ^1H NMR (DMSO- d_6 , 500 MHz): d (ppm) 12.64 (1H, s), 8.49-8.46 (1H, t, $J = 6.0$ Hz), 7.86-7.83 (2H, t, $J = 9.0$ Hz), 7.78 (1H, d, $J = 8.0$ Hz), 7.48-7.44 (1H, m), 7.38-7.33 (2H, m), 7.27-7.25 (1H, dd, $J = 6.8$ and 2.4 Hz), 4.65 (2H, s), 3.85 (2H, d, $J = 6.0$ Hz). ^{13}C NMR (DMSO- d_6 , 100 MHz): d (ppm) 171.49, 168.48, 155.93, 134.51, 129.78, 129.22, 127.96, 126.91, 124.33, 119.07, 107.93, 67.34, 40.86.

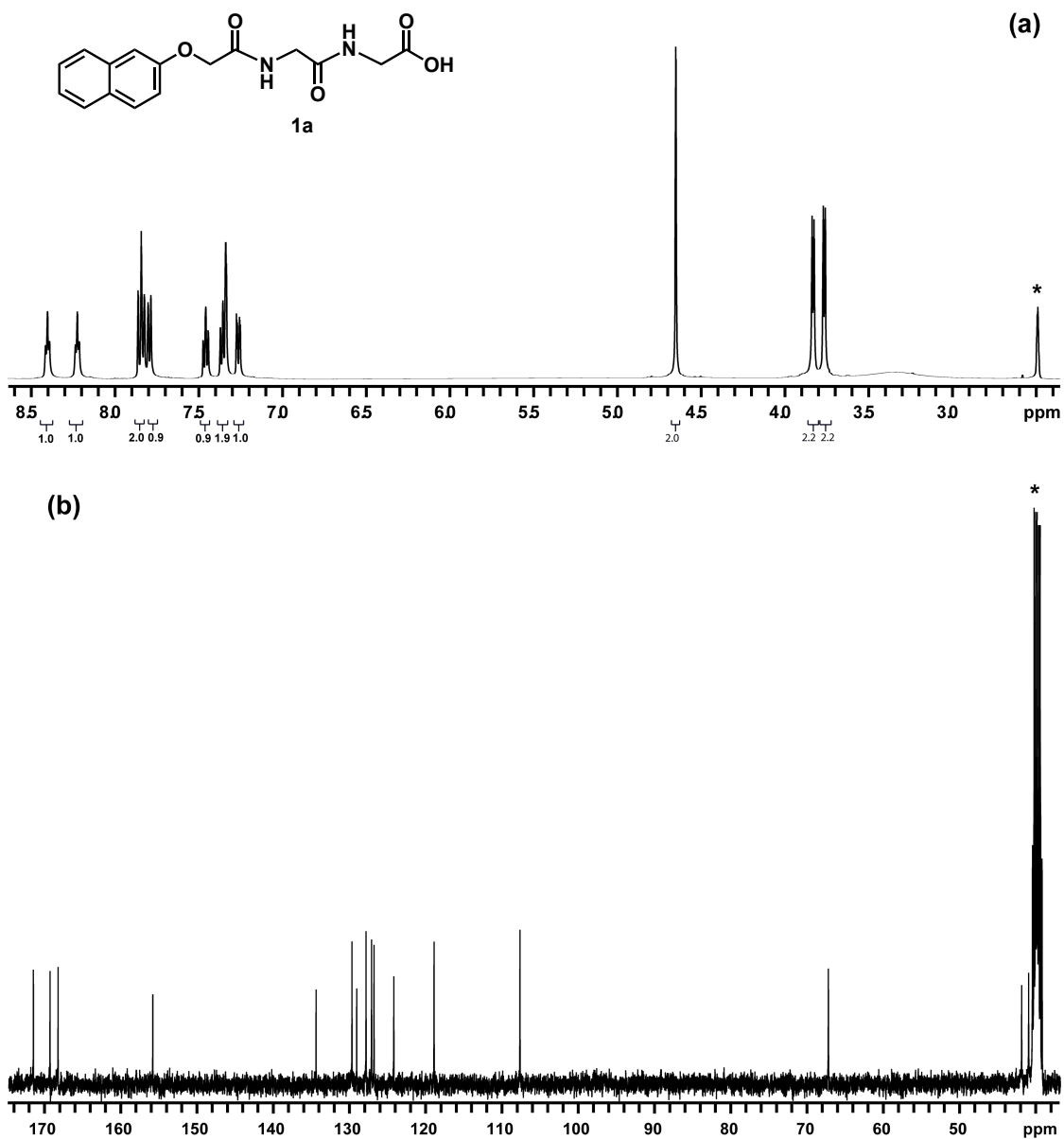


Figure S2. (a) ^1H NMR and (b) ^{13}C NMR spectra of **1a**. ^1H NMR (DMSO- d_6 , 500 MHz): d (ppm) 8.42-8.39 (1H, t, $J = 5.5$ Hz), 8.24-8.22 (1H, t, $J = 6.0$ Hz), 7.86-7.83 (2H, t, $J = 9.5$ Hz), 7.79 (1H, d, $J = 8.0$ Hz), 7.48-7.45 (1H, t, $J = 8.0$ Hz), 7.37-7.34 (2H, m), 7.28-7.25 (1H, dd, $J = 8.5$ and 2.5 Hz), 4.65 (2H, s), 3.83 (2H, d, $J = 6.0$ Hz), 3.76 (2H, d, $J = 5.5$ Hz). ^{13}C NMR (DMSO- d_6 , 100 MHz): d (ppm) 171.59, 169.41, 168.35, 155.93, 134.52, 128.81, 129.19, 127.96, 127.24, 126.92, 124.32, 119.04, 107.78, 67.33, 41.99, 41.07.

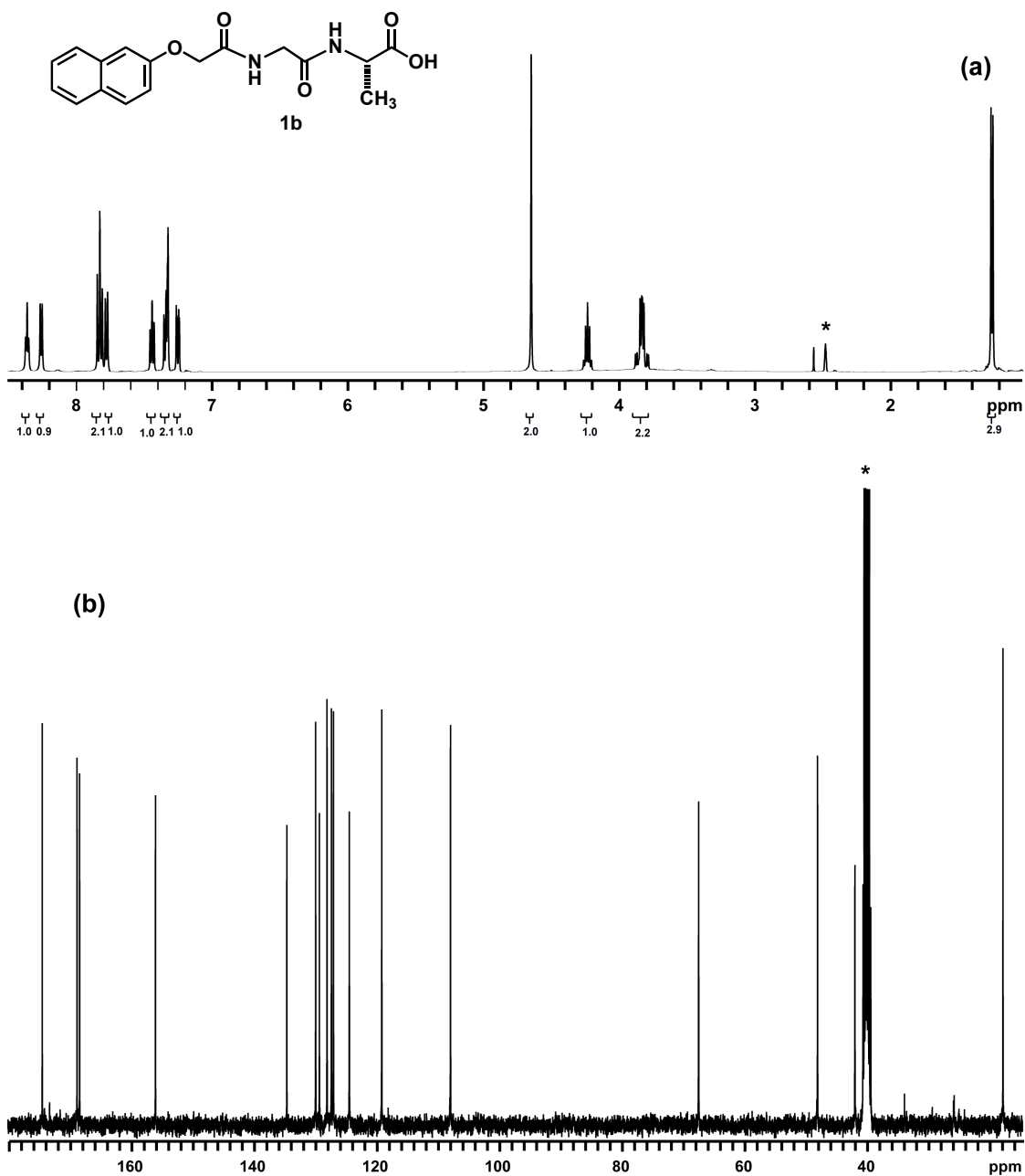


Figure S3. (a) ^1H NMR and (b) ^{13}C NMR spectra of **1b**. ^1H NMR (DMSO- d_6 , 500 MHz): d (ppm) 8.38-8.36 (1H, t, J = 6.0 Hz), 8.26 (1H, d, J = 7.5 Hz), 7.86-7.82 (2H, t, J = 9.0 Hz), 7.78 (1H, d, J = 10 Hz), 7.47-7.44 (1H, t, J = 7.0 Hz), 7.36-7.33 (2H, m), 7.27-7.25 (1H, dd, J = 8.5 and 2.5 Hz), 4.66 (2H, s), 4.27-4.21 (1H, m), 3.89-3.79 (2H, m), 1.26 (3H, d, J = 7.5 Hz). ^{13}C NMR (DMSO- d_6 , 100 MHz): d (ppm) 174.41, 168.73, 168.31, 155.94, 134.51, 129.81, 129.20, 127.95, 127.24, 126.91, 124.32, 119.02, 107.81, 67.34, 47.94, 41.85, 17.69.

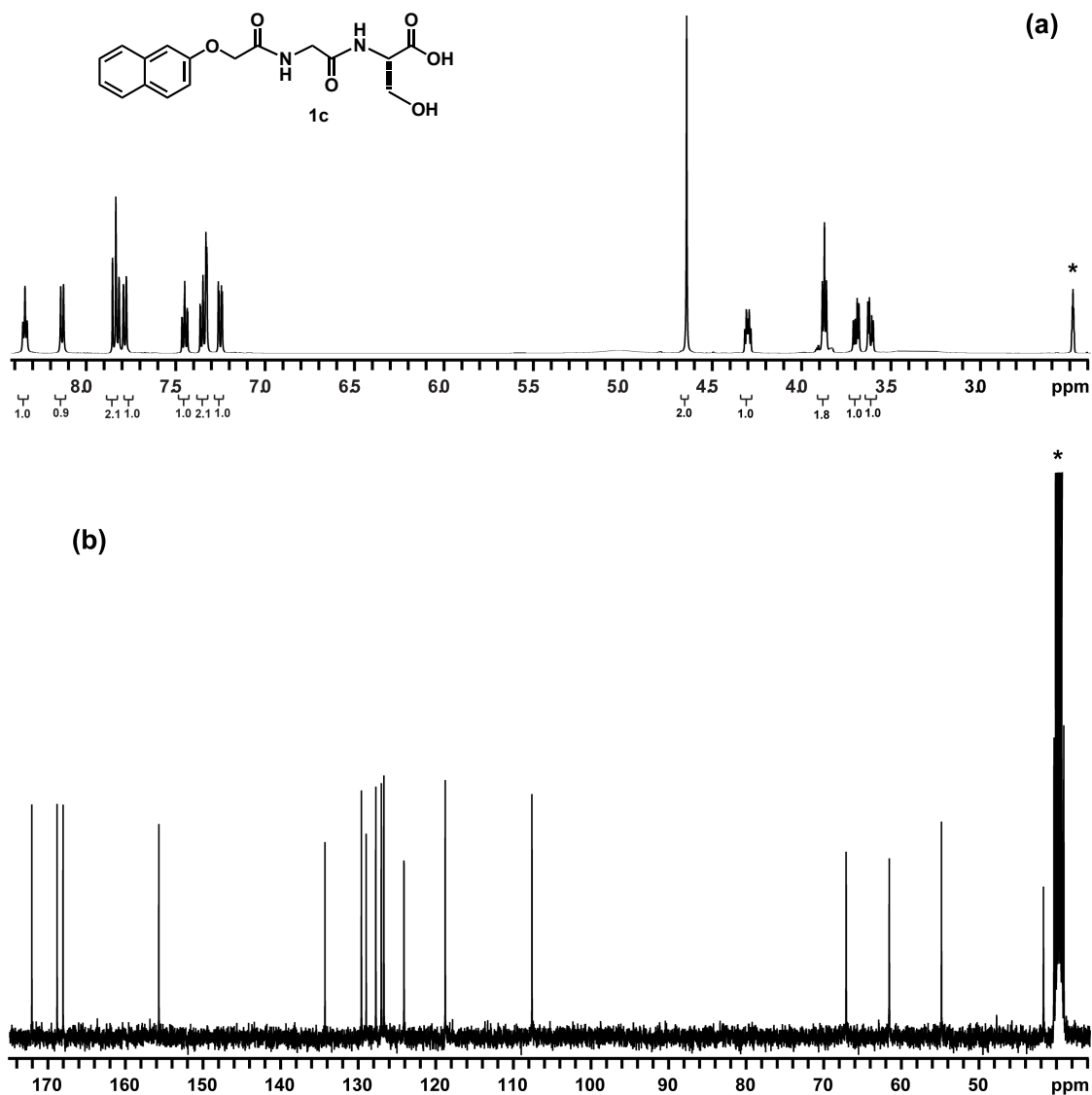


Figure S4. (a) ^1H NMR and (b) ^{13}C NMR spectra of **1c**. ^1H NMR (DMSO- d_6 , 500 MHz): d (ppm) 8.36-8.34 (1H, t, $J = 5.5$ Hz), 8.14 (1H, d, $J = 8.0$ Hz), 7.86-7.82 (2H, t, $J = 9.0$ Hz), 7.79 (1H, d, $J = 8.0$ Hz), 7.47-7.44 (1H, m), 7.37-7.33 (2H, m), 7.27-7.25 (1H, dd, $J = 9.0$ and 2.5 Hz), 4.65 (2H, s), 4.32-4.30 (1H, m), 3.89-3.87 (2H, t, $J = 6.0$ Hz), 3.72-3.69 (1H, m), 3.64-3.61 (1H, m). ^{13}C NMR (DMSO- d_6 , 100 MHz): d (ppm) 172.29, 169.03, 168.21, 155.93, 134.51, 129.81, 129.19, 127.96, 127.25, 126.92, 124.33, 119.02, 107.83, 67.34, 61.78, 55.05, 41.91.

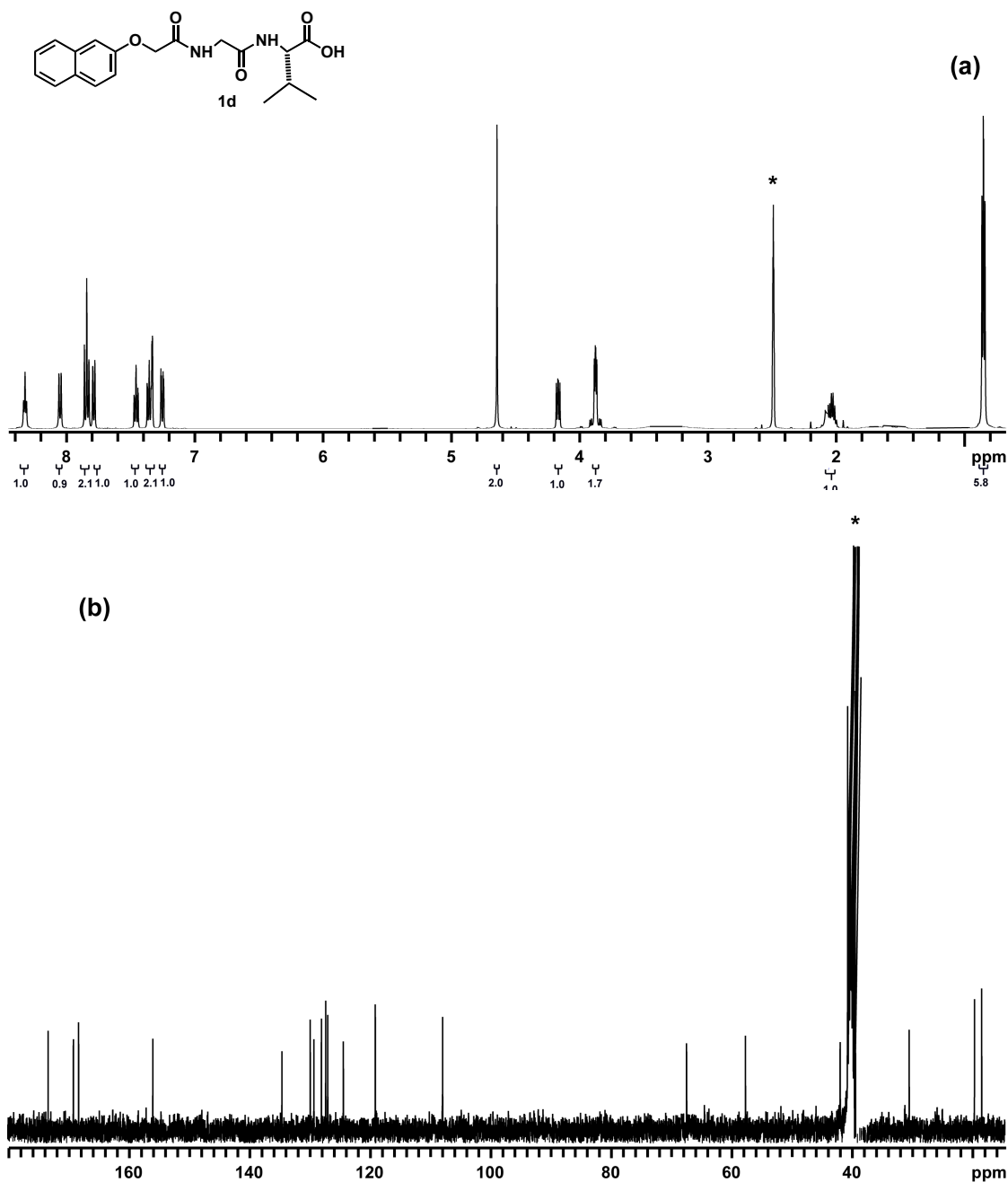


Figure S5. (a) ^1H NMR and (b) ^{13}C NMR spectra of **1d**. ^1H NMR (DMSO- d_6 , 500 MHz): d (ppm) 8.34-8.27 (1H, t, $J = 6.0$ Hz), 8.06-8.04 (1H, d, $J = 9.0$ Hz), 7.86-7.83 (2H, t, $J = 9.0$ Hz), 7.78 (1H, d, $J = 8.0$ Hz), 7.47-7.44 (1H, m), 7.37-7.33 (2H, m), 7.26-7.24 (1H, m), 4.64 (2H, s), 4.18-4.15 (1H, q, $J = 6.0$ Hz), 3.89-3.87 (2H, m), 2.05-2.01 (1H, m), 0.86-0.84 (6H, t, $J = 5.5$ Hz). ^{13}C NMR (DMSO- d_6 , 100 MHz): d (ppm) 173.32, 169.12, 168.26, 155.94, 134.51, 129.81, 129.21, 127.95, 127.24, 126.90, 124.32, 119.01, 107.83, 67.35, 57.57, 41.85, 30.39, 19.54, 18.36.

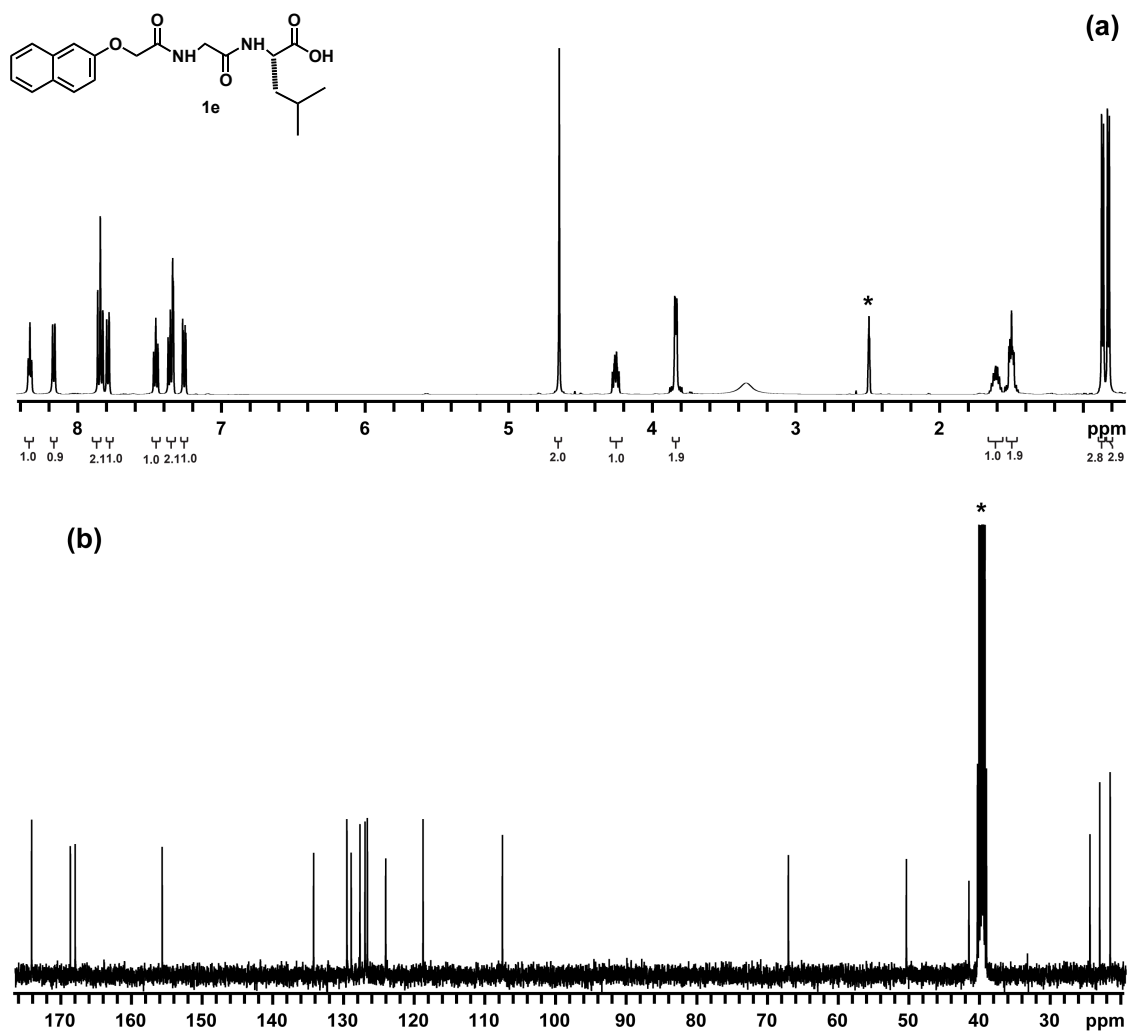


Figure S6. (a) ¹H NMR and (b) ¹³C NMR spectra of **1e**. ¹H NMR (DMSO-*d*₆, 500 MHz): d (ppm) 8.34-8.32 (1H, t, *J* = 6.0 Hz), 8.16 (1H, d, *J* = 8.0 Hz), 7.86-7.82 (2H, t, *J* = 9.0 Hz), 7.79 (1H, d, *J* = 8.0 Hz), 7.47-7.44 (1H, m), 7.37-7.33 (2H, m), 7.27-7.25 (1H, dd, *J* = 8.5 and 2.5 Hz), 4.65 (2H, s), 4.28-4.23 (1H, m), 3.84-3.83 (2H, dd, *J* = 2.0 and 6.0 Hz), 1.62-1.58 (1H, m), 1.52-1.48 (2H, m), 0.86 (3H, d, *J* = 6.5 Hz), 0.82 (3H, d, *J* = 6.5 Hz). ¹³C NMR (DMSO-*d*₆, 100 MHz): d (ppm) 174.42, 168.94, 168.29, 155.94, 134.51, 129.81, 129.19, 127.95, 127.24, 126.90, 124.31, 119.02, 107.79, 67.33, 50.63, 41.78, 24.65, 23.27, 21.79.

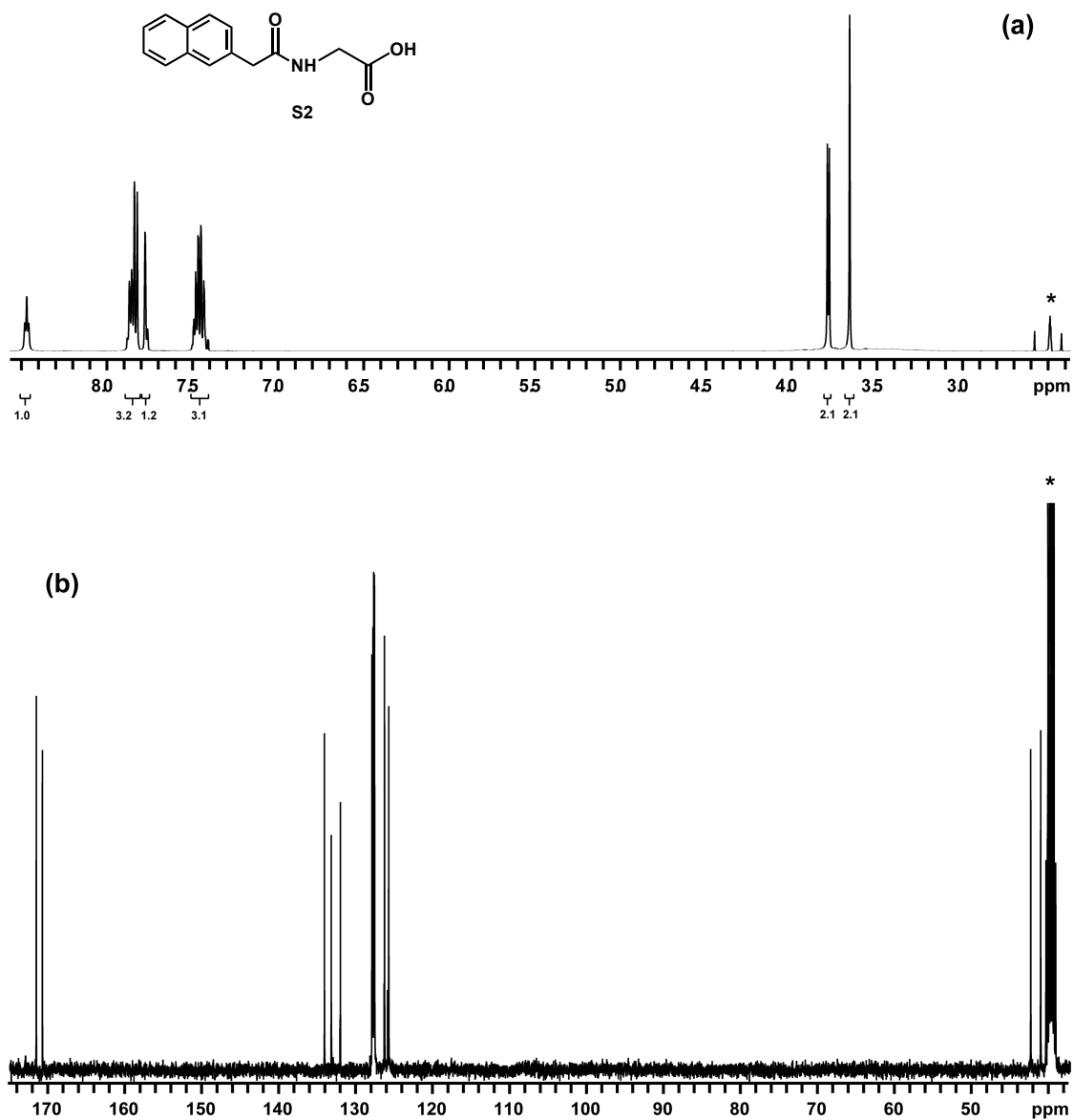


Figure S7. (a) ^1H NMR and (b) ^{13}C NMR spectra of **S2**. ^1H NMR (DMSO- d_6 , 500 MHz): d (ppm) 8.48-8.46 (1H, t, $J = 6.0$ Hz), 7.87-7.82 (3H, m), 7.78 (1H, s), 7.49-7.43 (3H, m), 3.79 (2H, d, $J = 6.0$ Hz), 3.66 (2H, s). ^{13}C NMR (DMSO- d_6 , 100 MHz): d (ppm) 171.74, 170.95, 134.30, 133.42, 132.22, 128.14, 128.00, 127.91, 127.81, 127.78, 126.49, 125.95, 42.54, 41.25.

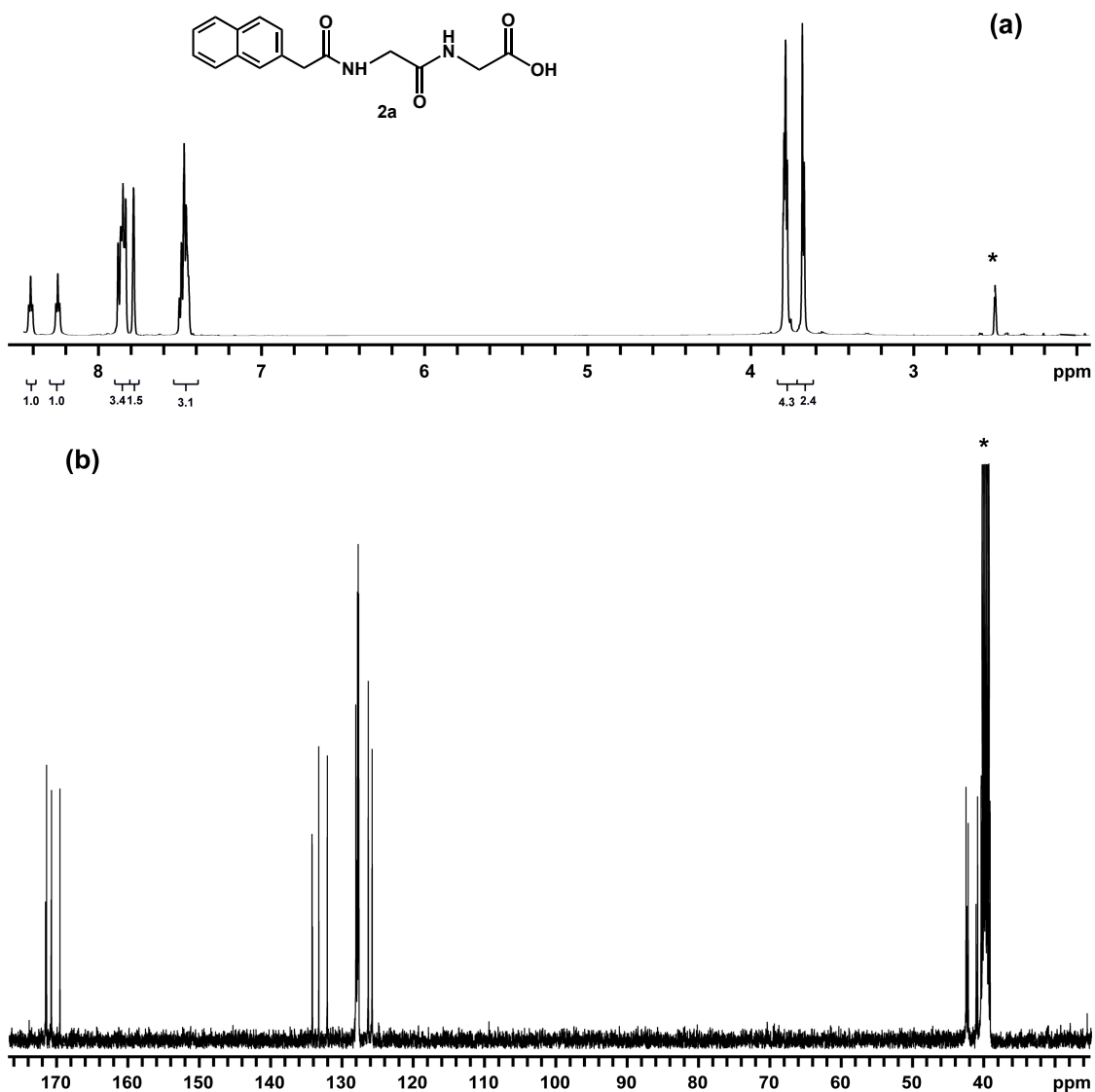


Figure S8. (a) ^1H NMR and (b) ^{13}C NMR spectra of **2a**. ^1H NMR (DMSO- d_6 , 500 MHz): d (ppm) 8.42-8.39 (1H, t, $J = 6.0$ Hz), 8.25-8.23 (1H, t, $J = 6.0$ Hz), 7.87-7.82 (3H, m), 7.77 (1H, s), 7.49-7.44 (3H, m), 3.79-3.76 (4H, m), 3.66 (2H, d, $J = 6.0$ Hz). ^{13}C NMR (DMSO- d_6 , 100 MHz): d (ppm) 171.34, 170.90, 169.60, 134.36, 133.42, 132.22, 128.22, 128.14, 127.99, 127.90, 127.85, 126.47, 125.93, 42.67, 42.35, 41.04.

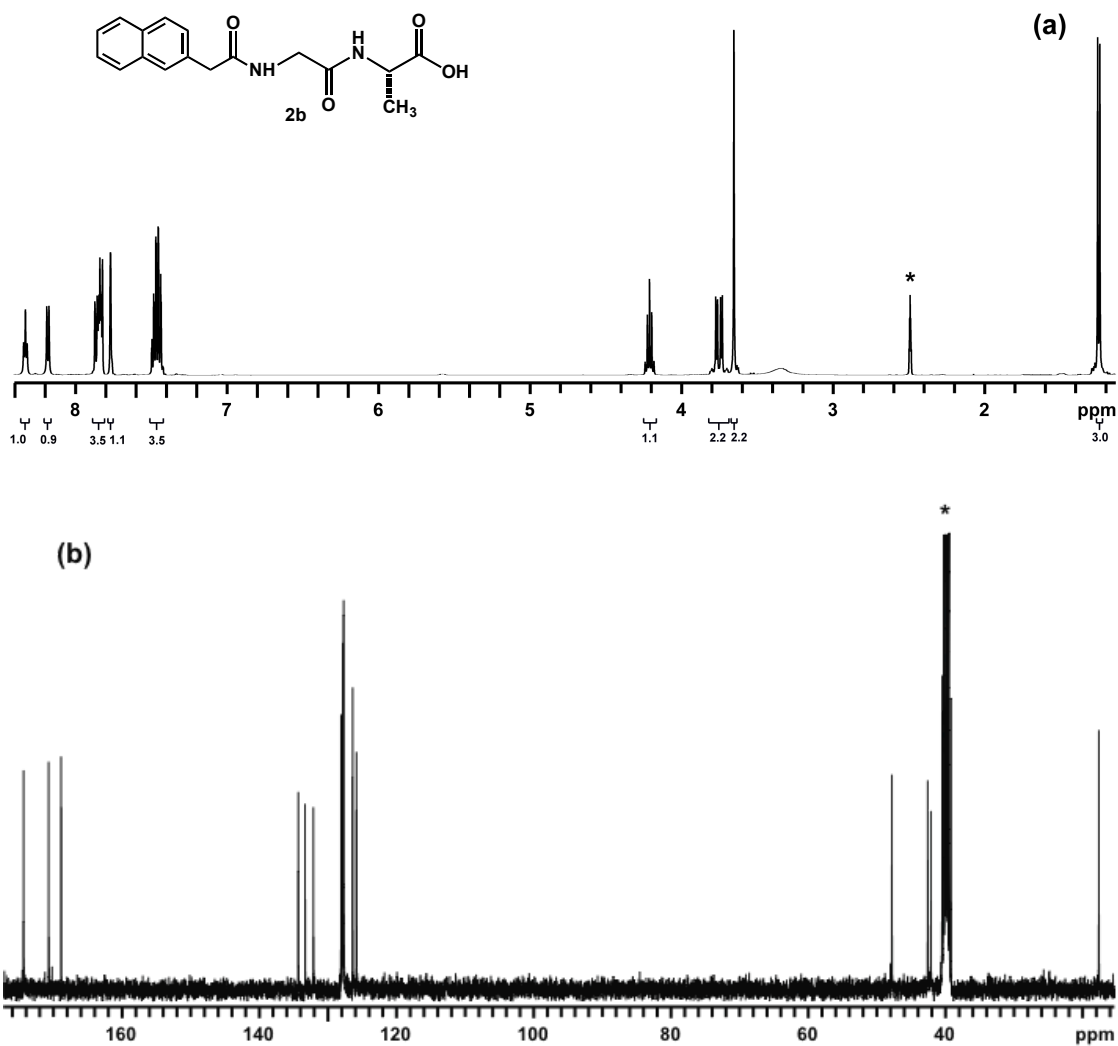


Figure S9. (a) ¹H NMR and (b) ¹³C NMR spectra of **2b**. ¹H NMR (DMSO-*d*₆, 500 MHz): d (ppm) 8.34-8.32 (1H, t, *J* = 6.0 Hz), 8.18 (1H, d, *J* = 7.0 Hz), 7.87-7.82 (3H, m), 7.76 (1H, s), 7.49-7.43 (3H, m), 4.22-4.19 (1H, t, *J* = 7.5 Hz), 3.77-3.73 (2H, dd, *J* = 6.0 Hz), 3.65 (2H, s), 1.25-1.23 (3H, d, *J* = 7.5 Hz). ¹³C NMR (DMSO-*d*₆, 100 MHz): d (ppm) 174.44, 170.79, 168.96, 134.41, 133.41, 132.21, 128.17, 128.00, 127.90, 127.82, 127.79, 126.48, 125.94, 47.88, 42.66, 42.19, 17.72.

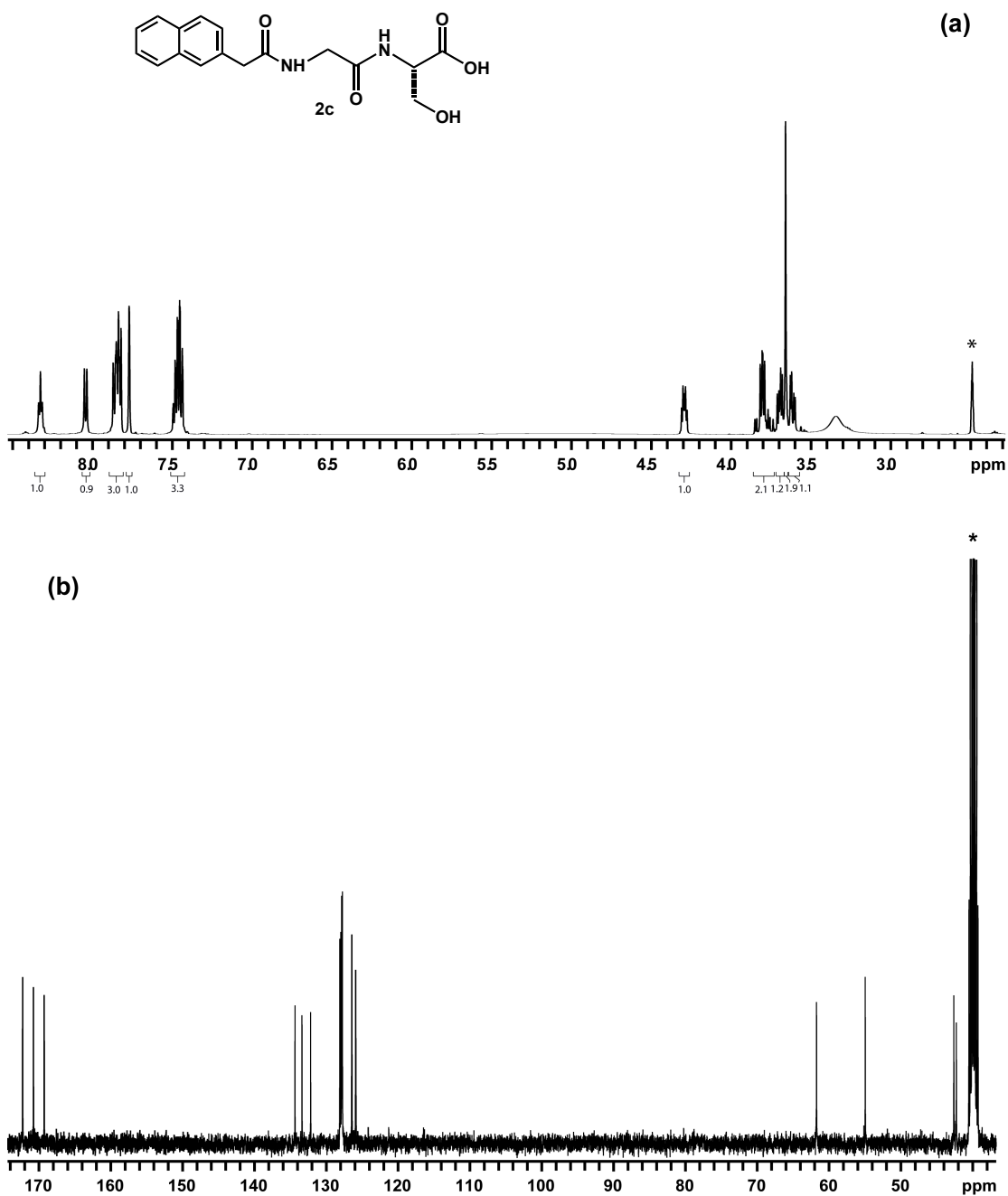


Figure S10. (a) ¹H NMR and (b) ¹³C NMR spectra of **2c**. ¹H NMR (DMSO-*d*₆, 500 MHz): d (ppm) 8.34-8.31 (1H, t, *J* = 11 Hz), 8.04 (1H, d, *J* = 8.0 Hz), 7.87-7.82 (3H, m), 7.77 (1H, s), 7.49-7.44 (3H, m), 4.31-4.28 (1H, m), 3.85-3.74 (2H, m), 3.71-3.69 (1H, m), 3.66 (2H, s), 3.63-3.60 (1H, m). ¹³C NMR (DMSO-*d*₆, 100 MHz): d (ppm) 172.31, 170.81, 169.31, 134.39, 133.42, 132.12, 128.16, 128.02, 127.90, 127.83, 127.79, 126.48, 125.94, 61.77, 54.99, 42.66, 42.31.

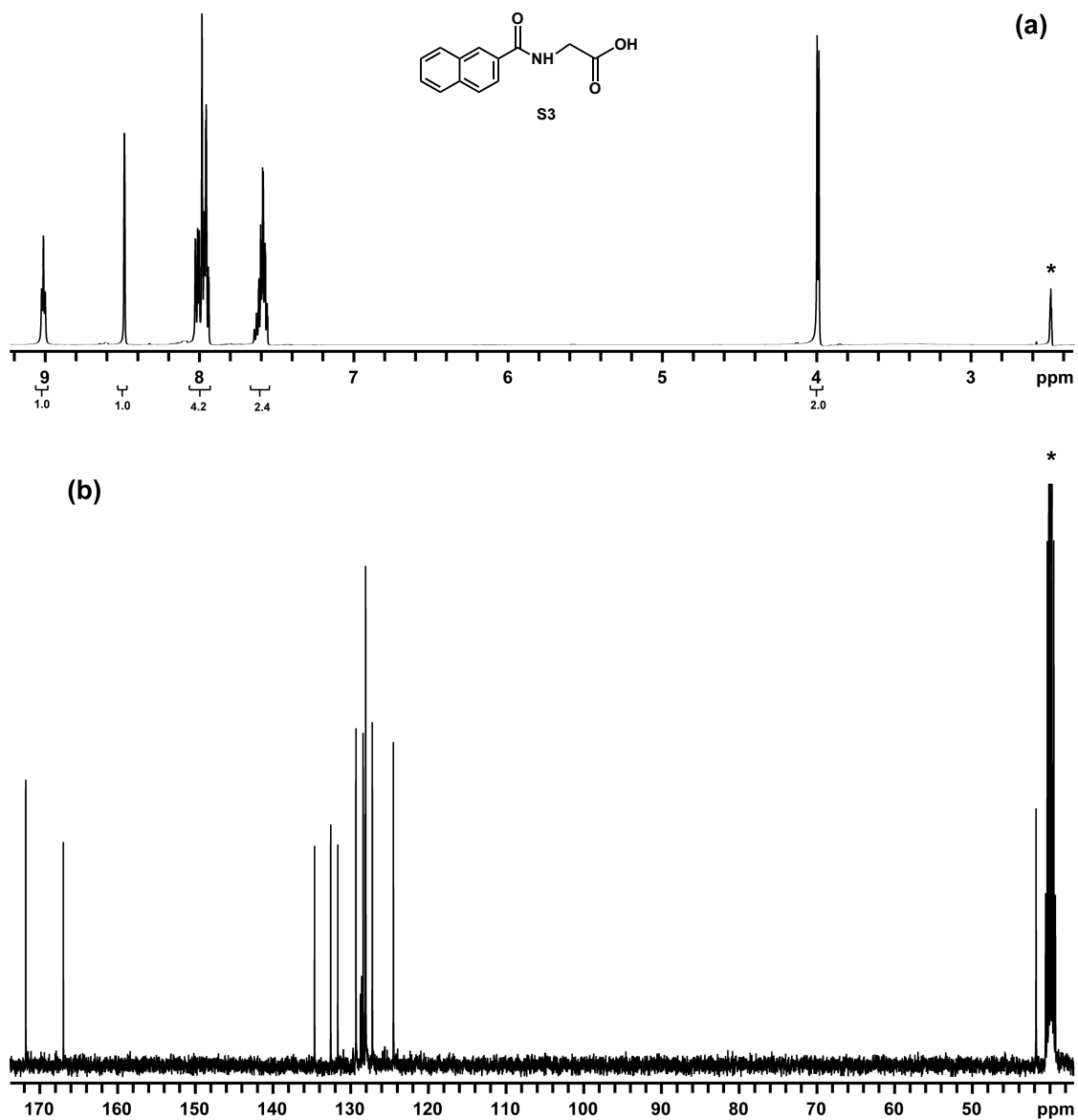


Figure S11. (a) ^1H NMR and (b) ^{13}C NMR spectra of **S3**. ^1H NMR (DMSO- d_6 , 500 MHz): d (ppm) 9.03-9.01 (1H, t, $J = 6.0$ Hz), 8.49 (1H, s), 8.04-7.95 (4H, m), 7.64-7.57 (2H, m), 4.00-3.99 (2H, d, $J = 6.0$ Hz). ^{13}C NMR (DMSO- d_6 , 100 MHz): d (ppm) 171.82, 166.98, 134.65, 132.57, 131.66, 129.32, 128.39, 128.13, 128.08, 128.07, 127.21, 124.51, 41.79.

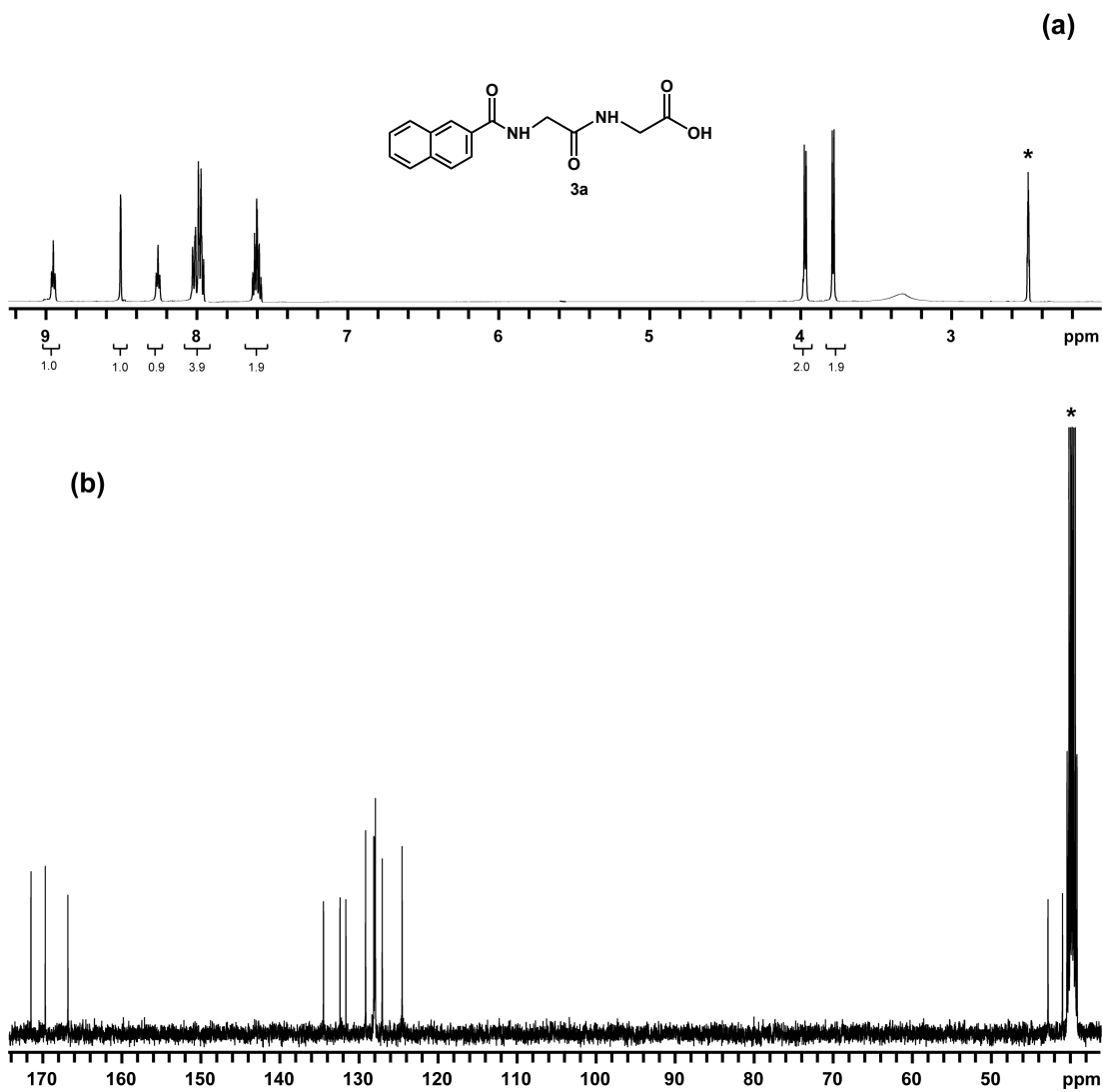


Figure S12. (a) ^1H NMR and (b) ^{13}C NMR spectra of **3a**. ^1H NMR (DMSO- d_6 , 500 MHz): d (ppm) 8.96-8.94 (1H, t, $J = 6.0$ Hz), 8.51 (1H, s), 8.27-8.25 (1H, t, $J = 6.0$ Hz), 8.03-7.95 (4H, m), 7.63-7.57 (2H, m), 3.97 (2H, d, $J = 6.0$ Hz), 3.78 (2H, d, $J = 6.0$ Hz). ^{13}C NMR (DMSO- d_6 , 100 MHz): d (ppm) 171.64, 169.83, 166.96, 134.63, 132.54, 131.79, 129.30, 128.26, 128.18, 128.09, 128.06, 127.19, 124.68, 42.96, 41.12.

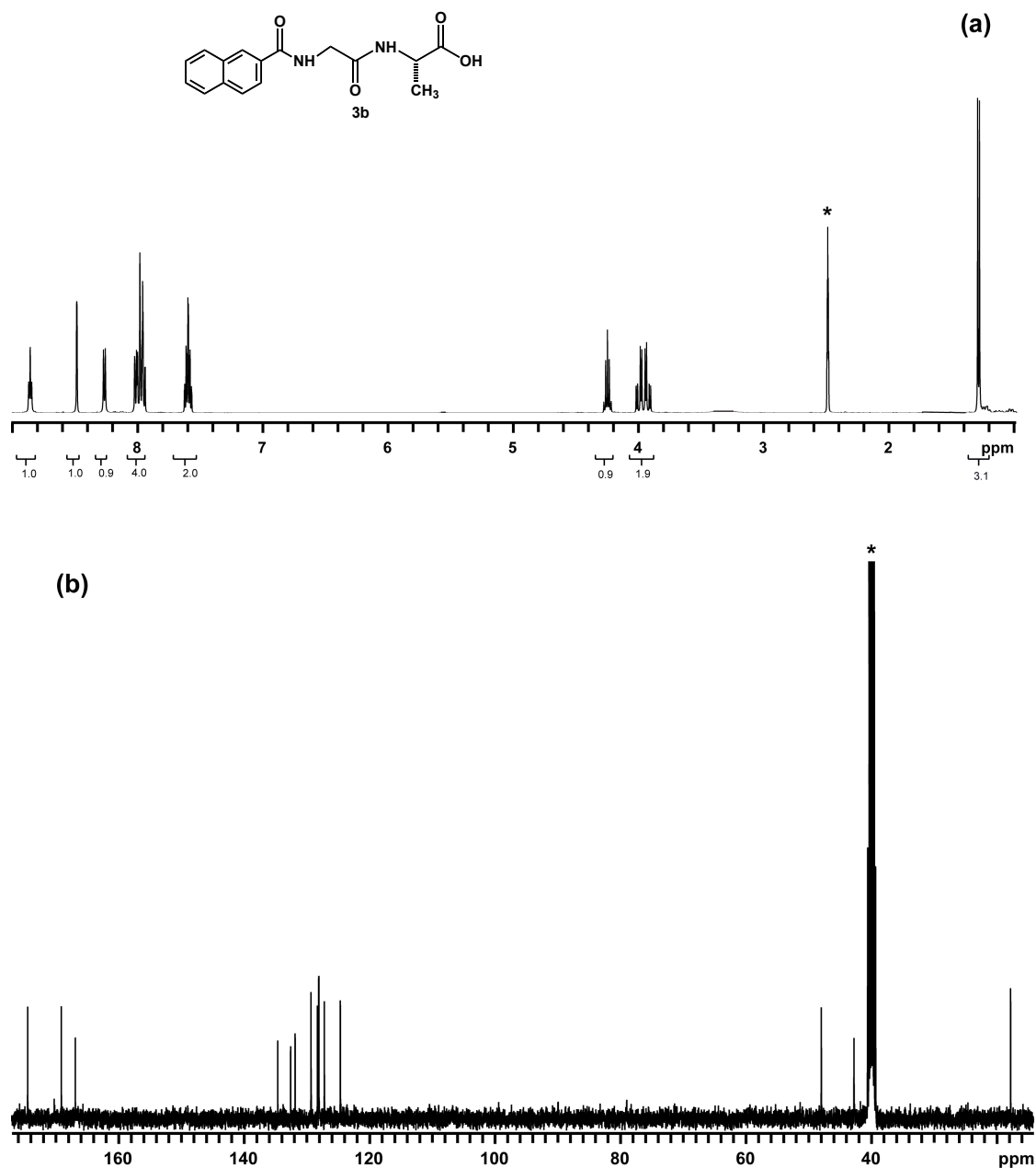


Figure S13. (a) ^1H NMR and (b) ^{13}C NMR spectra of **3b**. ^1H NMR (DMSO- d_6 , 500 MHz): d (ppm) 8.88-8.86 (1H, t, $J = 6.0$ Hz), 8.50 (1H, s), 8.27 (1H, d, $J = 7.5$ Hz), 8.03-7.95 (4H, m), 7.64-7.58 (2H, m), 4.29 (1H, m), 4.03-3.91 (2H, q, $J = 6.0$ Hz), 1.29 (3H, d, $J = 7.0$ Hz). ^{13}C NMR (DMSO- d_6 , 100 MHz): d (ppm) 174.48, 169.11, 166.88, 134.61, 132.55, 131.84, 129.30, 128.28, 128.11, 128.06, 127.18, 124.63, 47.95, 42.75, 17.78.

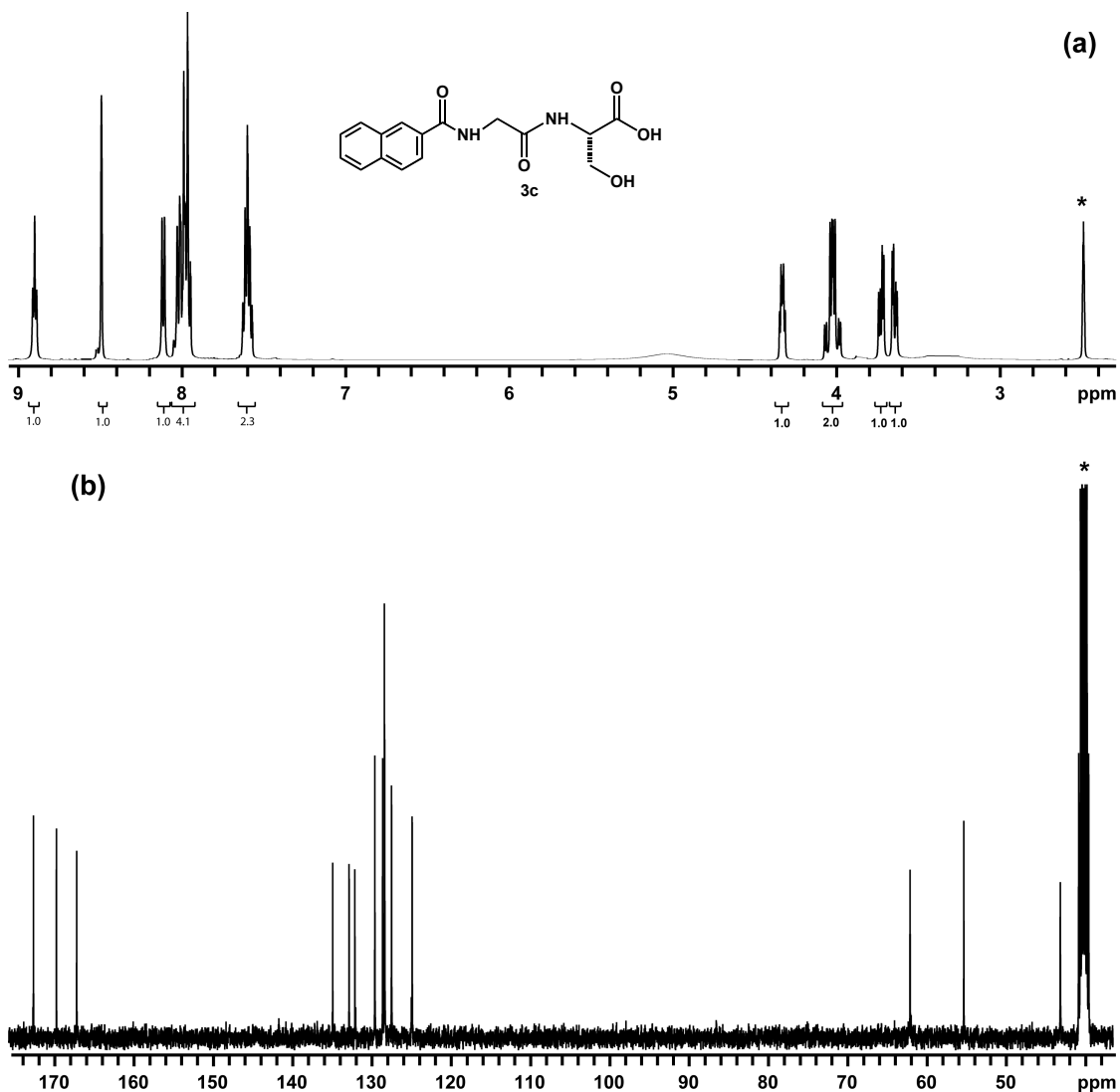


Figure S14. (a) ^1H NMR and (b) ^{13}C NMR spectra of **3c**. ^1H NMR (DMSO- d_6 , 500 MHz): d (ppm) 8.91-8.88 (1H, t, $J = 6.0$ Hz), 8.49 (1H, s), 8.11 (1H, d, $J = 7.5$ Hz), 8.03-7.95 (4H, m), 7.63-7.57 (2H, m), 4.35-4.31 (1H, m), 4.07-3.98 (2H, m), 3.74-3.71 (1H, dd, $J = 5.0$ and 11 Hz), 3.66-3.63 (1H, dd, $J = 4.0$ and 11 Hz). ^{13}C NMR (DMSO- d_6 , 100 MHz): d (ppm) 172.30, 169.46, 166.91, 134.62, 132.56, 131.83, 129.31, 128.33, 128.10, 128.06, 127.20, 124.61, 61.82, 55.04, 42.87.

IV. Measurement of Enthalpy and Entropy of Dissolution of Peptides¹

An 8 mL vial was charged with the corresponding naphthalene dipeptide (~ 30 mg) and water (~ 6 mL) (pH = 2, HCl) and the heterogeneous mixture was equilibrated for 24 h (without stirring) at each of the temperatures studied (25, 40, 50, 60, and 70 °C). At each temperature, a 200 μ L aliquot was taken from the solution with a micro-syringe and the syringe was rinsed with acetonitrile (2 x 200 μ L). The aliquot and combined rinses were further diluted with 2 mL of acetonitrile to achieve a final volume of 2.6 mL. The concentration of the naphthalene dipeptides was determined using UV-Vis spectroscopy and the extinction coefficient of each compound in acetonitrile at a fixed wavelength.

At each temperature, 3 different vials were set up and 3 aliquots were taken from each vial, producing a total of 9 samples at each temperature. The concentrations reported are the average of 9 samples.

To calculate the enthalpy and entropy of dissolution (ΔH_{diss} and ΔS_{diss} , respectively), van't Hoff plots were constructed based on the equation

$$\ln x = -\frac{\Delta H_{\text{diss}}}{RT} + \frac{\Delta S_{\text{diss}}}{R}$$

where x is the mole fraction solubility of the corresponding compound, R is the gas constant (1.98587 cal/mol \cdot K), and T is the temperature in K. From the slope, ΔH_{diss} was obtained and from the intercept, ΔS_{diss} was calculated. The reported errors for ΔH_{diss} and ΔS_{diss} were obtained from the statistical analysis of Sigmaplot 10. The individual errors reported on each point presented in the van't Hoff plots were calculated as the relative error

$$r.e. = \frac{\Delta x}{x}$$

where Δx is the error associated to the mole fraction and x is the mole fraction solubility of the corresponding compound

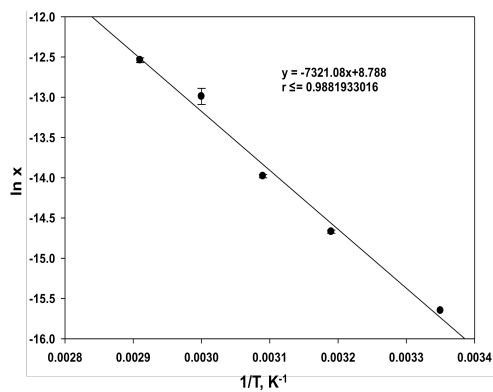


Figure S15. Representative van't Hoff plot of **1c** in H₂O (pH = 2).

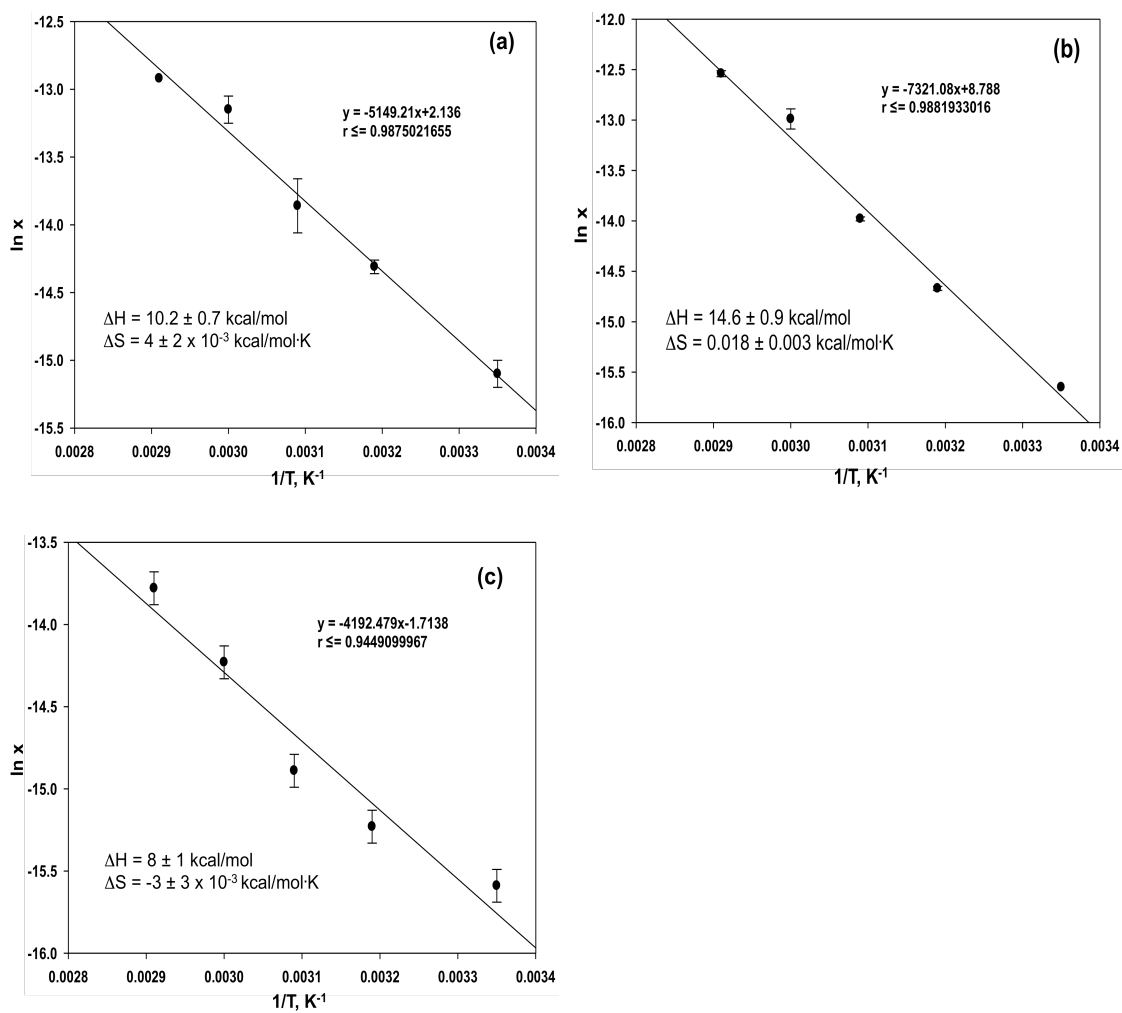


Figure S16. van't Hoff plots for **1b** (a), **1c** (b), and **1d** (c) in H₂O (pH = 2).

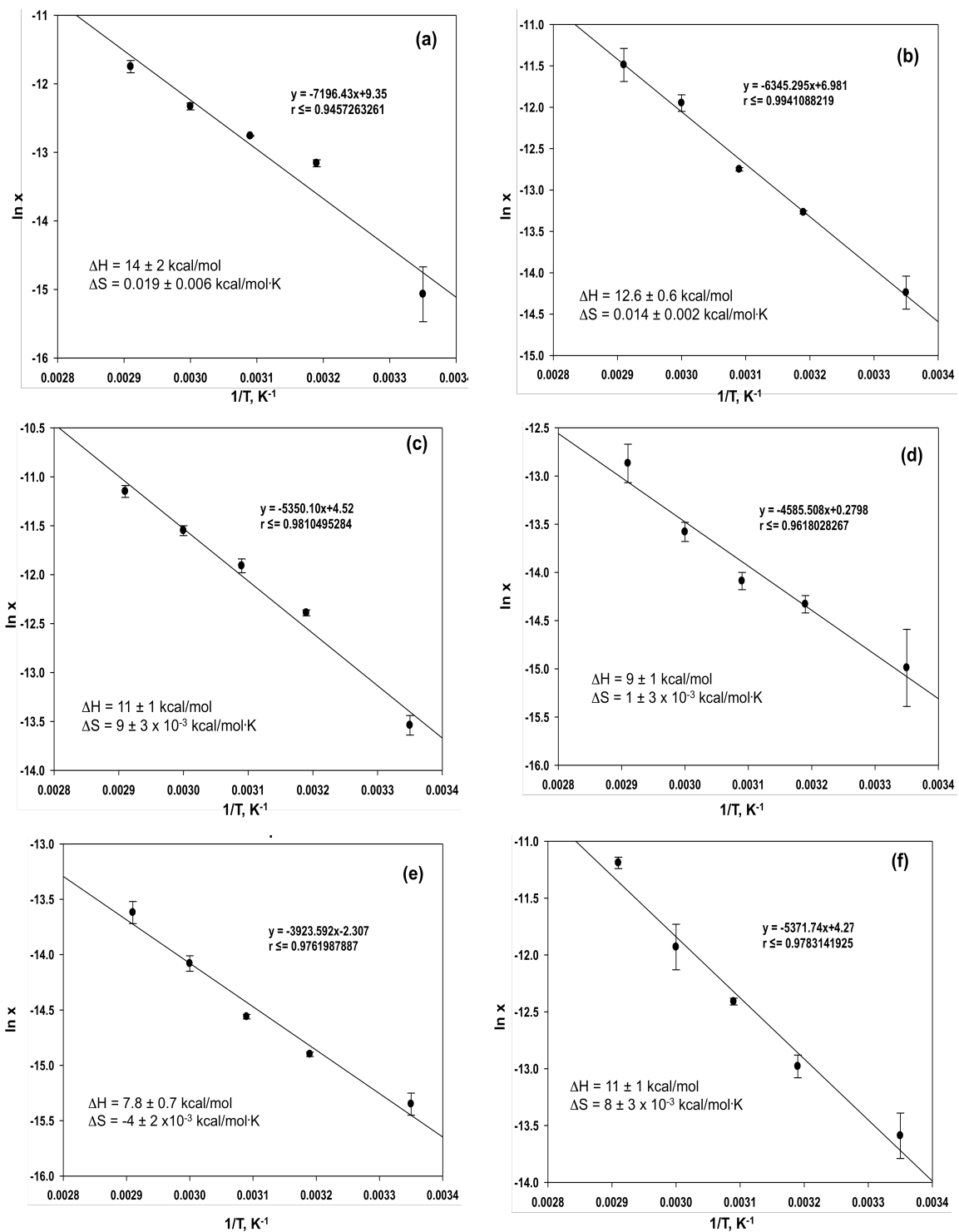


Figure S17. van't Hoff plots for **2a** (a), **2b** (b), **2c** (c), **3a** (d), **3b** (e), and **3c** (f) in H₂O (pH = 2).

Table S1. Room temperature solubilities for **1b-d**, **2a-c**, and **3a-c** in H₂O (pH = 2).

Dipeptide	RT Solubility (mg/mL)
1b	0.021 ± 0.002
1c	0.013 ± 0
1d	0.014 ± 0.002
2a	0.02 ± 0.01
2b	0.05 ± 0.01
2c	0.09 ± 0.01
3a	0.02 ± 0.01
3b	0.015 ± 0.002
3c	0.10 ± 0.01

Table S2. Enthalpy and entropy of dissolution for **1b-d**, **2a-c**, and **3a-c** in H₂O (pH = 2).

Dipeptide	ΔH_{diss} (kcal/mol)	ΔS_{diss} (kcal/mol·K)
1b	10.2 ± 0.7	4 ± 2 × 10 ⁻³
1c	14.6 ± 0.9	0.018 ± 0.003
1d	8 ± 1	-3 ± 3 × 10 ⁻³
2a	14 ± 2	0.019 ± 0.006
2b	12.6 ± 0.6	0.014 ± 0.002
2c	11 ± 1	9 ± 3 × 10 ⁻³
3a	9 ± 1	1 ± 3 × 10 ⁻³
3b	7.8 ± 0.7	-4 ± 2 × 10 ⁻³
3c	11 ± 1	8 ± 3 × 10 ⁻³

V. ^1H NMR spectra of **1a** and **1e**

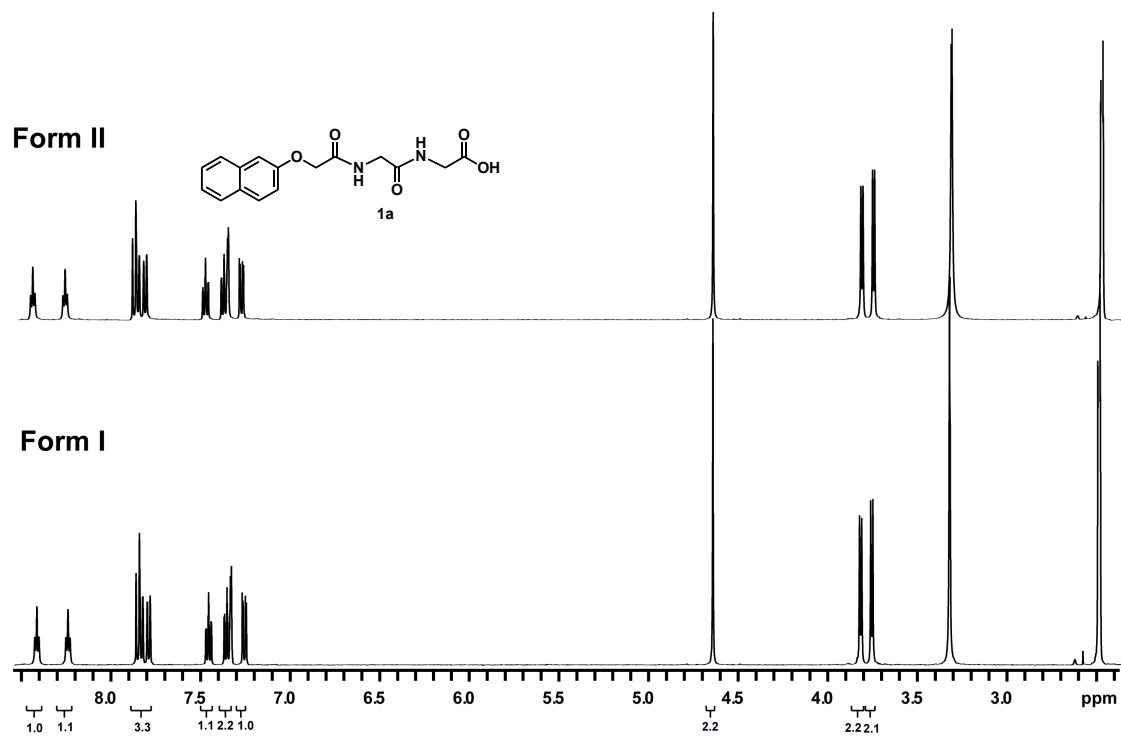


Figure S18. ^1H NMR spectra of Forms I and II of compound **1a** dissolved in $\text{DMSO}(d_6)$. Form I is the isolated powder from synthesis, Form II is the powder isolated after heating Form I in H_2O (pH = 2) at 70°C

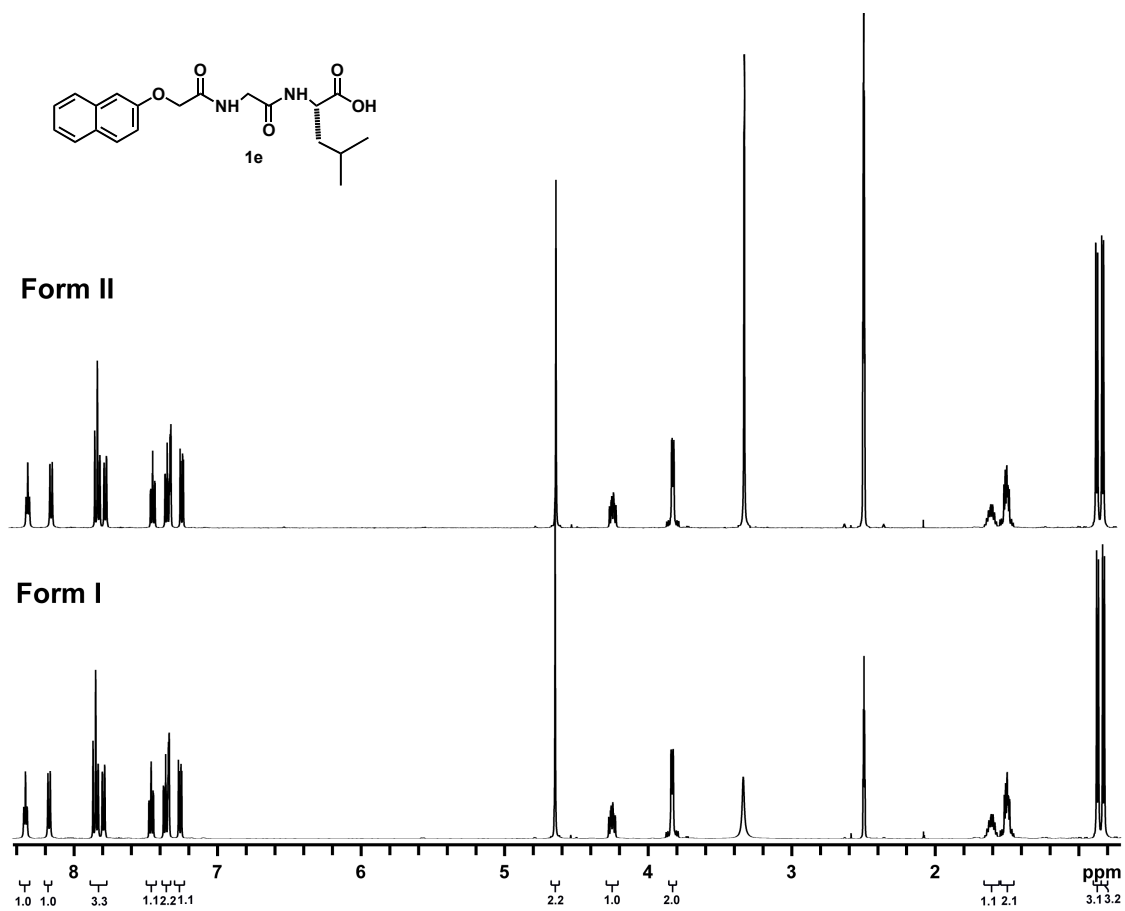


Figure S19. ^1H NMR spectra of Forms I and II of compound **1e** dissolved in $\text{DMSO}(d_6)$. Form I is the isolated powder from synthesis and Form II is the powder isolated after heating Form I in H_2O (pH = 2) at $40\text{ }^\circ\text{C}$.

VI. Powder X-ray Diffraction Patterns of Peptides

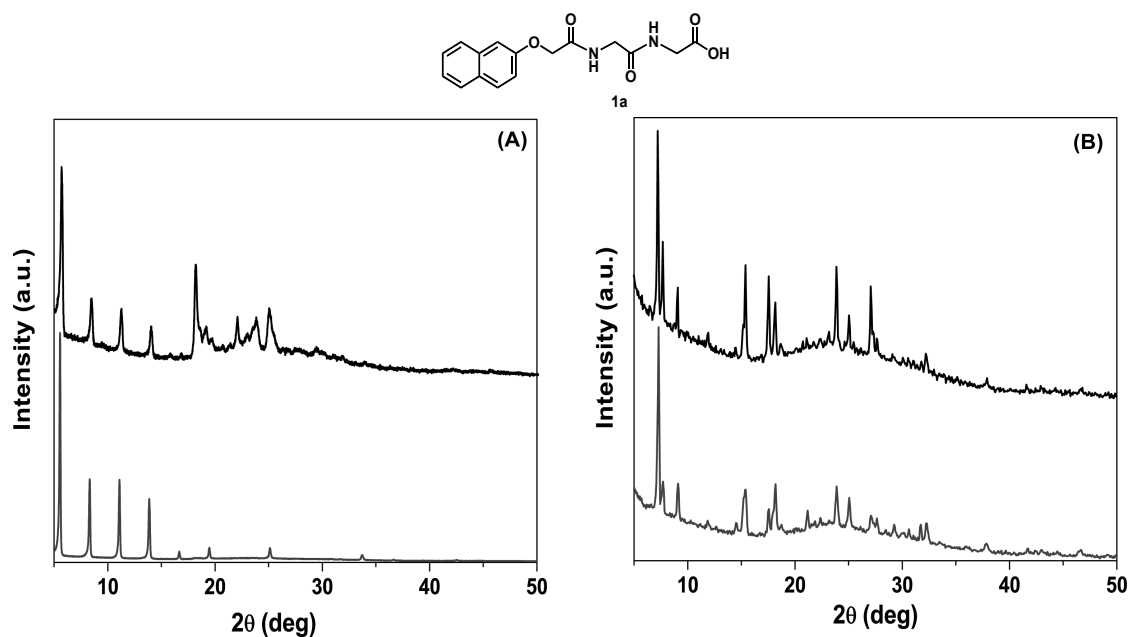


Figure S20. PXR D patterns for gelator **1a**: (A) Form I (top) and the air-dried gel (bottom), and (B) Form II (top) with the freeze-dried gel (bottom).

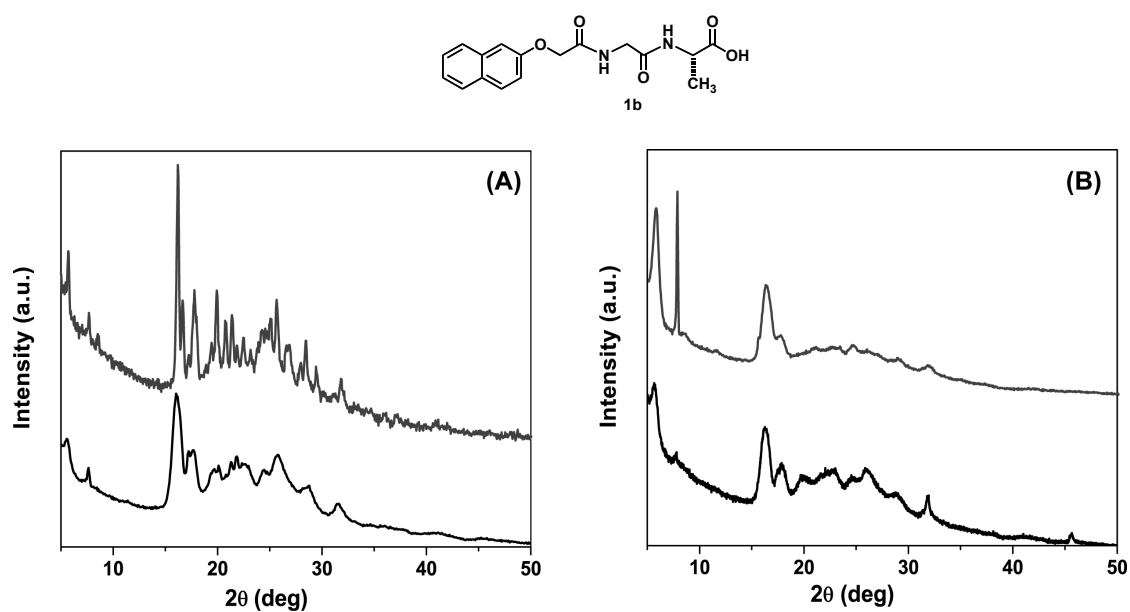


Figure S21. PXR D patterns for **1b** performed on the solid (A) before heating (bottom) and after heating (top) and (B) the bulk form (bottom) and the air-dried gel (top).

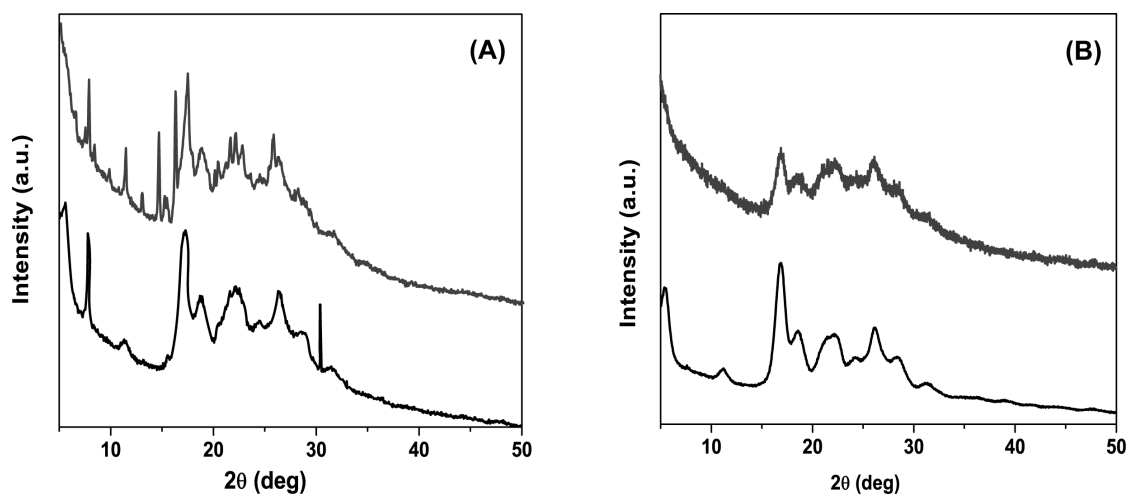
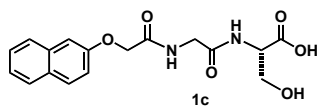


Figure S22. PXRD patterns of **1c** performed on the solid (A) before heating (bottom) and after heating (top) and (B) the bulk form (bottom) and the air-dried gel (top).

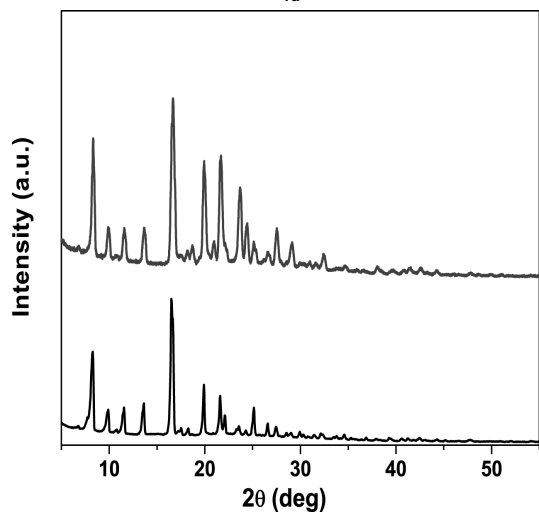
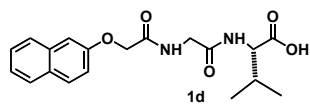


Figure S23. PXRD patterns of **1d** performed on the solid before heating (bottom) and after heating (top).

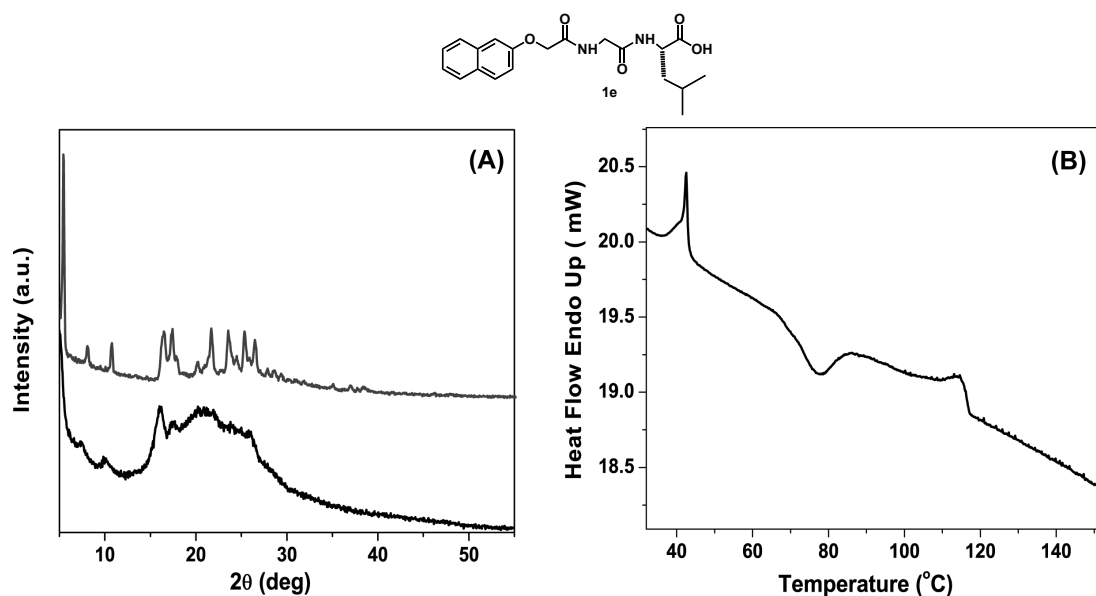


Figure S23. (A) PXR patterns of **1e** performed on the solid before heating (bottom) and after heating (top). Note that the solid visually changed appearance upon heating (at 40 $^{\circ}\text{C}$ in acidic water). This solid-solid transformation could also be observed by DSC (B).

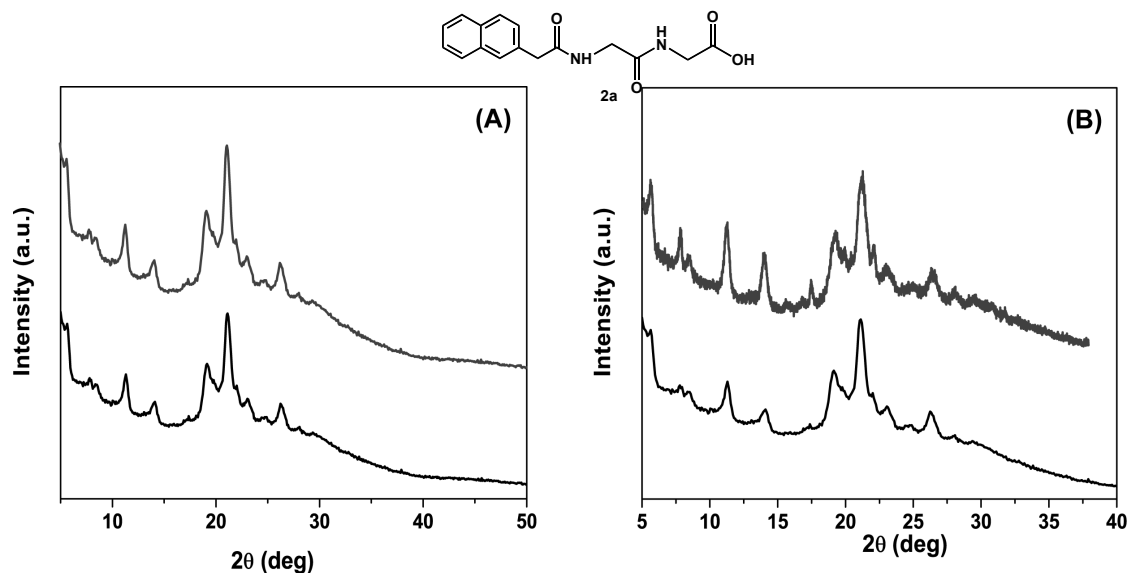


Figure S24. PXR patterns of **2a** performed on the solid (A) before heating (bottom) and after heating (top) and (B) the bulk form (bottom) and the air-dried gel (top).

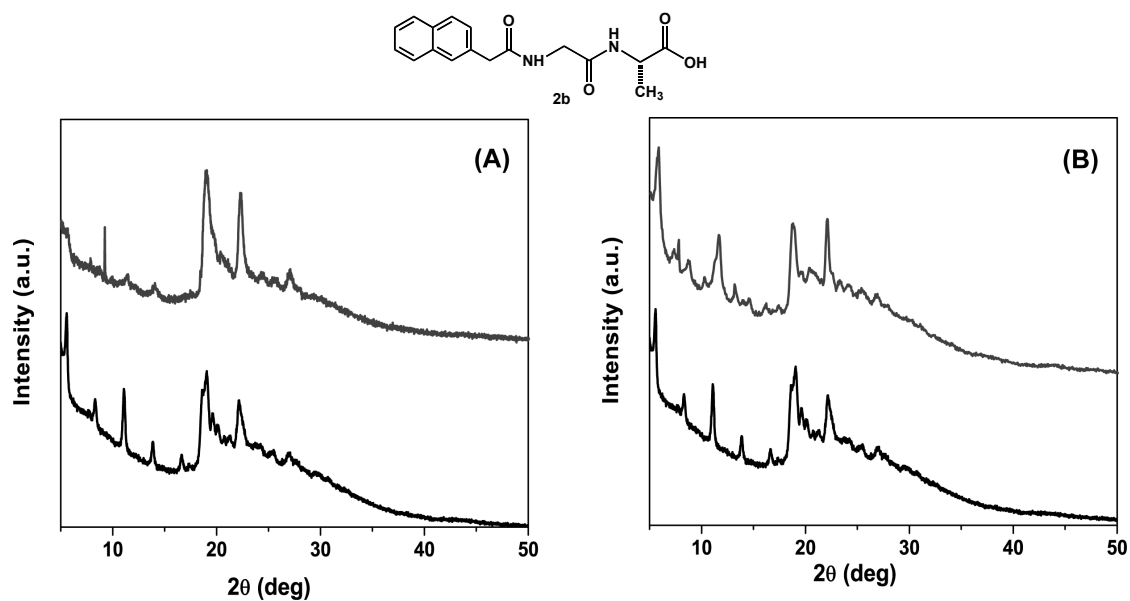


Figure S25. PXRD patterns of **2b** performed on the solid (A) before heating (bottom) and after heating (top) and (B) the bulk form (bottom) and the air-dried gel (top).

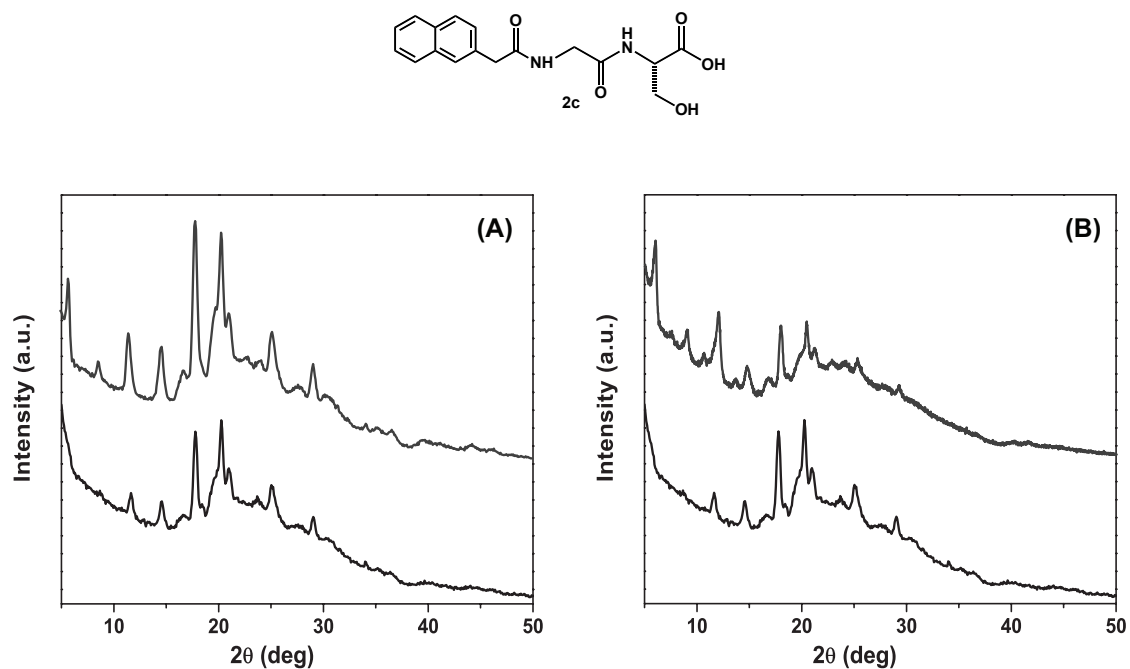


Figure S26. PXRD patterns of **2c** performed on the solid (A) before heating (bottom) and after heating (top) and (B) the bulk form (bottom) and the air-dried gel (top).

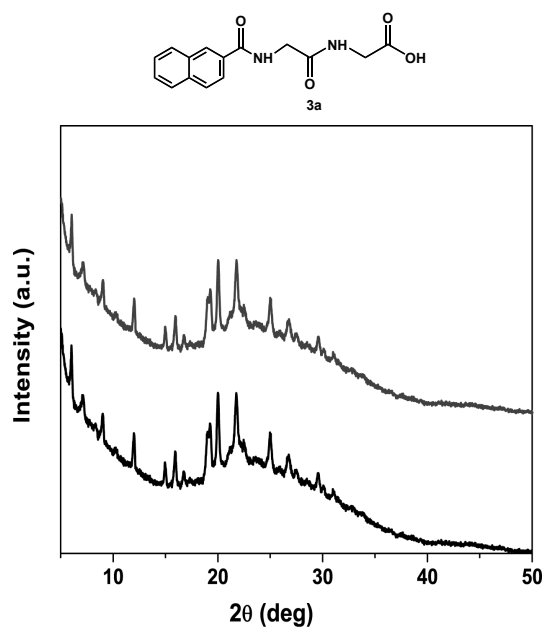


Figure S27. PXRD patterns of **3a** performed on the solid before heating (bottom) and after heating (top).

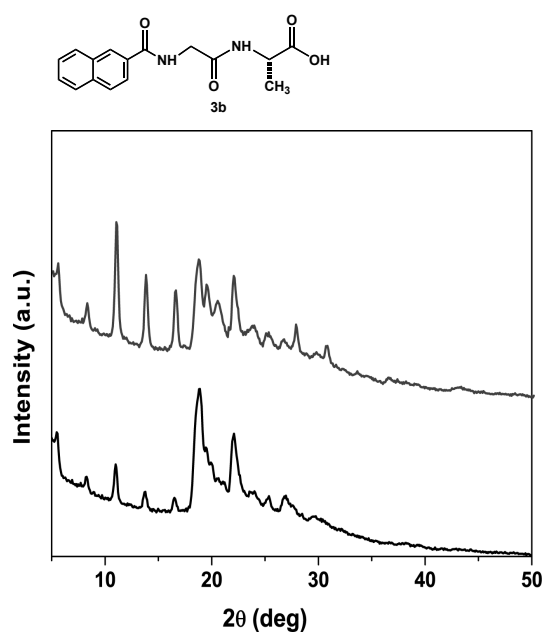


Figure S28. PXRD patterns of **3b** performed on the solid before heating (bottom) and after heating (top).

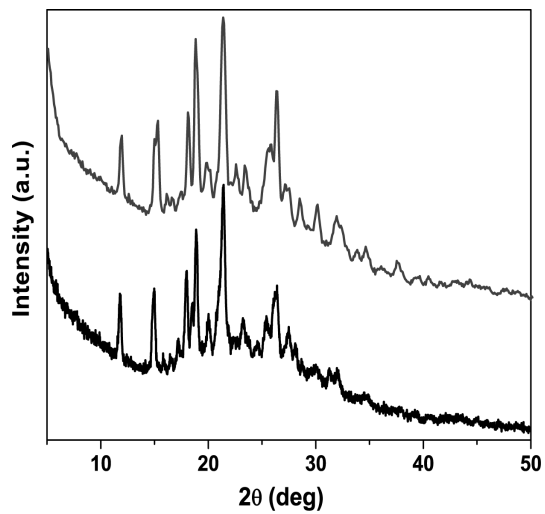
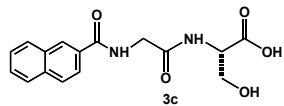


Figure S29. PXRD patterns of **3c** performed on the solid before heating (bottom) and after heating (top).

VII. Cgc of Pyridines¹

Pyridine	cgc (mg/mL) in 1/1 DMSO/H ₂ O	cgc (mg/mL) in 1/2 EtOH/H ₂ O
4a	30 ± 1	--
4b	6 ± 1	9 ± 1
5a	4.5 ± 0.5	9 ± 1
5b	13 ± 1	13 ± 1
5c	21 ± 1	28 ± 1
6a	18 ± 1	18 ± 1
6b	13 ± 1	13 ± 1
7	7.5 ± 0.5	13 ± 1

VIII. Measurements of Enthalpy and Entropy of Dissolution of Pyridines

An 8 mL vial was charged with the corresponding pyridine (~ 10 mg) and 1/1 DMSO/H₂O or 1/2 EtOH/H₂O (~ 6 mL) and the heterogeneous mixture was equilibrated for 24 h (without stirring) at each of the temperatures studied (25, 35, 45, 55 °C). For extremely soluble pyridines, equilibrium temperatures were selected as 25, 30, 35, 40 °C. For extremely insoluble pyridines, temperatures were 40, 50, 60, 70 °C. At each temperature, a 300 μ L aliquot was taken from the solution with a micro-syringe and the syringe was rinsed with DMSO or EtOH (300 μ L). The aliquot and combined rinses were further diluted with 1.5 mL of DMSO or EtOH to achieve a final volume of 2.1 mL. The concentration of the pyridines was determined using UV-Vis spectroscopy and the extinction coefficient of each compound in DMSO at a fixed wavelength.

At each temperature, 3 different vials were set up and 3 aliquots were taken from each vial, producing a total of 9 samples at each temperature. The concentrations reported are the average of 9 samples.

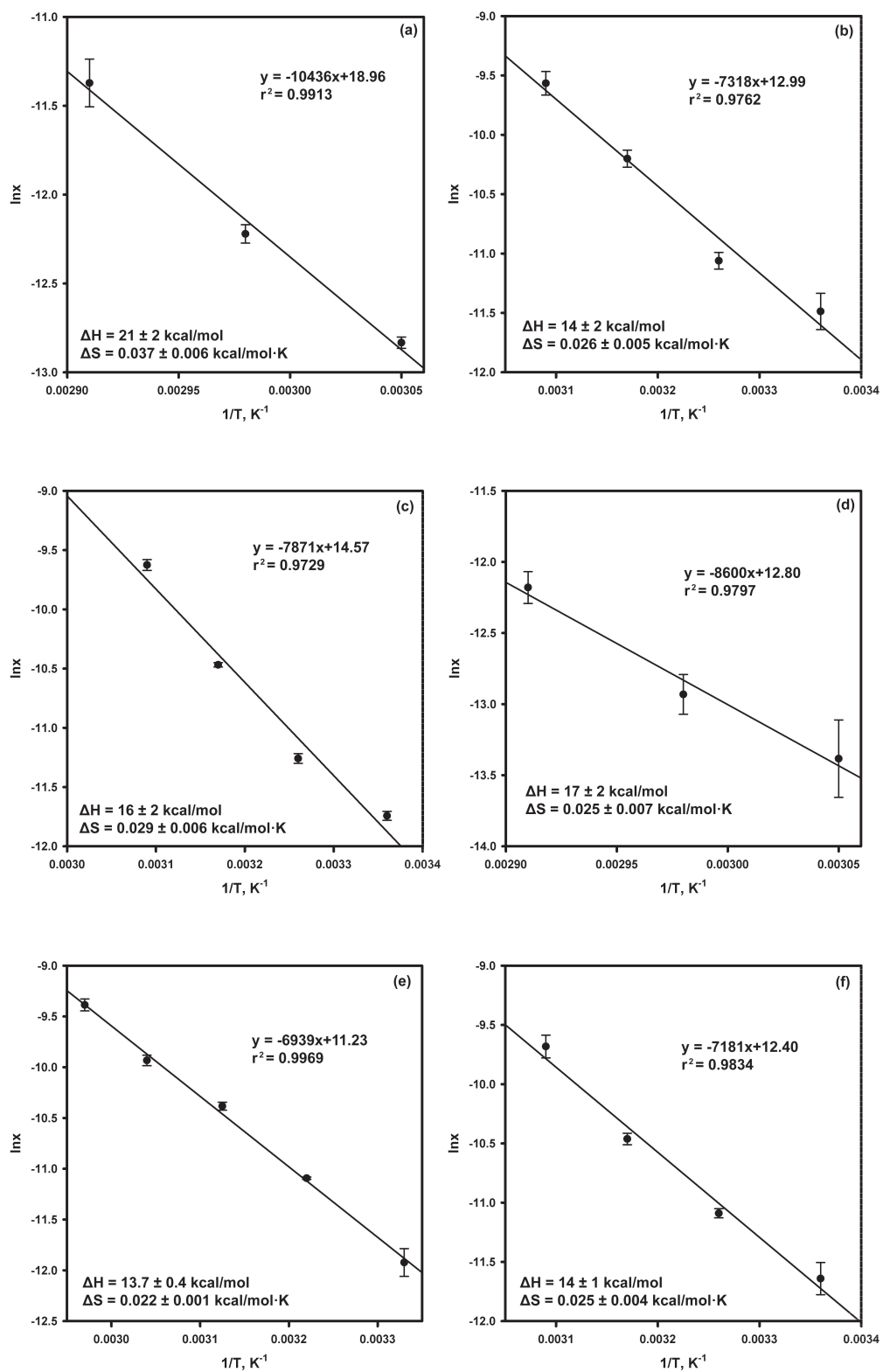


Figure S30. van't Hoff plots for **4a** (a), **4b** (b), **5a** (c), **5b** (d), **5c** (e), and **6a** (f) in 1/1 DMSO/H₂O.

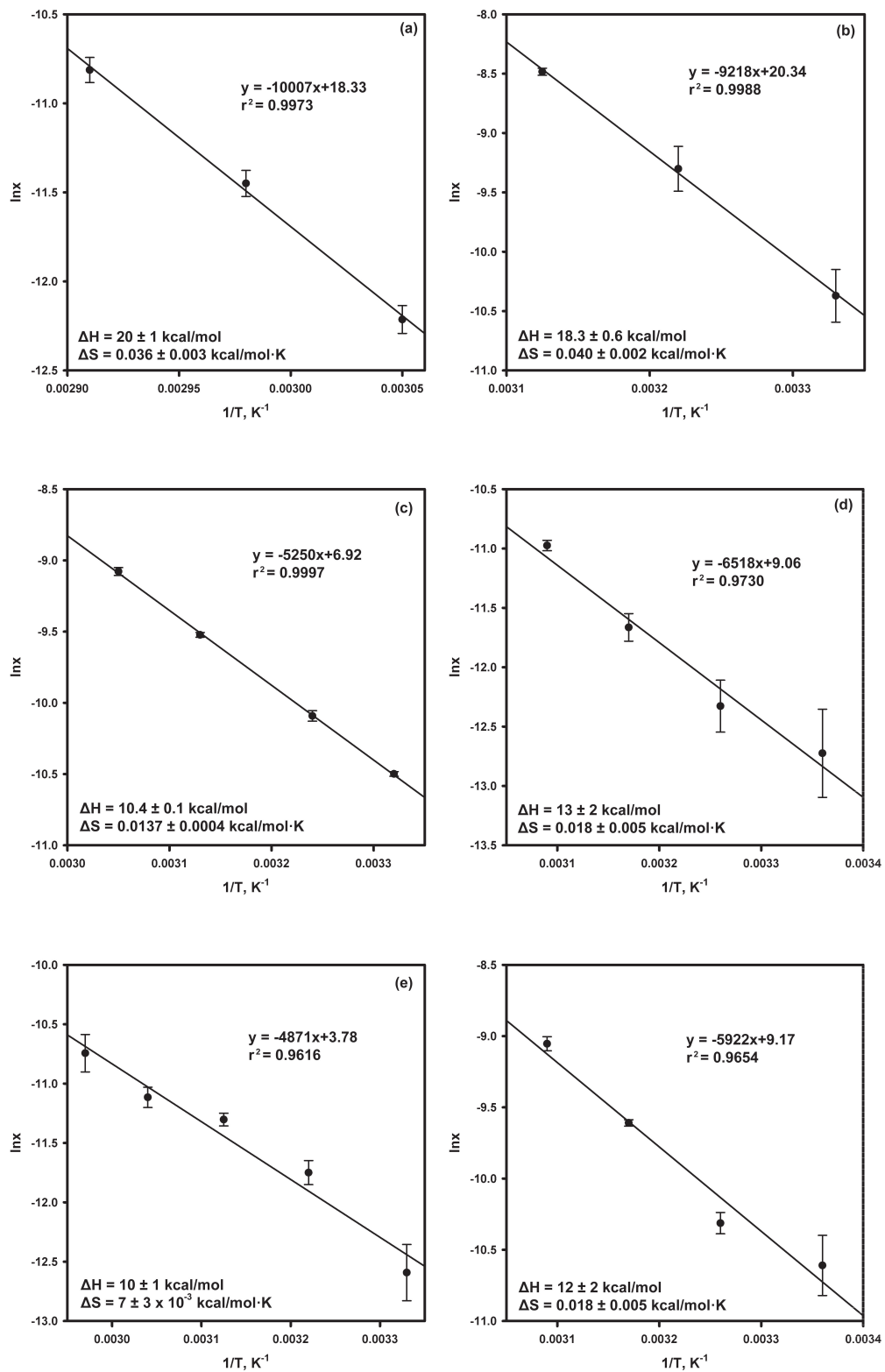


Figure S31. van't Hoff plots for **6b** (a), **7** (b), **8a** (c), **8b** (d), **8c** (e), and **11b** (f) in 1/1 DMSO/H₂O.

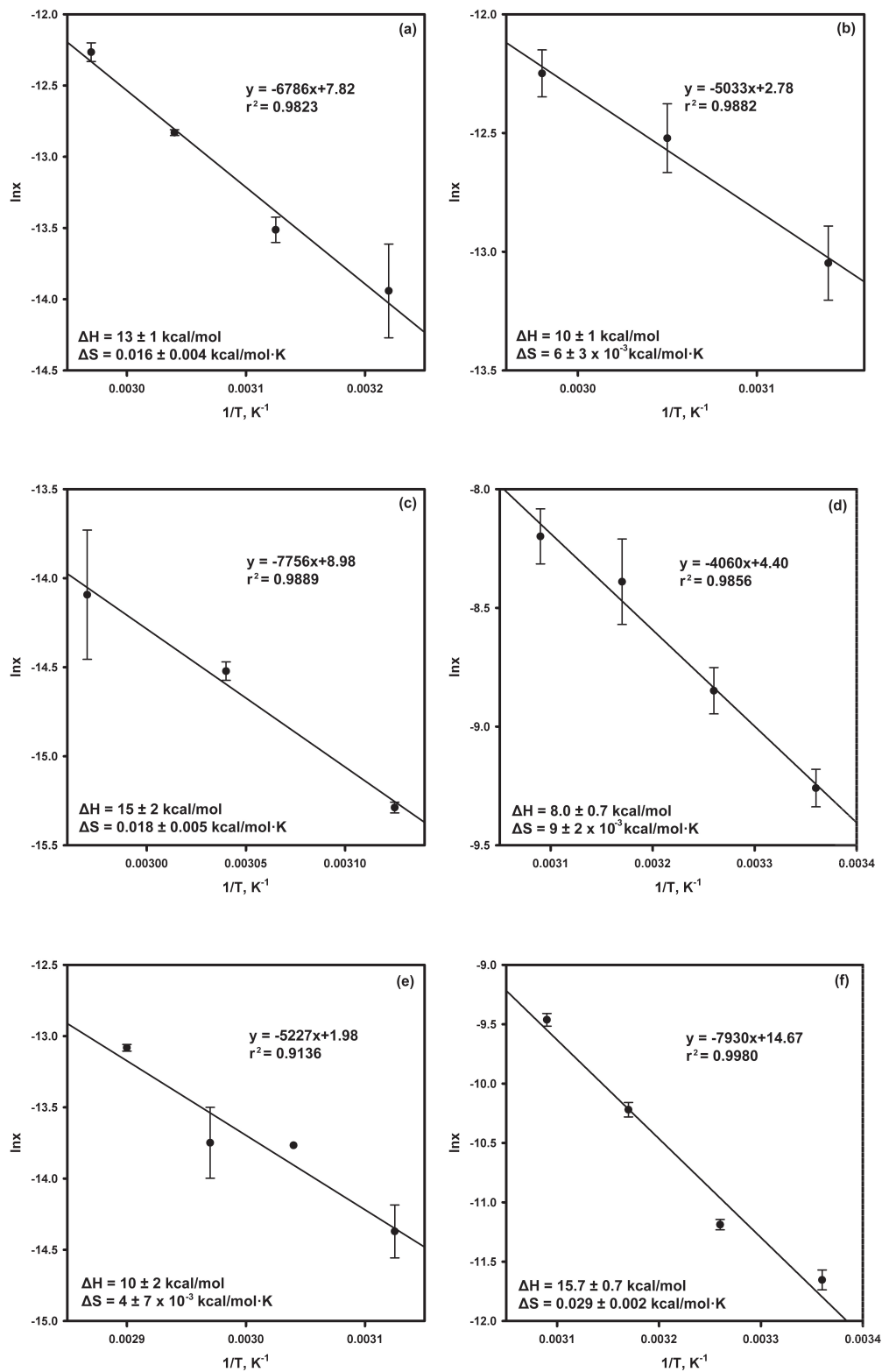


Figure S32. van't Hoff plots for **9b** (a), **9c** (b), **9d** (c), **10a** (d), **10b** (e), and **11a** (f) in 1/1 DMSO/H₂O.

Table S3. Enthalpy and entropy of dissolution for **4a-11b** in 1/1 DMSO/H₂O.

Pyridines	ΔH_{diss} (kcal/mol)	ΔS_{diss} (kcal/mol•K)
4a	21 ± 2	0.037 ± 0.006
4b	14 ± 2	0.026 ± 0.005
5a	16 ± 2	0.029 ± 0.006
5b	17 ± 2	0.025 ± 0.007
5c	13.7 ± 0.4	0.022 ± 0.001
6a	14 ± 1	0.025 ± 0.004
6b	20 ± 1	0.036 ± 0.003
7	18.3 ± 0.6	0.040 ± 0.002
8a	10.4 ± 0.1	0.0137 ± 0.0004
8b	13 ± 2	0.018 ± 0.005
8c	10 ± 1	7 ± 3 × 10 ⁻³
9b	13 ± 1	0.016 ± 0.004
9c	10 ± 1	6 ± 3 × 10 ⁻³
9d	15 ± 2	0.018 ± 0.005
10a	8.0 ± 0.7	9 ± 2 × 10 ⁻³
10b	10 ± 2	4 ± 7 × 10 ⁻³
11a	15.7 ± 0.7	0.029 ± 0.002
11b	12 ± 2	0.018 ± 0.005

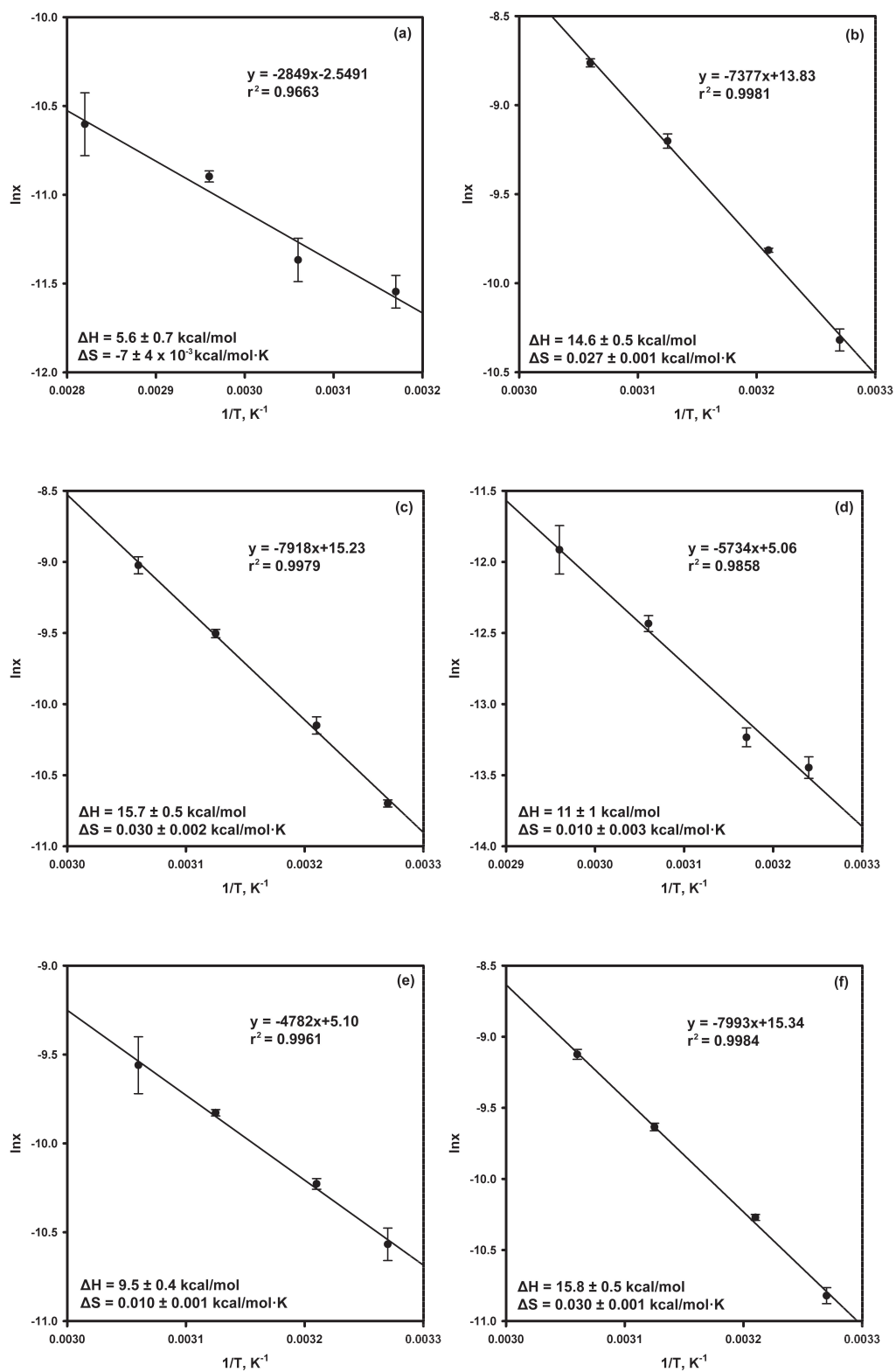


Figure S33. van't Hoff plots for **4a** (a), **4b** (b), **5a** (c), **5b** (d), **5c** (e), and **6a** (f) in 1/2 EtOH/H₂O.

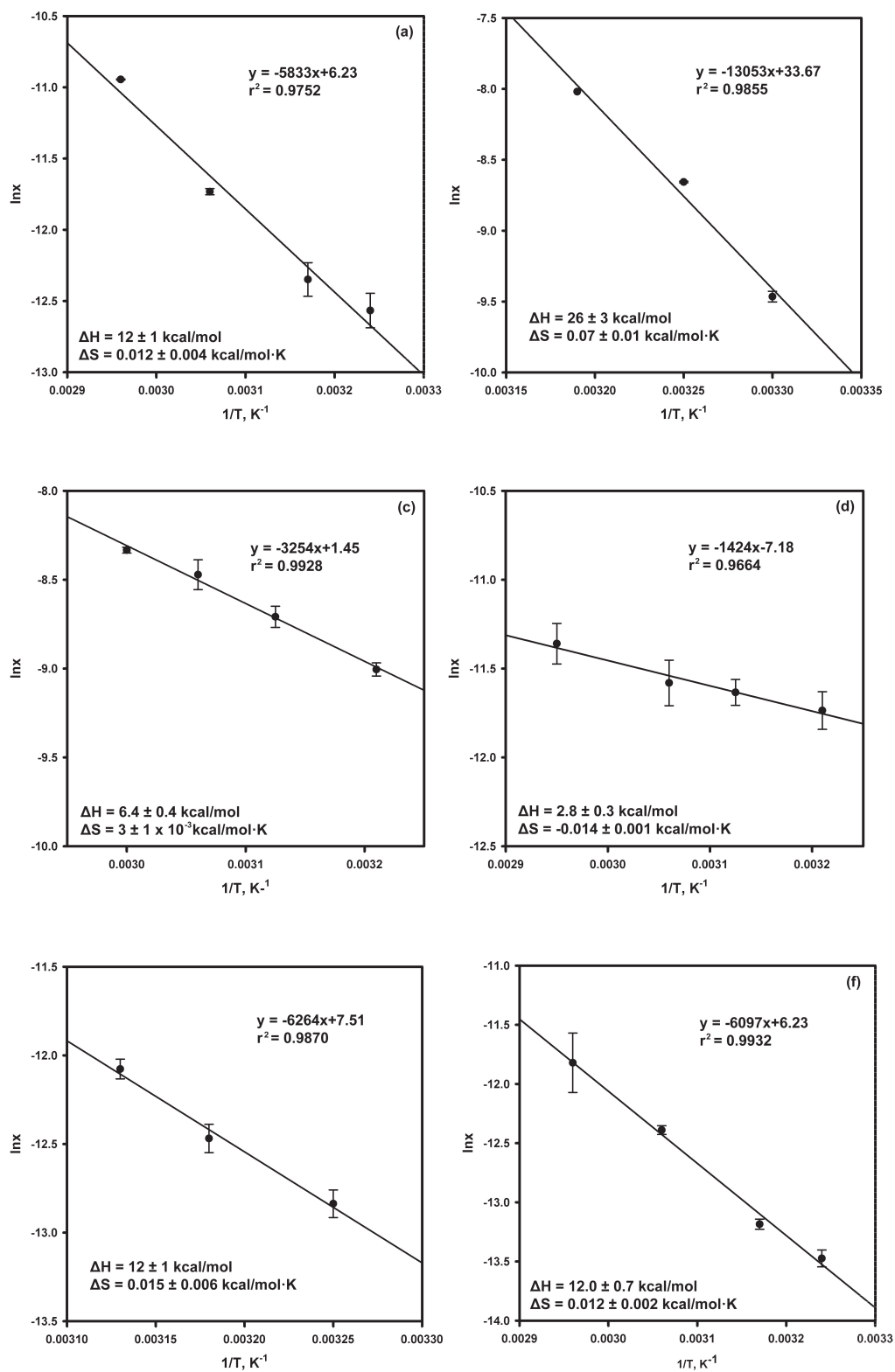


Figure S34. van't Hoff plots for **6b** (a), **7** (b), **8a** (c), **8c** (d), **9b** (e), and **9c** (f) in 1/2 EtOH/H₂O.

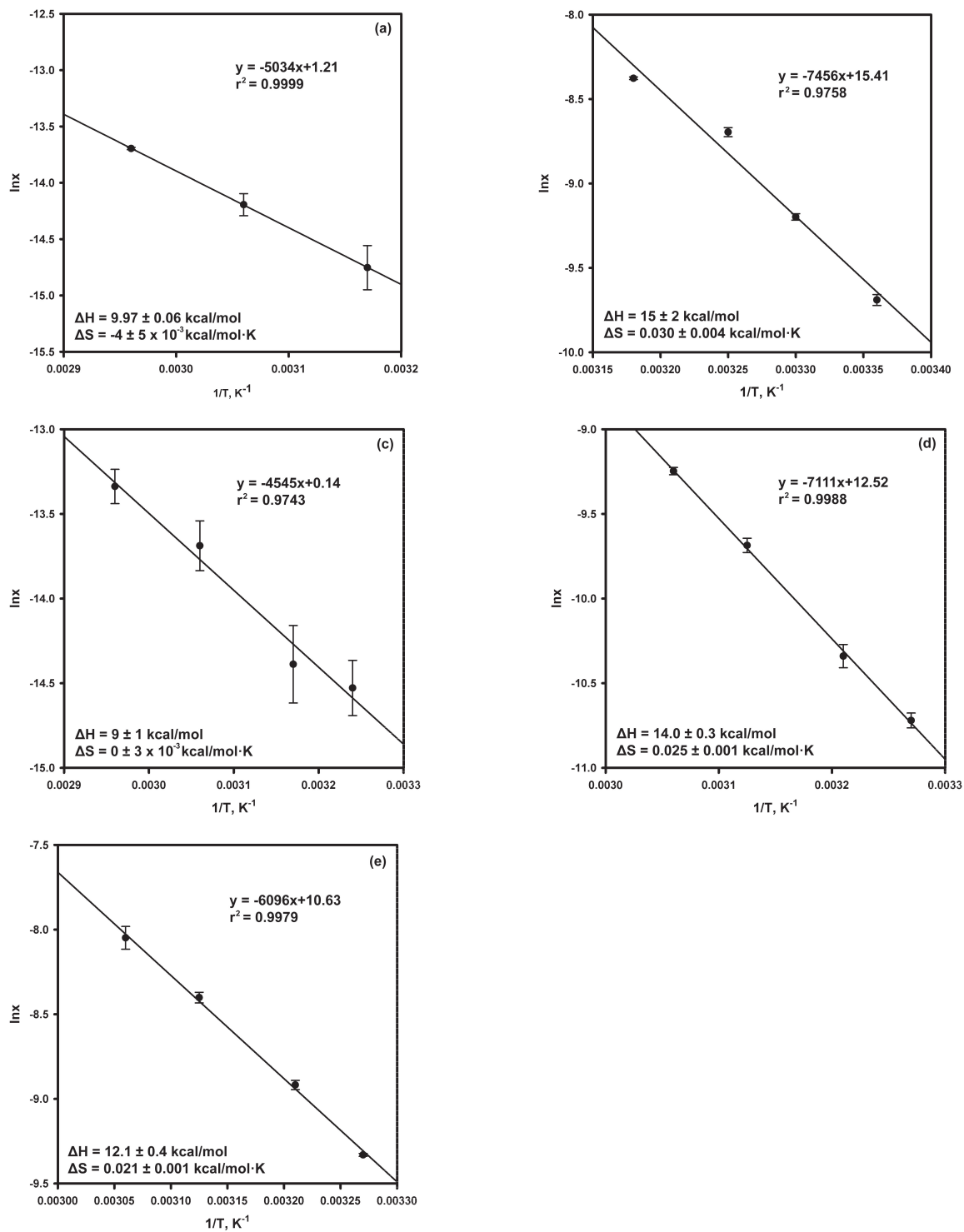


Figure S35. van't Hoff plots for **9d** (a), **10a** (b), **10b** (c), **11a** (d) and **11b** (e) in 1/2 EtOH/H₂O.

Table S4. Enthalpy and entropy of dissolution for **4a-11b** in 1/2 EtOH/H₂O.

Pyridines	ΔH_{diss} (kcal/mol)	ΔS_{diss} (kcal/mol·K)
4a	5.6 ± 0.7	-7 ± 4 × 10 ⁻³
4b	14.6 ± 0.5	0.027 ± 0.001
5a	15.7 ± 0.5	0.030 ± 0.002
5b	11 ± 1	0.010 ± 0.003
5c	9.5 ± 0.4	0.010 ± 0.001
6a	15.8 ± 0.5	0.030 ± 0.001
6b	12 ± 1	0.012 ± 0.004
7	26 ± 3	0.07 ± 0.01
8a	6.4 ± 0.4	3 ± 1 × 10 ⁻³
8c	2.8 ± 0.3	-0.014 ± 0.001
9b	12 ± 1	0.015 ± 0.006
9c	12.0 ± 0.7	0.012 ± 0.002
9d	9.97 ± 0.06	-4 ± 5 × 10 ⁻³
10a	15 ± 2	0.030 ± 0.004
10b	9 ± 1	0 ± 3 × 10 ⁻³
11a	14.0 ± 0.3	0.025 ± 0.001
11b	12.1 ± 0.4	0.021 ± 0.001

IX. Powder X-ray Diffraction Pattern of Pyridines

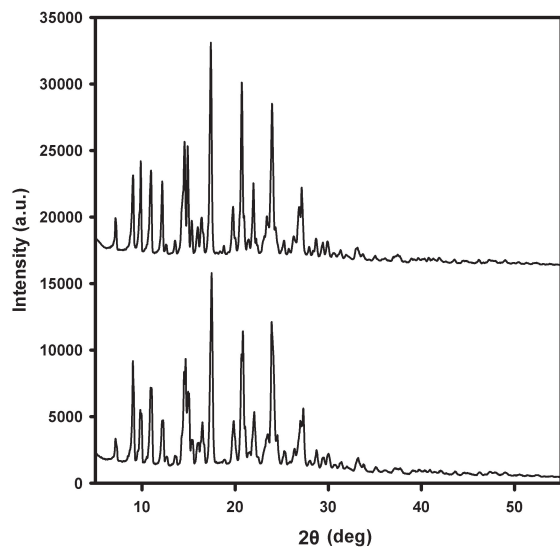


Figure S36. PXRD patterns of **4a** performed on the solid before heating (bottom) and after heating (top) in 1/1 DMSO/H₂O.

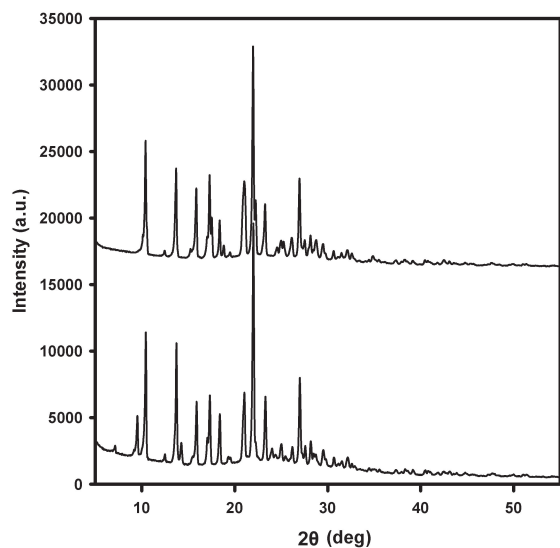


Figure S37. PXRD patterns of **4b** performed on the solid before heating (bottom) and after heating (top) in 1/1 DMSO/H₂O.

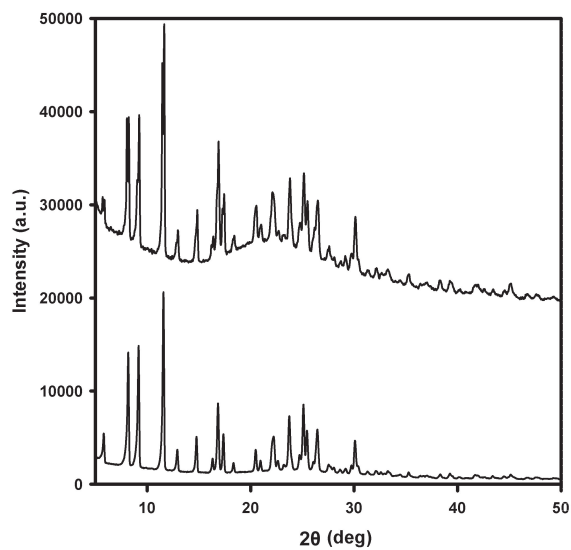


Figure S38. PXRD patterns of **5a** performed on the solid before heating (bottom) and after heating (top) in 1/1 DMSO/H₂O.

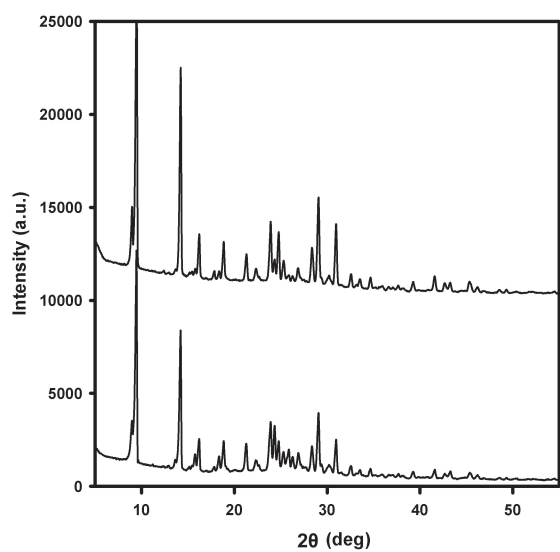


Figure S39. PXRD patterns of **5b** performed on the solid before heating (bottom) and after heating (top) in 1/1 DMSO/H₂O.

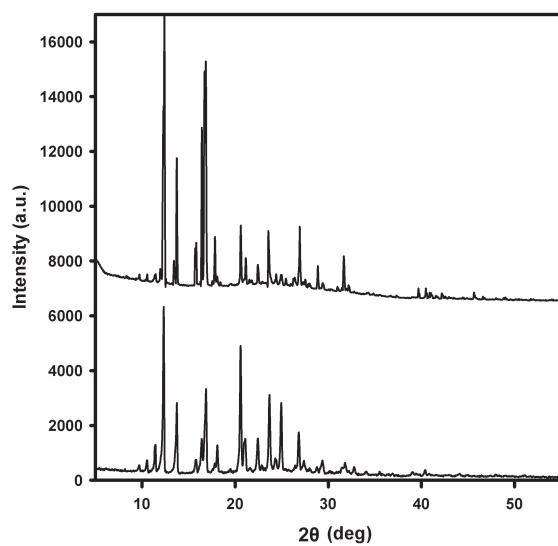


Figure S40. PXRD patterns of **5c** performed on the solid before heating (bottom) and after heating (top) in 1/1 DMSO/H₂O.

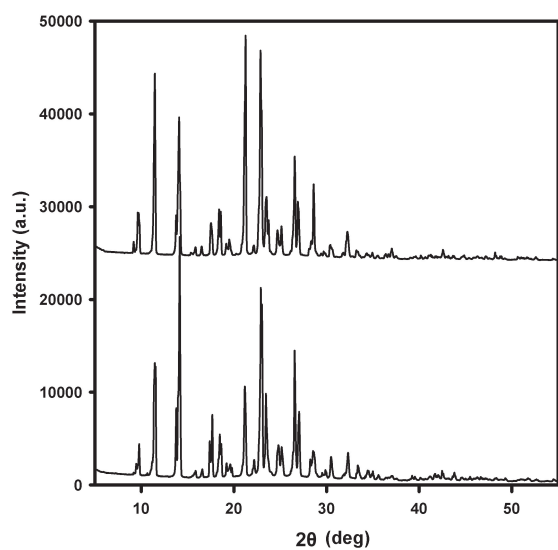


Figure S41. PXRD patterns of **6a** performed on the solid before heating (bottom) and after heating (top) in 1/1 DMSO/H₂O.

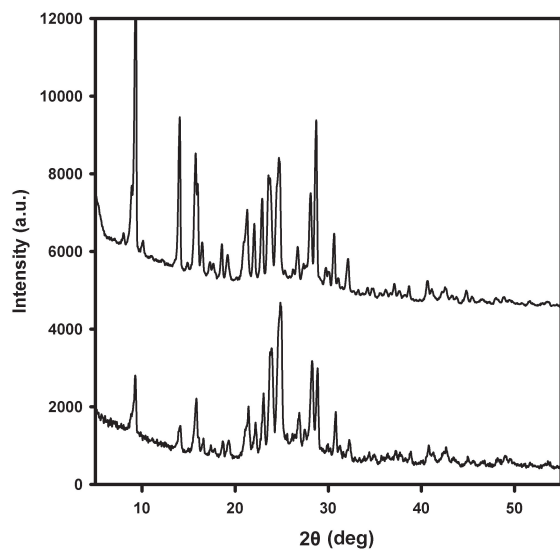


Figure S42. PXRD patterns of **6b** performed on the solid before heating (bottom) and after heating (top) in 1/1 DMSO/H₂O.

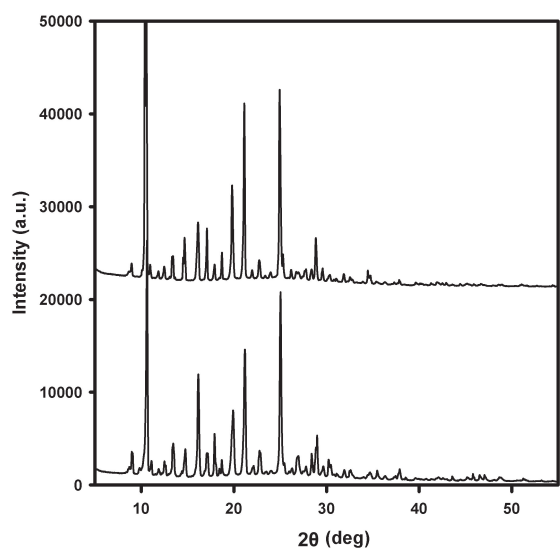


Figure S43. PXRD patterns of **7** performed on the solid before heating (bottom) and after heating (top) in 1/1 DMSO/H₂O.

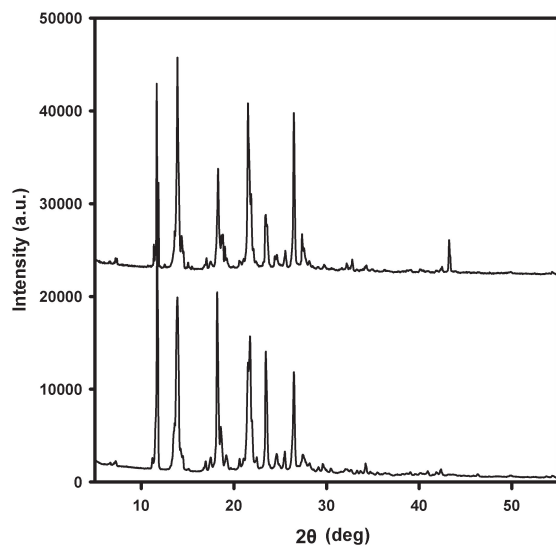


Figure S44. PXRD patterns of **8b** performed on the solid before heating (bottom) and after heating (top) in 1/1 DMSO/H₂O.

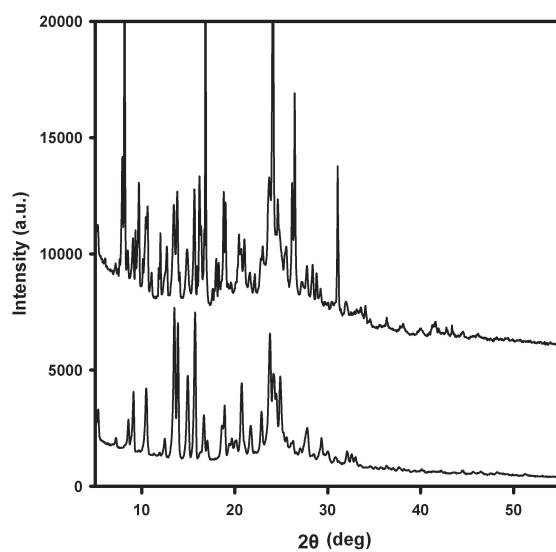


Figure S45. PXRD patterns of **9a** performed on the solid before heating (bottom) and after heating (top) in 1/1 DMSO/H₂O. Note that two patterns were different.

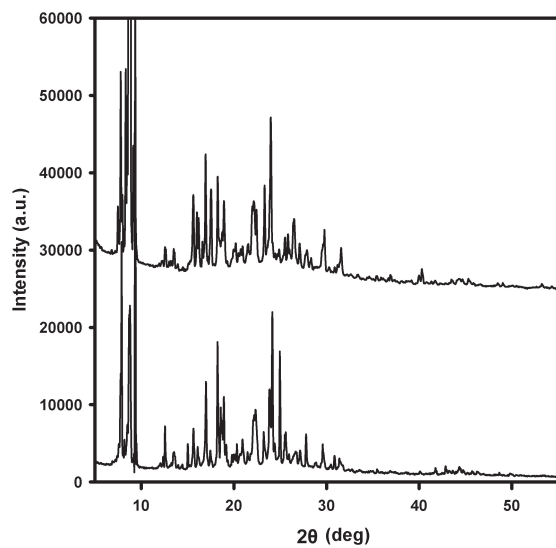


Figure S46. PXRD patterns of **9b** performed on the solid before heating (bottom) and after heating (top) in 1/1 DMSO/H₂O.

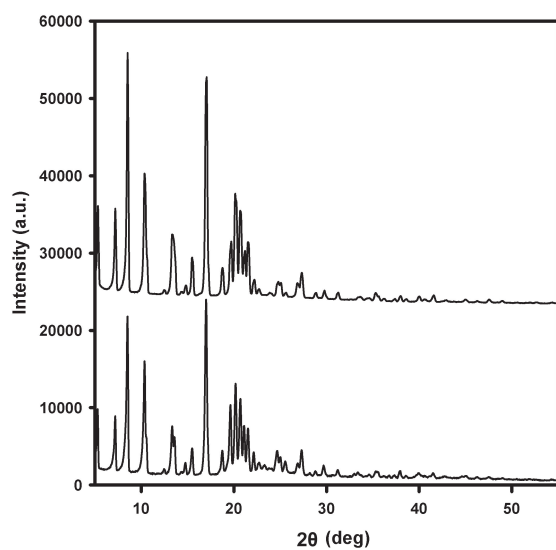


Figure S47. PXRD patterns of **9c** performed on the solid before heating (bottom) and after heating (top) in 1/1 DMSO/H₂O.

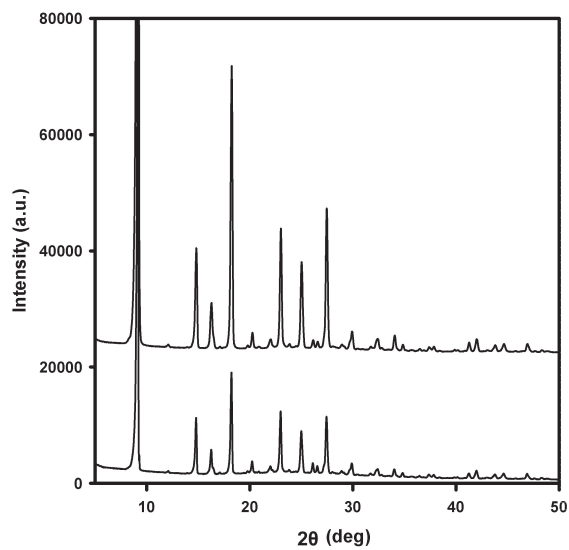


Figure S48. PXRD patterns of **9d** performed on the solid before heating (bottom) and after heating (top) in 1/1 DMSO/H₂O.

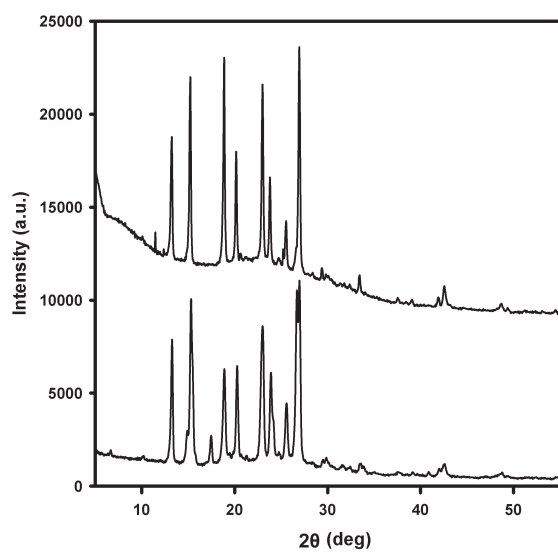


Figure S49. PXRD patterns of **10a** performed on the solid before heating (bottom) and after heating (top) in 1/1 DMSO/H₂O.

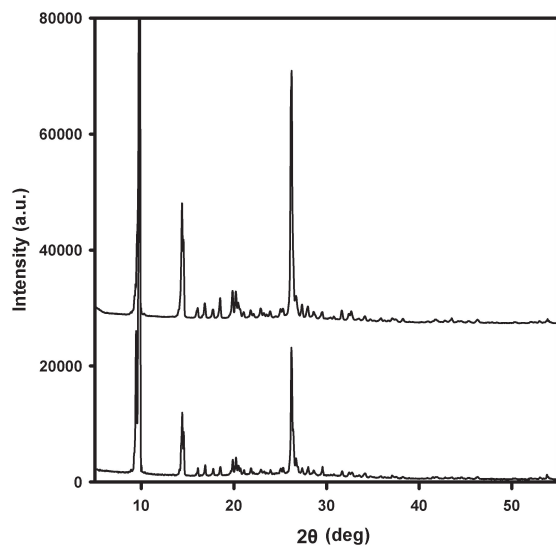


Figure S50. PXRD patterns of **10b** performed on the solid before heating (bottom) and after heating (top) in 1/1 DMSO/H₂O.

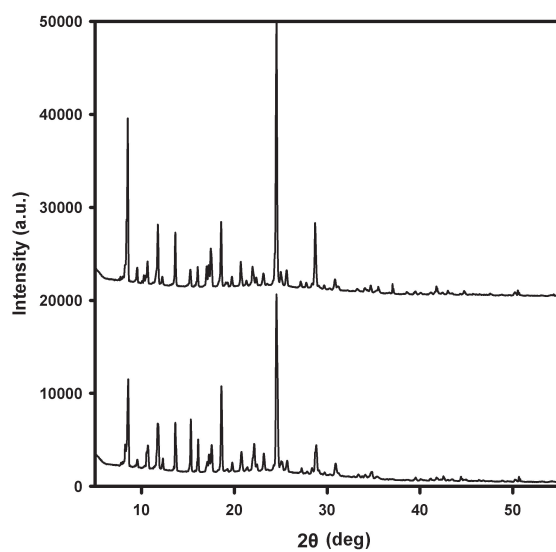


Figure S51. PXRD patterns of **11a** performed on the solid before heating (bottom) and after heating (top) in 1/1 DMSO/H₂O.

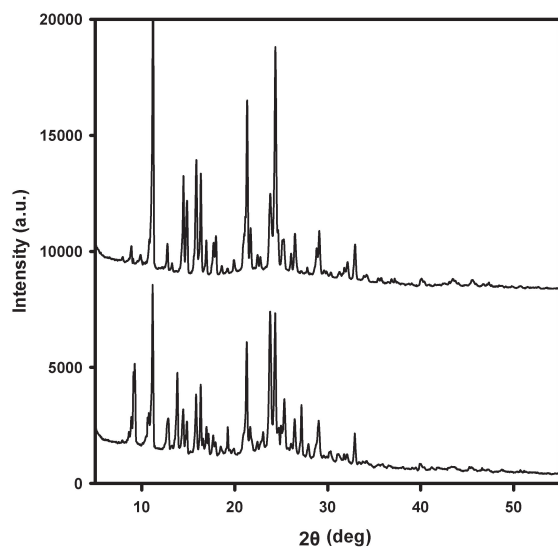


Figure S52. PXRD patterns of **11b** performed on the solid before heating (bottom) and after heating (top) in 1/1 DMSO/H₂O.

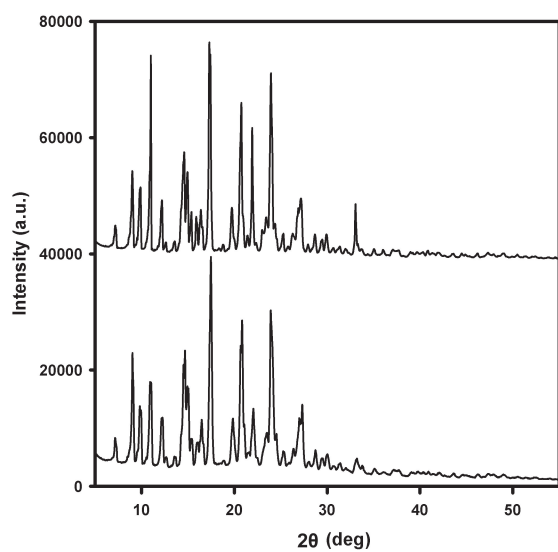


Figure S53. PXRD patterns of **4a** performed on the solid before heating (bottom) and after heating (top) in 1/2 EtOH/H₂O.

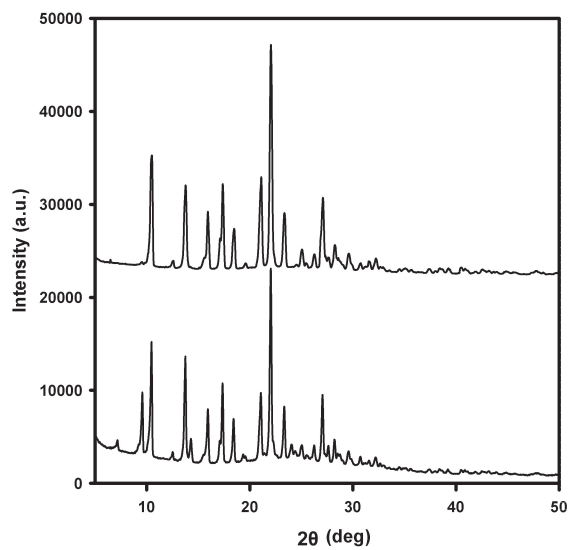


Figure S54. PXRD patterns of **4b** performed on the solid before heating (bottom) and after heating (top) in 1/2 EtOH/H₂O.

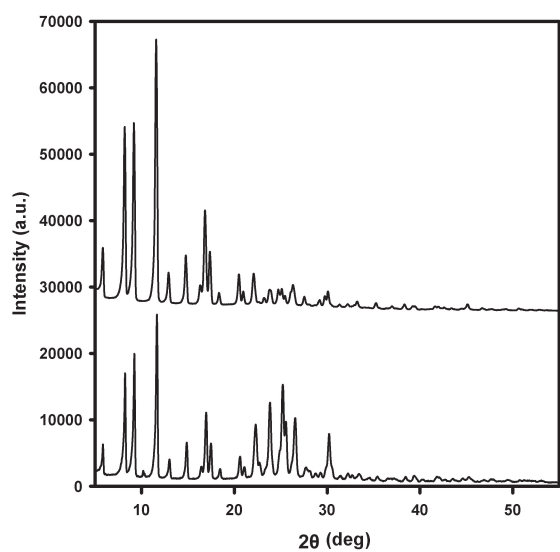


Figure S55. PXRD patterns of **5a** performed on the solid before heating (bottom) and after heating (top) in 1/2 EtOH/H₂O.

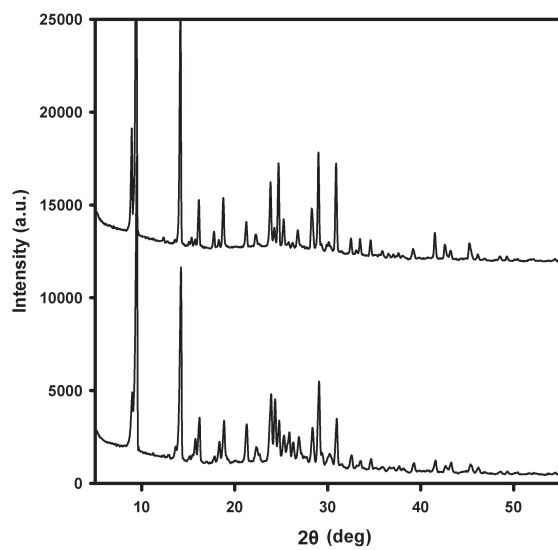


Figure S56. PXRD patterns of **5b** performed on the solid before heating (bottom) and after heating (top) in 1/2 EtOH/H₂O.

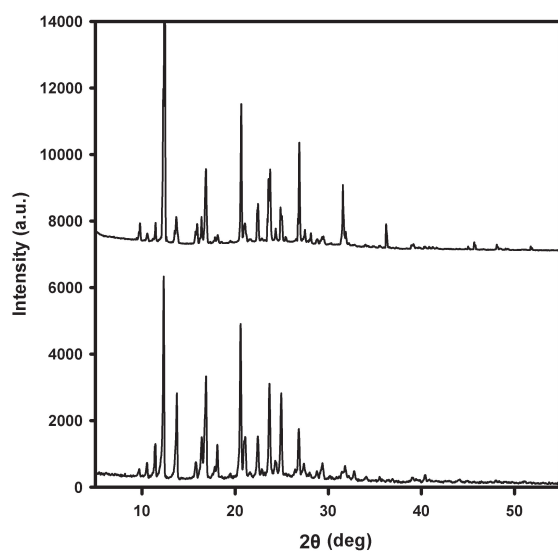


Figure S57. PXRD patterns of **5c** performed on the solid before heating (bottom) and after heating (top) in 1/2 EtOH/H₂O.

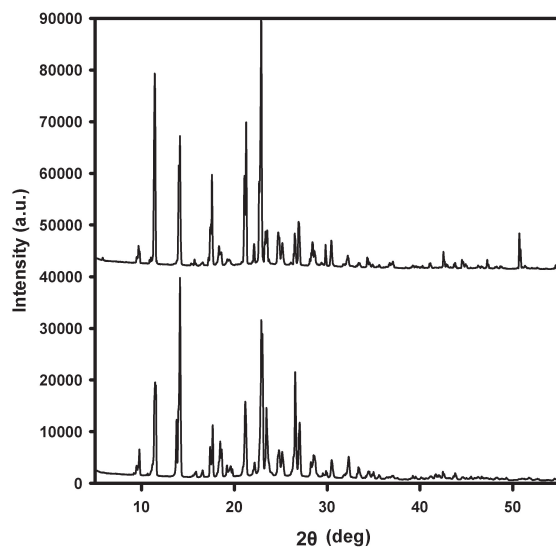


Figure S58. PXRD patterns of **6a** performed on the solid before heating (bottom) and after heating (top) in 1/2 EtOH/H₂O.

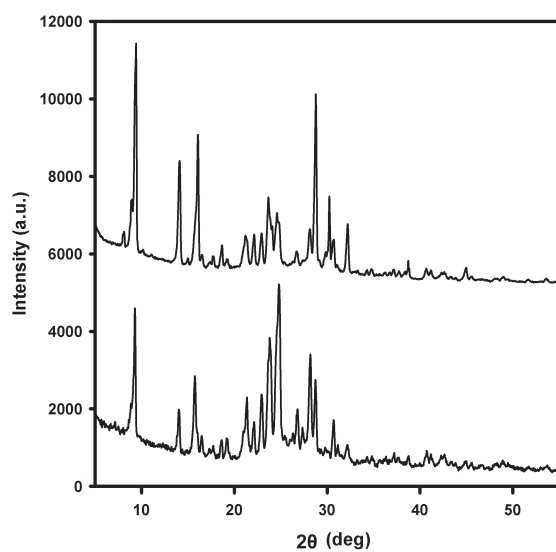


Figure S59. PXRD patterns of **6b** performed on the solid before heating (bottom) and after heating (top) in 1/2 EtOH/H₂O.

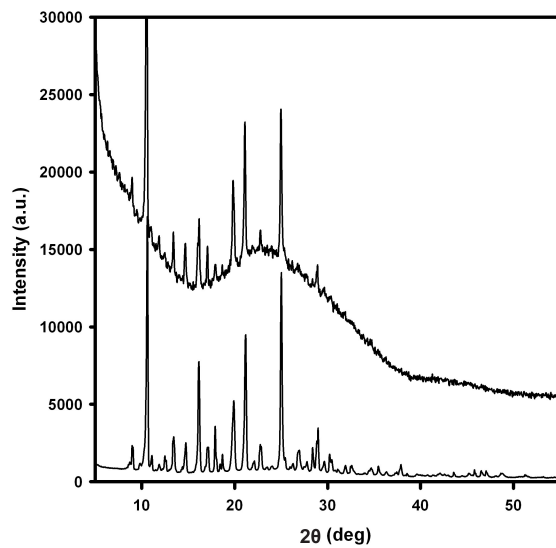


Figure S60. PXRD patterns of **7** performed on the solid (Form II) before heating (bottom) and after heating (top) in 1/2 EtOH/H₂O.

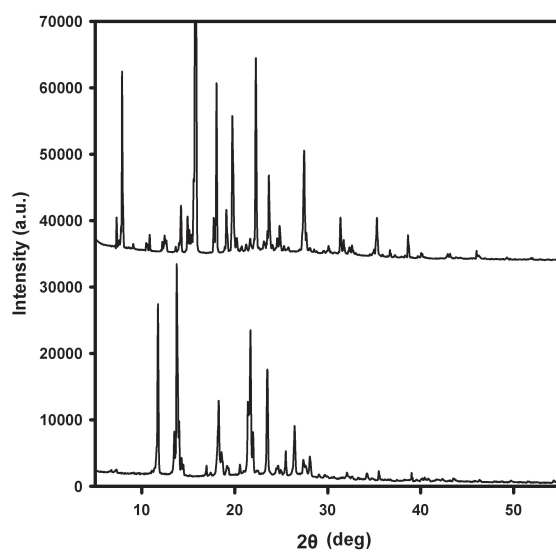


Figure S61. PXRD patterns of **8b** performed on the solid before heating (bottom) and after heating (top) in 1/2 EtOH/H₂O. Note that two patterns were different.

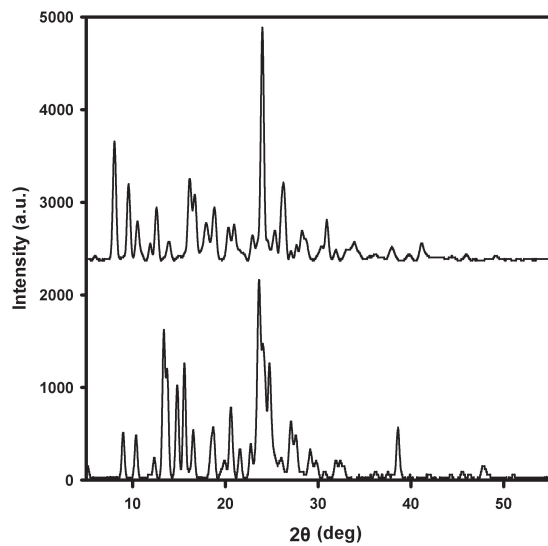


Figure S62. PXRD patterns of **9a** performed on the solid before heating (bottom) and after heating (top) in 1/2 EtOH/H₂O. Note that two patterns were different.

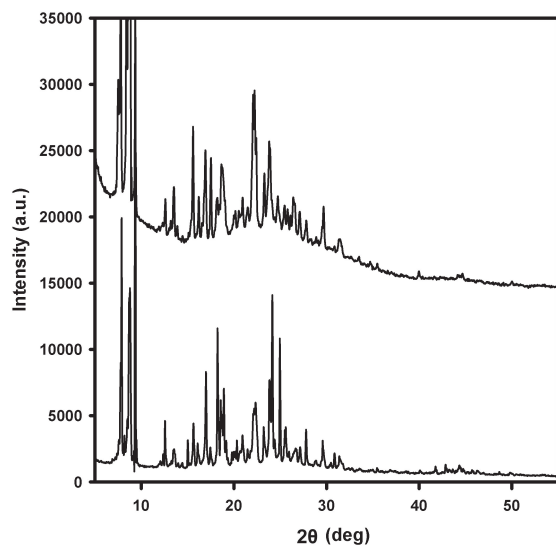


Figure S63. PXRD patterns of **9b** performed on the solid before heating (bottom) and after heating (top) in 1/2 EtOH/H₂O.

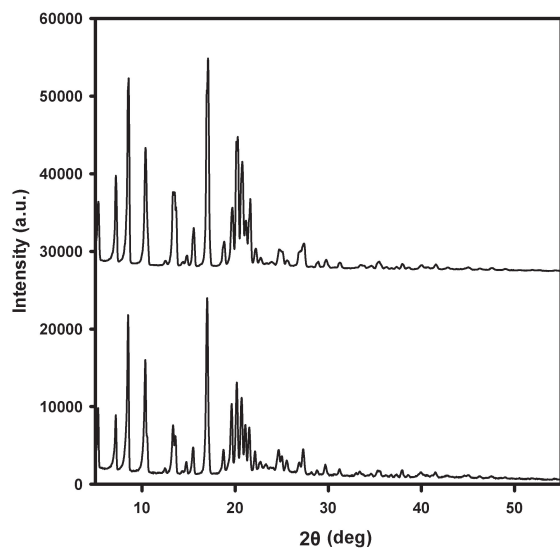


Figure S64. PXR D patterns of **9c** performed on the solid before heating (bottom) and after heating (top) in 1/2 EtOH/H₂O.

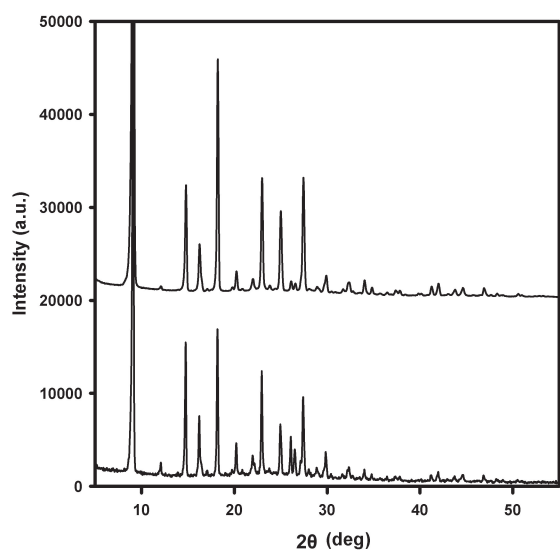


Figure S65. PXR D patterns of **9d** performed on the solid before heating (bottom) and after heating (top) in 1/2 EtOH/H₂O.

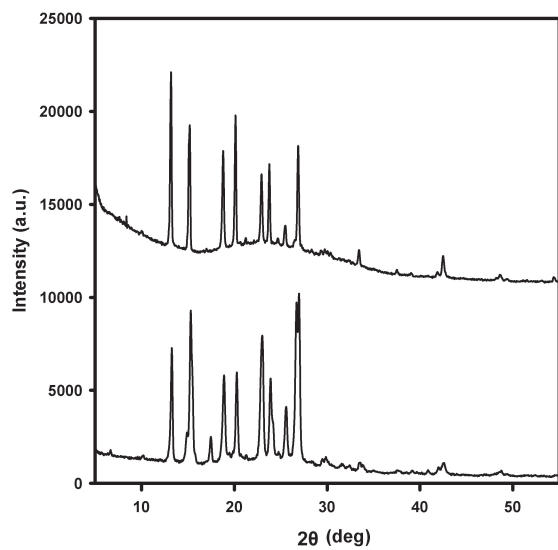


Figure S66. PXR D patterns of **10a** performed on the solid before heating (bottom) and after heating (top) in 1/2 EtOH/H₂O.

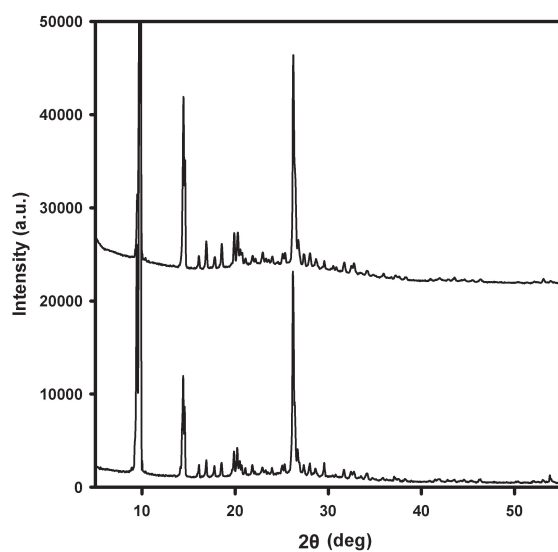


Figure S67. PXR D patterns of **10b** performed on the solid before heating (bottom) and after heating (top) in 1/2 EtOH/H₂O.

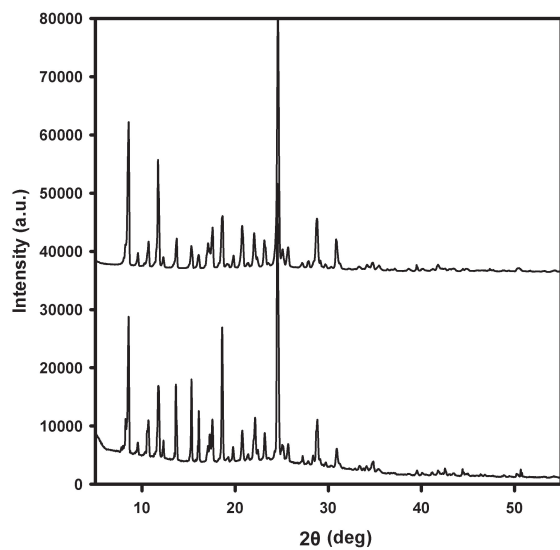


Figure S68. PXR D patterns of **11a** performed on the solid before heating (bottom) and after heating (top) in 1/2 EtOH/H₂O.

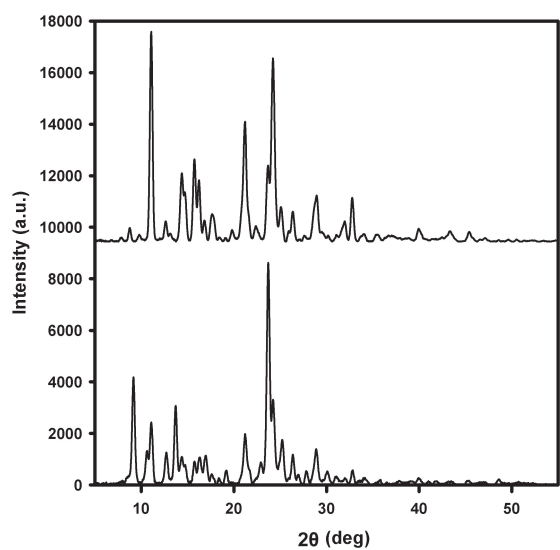


Figure S69. PXR D patterns of **11b** performed on the solid before heating (bottom) and after heating (top) in 1/2 EtOH/H₂O.

X. References

1. Chen, J.; Kampf, J. W.; McNeil, A. J. *Langmuir* **2010**, *26*, 13076-13080.
2. Yang, Z.; Liang, G.; Ma, M.; Gao, Y.; Xu, B. *J. Mater. Chem.* **2007**, *17*, 850-854.

Appendix 4

Appendix to Chapter 5: Detecting a Peroxide-based Explosive via Molecular Gelation

I. General Experimental

Commercially available reagents and solvents for the synthetic procedures were obtained from Sigma-Aldrich, Acros Organic, and Fisher Scientific and used as received. The syntheses were adapted from published literature procedures¹ as described in section II.

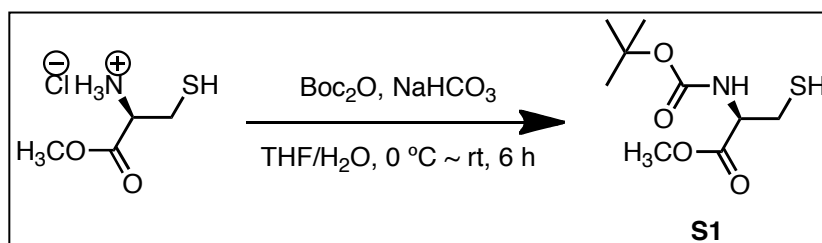
Synthesis of TATP:² All operations should be carried out behind a blast shield in the fume hood. TATP was synthesized on a 100-200 mg scale. A 4 mL vial was charged with a stir bar and placed in an ice-water bath. Acetone (200 μ L) and H₂O₂ (30%, 276 μ L) were added to the vial. Concentrated H₂SO₄ (20 μ L) was added to the solution drop-wise. The vial was capped and the homogeneous solution was stirred overnight at rt. The white precipitate was filtered and washed with H₂O (3 x 20 mL), and dried under air for 30-60 min. The typical yield was ~35-60% and the product was characterized by ¹H and ¹³C NMR spectroscopy. The product was stored at 4 °C and used without further purification.

NMR Spectroscopy: ¹H and ¹³C NMR spectra for all compounds were acquired at rt in DMSO-*d*₆ or CDCl₃ on a Varian vnmrs 500 operating at 500 and 126 MHz or a Varian MR 400 operating at 400 and 100 MHz, respectively. The chemical shift data are reported in units of δ (ppm) relative to tetramethylsilane (TMS) and referenced with residual solvent. Multiplicities are reported as follows: singlet (s), doublet (d), doublet of doublets (dd), triplet (t), quartet (q), quintet (quin), multiplet (m) and broad resonance (br).

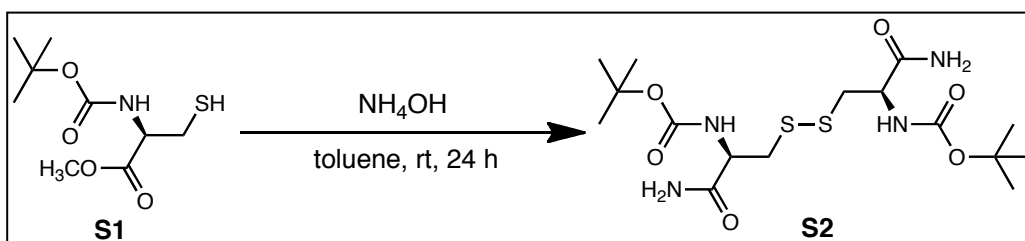
Mass Spectrometry: HRMS data was obtained on a Micromass Autospec Ultima Magnetic Sector mass spectrometer.

General Procedure for cgc Determination: A 4 mL vial was charged with ~2-3 mg of **2-7** and 0.30 mL MeOH. The mixture was sonicated while heating to the boiling point of MeOH and then allowed to cool to rt. The vial was inverted to examine if a stable gel formed. If a stable gel formed, 0.10 mL of MeOH was added and the procedure was repeated until an unstable gel was formed. The last concentration of the stable gel was recorded as critical gelation concentration (cgc).

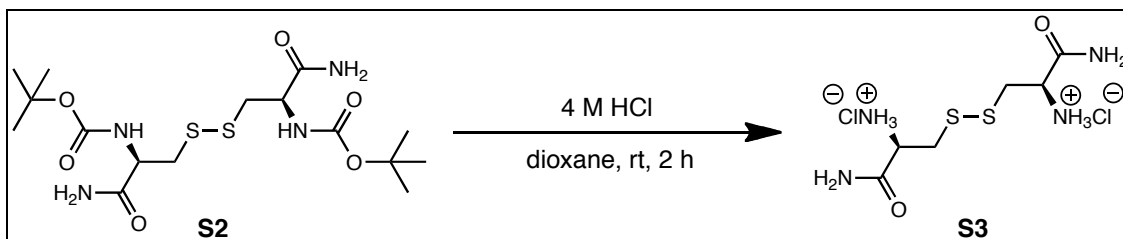
II. Syntheses



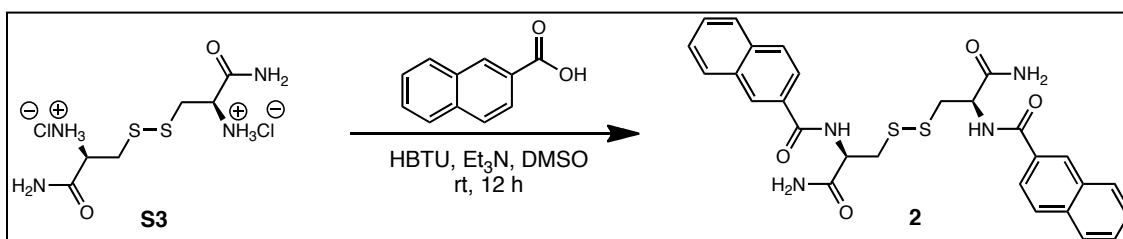
S1: A 250 mL round-bottom flask was charged with a stir bar, L-cysteine methyl ester (2.005 g, 11.73 mmol) and THF (15 mL) and cooled to 0 °C. To this solution, an aqueous solution of NaHCO₃ (2.3 M, 15 mL) was added, followed by the addition of di-*t*-butyl dicarbonate (2.427 g, 11.13 mmol). The ice-water bath was then removed and the solution was stirred at rt. After 6 h, the solution was concentrated under reduced pressure and the residue was adjusted to ~ pH 4 with saturated aqueous solution of citric acid. The mixture was then extracted with CH₂Cl₂ (3 x 30 mL). The organic layers were combined, washed with brine (50 mL), dried over MgSO₄, filter and concentrated in vacuo to give a colorless oil (2.577 g, 94%). HRMS (ESI): Calcd for C₉H₁₇NO₄S, 258.0770 [M + Na]⁺; Found 258.0770 .



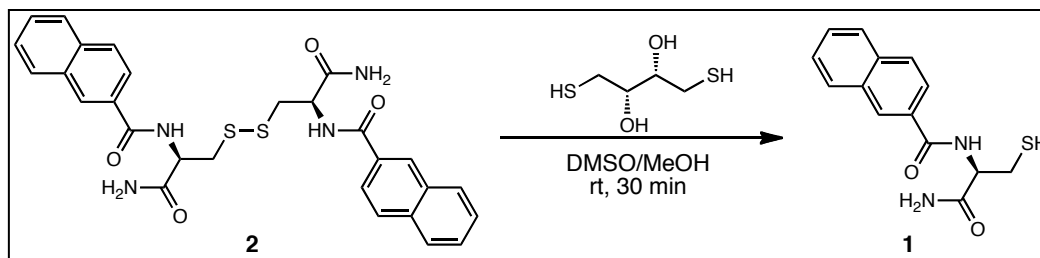
S2^{1a}: A 250 mL round-bottom flask was charged with a stir bar, **S1** (5.199 g, 22.12 mmol), toluene (15 mL) and NH₄OH (aq) (30%, 15 mL) and the heterogeneous mixture was stirred at rt. After 24 h, the reaction was concentrated under reduced pressure. The solid residue was filtered and the white solid was washed with H₂O (3 x 20 mL), MeOH (3 x 20 mL) and dried in vacuo to give a white solid (3.334 g, 69%). HRMS (ESI): Calcd for C₁₆H₃₁N₄O₆S₂, 461.1499 [M + Na]⁺; Found 461.1501.



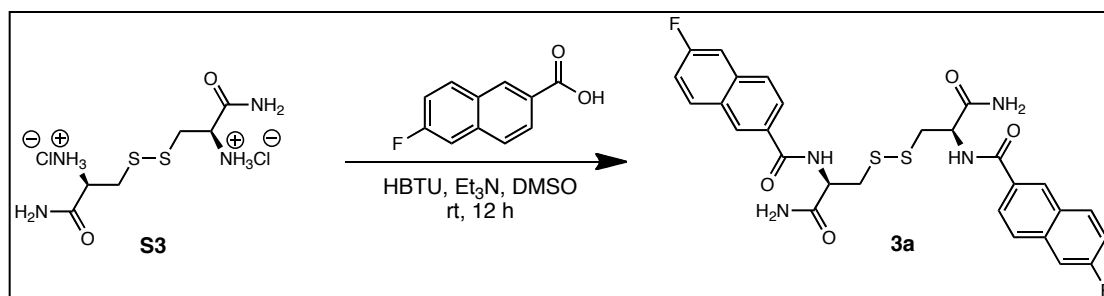
S3^{1b}: A 50 mL round-bottom flask was charged with a stir bar, **S2** (795 mg, 1.82 mmol) and dioxane (10 mL). To this mixture, HCl (10 mL, 4 M in dioxane) was added over 10 min and the mixture was stirred at rt. After 2 h, the solvent was evaporated under reduced pressure. The solid residue was filtered and the white solid was washed with acetone (3 x 20 mL) and dried in vacuo to give a white solid (535 mg, 95%). HRMS (ESI): Calcd for C₆H₁₄N₄O₂S₂, 239.0636 [M + H]⁺; Found 239.0637.



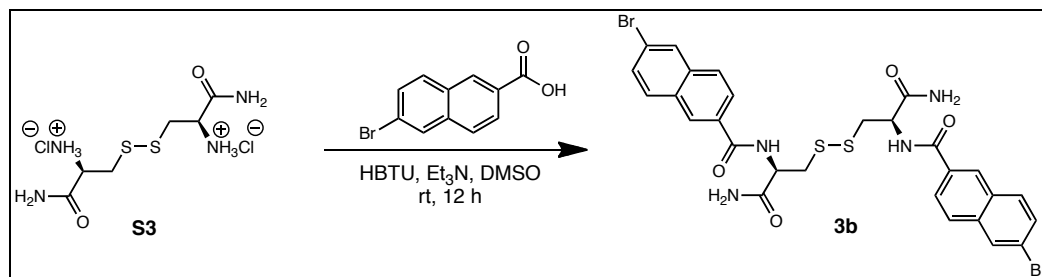
2^{1c}: A 50 mL round-bottom flask was charged with a stir bar, 2-naphthoic acid (111 mg, 0.645 mmol), HBTU (245 mg, 0.646 mmol) and anhydrous DMSO (10 mL). The solution was stirred at rt for 30 min. Sequentially, **S3** (100 mg, 0.323 mmol) and Et₃N (179 μL, 1.29 mmol) were added and the solution was stirred at rt. After 12 h, the solution was poured into H₂O (100 mL). The resulting precipitate was filtered and washed with H₂O (3 x 20 mL), MeOH (3 x 20 mL) and dried in vacuo to give a white solid (113 mg, 64%). HRMS (ESI): Calcd for C₂₈H₂₆N₄O₄S₂, 547.1468 [M + H]⁺; Found 547.1473.



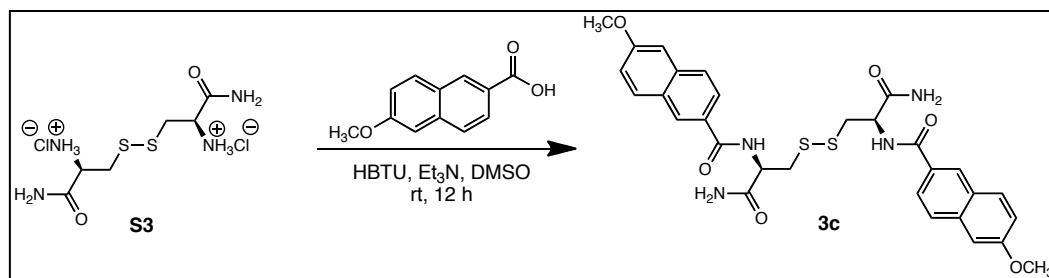
1: A 50 mL round-bottom flask was charged with a stir bar, **2** (200 mg, 0.366 mmol) and anhydrous DMSO (10 mL). To this mixture, a solution of dithiolthreitol (1.85 M, 1 mL MeOH) was added and the solution was stirred at rt. After 30 min, the mixture was poured into H₂O (100 mL) and extracted with EtOAc (3 x 30 mL). The organic layers were combined, washed with brine (2 x 30 mL), dried over MgSO₄, filtered and concentrated in vacuo to give a white solid (91 mg, 45%). HRMS (ESI): Calcd for C₁₄H₁₄N₂O₂S, 297.0674 [M + Na]⁺; Found 297.0672.



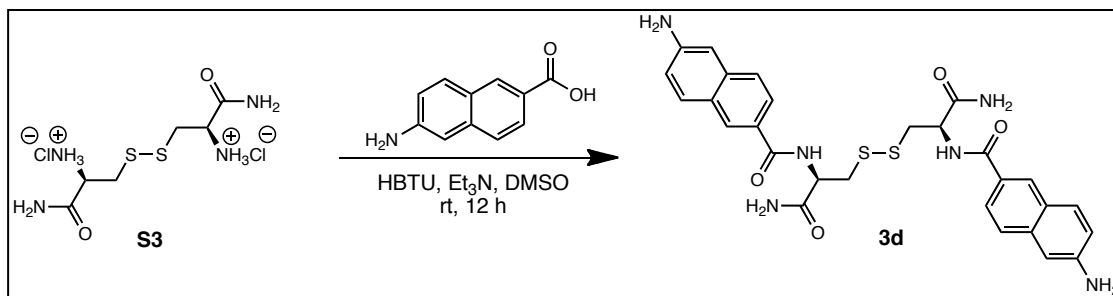
3a: A 50 mL round-bottom flask was charged with a stir bar, 6-fluoro-2-naphthoic acid (123 mg, 0.647 mmol), HBTU (245 mg, 0.646 mmol) and anhydrous DMSO (10 mL). The solution was stirred at rt for 30 min. Sequentially, **S3** (100 mg, 0.323 mmol) and Et₃N (179 μL, 1.29 mmol) were added and the solution was stirred at rt. After 12 h, the solution was poured into H₂O (100 mL). The resulting precipitate was filtered and washed with H₂O (3 x 20 mL), MeOH (3 x 20 mL) and dried in vacuo to give a white solid (92 mg, 49%). HRMS (ESI): Calcd for C₂₈H₂₆N₄O₆S₂, 583.1280 [M + H]⁺; Found 583.1301.



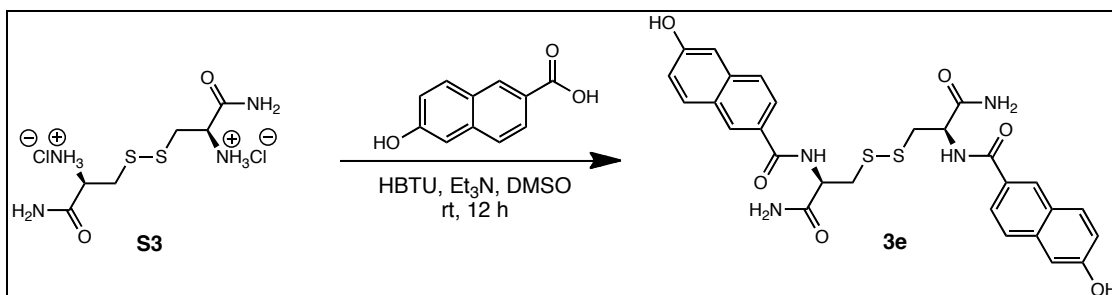
3b: A 50 mL round-bottom flask was charged with a stir bar, 6-bromo-2-naphthoic acid (162 mg, 0.645 mmol), HBTU (245 mg, 0.646 mmol) and anhydrous DMSO (10 mL). The solution was stirred at rt for 30 min. Sequentially, **S3** (100 mg, 0.323 mmol) and Et₃N (179 μ L, 1.29 mmol) were added and the solution was stirred at rt. After 12 h, the solution was poured into H₂O (100 mL). The resulting precipitate was filtered and washed with H₂O (3 x 20 mL), MeOH (3 x 20 mL) and dried in vacuo to give a white solid (138 mg, 61%). HRMS (ESI): Calcd for C₂₈H₂₄Br₂N₄O₄S₂, 724.9498 [M + Na]⁺; Found 724.9483.



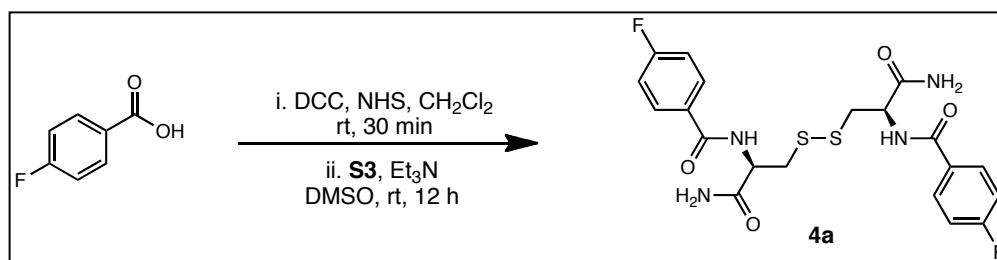
3c: A 50 mL round-bottom flask was charged with a stir bar, 6-methoxy-2-naphthoic acid (130 mg, 0.644 mmol), HBTU (245 mg, 0.646 mmol) and anhydrous DMSO (10 mL). The solution was stirred at rt for 30 min. Sequentially, **S3** (100 mg, 0.323 mmol) and Et₃N (179 μ L, 1.29 mmol) were added and the solution was stirred at rt. After 12 h, the solution was poured into H₂O (100 mL). The resulting precipitate was filtered and washed with H₂O (3 x 20 mL), MeOH (3 x 20 mL) and dried in vacuo to give a white solid (115 mg, 59%). HRMS (ESI): Calcd for C₃₀H₃₀N₄O₆S₂, 607.1685 [M + H]⁺; Found 607.1685.



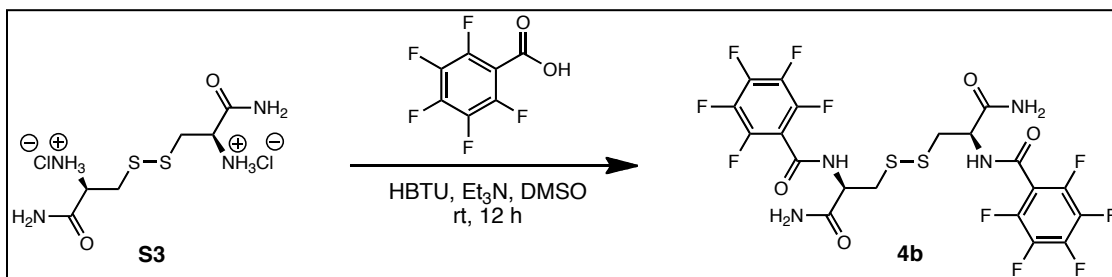
3d: A 50 mL round-bottom flask was charged with stir bar, 6-amino-2-naphthoic acid (0.300 g, 1.60 mmol), HBTU (0.608 g, 1.79 mmol) and anhydrous DMSO (15 mL). The solution was stirred at rt for 30 min. Sequentially, **S3** (0.249 g, 0.801 mmol) and Et₃N (0.47 mL, 3.2 mmol) were added and the solution was stirred at rt. After 12 h the solution was poured into H₂O (150 mL). The resulting precipitate was filtered, washed with H₂O (3 x 10 mL), MeOH (3 x 10 mL) and acetone (3 x 10 mL) to give a light brown solid (0.282 g, 61%). HRMS (ESI): Calcd for C₂₈H₂₈N₆O₄S₂, 599.1511 [M + Na]⁺; Found 599.1509.



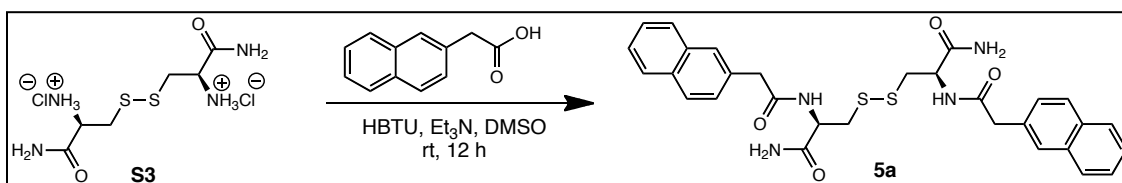
3e: A 50 mL round-bottom flask was charged with stir bar, 6-hydroxy-2-naphthoic acid (0.158 g, 0.839 mmol) and HBTU (0.318 g, 0.838 mmol) and anhydrous DMSO (10 mL). The solution was stirred at rt for 30 min. Sequentially, **S3** (0.130 g, 0.418 mmol) and Et₃N (0.26 mL, 1.8 mmol) were added and the solution was stirred at rt. After 12 h the solution was poured into H₂O (100 mL). The resulting precipitate was filtered, washed with H₂O (3 x 10 mL) and hexanes (3 x 10 mL). The crude product was recrystallized from MeOH/EtOAc (95:5) to give a white solid (0.077 g, 32%). HRMS (ESI): Calcd for C₂₈H₂₆N₄O₆S₂, 579.1367 [M + H]⁺; Found 579.1378.



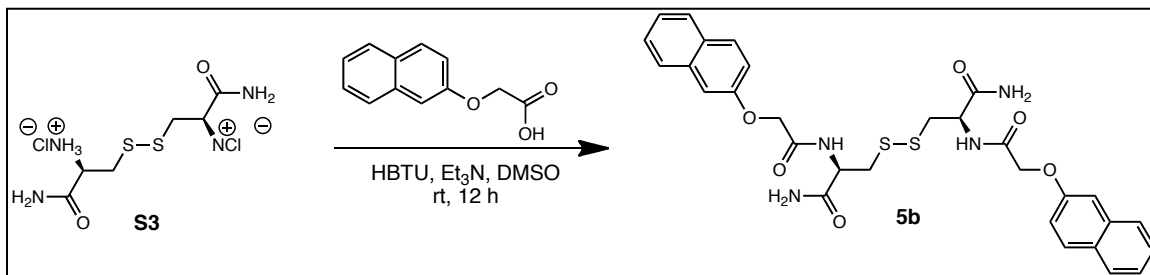
4a: In a 20 mL vial, 4-fluorobenzoic acid (0.200 g, 1.44 mmol) and N-hydroxysuccinimide (NHS, 0.164 g, 1.43 mmol) were dissolved in CH₂Cl₂ (10.0 mL) at rt. To this solution, N,N'-dicyclohexylcarbodiimide (DCC, 0.198 g, 0.960 mmol) was added and the solution was stirred at rt for 30 min. The precipitate was removed via filtration and the filtrate, which contains the intermediate, was evaporated under reduced pressure to obtain a white solid that was submitted to the next reaction without further purification. The solid obtained from previous step and **S3** (0.222 g, 0.714 mmol) were dissolved in anhydrous DMSO (10 mL) and stirred for 10 min at rt. Then Et₃N (4.0 mL, 2.9 mmol) was added at rt. After 12 h the reaction was poured into H₂O (100 mL). The resulting precipitate was filtered, washed with H₂O (3 x 10 mL), hexanes (2 x 10 mL), and cyclohexane/EtOH (1:1, 2 x 20 mL). The crude product was recrystallized from MeOH to give a white solid (0.139 g, 46%). HRMS (ESI): Calcd for C₂₀H₂₀F₂N₄O₄S₂, 505.0792 [M + Na]⁺; Found 505.0784.



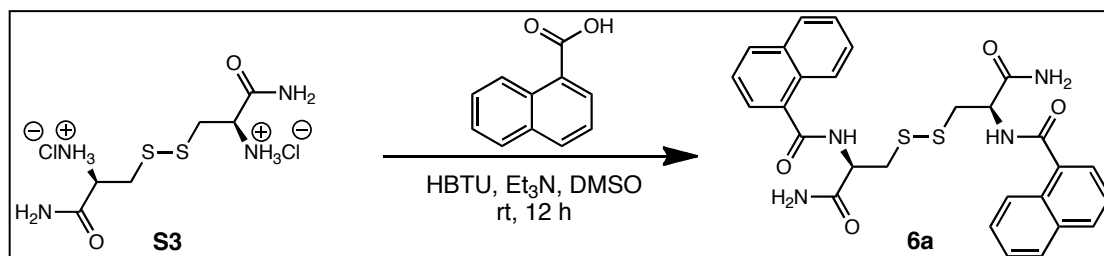
4b: A 50 mL round-bottom flask was charged with a stir bar, pentafluorobenzoic acid (72 mg, 0.34 mmol), HBTU (129 mg, 0.340 mmol) and anhydrous DMSO (10 mL). The solution was stirred at rt for 30 min. Sequentially, **S3** (53 mg, 0.17 mmol) and Et₃N (95 μ L, 0.68 mmol) were added and the solution was stirred at rt. After 12 h, the solution was poured into H₂O (100 mL). The resulting precipitate was filtered and washed with H₂O (3 x 20 mL) and dried in vacuo to give a pale brown solid (29 mg, 27%). HRMS (ESI): Calcd for C₂₀H₁₂F₁₀N₄O₄S₂, 627.0213 [M + H]⁺; Found 627.0220.



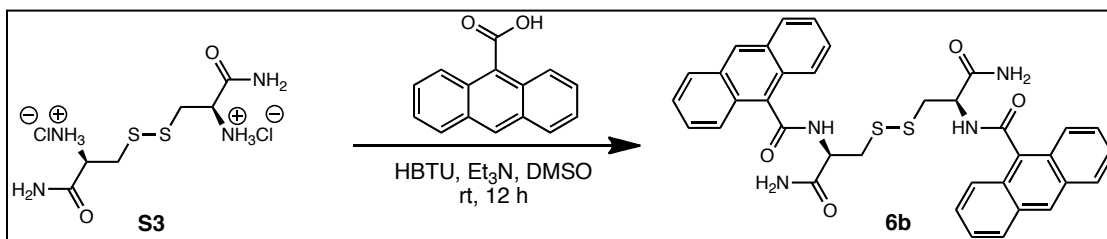
5a: A 50 mL round-bottom flask was charged with a stir bar, 2-naphthaleneacetic acid (120 mg, 0.645 mmol), HBTU (245 mg, 0.646 mmol) and anhydrous DMSO (10 mL). The solution was stirred at rt for 30 min. Sequentially, **S3** (100 mg, 0.323 mmol) and Et₃N (179 μ L, 1.29 mmol) were added and the solution was stirred at rt. After 12 h, the solution was poured into H₂O (100 mL). The resulting precipitate was filtered and washed with H₂O (3 x 20 mL), MeOH (3 x 20 mL) and dried in vacuo to give a white solid (114 mg, 62%). HRMS (ESI): Calcd for C₃₀H₃₀N₄O₄S₂, 597.1606 [M + H]⁺; Found 597.1605.



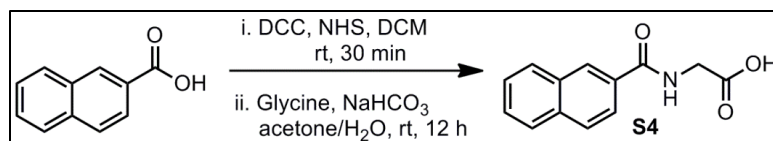
5b: A 50 mL round-bottom flask was charged with a stir bar, 2-naphthoxyacetic acid (130 mg, 0.644 mmol), HBTU (245 mg, 0.646 mmol) and anhydrous DMSO (10 mL). The solution was stirred at rt for 30 min. Sequentially, **S3** (100 mg, 0.323 mmol) and Et₃N (179 μ L, 1.29 mmol) were added and the solution was stirred at rt. After 12 h, the solution was poured into H₂O (100 mL). The resulting precipitate was filtered and washed with H₂O (3 x 20 mL), MeOH (3 x 20 mL) and dried in vacuo to give a white solid (158 mg, 81%). HRMS (ESI): Calcd for C₃₀H₃₀N₄O₆S₂, 629.1504 [M + Na]⁺; Found 629.1500. Elemental Analysis: Calcd. for C₃₀H₃₀N₄O₆S₂: C, 59.39; H, 4.98; N, 9.23; O, 15.82; S, 10.57; Found: C, 59.50; H, 4.93; N, 9.21; O, 15.94; S, 10.42.



6a: A 50 mL round-bottom flask was charged with a stir bar, 1-naphthoic acid (111 mg, 0.645 mmol), HBTU (245 mg, 0.646 mmol) and anhydrous DMSO (10 mL). The solution was stirred at rt for 30 min. Sequentially, **S3** (100 mg, 0.323 mmol) and Et₃N (179 μ L, 1.29 mmol) were added and the solution was stirred at rt. After 12 h, the solution was poured into H₂O (100 mL). The resulting precipitate was filtered and washed with H₂O (3 x 20 mL), MeOH (3 x 20 mL) and dried in vacuo to give a brown solid (102 mg, 58%). HRMS (ESI): Calcd for C₂₈H₂₆N₄O₄S₂, 547.1474 [M + H]⁺; Found 547.1474.

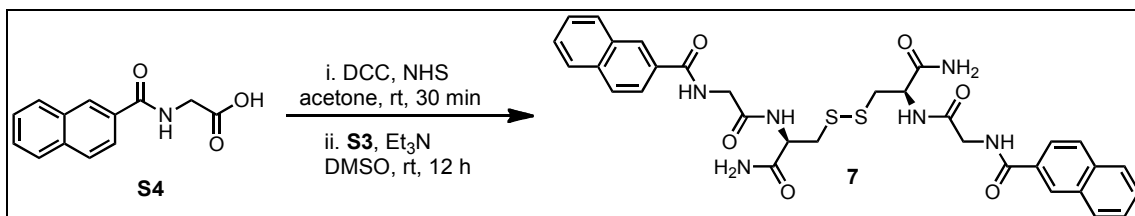


6b: A 50 mL round-bottom flask was charged with a stir bar, 9-anthracenecarboxylic acid (143 mg, 0.644 mmol), HBTU (245 mg, 0.646 mmol) and anhydrous DMSO (10 mL). The solution was stirred at rt for 30 min. Sequentially, **S3** (100 mg, 0.323 mmol) and Et₃N (179 μ L, 1.29 mmol) were added and the solution was stirred at rt. After 12 h, the solution was poured into H₂O (100 mL). The resulting precipitate was filtered and washed with H₂O (3 x 20 mL), MeOH (3 x 20 mL) and dried in vacuo to give a pale yellow solid (80 mg, 38%). HRMS (ESI): Calcd for C₃₆H₃₀N₄O₄S₂, 669.1606 [M + Na]⁺; Found 669.1604.



S4: In a 20 mL vial, 2-naphthoic acid (0.150 g, 0.871 mmol) and NHS (0.101 g, 0.869 mmol) were dissolved in CH₂Cl₂ (10.0 mL) at rt. To this solution, DCC (0.198 g, 0.960 mmol) was added and the final solution was stirred at rt for 30 min. The precipitate was removed via filtration and the filtrate, which contains the intermediate, was evaporated under reduced pressure to obtain a white solid that was submitted to the next reaction without further purification. Glycine (0.065 g, 0.87 mmol) and NaHCO₃ (0.146 g, 1.74 mmol) were dissolved in H₂O (6.0 mL) at rt and the solid obtained previously was dissolved in acetone (9.0 mL) and added to the aqueous solution. After 12 h, the reaction was evaporated under reduced pressure, and the residue re-dissolved in H₂O (~10 mL). The insoluble solid was filtered off and the filtrate was acidified to pH = 3 with dilute HCl to obtain a white precipitate. The solid was filtered, washed with H₂O (3 x 10 mL), hexanes (2 x 10 mL), CH₂Cl₂ (2 x 10 mL) and dried under vacuum to give a white

solid (0.145 g; 72%). HRMS (ESI): Calcd for $C_{13}H_{11}NO_3$, 230.0812 $[M + H]^+$; Found 230.0815.



7: In a 20 mL vial, **S4** (0.130 g, 0.567 mmol) and NHS (0.065 g, 0.57 mmol) were dissolved in acetone (12.0 mL) at rt. To this solution, DCC (0.129 g, 0.625 mmol) was added and the final solution was stirred at rt for 30 min. The precipitate was removed via filtration and the filtrate, which contains the intermediate, was evaporated under reduced pressure to obtain a white solid that was submitted to the next reaction without further purification. The solid obtained from previous step and **S3** (0.088 g, 0.28 mmol) were dissolved in anhydrous DMSO (15 mL) and stirred for 10 min at rt. Then Et₃N (0.16 mL, 1.1 mmol) was added at rt. After 12 h, the reaction was poured into H₂O (100 mL). The resulting precipitate was filtered, washed with H₂O (3 x 10 mL), hexanes (2 x 10 mL), and cyclohexane/EtOH (1:1, 2 x 20 mL) to give a white solid (0.124 g, 66%). HRMS (ESI): Calcd for $C_{32}H_{32}N_6O_6S_2$, 683.1722 $[M + Na]^+$; Found 683.1720.

III. ^1H and ^{13}C NMR Spectra

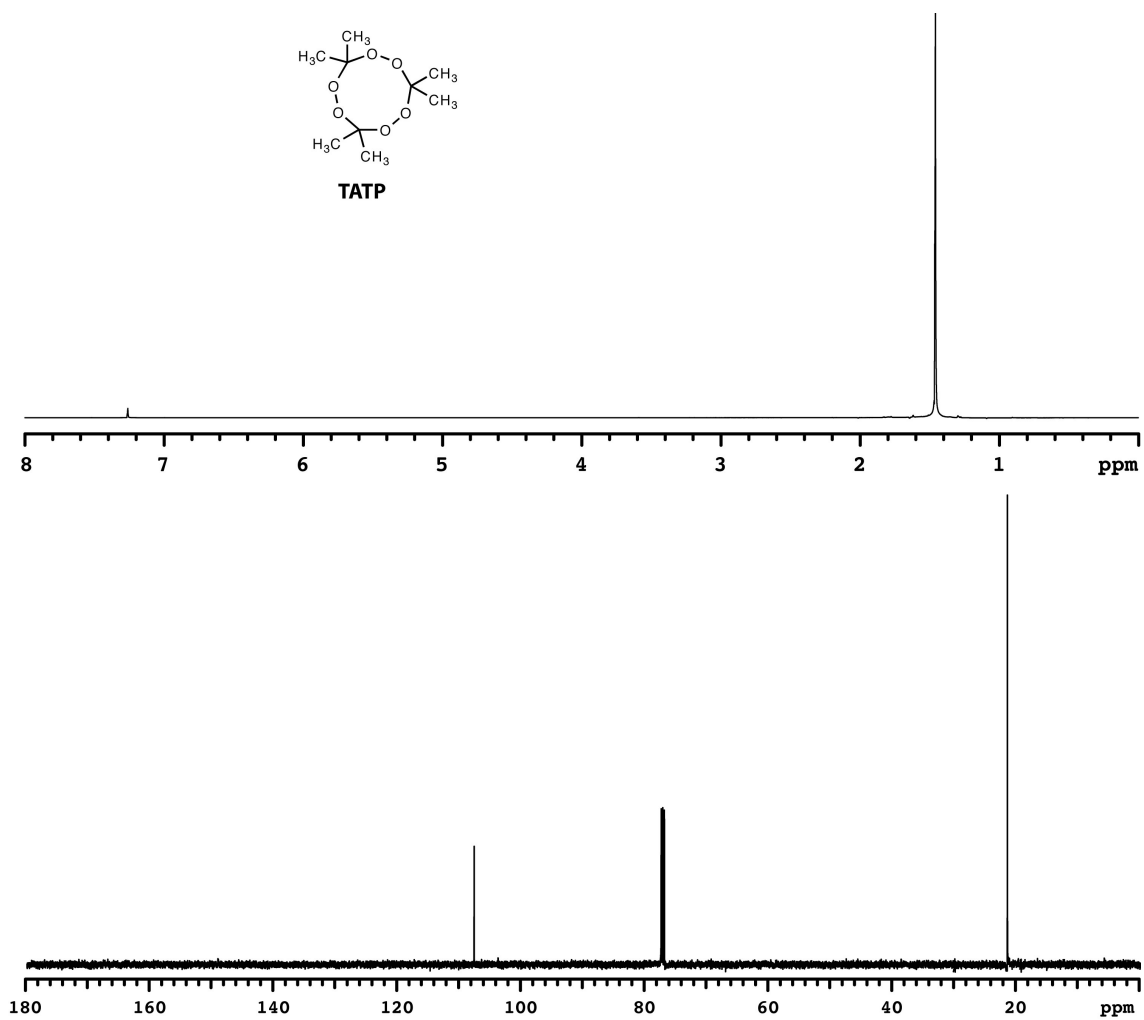


Figure S1. ^1H and ^{13}C NMR spectra of **TATP**. ^1H NMR (CDCl_3 , 500 MHz): δ 1.46. ^{13}C NMR (CDCl_3 , 125 MHz): δ 107.72, 21.54.

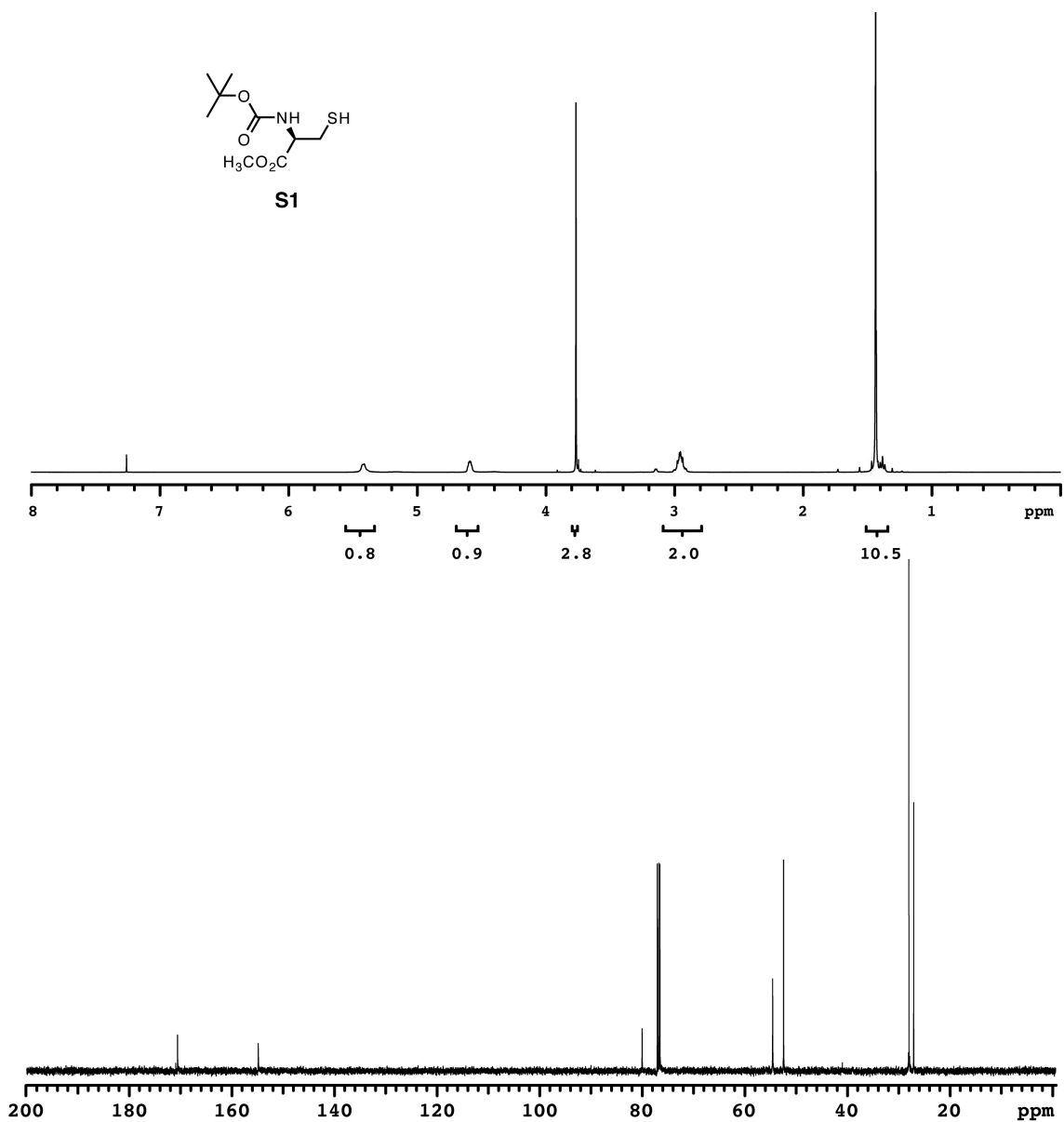


Figure S2. ¹H and ¹³C NMR spectra of **S1**. ¹H NMR (CDCl₃, 500 MHz): δ 5.42 (brs, 1H), 4.59 (brs, 1H), 3.77 (s, 3H), 2.95 (m, 2H), 1.43-1.37 (m, 10H). ¹³C NMR (CDCl₃, 125 MHz): δ 170.52, 154.79, 79.96, 54.52, 52.39, 27.98, 27.03.

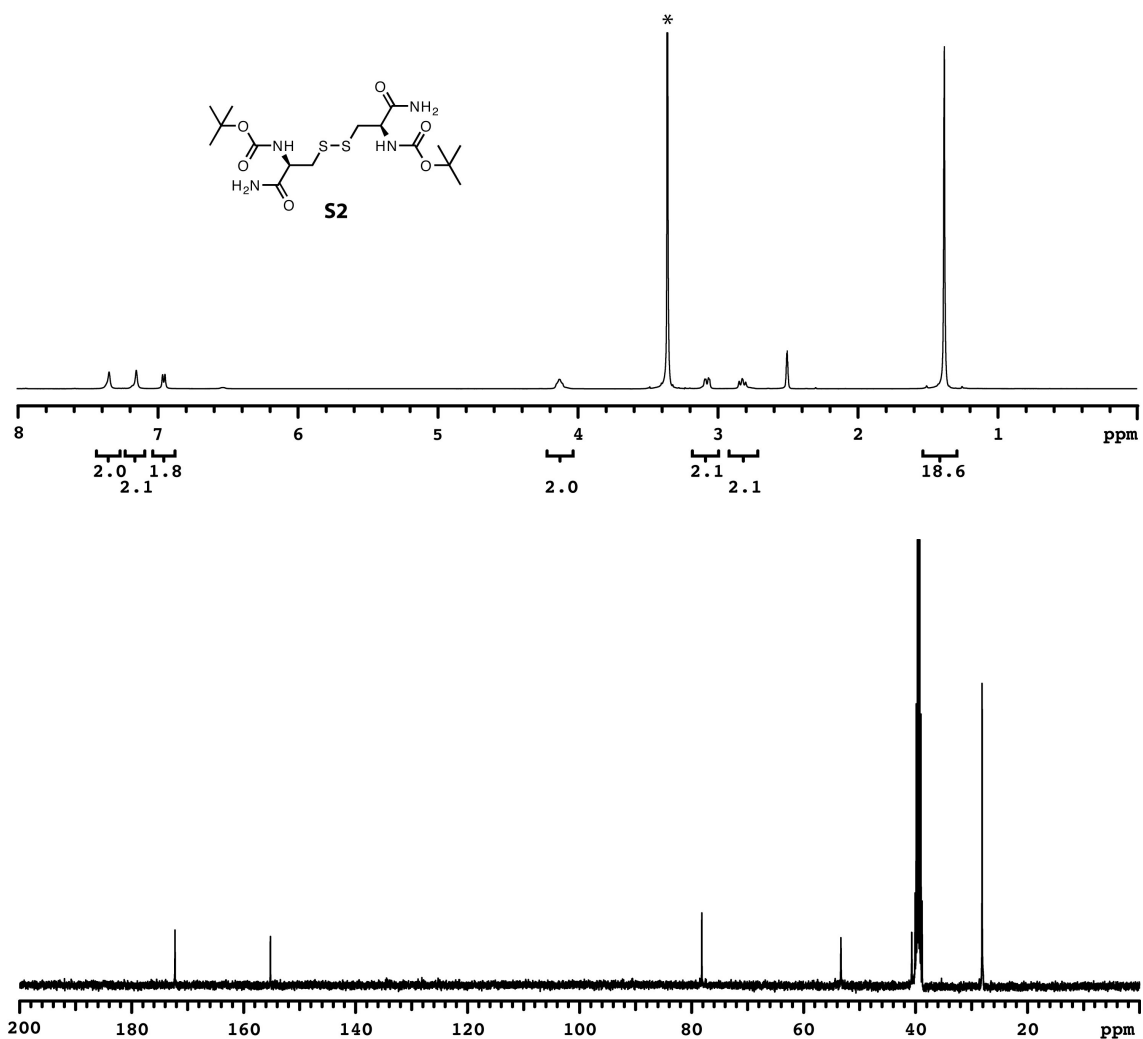


Figure S3. ^1H and ^{13}C NMR spectra of **S2**. ^1H NMR (DMSO- d_6 , 400 MHz): δ 7.33 (brs, 2H), 7.14 (brs, 2H), 6.94 (brm, 2H), 4.13 (brs, 2H), 3.08 (m, 2H), 2.83 (m, 2H), 1.38 (s, 18H). ^{13}C NMR (DMSO- d_6 , 100 MHz): δ 172.30, 155.26, 78.22, 53.38, 40.72, 28.16. *denotes H_2O .

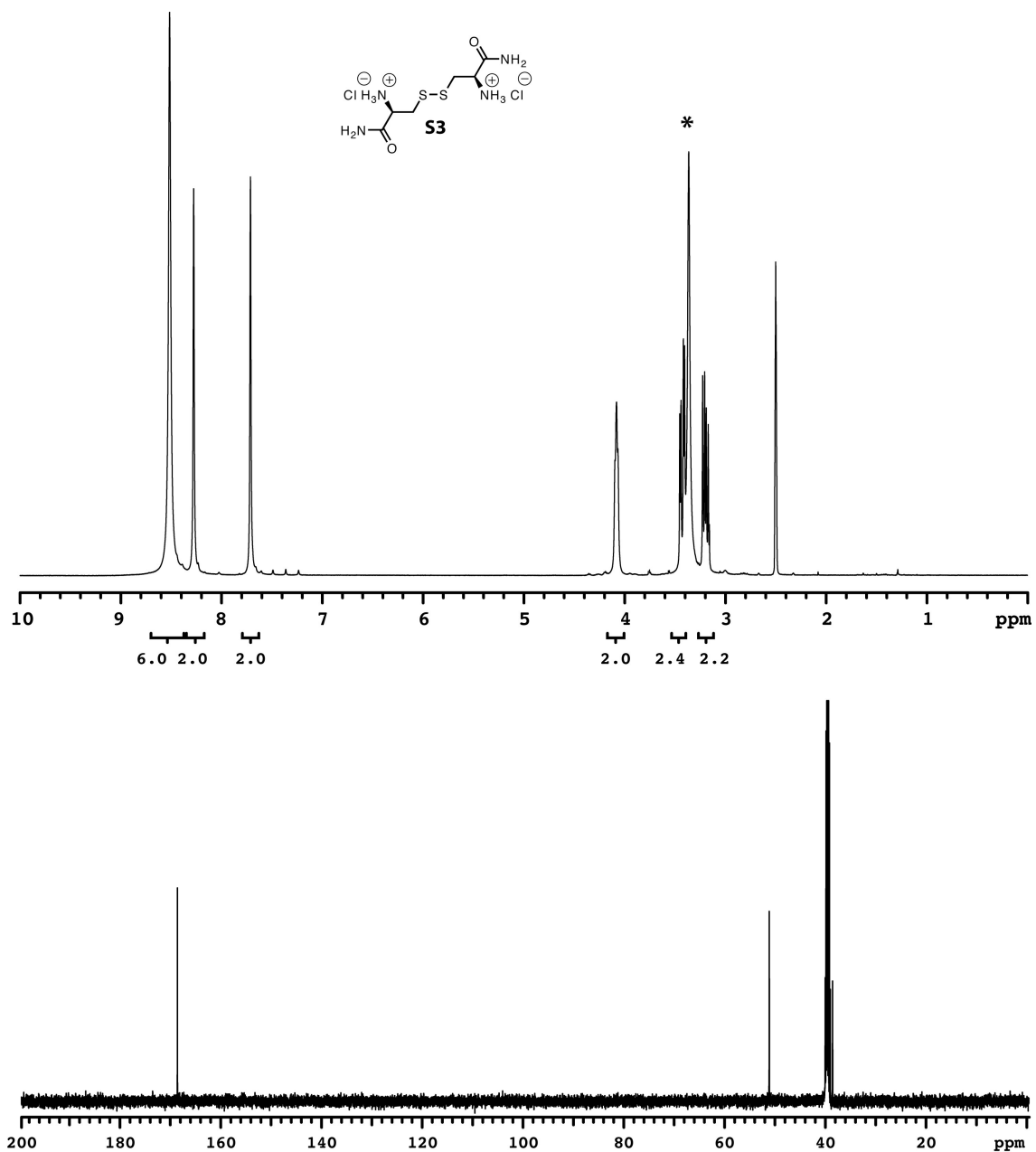


Figure S4. ^1H and ^{13}C NMR spectra of **S3**. ^1H NMR (DMSO- d_6 , 400 MHz): δ 8.52 (brs, 6H), 8.28 (s, 2H), 7.71 (s, 2H), 4.08 (brm, 2H), 3.46-3.40 (m, 2H), 3.20 (m, 2H). ^{13}C NMR (DMSO- d_6 , 125 MHz): δ 168.57, 51.10, 38.54. *denotes H_2O .

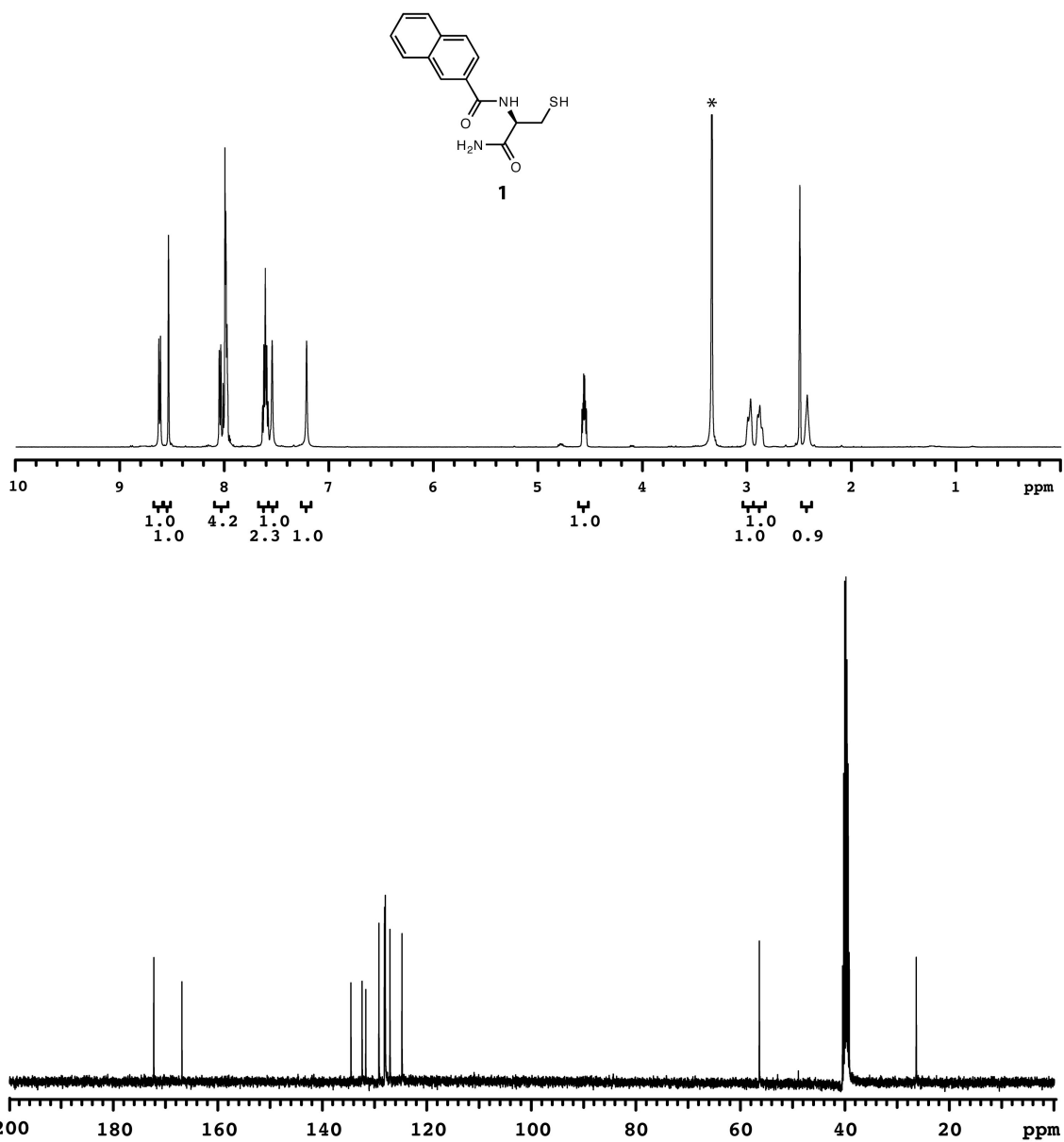


Figure S5. ^1H and ^{13}C NMR spectra of **1**. ^1H NMR (DMSO- d_6 , 500 MHz): δ 8.63 (d, J = 7.5 Hz, 1H), 8.54 (s, 1H), 8.06-7.98 (m, 4H), 7.62 (m, 2H), 7.55 (s, 1H), 7.22 (s, 1H), 4.56 (m, 1H), 2.98 (m, 1H), 2.89 (m, 1H), 2.43 (brs, 1H). ^{13}C NMR (DMSO- d_6 , 125 MHz): δ 171.95, 166.56, 134.22, 132.08, 131.38, 128.87, 127.82, 127.78, 127.67, 127.64, 126.75, 124.45, 56.07, 26.04. *denotes H_2O .

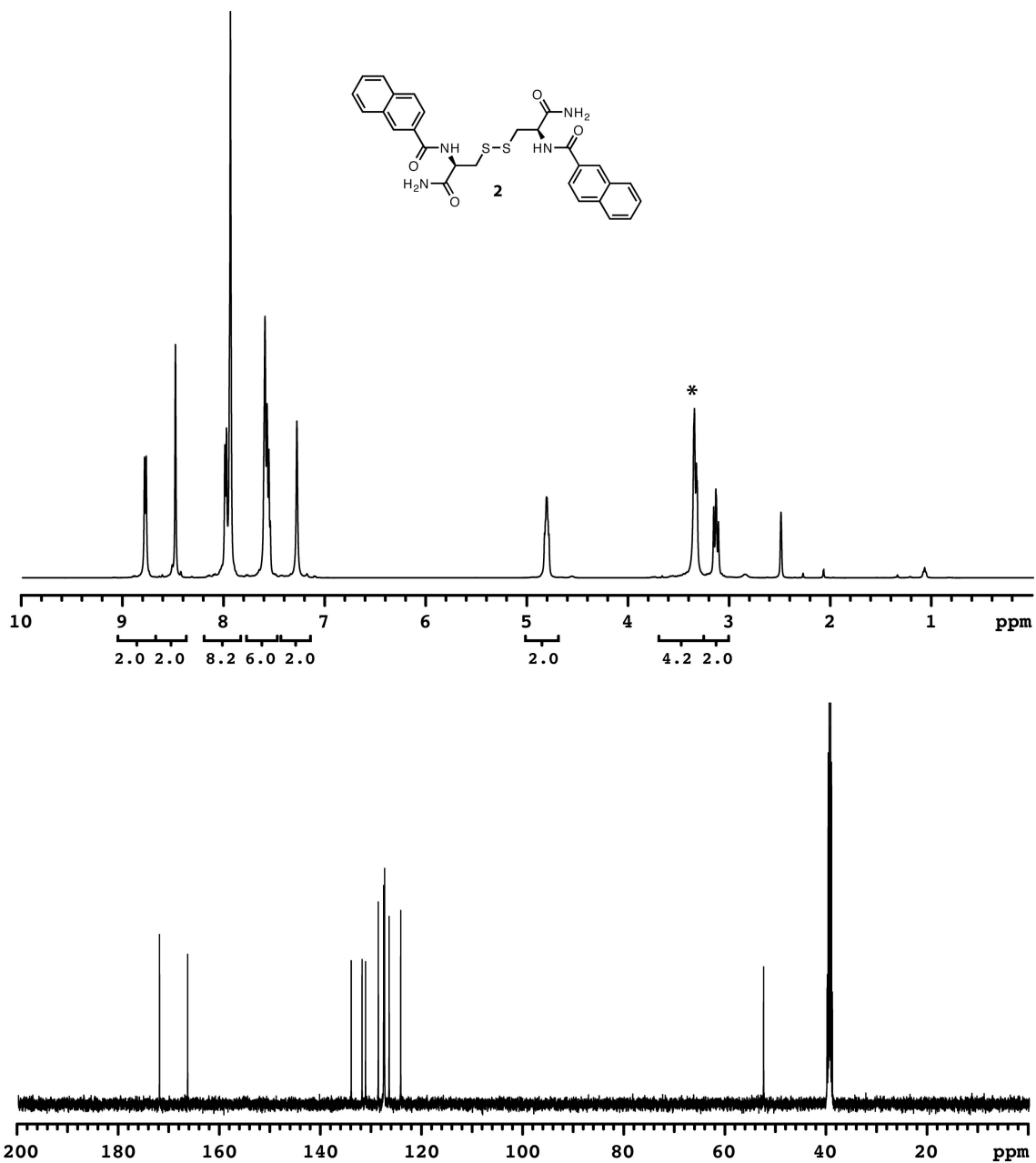


Figure S6. ^1H and ^{13}C NMR spectra of **2**. ^1H NMR (DMSO- d_6 , 500 MHz): δ 8.78 (d, J = 8.0 Hz, 2H), 8.49 (s, 2H), 8.00-7.95 (m, 8H), 7.60-7.55 (m, 6H), 7.29 (s, 2H), 4.82 (m, 2H), 3.33 (m, 2H), 3.15 (m, 2H). ^{13}C NMR (DMSO- d_6 , 125 MHz): δ 172.08, 166.52, 134.17, 132.03, 131.34, 128.82, 127.77, 127.71, 127.58, 126.68, 124.38, 52.61, 40.05. One aromatic carbon was not resolved. *denotes H_2O .

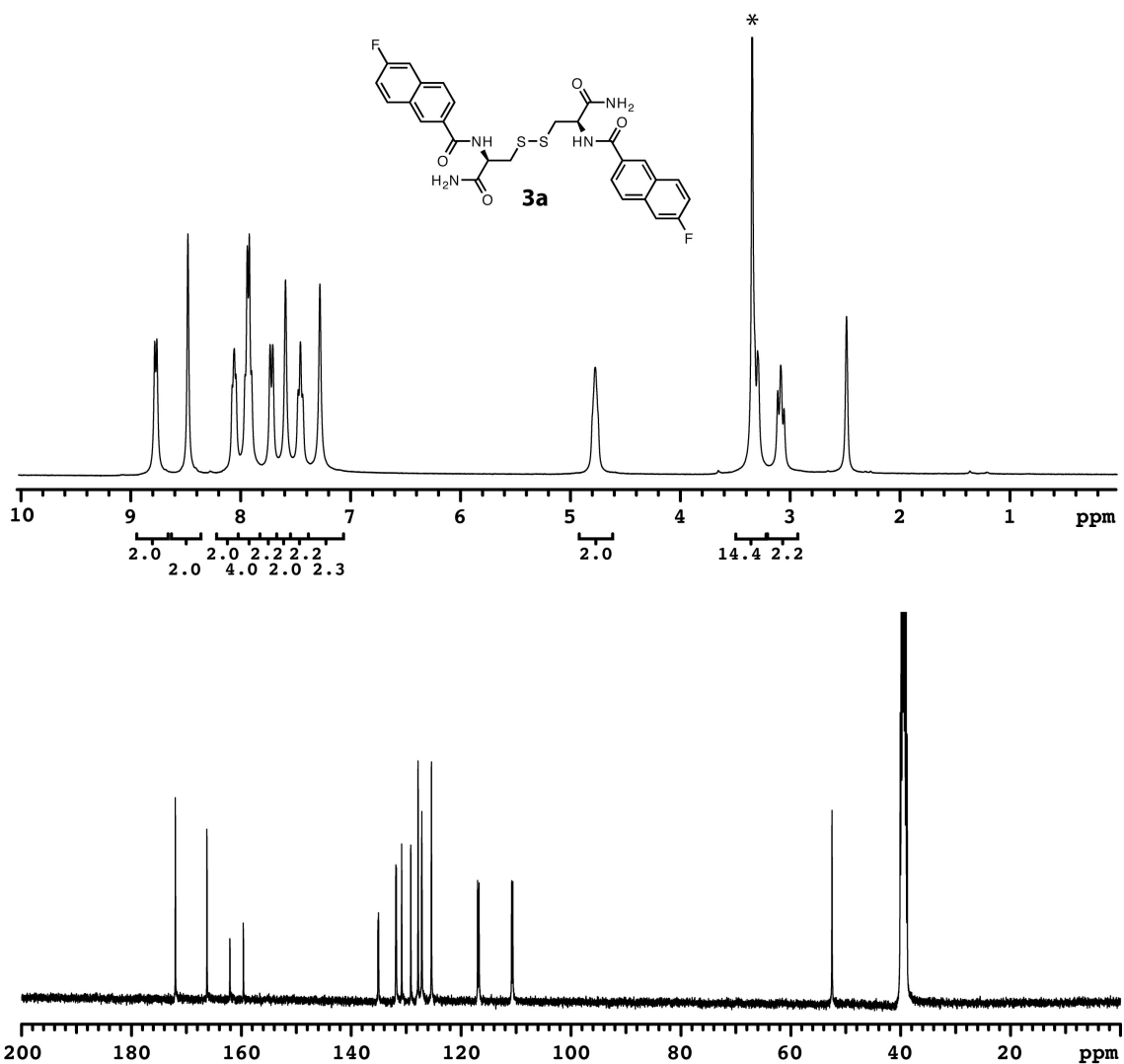


Figure S7. ^1H and ^{13}C NMR spectra of **3a**. ^1H NMR (DMSO- d_6 , 400 MHz): δ 8.78 (d, J = 7.6 Hz, 2H), 8.49 (s, 2H), 8.07 (m, 2H), 7.94 (m, 4H), 7.73 (d, J = 9.6 Hz, 2H), 7.61 (s, 2H), 7.47 (m, 2H), 7.29 (s, 2H), 4.79 (brs, 2H), 3.31-3.26 (m, 2H), 3.10 (m, 2H). ^{13}C NMR (DMSO- d_6 , 100 MHz): δ 172.50 (d, $J_{\text{F-C}}$ = 3.1 Hz), 166.30 (d, $J_{\text{F-C}}$ = 3.1 Hz), 160.90 (d, $J_{\text{F-C}}$ = 248 Hz), 135.17 (dd, $J_{\text{F-C}}$ = 3.1 Hz and 7.0 Hz), 131.88 (d, $J_{\text{F-C}}$ = 6.6 Hz), 130.85, 129.19 (d, $J_{\text{F-C}}$ = 2.7 Hz), 127.87, 127.19, 125.43, 116.90 (d, $J_{\text{F-C}}$ = 25.2 Hz), 110.73 (d, $J_{\text{F-C}}$ = 20.5), 52.53. One aliphatic proton was not resolved with DMSO. *denotes H_2O .

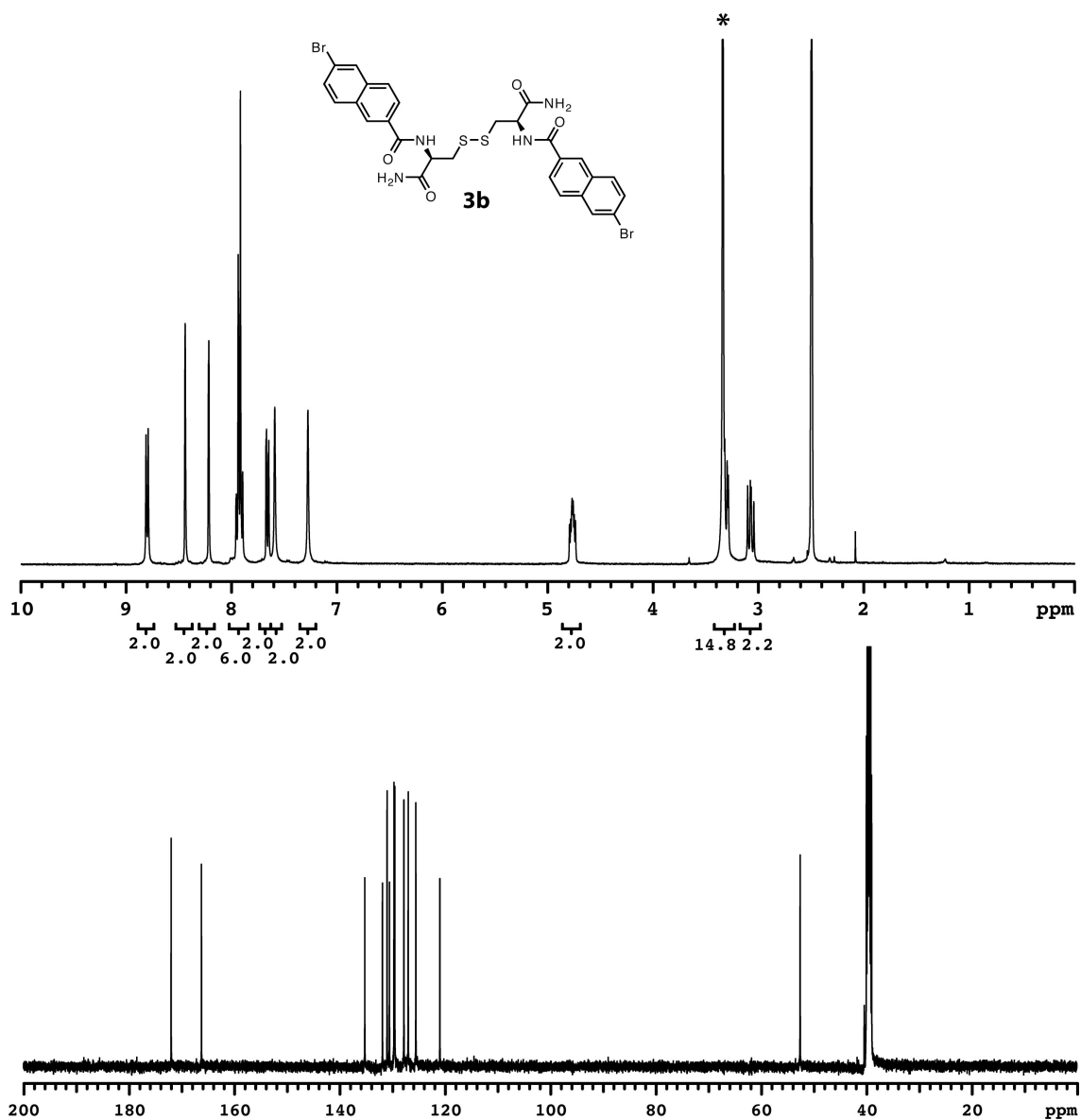


Figure S8. ^1H and ^{13}C NMR spectra of **3b**. ^1H NMR (DMSO- d_6 , 400 MHz): δ 8.81 (d, J = 8.4 Hz, 2H), 8.44 (s, 2H), 8.22 (s, 2H), 7.96-7.90 (m, 6H), 7.66 (m, 2H), 7.59 (s, 2H), 7.28 (s, 2H), 4.77 (m, 2H), 3.31-3.25 (m, 2H), 3.08 (m, 2H). ^{13}C NMR (DMSO- d_6 , 125 MHz): δ 171.97, 166.21, 135.21, 131.85, 130.97, 130.52, 129.67, 129.52, 127.78, 126.96, 125.51, 120.96, 52.57, 40.41. *denotes H_2O .

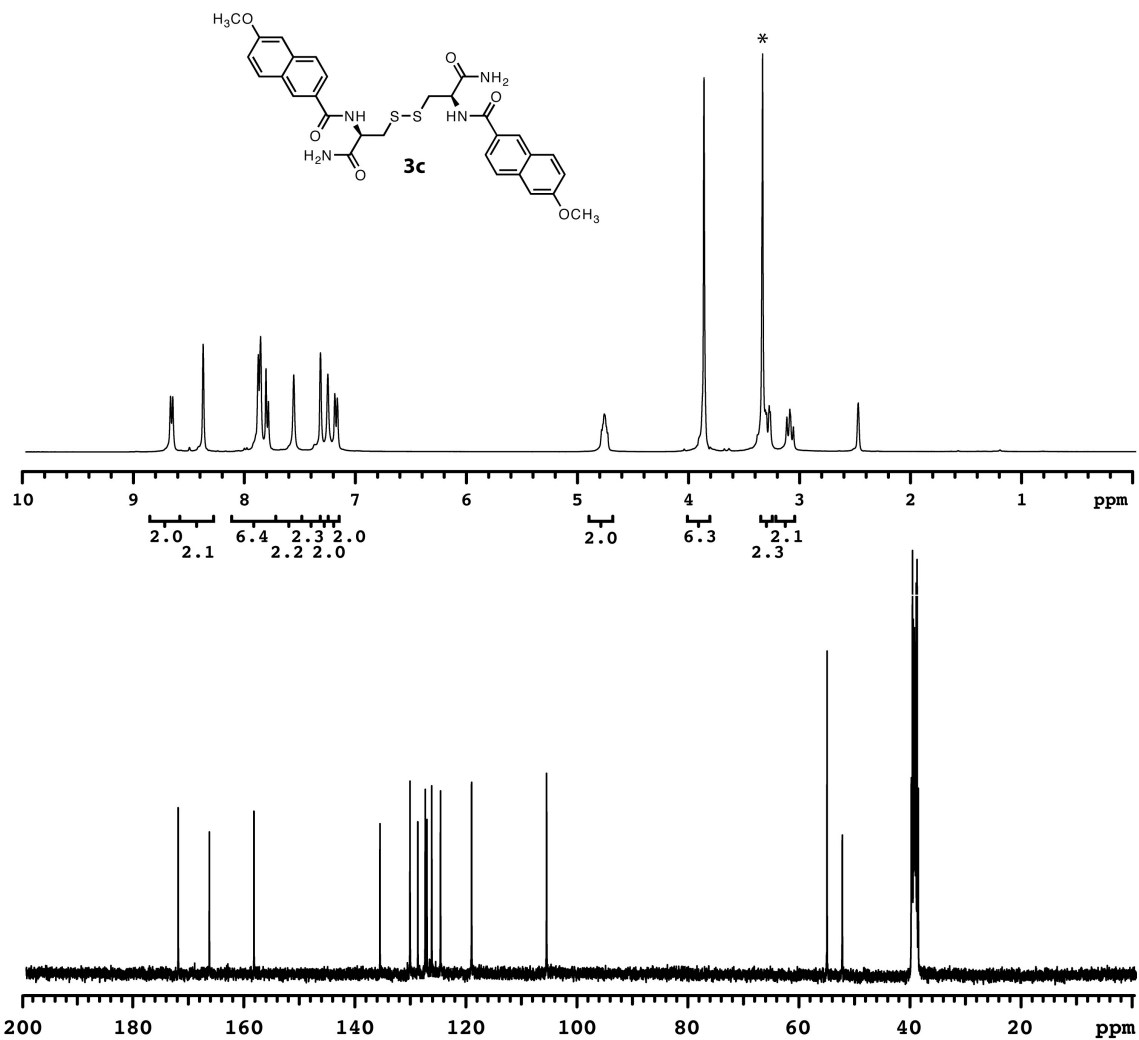


Figure S9. ^1H and ^{13}C NMR spectra of **3c**. ^1H NMR (DMSO- d_6 , 400 MHz): δ 8.69 (d, J = 8.0 Hz, 2H), 8.40 (s, 2H), 7.91-7.81 (m, 6H), 7.59 (s, 2H), 7.35 (s, 2H), 7.28 (s, 2H), 7.21 (d, J = 8.8 Hz, 2H), 4.79 (brm, 2H), 3.89 (s, 6H), 3.36-3.29 (m, 2H), 3.12 (m, 2H). ^{13}C NMR (DMSO- d_6 , 100 MHz): δ 172.20, 166.58, 158.54, 135.85, 130.44, 129.03, 127.69, 127.38, 126.52, 124.94, 119.34, 105.83, 55.31, 52.56, 40.05. *denotes H_2O .

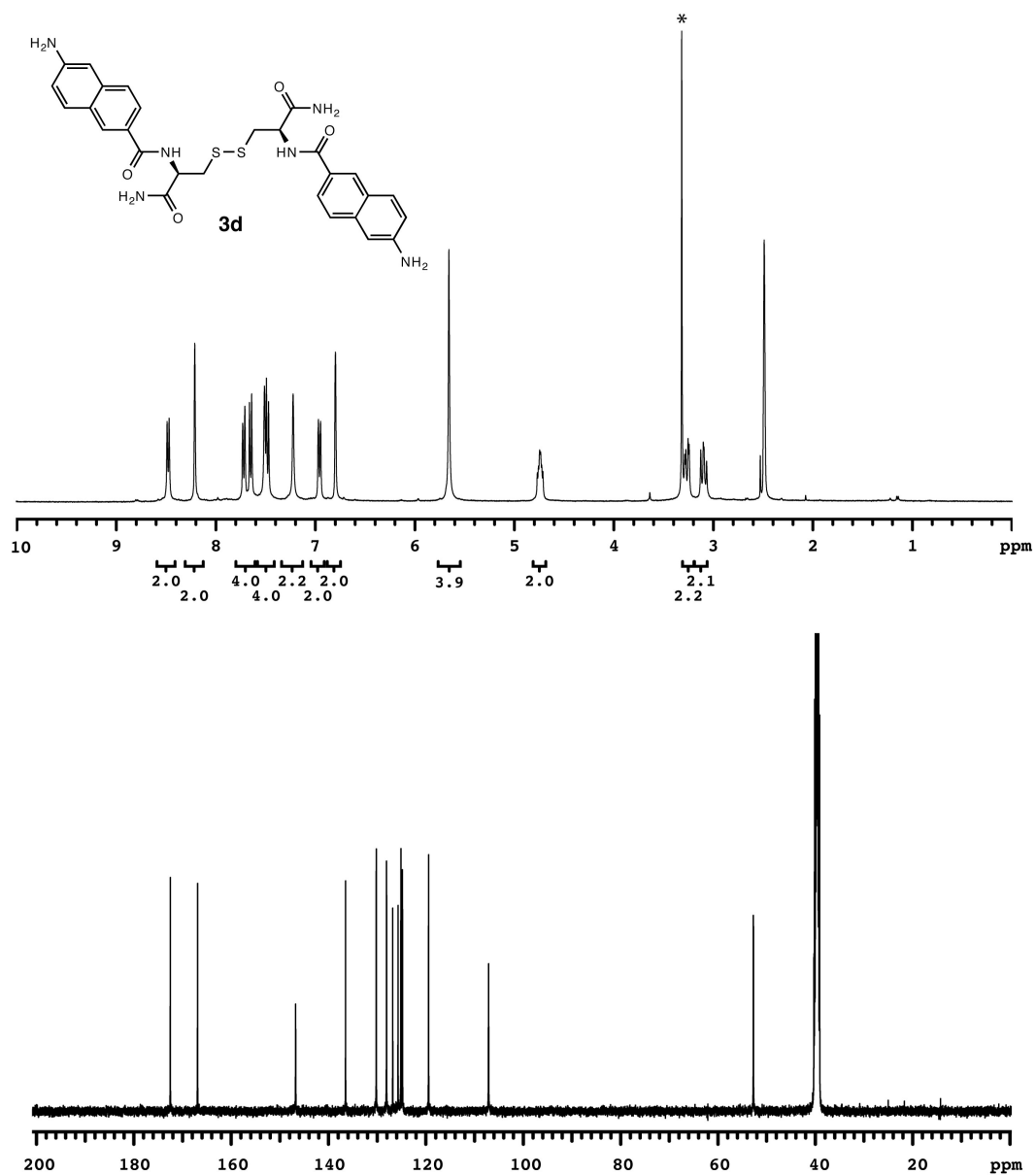


Figure S10. ^1H and ^{13}C NMR spectra of **3d**. ^1H NMR (DMSO- d_6 , 400 MHz): δ 8.49 (d, J = 8.0 Hz, 2H), 8.22 (s, 2H), 7.78-7.60 (m, 4H), 7.57-7.43 (m, 4H), 7.24 (s, 2H), 6.97 (d, J = 12.8 Hz, 2H), 6.81 (s, 2H), 5.67 (s, 4H), 4.75 (brm, 2H), 3.28 (m, 2H), 3.11 (m, 2H). ^{13}C NMR (DMSO- d_6 , 125 MHz): δ 172.82, 167.22, 147.07, 136.81, 130.51, 128.39, 127.13, 126.04, 125.45, 125.12, 119.76, 107.43, 53.03, 40.58. *denotes H_2O .

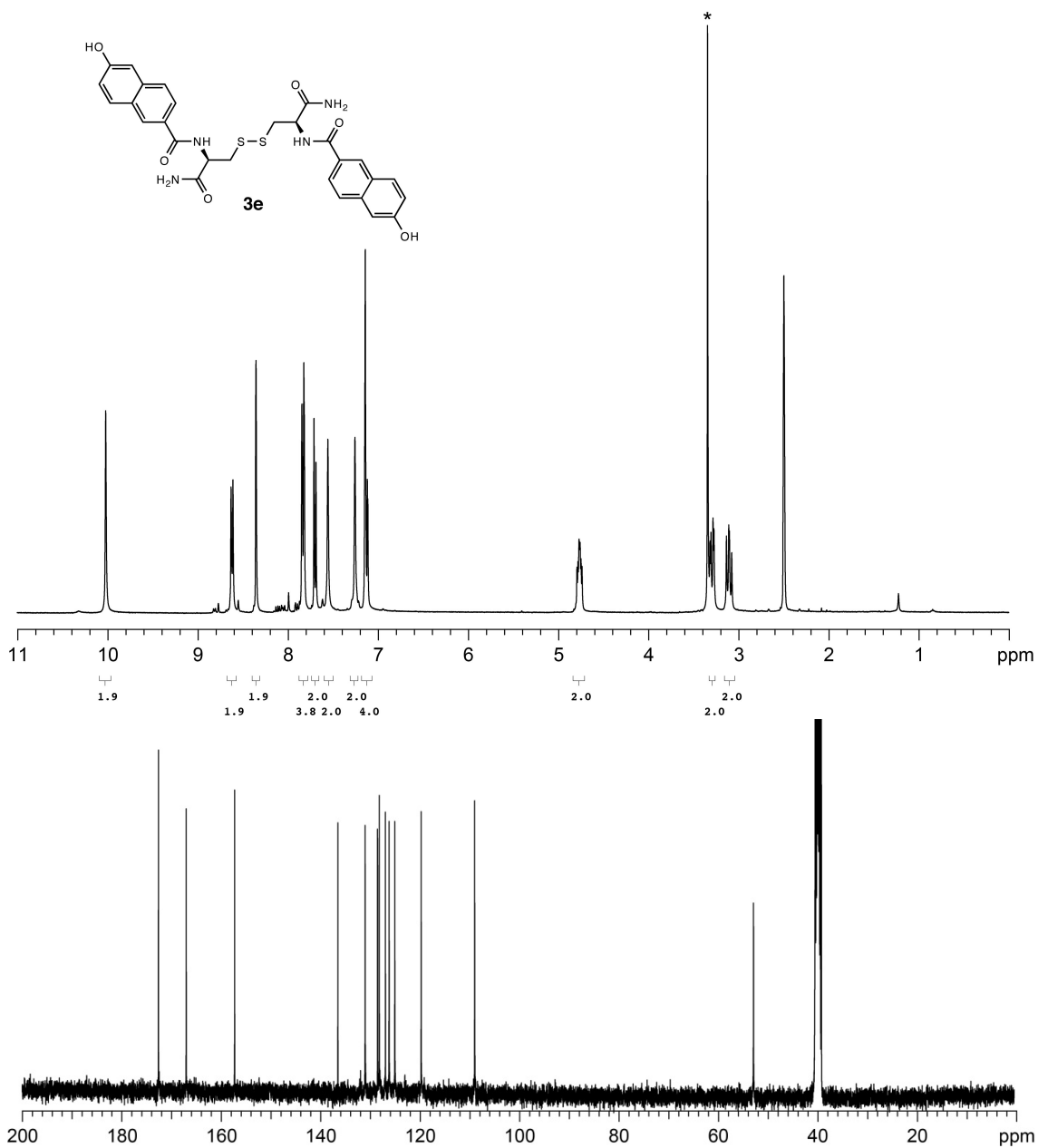


Figure S11. ^1H and ^{13}C NMR spectra of **3e**. ^1H NMR (DMSO- d_6 , 400 MHz): δ 10.03 (s, 2H), 8.62 (d, $J = 8.4$ Hz, 2H), 8.36 (s, 2H), 7.84 (d, $J = 8.8$ Hz, 4H), 7.70 (d, $J = 8.4$ Hz, 2H), 7.56 (s, 2H), 7.26 (s, 2H), 7.15-7.12 (m, 4H), 4.77 (m, 2H), 3.30 (m, 2H), 3.11 (m, 2H). ^{13}C NMR (DMSO- d_6 , 100 MHz): δ 172.64, 167.06, 157.31, 136.53, 131.06, 128.56, 128.23, 126.98, 126.24, 125.08, 119.80, 109.02, 52.95, 40.50. *denotes H_2O .

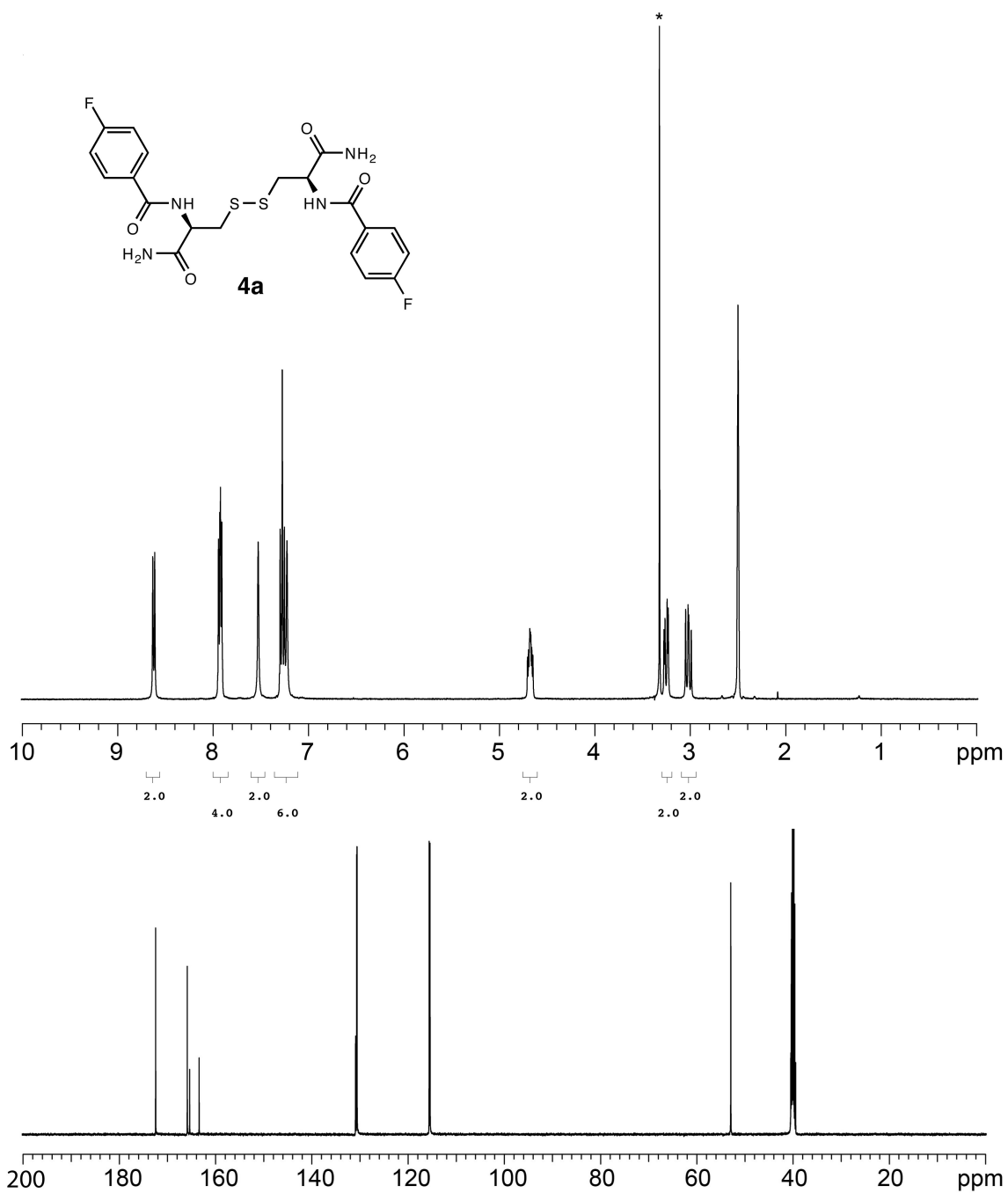


Figure S12. ^1H and ^{13}C NMR spectra of **4a**. ^1H NMR (DMSO- d_6 , 400 MHz): δ 8.62 (d, J = 5.0 Hz, 2H), 7.92 (m, 4H), 7.53 (s, 2H), 7.30-7.23 (m, 6H), 4.68 (m, 2H), 3.26 (m, 2H), 3.02 (m, 2H). ^{13}C NMR (DMSO- d_6 , 125 MHz): δ 172.46, 165.88, 164.40 (d, $J_{\text{F-C}}$ = 247 Hz), 130.91 (d, $J_{\text{F-C}}$ = 2.9 Hz), 130.64 (d, $J_{\text{F-C}}$ = 8.8 Hz), 115.53 (d, $J_{\text{F-C}}$ = 21 Hz), 52.94, 40.35. *denotes H_2O .

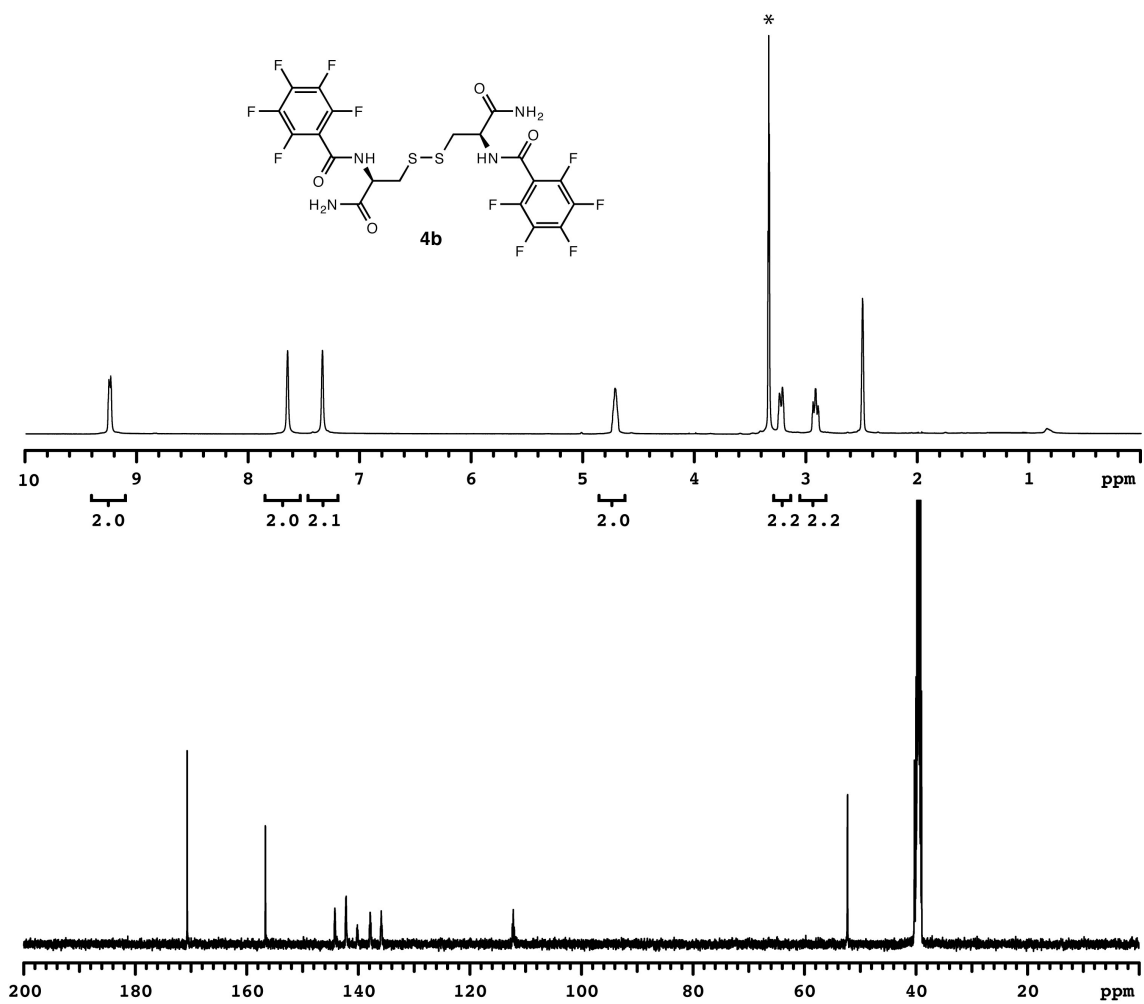


Figure S13. ¹H and ¹³C NMR spectra of **4b**. ¹H NMR (DMSO-*d*₆, 500 MHz): δ 9.25 (m, 2H), 7.65 (s, 2H), 7.34 (m, 2H), 4.72 (m, 2H), 3.23 (m, 2H), 2.92 (m, 2H). ¹³C NMR (DMSO-*d*₆, 125 MHz): δ 170.68, 156.66, 143.19 (d, *J*_{F-C} = 255 Hz), 141.17 (d, *J*_{F-C} = 251 Hz), 136.87 (d, *J*_{F-C} = 243 Hz), 112.22 (m), 52.26, 40.27. *denotes H₂O.

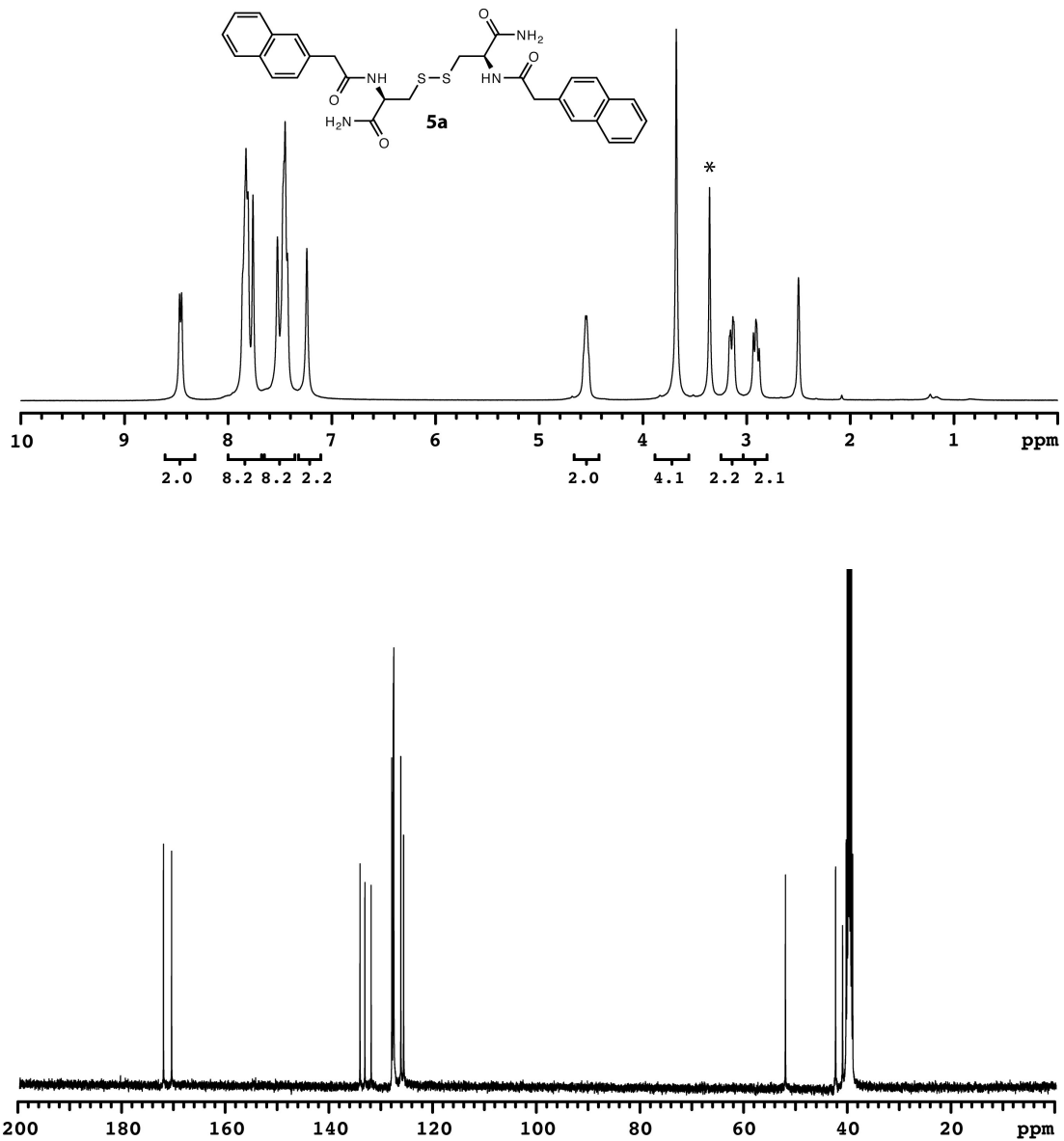


Figure S14. ^1H and ^{13}C NMR spectra of **5a**. ^1H NMR (DMSO- d_6 , 400 MHz): δ 8.45 (d, J = 8.0 Hz, 2H), 7.86-7.76 (m, 8H), 7.51-7.42 (m, 8H), 7.23 (s, 2H), 4.54 (brm, 2H), 3.67 (s, 4H), 3.18-3.10 (m, 2H), 2.95-2.84 (m, 2H). ^{13}C NMR (DMSO- d_6 , 100 MHz): δ 171.82, 170.25, 133.91, 132.96, 131.76, 127.77, 127.52, 127.47, 127.42, 127.38, 126.04, 125.49, 51.84, 42.17, 40.82. *denotes H_2O .

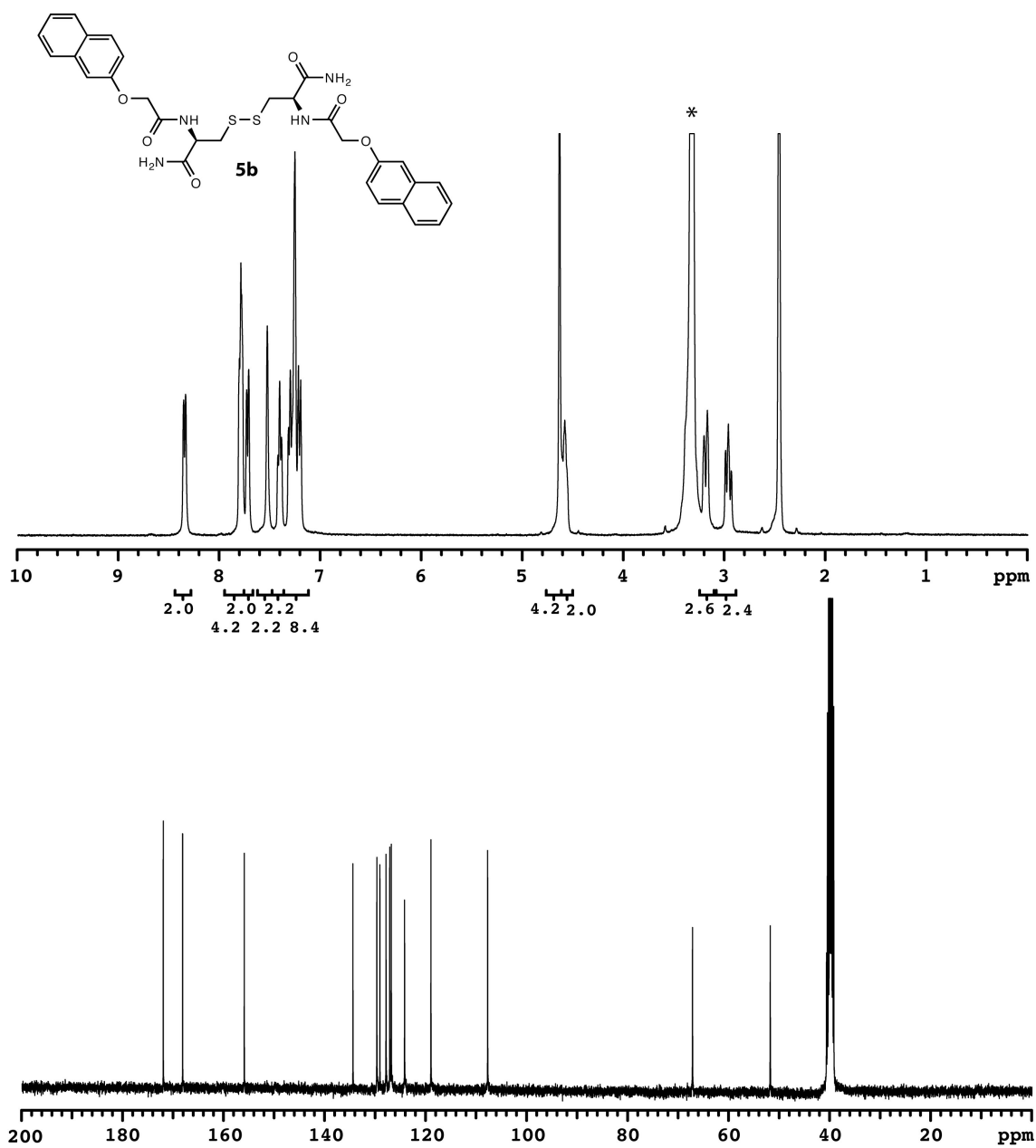


Figure S15. ^1H and ^{13}C NMR spectra of **5b**. ^1H NMR (DMSO- d_6 , 400 MHz): δ 8.38 (d, J = 7.6 Hz, 2H), 7.84-7.82 (m, 4H), 7.76 (d, J = 8.0 Hz, 2H), 7.57 (s, 2H), 7.44 (m, 2H), 7.36-7.24 (m, 8H), 4.67 (s, 4H), 4.62 (s, 2H), 3.23 (m, 2H), 3.00 (m, 2H). ^{13}C NMR (DMSO- d_6 , 100 MHz): δ 171.63, 167.80, 155.59, 134.08, 129.34, 128.74, 127.52, 126.79, 126.47, 123.85, 118.63, 107.40, 66.84, 51.44, 40.31. *denotes H_2O .

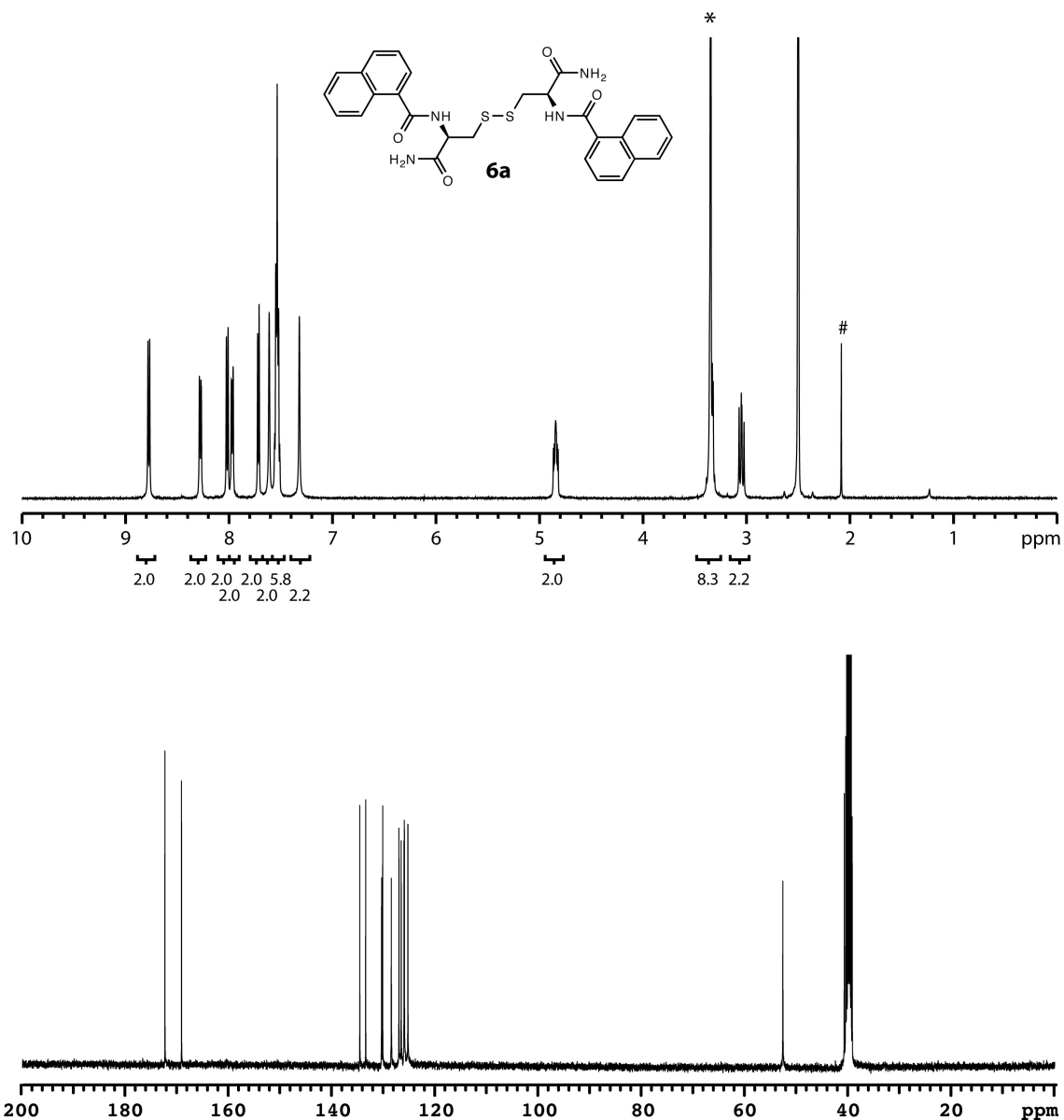


Figure S16. ¹H and ¹³C NMR spectra of **6a**. ¹H NMR (DMSO-*d*₆, 500 MHz): δ 8.78 (d, *J* = 8.5 Hz, 2H), 8.28 (d, *J* = 8.0 Hz, 2H), 8.02 (d, *J* = 8.5 Hz, 2H), 7.97 (m, 2H), 7.72 (d, *J* = 7.0 Hz, 2H), 7.61 (s, 2H), 7.56-7.51 (m, 6H), 7.32 (s, 2H), 4.81 (m, 2H), 3.43-3.28 (m, 2H), 3.01 (m, 2H). ¹³C NMR (DMSO-*d*₆, 100 MHz): δ 172.00, 168.79, 134.26, 133.11, 130.02, 129.82, 128.15, 126.67, 126.23, 125.68, 125.62, 124.94, 52.30, 40.41. *denotes H₂O. #denotes acetone.

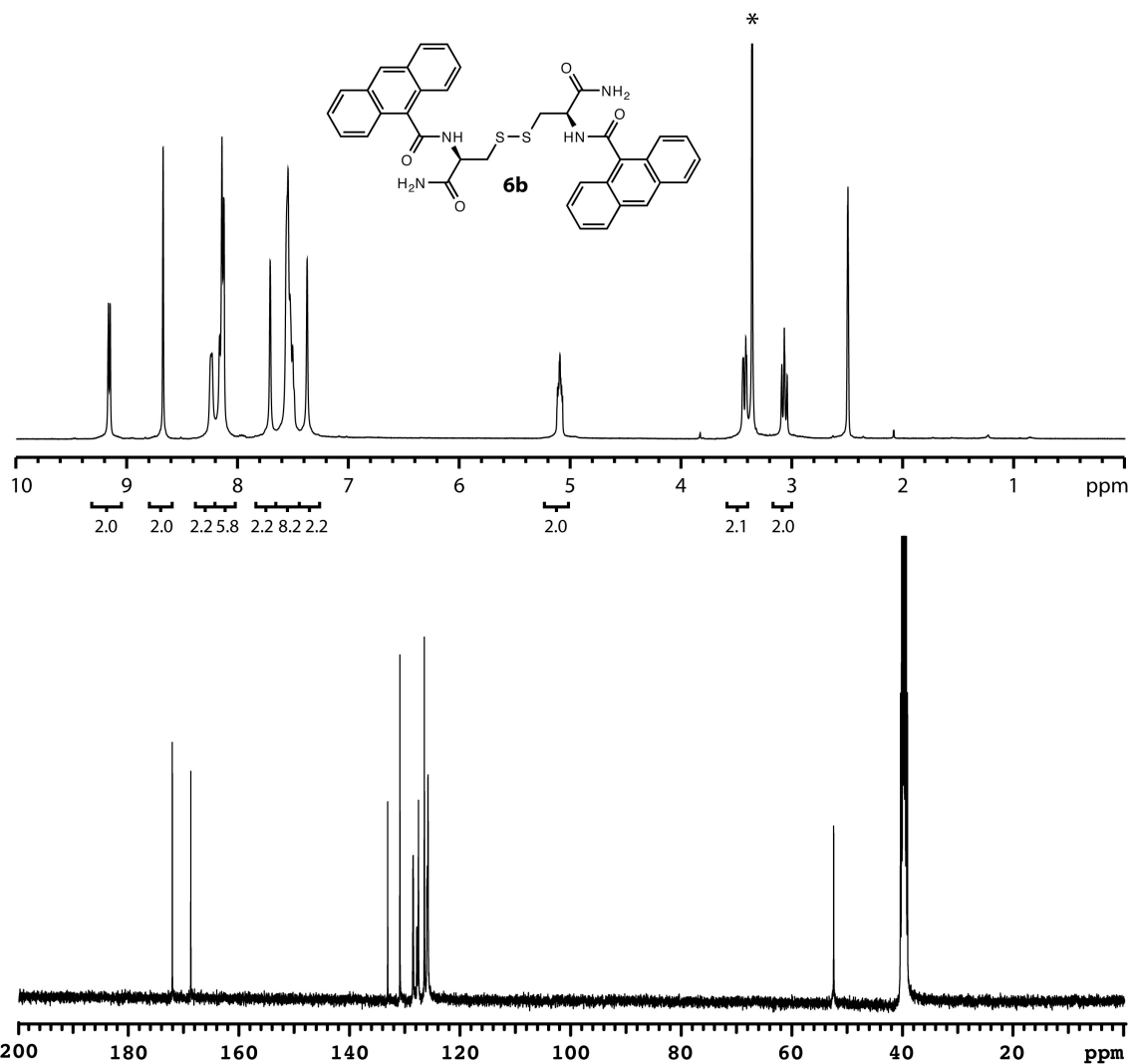


Figure S17. ^1H and ^{13}C NMR spectra of **6b**. ^1H NMR (DMSO- d_6 , 500 MHz): δ 9.16 (d, J = 8.0 Hz, 2H), 8.68 (s, 2H), 8.24 (brm, 2H), 8.17-8.13 (m, 6H), 7.71 (s, 2H), 7.55-7.51 (brm, 8H), 7.38 (s, 2H), 5.10 (m, 2H), 3.43 (m, 2H), 3.07 (m, 2H). ^{13}C NMR (DMSO- d_6 , 100 MHz): δ 171.82, 168.48, 132.87, 130.66, 128.27, 127.62, 127.31, 126.25, 125.70, 125.58, 52.22. *denotes H_2O .

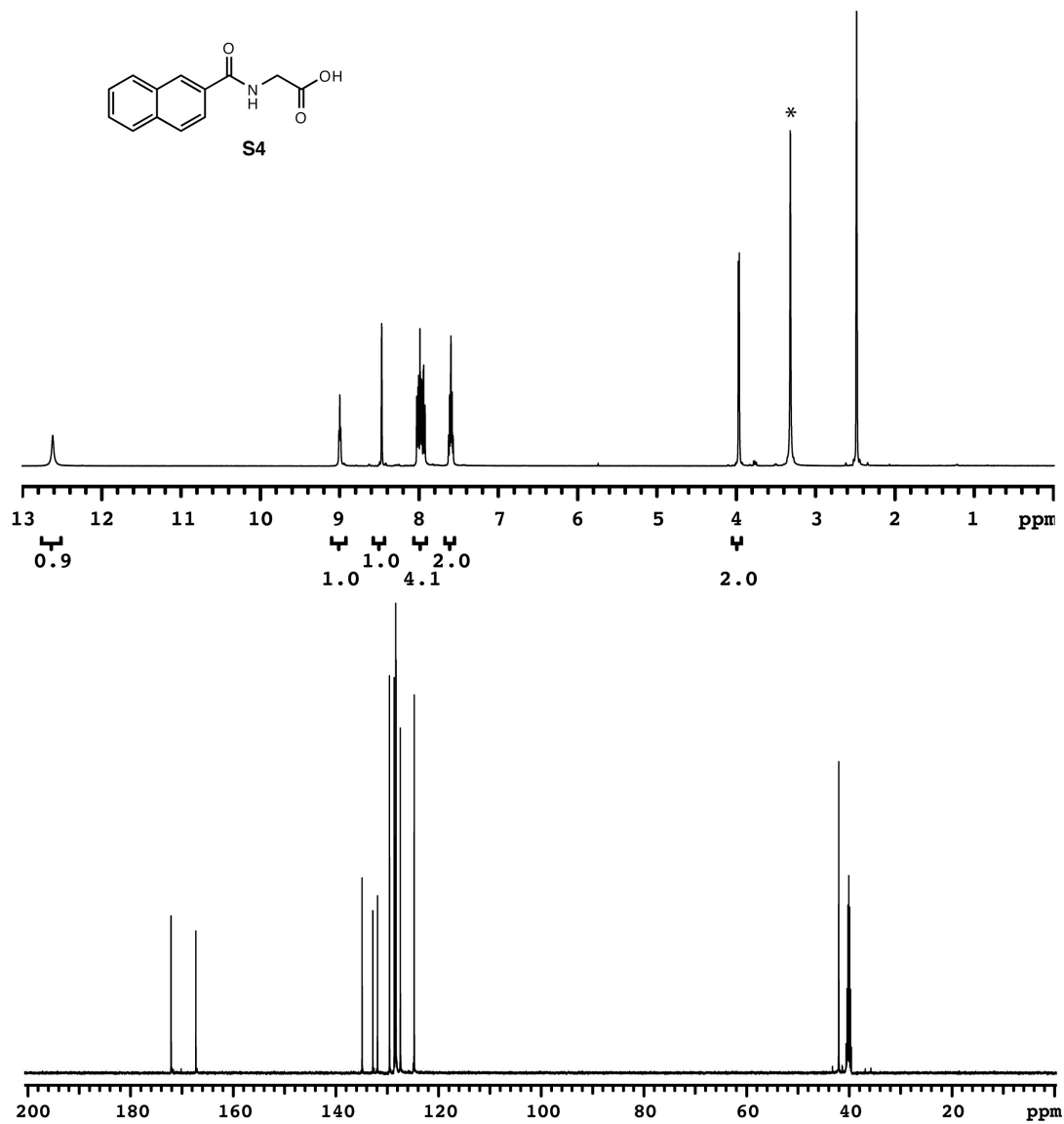


Figure S18. ¹H and ¹³C NMR spectra of **S4**. ¹H NMR (DMSO-*d*₆, 500 MHz): δ 12.63 (s, 1H), 9.02 (t, *J* = 6.0 Hz, 1H), 8.49 (s, 1H), 8.04-7.94 (m, 4H), 7.60 (m, 2H), 3.99 (d, *J* = 5.0 Hz, 2H). ¹³C NMR (DMSO-*d*₆, 125 MHz): δ 171.89, 167.06, 134.68, 132.59, 131.67, 129.34, 128.43, 128.28, 128.13, 128.09, 127.24, 124.54, 41.83. *denotes H₂O.

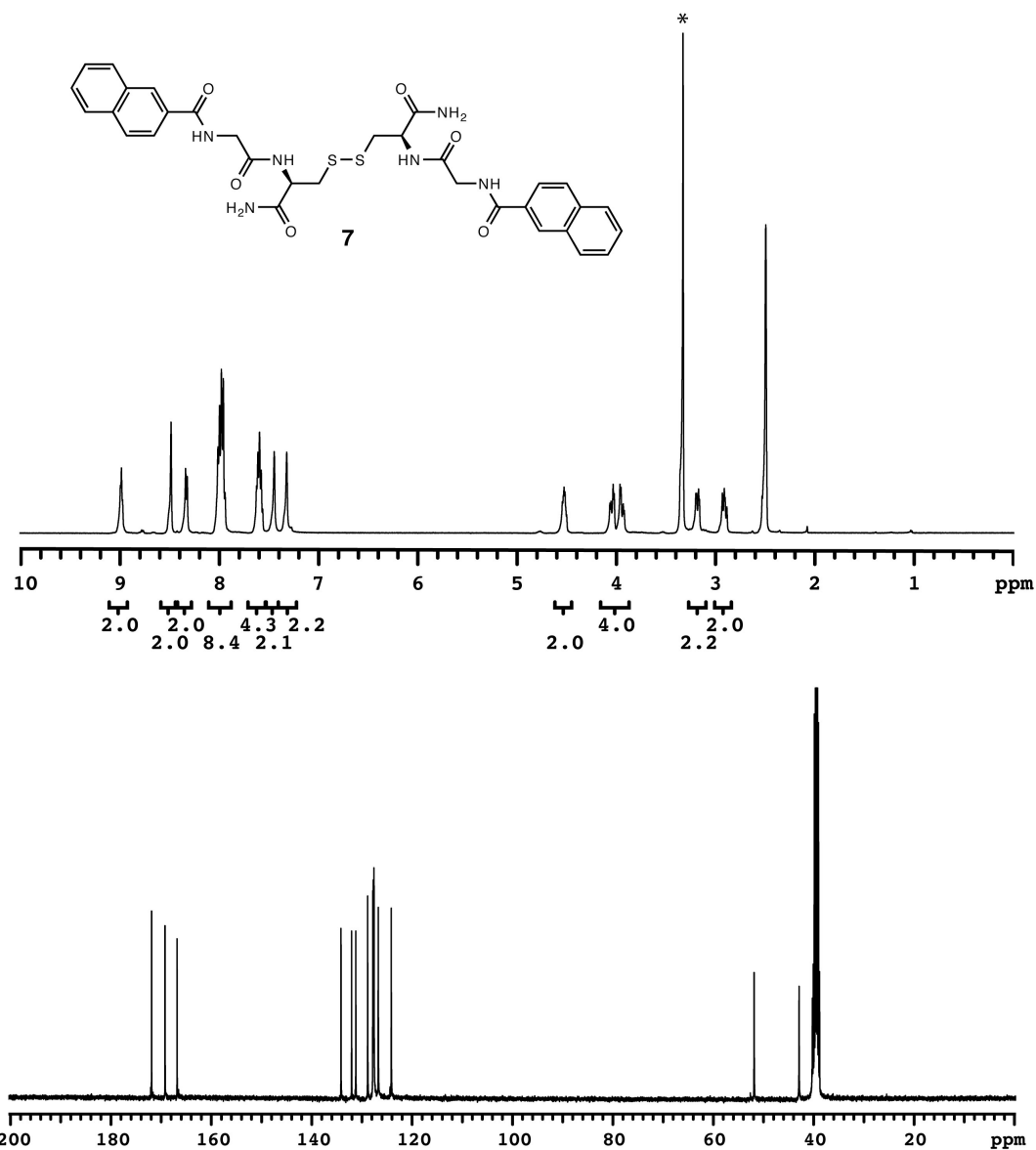


Figure S19. ^1H and ^{13}C NMR spectra of **7**. ^1H NMR (DMSO- d_6 , 500 MHz): δ 8.99 (m, 2H), 8.49 (s, 2H), 8.34 (d, $J = 8.5$ Hz, 2H), 8.02-7.95 (m, 8H), 7.63-7.57 (m, 4H), 7.45 (s, 2H), 7.33 (s, 2H), 4.50 (brm, 2H), 4.12-3.88 (m, 4H), 3.19 (m, 2H), 2.92 (m, 2H). ^{13}C NMR (DMSO- d_6 , 100 MHz): δ 172.37, 169.69, 167.29, 134.64, 132.53, 131.68, 129.32, 128.31, 128.20, 128.13, 128.06, 127.20, 124.62, 52.34, 43.38, 40.73. *denotes H_2O .

IV. In situ Gelation in a 4 mL Vial

A 4 mL vial was charged with **1** (5 mg, 0.018 mmol), TsOH (124 mg, 0.65 mmol, 36 equiv.) and MeOH (0.25 mL). Then TATP (0.25 mL, 45 mM in MeOH) was added to the vial. The mixture was shaken for 1-2 s and allowed to sit at rt. After 30 min, the vial was inverted and a stable gel was formed.

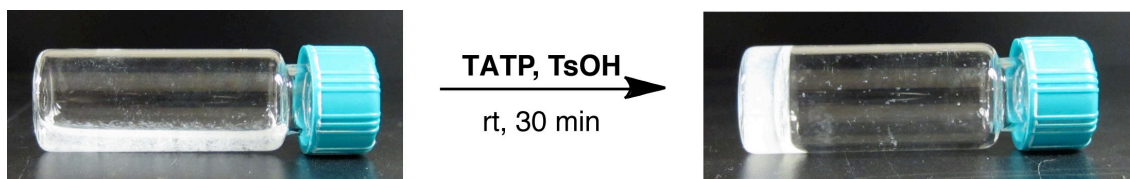
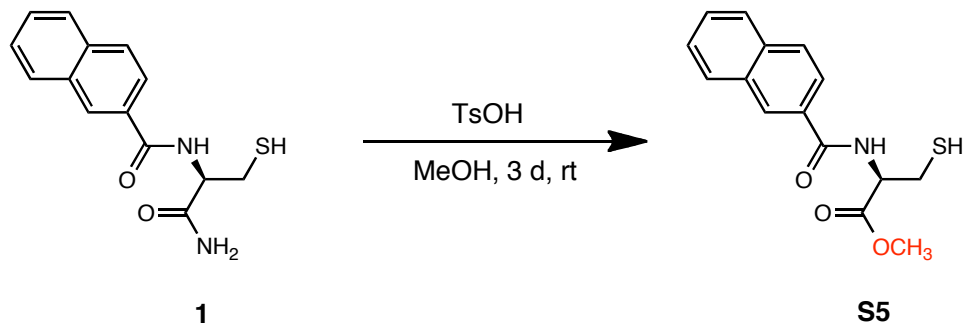


Figure S20. In situ gel formation triggered by oxidation of **1** under TATP/TsOH conditions.

V. Reaction of **1** under Acidic Conditions



A 20 mL vial was charged with **1** (11 mg, 0.040 mmol), TsOH (275 mg, 1.45 mmol) and MeOH (5 mL). After 3 d at rt, the solution was concentrated under reduced pressure. H₂O (20 mL) was added to the oily residue to generate a white suspension. The mixture was extracted with EtOAc (3 x 20 mL). The organic layers were combined, washed with brine (30 mL) and dried over MgSO₄, filtered and concentrated in vacuo to give a crude oil. The crude product was further purified via column chromatography (hexanes/EtOAc 1:1) to give a white solid of **S5** (9 mg, 78%). HRMS (EI): Calcd for C₁₅H₁₅NO₃S, 289.0773 M⁺; Found 289.0771.

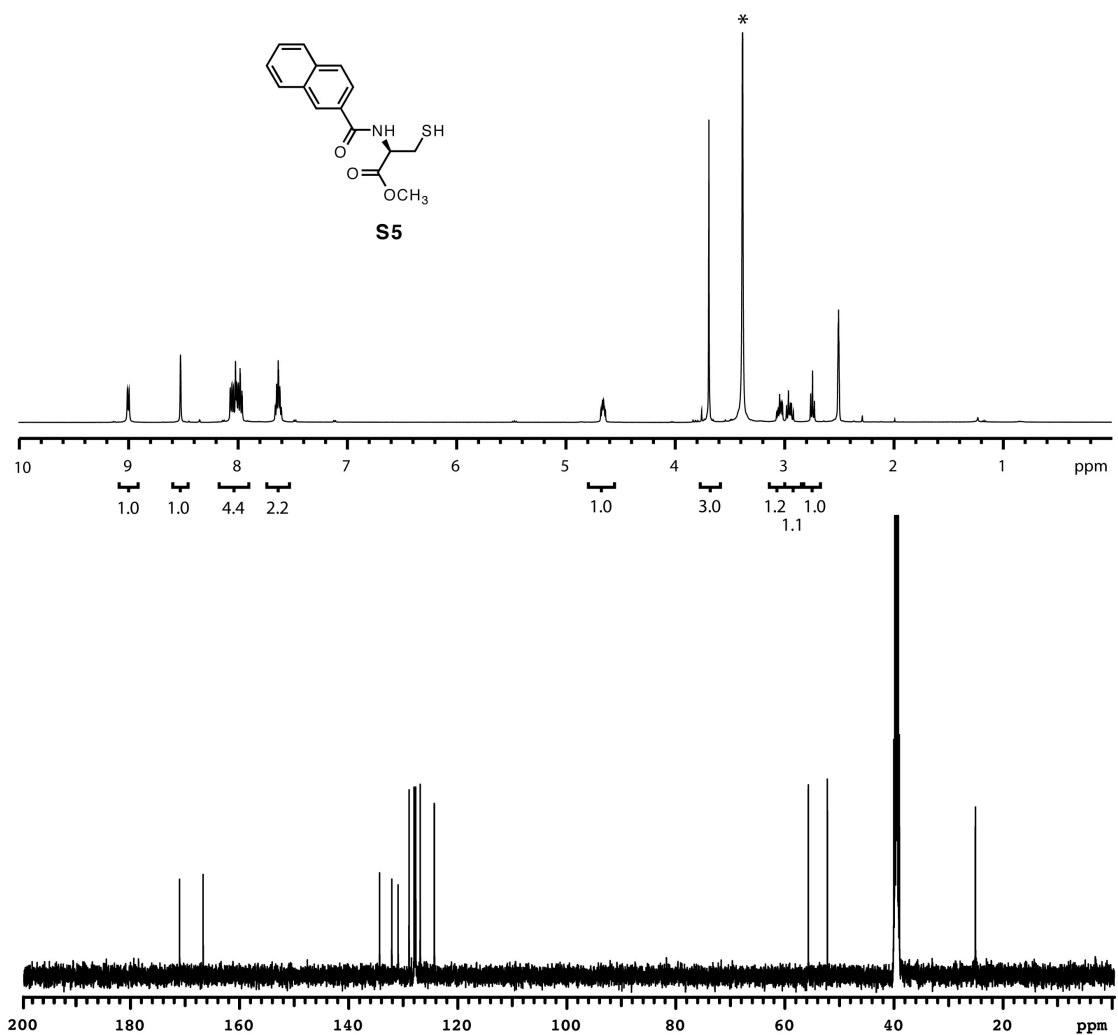


Figure S21. ^1H and ^{13}C NMR spectra of **S5**. ^1H NMR (DMSO- d_6 , 500 MHz): δ 9.01 (d, J = 7.5 Hz, 1H), 8.52 (s, 1H), 8.06-7.95 (m, 4H), 7.63 (m, 2H), 4.65 (m, 1H), 3.69 (s, 3H), 3.04 (m, 1H), 2.94 (m, 1H), 2.74 (t, J = 8.5 Hz, 1H). ^{13}C NMR (DMSO- d_6 , 125 MHz): δ 171.00, 166.68, 134.32, 132.08, 130.92, 128.92, 127.98, 127.90, 127.83, 127.69, 126.87, 124.28, 55.69, 52.20, 25.05. *denotes H_2O .

VI. Gelation Tests of 2-7

Table S1. Cgcs of **2**, **3a**, **4a** and **5b**.

Compound	cgc in MeOH (mM)	cgc in 1/1 (v/v) DMSO/H ₂ O (mM)	Compound	cgc in MeOH (mM)	cgc in 1/1 (v/v) DMSO/H ₂ O (mM)
2	4.6	0.55	5a	--	--
3a	6.5*	3.4	5b	8.5	1.5
3b	--	--	6a	--	--
3c	--	--	6b	--	--
3d	--	--	7a	--	--
3e	--	--	7b	--	--
4a	25	1.9	7c	--	--
4b	--	--			

(--) indicates nongelator under all conditions examined.

* Gelation was not observed for **3a** in MeOH via the general procedure on page S2. A stable gel was formed when a heated solution of **3a** was cooled to rt and then sonicated for ~ 30 s.

VII. Rate Measurements of TATP Degradation under Acidic Conditions

(1) Determining the reaction order in TATP

An NMR tube was charged with TATP (0.50 mL of 0.0491 M in CD₃OD) and 1,4-dioxane (10 μ L) as an internal standard. Then TsOH (50 μ L of 9.0 M in CD₃OD) was added and the NMR tube was capped and inverted twice to ensure complete mixing. ¹H NMR spectra were acquired over time to monitor the change in [TATP] (Figure S22). The same procedure was applied to three other samples where [TATP]₀ = 0.0614 M, 0.0369 M, 0.0246 M.

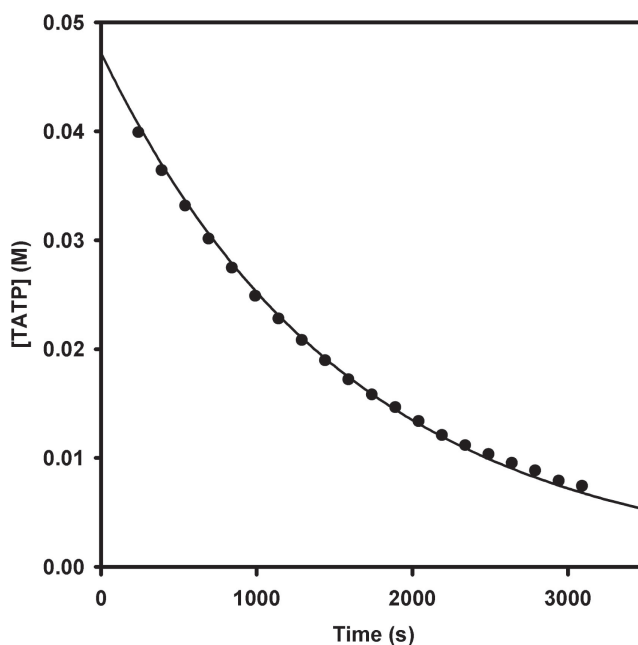


Figure S22. Plot of [TATP] versus time fit to $[TATP] = [TATP]_0 e^{-k_{\text{obs}} t}$, where $[TATP]_0 = 4.72 \pm 0.06 \times 10^{-2}$ and $k_{\text{obs}} = 6.26 \pm 0.08 \times 10^{-4}$.

Table S2. Rate constants of TATP degradation at different [TATP]₀.

Run	[TATP] ₀ (M)	k _{obs} (s ⁻¹)
A	$5.79 \pm 0.07 \times 10^{-2}$	$6.13 \pm 0.01 \times 10^{-4}$
B	$4.72 \pm 0.06 \times 10^{-2}$	$6.26 \pm 0.08 \times 10^{-4}$
C	$3.61 \pm 0.02 \times 10^{-2}$	$6.23 \pm 0.05 \times 10^{-4}$
D	$2.39 \pm 0.01 \times 10^{-2}$	$6.28 \pm 0.06 \times 10^{-4}$

(2) Determining reaction order in TsOH

A NMR tube was charged with TATP (0.50 mL of 0.0450 M in CD₃OD) and 1,4-dioxane (10 μ L) as an internal standard. Then TsOH (40 μ L of 9.0 M in CD₃OD) was added and the NMR tube was capped and inverted twice to ensure complete mixing. ¹H NMR spectra were acquired over time to monitor the change in [TATP]. The same procedure was applied to three other samples where [TsOH]₀ = 0.137 M, 0.350 M, 0.451 M and 0.578 M respectively.

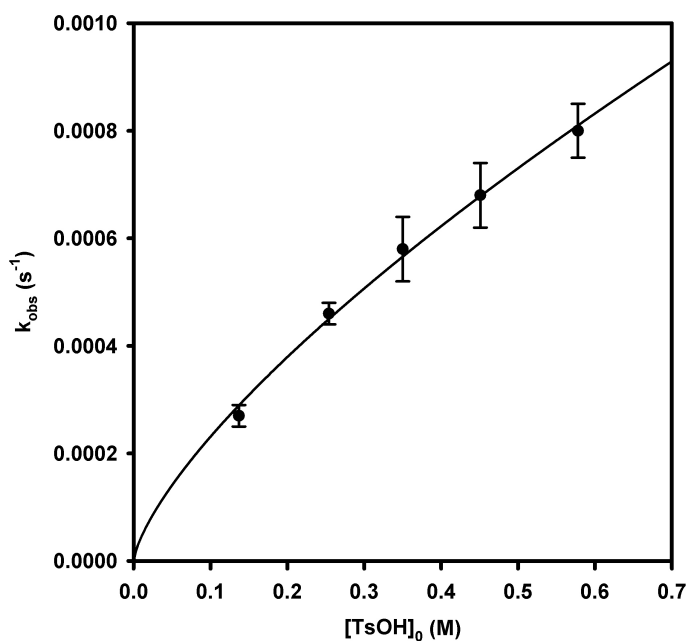


Figure S23. Plot of k_{obs} versus [TsOH] for the TsOH-induced TATP degradation ([TATP] = 0.0450 M), fit to $k_{\text{obs}} = a[\text{TsOH}]^n$, where $a = 1.20 \pm 0.04 \times 10^{-3}$ and $n = 0.72 \pm 0.03$.

Table S3. Data for the plot in Figure S23.

[TsOH] ₀ (M)	k _{obs} (s ⁻¹)
0.578	0.00080 ± 0.00005
0.451	0.00068 ± 0.00007
0.350	0.00058 ± 0.00006
0.254	0.00046 ± 0.00002
0.137	0.00027 ± 0.00002

VIII. Rate Measurement of Oxidation of 1 with H₂O₂

(1) Determining the reaction order in 1

An NMR tube was charged with 1 (0.50 mL of 5.48 mM in CD₃OD) and 1,3-dinitrobenzene (10 μL of 0.30 M in CD₃OD) as an internal standard. Then H₂O₂ (50 μL of 2.0 M in H₂O) was added and the NMR tube was capped and inverted twice to ensure complete mixing. ¹H NMR spectra were acquired over time to monitor the change in [1] (Figure S24). The same procedure was applied to another sample where [1]₀ = 3.32 mM.

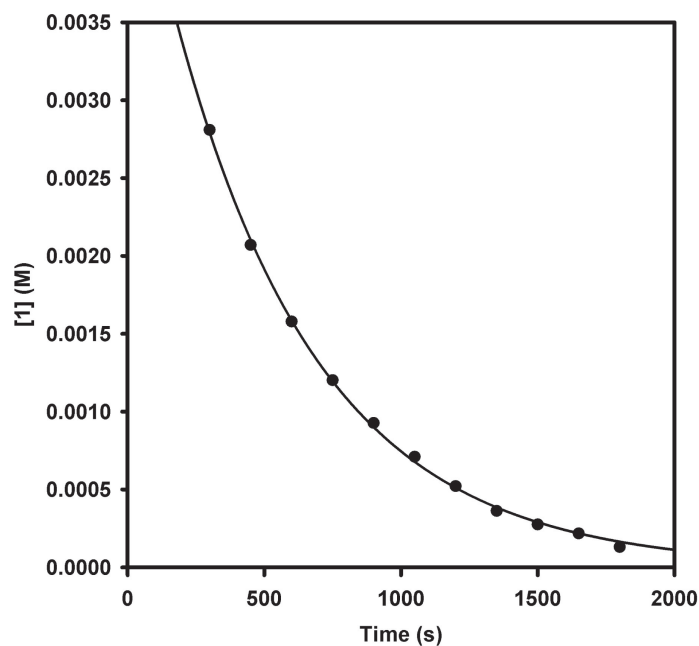


Figure S24. Plot of [1] versus time, fit to $[1] = [1]_0 e^{-k_{\text{obs}} t}$, where $[1]_0 = 4.8 \pm 0.1 \times 10^{-3}$ and $k_{\text{obs}} = 1.7 \pm 0.2 \times 10^{-3}$.

Table S4. Rate constants of thiol oxidation at different [1]₀.

Run	[1] ₀ (M)	k _{obs} (s ⁻¹)
A	$4.8 \pm 0.1 \times 10^{-3}$	$1.7 \pm 0.2 \times 10^{-3}$
B	$3.2 \pm 0.1 \times 10^{-3}$	$1.8 \pm 0.1 \times 10^{-3}$

(2) Determining the reaction order in H₂O₂

An NMR tube was charged with **1** (0.50 mL, 3.65 mM in CD₃OD) and 1,3-dinitrobenzene (10 μL, 0.30 M in CD₃OD) as an internal standard. Then H₂O₂ (50 μL, 2.0 M in H₂O) was added and the NMR tube was capped and inverted twice to ensure complete mixing. ¹H NMR spectra were acquired over time to monitor the change in [**1**]. The same procedure was applied to two other samples where [H₂O₂]₀ = 0.0904 and 0.271 M respectively. The reported data represent an average of 3 runs.

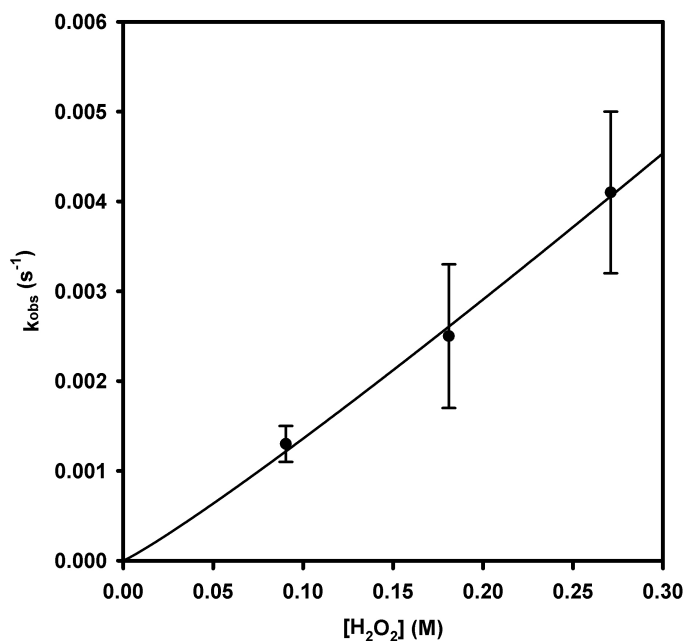
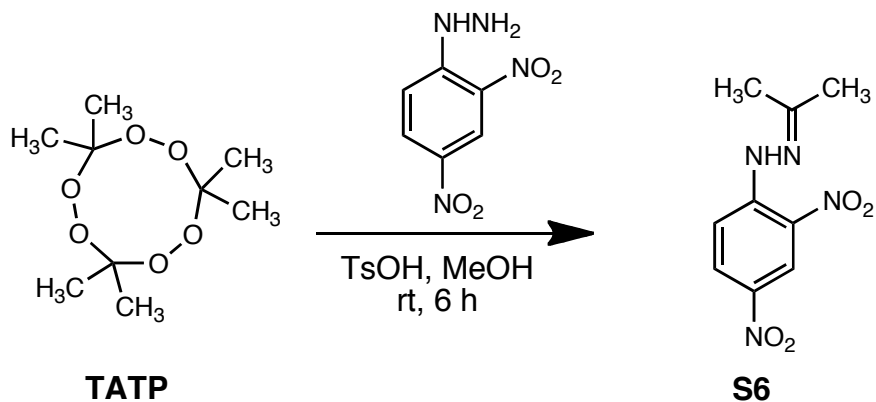


Figure S25. Plot of k_{obs} versus $[\text{H}_2\text{O}_2]$ for the oxidation of **1** by H₂O₂ ($[\text{1}] = 0.00365 \text{ M}$), fit to $k_{\text{obs}} = a[\text{H}_2\text{O}_2]^n$, where $a = 1.7 \pm 0.3 \times 10^{-2}$ and $n = 1.1 \pm 0.1$.

Table S5. Data for the plot in Figure S25.

[H ₂ O ₂] ₀ (M)	k _{obs} (s ⁻¹)
0.0904	1.3 ± 0.4 × 10 ⁻³
0.181	2.5 ± 0.8 × 10 ⁻³
0.271	4.1 ± 0.9 × 10 ⁻³

IX. Characterization of TATP Degradation Products



A 20 mL vial was charged with a stir bar, TATP (30 mg, 0.14 mmol), 2,4-dinitrophenylhydrazine (59 mg, 0.30 mmol), TsOH (959 mg, 5.05 mmol) and MeOH (3 mL). The mixture was stirred at rt. After 6 h, the heterogeneous mixture became homogeneous. The solution was poured into H₂O (~50 mL) and the resulting precipitate was filtered and washed with H₂O (3 x 20 mL) and dried in vacuo to give an orange solid **S6** (27 mg, 28%). Average yield was ~30% based on 2 runs. HRMS (EI): Calcd for C₉H₁₀N₄O₄, 238.0702 M⁺; Found 238.0703.

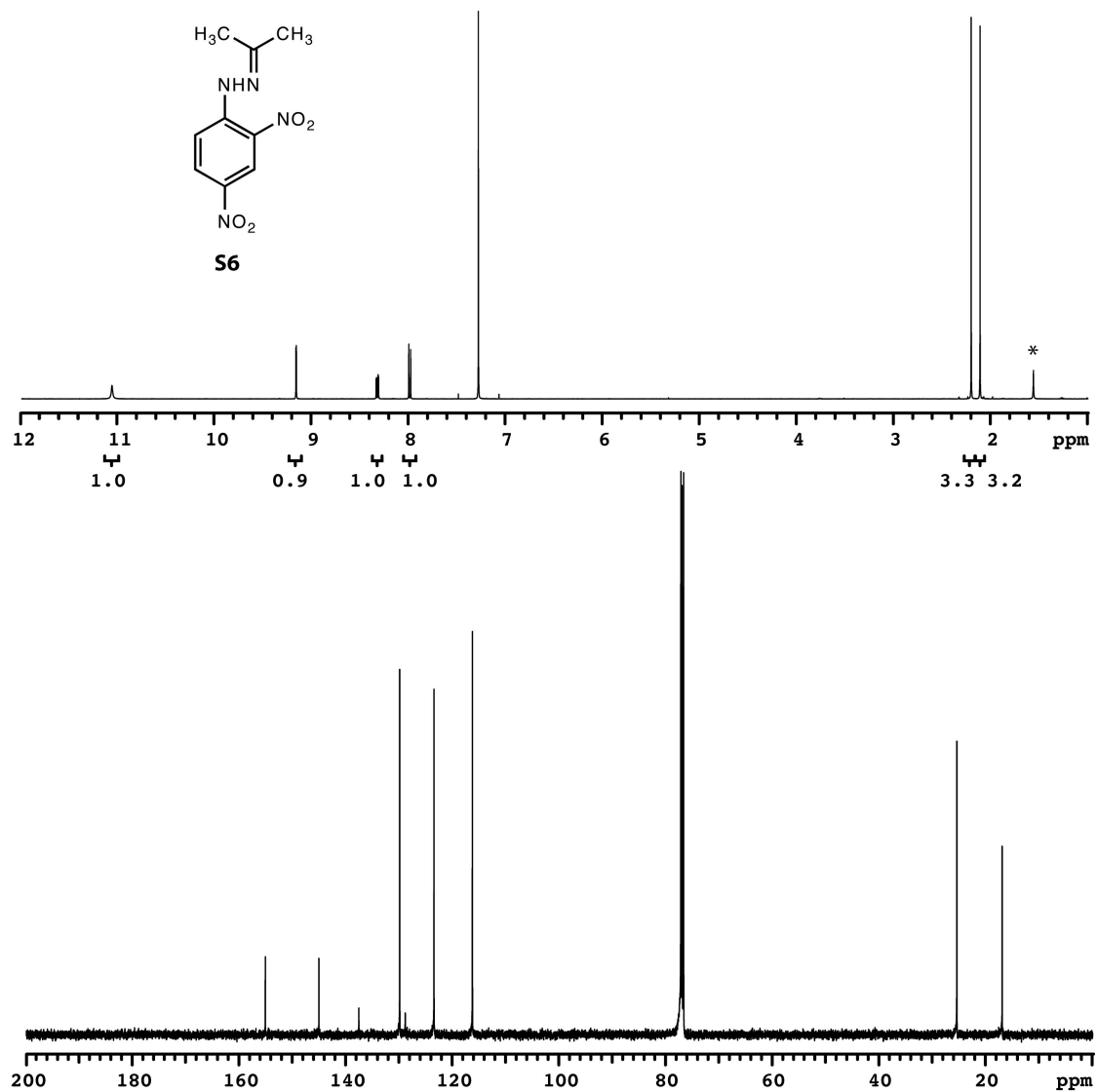
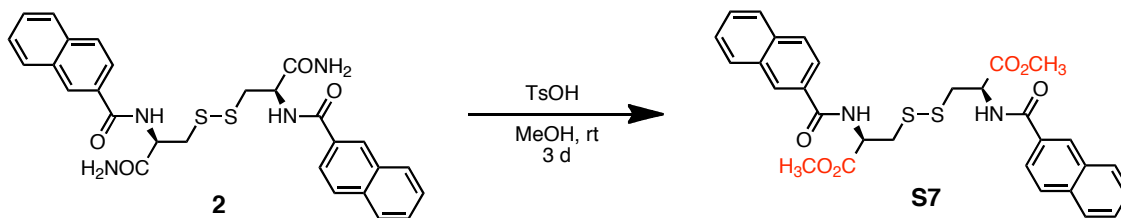


Figure S26. ^1H and ^{13}C NMR spectra of **S6**. ^1H NMR (CDCl_3 , 500 MHz): δ 11.04 (brs, 1H), 9.14 (d, $J = 2.5$ Hz, 1H), 8.30 (m, 1H), 7.97 (d, $J = 9.5$ Hz, 1H), 2.18 (s, 3H), 2.09 (s, 3H). ^{13}C NMR (CDCl_3 , 125 MHz): δ 154.93, 144.88, 137.38, 129.72, 128.69, 123.29, 116.10, 25.24, 16.75. *denotes H_2O .

X. Reaction of **2** under Acidic Conditions



A 20 mL vial was charged with **2** (67 mg, 0.12 mmol), TsOH (839 mg, 4.3 mmol) and MeOH (5 mL). The reaction conversions at 5 h and 24 h were ~ 10% and ~ 33% respectively, measured by ¹H NMR. After 3 d at rt, the undissolved **2** was removed by filtration and dried in vacuo (20 mg, 30%). The filtrate was concentrated under reduced pressure. H₂O (50 mL) was added to the oily residue to generate a white precipitate. The precipitate was isolated by filtration, washed with H₂O (3 x 20 mL) and dried in vacuo to give a white solid **S7** (36 mg, 50%). HRMS (EI): Calcd for **S7** C₃₀H₂₈N₂O₆S₂, 576.1389 M⁺; Found, 576.1389.

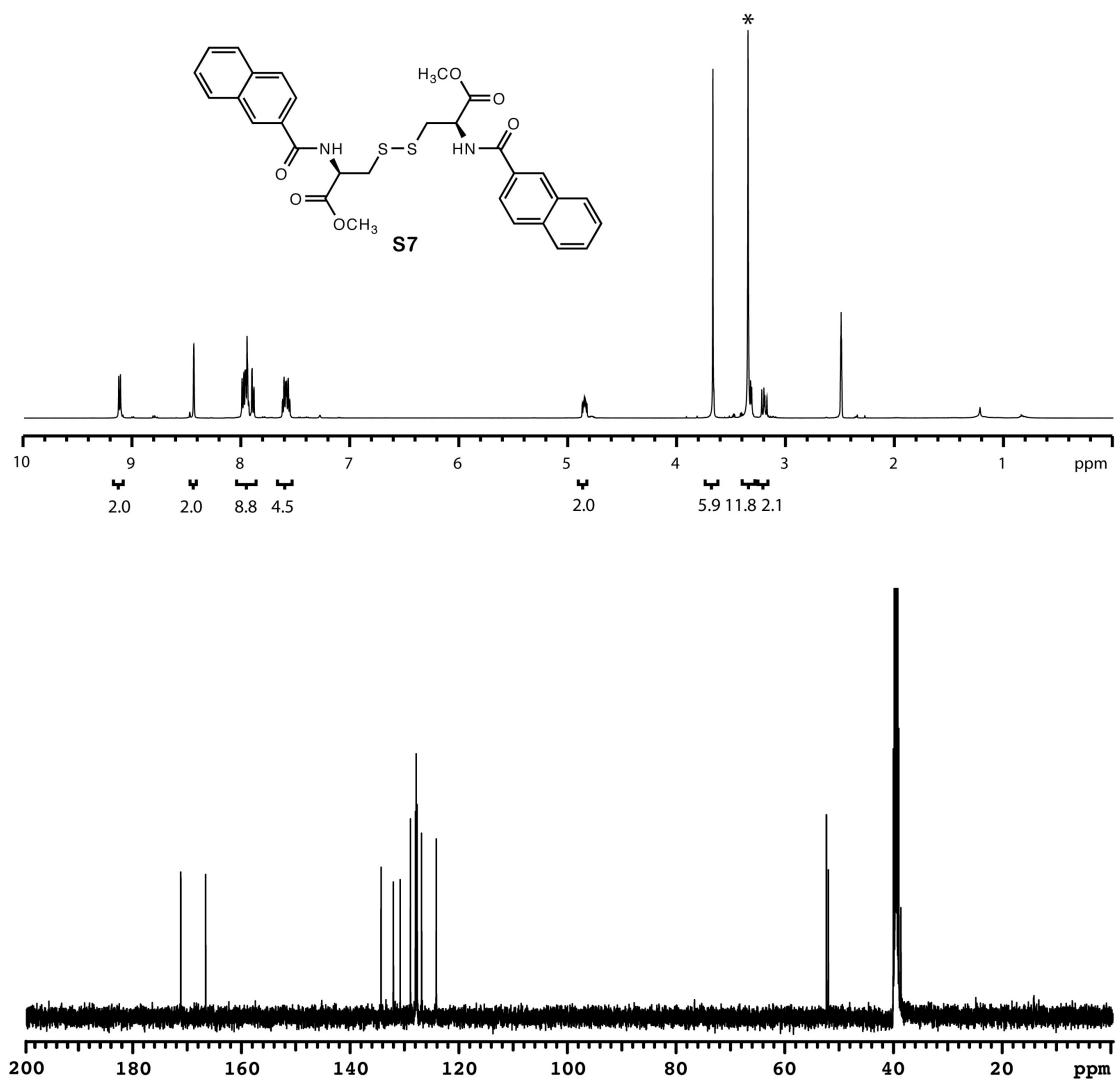


Figure S27. ^1H and ^{13}C NMR spectra of **S7**. ^1H NMR (DMSO- d_6 , 500 MHz): δ 9.13 (d, J = 7.5 Hz, 2H), 8.44 (s, 2H), 8.00-7.89 (m, 8H), 7.63-7.56 (m, 4H), 4.85 (m, 2H), 3.68 (s, 6H), 3.35-3.32 (m, 2H), 3.20 (m, 2H). ^{13}C NMR (DMSO- d_6 , 125 MHz): δ 171.15, 166.57, 134.28, 132.02, 130.77, 128.88, 127.96, 127.81, 127.64, 126.83, 124.12, 52.32, 51.97, 38.62. One aromatic carbon was not resolved. *denotes H_2O .

XI. Optimization of TATP Sensing Conditions in a Small Tube

Note that for experimental convenience, optimizations were performed with a stock solution of TATP. Also all reagents were combined in a 4 mL vial before transferring to the small tube.

(1) Optimization of [TsOH]

A 4 mL vial was charged with **1** (2 mg, 0.007 mmol), TsOH (different amounts as shown below) and MeOH (0.15 mL). Then TATP (0.15 mL of 45 mM in MeOH) was added to the vial. The mixture was shaken for 1-2 s and transferred to a small tube (4.6 mm I.D.). After 10 min, the tube was inverted to examine for gel formation.

Table S6. Optimization of [TsOH]

Equiv. of TsOH	6.1	13.7	25.2	36.7
At 10 min	Solution	Unstable gel	Gel	Gel
Equiv. of TsOH	49.0	61.3	73.5	85.8
At 10 min	Gel	Solution*	Solution*	Solution*

* The solution is attributed to the background reaction of **2** with TsOH in MeOH to generate **S7**.

(2) Optimization of [1]

A 4 mL vial was charged with MeOH (0.15 mL), **1** (different amounts as shown below) and TsOH (36 equiv. to **1**). Then TATP (0.15 mL, 45 mM in MeOH) was added to the vial. The mixture was shaken for 1-2 s and transferred to a small tube (4.6 mm I.D.). The sample was inverted to examine for gelation every 5 min.

Table S7. Optimization of [1]

[1] (mM)	12 mM	24 mM	36 mM
Observed Gelation	> 60 min	15 min	10 min

(3) Detection limit

A 4 mL vial was charged with **1** (3 mg, 0.011 mmol), TsOH (77 mg, 0.41 mmol, 37 equiv.) and MeOH (0.15 mL). Then TATP (0.15 mL, different concentrations in MeOH)

was added to the vial to generate the final [TATP] as shown below. The mixture was shaken for 1-2 s and transferred to a small tube (4.6 mm I.D.). The sample was inverted to examine for gelation every 5 min.

Table S8. Gelation time at various final [TATP]

[TATP] (mM)	4.5 mM	14 mM	32 mM	45 mM	180 mM
Observed Gelation	~ 30 min	10-15 min	5-10 min	5-10 min	~ 2 min

XII. TATP Detection at Different Sample Volumes

A 4 mL vial was charged with **1** (4 mg, 14 mmol), TsOH (99 mg, 0.52 mol) and MeOH (0.20 mL). Then TATP (0.20 mL of 45 mM in MeOH) was added to the vial. The mixture was shaken for 1-2 s and allowed to sit at rt. After 30 min, the vial was inverted and a stable gel was formed (Figure S28, left).

The procedure described above was repeated with all reagents increased by a factor of 10. A stable gel was observed after 30 min (Figure S28, right).

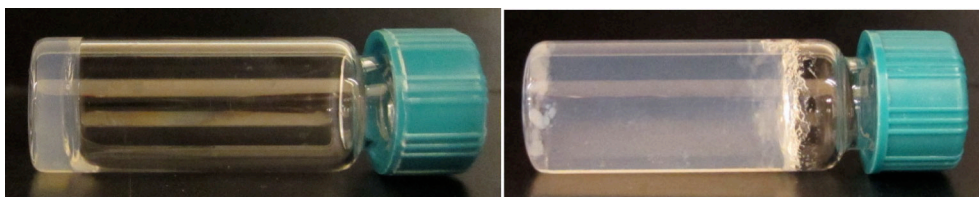


Figure S28. (left) A 0.4 mL gel of **1** triggered by 2 mg TATP and (right) a 4 mL gel of **1** triggered by 20 mg TATP.

XIII. Cgc Measurements in an NMR Tube

An NMR tube was charged with a suspension of **2** (0.30 mL, 4.6 mM in MeOH), heated to the boiling point of MeOH and then allowed to cool to room temperature. The tube was inverted to examine whether a stable gel formed. If a stable gel formed, 0.10 mL of MeOH was added and the procedure was repeated until an unstable gel was observed. The last concentration of a stable gel was recorded as the cgc.

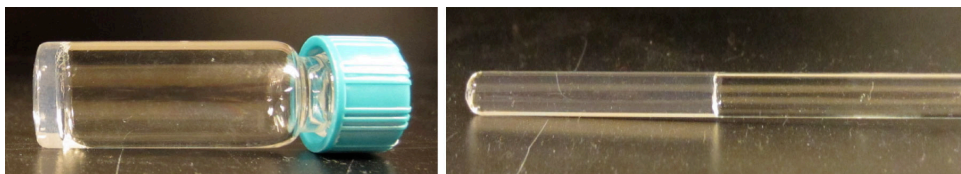


Figure S29. Gels of **2** at cgc (left) in a 4 mL vial and (right) in an NMR tube, both at a volume of 0.50 mL.

Table S9. Cgcs of **2** in a 4 mL vial and an NMR tube.

cgc in a 4 mL vial (mM)	cgc in an NMR tube (mM)
4.6	2.0

XIV. In situ Gelation in a Small Tube

A 4 mL vial was charged with **1** (3 mg, 0.011 mmol), TsOH (75 mg, 0.39 mmol, 36 equiv.) and MeOH (0.15 mL). Then TATP (0.15 mL, 45 mM in MeOH) was added to the vial. The mixture was shaken for 1-2 s and transferred to a small tube. After 8 min, the sample was inverted and a stable gel was observed.

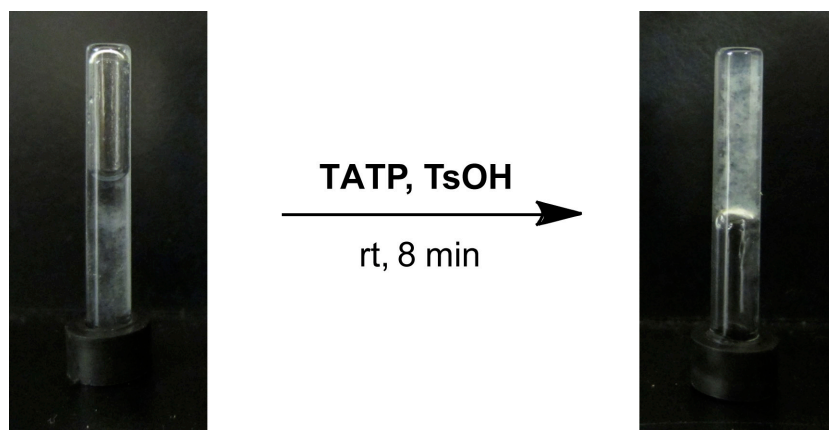
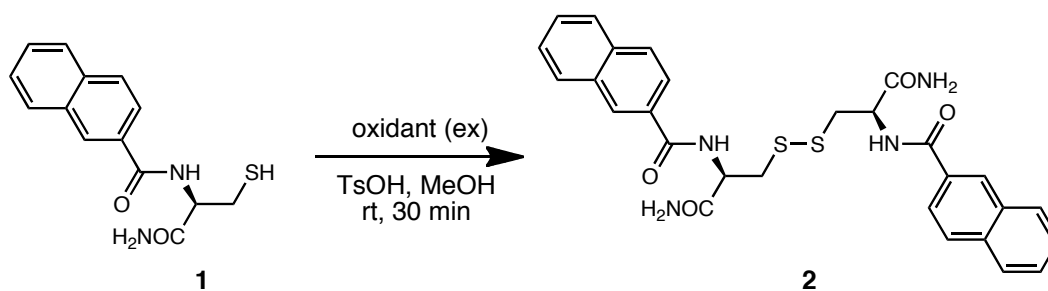


Figure S30. In situ gel formation triggered by the oxidation of **1** under TATP/TsOH conditions in a small tube.

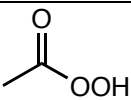
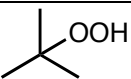
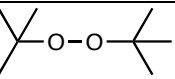
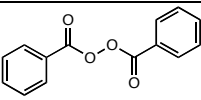
XV. Sensor Selectivity



A 4 mL vial was charged with **1** (2 mg, 0.007 mmol) and MeOH (1 mL). An excess amount of oxidant (10 equiv.) was added. Note that organic oxidants (e.g., NaOCl, peroxides) were added without dilution. Inorganic oxidants were added as aqueous solutions (0.1 mL, ~ 0.7 M in H₂O). After 30 min, the vial was inverted to check for gelation.

For screenings performed under acidic conditions, the same procedures were repeated except that TsOH (13 mg, 0.068 mmol) was added prior to the addition of oxidants.

Table S10. In situ gel screenings of **1** towards various oxidants.

[TsOH] (M)	NaOCl				
0	Gel	Gel	Gel	Solution	Solution
0.068	Gel	Gel	Gel	Gel	Solution
	K₂CrO₄	K₂Cr₂O₄	KClO₃	KI	NaNO₂
0	Gel	Gel	Solution	Solution	Solution
0.068	Gel	Gel	Solution	Solution	Solution

XVI. References:

1. (a) Lin, Y. A.; Chalker, J. M.; Floyd, N.; Bernardes, G. J. L.; Davis, B. G. *J. Am. Chem. Soc.* **2008**, *130*, 9642-9643. (b) Yanagisawa, H.; Ishihara, S.; Ando, A.; Kanazaki, T.; Miyamoto, S.; Koike, H.; Iijima, Y.; Oizumi, K.; Matsushita, Y.; Hata, T. *J. Med. Chem.* **1987**, *30*, 1984-1991. (c) Han, G.; Tamaki, M.; Hruby, V. J. *J. Peptide Res.* **2001**, *58*, 338-341.

2. (a) Matyas, R.; Pachman, J. *Propellants Explos. Pyrotech.* **2010**, *35*, 31-37. (b) Bellamy, A. J. *J. Forensic Sci.* **1999**, *44*, 603-608.